Transactions of the ASME®

Journal of Engineering for Gas Turbines and Power

Published Quarterly by The American Society of Mechanical Engineers

VOLUME 122 • NUMBER 4 • OCTOBER 2000

Technical Editor
H. D. NELSON (2001)

Associate Technical Editors
Advanced Energy Systems
M. J. MORAN (1999)
G. REISTAD (2002)
Fuels and Combustion Technologies
S. GOLLAHALLI (2001)
Gas Turbine (Review Chair)
D. WISLER (2001)
Gas Turbine
D. COOKE (1999)
M. MIGNOLET (2002)
Internal Combustion Engines
D. ASSANIS (2002)
Nuclear
R. DUFFEY (2001)
Power
D. LOU (2002)

BOARD ON COMMUNICATIONS
Chairman and Vice-President
R. K. SHAH

OFFICERS OF THE ASME
President, **JOHN R. PARKER**

Executive Director, **D. L. BELDEN**

Treasurer, **J. A. MASON**

PUBLISHING STAFF
Managing Director, Engineering
CHARLES W. BEARDSLEY

Director, Technical Publishing
PHILIP DI VIETRO

Managing Editor, Technical Publishing
CYNTHIA B. CLARK

Managing Editor, Transactions
CORNELIA MONAHAN

Production Coordinator
COLIN MCATEER

Production Assistant
MARISOL ANDINO

Transactions of the ASME, Journal of Engineering for Gas Turbines and Power (ISSN 0742-4795) is published quarterly (Jan., April, July, Oct.) by The American Society of Mechanical Engineers, Three Park Avenue, New York, NY 10016. Periodicals postage paid at New York, NY and additional mailing offices. POSTMASTER: Send address changes to Transactions of the ASME, Journal of Engineering for Gas Turbines and Power, c/o THE AMERICAN SOCIETY OF MECHANICAL ENGINEERS, 22 Law Drive, Box 2300, Fairfield, NJ 07007-2300.

CHANGES OF ADDRESS must be received at Society headquarters seven weeks before they are to be effective. Please send old label and new address.

STATEMENT from By-Laws. The Society shall not be responsible for statements or opinions advanced in papers or ... printed in its publications (B7.1, par. 3).

COPYRIGHT © 2000 by the American Society of Mechanical Engineers. For authorization to photocopy material for internal or personal use under circumstances not falling within the fair use provisions of the Copyright Act, contact the Copyright Clearance Center (CCC), 222 Rosewood Drive, Danvers, MA 01923, Tel: 978-750-8400, www.copyright.com.

INDEXED by Applied Mechanics Reviews and Engineering Information, Inc. Canadian Goods & Services Tax Registration #126148048

TECHNICAL PAPERS–SPECIAL ICE SECTION

Engine Design

Intake and Exhaust System Dynamics

In-Cylinder Processes

Alternative Fuels Combustion and Emissions

(Contents continued on inside back cover)

This journal is printed on acid-free paper, which exceeds the ANSI Z39.48-1992 specification for permanence of paper and library materials. ∞™
♲ 85% recycled content, including 10% post-consumer fibers.

Downloaded 03 Jun 2010 to 171.66.16.159. Redistribution subject to ASME license or copyright; see http://www.asme.org/terms/Terms_Use.cfm

(**Contents continued**)

Journal of Engineering for Gas Turbines and Power **OCTOBER 2000**

Volume 122, Number 4

TECHNICAL PAPERS

Gas Turbines: Ceramics

Gas Turbines: Coal, Biomass, and Alternative Fuels

Gas Turbines: Combustion and Fuel

Gas Turbines: Controls and Diagnostics

Gas Turbines: Cycle Innovations

Gas Turbines: Heat Transfer

Gas Turbines: Marine

Gas Turbines: Structures and Dynamics

Gas Turbines: Vehicular and Small Turbomachines

Journal of Engineering for Gas Turbines and Power

Preface: Special ICE Section

In recent years, the ever-increasing socioeconomic pressures for developing cleaner and more efficient means for converting chemical fuel energy into useful mechanical work have resulted in a dramatic growth in internal combustion engine research and development activities. As a natural outcome of this vigorous activity, a large number of technical papers dealing with various mechanical aspects of engine design, as well as with the basic thermo-fluid engine processes have been presented at the Fall and Spring Technical Conferences organized by the Internal Combustion Engine (ICE) Division of ASME. In 1999, the ICE Division has renewed its commitment to identify quality papers of long-term reference value for the journal. Therefore, a major section of this issue of the ASME JOURNAL FOR GAS TURBINES AND POWER is devoted to a selection of the highest quality ICE Papers presented at those meetings, and other papers of long-term reference value which were submitted directly to the journal. The contributions of the ICE Division Associates, the support of the ICE Executive Committee, and the ASME Editorial Staff, and above all the contributions of the authors and referees are gratefully acknowledged.

The papers that have been included in the special ICE section of this volume have been arranged in four topical areas: engine design, intake and exhaust system dynamics, in-cylinder processes, and alternative fuels combustion and emissions. As a special note, the lead paper for the ICE section, authored by Dan E. Richardson and entitled ‘‘Review of Power Cylinder Friction for Diesel Engines,’’ was presented at the 1999 Spring Technical Conference, Columbus, Indiana. This paper was selected as the most valuable technical paper presented at an ASME-ICE Division Meeting during 1999.

Dennis N. Assanis
Associate Editor
ICE Division

Review of Power Cylinder Friction for Diesel Engines

D. E. Richardson
Cylinder Systems Development,
Cummins Engine Company,
Columbus, IN 47201

Power cylinder friction is a major contributor to overall engine friction. For engines of the future to become more fuel efficient it will be necessary to reduce power cylinder friction. To be able to reduce the friction it is important to fully understand it. This paper is a review of power cylinder friction with a specific emphasis on diesel engines. This paper first describes how significant the contribution of power cylinder friction is compared to all the other losses of the engine. It compares the mechanical friction of the engine to the total energy produced by the engine. Then a comparison is made of the power cylinder friction to overall mechanical friction. A comparison of different methods of friction measurement is be made. The advantages and disadvantages are given for each method. There is also a comparison of motoring versus firing friction tests. An equation is given to estimate the effect of bore and stroke on power cylinder friction. Other equations for estimating power cylinder friction are also shown. More sophisticated cylinder kit models are reviewed. Finally a review is made of methods for reducing friction. These are based on a broad review from various companies. [S0742-4795(00)01604-5]

Power Cylinder Friction in Diesel Engines

The main focus of this review is primarily to examine those factors that will affect power cylinder friction in Diesel engines. The power cylinder components considered are: Pistons, Piston Rings, Liners/Bores, Connecting Rods, Piston Pins, and Oil. Spark Ignited (SI) engine operate on many of the same principles. Therefore, much of this review will be quoting from research centered on SI engines.

Power Cylinder Friction Contribution

The power cylinder is a major contributor to the overall mechanical friction of the engine. However compared to the total energy produced by the engine, the amount is small. This makes measurements of power cylinder friction difficult.

Mechanical Friction. The distribution of total energy [1,2] in a typical fired engine (diesel or SI) is shown in Fig. 1. McGeehan [3] reviewed the literature for piston and ring friction. He stated sources [4–7] that suggest that piston assembly friction could account for 58 percent to 75 percent of the total mechanical friction of an internal combustion engine. However, the sources quoted are based on technical papers written before 1969. Recent literature and experience at Cummins Engine Company suggests that the total friction due to Pistons, Rings, and Rod will contribute only 40 to 55 percent [8–12] (Fig. 2).

Power Cylinder Friction. Early motoring tests at Cummins found that the contribution of each cylinder kit component to motoring friction is shown in Table 1.

On Engine A, at the time (1983), it was determined that the contribution of each ring to the total ring pack friction is shown in Table 2.

Table 3 shows more recent data giving a breakdown of power cylinder component friction.

Other researchers [13,14] have found similar results. The combination of all the sources suggests that the typical frictional distribution between pistons, rings, and rods are shown in Fig. 3. The distribution of the ring friction is given in Figure 4.

Summary of Power Cylinder Friction Contribution. Table 4 gives the percent contribution of each power cylinder component with respect to: (1) total power cylinder friction, (2) total energy produced by the engine, and (3) work output power. The available energy for friction reduction would have to fall below these values.

Methods for Measuring Friction in an Engine

Measuring power cylinder friction is difficult. It can be seen in Table 4 that the total power cylinder friction is a small percentage

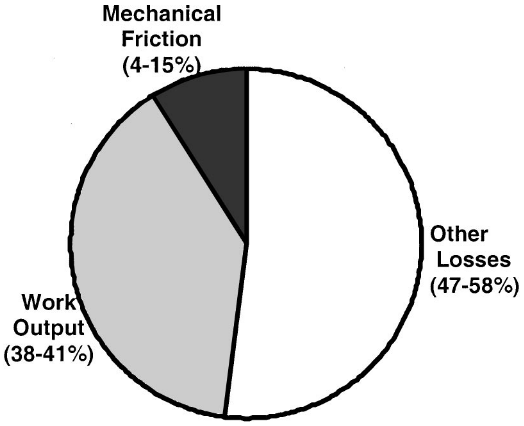

Fig. 1 Distribution of total energy in a fired engine

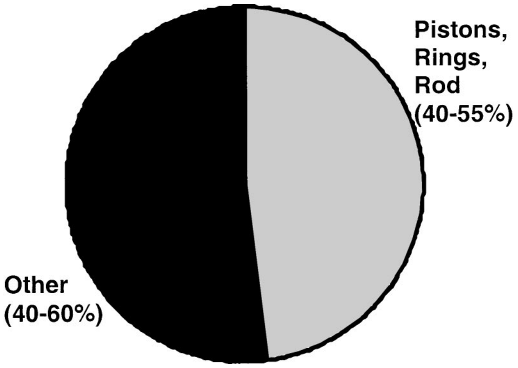

Fig. 2 Distribution of the total engine mechanical friction

Contributed by the Internal Combustion Engine Division of The American Society of Mechanical Engineers for publication in the ASME JOURNAL OF ENGINEERING FOR GAS TURBINES AND POWER. Manuscript received by the ICE Division January 15, 1999; final revision received by the ASME Headquarters April 2, 2000. Technical Editor: D. Assanis.

Table 1 Power cylinder motoring friction contributions

Motored:	Engine A	Engine B	Engine C
Rings:	28%	45%	52%
Piston & Skirt:	47%	32%	25%
Rod Bearing:	25%	23%	23%

Fired:	Engine A	Engine B
Rings:	20%	36%
Piston & Skirt:	62%	44%
Rod Bearing:	18%	20%

Table 2 Ring friction contribution

Top Ring:	13%
2nd Ring:	12%
Oil Ring:	75%

Table 3 Power cylinder motoring friction contributions (recent data)

Motored:	Engine		Ring
Rings:	37%	Top:	27%
Piston & Skirt:	30%	2nd:	22%
Rod Bearing:	33%	Oil:	51%

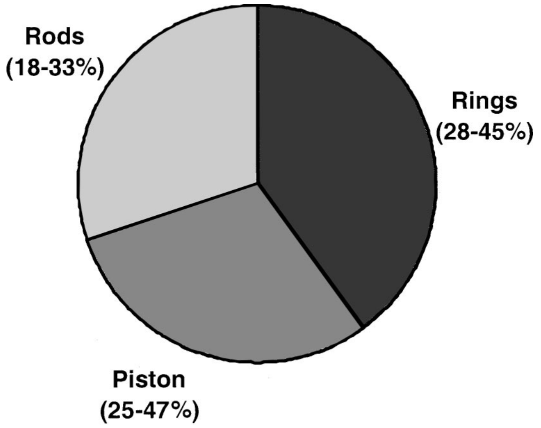

Fig. 3 Distribution of piston/ring/rod friction

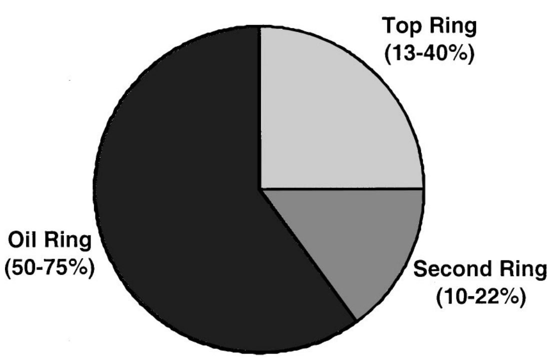

Fig. 4 Distribution of ring friction

Table 4 Percent friction

	% Power Cylinder	% Total Energy	% Work Output
Piston/Rings/Rods	100	1.6–8.3	4.1–20.9
Rods	18–33	0.29–2.7	0.74–6.8
Piston	25–47	0.40–3.9	1.02–9.8
Rings	28–45	0.45–3.7	1.15–9.4
Top	3.6–18.0	0.06–1.5	0.15–3.8
Second	2.8–9.9	0.05–0.8	0.11–2.1
Oil	14.0–33.8	0.23–2.8	0.58–7.0

of the Total Energy (IMEP) of the engine. When compared to the actual output power of the engine the percentage is a little higher. Individual components are even less. The accuracy of the measurement technique and equipment is very important to be able to quantify power cylinder friction.

The second problem with measuring power cylinder friction is isolating it from all the other friction. For example, it is difficult to separate piston friction from friction due to the overhead and very difficult to separate it from the ring friction. Some of the techniques for quantifying power cylinder friction are as follows:

1 Component removal—Remove a component and measure the overall change. This is not always possible. Also, removing components can affect the friction of the other components.

2 Difference testing—Measure the difference between two designs. This will not give the absolute magnitude of the component friction but will indicate the effect of a change.

3 Analytical modeling—Use an analytical model to predict the contribution of each component to friction. The model might be calibrated or verified by comparing to experimental data from a ‘‘difference test’’ or a ‘‘component removal’’ test.

Performance Measurements. Friction of the power cylinder may be evaluated by its effect on the overall engine performance. Here are two methods that can be used: (1) FMEP or P-V Diagrams or (2) Brake Specific Fuel Consumption (BSFC). However, in both cases, it is possible to test only relative differences between changes in the power cylinder. It is not possible to determine the absolute magnitude of friction.

In both of these cases it is necessary to accurately measure the performance of the engine. Therefore an engine must be run under very controlled circumstances. Little changes in parameters like intake manifold temperatures or pressures can significantly affect the results. Furthermore, the engine must be run in a well calibrated test cell to be able to detect the small differences that are present.

Even with the most care, test cell variability can be large compared to the desired measurement. Therefore it is imperative that multiple tests be made for each configuration and a statistical analysis used to determine the significance.

FMEP or P-V Diagram. Mean effective pressure (MEP) is a method to normalize loading on an engine per unit displacement volume. As a result, this is used to factor out the effect of engine size.

It is possible to calculate the total work done by the cylinder pressure and combustion by integrating the Pressure-Volume (P-V) diagram. This will give the Net Indicated Mean Effective Pressure (NIMEP).

$$NIMEP=\int_{0}^{360\cdot nr}\left(\frac{P}{nr\cdot D}\right)dV, \qquad (1)$$

where:

$NIMEP$=net indicated mean effective pressure
P=cylinder pressure
V=cylinder volume
nr=number of revolutions per cycle
D=engine displacement (volume)

For a four stroke engine it is sometimes useful to divide this integral into two sub integrals. The Pumping Mean Effective Pressure (PMEP) is determined by performing the integration of the intake and exhaust portions of the cycle. This the work that is required to purge the cylinder of exhaust gases and fill it with fresh. The Gross Indicated Mean Effective Pressure (GIMEP) is obtained by integrating over the compression and expansion portions of the cycle. It is an indication of the amount of work generated during the compression-combustion-expansion process.

The indicator of how much energy is delivered by the engine is Brake Mean Effective Pressure (BMEP):

$$BMEP=\left(\frac{BP\cdot nr}{D\cdot rpm}\right), \tag{2}$$

where

$BMEP$ =brake mean effective pressure
BP=brake power
nr=number of revolutions per cycle
D=engine displacement (volume)
rpm=revolutions per minute

The mechanical frictional energy loss is called Friction Mean Effective Pressure (FMEP). It is related to NIMEP and BMEP by the following:

$$NIMEP=BMEP+FMEP \tag{3}$$

or

$$FMEP=NIMEP-BMEP, \tag{4}$$

where

$NIMEP$ =net indicated mean effective pressure
$BMEP$ =brake mean effective pressure
$FMEP$ =friction mean effective pressure

To be able to use FMEP in evaluating power cylinder friction, it is necessary to measure cylinder pressure. This is required for the integration of Pressure and Volume to obtain the NIMEP. Figure 2 shows that the power cylinder friction is approximately 40 to 55 percent of the total mechanical friction or FMEP of the engine.

Brake Specific Fuel Consumption (BSFC). When cylinder pressure data are not available, it is possible to use BSFC measurements to determine a change in power cylinder friction. The difference in BSFC between two different configurations can be used to quantify the frictional changes. However, the power cylinder friction contribution is so low compared to the power output of the engine, these measurements can be difficult. In some cases only light load conditions are studied [15] to amplify the effect of a small friction reduction. If higher loads are studied, many repeat tests are required and statistical analysis should be employed to analyze the results.

Motoring Friction Measurements

Motoring Teardown. Motoring teardown engine tests are commonly used and probably the easiest technique to evaluate engine friction [10,12,16]. This type of testing involves rotating the engine with a motoring dynamometer and recording the torque required to maintain a constant speed. By removing components from the engine it is possible to determine their contribution to friction.

To measure power cylinder friction, the engine is first motored without the head. Then each of the piston rings are removed individually and the engine motored again. The difference in torque is attributed to the frictional contribution of that component. This is an example of a ''component removal'' test described above.

In the end the piston is removed (with the connecting rod) and the engine is motored again. The difference in torque is assigned to the piston and the rod. It is not possible to directly isolate the piston friction from the rod friction. Analytical techniques may be used to try to separate these contributions.

The problems with motoring teardown tests are

1 The effects of high cylinder pressures are not measured.
2 The test will not be operating at realistic temperatures compared to the fired engine.
3 It is not possible to truly isolate the contribution of each individual component. For example, if one ring is removed, it will allow more oil to flow to the remaining rings. This will reduce the overall friction.

Some of these issues are discussed in more detail below in comparing motoring friction with fired friction.

Pressurized Motoring Tests. To try to quantify the effects of pressure it is possible to motor the engine while supplying high pressure to the intake manifold. Then during compression, high cylinder pressures will be developed. The cylinder pressures can be controlled by the amount of boost or intake manifold pressure. By supplying sufficient boost pressure, peak cylinder pressures can be duplicated.

The problems with this test technique are

1 High temperatures of a fired engine are not included.
2 Air pumping losses and overhead friction will reduce the accuracy of the measurement.

Firing/Motoring Tests

Hot Shutdown. To quantify the effects of high temperature in a motoring test it is possible to fire the engine until stable temperatures are reached. Then the fueling to the injectors is stopped and the engine is motored [13]. Before the engine components have cooled the engine is motored and motoring torque is recorded.

The problems with this test technique are

1 High cylinder pressures of a fired engine are not included.
2 Air pumping losses and friction of all the other components that are required to fire the engine will reduce the accuracy of the measurement.

Willans Line. The Willans line is a method that can be used when sophisticated instrumentation is not available. Engine load is measured and plotted at constant engine speed as a function of engine fuel rate (or torque) [16,17]. The curve is then linearly extrapolated to zero fuel flow (or torque) which results in a negative load. This represents the losses of the engine. This method gives not only the mechanical friction but includes the pumping losses also.

The concern with this test technique is that it requires extrapolation which can be unreliable [16].

Free Deceleration Curves. The engine coast down test can be performed without a motoring dynamometer. The engine is run at full load and the appropriate speed until all temperatures are stabilized. The fuel is then cut off and the engine is allowed to decelerate. Haines [17] states that

> ''Total resistive torque can be calculated by the engine effective moment of inertia and the tangent to the deceleration curve at the speed point of interest. This has the advantage of being a simple test to run, and yielding values for the whole speed range. However, it must be borne in mind that transient conditions are not likely to give the same friction values as

> steady state. Also, cylinders are not operating at the pressures and temperatures prevailing during normal running and this will influence the results.''

Morse Test or Electronic Cylinder Disablement. In this test the engine is run at constant speed while the brake power is being measured by a dynamometer. Fueling to one or more cylinders at a time is cut off [17] and the resultant loss in power is measured. Unfortunately, these cylinders will not have the effect of the high cylinder pressure. It is also necessary to measure the cylinder pressure under ''both normal and disable cycles.'' The energy losses from the lack of fueling and the air pumping losses can then be determined.

Direct Friction Measurements. The following techniques are ways that offer the potential to measure power cylinder friction directly under fired conditions. These techniques were also reviewed by others [18,19]. However, separating the friction due to each individual component of the power cylinder is still very difficult to impossible.

The disadvantage to most of these methods is that they are much more complex than the previously mentioned methods. This requires significantly more in terms of instrumentation, setup, and/or analysis.

Moveable or Floating Bore. Many measurements of cylinder kit friction have been made by mounting the cylinder elastically. Friction is determined by measuring the forces acting on the cylinder liner as the piston reciprocates. It has been used by various researchers [18,20–24].

This technique is probably the most accurate method to quantify power cylinder friction. The friction is measured directly and does not require complex calculations. However, the problem with this technique is that extensive and costly modifications to the engine are required. Also great care is needed to balance the pressure effects on the liner.

Reciprocating Liner. Another method used was to mount the piston elastically and reciprocate the liner [22,25]. The friction is then measured in the piston. It is not possible to fire the engine under these conditions. However methods have been proposed to try to simulate cylinder pressures on the back of the rings.

Instantaneous IMEP. Uras and Patterson developed a technique called the ''Instantaneous IMEP'' friction measurement where strain gauges were installed on the connecting rod [26–29]. The forces acting through the connecting rod are measured. Pressure and inertial forces are calculated and subtracted from the results to obtain the friction contribution. However, the validity of this measurement depends highly on the accuracy of the cylinder pressure and connecting rod force measurements. The actual frictional forces are on the order of the error in the pressure measurements. This also requires detailed calculation of the pressure and inertial forces.

Fixed Sleeve. Ku and Patterson [30] tried a fixed sleeve method for measuring friction. This is a ''derivative of what has been called the 'moveable bore' method.'' In this method a thin liner is mounted rigidly inside a ''modified steel replica of the removable production liner.''

The friction forces are measured by strain gages mounted in the liner. Gas forces will act on the upper portion of the flexible sleeve and need to be subtracted from the total measured force. This requires the measurement of cylinder pressure.

This configuration also requires a smaller piston and rings to fit inside the apparatus. Therefore it is not possible to test actual production hardware.

(P-ω) Method. Another technique to quantify cylinder kit friction is referred to as the (P-ω) method. This technique, developed by Rezeka and Henein [31], measures the instantaneous changes in angular velocity of the flywheel that are caused by cylinder kit friction variations. This requires significant computation that makes the results difficult to obtain. However, very little modification to the engine is required.

Summary of Methods of Friction Measurements. Performance tests have the advantage of directly measuring the desired effect of reducing friction. Unfortunately, the potential changes in power cylinder friction are small and difficult to measure.

Motoring friction tests are relatively easy to perform and have high measurement accuracy. Unfortunately their results may not be representative of what is actually happening in a real engine because of lower cylinder pressures and/or lower temperatures.

Friction of the ring-pack and piston can be measured directly. However, direct measurements require major modifications to the engine. Techniques are available that require less modification but have greater error due to the calculations required.

Comparison of Motoring and Fired Engine Tests

Since motoring friction tests have been used to evaluate friction, it is necessary to review how accurate they might be. This type of testing does not have the high cylinder pressures and/or high temperatures of an operating engine.

Motoring Versus Fired: Moveable Bore Technique. At the Musashi Institute in Japan various studies have been made where cylinder kit friction has been measured. The ''moveable bore'' technique was used for their measurements. They compared the measured friction of a motored engine without gas pressure to a fired engine [20]. The following was their statement:

> . . . the value of the (motoring) friction force was nearly the same to the . . . piston assembly under firing operation. This is due to the differences in temperatures on the sliding surfaces . . . If the difference in oil temperature was taken into account, the friction force of the ring pack can be converted into a value which is about 85 percent of the value of piston assembly friction force under the same (fired) conditions.

This indicates that while increased cylinder pressures may tend to increase the power cylinder friction, lower viscosities due to higher temperatures will decrease friction. The net result is that the absolute value of the motored friction is almost the same as the friction in the fired engine.

In another report [32], friction was measured on a diesel engine with a bore of 137 mm and a stroke of 135 mm. The engine piston had three compression rings and an oil ring. It can be seen in Fig. 5 that as the load of the engine increases (no load to full load), friction significantly increased (approx. 40 percent) during the expansion stroke.

In part (a) of the figure the coolant water temperature was held constant. In regions other than the expansion stroke, the full load case actually had lower friction. This is presumably due to the higher temperatures causing a reduction in oil viscosity.

In part (b) of the figure the cylinder wall temperature was held constant (viscosity constant). The results show very little difference in friction other than during the high pressure regions of the stroke.

Other engine tests were conducted on gasoline engines [21]. Figure 6 shows the effect of engine load on measured friction. Measured friction is shown at no-load, half-load, and full-load. It should be remembered that gasoline engines will have lower cylinder pressure than diesel engines. However, the measured friction around Top Dead Center Firing (TDCF) changes significantly.

It is noted that friction in the intake and exhaust strokes of the cycle are not significantly affected by engine load.

Other researchers have also used the moveable bore technique for measuring cylinder kit friction. In one paper [18], motoring friction was compared with firing friction of the power cylinder at ''the same conditions (oil, water temperature, and speed).'' The conclusions were:

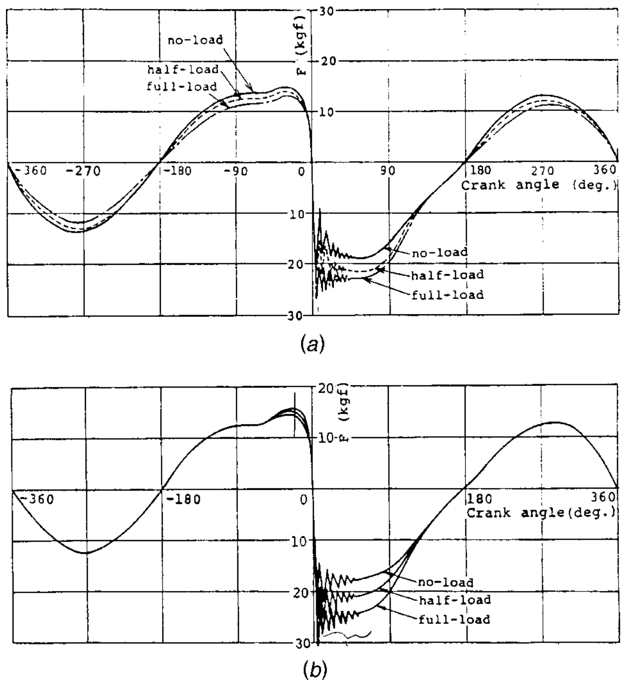

Fig. 5 The effect of engine load on cylinder kit friction (Moveable Bore [32]): (*a*) constant coolant water temperature; (*b*) constant cylinder temperature.

> Hydrodynamic forces during intake and exhaust strokes are reduced by 10 Newtons . . . At dead centers boundary friction peaks increase due to the reduced viscosity, and at power TDC the pressure effect is added. Overall friction losses are reduced and the essential part of the difference is due to temperature increase and to its effects on the effective viscosity.

This indicates that under some conditions that the overall friction of the fired engine may appear equivalent or even less than the motored friction.

Motoring Versus Fired: Instantaneous IMEP. At the University of Michigan, researchers have connected strain gages to the connecting rod of the engine. Through the strain measurements they can calculate the friction force of the power cylinder. They measured friction of a gasoline engine under motored and fired conditions [26]. Their statement on the differences is

> There is ample evidence to suggest that piston ring friction losses are different under motoring and firing conditions. As expected, losses under firing were considerably higher than motoring. The difference between FMEP's of firing and motoring is about 20kPa at 500 RPM.

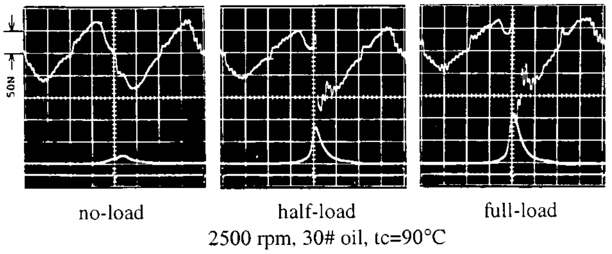

Fig. 6 The effect of engine load on cylinder kit friction (Moveable Bore [21])

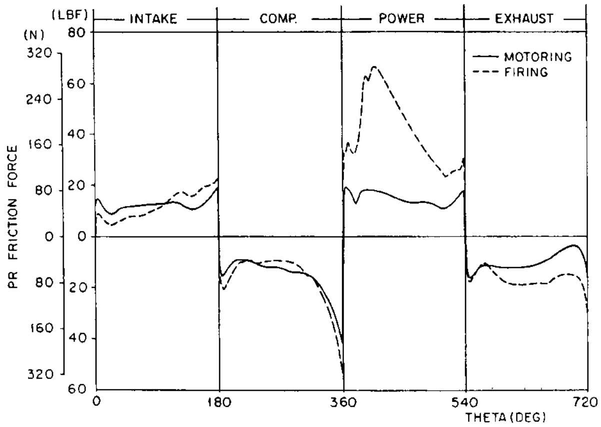

Fig. 7 Motoring versus firing friction—500 rpm (Instantaneous IMEP [29])

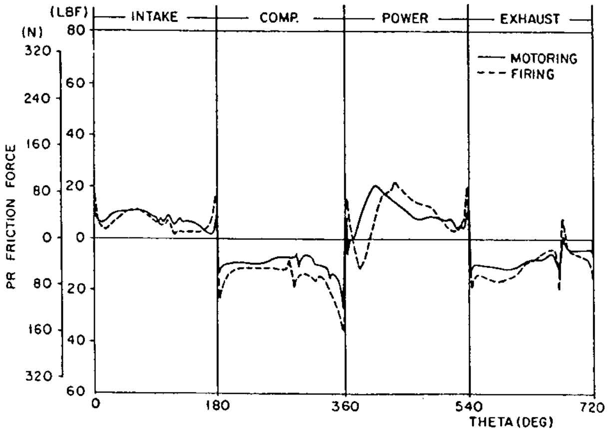

Fig. 8 Motoring versus firing friction—1100 rpm (Instantaneous IMEP [29])

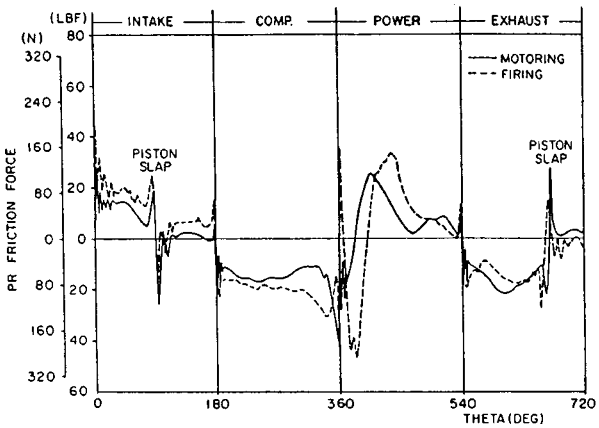

Fig. 9 Motoring versus firing friction—1640 rpm (Instantaneous IMEP [29])

In another paper [29], graphs showing motoring friction compared to fired friction are given at three speeds (500, 1100, and 1640 rpm, Fig. 7, Fig. 8, and Fig. 9). They state:

> Differences between motoring and firing are noticeable especially on the power and exhaust strokes. Intake and compression strokes are more similar . . . Firing friction forces are noticeably greater during the power stroke at 500 rpm. This is

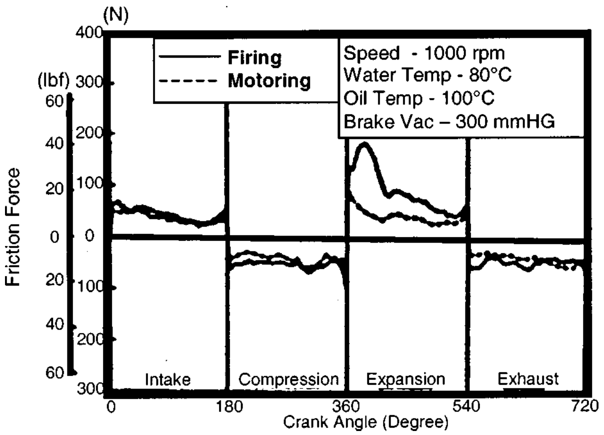

Fig. 10 Motoring versus firing friction—1000 rpm (Fixed Sleeve [30])

> attributed to the higher cylinder pressures. (At 1100 and 1640 rpm) the differences between motoring and firing friction are considerably less at these speeds except around top and bottom centers.

Some inaccuracies are observed in this type of measurement. Nevertheless, it can be seen that a fired engine can have higher power cylinder friction than a motored engine.

Motoring Versus Fired: Fixed Sleeve Method. At the University of Michigan, researchers have also connected strain gages to a thin walled cylinder liner to measure the cylinder kit friction [30]. Figure 10 shows a graph comparing motoring friction and fired friction at part load. This work was done on a gasoline engine. The statement in the paper is

> As might be expected, the firing friction differs, and is much larger than motoring friction during the expansion stroke. Elsewhere, the differences are more minor.

Once again it can be seen that the cylinder pressures and temperatures from combustion will affect the friction measurements.

Motoring Versus Fired: High Pressure Tests. A test was run at Cummins where the motoring friction was measured with a pressurized intake manifold. This made it possible to increase cylinder pressure by changing the intake manifold pressure. Figure 11 shows that an increase in the peak cylinder pressure can increase the measured frictional horsepower.

Motoring Versus Firing: Discussion. It can be seen above that the differences between fired cylinder kit friction and motored friction can be small to very large. In general it can be said that around Top Dead Center Firing (TDCF) the friction force will be greater in a fired engine due to the increased cylinder pressures and temperatures. However, around the dead centers an increase in friction force might not translate into significant frictional power losses. This is because the piston is moving very slowly at this point in the cycle.

At other parts of the cycle that do not have the high cylinder pressures, temperature effects will dominate. Temperature of a fired engine will be greater than a motored engine. This will cause a small reduction in friction force. However, since this happens when the piston is moving (mid stroke) relatively fast, the effect on friction power will be greater.

Various analytical models [14,33,34] from different companies have predicted that the piston skirt can deform under the high pressure loads in a diesel engine. A motored engine will not have these high pressure forces, the deformations will be small, and the effect on the lubrication might not be observed. A piston skirt might not have any skirt to bore contact in a motored engine, but in a fired engine there might be significant contact. Skirt to bore contact will result in high friction.

It should also be noted that the higher temperatures of a fired engine will affect clearances. In particular, the piston skirt clearance will become smaller. This will result in some increase in friction. It will also affect piston secondary motion.

Motoring Versus Firing: Model Predictions. A direct injection diesel engine was modeled to predict ring pack friction (not piston friction). Three cases were modeled

1. Fired
2. Motored (at typical cylinder kit temperatures for a motored test, this assumes that the oil has been heated so that the ring pack temperatures are 77°C)
3. Motored (at firing temperatures)

Figure 12 shows the predicted instantaneous ring pack friction force prediction over the entire cycle. This is different from the power cylinder friction measurements shown previously (Fig. 5 to Fig. 10) because it only includes the friction due to the rings. The model predicts significantly higher frictional forces around Top Dead Center Firing (TDCF) (during times of high cylinder pressure) for the fired case. The motored case at firing temperatures illustrates the effect of temperature. It has lower friction at the mid stroke because of the reduced viscosity of the oil. Yet there are slight peaks at the ends which indicate some asperity contact with the thinner oil around the dead centers.

The instantaneous friction power loss is shown in Fig. 13. It can be seen that the power loss goes to zero at the dead centers. The largest differences only occur from −30 to 90 deg. This is only about 17 percent of the cycle. It can also be seen that the motored case at firing temperatures results in lower instantaneous power loss over most of the cycle.

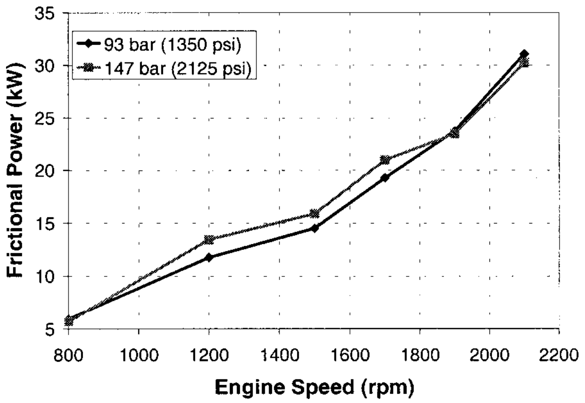

Fig. 11 Pressurized motoring friction test at two different peak cylinder pressures (93 and 147 bar)

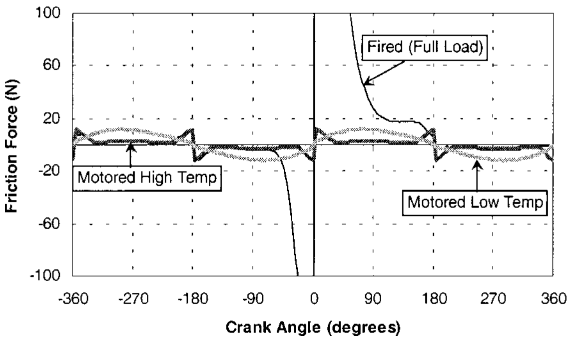

Fig. 12 Predicted instantaneous ring pack friction force (fired, motored, hot motored)

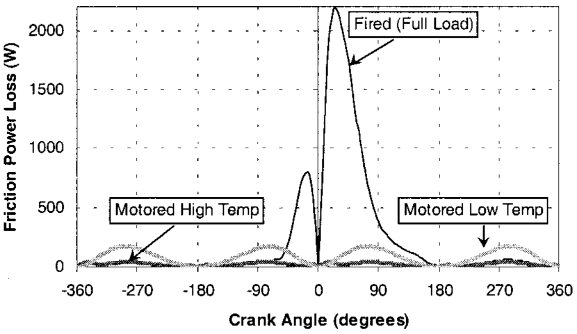

Fig. 13 Predicted instantaneous ring pack friction power loss (fired, motored, hot motored)

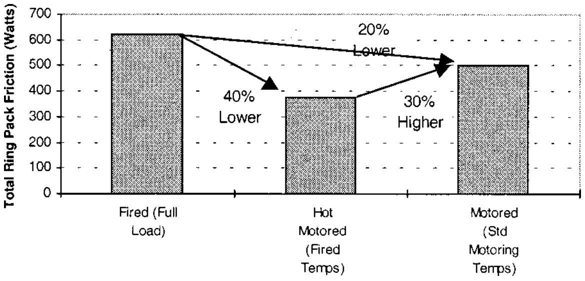

Fig. 14 Predicted average ring pack friction power loss (fired, motored, hot motored)

The total or average friction of the ring pack is shown in Fig. 14. It can be seen that just by removing the cylinder pressures, friction will be reduced by 40 percent. Then when motoring at the cooler temperatures (typical of a motored test), the friction increases 30 percent over the motoring case at fired temperatures.

Motoring Versus Firing: Conclusions

- Cylinder pressures will be significantly higher in a fired engine than motored engine. It was seen that changes in cylinder pressure can have a large effect on the cylinder kit friction force, especially around TDC. However, since the piston is not moving very fast, the increase in friction power loss will be small. Also the time of high pressure occurs during only 15 to 20 percent of the cycle. Some data showed that even during the mid-stroke the friction force differences were large. This will cause a large increase in friction power loss. Modeling suggests that the friction increase due to pressure alone can be up to 40 percent.
- Cylinder temperatures will be higher in a fired engine than a motored engine. This will result in lower viscosity oil and reduced friction. The reduced friction force occurs during mid-stroke when the piston is moving. The resulting reduction in friction power is then magnified. Modeling suggests that this effect may be as much as 30 percent or more.
- High cylinder temperatures also reduce clearances. This will cause some increase in friction and have some effect on piston secondary motion.
- The overall average cylinder kit friction of a fired engine will be 0 to 20 percent more than the friction of a motored engine.
- Even though the overall friction measurement might not be significantly different, the mechanisms of friction clearly are. A fired engine will have more friction around Top Dead Center Firing (TDCF) and less friction in the regions of low cylinder pressures. It is only through understanding these differences and designing the power cylinder appropriately that friction will be reduced on the power cylinder components.

Friction Correlations

The review by McGeehan [3] reports that the cylinder bore lubrication is predominantly hydrodynamic with localized contact between ring and bore at TDC firing [8,35,36]. Also, the degree of contact may increase during transient conditions. This is very apparent in examining a worn cylinder bore. There is very little wear anywhere on the bore other than at top ring reversal.

Stribeck Relation. Based on the Stribeck relationship, McGeehan's review [3] gives various equations based on different researchers results. The basic equation is

$$f=c\left(\frac{\mu v}{pw}\right)^{x}, \tag{5}$$

where

f=coefficient of friction
c=constant
μ=Dynamic viscosity
v=piston speed
p=effective pressure on ring
w=width of the ring
x=exponent (0.33–0.66)

Many empirical constants are given for the above equation corresponding to different ring face profiles. He also says that frictional losses are proportional to

$$Fp \propto v^{1.5}(\mu w)^{0.5}, \tag{6}$$

where

Fp=friction power
v=piston speed
μ=Dynamic viscosity
w=width of the ring

Parallel Plate Approximation. Using basic lubrication principles of oil being sheared between parallel plates, Patton et al. [9] developed the following proportionality for piston friction:

$$Fp \propto BV_p^2, \tag{7}$$

where

Fp=friction power
B=bore
V_p=Mean Piston Speed

This relationship can be modified further to be

$$Fp \propto BS^2 RPM^2, \tag{8}$$

where

Fp=friction power
RPM=revolutions/minute
B=bore
S=stroke

Based on the above equation it is possible to write the following relationship:

$$Fp = 1.48\times 10^{-13} BS^2 RPM^2 nc, \tag{9}$$

where

Fp=friction power of the piston rings and rods (KW)
RPM=revolutions/minute
B=bore (mm)
S=stroke (mm)
nc=number of cylinders,

where the constant (1.48×10^{-13}) was determined by a best fit through a series of motoring teardown tests (see below).

Correlation Results

Comparison of the Equation and Measured Data. The equation given above (Eq. 9) is compared to the motoring friction data as shown in Fig. 15, Fig. 16, and Fig. 17. These graphs show the piston and rod friction from motoring teardown tests. The correlation used (Eq. 9) for the piston friction in the graphs was based on a best fit for all the data. The figures show data for seven different engines. Other engines were also tested but not shown here. Of all the engines tested, the maximum deviation from this best fit line was 2.8 hp or 13 percent. All of the engines were run in one test cell at Cummins Engine Co. Oil temperature was controlled to 220 to 225 degrees Fahrenheit. The heads were removed so there was no coolant flow through the engine. Multiple torque readings were taken at each speed and then averaged.

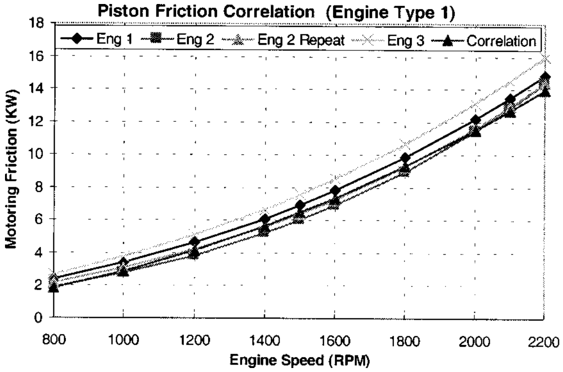

Fig. 15 Motoring friction and correlation for engine type 1

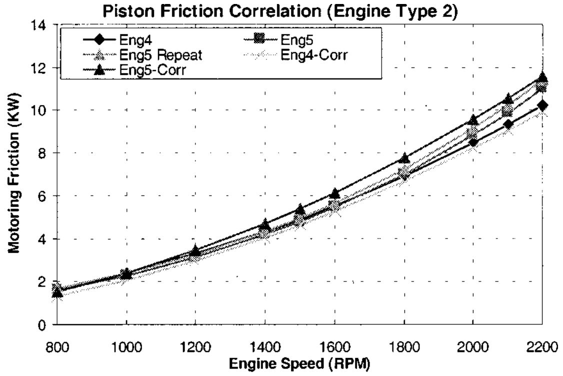

Fig. 16 Motoring friction and correlation for engine type 2

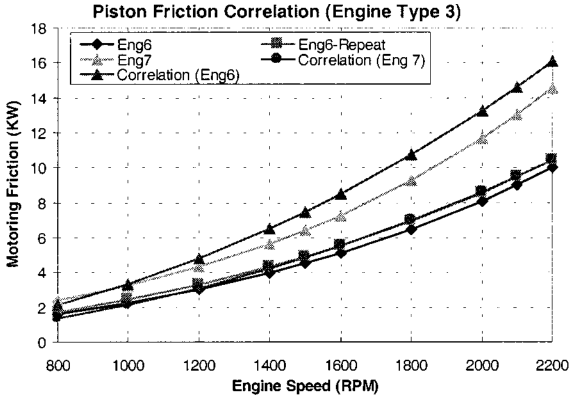

Fig. 17 Motoring friction and correlation for a DDC engine

Ranking the Engines. The correlation given above (Eq. 9) is governed by the effects of engine size (bore and stroke). Any deviations from the equation are effects of how the system is being lubricated. This offers a method for comparing engines of different size. In some cases the actual motoring torque is higher than the correlation, Fig. 15. This indicates a power cylinder that has higher motoring friction than the average. Others show lower torque than the correlation Fig. 17, indicating lower friction than the average.

Ring Mixed Lubrication. Patton et al. [9] also proposed a relationship for a piston ring in mixed lubrication. This is an arbitrary equation that gives an increase in friction force as the engine speed goes down.

$$Fp \propto \left(1+\frac{1000}{RPM}\right)^{*} S^{*}RPM, \tag{10}$$

where
Fp=friction power S=stroke
RPM=revolutions/minute

The original equation given by Patton et al. used mean piston speed. The mean piston speed is proportional to the Stroke * RPM and therefore was used in the above equation.

Pressure Effects On Ring Lubrication. A relationship related to the physics of the compression process and based on the work of Bishop [6] was used by Patton et al. [9].

$$Fp \propto BS^2RPM\left(\frac{P_i}{P_a}\right)[0.088r_c+0.182r_c^{(1.33-0.0238V_p)}], \tag{11}$$

where
Fp=friction power B=bore
RPM=revolutions/minute S=stroke
r_c=compression ratio P_i=intake pressure
V_p=mean piston speed P_a=atmospheric pressure

Windage Calculations. Thring [37] used the following formula to estimate the windage effects. This is the force that results when a solid body (such as a connecting rod) moves through a fluid.

$$F_d=\frac{1}{2}\rho_c v^3 c_d A \tag{12}$$

$$\rho_c=\left(1-\frac{Pc_{oil}}{100}\right)\rho_a+\left(\frac{Pc_{oil}}{100}\right)\rho_o, \tag{13}$$

where
F_d=drag force v=velocity of moving component
ρ_r=density of fluid c_d=drag coefficient
ρ_d=density of air A=frontal area
ρ_o=density of oil
Pc_{oil}=percent of oil in gases

Analytical Models

Detailed analytical models have been developed to predict the lubrication of the pistons and rings. These models are based on the fundamental equations for lubrication and kinematics.

Some of the analytical models that have been used are

- CASE—developed at Michigan State University (originally developed by Larry Bromlich at Computech) [38]
- MIT—developed through a consortium with industry [34,39,40].
- RINGPAK and PISDYN at Ricardo Software. RINGPAK models the lubrication of the ring pack. PISDYN models the lubrication of the piston [41–43].
- GLIDE—developed by AVL. There are separate models to predict ring dynamics and piston dynamics [44].
- FLARE—developed by GM [14,45,46]

Methods for Reducing Friction

The following recommendations and contributions were made in the literature from various companies for reducing friction.

Cummins Piston Ring Division [47,48]

- More conformable low tension oil ring
- Reduced compression ring cross-section
- Connecting rod guided by piston (constrain the rod from moving along the axis of the engine with the piston rather than between the crank throws)
- Reduced the piston mass

MAHLE [13,49]. Methods to reduce friction

- Ring Tension (0.018 hp/lb total, 1600 RPM)
- Ring Tension (0.045 hp/lb total, 4500 RPM)
- Fitting Clearance—0.8 hp
- Optimized Skirt Profile—0.8 hp
- Skirt Area Reduction—No Benefit
- Skirt Ovality—No Benefit
- Coated Skirt (Teflon and Xylan)—No Benefit
- Coated Piston (Grafal)—Shows a Benefit
- Coated Cylinder Liner With Low Tension Rings—Shows a Benefit
- Piston Weight—No Benefit

AVL [50]. Methods to reduce friction

- Smaller preload (tension) on the rings
- Smaller rings
- Increase cold clearance (will increase noise)
- Reduce contact surface (ovality or skirt pads)
- Reduce piston mass
- Increase liner temperature
- Reduce liner distortion
- Articulated piston has lower friction than a monoblock piston

Predominate Factors Affecting Friction

- Skirt profile (Contact area between piston and liner)
- Clearance
- Piston Mass
- Liner Temperature
- Piston Construction

Karl Schmidt [15]. Methods to reduce friction

- Reduced wall pressure (tension) on the rings
- Reduced axial ring height (1.5 to 3.5 percent reduction in BSFC)
- Reduced skirt area in the axial direction
- Separated bearing areas in the axial direction on the skirt
- Emralon Coated Skirt—Shows improvement (automotive)
- Reduced piston assembly mass
- Coolant out temp. (10°C change=>0.4 percent BSFC change)
- Oil temperature (10°C change=>0.3 to 1.5 percent BSFC change)

***T* And *N* Technologies [51].** Methods to reduce friction

- Oil Temperature
- AEconoglide piston—Reduced skirt-to-bore contact area. (33 percent reduction in piston friction)

Chevron Research [3]. Methods to reduce friction

- Reduce axial ring width
- Reduce bearing surface area of skirt (axial)
- Reduce piston weight to reduce side load
- Wrist-pin offset (1.6 mm, 1/16 in)
- Barrel-faced profiles
- Reduce linear speed
- Smoother cylinder bore finishes
- Additives that reduce the coefficient of friction in mixed or boundary lubrication

Predominate Factors Affecting Ring Friction

- Gas loading
- Number of Rings
- Ring size
- Ring design

Ford Motor Co. [8,10,52]. Methods to reduce friction

- Reduce ring tension (44 percent reduction in tension=>22 percent reduction in ring friction)
- Reduce ring axial width
- Reduce skirt area (circumferentially)—No Effect
- Reduce mass—25 percent Reduction=>0.1 psi MEP
- Moly coated top ring
- Ring materials and coatings
- Reduce the number of rings (4 percent reduction with 2 ring versus 3 ring)
- Optimized ring face profiles
- Low friction skirt and roller follower coatings—8 percent

General Motors [14,45]. Methods to reduce friction

- Reduce oil ring tension (0.02 hp/lb)
- Reduce top ring tension
- Reduce top ring axial width
- Increase skirt clearance (friction changes of 35 to 40 percent)
- Reduce skirt width (Circumferential)—Little Effect
- Skirt cam drop (ovality)
- Reduce reciprocating mass
- Reduce oil temperature
- Pin offset

Southwest Research Institute [37]. Methods to reduce friction

- Reduce oil ring tension
- Reduce windage or percent of oil in the air
- Reduce maximum cylinder pressure

Musashi Institute of Technology [20]. Methods to reduce friction

- Reduce axial width of rings
- Reduce axial width and contact pressure
- Reduce viscosity (viscosity has a significant effect)
- Increase the piston clearance (negligible effect)
- Surface finish (negligible effect)

Friction Reduction Summary. Almost every company surveyed claimed that reducing ring tension (oil ring in particular) and top ring width would reduce friction.

Efforts to reduce piston skirt friction yielded mixed results. Some said that reducing the contact area of the piston skirt would reduce friction while others said it would not. In most cases, when the skirt area was reduced axially generally a friction benefit was observed. When the skirt area was reduced circumferentially there was little benefit. This may be because a piston is typically made with a large ovality. Increasing the ovality or cutting back the sides might have a minor effect that might not be measurable. See the section below on Piston Skirt Friction for additional information about reducing the skirt contact area.

Increasing skirt clearance was another way to reduce friction, but it was noted that this might increase cavitation problems. Reduced mass of the piston was cited by many as a way to reduce friction. Piston mass is also discussed below.

Individual Components: Piston

Piston Skirt Friction. Piston skirt friction is strongly dependent on two factors:

1. Whether the skirt contacts the cylinder bore
2. How the skirt shears the oil

Skirt/Bore Contact. A well designed piston skirt will have very little skirt to bore contact. This is because the lubricating oil film will support the piston and prevent contact with the bore. However, if the piston skirt breaks through the lubricating film, the resulting asperity contact will cause high friction. Analytical models [14,33,34] are available that attempt to predict the lubricating film between the piston skirt and the cylinder bore.

If there is skirt/bore contact, reductions in friction may be obtained by:

1 Changing the profile of the piston skirt to prevent contact
2 Putting a low friction coating on the piston

It should be noted that low friction coatings on the skirt will have very little effect on friction if the skirt does not contact the cylinder bore.

Skirt and Oil Shearing Area. The second major friction loss for piston skirts is through the shearing of the oil. To reduce this it is necessary to reduce the shearing area of the oil. The skirt shearing area may be reduced in a number of ways:

Axial:	Reduced skirt length
	Axial profile (Double hump, barrel shape)
Circumferential:	Increased ovality
	Circumferential profile
	Regions where the skirt is cut back
Other:	Pads

In all cases the skirt profiles, shape, and stiffness should be designed to enhance the hydrodynamic oil film. If reducing the skirt shearing area induces skirt to bore contact, then no friction reduction will be observed. There may even be an increase in friction. If skirt to bore contact already exists in a piston design, attempting to reduce the shearing area will have little to no effect. The skirt fatigue strength should also be evaluated with each new design.

Piston Mass. The engine is a reciprocating machine. Therefore, most of the energy that is spent in accelerating the piston is regained during the deceleration. If the piston mass is increased, differences in the overall losses are due to increased friction caused by higher side loads from the piston or inertial loads on the pin. In a medium speed diesel engine, these forces are not as large as the forces caused by the cylinder pressure and the effect is small. The effect may be larger in small high speed engines.

Individual Components: Top Ring

Analytical modeling was performed to analyze how to reduce top ring friction in a diesel engine. The cylinder kit model used was the Ricardo RINGPAK model version 2.0. The following configurations were modeled:

1 Standard Ring
2 Standard Ring with Barrel Skewed Toward the Bottom
3 Reduced Width Ring (Fig. 18)
4 Reduced Width Ring with Barrel Skewed Toward the Bottom.

The details are given in Table 5 and Fig. 18.

Analysis. The predicted instantaneous friction of the top ring is shown in Fig. 19. The two cases shown are based on the nominal barrel drops. The predicted instantaneous power loss is shown in Fig. 20. In both graphs the peak values for the reduced width top ring were 15 percent lower than the standard ring.

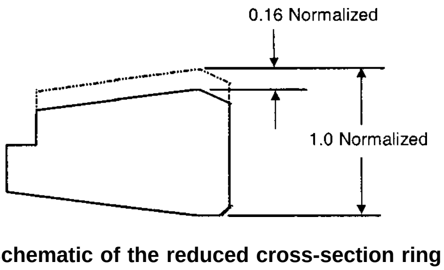

Fig. 18 Schematic of the reduced cross-section ring that was modeled (dimensions are normalized)

Table 5 Top ring design features

Engine:	Diesel Engine
Cylinder Pressures:	Rating (1800 RPM, Full Load)
Top Ring Nominal Width:	(Normalized Dimensions)
Nominal Width	1.0
Nominal Centered Barrel Drop	1.0
Nominal Skewed Barrel Case	0.83 Bottom, 2.5 Top, Peak @1/3 width toward bottom side
Top Ring Reduced Width:	(Normalized Dimensions)
Nominal Width	0.84
Nominal Centered Barrel Drop	0.83
Nominal Skewed Barrel Case	0.66 Bottom, 2.1 Top, Peak @1/3 width toward bottom side

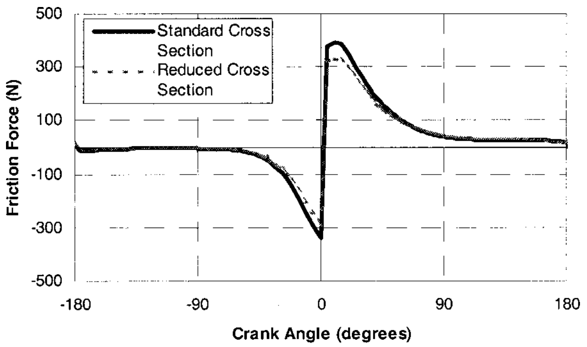

Fig. 19 Predicted instantaneous friction force on top ring

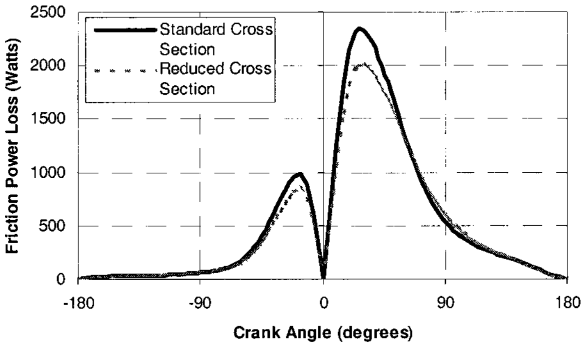

Fig. 20 Predicted instantaneous power loss on top ring

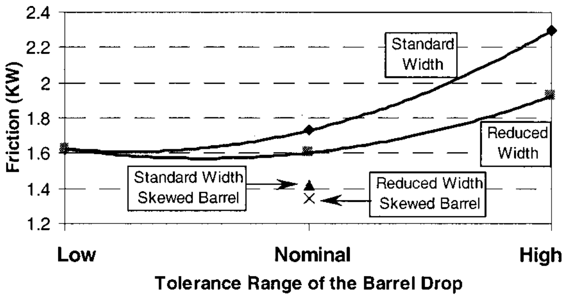

Fig. 21 Top ring friction versus barrel drop (cycle averaged friction for six cylinders)

The model predicts a fairly large effect on friction due to the barrel drop. This can affect the conclusions about the reduced cross-section ring. The results are shown in Fig. 21. In this figure, the overall friction losses for a six cylinder engine are plotted. It can be seen that there is very little predicted benefit of the reduced cross-section ring at the low end of the barrel drop specification.

At the nominal barrel drop there is a 0.11 KW (0.15 hp) benefit. There is a 0.34 KW (0.45 hp) benefit in friction at the high end of the specification.

Since the barrel drop was so significant, a skewed profile was modeled. It can be seen that the results are significant. In this case the benefit of the reduced cross-section and skewed barrel was 0.37 KW (0.5 hp). The benefit of just the skewed barrel with the standard width is 0.30 KW (0.4 hp).

It should be noted that the skewed barrel profiles used in these calculations were not optimized. Also the manufacturing feasibility was not investigated.

Discussion on the Effect of Barrel Profiles. The effect of the barrel drop is not as simple. The only way to accurately predict its overall effect is through a cylinder kit model. However, the following attempts to explain some of the effects.

Pressure Forces Acting on the Ring. The barrel shape and height will affect the pressure forces acting on the piston ring. A schematic of the effect is shown in Fig. 22. In the figure it is assumed that the pressure above the ring is greater than the pressure below. This is the case with the top ring near Top Dead Center (TDC).

The region on the top side of the ring where oil does not contact the ring face is labeled region ‘‘A.’’ In this region the pressure in front of the ring and behind are equal and have a net radial force of zero. In regions ‘‘B’’ and ‘‘C’’ there is a pressure difference that results in a net outward force. If region ‘‘A’’ is increased then regions ‘‘B’’ and/or ‘‘C’’ will be reduced. This will result in an overall decrease in the net radial force acting on the ring and as a result friction will be reduced.

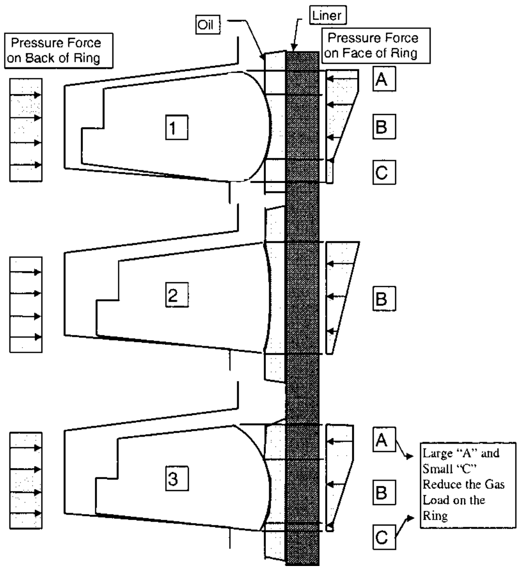

Fig. 22 Schematic of pressure forces acting on the top ring (1. large barrel drop, 2. small barrel drop, 3. skewed barrel)

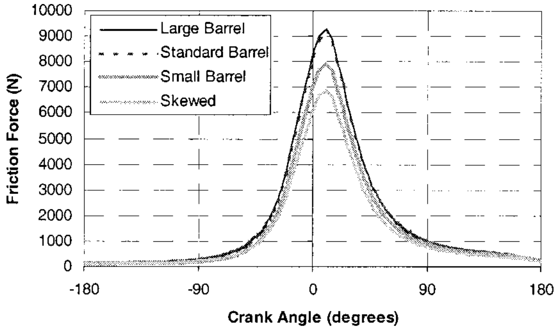

Fig. 23 Radial gas pressure force acting on the top ring

The region where the oil film contacts the ring face is labeled ‘‘B.’’ In the figure it is shown as a linear distribution of pressure on the face of the ring. This is not correct. It is only for illustration. There is a hydrodynamic wedge effect created by the profile of the ring which gives a non-linear pressure distribution. The net radial force acting on the ring in this region depends on this pressure distribution.

The section below where the oil film contacts the face of the ring is labeled ‘‘C.’’ In this region the low pressure below the ring acts on the face and the high pressures of combustion act on the back of the ring. The difference in these forces results in a net radial force acting on the ring. Minimizing this region will reduce the radial forces on the ring and reduce friction.

It can be seen that the skew barrel maximizes section ‘‘A’’ and minimizes section ‘‘B.’’ Both of these are favorable to reducing friction of the ring.

Figure 23 shows a comparison of the net pressure forces acting on the top ring for different barrel drop configurations. It can be seen that the small barrel drop and skew barrel both significantly reduce the radial gas pressure force acting on the ring.

Instantaneous Friction Force. Figure 24 shows the predicted instantaneous friction force for the top ring with various barrel drops. Figure 25 shows the corresponding power loss. It can be seen that the small barrel drop has the lowest friction around the 0 deg. However, because the piston is moving so slowly at that time the overall effect of friction power is not as significant. The skewed barrel has the lowest friction power lost.

Top Ring Friction Summary

- It is possible to reduce friction by reducing the cross-section of the top ring. This result is strongly affected by the barrel drop of the rings.

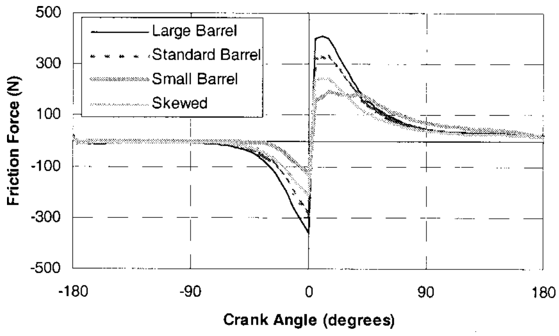

Fig. 24 Effect of ring face profile on predicted instantaneous friction force of the top ring

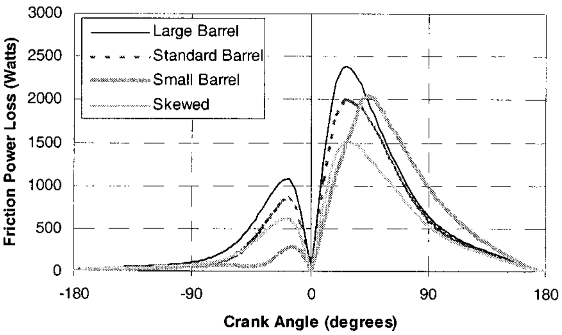

Fig. 25 Effect of ring face profile on predicted instantaneous friction power loss of the top ring

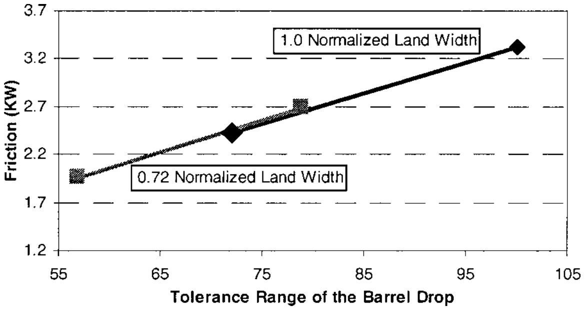

Fig. 26 Effect of oil ring tension on friction for two cases

- A skewed barrel for the top ring profile offers another potential reduction in friction. The friction reductions due to ring face profiles will diminish as the ring wears.

Individual Components: Oil Ring

Oil ring friction is predominately affected by ring tension. The face of the oil ring usually comprises very small rails or lands. These are too small to generate a hydrodynamic oil film which results primarily in asperity contact between ring face and bore. Reducing tension will reduce the friction losses. Too much reduction in tension will cause an increase in oil consumption. Figure 26 shows the analytical predictions for two cases with different land widths.

There are future technologies that are being developed to be able to reduce oil ring tension without a loss in oil consumption. One of these new technologies is the plastic oil ring [47].

Individual Components: Liner or Bore

Low friction liner or bore coatings may reduce friction during times of metal to metal contact. This can occur with the skirt and the rings. The top ring primarily contacts the bore near Top Dead Center Firing (TDCF). However the piston is moving very slowly, so the friction power differences will be small. The biggest reduction may occur by reducing the friction between the oil ring face and the bore. Because of the high unit pressures of the oil ring, there is significant potential for metal to metal contact.

A coated liner was engine tested [49] by Mahle. The results showed very little reduction due to the coating itself. However, they claimed that because of the coating it was possible to use rings with lower tension without losing oil consumption. Because of the lower ring tension the friction was reduced. But it was only possible, they claim, because of the liner coating.

Individual Components: Oil

Oil Formulation. A reduced viscosity oil offers the potential for reduced friction because of the lower shear force. A significant trend has been observed in the automotive industry to reduce oil viscosity for improved fuel economy. This is an important trend that will most likely be followed by the Diesel engine industry in the near future.

A significant literature review of ‘‘The Relationship Between Oil Viscosity and Engine Performance’’ was made by Steward and Selby [53]. The report shows a number of examples of how reducing oil viscosity will reduce engine friction. It was also shown that reducing the viscosity could cause significant increases in wear. However, cases were also shown where different additives to the oil could lessen or eliminate the effect of the low viscosity on wear.

Other researchers [54,55] also found an improvement in fuel economy with low viscosity oils. It was found that an appropriate friction modifier in the oil formulation could further improve the results. Kennedy and Moore [56] claim that ‘‘the fuel economy effects of friction modifer, viscosity index improver, and viscosity grade can be as much as five times greater than the effects of ZDP (zinc dialkyldithiophosphate) or overbased metal detergent.’’ They found that ZDP additives actually increase friction and are ‘‘antagonistic to friction modifiers.’’ It is also reported ‘‘that SAE 5W-30 oils are not inherently more fuel efficient than their 10W-30 counterparts in the Sequence VI tests.’’ But the ‘‘SAE 5W-30 oils are somewhat more responsive to friction modifiers than 10W-30s.’’

Research by Moore [57] with a capacitance film thickness transducer showed that fuel economy and cylinder wear were improved when a SAE 10W-30 oil was used rather than 15W-40 (Volvo TD 100G).

A study at Chevron [58] on 44 diesel engine field test engines found no statistically significant difference in fuel consumption between SAE 15W-40 and SAE 30. The study did show a 30 percent oil consumption advantage of the SAE 15W-40 over SAE30. They also demonstrated [59] with 15W-40, SAE 40, and 15W oils that the there was a significant effect of the multigrade oil (i.e., V.I. improver) in minimizing oil consumption and soluble fraction of the particulate. Also there was no statistical difference between exhaust particulates of SAE 10W-30 and 15W-40 oils.

Chevron also tested three oils using a Mack EM-6-300L with high top ring pistons. The oils tested were 10W-30, 10W-40, and 15W-40. Tests showed that all oils provided low oil consumption and equal wear. Radioactive wear testing on a DDC series 60 diesel engine showed no difference in wear between an SAE 15W-40 and 20W-40 oils. But an SAE 10W-30 resulted in higher ring face wear than both.

This result seems to contradict the work done by Moore [57] stated above. However, the difference may be caused by a number of things. It is possible that the differences in lubricant formulation, engine loading was different, and/or design of the power cylinder could have caused this difference.

Furuhama and Sasaki [21] found that oil viscosity was ‘‘useful for improved fuel economy.’’ However, there is a risk of breakdown in the oil film. They found that a multigrade 10W-30 oil would help prevent breakdown of the oil film at the combustion Top Dead Center (TDC) when compared to a single grade oil.

In the hydrodynamic region, Gauthier et al. [18] state that the polymer in a multigrade oil ‘‘induces a considerable decrease in friction loss and energy consumption as compared to the Newtonian oil with the same final viscosity. However, this reduction is obtained through a large decrease in effective viscosity and in thickening effect of the polymer.’’ In the boundary lubricated regions (around the dead centers) it was found that friction force with polymer thickened oil is not very different from the friction force with the base oil alone. In fact, it was found that the polymer type oils give an increase in boundary friction.

As indicated above, lower viscosity oils may lead to increased wear. In particular, wear will increase around Top Ring Reversal of the cylinder bore. This increase in wear may be reduced or eliminated by:

- Improved oil formulations
- More wear resistant materials
- Improved piston and ring designs

Oil Degradation. Researchers at Shell investigated the effects of lubricant degradation on the friction in the piston ring pack [60]. They sampled oil from behind the top ring in an operating engine. The viscometrics of the oil was measured and put in their lubrication model. In the extreme case, degradation increased the predicted friction losses of the ring pack by up to 40 percent.

Oil Windage. Friction can also be affected by crankshaft moving through the oil in the crankcase. This may be through the liquid oil or the oil that is in vapor form. The effect of the crank spinning through air and oil vapor was studied by Thring [37]. The crankcase oil level can significantly affect the windage losses. It has been found that it is possible to reduce parasitic losses in some engines by just reducing the oil level.

Oil Temperatures. Oil temperatures effect the viscosity of the oil. This will affect the friction power losses [49] of the power cylinder. Higher temperatures will reduce the viscosity and reduce friction. Temperatures of the oil on the bore are primarily controlled by the coolant temperature. If temperatures become too high, loss of lubrication can result leading to high wear and/or scuffing.

Oil Summary. Friction reduction is possible with a lower viscosity oil. It is important that a multigrade oil is used to help maintain low oil consumption. Increased wear is also a concern that will need to be addressed.

Overall Conclusions

- Power cylinder friction constitutes a significant portion of the total mechanical friction of the engine. However, as a percent of the total energy developed by the engine it is a small percentage (1.6 to 8.3 percent). Each individual component will result in an even smaller percentage of the total energy. Relative to the work output (brake power) the percent is a little higher (4.1 to 20.9 percent).
- Power cylinder friction can be difficult to measure. Various methods were given. The method that is used will depend on capabilities, accuracy needed, and the amount of money for this type of testing.
- It was shown that power cylinder friction of a fired engine can be almost equal to a motored engine and in some cases it will be higher (0 to 20 percent). High cylinder pressures will tend to increase friction while higher temperatures will tend to reduce friction.
- Even though the overall friction measurement might not be significantly different in a motored versus fired engine, the mechanisms for friction are significantly different. A fired engine will have more friction around TDCF and less friction in the regions of low cylinder pressures. It is only through understanding these differences and designing the power cylinder appropriately that friction will be reduced on the power cylinder components.
- Various methods for predicting friction were given. The most accurate method for predicting power cylinder friction is by using analytical models that predict the lubrication and kinematics of the power cylinder. Other empirical correlations were given to estimate friction.
- A review of the literature from various companies suggested various ways to reduce power cylinder friction. The small top ring widths and low ring tension (oil ring in particular) are common ways to reduce friction. Some friction benefits can be obtained through modifications to the piston skirt. Reduced friction can also be achieved by appropriate oil specifications.
- Friction reductions with oil lower viscosity oils offer the potential of reducing friction. However the oil must be formulated appropriately to minimize possible increases in wear. Design changes to the power cylinder may also be made to minimize the wear.

Acknowledgments

Thanks and credit goes to Rod Radovanovic and Lori Rosenthal at Cummins for the early motoring friction work that they did that is quoted in this paper.

References

[1] Primus, R. J., and Flynn, P. F., 1986, ''The Assessment of Losses in Diesel Engines Using Second Law Analysis,'' *Computer-Aided Engineering and Energy Systems*, Vol. 3, Second Law Analysis and Modeling, ASME, New York, pp. 61–68.

[2] Rao, V. D. N., et al., 1997, ''Engine Studies of Solid Film Lubricant Coated Pistons,'' SAE Paper 970009.

[3] McGeehan, J. A., 1978, ''Literature Review of the Effects of Piston Ring Friction and Lubricating Oil Viscosity on Fuel Economy,'' SAE Paper 780673.

[4] Rogowski, A. R., 1961, ''Method of Measuring the Instantaneous Friction of Piston Friction of Piston Rings in a Firing Engine,'' SAE Paper 379F.

[5] Cleveland, A. E., and Bishop, I. N., 1960, ''Several Possible Paths to Improved Part-Load Economy of Park-Ignition Engines,'' SAE Paper 150A.

[6] Bishop, I. N., 1965, ''Effect of Design Variables on Friction and Economy,'' SAE Paper 812A.

[7] Ricardo, H., and Hempson, J. G. G., 1968, *The High Speed Internal Combustion Engine*, 5th ed., Blackie, London, pp. 139–141.

[8] Ting, L. L., 1985, ''A Review of Present Information on Piston Ring Tribology,'' SAE Paper 852355.

[9] Patton, K. J., Nitschke, R. G., and Heywood, J. B., 1989, ''Development and Evaluation of a Friction Model for Spark-Ignition Engines,'' SAE Paper 890836.

[10] Kovach, J. T., Tsakiris, E. A., and Wong, L. T., 1982, ''Engine Friction Reduction for Improved Fuel Economy,'' SAE Paper 820085.

[11] Hami, K., et al., 1990, ''Development of a Friction Prediction Model for High Performance Engines,'' Lubr. Eng., **47**, No. 7, pp. 567–573.

[12] Koch, F., et al., ''PIFFO—Piston Friction Force Measurements During Engine Operation,'' SAE Paper 960306.

[13] Betz, G., Gabele, H., and Assmus, H-O, 1989, ''Friction Power and Noise Behaviour of the Piston Assembly,'' IMechE, C375/019.

[14] Goenka, P. K., and Meernik, P. R., 1992, ''Lubrication Analysis of Piston Skirts,'' SAE Paper 920490.

[15] Essig, G., 1984, ''Recent KS Work on the Reduction of Passenger Car Engine Fuel Consumption,'' SAE Paper 841224.

[16] Winterbone, D. E., and Tennant, D. W. H., 1981, ''The Variation of Friction and Combustion Rates During Diesel Engine Transients,'' SAE Paper 810339.

[17] Haines, S. N. M., and Shields, S. A., 1989, ''The Determination of Diesel Engine Friction Characteristics by Electronic Cylinder Disablement,'' Journal of Power Engineering, **203**, pp. 203–204.

[18] Gauthier, A., Constans, B., Parrin, H., and Roux, F., 1983, ''Lubricants Effects on Piston/Rings/Liner Friction in an Instrumented Single Cylinder Diesel Engine,'' SAE Paper 872034.

[19] Ciulli, E., 1992, ''A Review of Internal Combustion Engine Losses: Part 1—Specific Studies on the Motion of Pistons, Valves and Bearings,'' J. Autom. Eng., **206**, pp. 223–236.

[20] Furuhama, S., Takiguchi, M., and Tomizawa, K., 1981, ''Effect of Piston and Piston Ring Designs on the Piston Friction Forces in Diesel Engines,'' SAE Paper 810977.

[21] Furuhama, S., and Sasaki, S., 1983, ''New Device for the Measurement of Piston Frictional Forces in Small Engines,'' SAE Paper 831284.

[22] Eilon, S., and Saunders, O. A., 1957, ''A Study of Piston Ring Lubrication,'' Proc. Inst. Mech. Eng., **171**, No. 11, pp. 427–433.

[23] Parker, D. A., et al., 1989, ''The Measurement and Reduction of Piston Assembly Friction,'' SAE Paper 890417.

[24] Yun, J. E., and Kim, S. S., 1992, ''An Improved Approach to the Instantaneous IMEP Method for Piston-Ring Assembly Friction Force Measurement,'' JSME Int. J., Ser. II, **35**, No. 2, pp. 310–318.

[25] DeFarro Barros, A., and Dyson, A., 1960, ''Piston Ring Friction-Rig Measurements with Low Viscosity Oils,'' J. of Inst. of Petroleum, **46**, No. 433, pp. 1–18.

[26] Uras, H. M., and Patterson, D. J., 1983, ''Measurement of Piston and Ring Assembly Friction Instantaneous IMEP Method,'' SAE Paper 830416.

[27] Uras, H. M., and Patterson, D. J., 1985, ''Oil and Ring Effects on Piston-Ring Assembly Friction by the Instantaneous IMEP Method,'' SAE Paper 850440.

[28] Uras, H. M., and Patterson, D. J., 1987, ''Effect of Some Piston Variables on Piston and Ring Assembly Friction,'' SAE Paper 870088.

[29] Uras, H. M., Patterson, D. J., 1984, ''Effect of Some Lubricant and Engine Variables on Instantaneous Piston and Ring Assembly Friction,'' SAE Paper 840178.

[30] Ku, Y., and Patterson, D. J., 1988, ''Piston and Ring Friction by the Fixed Sleeve Method,'' SAE Paper 880571.

[31] Rezeka, S. F., and Henein, N. A., 1984, ''A New Approach to Evaluate Instantaneous Friction and its Components in Internal Combustion Engines,'' SAE Paper 840179.

[32] Takiguchi, M., and Furuhama, S., 1979, ''Measurement of Piston Friction Force in Actual Operating Diesel Engine,'' SAE Paper 790855.

[33] Dursunkaya, Z., et al., 1993, ''A Model of Piston Secondary Motion and Elastohydrodynamic Skirt Lubrication,'' ASME Paper 93-ICE-7.

[34] Wong, V. W., et al., 1994, ''A Numerical Model of Piston Secondary Motion and Piston Slap in Partially Flooded Elastohydrodynamic Skirt Lubrication,'' SAE Paper 940696.

[35] DeFarro Barros, A., and Dyson, A., 1960, ''Piston Ring Friction-Rig Measurements with Low Viscosity Oils,'' J. Inst. Pet., **46**, No. 433, pp. 1–18.

[36] Rhodes, M. L. T., 1970, ''Piston Research and Development Techniques,'' AED Group Symp, UK.

[37] Thring, R. H., 1992, ''Engine Friction Modeling,'' SAE Paper 920482.

[38] CASE Web Page, http://www.egr.msu.edu/ERL/case/case.htm.

[39] Tian, T., Wong, V. W., Heywood, J. B., 1996, ''A Piston Ring-Pack Film Thickness and Friction Model for Multigrade Oils and Rough Surfaces,'' SAE Paper 962032.

[40] Tian, T., Wong, V. W., and Heywood, J. B., 1998, ''Modeling the Dynamics and Lubrication of Three Piece Oil Control Rings in Internal Combustion Engines,'' SAE Paper 982657.

[41] Keribar, R., Dursunkaya, Z., and Flemming, M. F., 1991, ''An Integrated Model of Ring Pack Performance,'' ASME J. Eng. Gas Turbines Power, **113**, pp. 382–389.

[42] Keribar, R., Dursunkaya, Z., and Ganapathy, V., 1993, ''An Integrated Design

Analysis Methodology to Address Piston Tribological Issues,'' SAE Paper 930793.
[43] Ricardo Software Home Page, http://www.ricardo.com/software.htm.
[44] AVL GLIDE Home Page, http://www.avl.com/html/2901.htm.
[45] Paranjpe, R. S., and Cusenza, A., 1992, ''FLARE: An Integrated Software Package for Friction and Lubrication Analysis of Automotive Engines: Part II—Experimental Validation,'' SAE Paper 920488.
[46] Jeng, Y. R., 1992, ''Friction and Lubrication Analysis of Piston-Ring Pack,'' SAE Paper 920492.
[47] Cullen, J. A., Dixon, R. F., and Ma, J., 1996, ''Plastic Oil Rings for Diesel Engines: A Preliminary Evaluation,'' SAE Paper 960049.
[48] Cullen, J. A., and Frodsham, G. A., 1997, ''Reduced Cross Section Compression Rings for Diesel Engines,'' SAE Paper 971146.
[49] Schelling, H., and Freier, R, 1993, ''Parameters for Frictional Losses in Pistons,'' SAE Paper 937083.
[50] ''Engine Friction Review,'' 1988, AVL Technical Report, C&I Report 15, Aug. 1988.
[51] Parker, D. A., Adams, D. R., and Donnison, G., 1989, ''The Measurement and Reduction of Piston Assembly Friction,'' IMechE, C375/017, pp. 27–34.
[52] Wade, W. R., et al., 1984, ''Combustion, Friction and Fuel Tolerance Improvements for the IDI Diesel Engine,'' SAE Paper 840515.
[53] Stewart, R. M., and Selby, T. W., 1977, ''The Relationship Between Oil Viscosity and Engine Performance—A Literature Search,'' SAE Paper 770372.
[54] Hamaguchi, H., Maeda, Y., and Maeda, T., 1981, ''Fuel Efficient Motor Oil for Japanese Passenger Cars,'' SAE Paper 810316.
[55] Griffiths, D. W., and Smith, D. J., 1985, ''The Importance of Friction Modifiers in the Formulation of Fuel Efficient Engine Oils,'' SAE Paper 852112.
[56] Kennedy, S., and Moore, L. D., 1987, ''Additive Effects on Lubricant Fuel Economy,'' SAE 872121.
[57] Moore, S. L., 1986, ''Fuel Efficient Lubricants—Performance and Protection in a Highly Rated Turbocharged Diesel Engine,'' The Inst. of Mech. Engineers, Seminar and Exhibition, Dec. 2, 1986.
[58] McGeehan, J. A., 1983, ''Effect of Piston Deposits, Fuel Sulfur, and Lubricant Viscosity on Diesel Engine Oil Consumption and Cylinder Bore Polishing,'' SAE Paper 831721.
[59] McGeehan, J. A., et al., 1993, ''Selecting Diesel Crankcase Oils for Low-Sulfur Fuel,'' SAE Paper 932845.
[60] Taylor, R. I., and Bell, J. C., 1993, ''The Influence of Lubricant Degradation on Friction in the Piston Ring Pack,'' Paper presented at the 20th Leeds/Lyon Symposium on Tribology, Lyon, 7–11 September 1993.

Predicted Effects of Cylinder Kit Wear on Blowby and Oil Consumption for Two Diesel Engines

D. E. Richardson
Cylinder Systems Development,
Cummins Engine Company,
Charleston, SC 29405
e-mail: dan.e.richardson@cummins.com

S. A. Krause
Federal-Mogul Power Train Systems
e-mail: steven_krause@fmo.com

Durability is very important for current diesel engines. Diesel engine manufacturers are trying to make the engines live as long as possible before overhaul. The time to overhaul for an engine is usually dictated by high oil consumption or blowby. Therefore, it is necessary to understand how wear affects the cylinder kit dynamics, oil consumption, and blowby in an engine. This paper explores the effect of power cylinder component (rings and cylinder bore) wear by using a cylinder kit dynamics model. The model predicts how wear will affect ring motion, inter-ring gas pressure, blowby, etc. The parameters studied were: liner wear, ring face wear, and ring side wear. Two different engines were modeled. The characteristics of these two engines are very different. As a result, the effects of wear are different and the corresponding durability will be different. This illustrates the need to model each individual type of engine separately. The modeling shows that top ring face wear is very significant for maintaining good oil and blowby control. Liner wear is important, but does not have as large an effect as ring wear. The effects of side wear are significant for these two cases. [S0742-4795(00)00203-9]

Background

To meet the durability goals that are required to be competitive in the future it is necessary to better understand the effects of wear in the engine. In particular, the cylinder kit components can contribute significantly to the perceived durability of the overall engine. When an engine has high blowby or high oil consumption the engine is perceived as ''worn out.'' As a result it is necessary to understand how cylinder kit wear affects the performance (oil consumption and blowby) of the engine.

This report addresses the issue through cylinder kit modeling. The advantage of the cylinder kit model is that many different cases can be tested in a relatively short period of time. This also is only a fraction of the cost of engine tests. It is also easy to separate out the contribution of each component.

The parameters that are studied are: liner wear, ring face wear, and ring side wear. There are other factors that will affect oil consumption and blowby that are not included in this report. Some of these factors are carbon on the piston and liner, turbocharger, valve guides, etc.

A significant amount of work has been done developing cylinder kit models [1–4]. The cylinder kit dynamics code that was used for this analysis was the Ricardo RINGPAK, public domain version [4]. Much of the modeling work in the past has been either to validate the model or to help solve a problem. In particular, oil consumption and blowby have been a particular focus of the work. The unique aspect of this work is it attempts to take the predictions to investigate the effects on long term durability of the power cylinder.

Modeled Cylinder Kit Wear

To run the cylinder kit models it is necessary to specify the type of wear that is present. In some cases it was not possible to model the wear exactly, and approximations had to be made. This section describes the assumptions that were used for the wear calculations.

There are two engines that were studied. Details of the engine ratings and sizes are not given. This is because the objective is to illustrate a technique not give a detailed review of the performance characteristics of a particular engine.

Both engines studied have low oil consumption. However, ring motion and gas flows through the ringpacks are significantly different. This is because both engines rely on different mechanisms to lower oil consumption. As a result, both must be studied separately.

Liner Wear

Diesel Engine No. 1. Actual liner wear data from an engine of the same type that had relatively high liner wear (26 microns maximum depth) was obtained. The wear trace from this one case was then scaled up to simulate increased wear. Two methods were used for scaling the wear profile. In one case the width of the wear band was held constant and the depth of wear was increased (Fig. 1). In the other case both the width and depth of the wear band were increased (Fig. 2). The amount that the wear depth was increased was arbitrarily chosen to be 50, 100, and 150 microns.

Diesel Engine No. 2. A similar approach was used for modeling the liner wear on Diesel Engine No. 2. The graphs shown in

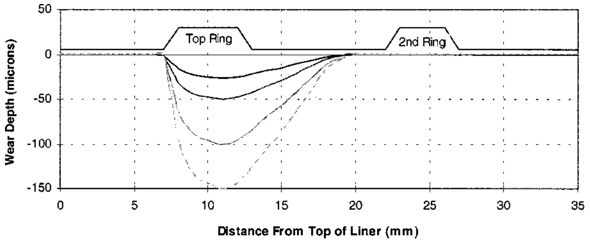

Fig. 1 Diesel engine No. 1 linear wear used in model (width constant)

Contributed by the Internal Combustion Engine Division of THE AMERICAN SOCIETY OF MECHANICAL ENGINEERS for publication in the ASME JOURNAL OF ENGINEERING FOR GAS TURBINES AND POWER. Manuscript received by the ICE Division November 2, 1998; final revision received by the ASME Headquarters November 22, 1999. Technical Editor: D. Assanis.

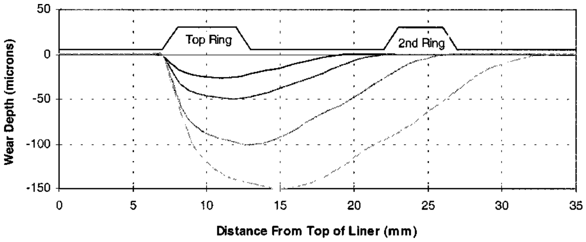

Fig. 2 Diesel engine No. 1 linear wear used in model (width increasing)

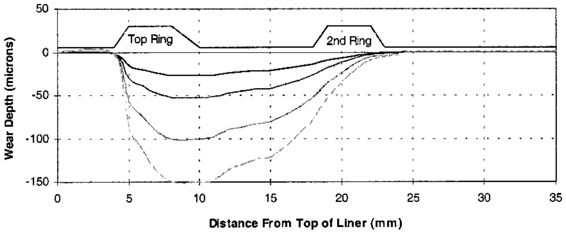

Fig. 3 Diesel engine No. 2 linear wear used in model (width constant)

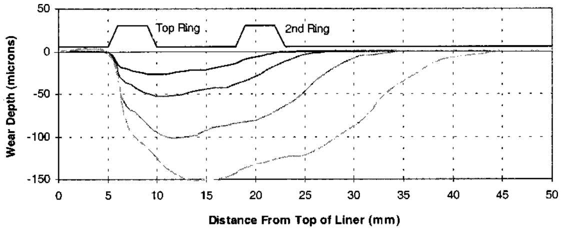

Fig. 4 Diesel engine No. 2 linear wear used in model (width increasing)

Fig. 3 and Fig. 4 are based on actual measured liner wear for one engine. The data were then scaled to obtain wear depths of 26, 50, 100, and 150 microns.

Comments. It should be noted that in the figures, the ring locations when the piston is at Top Dead Center (TDC) are shown schematically. In the case where the width of the wear band does not increase, the second ring does not reach the worn portion of the liner on Diesel Engine No. 1. On Diesel Engine No. 2 the second ring only slightly enters the worn region. For both Diesel Engine No. 1 and Diesel Engine No. 2 in the case where the width of the wear band increases the second ring is significantly affected by the liner wear.

Description of Liner Wear Modeling. The cylinder kit dynamics code that was used for the modeling did not inherently include the effect of liner wear. To be able to model this effect, the source code of the program was modified. The program was altered such that end gap of the rings would increase because of the wear step. As a result, the end gap only increases around TDC. This is shown in Fig. 5 for the largest wear case of Diesel Engine No. 1 (see Fig. 1).

The model does not include the effect of the radial inertia of the ring as it conforms to the wear scar. This can affect the oil film thickness predictions.

Ring Face Wear. Wear of the ring face was considered at the same levels as the liner wear. Wear depths of 26, 50, 100, and 150 microns were modeled. Two factors were included in the model for ring face wear.

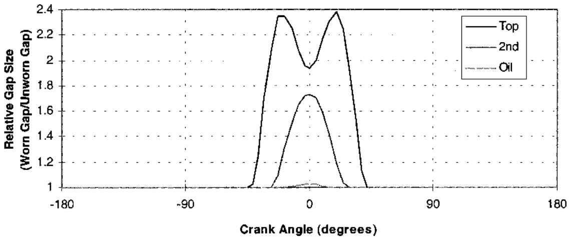

Fig. 5 Increase in ring end gap because of the worn liner (diesel engine No. 1, Ref. Fig. 2, 150 micron wear depth)

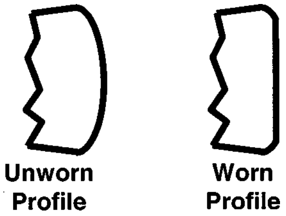

Fig. 6 Schematic of unworn and worn top ring face profiles

1. It was assumed that the face profile of the ring was nearly flat (Fig. 6) due to wear.
2. The ring end gap was increased by the corresponding amount of the wear. This was determined by the following formula:

$$\text{Increase in Gap Width} = 2\pi(\text{wear Depth}). \tag{1}$$

Ring Side Wear. The wear of the side of the ring was modeled by decreasing the width of the ring in the model. This was done at wear depths of 26, 50, 100, and 150 microns also.

Results

Summary of Diesel Engine No. 1 Results. Diesel Engine No. 1 was modeled at 1800 RPM and 1460 N-m torque.

Diesel Engine No. 1 Ring-Pack Dynamics. There are two distinct modes of ringpack dynamics that occurred as a result of varying amounts of wear on Diesel Engine No. 1. These modes will be labeled Mode 1 and 2 as described below. The predicted inter-ring gas pressure is shown in Fig. 7 and the corresponding ring motion is shown in Fig. 8.

Mode 2 ringpack dynamics is characteristic of the more highly worn top ring face and liner on this engine. It can be seen that in Mode 2, the inter-ring gas pressure is higher than the cylinder pressure for much of the cycle (Fig. 7). This holds the top ring up on the top side of the ring groove (Fig. 8). This type of behavior causes an increase in blowby because of the high inter-ring gas pressure. Also, the high inter-ring gas pressure might be bad for

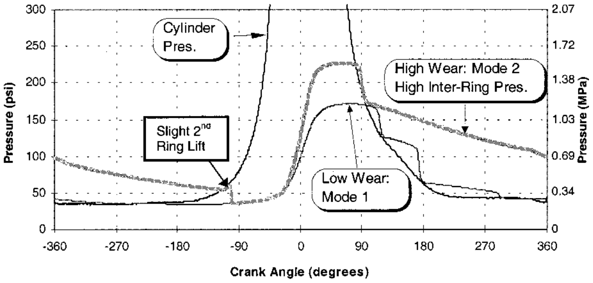

Fig. 7 Predicted inter-ring gas pressure-diesel engine No. 1 engine (mode 1=low wear, mode 2=high wear)

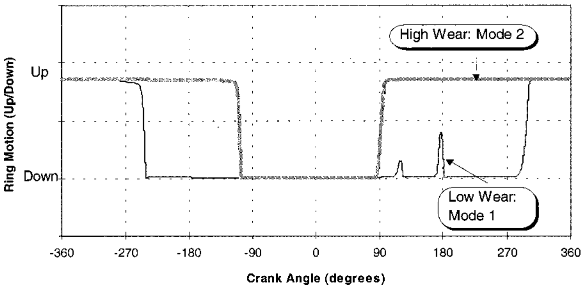

Fig. 8 Predicted top ring motion-diesel engine No. 1 engine (mode 1=low wear, mode 2=high wear)

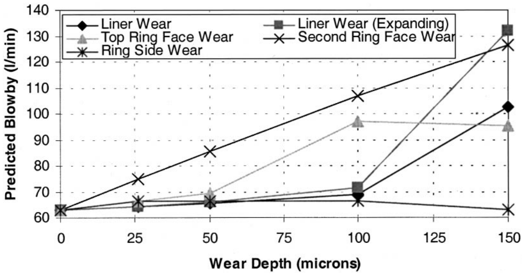

Fig. 9 Predicted effect of wear on blowby-diesel engine No. 1 engine (1800 rpm, full load, single factor effect)

oil consumption. It provides a continuous spray of gases and oil from the second land to the combustion chamber through the end gap over much of the cycle.

Mode 1 ringpack dynamics is characteristic of unworn and lightly worn top ring face and liner. In Mode 1 the top ring lifts up partially, but does not stay up. As a result the inter-ring gas pressure closely follows the cylinder pressure after 90° ATDC. This results in lower blowby because the gas pressure that builds up on the second land vents upward around the back of the top ring rather than downward past the second ring which is blowby. This type of behavior might be better for oil control because there are only a couple of brief times that the top ring lifts partially. Oil and gas flow will be restricted when it has to flow around the back of the ring as opposed to a direct flow through the end gap. Also, the gas forces blowing gas and oil upward are smaller than in Mode 2 type behavior. As wear increases on the top ring face and liner it causes the ring pack dynamics to switch from mode 1 to mode 2.

In each of these Modes of ringpack behavior, the second ring motion is very stable. The second ring remains seated on the bottom side of the ring groove throughout the cycle. As a result, the ring acts as a good gas seal which results in relatively low blowby when compared to Diesel Engine No. 2 (see below). In Mode 2 there is a very small lift of the second ring that occurs about −100° BTDC. This causes the sudden drop in predicted inter-ring gas pressure at that time.

Diesel Engine No. 1 Blowby Predictions—Single Factor Effects The effect of each type of wear was considered independent of all the other types of wear. For example, when top ring face wear was modeled, the liner and second ring were not considered to be worn. This was done to determine the contribution of each factor to the increase in blowby. The model results of Diesel Engine No. 1 are shown in Fig. 9.

It is noted that liner wear does not significantly affect the predicted blowby until the wear becomes greater than 100 microns. At this point the mode of ring dynamics change from Mode 1 type behavior to Mode 2.

Top ring wear starts to affect blowby after only 50 microns of wear. Once again this is because of the change in ring dynamic behavior from Mode 1 to Mode 2.

The second ring face wear has the most significant effect on blowby for Diesel Engine No. 1 engine. Blowby increases continuously as the ring wears. The ring pack behavior caused by this type of wear is always Mode 1. It never transitions to Mode 2. The increase in blowby is solely due to the increase in the gas flow area through the second ring.

There is no significant effect on ring motion or blowby due to side wear on the top or second ring.

Diesel Engine No. 1 Oil Consumption Predictions. There is currently no reliable model to predict absolute levels of oil consumption changes. However, inferences can be made about the effect of the ringpack dynamics on oil consumption.

As mentioned above, it is thought that the Mode 1 type of ringpack dynamics will be better for oil control than Mode 2. This is because in Mode 2 the gas flow from the second land into the combustion chamber will increase. This reverse flow is called ''blowback.'' Oil will be carried with the gases that blowback into the cylinder. This has the potential for being burned and causing an increase in oil consumption. The model predictions on ''blowback'' are shown in Fig. 10.

It can be seen that as wear of the top ring face and liner increases, the blowback will increase. The sudden increases in blowback are due to the change in the mode of ringpack dynamics. Also it can be seen that wear of the second ring will cause a net decrease in blowback. This is because of the increased downward flow of the gases due to the increase in gas flow area caused by the worn ring face.

Another parameter that is considered to affect oil consumption is the oil film thickness under the top ring. Figure 11 shows a comparison of the predicted film thickness for the unworn and worn rings. The figure predicts radial ring collapse for both the worn and unworn rings. This can occur when the pressure below the top ring becomes larger than the pressure above the ring. This type of pressure imbalance will try to force the ring up off the bottom side of the groove and/or collapse the ring radially inward

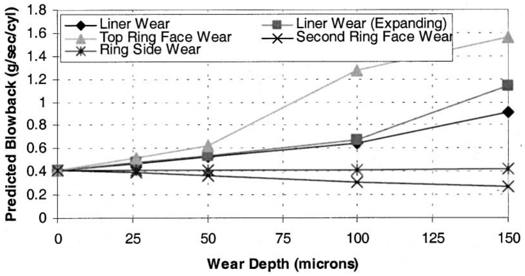

Fig. 10 Predicted effect of wear on blowback-diesel engine No. 1 engine (gas flow from the second land to the combustion chamber)

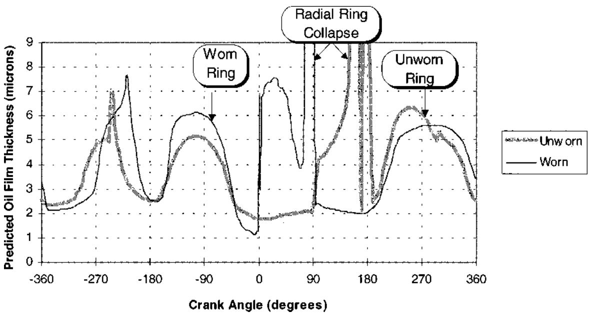

Fig. 11 Predicted oil film thickness under the top ring-diesel engine No. 1 engine (unworn ring versus worn ring—150 microns wear)

[5]. If inertial and/or oil suction forces prevents the ring from lifting upward, the ring will collapse radially inward. When the ring collapses, oil and gases will blow past the front of the ring and into the combustion chamber. Once the oil has been blown into the combustion chamber it is susceptible to being consumed.

It is thought oil consumption will be lower when the radial ring collapse occurs late in the cycle rather than early. This is because there will be less opportunity for the oil that is blown upward to be burned if it occurs later in the cycle. It can be seen that the unworn ring will perform better than the worn ring (because radial collapse occurs later in the cycle). The earlier radial collapse of the worn ring occurs primarily because of the higher inter-ring gas pressures caused by the increased gas flow areas. Once again, this is an indication that oil consumption will get worse with the worn ring.

It is also observed that the oil film thickness under the top ring just after TDC (0 deg) is large for the worn case. This is caused by the flat profile of the worn ring face and the pressure forces that act on the ring. This will be described in more detail for Diesel Engine No. 2 (Fig. 17). This could also be a cause for increased oil consumption.

Diesel Engine No. 1 Experimental Results. The advantage of the cylinder kit model is that it is very inexpensive to run different cases. However, it was necessary to verify the model at a few key conditions. As a result, two engine tests were run with ''artificial wear'' machined into the liners per the dimensions shown in Fig. 1. Two cases were tested: 100 and 150 microns liner wear depth. These two wear amounts were chosen because the model showed a step change in ring dynamics and gas flow between these two values. The results are seen in Table 1.

In Table 1 and Fig. 12 it can be seen that the step change in blowby and oil consumption that was predicted between 100 and 150 microns of liner wear was observed experimentally. There is a very good correlation of the predicted blowby and actual.

Table 1 Percent increase in blowby and oil consumption due to wear

	100 microns	150 microns
Blowby Increase		
Predicted	9%	63%
Actual	19%	100%
Oil Consumption Increase		
Predicted	Small Increase	Step Change Increase
Actual	77%	225%

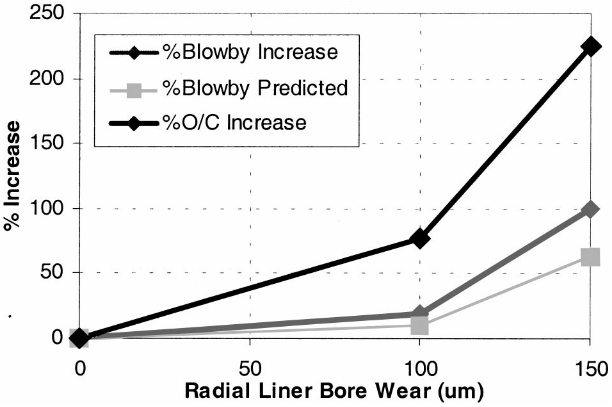

Fig. 12 Predicted increases in blowby and oil consumption with linear wear (experimental and predicted)

Diesel Engine No. 1 Conclusions

- There are two distinct types of ring motion on Diesel Engine No. 1 that can result from wear. When wear reaches a certain level, the ringpack dynamics change. This causes a sudden increase in blowby.
- The change in ring pack dynamics predicted as a result of wear, causes an increase in oil consumption. This is due to an increase in oil blown into the combustion chamber by the high inter-ring gas pressures.
- The changes in blowby and oil consumption because of wear will likely result in a perception that the engine is ''worn out.''
- Face wear of the top ring will result in the change of ringpack dynamics sooner than liner wear. This indicates that it is more important to have low ring wear than liner wear to achieve better durability.
- Face wear of the second ring will result in a large change in blowby. However, the ringpack dynamics do not change significantly. As a result, it might not adversely affect oil consumption. If blowby is the major consideration in the perceived durability, this might be important. If oil consumption is the major factor, then second ring wear is not so important.
- Top and second ring side wear does not significantly affect blowby or ringpack dynamics in the predictions.
- Oil film thickness predictions suggest that the oil consumption will get worse as the top ring face wears.
- Model predictions were verified with of engine tests. These tests showed the step change in oil consumption and blowby predicted between 100 and 150 microns of liner wear.

Summary of Diesel Engine No. 2 Results. Diesel engine No. 2 was modeled at 1800 rpm and 1460 N-m torque.

Diesel Engine No. 2 Ring-Pack Dynamics. There is only one type of general ring motion and inter-ring gas pressure behavior on Diesel Engine No. 2. This is true regardless of the wear that occurs on the cylinder kit parts. The predictions of inter-ring gas pressure are shown in Fig. 13 and ring motion is shown in Fig. 14. It can be seen that the inter-ring gas pressure is very low on Diesel Engine No. 2. This is because the second ring is unstable between

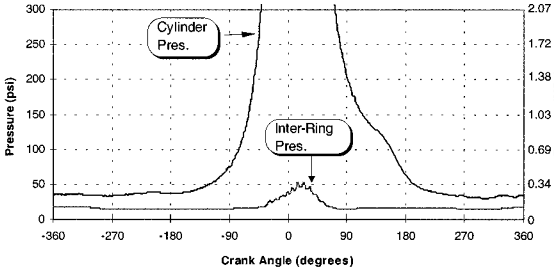

Fig. 13 Predicted inter-ring gas pressure-diesel engine No. 2 engine

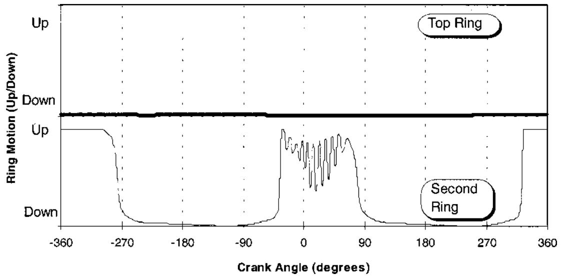

Fig. 14 Predicted ring motion-diesel engine No. 2 engine

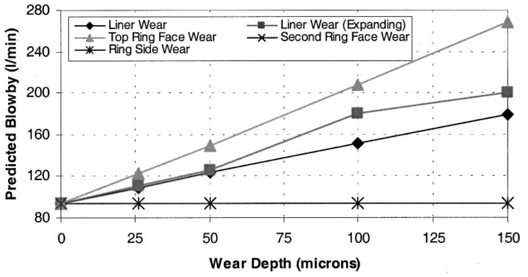

Fig. 15 Predicted effect of wear on blow by-diesel engine No. 2 engine (1800 rpm, full load, single factor effect)

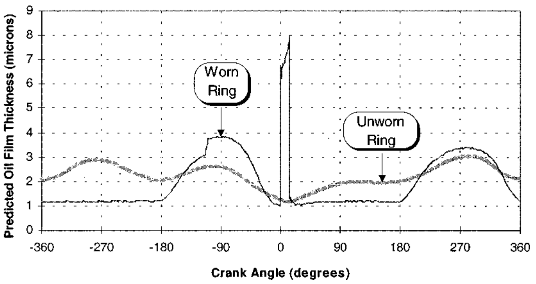

Fig. 16 Predicted oil film thickness under the top ring-diesel engine No. 2 engine (unworn ring versus worn ring—150 microns wear)

−50 deg and 70 deg. As the ring moves up and down, the gases vent around the back of the ring. As a result, the primary leakage path for blowby is around the back of the ring. In short, the second ring on Diesel Engine No. 2 does not seal the inter-ring gases. This causes Diesel Engine No. 2 to have higher blowby than Diesel Engine No. 1. This same type of inter-ring gas pressure (and ring motion) has been observed experimentally on another engine [5]. As a result it was felt that this type of prediction is accurate.

Diesel Engine No. 2 Blowby Predictions—Single Factor Effects The prediction of blowby caused by the wear of each component is shown in Fig. 15. It should be noted that the blowby on Diesel Engine No. 2 is much more sensitive to top ring face wear and liner wear. The increases in blowby are much more significant than what was observed on Diesel Engine No. 1. This is because the second ring does not seal gases. Any increases in the amount of gases that flow into the inter-ring region will result in blowby on Diesel Engine No. 2. As a result, when the top ring end gap flow area increases due to wear, blowby will go up. On Diesel Engine No. 1 this effect is moderated because of the seal caused by the second ring.

The second thing that should be noted is that the wear of the ring will cause higher increases in blowby than a corresponding wear of the liner. This is because when the top ring face wears, the gas flow area at the gap is increased over the entire cycle. However, liner wear only increases the gap flow area around TDC. Once again, this illustrates that it is more important to have low ring wear than liner wear.

It is interesting to note that second ring face wear had no significant effect on blowby. This is because the primary gas flow is around the back of the second ring. The increase in gas flow area in the end gap caused by wear of the second ring face, does not affect blowby.

The side wear of the top and second rings does not affect the predicted blowby.

Diesel Engine No. 2 Oil Consumption Predictions. No significant changes in the ring motion or inter-ring gas pressure are predicted as a result of wear. Since the inter-ring gas pressures are so low on Diesel Engine No. 2, there is **no** predicted ''blowback'' (see above for description on Diesel Engine No. 1) for any of the cases modeled. As a result there should be no loss in oil control as the engine wears due to gas flows and ringpack dynamics.

Figure 16 shows the predicted oil film thickness under the top ring for the unworn and worn rings. The worn ring shows an increase in film thickness just after TDC (0 deg). This may cause an increase in oil consumption. However in other locations the oil film thickness for the worn ring is low when the piston is descending and high when the piston is rising. This is an ideal type of scraping action for the ring and might lower oil consumption. Because of these two conflicting results it is not possible to predict the final effect on oil consumption.

An unusual spike occurs in the oil film thickness starting at 0 deg for the worn ring case. To model a worn ring, a very flat face profile was used. It is believed that the spike in oil film thickness is caused the combination of the flat profile and changing boundary conditions at top ring reversal. At the ring reversal the high pressure above the ring will extend over a larger portion of the ring face and cause the ring to move back. This is shown in a very simple schematic in Fig. 17.

Diesel Engine No. 2 Conclusions

- Blowby on Diesel Engine No. 2 is much more sensitive to wear than Diesel Engine No. 1. For equivalent amounts of wear the blowby increase in Diesel Engine No. 2 will be significantly more than Diesel Engine No. 1.
- Blowby is affected more by top ring face wear than liner wear. This indicates it is more important to have low ring wear than liner wear for good blowby control.

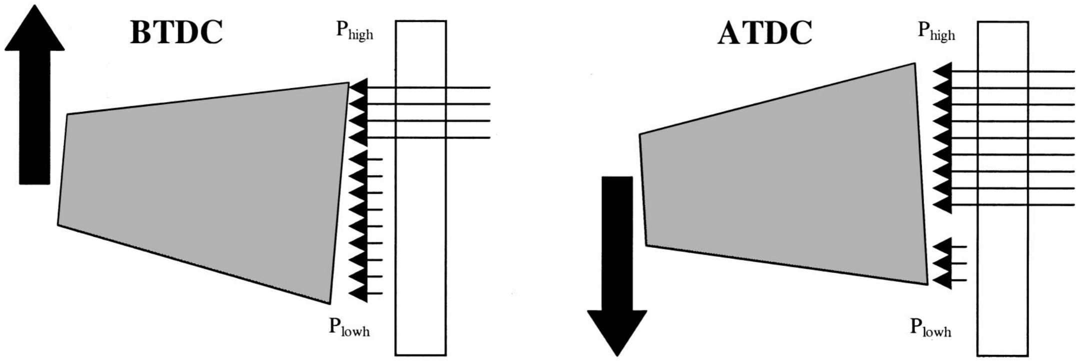

Fig. 17 Simple schematic of radial pressure forces acting on the ring face

- The ringpack dynamics on Diesel Engine No. 2 are very stable and are not significantly affected by wear of the components. As a result, there might not be very much change in oil consumption.

Overall Conclusions

- Wear of the top ring face and wear of the liner increase blowby on Diesel Engine No. 2 engine more than Diesel Engine No. 1. However, the ringpack dynamics do not change on Diesel Engine No. 2 while they do no Diesel Engine No. 1. This indicates that Diesel Engine No. 1 oil consumption might deteriorate more with wear than Diesel Engine No. 2.
- If blowby is the major factor in perceived durability, then Diesel Engine No. 2 will have less apparent durability than Diesel Engine No. 1. If oil consumption is the major factor in perceived durability, Diesel Engine No. 1 will have lower apparent durability.
- Top ring face wear affects blowby and ringpack dynamics more than liner wear. The increase in blowby is due primarily to the increase in end gap caused by the wear of the ring or liner. When the ring wears the end gap will be increased over the entire cycle whereas liner wear will only increase the end gap around TDC. As a results it is more important to maintain low ring wear than liner wear for improved durability.
- The second ring face wear significantly affects blowby on Diesel Engine No. 1 but has little effect on ringpack dynamics. As a result, oil consumption might not be adversely affected by second ring face wear on Diesel Engine No. 1. On Diesel Engine No. 2, the second ring face wear has no significant effect on blowby or ringpack dynamics.
- Top and second ring side wear do not significantly affect blowby or ringpack dynamics in the predictions for Diesel Engine No. 1 and Diesel Engine No. 2. However, if the side wear becomes too large, pounding of the ring might cause a breakage that will cause a loss of blowby and oil control. This was not modeled.
- The predicted effect of wear on Diesel Engine No. 1 and Diesel Engine No. 2 engines were very different. As a result, it can be seen that the results shown here are not directly transferable to different engines. Each engine needs to be modeled to determine the effect of wear on its durability.

References

[1] Mayer, J. E., 1974, ''Piston Ring Lubrication and Cylinder Bore Wear Analysis, Part I—Theory,'' J. Lubr. Technol., pp. 305–314.

[2] Namazian, M., and Heywood, J. B., 1982, ''Flow in the Piston-Cylinder-Ring Crevices of a Spark-Ignition Engine: Effect on Hydrocarbon Emissions, Efficiency and Power,'' SAE Paper 820088.

[3] Kuo, T., et al., 1989, ''Calculation of Flow in the Piston-Cylinder-Ring Crevices of a Homogeneous-Charge Engine and Comparison with Experiment,'' SAE Paper 890838.

[4] Keribar, R., Dursunkaya, Z., and Flemming, M. F., 1991, ''An Integrated Model of Ring Pack Performance,'' ASME J. Eng. Gas Turbines Power, pp. 382–389.

[5] Richardson, D. E., 1996, ''Comparison of Measured and Theoretical Inter-Ring Gas Pressure on a Diesel Engine,'' SAE Paper 961909.

A Probabilistic Approach to Engine Balance

Dinu Taraza
Mechanical Engineering Department,
Wayne State University,
Detroit, MI 48202

The paper presents an original probabilistic model of the balance of internal combustion engines. The model considers the manufacturing tolerances and predicts the most probable value of the first-order residual unbalance for engines that—theoretically—have the first order forces and moments balanced. It has been found that, assuming normal distributions of the geometric and mass parameters of the reciprocating mechanisms of a multicylinder engine, the unbalancing forces and moments are statistically distributed according to a Rayleigh law. The mode of the Rayleigh distribution, which represents the most probable value of the residual unbalance, is expressed in terms of the statistical characteristics of the parameters subjected to manufacturing tolerances. In this way, the tolerances and, especially the ones admitted for the reciprocating masses, are directly correlated to the expected value of the residual unbalance making it possible to establish reasonable limits for these tolerances. Validation of the probabilistic balance model is demonstrated by computer simulation. [S0742-4795(00)01704-X]

Introduction

The classical theory of the reciprocating internal combustion engine balance is based on the assumption that all reciprocating mechanisms of a multicylinder engine are perfectly identical. In this case, for certain angular arrangements of the cranks around the axis of the crankshaft some harmonic components of the resultant Reciprocating Inertia Forces (REIF) may be perfectly balanced.

Actually, the manufacturing tolerances of the parts belonging to the reciprocating mechanisms of the same engine determine slightly different values of the reciprocating inertia forces for the different cylinders of the engine. In this situation, a perfect balance is no more possible and residual unbalances subsist for harmonic orders that, according to the classical theory are completely balanced.

This situation is especially important for all engines having the second order REIF balanced according to the classical theory of balance. For these engines, the major unbalance is caused by the first order residual unbalance of the REIF which is several times larger than the unbalance predicted by the classical theory.

In order to be able to predict the most probable value of the residual unbalance and to correlate it to the manufacturing tolerances, a probabilistic approach is used to formulate a random-vector interpretation of the first order REIF.

Random Vector Interpretation of the First Order REIF

According to the classical theory of balance [1,2] the first order REIF corresponding to cylinder ‘‘*j*’’ may be interpreted[1] as the projection on the cylinder axis of a constant modulus vector

$$|F_{I_j}| = (m_{tr})_j r_j \omega^2, \tag{1}$$

which rotates with the same speed as the crankshaft and is directed along the axis of the crank corresponding to cylinder ‘‘*j*’’.

The classical theory of balance doesn't make any difference between the reciprocating masses m_{tr} and crank radii r belonging to the different cylinders of the same engine. At the same time, the angular position of the cranks θ_j are considered perfectly equal to the theoretical firing interval of the engine.

Actually, all these magnitudes are subjected to manufacturing tolerances and take slightly different values for the different cylinders of the same engine:

$$\left[\begin{array}{l} (m_{tr})_j = \overline{m}_{tr} \pm \Delta m_{tr} \\ r_j = \overline{r} \pm \Delta r \\ \theta_j = \overline{\theta}_j \pm \Delta \theta \end{array}\right. . \tag{2}$$

In mass production, the machined dimensions could be considered as distributed according to a normal law

$$f(z) = \frac{1}{\sqrt{2\pi}\sigma_z} \exp\left[-\frac{1}{2}\left(\frac{z-\overline{z}}{\sigma_z}\right)^2\right], \tag{3}$$

where $\overline{z}$ represents the mean value of the random variable z and σ_z its standard deviation. According to the properties of the normal distribution, 99.73 percent of all possible values of a normally distributed random variable are situated in the interval $\overline{z} \pm 3\sigma_z$. Consequently, the nominal dimensions specified on the technical drawing may be considered as mean values and the corresponding tolerances as $\pm 3\sigma$ limits:

$$\left[\begin{array}{l} \sigma_m = \frac{1}{3}\Delta m_{tr} \\ \sigma_r = \frac{1}{3}\Delta r \\ \sigma_\theta = \frac{1}{3}\Delta \theta \end{array}\right. . \tag{4}$$

In this situation, the vector representing the REIF for the cylinder ‘‘*j*’’ will have a modulus equal to the product of two normally distributed random variable and will be situated in the tolerance field of the angular position of the crank corresponding to cylinder ‘‘*j*’’ (Fig. 1).

The modulus of the random vector $|F_{ij}|$ representing the REIF of cylinder ‘‘*j*’’ results as a product of two independent random variables, normally distributed. According to the algebra of normal functions [4], this is also a normally distributed random variable whose mean value and standard deviation are (see table in Appendix A):

$$\overline{F}_{I_j} = \overline{m}_{tr}\overline{r}\omega^2 \tag{5}$$

---

[1] The first order residual unbalance is treated for normal reciprocating mechanisms without off-set.

Contributed by the Internal Combustion Engine Division of THE AMERICAN SOCIETY OF MECHANICAL ENGINEERS for publication in the ASME JOURNAL OF ENGINEERING FOR GAS TURBINES AND POWER. Manuscript received by the Internal Combustion Engine Division June 1, 1999; final revision received by the ASME Headquarters August 31, 1999. Technical Editor: D. Assanis.

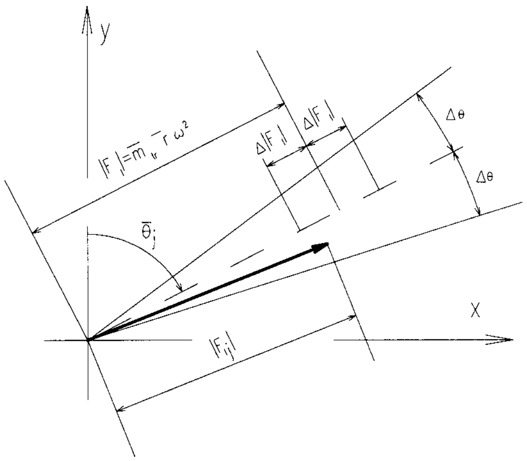

Fig. 1 The random vector interpretation of the first order REIF, considering manufacturing tolerances

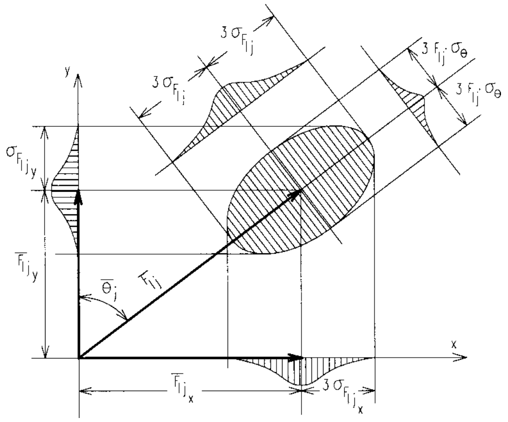

Fig. 2 Statistical distribution of the random vector interpreting the first order REIF for an arbitrary cylinder "*j*"

$$\sigma_{I_j}=\omega^2\sqrt{\overline{m}_{tr}^2\sigma_r^2+\overline{r}^2\sigma_m^2+\sigma_r^2\sigma_m^2}\cong\omega^2\sqrt{\overline{m}_{tr}^2\sigma_r^2+\overline{r}^2\sigma_m^2}. \tag{6}$$

The tolerances affecting the angular positions of the cranks determine a normal distribution of the random vector $|\overline{F_{ij}}|$ around the direction specified by $\overline{\theta}_j$. Consequently, this random vector will be distributed according to a two-dimensional normal law, its tip being situated in the dispersion ellipse having as half axes $3\sigma_{|F_{ij}|}$ and $3F_{ij}\sigma_\theta$ (Fig. 2).

The first order residual unbalance has two aspects: the unbalance produced by the resultant of all first order random vectors and the unbalance produced by the external moment of these vectors with respect to the middle point of the crankshaft's axis.

Residual Unbalance of the First Order REIF

In order to determine the first order force unbalance produced by the REIF in a multicylinder engine the resultant of all random vectors corresponding to the engine's cylinders must be calculated. This calculation may be performed by adding the projections of the random vectors on the axes of the coordinate system.

The projected vectors will be also normally distributed random vectors (see Fig. 2) and their statistical characteristics may be determined according to the table in Appendix A

$$\left[\begin{aligned}&\overline{F}_{I_{j_x}}=\overline{F}_{I_j}\sin\overline{\theta}_j=\omega^2\overline{m}_{tr}\overline{r}\sin\overline{\theta}_j\\&\sigma^2_{F_{I_{j_x}}}=\sigma^2_{F_{I_j}}\sin^2\overline{\theta}_j+\overline{F}^2_{I_j}\sigma^2_\theta\cos^2\overline{\theta}_j\end{aligned}\right. \tag{7}$$

$$\left[\begin{aligned}&\overline{F}_{I_{j_y}}=\overline{F}_{I_j}\cos\overline{\theta}_j=\omega^2\overline{m}_{tr}\overline{r}\cos\overline{\theta}_j\\&\sigma^2_{F_{I_{j_y}}}=\sigma^2_{F_{I_j}}\cos^2\overline{\theta}_j+\overline{F}^2_{I_j}\sigma^2_\theta\sin^2\overline{\theta}_j.\end{aligned}\right. \tag{8}$$

This pair of random vectors, resulting from the projection of the same random vector are correlated random variables, the coefficient of correlation being [3]

$$\rho_{x_jy_j}=\frac{\tan 2\overline{\theta}_j}{2}\,\frac{\sigma^2_{F_{I_{j_y}}}-\sigma^2_{F_{I_{j_x}}}}{\sigma_{F_{I_{j_x}}}\sigma_{F_{I_{j_y}}}} \tag{9}$$

and the covariance corresponding to this coefficient of correlation is

$$K_{x_jy_j}=\rho_{x_jy_j}\sigma_{F_{I_{j_x}}}\sigma_{F_{I_{j_y}}}=\frac{\sin 2\overline{\theta}_j}{2}\left[\sigma^2_{F_{I_j}}-\overline{F}^2_{I_j}\sigma^2_\theta\right]. \tag{10}$$

The resultant random vector representing the first order residual unbalance is obtained by calculating, first, its components on the coordinate axes as sums of the components of the random vectors corresponding to the engine's cylinders. The components of the resultant random vector are correlated random variables and their covariance is equal to the sum of the covariances of all pairs of components [3]:

$$K_{xy}=\sum_{j=1}^{N}K_{x_jy_j}=\frac{1}{2}\left[\sigma^2_{F_{I_j}}-\overline{F}^2_{I_j}\sigma^2_\theta\right]\sum_{j=1}^{N}\sin 2\overline{\theta}_j. \tag{11}$$

Consequently, if the following condition is fulfilled:

$$\sum_{j=1}^{N}\sin 2\overline{\theta}_j=0, \tag{12}$$

the components of the resultant random vector have a covariance and, respectively, a coefficient of correlation equal to zero.

Condition (12) is fulfilled for all engines that are theoretically balanced with respect to the second-order REIF. In this case the angular directions θ_j are uniformly distributed around the crankshaft's axis and the resultant random vector doesn't have any preferential orientation. In contrast, if the second-order unbalance subsists, the first order vectors are opposing each other (as in the case of the four stroke, four cylinder in-line engine) and all the cranks of the crankshaft are situated in the same plane that determines a preferential direction for the first order random vector.

As it was mentioned before, the first order residual unbalance is especially important for engines that are theoretically balanced with respect to the second order REIF. In this case, the components of the resultant random vector may be treated as independent random variables and their statistical characteristics may be calculated according to the formulas presented in the table in Appendix A.

Because the engine is theoretically balanced with respect to the first order REIF,

$$\sum_{j=1}^{N}\sin\overline{\theta}_j=\sum_{j=1}^{N}\cos\overline{\theta}_j=0,$$

the mean values of the components of the resultant random vector are equal to zero:

$$\left[\begin{aligned}&\overline{R}_{I_x}=\sum_{j=1}^{N}\overline{F}_{I_{j_x}}=\overline{m}_{tr}\overline{r}\omega^2\sum_{j=1}^{N}\sin\overline{\theta}_j=0\\&\overline{R}_{I_y}=\sum_{j=1}^{N}\overline{F}_{I_{j_y}}=\overline{m}_{tr}\overline{r}\omega^2\sum_{j=1}^{N}\cos\overline{\theta}_j=0\end{aligned}\right. \tag{13}$$

and the standard deviations of these components are

$$\left[\begin{aligned}\sigma_{R_{I_x}}^2 &= \sum_{j=1}^{N} \sigma_{F_{I_{j_x}}}^2 = \frac{\omega^4}{9}\left[(\overline{m}_{tr}^2 \Delta r^2 + \overline{r}^2 \Delta m_{tr}^2)\sum_{j=1}^{N} \sin^2 \overline{\theta_j}\right.\\ &\qquad \left. + (\overline{m}_{tr}\overline{r}\Delta\theta)^2 \sum_{j=1}^{N} \cos^2 \overline{\theta_j}\right]\\ \sigma_{R_{I_y}}^2 &= \sum_{j=1}^{N} \sigma_{F_{I_{j_y}}}^2 = \frac{\omega^4}{9}\left[(\overline{m}_{tr}^2 \Delta r^2 + \overline{r}^2 \Delta m_{tr}^2)\sum_{j=1}^{N} \cos^2 \overline{\theta_j}\right.\\ &\qquad \left. + (\overline{m}_{tr}\overline{r}\Delta\theta)^2 \sum_{j=1}^{N} \sin^2 \overline{\theta_j}\right]\end{aligned}\right. \quad (14)$$

For all engines that are theoretically balanced with respect to the second order REIF the following condition is fulfilled:

$$\sum_{j=1}^{N} \cos 2\overline{\theta_j} = 0,$$

and taking into account the trigonometric relations

$$\left[\begin{aligned}\sum_{j=1}^{N} \sin^2 \overline{\theta_j} &= \frac{1}{2}\left(N - \sum_{j=1}^{N} \cos 2\overline{\theta_j}\right)\\ \sum_{j=1}^{N} \cos^2 \overline{\theta_j} &= \frac{1}{2}\left(N + \sum_{j=1}^{N} \cos 2\overline{\theta_j}\right)\end{aligned}\right. \quad (15)$$

finally, the following formula is obtained:

$$\sigma_{R_I} = \sigma_{R_{I_x}} = \sigma_{R_{I_y}} = \frac{\omega^2}{3}\sqrt{\frac{N}{2}[\overline{m}_{tr}^2 \Delta r^2 + \overline{r}^2 \Delta m_{tr}^2 + (\overline{m}_{tr}\overline{r}\Delta\theta)^2]}. \quad (16)$$

In conclusion, the components of the first order resultant random vector are degenerated random variables having the mean value equal to zero and the dispersion ellipse of the resultant force R_I reduced to a circle with the center in the origin of the coordinate axes (Fig. 3).

The probability that the modulus of the first order random vector R_I will be included in the interval between zero and $|R|$ is given by [3]:

$$P[0 \leqslant |R_I| \leqslant |R|] = 1 - e^{-h^2/2}, \quad (17)$$

where parameter h represents the ratio between the area of the circle of radius R and that of the unity dispersion circle of radius σ_{RI}:

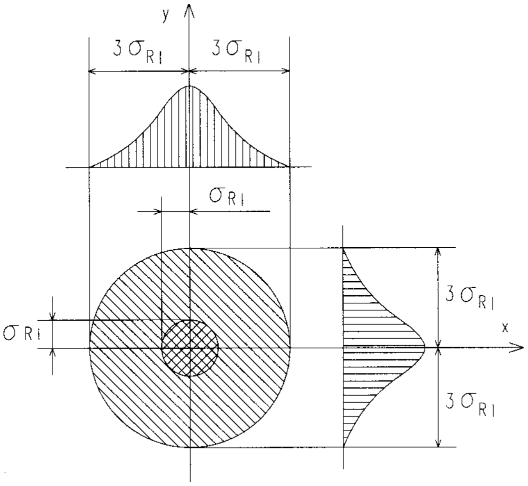

Fig. 3 Statistical distribution of the resultant first order random vector

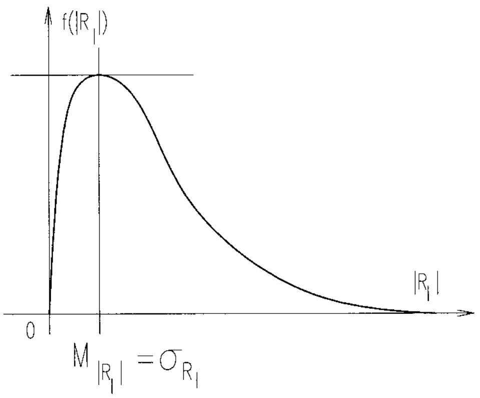

Fig. 4 Rayleigh density of probability function

$$h^2 = \frac{\pi R_I^2}{\pi \sigma_{R_I}^2} = \frac{R_I^2}{\sigma_{R_I}^2}. \quad (18)$$

The probability expressed by relation (17) represents the distribution function of the modulus of the first order random vector R_I and its differential with respect to R_I is the probability density function of $|R_I|$:

$$f(|R_I|) = \frac{|R_I|}{\sigma_{R_I}^2} \exp\left[-\frac{R_I^2}{2\sigma_{R_I}^2}\right]. \quad (19)$$

Function (19) is the well known Rayleigh distribution and is represented in Fig. 4. The mode of this function expresses the most probable value of the random variable $|R_I|$ and is equal to the radius of the unity dispersion circle:

$$M_{|R_I|} = \sigma_{R_I}. \quad (20)$$

The median of the probability density function (19) is equal to the expected mean value of the random variable $|R_I|$ and is given by [3]:

$$m_{R_I} \cong 1.25\sigma_{R_I}. \quad (21)$$

If the manufacturing tolerances are expressed as fractions of the corresponding nominal value

$$\left[\begin{aligned}\varepsilon_r &= \Delta r/\overline{r}\\ \varepsilon_m &= \Delta m_{tr}/\overline{m}_{tr},\end{aligned}\right. \quad (22)$$

and $|F_I|$, the nominal value of the first order REIF is taken as a reference, the most probable value of the first order force unbalance may be expressed as

$$\frac{|R_I|}{|F_I|} = \frac{1}{3}\sqrt{\frac{N}{2}[\varepsilon_r^2 + \varepsilon_m^2 + (\Delta\theta)^2]}. \quad (23)$$

Based on Eq. (23), the manufacturing tolerances, and especially those regarding the reciprocating masses, may be judiciously determined in order to assure a smooth running of the engine.

Residual Unbalance of the First Order External Moment Produced by the REIF

In order to determine the most probable value of the first order residual moment of the REIF additional magnitudes subjected to manufacturing tolerances shall be considered: the distances separating the cylinders along the crankshaft's axis. These distances are usually expressed with respect to either the middle, or the last journal bearing depending on whichever controls the axial position of the crankshaft.

With respect to this reference, the position of the axis of cylinder ''j'' may be expressed as:

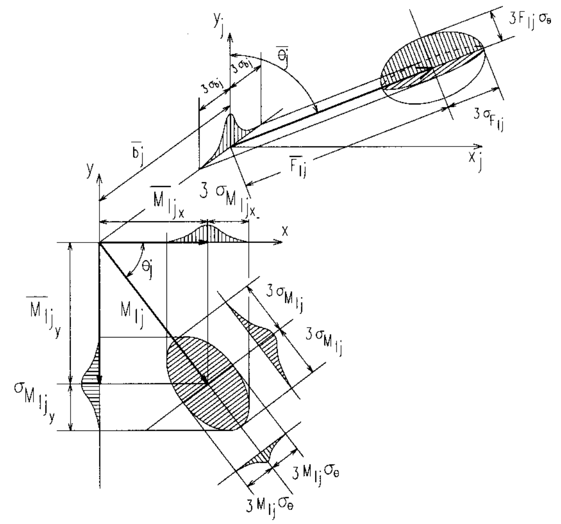

Fig. 5 Random vector interpretation of the first order moment of the REIF, for an arbitrary cylinder "*j*"

$$b_j = b_j \pm \Delta b_j \tag{24}$$

and, again, considering the manufacturing tolerances as ±3σ limits, the standard deviation of these random variables are:

$$\sigma_{b_j} = \tfrac{1}{3}\Delta b_j \quad j = 1,2,\ldots,N. \tag{25}$$

Consequently, the first order random vector representing the REIF of cylinder "j" will be tridimensionally normal distributed, its tip being situated inside the dispersion ellipsoid (Fig. 5) having the half axes equal to $3\sigma_{FIj}$, $3F_{Ij}\sigma_\theta$, and $3\sigma_{bj}$.

The moment of this random vector with respect to the reference point O is also a random vector, normally distributed in the plane xOy (Fig. 5), its mean value and standard deviation being:

$$\left[\begin{aligned} &\overline{M}_{I_j} = \overline{b}_j \overline{F}_{I_j} = \overline{m}_{tr}\overline{r}\overline{b}_j\omega^2 \\ &\sigma_{M_{I_J}} = \sqrt{\overline{F}^2_{I_J}\sigma^2_{b_j} + \overline{b}^2_j\sigma^2_{F_{I_j}} + \sigma^2_{b_j}\sigma^2_{F_{I_J}}} \\ &\qquad \cong \omega^2\sqrt{(\overline{m}_{tr}\overline{r})^2\sigma^2_{b_j} + (\overline{m}^2_{tr}\sigma^2_r + \overline{r}^2\sigma^2_m)\overline{b}^2_j} \end{aligned}\right. . \tag{26}$$

The tip of the random vector M_{IJ} is included in the dispersion ellipse having the half axes equal to $3\sigma_{MIj}$ and $3M_{Ij}\sigma_\theta$, respectively (Fig. 5). The projections of this vector on the axes of the coordination system xOy are normally distributed random vectors having the following statistical characteristics:

$$\left[\begin{aligned} &\overline{M}_{I_{j_x}} = \overline{M}_{I_j}\cos\overline{\theta}_j = \overline{m}_{tr}\overline{r}\overline{b}_j\omega^2\cos\overline{\theta}_j \\ &\sigma^2_{M_{I_{J_x}}} = \sigma^2_{M_{I_j}}\cos^2\overline{\theta}_j + \overline{M}^2_{I_j}\sigma^2_\theta\sin^2\overline{\theta}_j \end{aligned}\right. \tag{27}$$

$$\left[\begin{aligned} &\overline{M}_{I_{j_y}} = \overline{M}_{I_j}\sin\overline{\theta}_j = \overline{m}_{tr}\overline{r}\overline{b}_j\omega^2\sin\overline{\theta}_j \\ &\sigma^2_{M_{I_{j_y}}} = \sigma^2_{M_{I_j}}\sin^2\overline{\theta}_j + \overline{M}^2_{I_j}\sigma^2_\theta\cos^2\overline{\theta}_j \end{aligned}\right. \tag{28}$$

$$K_{M_{I_J}} = \frac{\sin 2\overline{\theta}_j}{2}(\sigma^2_{M_{I_j}} - \overline{M}^2_{I_j}\sigma^2_\theta). \tag{29}$$

The components of the resultant first order moment vector may be calculated by adding the respective components of the individual random moment vectors corresponding to the engine's cylinders. Based on formulas presented in the table in Appendix A, the statistical characteristics of the components of the resultant first-order moment vector are

$$\left[\begin{aligned} &\overline{M}_{I_x} = \sum_{j=1}^{N}\overline{M}_{I_{j_x}} = \omega^2\overline{m}_{tr}\overline{r}\sum_{j=1}^{N}\overline{b}_j\cos\overline{\theta}_j \\ &\sigma^2_{M_{I_x}} = \sum_{j=1}^{N}\sigma^2_{M_{I_{j_x}}} = \omega^4\left[\overline{m}^2_{tr}\overline{r}^2\sum_{j=1}^{N}\sigma^2_{b_j}\cos^2\overline{\theta}_j + (\overline{m}^2_{tr}\sigma^2_r + \overline{r}^2\sigma^2_m)\sum_{j=1}^{N}\overline{b}^2_j\cos^2\overline{\theta}_j + (\overline{m}_{tr}\overline{r}\sigma_\theta)^2\sum_{j=1}^{N}\overline{b}^2_j\sin^2\overline{\theta}_j\right] \end{aligned}\right. \tag{30}$$

$$\left[\begin{aligned} &M_{I_y} = \sum_{j=1}^{N}\overline{M}_{I_{j_y}} = \omega^2\overline{m}_{tr}\overline{r}\sum_{j=1}^{N}\overline{b}_j\sin\overline{\theta}_j \\ &\sigma^2_{M_{I_y}} = \sum_{j=1}^{N}\sigma^2_{M_{I_{j_y}}} = \omega^4\left[\overline{m}^2_{tr}\overline{r}^2\sum_{j=1}^{N}\sigma^2_{b_j}\sin^2\overline{\theta}_j + (\overline{m}^2_{tr}\sigma^2_r + \overline{r}^2\sigma^2_m)\sum_{j=1}^{N}\overline{b}^2_j\sin^2\overline{\theta}_j + (\overline{m}_{tr}\overline{r}\sigma_\theta)^2\sum_{j=1}^{N}\overline{b}^2_j\cos^2\overline{\theta}_j\right] \end{aligned}\right. \tag{31}$$

$$\begin{aligned} K_{M_I} &= \sum_{j=1}^{N}K_{M_{I_j}} \\ &= \frac{\omega^4}{2}\left[\overline{m}^2_{tr}\overline{r}^2\sum_{j=1}^{N}\sigma^2_{b_j}\sin 2\overline{\theta}_j + (\overline{m}^2_{tr}\sigma^2_r + \overline{r}^2\sigma^2_m)\right. \\ &\quad \left.\times\sum_{j=1}^{N}\overline{b}^2_j\sin 2\overline{\theta}_j - (\overline{m}_{tr}\overline{r}\sigma_\theta)^2\sum_{j=1}^{N}\overline{b}^2_j\sin 2\overline{\theta}_j\right]. \end{aligned} \tag{32}$$

If the first-order external moment of the REIF is theoretically balanced the following condition is fulfilled:

$$\sum_{j=1}^{N}\overline{b}_j\cos\overline{\theta}_j = \sum_{j=1}^{N}\overline{b}_j\sin\overline{\theta}_j = 0, \tag{33}$$

and the components of the first order moment vector are degenerated random variables having their mean values equal to zero:

$$\overline{M}_{I_x} = \overline{M}_{I_y} = 0. \tag{34}$$

Taking into account relations (4), (5), (22), (30), (31), and (32) the standard deviations may be written as

$$\begin{aligned} \sigma^2_{M_{I_x}} = \frac{1}{2}\left[\frac{\overline{F}_I}{3}\right]^2 &\left\{\sum_{j=1}^{N}(\Delta b_j)^2 + \sum_{j=1}^{N}(\Delta b_j)^2\cos 2\overline{\theta}_j + [\varepsilon^2_r + \varepsilon^2_m\right. \\ &\left. + (\Delta\theta)^2]\sum_{j=1}^{N}\overline{b}^2_j + [\varepsilon^2_r + \varepsilon^2_m - (\Delta\theta)^2]\sum_{j=1}^{N}\overline{b}^2_j\cos 2\overline{\theta}_j\right\} \end{aligned} \tag{35}$$

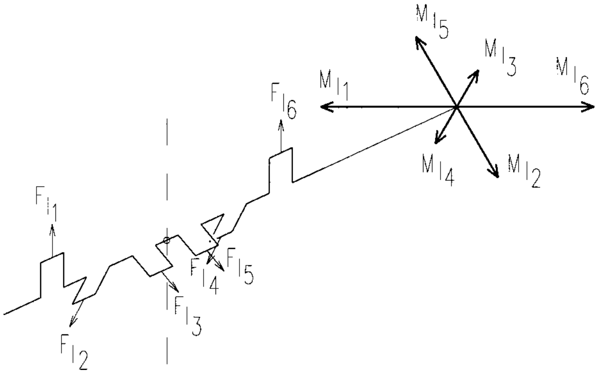

Fig. 6 The first order vector moments for a four stroke, six cylinder engine

$$\sigma^2_{M_{I_y}}=\frac{1}{2}\left[\frac{\overline{F_I}}{3}\right]^2\left\{\sum_{j=1}^{N}(\Delta b_j)^2-\sum_{j=1}^{N}(\Delta b_j)^2\cos 2\overline{\theta_j}+[\varepsilon_r^2+\varepsilon_m^2+(\Delta\theta)^2]\sum_{j=1}^{N}\overline{b_j^2}-[\varepsilon_r^2+\varepsilon_m^2-(\Delta\theta)^2]\sum_{j=1}^{N}\overline{b_j^2}\cos 2\overline{\theta_j}\right\} \tag{36}$$

and the covariance as

$$K_{M_I}=\frac{1}{2}\left[\frac{\overline{F_I}}{3}\right]^2\left\{\sum_{j=1}^{N}(\Delta b_j)^2\sin 2\overline{\theta_j}+[\varepsilon_r^2+\varepsilon_m^2-(\Delta\theta)^2]\sum_{j=1}^{N}\overline{b_j^2}\sin 2\overline{\theta_j}\right\}. \tag{37}$$

Equation (37) shows that, even if the second-order REIF are theoretically balanced, the components of the resultant first order external moment are correlated random variables. This situation is determined by the fact that the moment vectors corresponding to different cylinders have different magnitudes and the residual value of their sum will have a preferential direction determined by the larger pair of opposite vectors (Fig. 6).

In this case the system of coordinates is not a principal system for the dispersion ellipse. The axes of the principal system $\zeta O\eta$ (Fig. 7) are rotated with respect to the considered system by an angle α [3]:

$$\tan 2\alpha=\frac{2K_{M_I}}{\sigma^2_{M_{I_x}}-\sigma^2_{M_{I_y}}}. \tag{38}$$

Considering Eqs. (35)–(38) this angle may be calculated by the following relation:

$$\alpha=\frac{1}{2}\tan^{-1}\left[\frac{\sum_{j=1}^{N}(\Delta b_j)^2\sin 2\overline{\theta_j}+[\varepsilon_r^2+\varepsilon_m^2-(\Delta\theta)^2]\Sigma_{j=1}^{N}\overline{b_j^2}\sin 2\overline{\theta_j}}{\sum_{j=1}^{N}(\Delta b_j)^2\cos 2\overline{\theta_j}+[\varepsilon_r^2+\varepsilon_m^2-(\Delta\theta)^2]\Sigma_{j=1}^{N}\overline{b_j^2}\cos 2\overline{\theta_j}}\right] \tag{39}$$

and the half axes of the dispersion ellipse: $3\sigma_{M_{I_\zeta}}$, $3\sigma_{M_{I_\eta}}$ may be determined from [3]:

$$\begin{cases}\sigma^2_{M_{I_\zeta}}=\sigma^2_{M_{I_x}}\cos^2\alpha+\sigma^2_{M_{I_y}}\sin^2\alpha+K_{M_I}\sin 2\alpha\\ \sigma^2_{M_{I_\eta}}=\sigma^2_{M_{I_x}}\sin^2\alpha+\sigma^2_{M_{I_y}}\cos^2\alpha-K_{M_I}\sin 2\alpha\end{cases}. \tag{40}$$

The probability that the module of the vector representing the first order external moment would be included in the interval between zero and $|M|$ is given by a relation similar to (17) where the parameter h^2 takes the following expression:

$$h^2=\frac{\pi M_I^2}{\pi\sigma_{M_{I_\zeta}}\sigma_{M_{I_\eta}}} \tag{41}$$

and the probability density function of this random vector is given by a modified Rayleigh distribution

$$f(|M_I|)=\frac{|M_I|}{\sigma_{M_{I_\zeta}}\sigma_{M_{I_\eta}}}\exp\left[-\frac{M_I^2}{2\sigma_{M_{I_\zeta}}\sigma_{M_{I_\eta}}}\right]. \tag{42}$$

Again, the most probable value of the residual first order external moment is equal to the mode of this function

$$|M_I|=\sqrt{\sigma_{M_{I_\zeta}}\sigma_{M_{I_\eta}}}, \tag{43}$$

and its mean value is

$$m_{M_I}\cong 1.25|M_I|. \tag{44}$$

Formulas (20) and (43) could be used to estimate the most probable value of the first order unbalance caused by the resultant force and external moment of the REIF.

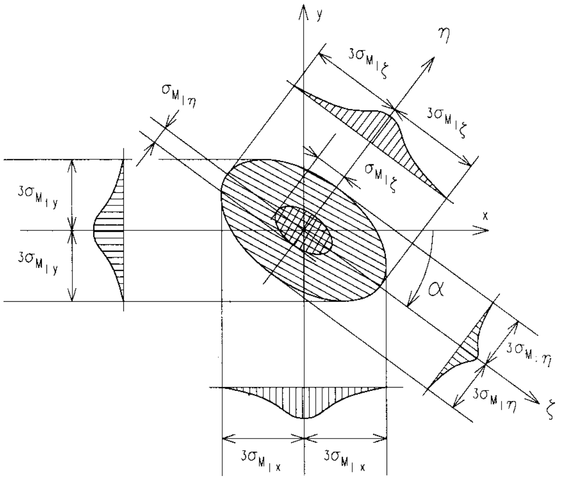

Fig. 7 Position of the principal axes of the dispersion ellipse

Numerical Simulation

In order to determine the significance of the residual first order unbalance and to check the validity of the formulas established by the probabilistic approach a particular case has been analyzed.

The considered engine is an automotive, four stroke, six cylinder diesel engine characterized by the following parameters:

$$m_{tr}=1000\pm 5\text{ g}\quad \varepsilon_m=0.005$$

$$r=50\pm 0.05\text{ mm}\quad \varepsilon_r=0.001$$

$$\theta_j=j\times 120°\pm 15'\quad \Delta\theta=0.00436\text{ rad}$$

$$j=1,2,\ldots,6.$$

The cylinders are symmetrically situated with respect to the middle journal bearing which is also the axial bearing of the crankshaft:

$$b_1=300\pm 0.2\text{ mm}\quad b_6=-300\pm 0.2\text{ mm}$$

$$b_2=180\pm 0.2\text{ mm}\quad b_5=-180\pm 0.2\text{ mm}$$

Table 1 Comparison between simulation and calculation based on the probabilistic model of the REIF

Calculated with formula ( )	Numerical simulation
$R_{I_x} = R_{I_y} = 0$ (13)	$R_{I_x} \cong 9.064 \times 10^{-5} \lvert F_I \rvert$ $R_{I_y} \cong 1.339 \times 10^{-4} \lvert F_I \rvert$
$\sigma_{R_{I_x}} = \sigma_{R_{I_y}} \cong 3.873 \times 10^{-3} \lvert F_I \rvert$ (16)	$\sigma_{R_{I_x}} \cong 3.894 \times 10^{-3} \lvert F_I \rvert$ $\sigma_{R_{I_y}} \cong 3.931 \times 10^{-3} \lvert F_I \rvert$
$m_{R_I} \cong 4.84 \times 10^{-3} \lvert F_I \rvert$ (21)	$m_{R_I} \cong 4.96 \times 10^{-3} \lvert F_I \rvert$
$\mathrm{M}_{I_x} = \mathrm{M}_{I_y} = 0$ (34)	$\mathrm{M}_{I_x} \cong -9.092 \times 10^{-6} \lvert F_I \rvert \; m$ $\mathrm{M}_{I_y} \cong -5.194 \times 10^{-6} \lvert F_I \rvert \; m$
$\sigma_{\mathrm{M}_{I_x}} \cong 0.836 \times 10^{-3} \lvert F_I \rvert \; m$ (35) $\sigma_{\mathrm{M}_{I_y}} \cong 0.766 \times 10^{-3} \lvert F_I \rvert \; m$ (36)	$\sigma_{\mathrm{M}_{I_x}} \cong 0.832 \times 10^{-3} \lvert F_I \rvert \; m$ $\sigma_{\mathrm{M}_{I_y}} \cong 0.776 \times 10^{-3} \lvert F_I \rvert \; m$
$K_{\mathrm{M}_I} \cong -1.937 \times 10^{-8} F_I^2 \; m^2$ (37)	$K_{\mathrm{M}_I} \cong -1.973 \times 10^{-8} F_I^2 \; m^2$
$\alpha \cong -9.55^o$ (39)	$\alpha \cong -11.87^o$
$m_{\mathrm{M}_I} \cong 1.00 \times 10^{-3} \lvert F_I \rvert \; m$ (44)	$m_{\mathrm{M}_I} \cong 1.015 \times 10^{-3} \lvert F_I \rvert \; m$

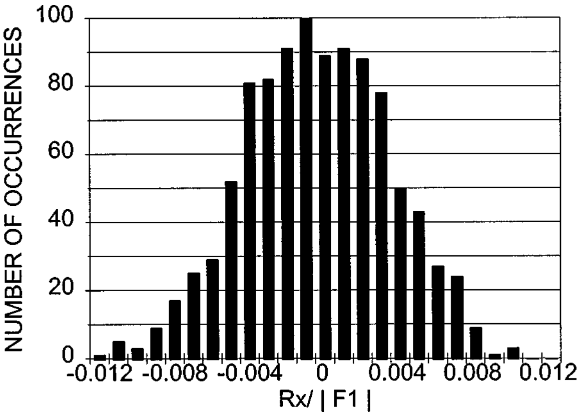

Fig. 8 **Histogram of the *x*-axis component of the resultant first order random vector R_I**

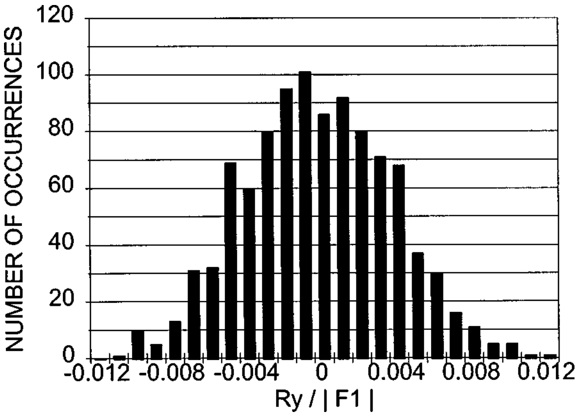

Fig. 9 **Histogram of the *y*-axis component of the resultant first order random vector R_I**

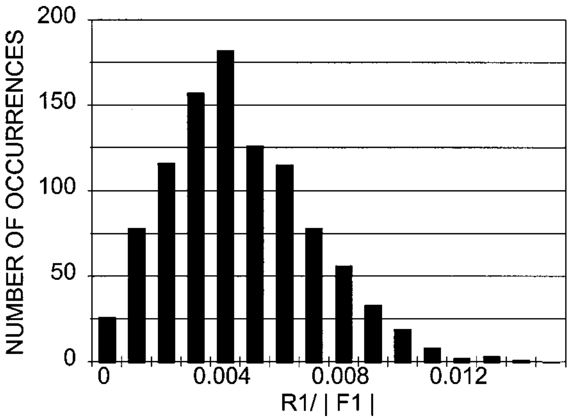

Fig. 10 **Histogram of the modulus of the first order random vector R_I**

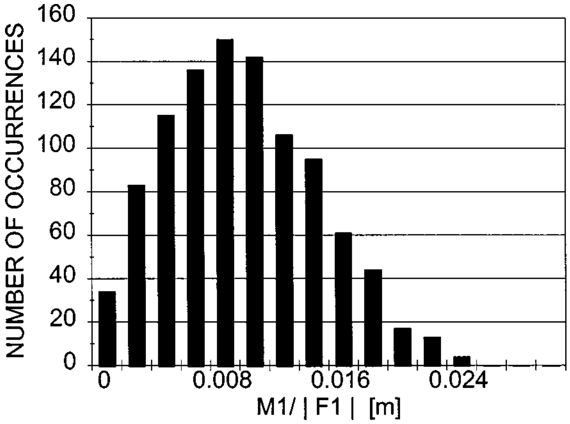

Fig. 11 **Histogram of the modulus of the first order random vector M_I**

$$b_3 = 60 \pm 0.2 \ \text{mm} \quad b_4 = -60 \pm 0.2 \ \text{mm}.$$

According to the classical theory of balance, the most significant unbalance of this engine is the sixth-order force unbalance which has a value six time larger than the module of the sixth order harmonic component of the REIF. For the considered engine ($\Lambda = 0.25$) the sixth order harmonic component is 0.000072 $|F_I|$ and the resulting unbalance: $|R_{VI}| = 6 \times 0.000072 |F_I| = 4.32 \times 10^{-4} |F_I|$.

Using formula (23) the most probable value of the first order residual force unbalance is determined:

$$|R_I| = \frac{F_I}{3} \sqrt{\frac{6}{2}(0.001^2 + 0.005^2 + 0.00436^2)} \cong 3.87 \times 10^{-3} |F_I|.$$

In spite of the fact that the manufacturing tolerances are extremely low, the residual unbalance is almost nine times larger than the theoretical unbalance of this engine.

For checking the results obtained by the probabilistic approach, a computer code was developed to simulate by random number generation the manufacturing tolerances. The simulation was calibrated to produce standard deviations for the manufacturing tolerances in accordance with relations (4) and (25) and the data resulting from this simulation showed a good agreement with the calculation made with formulas developed in this paper. At the same time, the simulations show that, in mass production, some engines will exhibit an even larger unbalance than the one predicted by formulas (23) and (43).

A typical result obtained in such a simulation considering 1000 random generated samples is presented in comparison with the probabilistic calculations in Table 1.

The histograms obtained from the simulated data are presented in Fig. 8–11. As it could be seen they approximate fairly well the predicted probability density functions.

Conclusions

The classical theory of balance assumes all reciprocating mechanisms of a multicylinder engine perfectly identical. In this case, many harmonic components of the REIF may be balanced.

The manufacturing tolerances introduce small differences between the dimensions and masses of the reciprocating mechanisms of the same multicylinder engine. In this situation, residual unbalances of the REIF subsist for harmonic orders that theoretically should be balanced.

The residual unbalance is especially important for engines that are theoretically balanced with respect to the second order REIF. In this case the most significant unbalance of the engine is the residual first order unbalance which is several times larger than the unbalance predicted by the classical theory of balance.

Applying methods specific to the theory of probability and mathematical statistics a probabilistic model of the REIF and methods to determine the most probable value of the residual unbalance are established.

The formulas developed in this paper may be used to correlate the manufacturing tolerances with the expected residual unbalance.

Nomenclature

b = distance measured along the crankshaft's axis
r = crank radius
l = length of the con-rod
m_{tr} = reciprocating mass
F = force
K = covariance
M = moment
N = total number of cylinders of a given engine
R = resultant
Δm = mass tolerance
Δr = tolerance of the crank radius
$\Delta\theta$ = tolerance of the angular position of a crank
ε = relative deviation with respect to nominal value
$\Lambda = r/l$ = parameter of the reciprocating mechanism
θ = angular position
ρ = coefficient of correlation
ω = angular velocity of the crankshaft
σ = standard deviation

Indices

j = relative to an arbitrary cylinder "j"
m = relative to the reciprocating mass
r = relative to crank radius
x = relative to Ox axis
y = relative to Oy axis
I = relative to the first harmonic order
F = relative to force
M = relative to moment
ζ = relative to Oζ axis
η = relative to Oη axis
θ = relative to the angular position of a crank

Appendix A

Table A1 Statistical characteristics of random variables obtained as a result of algebraic operations applied to normally distributed random variables [4]

Algebraic operation	Statistical characteristics Independent random variables
Addition $z = x + y$	$\bar{z} = \bar{x} + \bar{y}$ $\sigma_z = \sqrt{\sigma_x^2 + \sigma_y^2}$
Subtraction $z = x - y$	$\bar{z} = \bar{x} - \bar{y}$ $\sigma_z = \sqrt{\sigma_x^2 + \sigma_y^2}$
Multiplication $z = x.y$	$\bar{z} = \bar{x}.\bar{y}$ $\sigma_z = \sqrt{\bar{x}^2\sigma_y^2 + \bar{y}^2\sigma_x^2 + \sigma_x^2\sigma_y^2}$
Function $y = f(x)$	$\bar{y} = f(\bar{x})$ $\sigma_y = [f'(\bar{x})]\sigma_x$

References

[1] Baranescu, G., 1975, *Teoria Echilibrajului Motoarelor cu Ardere Interna in Linie* (*Theory of In-Line Engines Balance*), Academia RSR, Bucharest.
[2] Taraza, D., 1985, *Dinamica Motoarelor cu Ardere Interna* (*Dynamics of I. C. Engines*), EDP, Bucharest.
[3] Ventsel, H., 1973, *Theorie des Probabilites* (*Theory of probability*) MIR, Moscow.
[4] Haugen, E. B., 1968, *Probabilistic Approaches to Design*, Wiley, New York.

Validation of a New TVD Scheme Against Measured Pressure Waves in the Inlet and Exhaust System of a Single Cylinder Engine

M. Vandevoorde

R. Sierens

E. Dick

Department of Mechanical and Thermal Engineering,
University of Gent, Belgium

Recently a new TVD scheme was presented by the authors and a comparison was made with other algorithms for two engine related test cases (the shock tube and the tapered pipe). It was shown that the new scheme combines high accuracy with exact conservation of the mass flow, even in tapered pipes. In this paper the pressure waves in the inlet and exhaust system of a single cylinder engine are measured and compared to calculations with the new algorithm. The comparison is made under motoring and firing conditions of the engine with two different external mixture formation systems (different fuels: gasoline and methane). Modifications on intake and exhaust pipe configuration clearly show their influence on the pressure wave development. The importance of the loss coefficients for the flow through the inlet and exhaust valves (mass flow coefficient) is demonstrated. A test rig has been built to obtain these coefficients under steady-state conditions as a function of valve lift and mass flow rate. It is shown that for this engine configuration the measured steady-state loss coefficients are not reliable at low valve lifts. This can be explained by the influence of the Reynolds number and the appearance of a transition zone. For all mentioned comparisons the agreement is excellent. The next phase will be to evaluate the code for multi-cylinder engines under atmospheric and turbo-charged conditions. [S0742-4795(00)00204-0]

Introduction

For more than 30 years, single cylinder engines have been used for validation of computer codes simulating the gas exchange process of IC engines (e.g., [1]). Of course, over the years improvements have been made in the measuring techniques (e.g., transducers) and the data acquisition system. But mainly, the engine in its most simple configuration is still an adequate tool to validate new computer algorithms.

The first gas dynamic computer code for the calculation of the unsteady flow in engine intake and exhaust system was based on the method of characteristics (solution of the differential characteristic equations). Then Lax-Wendroff methods where introduced, where differentials are replaced by differences with a second order accuracy. Flux correction techniques are necessary to reduce the inherent overshoots. Further, the centered Lax-Wendroff schemes were extended to first order upwind schemes.

Recently TVD (Total Variation Diminishing) schemes were introduced for the simulation of the gas exchange process in IC engines [2,3]. TVD schemes are an extension of first order upwind schemes by the use of non-linear techniques (the so-called limiters) to achieve second order accuracy.

The authors have developed a new cell-vertex TVD scheme with the superbee limiter in two stage form [4,5]. Basically the method is a one-dimensional variant of the polynomial Flux Difference Splitting (FDS) technique as developed in [6–8]. In [4] the authors have made a comparison of different numerical algorithms (the method of characteristics, different Lax-Wendroff schemes, first order upwind schemes, the classic TVD schemes) with the new TVD scheme for two test cases: the shock tube and the tapered pipe. None of the earlier methods combine high accuracy for pressure wave calculations and correct calculations for tapered pipes. Even the classic TVD schemes have local discretization errors at places with an area variation.

The new TVD scheme has both a high accuracy for the first test case (shock tube) and an exact conservation of the mass flow in the second test case (tapered pipe). The new scheme is described in detail in [5].

In this paper, the new TVD scheme is tested against measurements in the inlet-and exhaust system of a one-cylinder engine.

1 Numerical Algorithm

The one-dimensional unsteady gas flow in a pipe is described by the following basic equations

The Continuity Equation

$$\frac{\partial \rho S}{\partial t}+\frac{\partial \rho u S}{\partial x}=0, \tag{1}$$

The Momentum Equation

$$\frac{\partial \rho u S}{\partial t}+\frac{\partial \rho u^2 S}{\partial x}=-\frac{\partial p S}{\partial x}+p\frac{\partial S}{\partial x}-f\frac{\rho u^2}{2}\frac{u}{|u|}O, \tag{2}$$

The Energy Equation

$$\frac{\partial \rho E S}{\partial t}+\frac{\partial \rho E u S}{\partial x}=-\frac{\partial p u S}{\partial x}+q\rho S \tag{3}$$

The nomenclature is as follows:

e = specific internal energy [J/kg]
E = $e+u^2/2$: specific total mechanical energy [J/kg]

Contributed by the Internal Combustion Engine Division of THE AMERICAN SOCIETY OF MECHANICAL ENGINEERS for publication in the ASME JOURNAL OF ENGINEERING FOR GAS TURBINES AND POWER. Manuscript received by the ICE Division June 1, 1999; final revision received by the ASME Headquarters July 17, 1998. Technical Editor: D. Assanis.

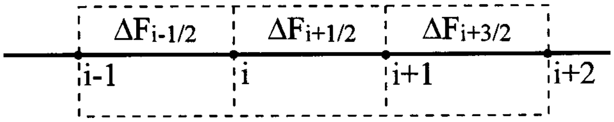

Fig. 1 Cell-vertex finite volume method

f = friction coefficient $[-]$
O = internal contour of the pipe [m]
p = pressure [N/m^2]
q = heat transfer added through the wall [J/(kg.s)]
S = section of the pipe [m^2]
t = time [s]
u = (convective) velocity along the x co-ordinate [m/s]
$|u|$ = absolute value of u
x = co-ordinate along the axis of the pipe [m]
ρ = density [kg/m^3]

This set of hyperbolic partial differential equations expresses the conservation of mass, momentum, and energy for a system with friction, heat transfer, and a variable section. After division by the section S, the equations can be written in short form as

$$\frac{\partial \xi}{\partial t}+\frac{1}{S}\frac{\partial F}{\partial x}-\frac{P}{S}=B, \tag{4}$$

with the vector of conserved variables

$$\xi=[\rho,\ \rho u,\ \rho E]^T, \tag{5}$$

the fluxvector

$$F=[\rho u S,\ (\rho u u+p)S,\ \rho H u S]^T, \tag{6}$$

the pressure term

$$P=\left[0,\, p\,\frac{\partial S}{\partial x},\, 0\right]^T, \tag{7}$$

and the source term

$$B=\left[0,\, -f\,\frac{\rho u^2}{2}\,\frac{u}{|u|}\,\frac{O}{S},\ q\rho\right]^T. \tag{8}$$

The new TVD scheme is a so-called cell-vertex finite volume method. In a cell-vertex formulation, the control volumes are formed by the cells in the grid. In one dimension these are the segments between the vertices of the grid as shown in Fig. 1. The term vertex is added to the denomination of the method to indicate that the variables are stored at the vertices of the grid.

An obvious difficulty with the cell-vertex finite volume method is the way in which updates of the variables in the nodes are to be constructed from the flux balances. The flux difference ΔF in each volume has to be distributed to the nodes of that volume. This distribution is done using upwinding technique, so that a node intercepts the information from the physically relevant direction. Second order accuracy for the space derivative is obtained by the use of non-linear combinations (limiters) of the flux differences.

The second order accurate scheme is described by

$$\xi_i^{n+1}=\xi_i^n-\frac{\Delta t}{S_i\Delta x}(F_L^n-F_R^n)+\Delta t B_i^n \tag{9}$$

with

$$F_L^n=D^-_{i+1/2,n}\Delta F^n_{i+1/2}+\frac{1}{2}\,\mathrm{Lim}(D^+_{i+1/2,n}\Delta F^n_{i+1/2},D^+_{i+1/2}\Delta F^n_{i-1/2})$$
$$-\frac{1}{2}\,\mathrm{Lim}(D^-_{i+1/2,n}\Delta F^n_{i+1/2},D^-_{i+1/2,n}\Delta F^n_{i+3/2}). \tag{10}$$

$$F_R^n=D^+_{i-1/2,n}\Delta F^n_{i-1/2}-\frac{1}{2}\,\mathrm{Lim}(D^+_{i-1/2,n}\Delta F^n_{i-1/2},D^+_{i-1/2}\Delta F^n_{i-3/2})$$
$$+\frac{1}{2}\,\mathrm{Lim}(D^-_{i+1/2,n}\Delta F^n_{i-1/2},D^-_{i-1/2,n}\Delta F^n_{i+1/2}). \tag{11}$$

The superscript n means that the variables have to be taken at time level n. The flux differences ΔF are calculated by

$$\Delta F^n_{i+1/2}=F^n_{i+1}-F^n_i-(S_{i+1}-S_i)\,\frac{p^n_{i+1}+p^n_i}{2}, \tag{12}$$

with the fluxes F defined in (6). Lim is the limiter used. The superbee limiter gives the best overall performance with this TVD scheme [4] and it is defined as follows:

$$\mathrm{superbee}(a,b)=\mathrm{sign}(a)\max(0,\max(\min(2abs(a),\mathrm{sign}(a)b),$$
$$\min(abs(a),2\,\mathrm{sign}(a)b))).$$

The matrices $D^-_{i-1/2}$ and $D^+_{i+1/2}$ originate from a flux difference splitting technique. The technique used here is the polynomial flux-difference splitting technique developed by one of the present authors [7], adapted for the cell vertex TVD scheme in [5].

Second order accuracy for the time derivative is obtained by multistage algorithms: the time step from n to $n+1$ is hereby divided into several stages. If the coefficients in these stages are well chosen an increase in the number of stages can result in an increase in the allowable CFL number and an increase in time accuracy.

Equation (9) symbolically gives the one-stage scheme. The two-stage cell-vertex TVD scheme with second order time accuracy is written as

$$\xi_i^{n+1/2}=\xi_i^n-\frac{\Delta t}{2S_i\Delta x}(F_L^n-F_R^n)+\frac{\Delta t}{2}B_i^n \tag{13}$$

$$\xi_i^{n+1}=\xi_i^n-\frac{\Delta t}{S_i\Delta x}(F_L^{n+1/2}-F_R^{n+1/2})+\Delta t B_i^{n+1/2}. \tag{14}$$

It is this two-stage form that is used for the calculations in this paper.

The thermodynamic cycle of the cylinder is calculated from the moment the inlet valve closes (trapped conditions) until the exhaust valve opens (release conditions) without or with combustion (motored or fired engine). The thermodynamic model for the two-zone combustion is based on the model by Tabaczynski et al. [9–11], but will not be described further. The only importance here is that the thermodynamic model correctly predicts the release conditions. When one or two of the valves are open, the cylinder conditions are calculated as a boundary condition for the gasdynamic model.

2 Description of the Test Rig

The experiments are carried out on a single cylinder four-stroke CFR engine with the following characteristics:

bore: 82.55 mm
stroke: 114.2 mm
swept volume 612.5 cm^3
compression ratio: 6.29
engine speed (constant): 600 rpm
inlet valve opens (IVO): 12°ca *after* TDC
inlet valve closes (IVC): 30°ca after BDC
exhaust valve opens (EVO): 31°ca before BDC
exhaust valve closes (EVC): 5°ca after TDC

The engine is connected to an electric brake. Figure 2 shows the geometry of the inlet and exhaust system of the engine. The first part in the inlet system is a buffer vessel of 209 1. It is installed to minimize the flow pulsation for a diaphragm type flow meter placed in front, but the pulsation remained too large to do a cor-

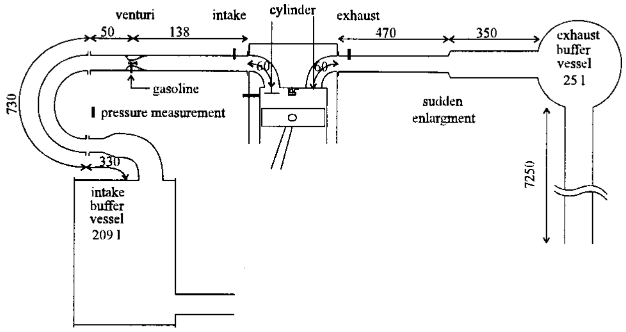

Fig. 2 Geometry of the inlet and exhaust system

rect mass flow measurement. This is due to the strong activation of a single cylinder at low engine speed. The buffer vessel is connected to the cylinder head via a tapered pipe ($L=330$ mm), an elastic pipe ($L=730$ mm, $\varnothing=31.75$ mm, 180 deg bend) and again a straight pipe ($L=188$ mm, $\varnothing=31.75$ mm). The intake port channel ($L=60$ mm, $\varnothing=31.75$ mm) has a 90 deg bend in the cylinder head. The venturi is positioned at 198 mm before the intake valve (intake port included).

The exhaust system consists of a 90 deg bend through the exhaust port channel ($L=60$ mm, $\varnothing=31.75$ mm) followed by a straight pipe ($L=470$ mm, $\varnothing=31.75$ mm) and a sudden section change to a straight pipe ($L=350$ mm, $\varnothing=53$ mm). The end of the second pipe is connected to a buffer vessel of 25 l. In this buffer vessel water can be injected by a spray to reduce the gas temperature. For the pressure measurements however no water has been injected. Finally there is a pipe leading from the buffer to the atmosphere ($L=7250$ mm, $\varnothing=53$ mm).

Three high pressure piezo-electric transducers are installed: one inside the cylinder (Type Kistler QC32c, flush with the wall), one in the intake channel (type Kistler QC32c, 90 mm before the intake valve) and one in the exhaust channel (type AVL 8QP500, 100 mm after the exhaust valve). To obtain accurate pressure measurements water cooled transducers are used (these are certainly necessary for in-cylinder and exhaust measurements). The quartz transducers used for the dynamic measurements have a natural frequency of 70 kHz and a linearity better than 0.2 percent FSO. Calibration is done for the combination transducer+cables+charge amplifier before each set of tests. For the in-cylinder measurements the log p-log V diagrams of the motoring and firing cycles are used to verify the absolute pressure level, the position of the TDC and the compression ratio. Also for the in-cylinder measurements under firing conditions, thermal shock error can not be avoided, but the transducer used is one of the best on the market in this respect, as own research has indicated [12].

A PC based data acquisition system is used to store the pressure data at a sample interval of 1 deg crank angle. The sample pulses are given by a CAM (crank angle marker) encoder combined with an interpolator. The position of TDC has been located using an A VL 428 TDC sensor, with an accuracy higher than 0.1 deg ca.

Different fuels can be used in the engine by changing the external mixture formation system. A set of tests is carried out with gasoline. An adjustable amount of fuel is added to the air in a venturi (Fig. 3). There is no throttle valve in the inlet pipe. The regulation of the amount of fuel is done by increasing the fuel pressure (height position of the fuel reservoir) as it is done in the normal use of a CFR engine for defining the octane number of a fuel.

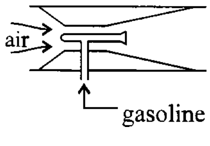

Fig. 3 Venturi (gasoline)

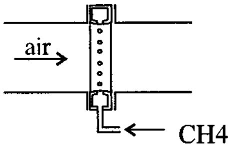

Fig. 4 Gas supply ring (methane)

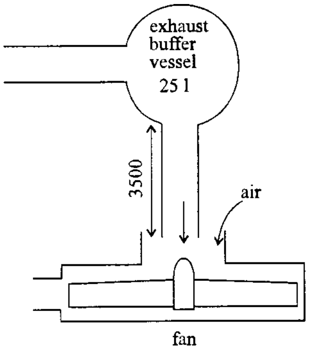

Fig. 5 Disposal of exhaust gases (methane)

A second set of tests is carried out with methane. In this case the fuel is added to the air with a simple fuel pressure line to a ring around the air intake pipe (Fig. 4) at the same location as the venturi for gasoline use. The methane is stored in a pressure vessel and the amount of fuel is again obtained by increasing the pressure in the CH4 line to the ring (rough regulation by a relief valve after the vessel, and fine adjustment by a second valve just before the ring). In the latter case modifications are done to the exhaust system (Fig. 5). The pipe coming from the exhaust buffer is made shorter ($L=3500$, $\varnothing=53$ mm) and for safety reasons a fan is located at the end of it to prevent any methane to accumulate. The fan decreases the pressure in the exhaust system with only 3 cm H2O.

The experiments are done under motoring and firing conditions of the engine.

3 Steady Flow Discharge Coefficients

3.1 Definition and Background. The mass flow rate through a poppet valve is usually described by the equation for compressible flow through a flow restriction. This equation is derived from a one-dimensional isentropic flow analysis.

The real mass flow is smaller than the theoretical mass flow because of a reduction in effective flow area due to the flow separation from wall and valve, heat transfer and friction and by a nonuniform distribution of the flow around the contour of the valve. The real gas flow effects are included by means of an experimentally determined discharge coefficient C_D, where

$$C_D=\frac{\dot{m}_{\text{real}}}{\dot{m}_{\text{theror}}} \tag{15}$$

with

C_D = discharge coefficient [−]
$\dot{m}$ = mass flow [kg/s]

and subscripts

real = measured on the test rig
theor = from theoretical calculation

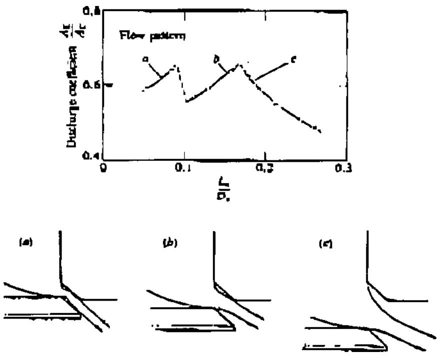

Fig. 6 Discharge coefficient of an inlet poppet valve [13]

In addition to valve lift, the performance of the inlet valve assembly is influenced by the following factors: valve seat width, valve seat angle, rounding of the seat corners, port design, and cylinder head shape.

The value of C_D and the choice of a reference area are linked together: their product $C_D A_R$, is the effective flow area of the valve assembly A_E. Several reference areas may be chosen, but only two different approaches are commonly used.

The first approach is to use the curtain area A_C, where

$$A_C = \pi D_v L_v \tag{16}$$

with

A_C = curtain area, [m^2]
L_v = valve lift, [m]
D_v = valve diameter, [m]

It is the most convenient reference area in practice since it varies linearly with valve lift and is simple to determine. Figure 6 shows the results of steady flow tests on a typical inlet valve configuration with a sharp-cornered valve seat [13]. The discharge coefficient based on valve curtain area is a discontinuous function of the valve lift/diameter ratio. The three segments shown correspond to different flow regimes as indicated. At very low lifts, the flow remains attached to the valve head and seat, giving high values for the discharge coefficient. At intermediate lifts, the flow separates from the valve head at the inner edge of the valve seat as shown. An abrupt decrease in discharge coefficient occurs at this point. The discharge coefficient then increases with increasing lift since the size of the separated region remains approximately constant while the minimum flow area is increasing. At high lifts, the flow separates from the inner edge of the valve seat as well.

The second approach is to use the geometric minimum flow area A_M. The geometric minimum flow area is a complex function of valve and valve seat dimensions. The transition points in Fig. 6 can also be seen as sudden changes in geometric minimum area. In this way, the C_D value is a much more continuous function of the valve lift/diameter ratio.

In either way it is clear that the effective flow area A_E shows a discontinuous behavior, and in this paper the first approach is used.

In order, first to obtain the mass flow coefficients for the valves of the CFR engine, second to verify if these coefficients can be used to predict dynamic behavior, and third to investigate the Reynolds number influence on these flow coefficients, a test rig was constructed. Figure 7 shows the test set up, for the normal inlet flow through the inlet valve with R the rotary compressor (type Vortech V-1), the valves V1 and V2 to regulate the mass flow, the diaphragm type mass flow meter F and the system S to set the inlet or exhaust valve lift to a certain position. The static pressures are measured at different locations as a function of the valve lift and of the mass flow rate.

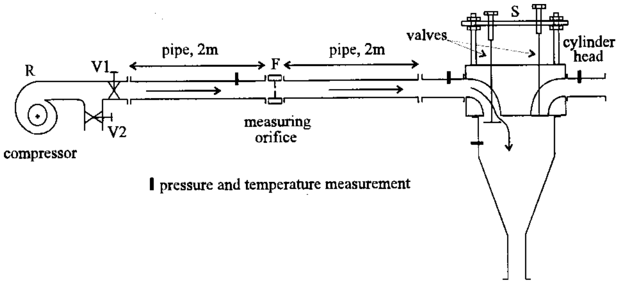

Fig. 7 Test rig for steady-state flow through a valve

The air delivered by the compressor is blown through the cylinder head of the engine (from inlet valve to cylinder liner, from cylinder liner to inlet or exhaust valve and from exhaust valve to cylinder liner, so taking into account also back-flow situations). In this way, a complete range of flow levels at each valve lift increment can be used for the measurements.

The real mass flow is determined by measuring the pressure drop across a diaphragm. It is good practice to limit this pressure drop to about 125 mm H_2O. For smaller pressure drops, air can be treated as an incompressible fluid. A disadvantage of the diaphragm is that the pressure difference across the device varies with the square of the flow rate. It follows that a turn down in flow rate of 10:1 corresponds to a reduction in pressure difference of 100:1, implying insufficient precision at low flow rates. This is solved by using different orifice diameters for different mass flow ranges

The relevant mass flow range for this engine is from 0 to 0.02 kg/s. This range is subdivided into three smaller ranges that each can be measured with one orifice giving allowable pressure drops. The measurements have been done per 1/2 mm valve lift, for each valve and for each flow direction. It is important to notice that in the experiments the compressor always blows the flow in the desired direction. In normal engine operation the flow is sucked through the inlet valve. This is no problem since the two flows have to be compared by the Mach and Reynolds number and not by the absolute value of the pressure.

The calculation of the mass flow from the pressure drop across the orifice is done according the ISO 5167-1 norm.

In many engine designs the port and valve assembly are used to create a rotational motion (swirl) inside the engine cylinder during the induction process, or the cylinder can be shaped to restrict the flow through one side of the valve opening to generate swirl. Swirl generation significantly reduces the valve flow coefficient. The measurement of the flow coefficient is done on the cylinder head including the intake and exhaust port channels. So the pressure drop across a valve includes these channels. The disadvantage is that the losses in these pipes are included in the flow coefficient. Ideally losses should be determined separately from the valve flow coefficient, so that the effect of the shape of the intake and exhaust port on its own could be investigated.

3.2 Steady Flow Results and Discussion. The result of the measurements for the flow from the inlet to the cylinder are shown in Fig. 8 and Fig. 9. Figure 8 gives the C_D value for a certain valve lift, as a function of the Reynolds number. The Reynolds number is calculated based on the diameter of the pipe before the valve and the velocity before the valve. It is clear that for a certain valve lift there is a significant effect of the Re number. For low valve lifts (0.5,1,1.5 mm) the value of C_D increases with the Re number to a limit value at high Re numbers. For medium valve lifts (2,3 mm) the Re effect has become less, where for high valve lifts (5,6 mm) there is a minimum in C_D with Re number. The importance of the valve lift itself on C_D remains. Figure 9 displays the same results as a function of valve lift only. From Fig. 8 it is clear that for most valve lifts the largest C_D

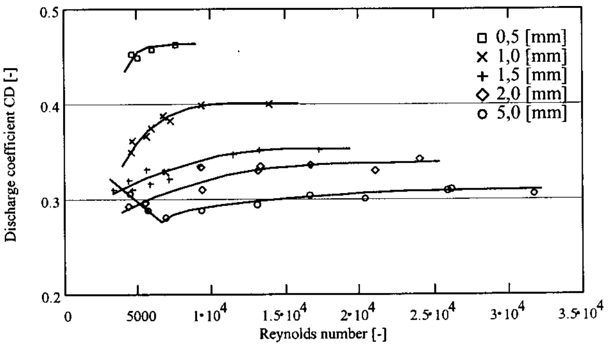

Fig. 8 Discharge coefficient for inlet valve

values occur at high Re number only, or at high and very low Re number together (e.g., 5 mm). That is why in Fig. 9 the largest C_D coefficients for each valve lift correspond to measurements with flow of high Re number or very low Re number.

The lowest C_D coefficients for each valve lift correspond to measurements with flow of low Re number.

For the exhaust valve the Reynolds number is calculated based on the diameter of the pipe after the valve and the velocity after the valve. The results are shown in Fig. 10 and Fig. 11. At low valve lifts, the C_D value increases with the Re number to a limit value at high Re (alike the inlet valve). At 4 (and 5) mm valve lift the C_D value at low Reynolds is high, but there is a sudden transition to a lower value at about Re 7500 followed by a restoration at higher Re. At 6 mm valve lift, the C_D value increases very fast with (low) Re number, followed by an abrupt decrease and restoration. Figure 11 displays the same results as a function of valve lift only. From Fig. 10 it is clear that for most valve lifts the lowest C_D values occur at low Re number, so in Fig. 11 the lowest C_D coefficients for each valve lift correspond to measurements with flow of low Re number.

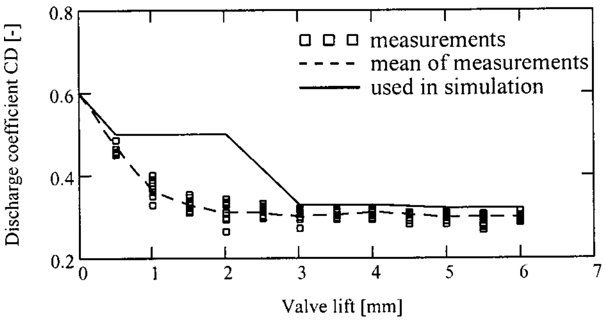

Fig. 9 Discharge coefficient for inlet valve

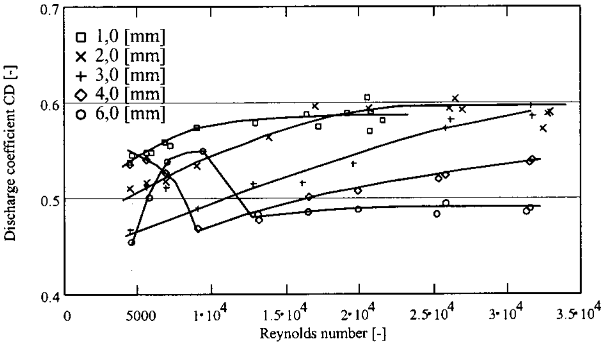

Fig. 10 Discharge coefficient for exhaust valve

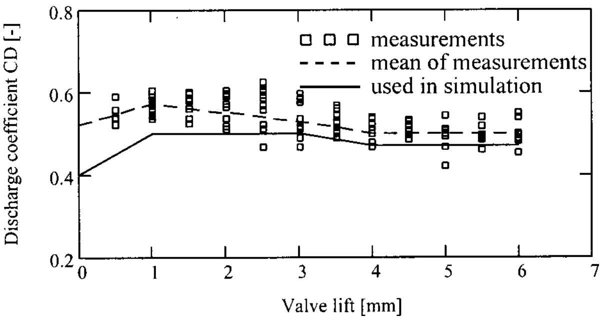

Fig. 11 Discharge coefficient for exhaust valve

The C_D coefficients used for the simulations however are not the same as the measured ones. The coefficients used are shown in Fig. 9 and Fig. 11 (full line). The coefficients used in the simulation were determined starting from the measured ones in steady flow with introduction of changes in order to take account of transient effects in such a way that agreement with the measurements could be obtained (see section 4). For the inlet valve (Fig. 9) the used C_D value stay relatively high (about 0.5) at valve lifts below 2 mm but drops (between 2 and 3 mm) to approximately the measured values. So for high valve lifts the largest of the measured values are found. As explained in a previous paragraph, these measurements can correspond to flow with high Re number. It seems as if the C_D value for low lifts is to be held until a sudden transition reduces the C_D value. In Fig. 12(*a*) the Reynolds number (from simulation) in the last node before the intake valve is shown together with the valve lift (dimensionless). At high valve lifts the Re number is also high. This explains why after the transition the measured C_D values with high Re number are found. Because the inlet valve opens relatively late (12°ca after TDC) and has no overlap with the exhaust valve (closes at 5°ca after TDC) there is a large acceleration of the flow into the cylinder when the inlet valve opens. This acceleration introduces sudden transition phenomena where on the steady test rig the transition (when the flow is gradually increased) is much smoother. This explains the necessary difference between the measured and used C_D values at low valve lifts.

Also for the exhaust valve, other coefficients than the ones measured on the static test rig are used for the simulations. Again at low lifts the measured and used coefficients are not the same. For low valve lifts the C_D values used are lower than the measured ones, and for lifts above 2 mm the lowest of the measured values are used. The lowest values of the measurements correspond to flow with low Re number Fig. 12(*b*) shows the Reynolds number in the first node after the exhaust valve (from simulation) together with the exhaust valve lift (dimensionless). At high valve lifts, the Reynolds number is low (even reversed flow occurs). This explains the trend to follow the measured C_D values with low Reynolds numbers for high valve lifts. The blow down pulse at the opening of the exhaust valve gives flow conditions that are very difficult to reproduce at a steady test rig. It is not surprising

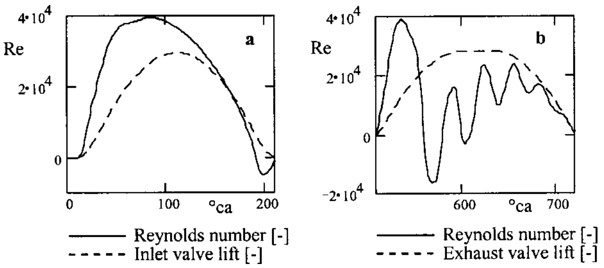

Fig. 12 Reynolds number and valve lift

that in the region of low valve lifts differences occur between measured C_D values and values necessary for good simulation results.

The coefficients used in the simulation program have been tuned to reproduce the correct pressure traces inside and out the cylinder. It has to be noted that the same set of coefficients is used for all the simulations. As will be shown later, the C_D coefficients have a large influence on the pressure traces.

4 Simulation Results

For the complete test rig as shown in Fig. 2 the simulation results are shown in Fig. 13. Figure 13(*a*) shows the measured (full line) and calculated (dashed line) pressure at the position of the pressure transducer in the inlet pipe. There is a strong pressure drop due to the large section reduction in the venturi. The section before and after the venturi has ∅31.75 mm while in the ''throat'' section of the venturi this is reduced to ∅12 mm. There is a small amount of back flow through the inlet valve near its closing point (210°ca). The shape of the calculated mass flow curve is the same as the Reynolds curve in Fig. 12(*a*). It is clear on Fig. 12(*a*) that the calculated mass flow (Reynolds number) becomes negative when the inlet valve closes. On the pressure trace a pressure build up (larger than atmospheric pressure) is noticed near closing of the inlet valve. This is due to the inertia effects of the flow. After closing of the inlet valve, the pressure waves can travel back and forth from the buffer vessel (because of the large volume this is almost an open end boundary) to the inlet valve (closed end boundary). An error in the length of the complete inlet pipe would be easy to find since the simulated and measured pressure traces would not be in phase. Due to friction and passage through the venturi the amplitude of the pressure wave declines.

Figure 13(*b*) shows the low pressure part of the cylinder pressure. Via the valve boundary condition the flow in inlet and cylinder are linked. In this boundary condition a mass flow coefficient is necessary. Because the inlet valve opens relatively late (12°ca after TDC) and has no overlap with the exhaust valve (closes at 5°ca after TDC) there is a pressure drop in the cylinder when both valves are closed. Next the inlet valve opens with a large acceleration of the flow due to the large pressure difference before and after the valve. This is why in Fig. 12(*a*) the maximum flow rate occurs early in the intake stroke (max flow reached at 65°ca remains almost constant to 100°ca). For the second half of the intake stroke (100°ca–210°ca) the piston speed decreases and the large pressure difference is levelled, so intake and cylinder pressure follows the same (increasing) trend until the inlet valve closes.

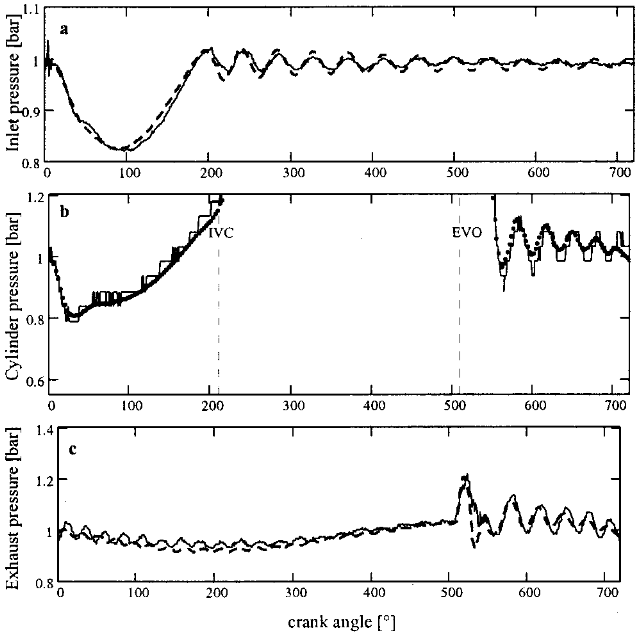

Fig. 13 Comparison of measured and calculated pressure diagrams (initial test set-up, gasoline)

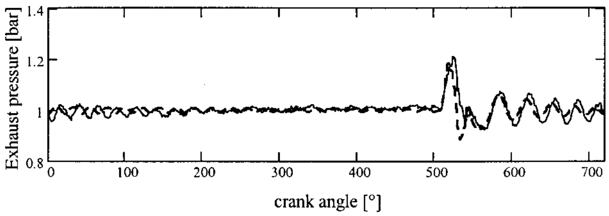

Fig. 14 Comparison of measured and calculated pressure in the exhaust pipe (without exhaust buffer vessel)

The thermodynamic cycle calculation is not the subject of this paper, but provides the correct release conditions for the flow. When the exhaust valve opens, a large pressure difference (3 to 4 bar in the cylinder versus about 1 bar in the exhaust system) over this valve exists. A large (steep) pressure wave is released in the exhaust pipe. The in-cylinder view of this phenomenon (Fig. 13(*b*)) is characterized by a steep pressure drop followed by pressure oscillations due to reflections of the pressure wave in the exhaust system through the exhaust valve in the cylinder. Figure 13(*c*) shows the measured and calculated pressure in the exhaust pipe, at the location of the pressure transducer. The steep pressure wave is noticed as soon as the exhaust valve opens. This wave however is partly destroyed by reflection on the sudden section change. This sudden section change causes a reflection and a transmission of an incoming wave. When this abrupt pressure phenomenon has settled, only travelling waves can be seen in the exhaust pipe. These waves can also be noticed on the pressure trace in the cylinder.

The pressure in the exhaust system has also a component with longer wave-length than the previously mentioned waves. This is the result of a dynamic action between the buffer vessel and the very long (7.25 m) pipe connected to it. In order to show the effect on measurement and simulation, the exhaust buffer and the long pipe connected to it were removed. Figure 14 shows the measured and simulated pressure trace in this case. Now the pressure in the exhaust system before the exhaust valve opens is constant and equal to atmospheric pressure. The rest of the wave action can be explained in a similar way as before.

For comparison, a simulation without ignition (motored engine) is shown in Fig. 15. There is a significant difference in the pressure during the exhaust stroke (both in the cylinder and in the

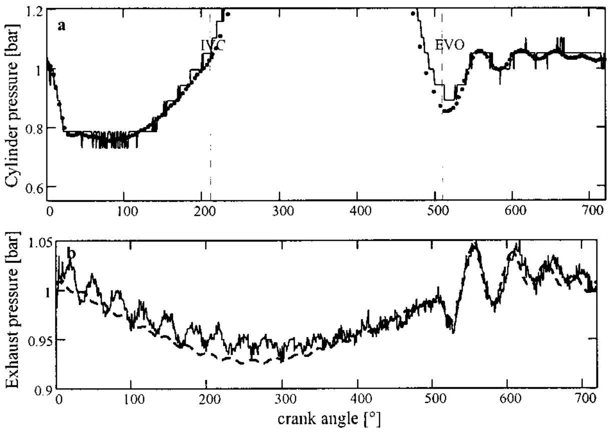

Fig. 15 Comparison of measured and calculated pressure diagrams during motoring

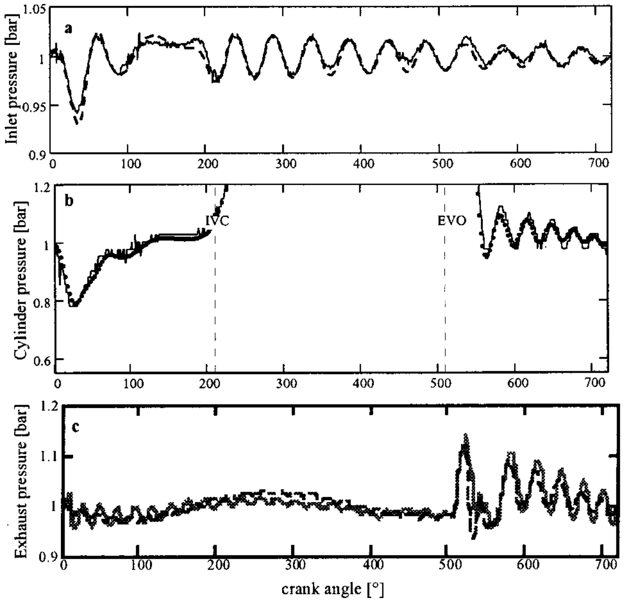

Fig. 16 Comparison of measured and calculated pressure diagrams (modified test set-up, methane)

exhaust pipe). Because of cooling effects during compression and expansion, the cylinder pressure at the end of the expansion stroke is lower than the pressure in the exhaust pipe. When the exhaust valve opens, a flow from the exhaust pipe into the cylinder occurs. This can be seen on the cylinder pressure trace, Fig. 15(*a*) (pressure increases when EVO) and on the exhaust pressure trace, Fig. 15(*b*) (when EVO there is a pressure drop). The pressure wave amplitudes are smaller than with combustion and the pressure trace does not show the blow down pulse.

With the modified engine as described in section 2 to allow for gaseous fuels, similar tests were carried out. The most important modifications are the replacement of the gas venturi by a gas supply ring, and a fan. The last pipe in the exhaust system was made shorter (3.5 m instead of 7.25 m).

Figure 16(*a*) shows the measured and calculated pressure traces in the inlet pipe at the same location as the case with the venturi. It is clear that the pressure drop is much smaller now, because of the very small obstruction of this ring for the flow. After an initial pressure drop the flow during the intake stroke is much more influenced by pressure waves than in the case with venturi (the venturi acts as an obstruction for pressure waves). Again a small pressure build up is noticed when IVC due to the pressure build up in the cylinder after BDC (a small amount of back flow in the inlet pipe).

The pressure drop in the cylinder (Fig. 16(*b*)) due to the late opening of the inlet valve is reduced fast because the flow in the inlet pipe shows much less resistance than when a venturi is installed. In the interval 100°ca–200°ca the pressure is nearly the atmospheric pressure. For the exhaust pressure trace (Fig. 16(*c*)) the same conclusions hold as for the case with venturi. Because the last pipe is shorter the action between buffer vessel and pipe is different.

For this simulation the fuel rate was measured by putting the methane bottle on a balance. Together with a gas analysis (and the engine speed), the amount of trapped air per cycle can be calculated. It is verified that with the used flow coefficients the error on the trapped mass was smaller than 1 percent.

The calculations shown are independent of the grid resolution. In fact changing the spacing between the nodes from 10 mm to 100 mm in the calculations gives no significant change to the result.

As an indication of the importance of the flow coefficients, a simulation has been carried out using the mean C_D coefficients (dashed lines on Fig. 9 and 11) for inlet and exhaust valve. The result is shown in Fig. 17 and has to be compared to Fig. 16(*b*) where the correct values were used. The pressure during the intake stroke shows that the resistance to the flow is too large and thus the simulated pressure is too low compared to the measurement. This is because the mean C_D coefficients for the inlet valve are too low during the first part of the intake stroke. Tuning the C_D coefficients until the measured pressure in the cylinder is obtained for the intake stroke results in the full line in Fig. 9.

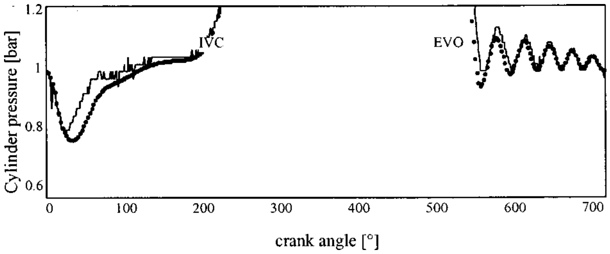

Fig. 17 Comparison of measured and calculated pressure diagrams with measured C_D coefficients

For the exhaust stroke the blow down pulse releases the pressure too fast because the C_D coefficients in the first part of the exhaust stroke are too large. This makes that the wave action in the cylinder and the exhaust system is wrong. Tuning the C_D coefficients until the measured cylinder pressure is obtained for the exhaust stroke results in the full line in Fig. 11.

Conclusions

The pressure-time history in the inlet-and exhaust pipe and in the cylinder of a single cylinder engine was calculated with a new TVD scheme (two stage cell-vertex TVD scheme with superbee limiter).

Comparison was made with measured pressure traces for different engine configurations under motoring and firing conditions. The firing tests were done with gasoline (venturi type mixture system), methane (ring type mixture system) and with modified exhaust systems. For each configuration the comparison is excellent provided that the C_D values are tuned properly.

Attention was paid to the flow discharge coefficients of the inlet-and exhaust valve. Therefore a special steady flow test rig was built and the flow discharge coefficients were measured as function of the valve lift and the mass flow rate (Reynolds number). It was observed that steady state flow coefficients at low valve lifts have to to be modified for transient effects in order to be useful in simulations.

Acknowledgment

The research reported in this paper was supported by the IWT (Flemish institute for the stimulation of scientific-technological research in industry), Belgium and by TNO, Road-Vehicles Research Institute, Delft, The Netherlands.

References

[1] Goyal, M., Scharpf, G., and Borman, G., 1967, ''The Simulation of Single Cyclinder Intake and Exhaust Systems,'' SAE Paper 670478.
[2] Pearson, R. J., 1994, ''Numerical Methods for Simulating Gas Dynamics in Engine Manifolds,'' Ph.D. thesis, Department of Mechanical Engineering, UMIST.
[3] Corberán, J. M., and Gascón, M. L., 1995, ''TVD Schemes for the Calculation of Flow in Pipes of Variable Cross-Section,'' Math. Comput. Model., **21**, No. 3, pp. 85–92.
[4] Vandevoorde, M., Sierens, R., Dick, E., Vierendeels, J., and Baert, R., 1997, ''Comparison of Algorithms for Unsteady Flow Calculation in Inlet and Exhaust Systems of IC Engines,'' ASME J. Eng. Gas Turbines and Power, **122**, No. 4, pp. 541–548.
[5] Vandevoorde, M., Vierendeels, J., Dick, E., and Sierens, R., 1998, ''A New

TVD Scheme for the Calculation of the One-Dimensional Flow in Inlet and Exhaust Pipes of Internal Combustion Engines,'' Journal of Automotive Engineering (Part D), **212**, pp. 437–448.

[6] Roe, P. L., 1981, ''Approximate Riemann Solvers, Parameters Vectors, and Difference Schemes,'' J. Comput. Phys., **43**, pp. 357–372.

[7] Dick, E., 1988, ''A Flux Difference Splitting Method for the Steady Euler Equations,'' J. Comput. Phys., **76**, pp. 19–32.

[8] Dick, E., 1990, ''Multigrid Formulation of Polynomial Flux-Difference Splitting for Steady Euler Equations,'' J. Comput. Phys., **91**, pp. 161–173.

[9] Tabaczynski, R. J., Ferguson, C. R., and Radhakrishnan, K., 1977, ''A Turbulent Entrainment Model for Spark-Ignition Engine Combustion,'' SAE Paper 770647.

[10] Hires, S. D., Tabaczynski, R. J., and Novak, J. M., 1978, ''The Prediction of Ignition Delay and Combustion Intervals for a Homogeneous Charge Spark Ignition Engine,'' SAE Paper 780232.

[11] Tabaczynski, R. J., Trinker, F. R., and Shannon, B. A. S., 1980, ''Further Refinement and Validation of a Turbulent Flame Propagation Model for Spark Ignition Engines,'' Combust. Flame, **39**, pp. 111–121.

[12] Sierens, R., Rosseel, E., and Baert, R., 1999, ''Evaluating Piezo-Electric Transducer Response to Thermal Shock Using In-Cylinder Pressure Data,'' SAE Paper 1999-01-0935.

[13] Heywood, J. B., 1988, *Internal Combustion Engine Fundamentals*, ISBN 0-07-100499-8, McGraw-Hill, New York.

M. Vandevoorde
Atlas Copco Airpower, Industrial Air Division,
Wilrijk, Belgium

J. Vierendeels

R. Sierens

E. Dick

Department of Flow,
Heat and Combustion Mechanics,
Ghent University, Belgium

R. Baert
TNO Road-Vehicles Research Institute,
Delft, The Netherlands

Comparison of Algorithms for Unsteady Flow Calculations in Inlet and Exhaust Systems of IC Engines

A comparison of different numerical algorithms used in commercial codes for the calculation of the one-dimensional unsteady flow in the pipes of the inlet and exhaust systems of internal combustion engines is presented in this work. The comparison is made between the Method Of Characteristics (MOC), different Lax-Wendroff schemes, first order upwind schemes and the newest TVD (Total Variation Diminishing) schemes. These algorithms are representative for the complete evolution noticed in the computer codes from the beginning of their use to the present state of the art. Two models of realistic problems in engine simulation tasks are considered: the shock tube calculation (so called Sod's problem) and the calculation in a tapered pipe. The first test case simulates the exhaust valve opening and releasing a pressure (shock)wave in the exhaust manifold while the other test case covers any gradual variation in the cross section of the manifold pipes. For both test cases computed results are compared with an exact solution and computer time and accuracy are evaluated. None of the examined schemes is completely satisfactory. They either show too much overshoots (for the first test case), or they have local discretization errors (at the section changes of the second test case). A new TVD scheme is proposed that does not introduce any of the foregoing inaccuracies. With this scheme overshoots and dips are eliminated and mass balances are fulfilled, while maintaining high accuracy. [S0742-4795(00)00304-5]

Introduction

The lay-out of the intake and exhaust system of a reciprocating internal combustion engine is an important aspect of its design. Because this design governs the gas flow into and out of the engine's cylinders, it affects both volumetric efficiency and residual gas fraction, which in turn have an important influence on fuel consumption and emissions.

Initially ''filling and emptying'' models were used to describe the engine as a series of volumes (cylinders, manifolds, filters, coolers) that exchange mass, while neglecting the gas dynamics taking place in the pipes connecting these volumes. Computer codes taking this approach are still being used by engine designers. A well-known example is TRANSENG, a code which was developed by Watson and co-workers at Imperial College [1] and which initially was advocated by him as a tool in the development of engine control strategies. However, from the start it was realized that this approach has its shortcomings because it neglects the wave action effects in the pipes. Especially for engines with complex intake and exhaust manifolds (the larger marine engines and the small automotive engines) this leads to errors. That is why already more than 30 years ago gas dynamic models were introduced to study the engine gas exchange process in these engines.

Gas dynamic models solve the mass, momentum, and energy conservation equations for the unsteady compressible flow in the intake and exhaust. The gas exchange process calculated with these models is then linked to a zero dimensional thermodynamic model of the in-cylinder combustion process.

Most calculations of the gas dynamics have been based on one-dimensional formulations of the governing equations. The first computer code taking this approach was developed by Benson et al. [2] at UMIST. This code was based on the method of characteristics. Different versions of this code were used for almost three decades in the development of intake and exhaust systems and it was licensed to a great number of companies. Similar codes evolved at other places (e.g., Blair and co-workers at the Queen's University of Belfast [3]). Soon however the computational advantages of the differential methods were pointed out (Lax-Wendroff [4], Richtmyer [5]). It was the start of a whole family of codes using the Lax-Wendroff method. In Germany, industry and universities worked together for years in the development and validation of a computer code taking this approach (Seifert [6,7]). Because these Lax-Wendroff methods can handle discontinuities but cause local overshoots, flux correction techniques were introduced next (Bulaty and Niessner [8]) to further improve them.

Most commercial codes currently available use some form of these finite volume methods (WAVE, PROMO, BOOST, GTI). At the same time some other commercial codes still use the method of characteristics (MERLIN, ICENG). However, both approaches were already developed some time ago and start to be somewhat outdated. Nowadays, TVD (Total Variation Diminishing) schemes are being introduced for the simulation of the gas exchange process in IC engines (Winterbone and Pearson form UMIST [9], Blair et al. [10]). Such schemes are well-known amongst Computational Fluid Dynamics practitioners but are rather new for most of the engine developers.

This paper gives a general overview of the evolution of the above mentioned algorithms, without going into details. The algorithms mentioned in Table 1 are applied to two test cases that are representative for internal combustion engines. The actual inlet and exhaust systems of internal combustion engines are much more complicated than the two test cases used in this paper. The test cases are meant for an analysis of fundamental properties of the schemes. Other and newer, one-dimensional schemes are continuously being investigated and presented in the literature. They are however not included in this comparison. Similarly, although

---

Contributed by the Internal Combustion Engine Division of THE AMERICAN SOCIETY OF MECHANICAL ENGINEERS for publication in the ASME JOURNAL OF ENGINEERING FOR GAS TURBINES AND POWER. Manuscript received by the ICE Division April 7, 2000; final revision received by the ASME Headquarters April 17, 2000. Technical Editor: D. Assanis.

Table 1 Numerical schemes

No	Scheme
1	MOC
2	Richtmyer
3	Ni
4	FCT
5	Upwind, 1st order
6	TVD, 1 stage, minmod limiter
7	TVD, 2 stage, minmod limiter
8	TVD, 4 stage, minmod limiter
9	TVD, 1 stage, superbee limiter
10	TVD, 2 stage, superbee limiter
11	TVD, 4 stage, superbee limiter
12	ENO, 1 stage, minmod limiter
13	upwind, cell-vertex, 1st order
14	TVD, 1 stage, minmod, cell-vertex
15	TVD, 2 stage, minmod, cell-vertex
16	TVD, 4 stage, minmod, cell-vertex
17	TVD, 1 stage, superbee, cell-vertex
18	TVD, 2 stage, superbee, cell-vertex
19	TVD, 4 stage, superbee, cell-vertex

two and three-dimensional simulation models have been introduced for complex boundaries (e.g., exhaust pipe junctions and converter systems (Zhao and Winterbone [11], Flamang and Sierens [12])), especially when the shape effects of these boundaries are investigated, these models are not considered here.

1 Test Cases

Two different test cases are used for the comparison of the different algorithms.

1.1 The Shock-Tube Calculation. This test case is generally called Sod's problem [13] and is used here to compare the accuracy and calculation time of the numerical schemes. It is representative for an exhaust valve which opens infinitely fast. For the numerical schemes it forms a severe test. Quality differences of the schemes can be clearly shown. Further it is interesting because the analytical solution (=exact solution) is known (as long as the waves do not interfere with reflected waves), and this analytical solution can serve as a reference for the comparison.

The problem consists of a pipe with constant section connected to a reservoir on the left side and to the atmosphere on the right side with $p_{\mathrm{res}} > p_{\mathrm{atm}}$ (Fig. 1). Within the pipe a diaphragm separates a volume of gas at reservoir conditions from that same gas at atmospheric conditions. At $t<0$ the gas is at rest. The changes of the gas are calculated when the diaphragm is broken at $t=0$. The gas flow is from left to right in Fig. 1.

At $t=0$ the diaphragm is broken and the following changes occur:

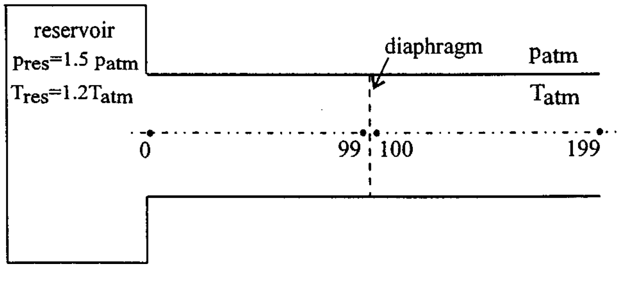

Fig. 1 The shock-tube test case

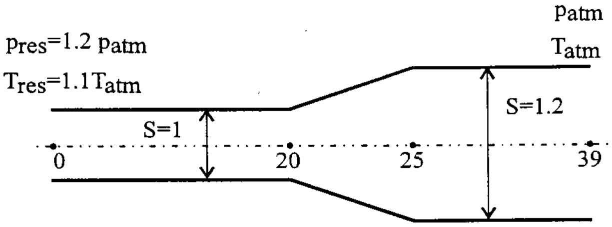

Fig. 2 Tapered pipe test case

- a shock wave (sudden change of pressure, density and velocity)
- an expansion wave (gradual change of pressure, density, and velocity)
- a contact discontinuity (sudden change of density, with constant pressure and velocity)

For the calculations the initial conditions have been set at $p_{\mathrm{res}} = 1.5 p_{\mathrm{atm}}$; $\rho_{\mathrm{res}} = 1.25 \rho_{\mathrm{atm}}$ therefore $T_{\mathrm{res}} = 1.2 T_{\mathrm{atm}}$. The gas is assumed to be perfect ($\kappa = 1.4$).

1.2 Calculation for a Pipe With a Gradual Area Change (Tapered Pipe). This test case is selected in particular to look at the accuracy when area variations are included.

Due to its theoretical constitution the method of characteristics has difficulties to comply with the law of conservation of mass when applying it to a flow through a pipe with a gradual area change. Van Hove and Sierens [14] demonstrated that the cycle integrated mass flow is not constant in all mesh points of a tapered pipe. This results in an error of the mass balance of the engine. The total mass of the exhaust gases for each cycle differs from the total of mass of admitted air and fuel. This effect is not so important for natural aspirated engines, but it can cause severe errors when estimating the operating point of the compressor and turbine of a turbocharged engine from the above mentioned intake and exhaust flows.

The other methods that are considered in this study are based on a fixed grid in the pipe, and because they directly discretize the conservative equations they have the mass conservation property automatically. However, they show a different problem with this test case. The calculated properties (pressure, density, temperature, . . .) have a dip or an overshoot in the nodes where the area changes (nodes 20 and 25 on Fig. 2).

Because in the manifold of reciprocating engines area variations are obvious and frequent, this problem is considered important enough to be investigated. In this test case an area change of 20 percent is taken. The initial conditions have been set at: $p_{\mathrm{res}} = 1.2 p_{\mathrm{atm}}$, $T_{\mathrm{res}} = 1.1 T_{\mathrm{atm}}$. Again the gas is assumed to be perfect.

2 Numerical Algorithms

The one-dimensional unsteady gas flow in a pipe is described by the following basic equations:

The Continuity Equation.

$$\frac{\partial \rho.S}{\partial t}+\frac{\partial \rho.u.S}{\partial x}=0 \tag{1}$$

The Momentum Equation.

$$\frac{\partial \rho.u.S}{\partial t}+\frac{\partial \rho.u^{2}.S}{\partial x}=-\frac{\partial p.S}{\partial x}+p.\frac{\partial S}{\partial x}-f.\frac{\rho.u^{2}}{2}.\frac{u}{|u|}.O \tag{2}$$

The Energy Equation.

$$\frac{\partial \rho.E.S}{\partial t}+\frac{\partial \rho.E.u.S}{\partial x}=-\frac{\partial p.u.S}{\partial x}+q.\rho.S \tag{3}$$

This set of hyperbolic partial differential equations is in conservative form and describes the conservation of mass, momentum, and energy. For a periodic flow the integration of mass through an area of the pipe during one complete period has to be constant, but momentum and energy are lost due to wall friction and heat transfer.

In the following sections, the properties of the schemes are discussed. A summary of the basic features of the schemes is given in the appendix.

2.1 Method of Characteristics (MOC). This method does not discretize equations (1) to (3) but a set of normal differential equations. These so-called characteristic non-dimensional equations are obtained by rearranging the initial equations, using Riemann variables λ and β (characteristic combinations of density, pressure and velocity) and normalizing the equations by dimensionless variables along the characteristic directions (each of the Riemann variables is moving along the pipe in a certain direction with a certain speed).

In the continuous domain both sets of equations are equivalent. However, discretization of the equations generates discretization errors. Because the discrete or algebraic equations do not express explicitly the conservation of mass, momentum and energy, the discretization errors introduce conservation errors, especially for important area changes of a pipe.

The original method of Jenny [15] was a completely graphical method. For the pressure wave characteristics (these are the characteristics which follow the pressure waves) as well as for the particle characteristic (this is the characteristic which follows the mass transportation and as a consequence the contact discontinuity; it is generally called the path line) trajectories are drawn and followed during the time evolution. Because this method is very time consuming, Benson et al. [2] developed a hybrid method. In this hybrid method the pressure wave characteristics are calculated with a simple first-order mesh method, in combination with the original method for the particle characteristic. This implies that the accuracy of the pressure waves is first order, while the contact discontinuity is followed with path lines and is therefore given an exact calculation. It is the hybrid method of Benson that is used as MOC for the first test case. In [14] a new algorithm is described that fulfils the law of conservation of mass in tapered pipes while using the hybrid method of characteristics. The key idea of this adapted method is to concentrate any area change over one mesh length in the mesh points instead of using an area gradient along the characteristic lines. Its disadvantage is that the computing time increases. This adapted method is used as MOC for the second test case.

2.2 Lax-Wendroff Schemes (LW). Lax-Wendroff schemes are finite volume schemes, directly discretizing the conservative set of Eqs. [4] When applied to the conservative form of the gas flow equations, these schemes guarantee the conservation of mass, momentum and energy, even for the discretized equations. In a finite volume method (FVM) the contact discontinuity is not followed explicitly (like the MOC does with the path line) but a single fixed grid is used. With FVM schemes the pressure waves and the contact discontinuity are given the same numerical treatment. The order of accuracy implied by the numerical scheme therefore applies to both phenomena.

With the Lax-Wendroff scheme it is possible to achieve second order accuracy (for both the spatial and time derivative). For the calculation of pressure waves this is a major improvement to the MOC, but on the other hand the exact representation of the contact discontinuity in the MOC is lost. In fact, the large overshoots in the calculation of discontinuities are a major drawback of the LW scheme. They are calculated with large oscillations which are clearly unphysical and lead to problems in the simulation of non steady flow in exhaust systems of engines. Furthermore, some of the finite volume schemes show discretization errors at section changes when calculating tapered pipes (which, however, does not influence the total integrated mass during one cycle).

In this study three well known and ''state of the art'' two-step LW based schemes have been examined: the Richtmyer scheme (with a Runge-Kutta like integration method) [5], the Ni scheme [16], and the MacCormack variant [17] (with a predictor-corrector like integration method). The MacCormack variant did not show any difference from the Richtmyer scheme and will not be explicitly mentioned anymore. For the constant section test case the results obtained with the Richtmyer and the Ni scheme are similar (this is not surprising because they originate from the same theory). For the second test case however the Richtmyer scheme shows a discretization error at section changes whereas the Ni scheme (due to its construction) does not show this problem.

A further extension, specifically meant to eliminate overshoots, is the FCT (flux corrected transport) approach as developed by Book et al. [18] and Boris and Book [19]. These FCT algorithms are generally accepted and they are considered to be very efficient. Mathematically it is obvious that this was the first attempt to achieve what nowadays the TVD schemes realize. Although it is a major improvement to the LW method this method has a severe deficiency. The conservative property of the LW method is lost. The FCT method checks for changes in the calculated properties, then applies a diffusion followed by an anti-diffusion. It is clearly seen that the overshoots in the calculation of the traveling waves in the constant section test-case are nearly eliminated (both in the Ni and Richtmyer scheme). But because the FCT algorithm cannot distinguish between overshoots that are unphysical and gradients in the solution, the diffusion and anti-diffusion are also applied to the latter. This results in a Ni scheme that originally performed well in the second test case and that with FCT correction has the same problem as the Richtmyer scheme.

2.3 First-Order Upwind Scheme. The LW schemes mentioned above are central schemes (Centered Space). In such schemes information is obtained from the whole environment (nodes $i-1,i,i+1$) for the calculation of the new value in one particular node *i*, even from directions where this is physically not correct. This leads to overshoots in the calculation of discontinuous phenomena.

With upwind schemes the information is only obtained from the relevant physical directions, eliminating the cause for the overshoots at discontinuities. As mentioned before, with FVM schemes the order of accuracy in the scheme will be noticed in the calculations. These upwind schemes have first order accuracy.

The method used in this study is a one-dimensional variant of the polynomial Flux Difference Splitting (FDS) technique as developed by one of the authors [20–22].

2.4 Existing TVD Schemes (Total Variation Diminishing). TVD schemes imply that the solution shows no numerical oscillations [23,24]. They are an extension of the first order upwind schemes by the use of non-linear techniques (the so-called limiters) to achieve second order accuracy. The kind of limiter used has an important influence on the results.

Besides second order accuracy for the spatial derivative, the first generation of TVD schemes only had first order accuracy in time. The algorithms are ''one step and one stage,'' which means that the time step from *n* to $n+1$ (one step) goes in one stage. It is also possible to adapt multi-stage algorithms, by dividing a step in a number of sub-steps or stages. So a ''four-stage stepping'' indicates that four sub-steps are used. If the coefficients for these sub-steps are correctly chosen, an increase of the number of sub-steps also increases the time accuracy of the scheme.

In this work, modified Runge-Kutta methods for the time-integration have been used with well defined sets of coefficients to allow for a higher CFL number (this is an indicator of the allowable size of timestep, depending on the velocity of sound and the mesh length).

In this study different TVD schemes have been programmed,

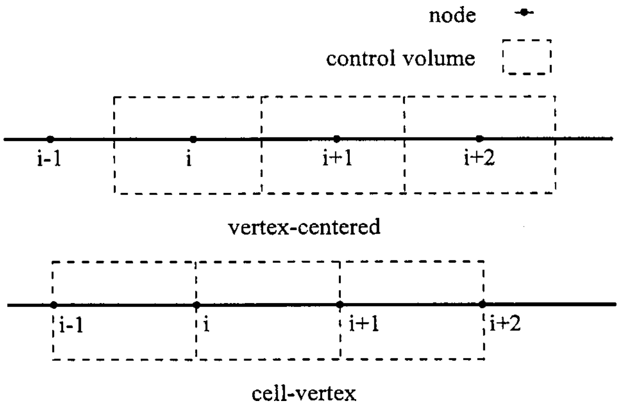

Fig. 3 Location of the control volumes

with one, two or four stages and with the minmod and superbee limiter. The results are extremely good for the two stage TVD with the superbee limiter. However, note that the problem with the calculation of the second test problem remains; there are local discretization errors at section changes. A further problem comes from the limiters. None of them is able to act in a physical correct way at the nodes where the section changes.

It can be shown that the TVD schemes switch back to first-order accuracy for the nodes around discontinuous phenomena. To prevent this, Harten et al. [25] developed the ENO (Essentially Non-Oscillatory) scheme. This results in an even higher accuracy, but there is no improvement for the second test case.

2.5 New Developed TVD Scheme. Especially to eliminate the existing problem at the nodes with a section variation, a new scheme is proposed. The previous FVM schemes are of the so called vertex-centered type. This means that the nodes are located in the center of the control volumes (Fig. 3 top). The control volumes are the volumes on which the equations (1, 2, 3) are discretized.

It also implies that the fluxes at the sides of the control volumes will be equal. The results of the calculations however are always shown in the nodes themselves. Identity of the fluxes *in* the nodes is in no way imposed by the numerical scheme, so the error that is seen on the graphs is the numerical discretization error.

It is clear that the only way to actually fulfil the flux balances *in* the nodes is to express the fluxes *in* the nodes themselves. This is achieved by the new cell-vertex TVD scheme (Fig. 3 bottom).

Now the numerical scheme imposes identity of the fluxes in the nodes for the steady solution so that the verification of the balances shows a perfect conservation even at nodes with section variation.

In the cell-vertex formulation, the fluxes are calculated on the boundaries of the control volumes. A flux difference Δf in each volume is obtained which has to distributed to the nodes of that volume. The distribution is done in an upwind way, so that a node intercepts the information from the physical relevant direction. The second order accuracy is obtained in a similar way as with the common TVD scheme. The complete system is second order accurate for the space derivative and first order accurate for the time derivative.

The influence of the limiter and of multi-stage algorithms for the time integration remains, and the same numerical accuracy as with the vertex-centered TVD scheme is obtained, but also the second test case is now calculated very well. Note that it is the only scheme that has these good results for the second, as well as the first test case (the Ni scheme has too much overshoots to be useful in an engine simulation code). A complete description of the algorithm is given in [26].

3 Comparison of the Different Algorithms

3.1 Shock Tube Calculation

3.1.1 Graphs: Comparison With the Exact Solution. In Figs. 4 and 5 a comparison is made of the different changes mentioned in §1.1 against the exact solution. Solutions are shown as linearly varying between grid nodes. An exact discontinuity is represented as a linear variation between two grid nodes.

Figure 4 shows the comparison of the MOC (with a CFL number of 0.95) and the LW-Richtmyer variant. The velocity profile (u) is used for the comparison of the expansion wave (graph on the left) and the shock wave (graph on the right). Because no contact discontinuity is seen on the velocity profile (pressure and velocity are the same over the contact discontinuity) the velocity of sound is used (graph in the middle).

With the MOC the contact discontinuity is very well simulated. This is due to the entropy transport along the particle characteristic which is correctly represented in the MOC. For the pressure waves (λ and β characteristics) a first order mesh method is applied with CFL<1 which results in numerical viscosity and first order accuracy on the pressure waves.

The Richtmyer variant is presented. Other calculations for this test case have shown that there is no difference between the Richtmyer and Ni schemes. The velocity profiles show overshoots due to the information stream opposite to the characteristic direction. The shock and expansion waves are better represented (apart from the oscillations), due to the second order accuracy. The contact discontinuities are treated in the LW schemes in the same way as the pressure waves, and are therefore less accurate than in the MOC.

The LW schemes with FCT give very good results. Nearly all overshoots disappear. It is the same with the first order upwind scheme, although this last scheme has the disadvantage of a low accuracy.

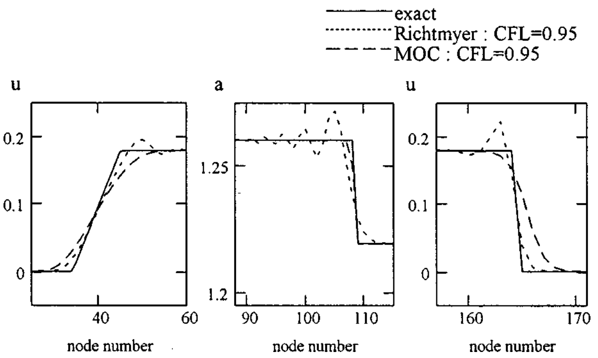

Fig. 4 Velocity and velocity of sound as a function of the location in the pipe (test case 1)

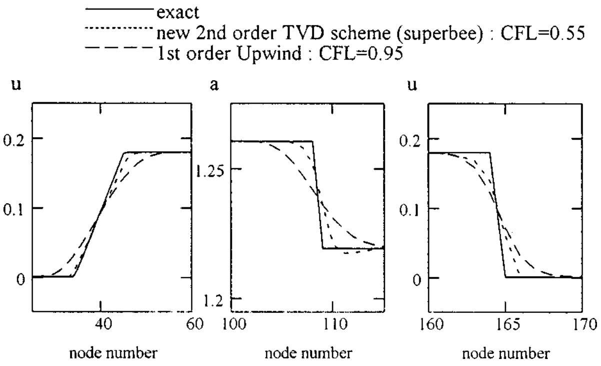

Fig. 5 Velocity and velocity of sound as a function of the location in the pipe (test case 1)

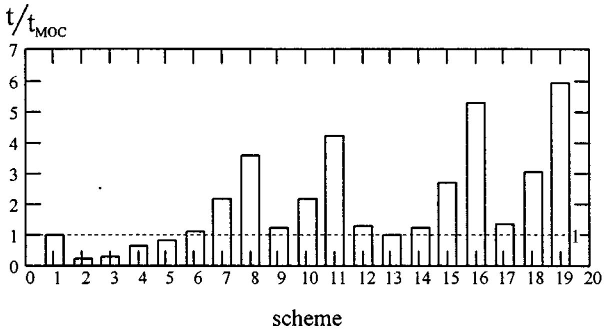

Fig. 6 Computer time relative to the MOC (test case 1)

Very good results are obtained with the TVD, two stages and superbee limiter (vertex-centered) and the cell-vertex TVD schemes. Figure 5 shows the results of the first order upwind scheme and the cell-vertex TVD (2 stage, superbee limiter) scheme.

3.1.2 Computer Time. A comparison of the computer time for the 19 schemes listed in Table 1 is made. For the flow of Fig. 1 and with a given CFL value, the time in seconds for the schemes to reach a given point in time (this point is the same for all the schemes) is plotted in Fig. 6. The plot is made relative to the time needed by the MOC. The MOC used is the hybrid method of Benson, without adapted algorithm for area changes and has an index value of 1.

As already known from other references [9,10], the LW schemes consume less computer time than the MOC. This is also the case for the first order upwind method. It is noted that the allowable CFL-number does not increase proportional to the number of stages so that the computer time for the TVD schemes increases gradually with the number of stages.

The extra work effort is restricted for the ENO method (compare ENO 1 stage with TVD 1 stage). It is remarkable that the cell-vertex TVD schemes from 2 stages on, ask much more computer time than the original TVD schemes (schemes 15, 16, and 18, 19 in comparison with the schemes 7, 8, and 10, 11).

3.1.3 Accuracy. For the same test case and the 19 schemes of Table 1, the calculation is stopped at a certain point in time and the accuracy is examined at that moment by comparing against the exact analytical solution. So a calculation for each scheme at the same moment in time is obtained, and a comparison is possible. The criterion for the error is taken as the summation of all absolute values of the differences to the analytic solution, and this for all mesh points:

$$\sum_{\text{all meshes}} |\text{calculated-analytical solution}|$$

In this way an error for the pressure, the velocity, the density and velocity of sound evolution is obtained. Because the error on pressure and velocity evolution has the same trend, only one of these will be used for discussion. The same holds for the density and velocity of sound evolution. The error developments related to the error with the MOC, are plotted in the Fig. 7.

The LW variants, the Richtmyer and Ni schemes score well for velocity (and pressure) profiles. This is due to the fact that they are second order accurate, but partly compensated by the overshoots. Their performances on density and velocity of sound are less, for the same reason as for the (first order) upwind scheme. Although the last mentioned scheme is a first order accuracy scheme (as can be seen immediately on the comparison of pressure and velocity), it does not generate overshoots, but Fig. 7 shows that the velocity of sound (and density) is less accurate than for the MOC. As mentioned before, it is due to the perfect representation of the contact discontinuity by the MOC, which is not the case for the Richtmyer, Ni and upwind schemes. Because in the pressure development the contact discontinuity does not interfere, it is quite possible that a certain scheme has a better performance for the pressure values than the MOC, without the certainty that this is also true for the velocity of sound.

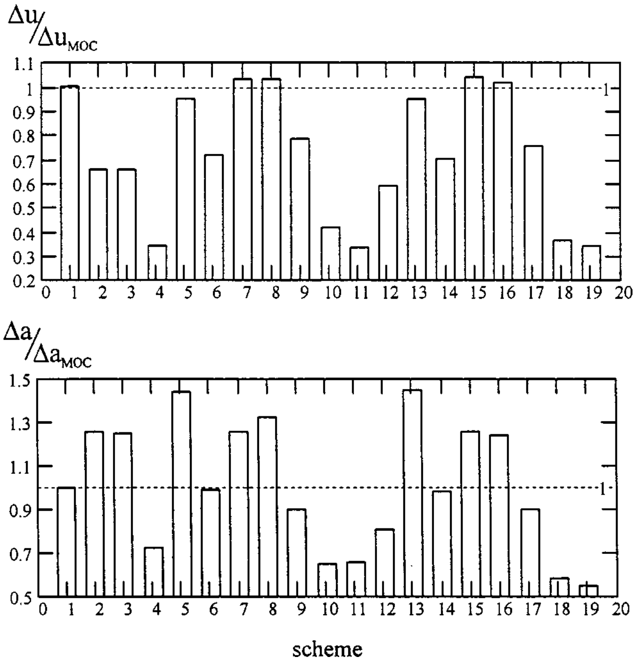

Fig. 7 Errors on the velocity and velocity of sound calculations (relative to the MOC, test case 1)

The influence of the overshoots on the error is recognized by comparing the Richtmyer with the FCT scheme. The differences of the two schemes are the overshoots. The FCT scheme presents very good results.

Surprisingly the TVD schemes with minmod limiter show no real improvement against the MOC. In the TVD schemes the best accuracy is obtained by the superbee limiter. The ENO scheme, although one stage and with the minmod limiter, gives good results as well. For the cell-vertex TVD schemes, the same conclusions can be made as for the original TVD schemes.

3.2 Tapered Pipe Calculations

3.2.1 Graphs. In the Figures 8 and 9 the mass flow is calculated as a function of the mesh points and this for the different schemes: Fig. 8 shows a comparison of Richtmyer, Ni and Lax-Wendroff with FCT after 5000 and 10,000 timesteps. Figure 9 shows the existing TVD (second order, superbee) against the new TVD (second order, superbee) scheme.

The MOC studied here uses the method proposed by Van Hove and Sierens [14] to fulfil the law of conservation of mass. But for this test case, the computer time increases from 26.48 to 52.19 s. This is due to the fact that in each of the considered section area changes a Newton-Raphson iteration method is necessary for the corrections.

For this test case there is a big difference in the different variants, e.g., in the Richtmyer scheme the mass balance seems to be violated, due to an inherent error in describing the section with this scheme. The Ni scheme is considered to be the best LW scheme.

LW with FCT uses a predictor-corrector technique with a strong diffusion in the predictor step and a *nearly equal* anti-

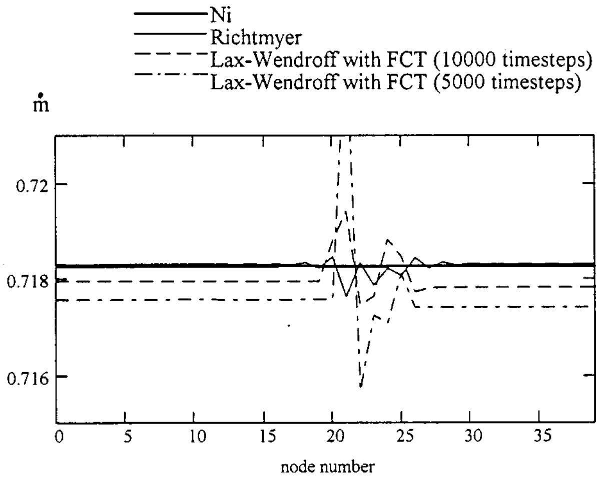

Fig. 8 Mass flow in the mesh points of the pipe (test case 2)

diffusion in the corrector step. For a tapered pipe, where a gradient in the solution is obvious, a steady solution is not possible anymore.

With the existing second order TVD method dips are seen in the boundaries of the tapered pipe (mesh points 20 and 25). This is due to the fact that the mass flows are presented *in* the mesh points, but the mass balances in the scheme are calculated (and solved) *between* the mesh points. In the existing TVD schemes, limiters not capable to handle nodes at section changes also introduce local errors.

Finally, with the new developed cell-vertex TVD scheme, the balances can be solved correctly and the dips are eliminated, while maintaining the high accuracy. With TVD, two step, superbee limiter and cell vertex formulation very good results are obtained.

3.2.2 Accuracy and Computer Time. The test case of Fig. 2 is calculated for a dimensionless time of 5000 (at that time the solution is converged).

For each of the schemes of Table 1, Fig. 10 gives the error of the calculated mass flow against the analytical value. This is the discretization error of the scheme. For all schemes this error is of the order of 0.5 percent. Attention has to be drawn to the error value for the FCT scheme, because this is not an end value (no steady solution because there is no complete compensation of the diffusion and anti-diffusion operators).

There exists also the error on the mass conservation of the scheme, which means the difference of the mass flow at the beginning and end of the pipe. It has been verified that all schemes (the MOC used is implemented with the new algorithm) have an error of the order of 0.001 percent or less.

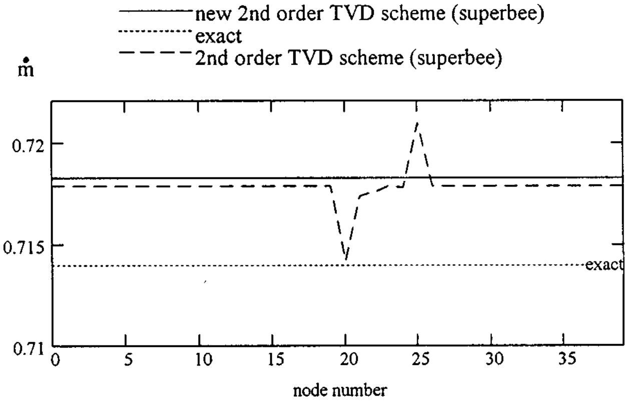

Fig. 9 Mass flow in the mesh points of the pipe (test case 2)

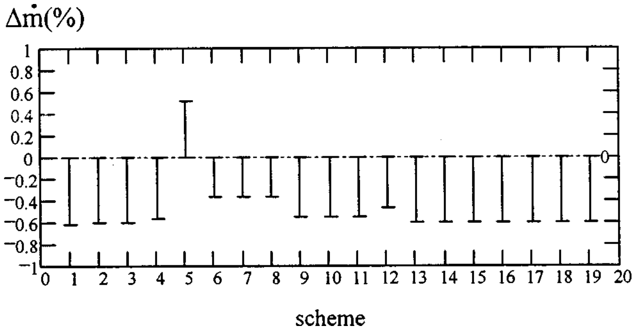

Fig. 10 Error on the calculated mass flow (test case 2)

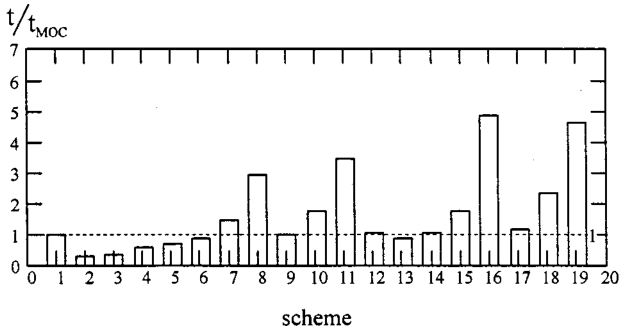

Fig. 11 Computer time related to the MOC (test case 2)

Finally, Fig. 11 gives the computer time. For these schemes that allow inherently for area changes, the computer time has the same trend as in the Fig. 6. For the MOC with adapted algorithm for area changes the computer time doubles for this test case in comparison to the first test case.

For the four stage cell-vertex TVD scheme the computer time consumption is about two times higher than for the two stage scheme but there is almost no improvement in accuracy when going from a two stage to a four stage scheme. Therefore the two stage TVD scheme in cell-vertex form employing the superbee limiter is the best of the considered schemes.

Conclusions

Different numerical schemes have been compared for two test cases: the shock tube calculation and the calculation in a tapered pipe. The response of the different schemes to these test cases is indicative of their capability to calculate the gas flows of the inlet and exhaust systems of IC engines.

With the first test case the attention is focused on the accuracy of the pressure wave calculation and simulation of the contact discontinuities. Where numerical schemes based on the Lax-Wendroff approach generate non-physical overshoots, low order schemes are too dissipative and thus generate a large error.

In the second test case the fulfilment of the law of conservation of mass for the different schemes is examined. Mass conservation between inlet and outlet of the pipe is achieved for all discretization methods and for the adapted method of characteristics. However, local discretization errors at places with an area variation are inherent to these numerical schemes.

All this proves that none of the existing schemes is ideal for the simulation work in IC engines.

Therefore a new scheme was developed. The new scheme that does not introduce any of the mentioned inaccuracies is a TVD scheme of the cell-vertex type. This scheme with the superbee limiter in two stage form has both a high accuracy for the first test case and an exact representation of the mass flow in the second test case together with an acceptable computer time.

Acknowledgment

The research reported in this paper was supported by the IWT (Flemish institute for the stimulation of scientific-technological research in industry) and by TNO, Road-Vehicles Research Institute, Delft, The Netherlands.

Nomenclature

a = speed of sound, [m/s]
c_p = heat capacity at constant pressure, [J/(kg.K)]
c_v = heat capacity at constant volume, [J/(kg.K)]
e = specific internal energy, [J/kg]
E = $e+\mathbf{u}^2/2$=specific total mechanical energy, [J/kg]
f = friction coefficient, [$-$]
$\dot{m}$ = mass flow, [kg/s]
O = internal contour of the pipe, [m]
p = pressure, [N/m^2]
q = heat transfer to the wall, [J/(kg.s)]
S = section of the pipe, [m^2]
t = time, [s]
T = temperature, [K]
u = (convective) velocity along the, [m/s]
x = co-ordinate via the axis of the pipe, [m]
$\Delta\dot{m}$ = mass flow difference, [kg/s]
κ = c_p/c_v=ratio of the heat capacities, [$-$]
ρ = density, [kg/m^3]

Subscripts

res = reservoir
atm = atmosphere

Acronyms

CFL = Courant Friedrichs Lewy number
ENO = essentially non-oscillatory
FCT = flux corrected transport
FDS = flux difference splitting
FVM = finite volume method
LW = Lax-Wendroff
MOC = method of characteristics
TVD = total variation diminishing

Appendix

Basic Features of the Numerical Schemes.

	advantage	disadvantage
MOC (Benson) (1)	+ exact calculation of contact discontinuity	- 1st order accurate (space and time) for the pressure waves - adaptation necessary for mass conservation in tapered pipes
LW → Richtmyer (2)	+ 2nd order accurate (space and time) for all phenomena	- non physical overshoots - discretization errors at section changes
LW → Ni (3)	+ 2nd order accurate (space and time) for all phenomena	- non physical numerical oscillations for all phenomena
LW + FCT (4)	+ 2nd order accurate (space and time) for all phenomena + no numerical oscillations	- unable to reach steady solution for tapered pipe - conservation of mass, momentum and energy is lost - discretization errors at section changes
1st order upwind (5)	+ no numerical oscillations	- 1st order accurate (space and time) for all phenomena - discretization errors at section changes
existing TVD schemes (6,7,8,9,10,11)	+ no numerical oscillations + 2nd order accurate (space) + 2nd order accurate (time) for multi-stage versions	- discretization errors at section changes
ENO (12)	+ no numerical oscillations + 3rd order accurate (space) + 2nd order accurate (time) for multi-stage versions	- discretization errors at section changes
1st order upwind, cell-vertex (13)	+ no numerical oscillations	- 1st order accurate (space and time) for all phenomena
new TVD scheme (14,15,16,17,18,19)	+ no numerical oscillations + 2nd order accurate (space) + 2nd order accurate (time) for multi-stage versions	

References

[1] Watson, N., and Janota, M. R., 1971, ''Non-Steady Flow in an Exhaust System With a Pulse Converter Junction,'' IMechE Conf. Internal Flows, Salford, pp. D17–D28.

[2] Benson, R. S., 1982, *The Thermodynamics and Gas Dynamics of Internal Combustion Engines*, J. H. Horlock and D. E. Winterbone, eds., Clarendon Press.

[3] Blair, G. P., and Gouldburn, J. R., 1967, ''The Pressure Time History in the Exhaust System of a High-Speed Reciprocating Internal Combustion Engine,'' SAE Paper 670477.

[4] Lax, P. D., and Wendroff, B., 1960, ''Systems of Conservation Laws,'' Commun. Pure Appl. Math., **13**, pp. 217–237.

[5] Richtmyer, R. D., and Morton, K. W., 1967, *Difference Methods for Initial Value Problems*, Wiley, New York.

[6] Seifert, H., 1960, ''Die Analyze instationärer Strömungsvorgänge in Ansaugleitungen an Mehrzylinder-Verbrennungsmotoren,'' FISITA, Tokyo.

[7] Seifert, H., 1978, ''Erfahrungen mit einem mathematischen Modell zur Simulation von Arbeitsverfahren in Verbrennungsmoteren,'' MTZ, **39**, (7/8 and 12) Tokyo.

[8] Bulaty, T., and Niessner, H., 1985, ''Calculation of 1-D Unsteady Flows in Pipe Systems of I.C. Engines,'' J. Fluids Eng., **107**, pp. 407–412.

[9] Pearson, R. J., 1994, ''Numerical Methods for Simulating Gas Dynamics in Engine Manifolds,'' Ph.D. thesis, Department of Mechanical Engineering, UMIST.

[10] Kirkpatrick, S. J., Blair, G. P., Fleck, R., and McMullan, R. K., 1994, ''Experimental Evaluation of 1-D Computer Codes for the Simulation of Unsteady Gas Flow Through Engines—A First Phase,'' Queen's University of Belfast, SAE Paper 941685.

[11] Zhao, Y., and Winterbone, D. E., 1991, ''Numerical Simulation of Multi-Dimensional Flow and Pressure Dynamics in Engine Intake Manifolds,'' IMechE Paper C430/039.

[12] Flamang, P., and Sierens, R., 1989, ''Experimental and Theoretical Analysis of the Flow in Exhaust Pipe Junctions,'' IMechE Paper C382/082.

[13] Sod, G. A., 1978, ''A Survey of Several Finite Difference Methods for Systems of Nonlinear Hyperbolic Conservation Laws,'' J. Comput. Phys., **27**, pp. 1–31.

[14] Van Hove, W., and Sierens, R., 1991, ''Calculation of the Unsteady Flow in Exhaust Pipe Systems: New Algorithm to Fulfill the Conservation Law in Pipes With Gradual Area Changes,'' Proc. Inst. Mech. Eng., **205**, Part D, pp. 245–250.

[15] Jenny, E., 1950, ''Unidimensional Transient Flows With Consideration of Friction and Change of Section,'' Brown Boveri Rev., **37**, No. 11, pp. 447–461.

[16] Ni, R. H., 1982, ''A Multiple Grid Scheme for Solving the Euler Equations,'' AIAA J., **20**, pp. 1565–1571.

[17] MacCormack, R. W., 1969, ''The Effect of Viscosity in Hypervelocity Impact Cratering,'' AIAA Paper 69-354.

[18] Book, D. L., Boris, J. P., and Hain, K., 1975, ''Flux Corrected Transport II: Generalizations of the Method,'' J. Comput. Phys., **18**, pp. 248–283.

[19] Boris, J. P., and Book, D. L., 1976, ''Flux-Corrected Transport III: Minimal-Error FCT Algorithms,'' J. Comput. Phys., **16**, pp. 85–129.

[20] Roe, P. L., 1981, ''Approximate Riemann Solvers, Parameters Vectors and Difference Schemes,'' J. Comput. Phys., **43**, pp. 357–372.

[21] Dick, E., 1988, ''A Flux Difference Splitting Method for the Steady Euler Equations,'' J. Comput. Phys., **76**, pp. 19–32.

[22] Dick, E., 1990, ''Multigrid Formulation of Polynomial Flux-Difference Splitting for Steady Euler Equations,'' J. Comput. Phys., **91**, pp. 161–173.

[23] Harten, A., 1983, ''High Resolution Schemes for Hyperbolic Conservation Laws,'' J. Comput. Phys., **49**, pp. 357–393.

[24] Chakravarty, S. R., and Osher, S., 1985, ''A New Class of High Accuracy TVD Schemes for Hyperbolic Conservation Laws,'' AIAA Paper 85-0363.

[25] Harten, A., and Osher, S., 1987, ''Uniformly High-Order Accurate Nonoscillatory Schemes I,'' SIAM J. Numer. Analy., **24**, pp. 279–309.

[26] Vandevoorde, M., Vierendeels, J., Dick, E., and Sierens, R., 1998, ''A New Total Variation Diminishing Scheme for the Calculation of One-Dimensional Flow in Inlet and Exhaust Pipes of Internal Combustion Engines,'' Proc. Inst. Mech. Eng., **212**, Part D. pp. 437–448.

Two-Dimensional Simulation of Wave Propagation in a Three-Pipe Junction

R. J. Pearson[1]
M. D. Bassett
P. Batten[2]
D. E. Winterbone

Department of Mechanical Engineering,
UMIST,
Manchester, England

The modelling of wave propagation in complex pipe junctions is one of the biggest challenges for simulation codes, particularly those applied to flows in engine manifolds. In the present work an inviscid two-dimensional model, using an advanced numerical scheme, has been applied to the simulation of shock-wave propagation through a three-pipe junction; the results are compared with corresponding schlieren images and measured pressure-time histories. An approximate Riemann solver is used in the shock-capturing finite volume scheme and the influence of the order of accuracy of the solver and the use of adaptive mesh refinement are investigated. The code can successfully predict the evolution and reflection of the wave fronts at the junctions whilst the run time is such as to make it feasible to include such a model as a local multi-dimensional region within a one-dimensional wave-action simulation of flow in engine manifolds.

[S0742-4795(00)01304-1]

Introduction

One-dimensional ''wave-action'' codes are now applied extensively in the design of manifolds for internal combustion engines [1–3]. Such codes can be used for the prediction of performance, turbocharger matching studies [4,5], and the calculation of noise levels radiated from the ends of the intake and exhaust systems [2,4,5]. The modelling of complex pipe junctions, however, remains a major challenge since the geometry of such junctions cannot be represented using a one-dimensional approach as these junctions often produce strong directional effects on the waves which propagate through them.

The usual assumption made at pipe boundaries is that the flow behaves in a quasi-steady manner, implying that the boundary regions are defined by infinitesimal control volumes with no mass or energy storage capacity; this means $(\partial p/\partial x)\gg(\partial p/\partial t)$. Real pipe junctions violate this criteria, most obviously in the cases of the four or five-into-one junctions in the exhaust systems of very high-performance engines. These junctions also give considerably different reflection and transmission characteristics depending on which branch of the junction a wave enters—this effect is referred to as ''directionality''. The directionality of junctions is used beneficially in ''pulse converters'' to enable several cylinders to be connected together without the waves generated by their respective blowdown pulses adversely affecting the scavenging of the other cylinders.

In order to characterize directionality effects one-dimensional ''pressure-loss'' models of junctions have been devised which require empirical data, obtained from steady flow tests, relating the pressure drop across the junction in the various directions to the pressure ratio [6–9]. Obtaining such data is extremely time consuming and the simulation model cannot be used as a design procedure since the junctions have to be manufactured before their characteristics are known. Multi-dimensional models of the unsteady flow in pipe junctions offer the prospect of removing both the need to use empirical data and the limitation of the quasi-steady assumption.

Multi-dimensional models of inviscid flows in manifolds, based on the fluid-in-cell (FLIC) method, have been used in entire engine intake manifolds [10–12]. Flamang and Sierens [13] have also illustrated that it is possible to use inviscid codes in steady-flow calculations to obtain the coefficients required by the pressure-loss models described above.

In the past 15 years major developments in numerical methods for wave propagation phenomena have produced robust and efficient numerical schemes of high accuracy [14]. In the present work an inviscid model based on a modern high-resolution shock-capturing scheme is used to simulate the propagation of shock waves in three-pipe junctions. The results are compared with corresponding schlieren images and pressure-time histories measured in the ducts. These test cases provide a rigorous examination of the capabilities of the multi-dimensional model and lay the foundations for the next phase of the work which is to ''embed'' such a model in an otherwise one-dimensional engine simulation.

Governing Equations

The governing equations of two-dimensional *inviscid* flow, in differential conservation law form are

$$\frac{\partial \mathbf{W}}{\partial t}+\frac{\partial \mathbf{F}}{\partial x}+\frac{\partial \mathbf{G}}{\partial y}=0, \tag{1}$$

where

$$\mathbf{W}=\begin{bmatrix}\rho\\ \rho u\\ \rho v\\ \rho e_0\end{bmatrix};\quad \mathbf{F}=\begin{bmatrix}\rho u\\ p+\rho u^2\\ \rho u v\\ \rho u h_0\end{bmatrix};\quad \mathbf{G}=\begin{bmatrix}\rho v\\ \rho u v\\ p+\rho v^2\\ \rho v h_0\end{bmatrix}, \tag{2}$$

and

$$e_0=e+\tfrac{1}{2}(u^2+v^2). \tag{3}$$

The relationships formed by substituting the elements of the **W**, **F**, and **G** vectors into Eq. (1) are the continuity, momentum (*x*-direction), momentum (*y*-direction), and energy equations, respectively. The equation set contains one more unknown than there are equations and therefore additional information is required to obtain a closure. Using the ideal gas state equation,

$$\frac{p}{\rho}=RT, \tag{4}$$

---

[1] Current address: Lotus Engineering, Hethel, Norfolk, England.

[2] Current address: Metacomp Technologies Inc., Westlake Village, California, USA.

Contributed by the Internal Combustion Engine Division of THE AMERICAN SOCIETY OF MECHANICAL ENGINEERS for publication in the ASME JOURNAL OF ENGINEERING FOR GAS TURBINES AND POWER. Manuscript received by the ICE Division November 5, 1998; final revision received by the ASME Headquarters May 9, 2000. Technical Editor: D. Assanis.

constrains its internal energy to be a function only of temperature of the gas and, in the special case of the fluid being a perfect gas, the internal energy and temperature are related as

$$e=c_vT. \tag{5}$$

In this equation c_v, the specific heat capacity at constant volume, is a constant.

Numerical method

Much work has been done in the last two decades on numerical methods for compressible flows [14]. Schemes based on solving a series of interface (or Riemann) problems between adjacent computational cells have largely replaced those derived purely from Taylor series expansions. Generically these schemes, based on the solution of the Riemann problem, are called Godunov-type methods [15], and introduce, in an explicit manner, the physics of wave propagation into the solution procedure.

Godunov-Type Schemes. Godunov-type schemes solve the initial value problem which evolves from the interaction of fluid states on either side of an interface. Godunov [15] supposed that the initial data in the solution domain could be replaced by a set of piecewise-constant states with discontinuities at $x_{i\pm1/2}$ as shown in Fig. 1 for the one-dimensional case. The piecewise-constant data is taken to represent the integral average of the initial data over the interval $x_{i-1/2}$ to $x_{i+1/2}$.

The integral form of the one-dimensional Eqs. (1) becomes

$$\int_x\int_t \frac{\partial \mathbf{W}}{\partial t}+\frac{\partial \mathbf{F}}{\partial x}=0, \tag{6}$$

where

$$\mathbf{W}=\begin{bmatrix}\rho\\ \rho u\\ \rho e_0\end{bmatrix};\quad \mathbf{F}=\begin{bmatrix}\rho u\\ p+\rho u^2\\ \rho u h_0\end{bmatrix}. \tag{7}$$

On integration this equation gives

$$(\mathbf{W}_i^{n+1}-\mathbf{W}_i^n)\Delta x+(\mathbf{F}_{i+1/2}^n-\mathbf{F}_{i-1/2}^n)\Delta t=0, \tag{8}$$

where **W** represents the average of dependent variables for the cell shown in Fig. 2 and is given by

$$\mathbf{W}_i=\frac{1}{\Delta x}\int_{x_{i-1/2}}^{x_{i+1/2}}\mathbf{W}dx, \tag{9}$$

and **F** is the average flux across the cell boundaries over an interval of time Δt, given by

$$\mathbf{F}_{i\pm1/2}=\frac{1}{\Delta t}\int_{t^n}^{t^{n+1}}\mathbf{F}dt. \tag{10}$$

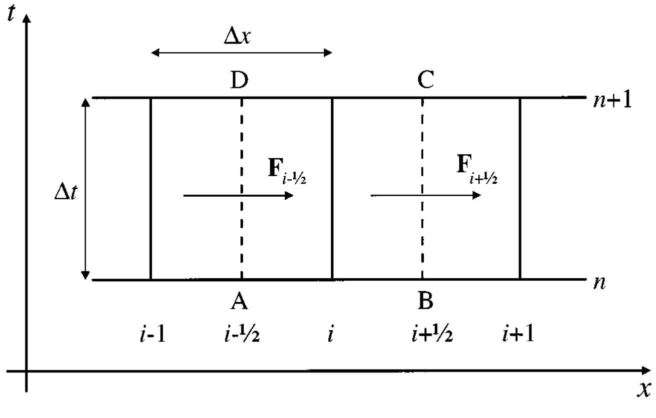

Fig. 1 Control volume for computational cell

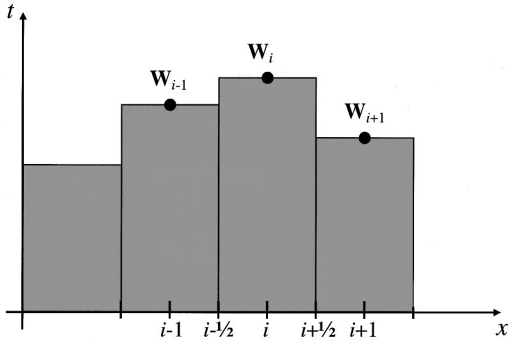

Fig. 2 Piecewise-constant reconstruction

For Godunov-type schemes the solution vector is updated by rewriting Eq. (8) as

$$\mathbf{W}_i^{n+1}=\mathbf{W}_i^n-\frac{\Delta t}{\Delta x}[\mathbf{F}^*_{i+1/2}(\mathbf{W}_i^n,\mathbf{W}_{i+1}^n)-\mathbf{F}^*_{i-1/2}(\mathbf{W}_{i-1}^n,\mathbf{W}_i^n)], \tag{11}$$

where $\mathbf{F}^*_{i+1/2}(\mathbf{W}_i^n,\mathbf{W}_{i+1}^n)$ represents the flux (10) given by the solution of the Riemann problem at $i+1/2$ formed by the piecewise-constant states in the cells at i and $i+1$.

Godunov's original method employs the exact solution to the Riemann problem [16] to find the inter-cell fluxes; this involves iterative procedures and can impose a large burden on computing resources for multi-dimensional calculations. Many ''approximate Riemann solvers'' have now emerged in the literature [14,17] which are significantly less demanding of computing time than the calculation of the exact solution. The solution method used in the present work is based on a modification, due to Toro et al. [18], of the approximate Riemann solver proposed by Harten et al. [19]. This Riemann solver reduces the computational effort required using an ''exact'' Riemann solver by approximately 40 percent.

High-Resolution Godunov-Type Schemes Using Gradient Limiters. Piecewise-constant reconstruction of the data resulting from the solution of the Riemann problem gives only first-order spatial accuracy; second-order accuracy can be obtained by using a piecewise-linear reconstruction. A straightforward approach to this linear reconstruction however, leads to the spurious oscillations which are produced by any second-order scheme with constant coefficients [17]. This problem can be overcome by the use of so-called gradient limiters [20] to modify the reconstruction so that the total variation of the reconstructed data does not exceed that of the initial data, thereby satisfying the total variation diminishing (TVD) condition [21]. This generic approach was termed MUSCL (Monotonic Upstream Scheme for Conservation Laws) by van Leer [20].

Equation (1) can be written, for an arbitrary control volume Ω, as

$$\frac{\partial}{\partial t}\int_\Omega \mathbf{W}d\Omega+\oint_S \vec{\mathbf{F}}\cdot d\vec{\mathbf{S}}=0. \tag{12}$$

This equation asserts that the time variation of the integral averaged solution, **W**, within the volume, Ω, depends only on the surface values of the fluxes. For any computational mesh with vertices ABC equation (12) can be written as

$$\frac{\partial}{\partial t}\int_\Omega \mathbf{W}d\Omega+\oint_{ABC}(\mathbf{F}dy-\mathbf{G}dx)=0, \tag{13}$$

where **F** and **G** are the Cartesian components of the flux vector $\vec{\mathbf{F}}$ and are given in Eqs. (2). The flux across side AB of this control volume is

$$\vec{\mathbf{F}}=\mathbf{F}_{AB}(y_B-y_A)-\mathbf{G}_{AB}(x_B-x_A)=\vec{\mathbf{F}}[R_0(\mathbf{W}_L,\mathbf{W}_R)], \tag{14}$$

where $R_0(\mathbf{W}_L, \mathbf{W}_R)$ is the interface solution of the Riemann problem defined by the two interpolated states $\mathbf{W}_L$ and $\mathbf{W}_R$, either side of the interface AB. A gradient limiter is employed to ensure monotonicity of the interpolated data. In the present work a two-cycle limiter is used, which is a modified version of the scheme described by Batten et al. [22].

Results

This section describes the application of the code to the simulation of shock-wave propagation through junctions formed by the intersection of three pipes. The junction considered in this phase of the work is a 180 deg junction, where two adjacent pipes merge to become one pipe of cross-sectional area equivalent to sum of the individual pipes. A shock tube rig was constructed for the purposes of obtaining schlieren images of the waves in the junction.

Schlieren Images. Figure 3 shows the general arrangement of experimental rig developed for visualizing the density gradients (schlieren images) induced by the propagating wave. The driving tube and shock tube (pipe 1) are separated by a diaphragm which bursts when the pressure difference reaches a certain value. Since the schlieren method produces two-dimensional images the tubes were square and rectangular in section. Three piezo-resistive pressure transducers were located around the junction—one transducer in each pipe. The signal from the transducer in pipe 1 was used, via a time-delay circuit, to trigger an argon-spark-flash unit and a CCD camera. The image acquired by the CCD camera was frozen by the short duration of the light source and a sequence of images of a propagating wave front was thus constructed. This was possible because the results were found to be highly repeatable.

Figure 4 shows the schlieren image obtained 200 μs after the wave has reached the pressure transducer in pipe 1. The wave has emerged from pipe 1 in which it was propagating from left to right. On reaching the junction the wave-front expands in a more or less spherical manner (cylindrical in two-dimensions) so that it expands around the bend into pipe 3, as well as continuing in the original direction of its travel into pipe 2. A rarefaction wave is reflected backwards into pipe 1 when the shock wave encounters the area expansion formed at the pipe junction and a vortex is formed at the ''tongue''. The distortion of the wave front from a cylindrical form arises because the propagation speed in each pipe is the sum of the speed of sound and the flow velocity.

The simulated results shown in Fig. 5(*a*) were produced with the coarse mesh, using no adaptive refinement, shown in Fig. 5(*b*). The narrow cells in the center of the grid are caused by the need to represent the ''tongue'' of the junction. Clearly these density contours give a very crude depiction of the wave front. Figure 6(*a*) shows how the resolution is improved by adaptively refining the grid to the extent shown in Fig. 6(*b*); this result was achieved using approximately 11,000 cells. The grid refinement was activated when the density gradient between computational cells exceeded a given criteria.

Figures 7(*a*)–(*d*) show a schlieren image, a predicted schlieren image, and predicted density contours and velocity vectors at $t = 250\ \mu$s. Since the schlieren system measures density *gradient* it is more appropriate to compare the measured images with the magnitude of the gradient of the density field predicted by the code, namely

$$\sqrt{\left(\frac{\partial \rho}{\partial x}\right)^2 + \left(\frac{\partial \rho}{\partial y}\right)^2}. \tag{15}$$

Figure 7(*b*) shows a predicted ''schlieren'' image of the wave system which is directly comparable with the measured image shown in Fig. 7(*a*). This was produced using a significantly higher grid refinement level than that shown in Fig. 6(*b*).

Figures 8(*a*)–(*d*) shows the schlieren image and predicted results at $t = 350\ \mu$s. By this time the shock front has reflected from the lower wall and started to bend around the growing vortex created at the tongue of the junction. Eventually a portion of this wave-front is transmitted back into pipe 1. The vortex produced in the predicted results is due entirely to the numerical viscosity introduced by the discretization process, there being no explicit model of the fluid viscosity in the simulation. In spite of this the predicted schlieren results shown in Fig. 8(*b*) are remarkably similar to the measured schlieren image. The vortex is illustrated clearly in the velocity vectors shown in Fig. 8(*d*). At $t = 500\ \mu$s (Fig. 9(*a*)) the vortex has detached itself from the tongue of the junction. The reflected wave from the bottom wall is just entering the mouth of pipe 1 and has reflected off the top wall of pipe 2. This situation is reliably mimicked by the simulation (Fig. 9(*b*)–(*d*)).

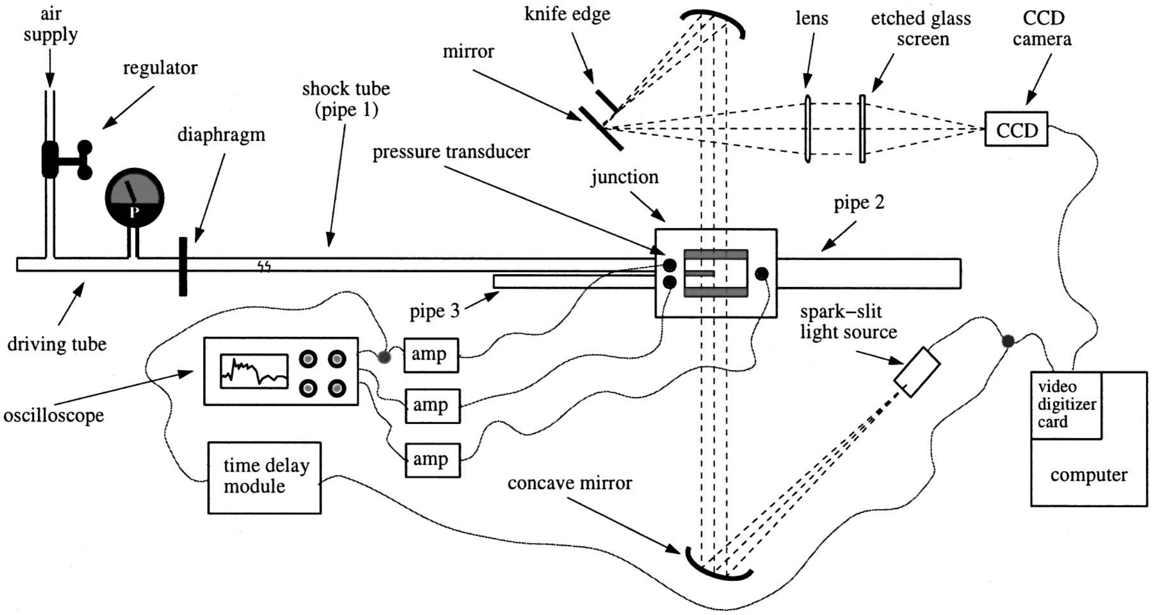

Fig. 3 General arrangement of schlieren system

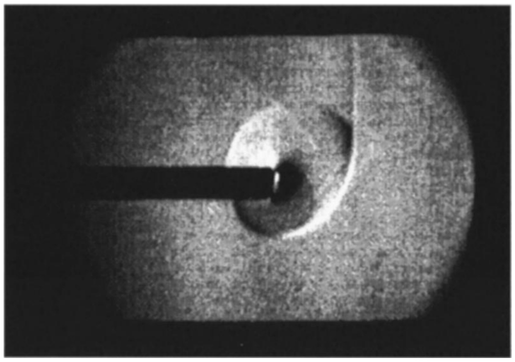

Fig. 4 Schlieren image at 200 microseconds

Numerical viscosity arises from the discretisation of the governing equations of flow and has the effect of introducing a mesh-dependent artificial mass diffusion, viscosity, and heat conduction in the continuity, momentum, and energy equations, respectively. These effects are often collectively termed ''numerical viscosity'' and are grid dependent. The focus of this paper is, however, on the modelling of the *propagation* phenomena of the waves in the pipes. The fluid flow field is driven by the pressure wave phenomena and thus the detailed flow field in the immediate vicinity of the junction is of secondary interest. It will be seen, indeed it is an aim of the paper to show, that it is possible to predict the mean pressure levels in the pipes even with an extremely coarse grid in which the fluid flow field is very poorly resolved.

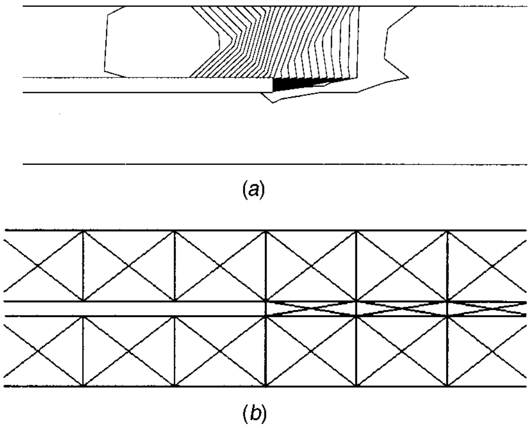

(*a*)

(*b*)

Fig. 5 (*a*) Density contours at 200 microseconds (unrefined grid); (*b*) unrefined grid

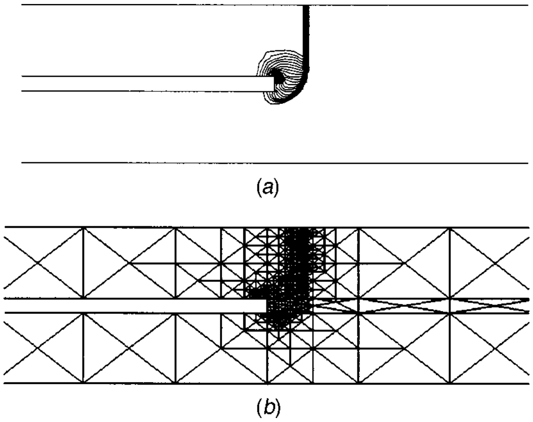

(*a*)

(*b*)

Fig. 6 (*a*) Density contours at 200 microseconds (refined grid); (*b*) refined grid at 200 microseconds

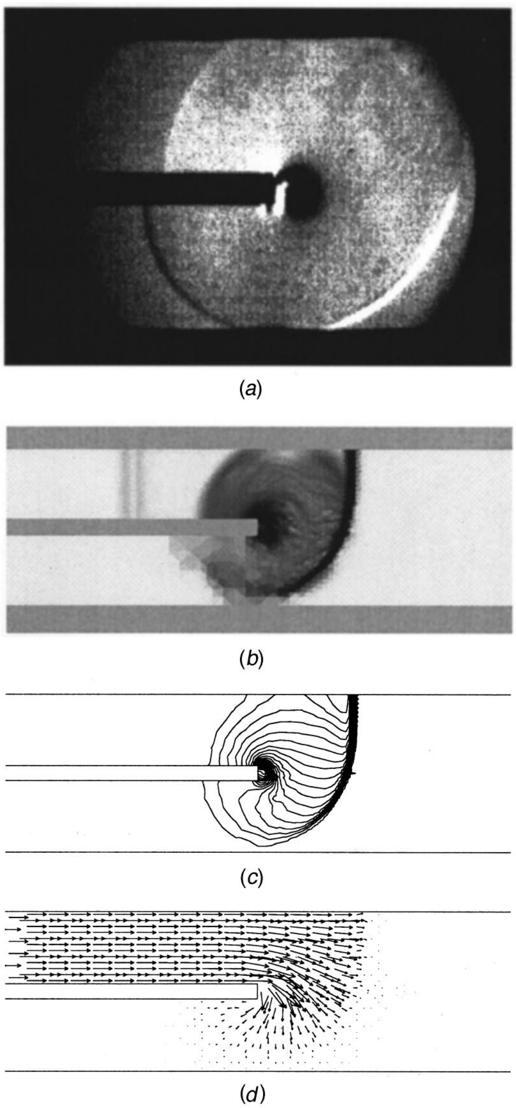

(*a*)

(*b*)

(*c*)

(*d*)

Fig. 7 (*a*) Schlieren image at 250 microseconds; (*b*) simulated schlieren image at 250 microseconds; (*c*) density contours at 250 microseconds; (*d*) velocity vectors at 250 microseconds

Pressure-Time Histories. Pressure-time histories at the transducer locations are shown in Figs. 10(*a*) and 10(*b*). It can be seen that the transmitted wave amplitude in pipe 3 is substantially smaller than both the original wave and the wave amplitude in pipe number 2. These differences in the mean level of the wave are an effect of the junction geometry on the propagation of the wave-front and it is this effect which cannot be captured directly by a one-dimensional model.

The high frequency oscillations which can be seen in the measured pressures in pipes 2 and 3 result from the transverse motion of a wave-front across the pipes. The simulation results shown in Fig. 10(*a*) predict accurately the mean levels of the transmitted pressures in pipes 2 and 3 (P2 and P3 in the diagrams). The simulated results shown in this figure were produced using an unrefined mesh of the form shown in Fig. 5(*b*). It does not seem possible to resolve the pressure caused by the transverse propagation of the waves in pipes 2 and 3 using this coarse mesh. Two predicted results are shown in each pipe, corresponding to first and second-order spatial accuracy. The results obtained using

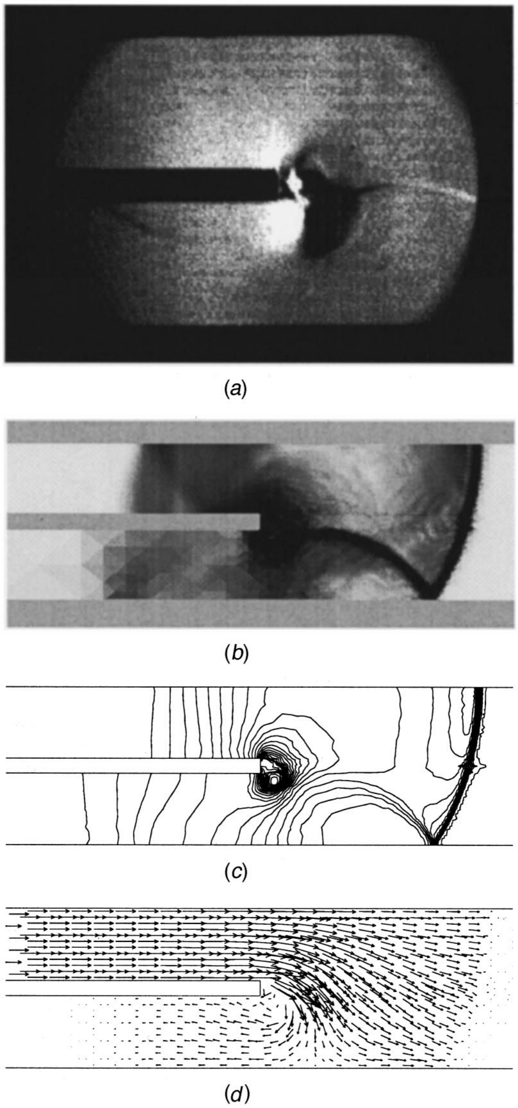
(a)

(b)

(c)

(d)

Fig. 8 (***a***) **Schlieren image at 350 microseconds;** (***b***) **simulated schlieren image at 350 microseconds;** (***c***) **density contours at 350 microseconds;** (***d***) **velocity vectors at 350 microseconds**

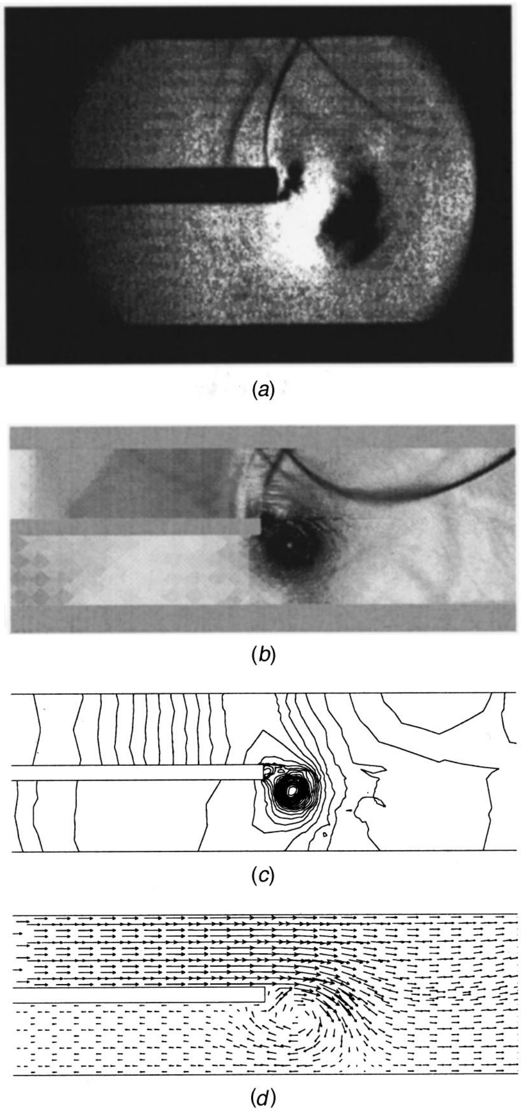
(a)

(b)

(c)

(d)

Fig. 9 (***a***) **Schlieren image at 500 microseconds;** (***b***) **simulated schlieren image at 500 microseconds;** (***c***) **density contours at 500 microseconds;** (***d***) **velocity vectors at 500 microseconds**

second-order spatial accuracy retain a steeper profile of the propagating shock waves than those produced when using first-order spatial accuracy.

Figure 10(*b*) shows that the pressure variations induced by the first three transverse wave oscillations in pipe 2 can be partially resolved by using adaptive grid refinement. An enlarged view of the pressure variation in pipe 2 is shown in Fig. 10(*c*). The shock wave gradient is significantly steeper compared with the results obtained without grid refinement. An improvement in the shock wave resolution also occurs when using first-order spatial accuracy with mesh refinement but the transverse oscillations remain unresolved.

The ability to predict the mean pressure levels of the waves propagating through the junction has a major bearing on the accuracy of volumetric efficiency predictions obtained using engine simulation programs and it is clear that the two-dimensional model used in this work affords such a facility for the square section pipes considered. The transverse component of the wave propagation would be of significance in predicting the noise spectrum radiated from the end of the pipe. However waves in engine manifolds can have wavelengths of the order of one meter or more and would thus not produce such strong transverse effects.

Wave propagation through 90 and 45 deg junctions have also been successfully simulated, as described by Pearson et al. [23] Figures 11 and 12 show measured and predicted results for a 45 deg junction with a nozzle in the pipe form which the shock emerges. Again, good correlation is obtained between the measured and predicted wave patterns (Fig. 11). After 0.3 ms the incident shock wave has propagated a significant distance away from the junction in each of the exit tubes and has reflected back from the wall opposite the entrance to the shock tube—this portion of the wave is approaching or is passing through the vortices at the exit to the shock tubes.

Figure 12 presents the pressure/time diagrams for the wave situation described in the previous area. It is clear that the nozzle in tube 1—the shock tube—has mitigated the amplitude of the pressure waves in the exit tubes. These extra losses are at the expense of having a larger pressure rise in the shock tube—indeed the pressure in the shock tube rises up to a time of 0.6 ms after the shock wave has first passed the transducer in that pipe due to the gradual reflection of a wave of increased amplitude along the nozzle-section of the junction.

Since the calculation techniques is based on a robust shock-capturing scheme the model is capable of handling much greater

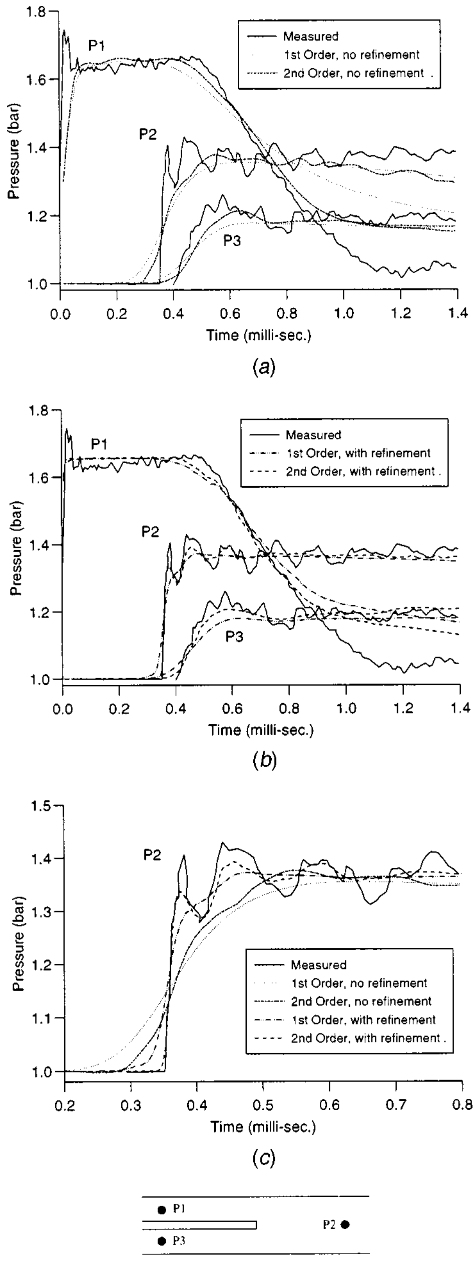

(*a*)

(*b*)

(*c*)

(*d*)

Fig. 10 (*a*) Pressure histories; (*b*) pressure histories; (*c*) pressure histories; (*d*) location of pressure transducers

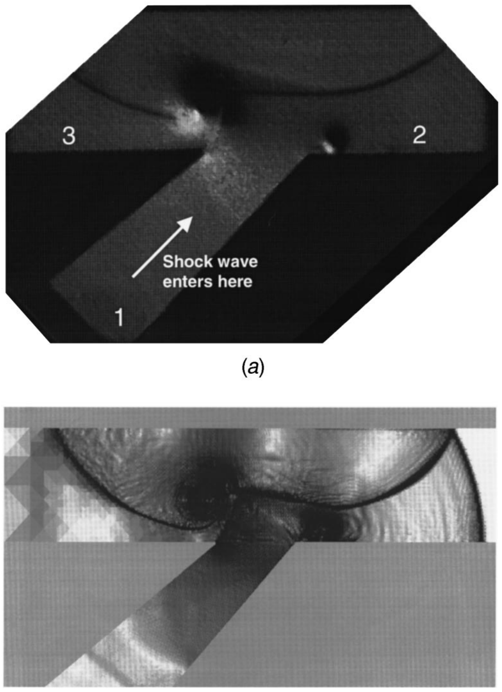

(*a*)

(*b*)

Fig. 11 (*a*) Schlieren image for 45 deg junction with a nozzle; (*b*) simulated schlieren image for 45 deg junction with a nozzle

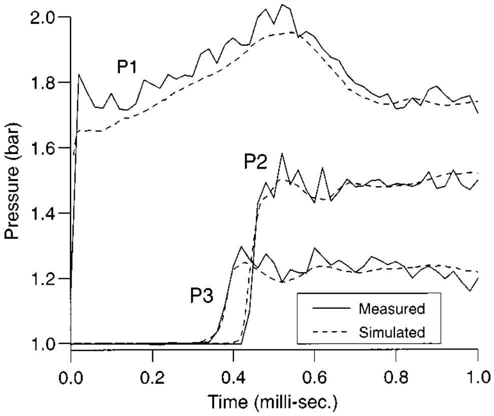

Fig. 12 Pressure histories for 45 deg junction with a nozzle

wave strengths than those used in the present work. Results for pressure ratios of 4 to 1 are shown by Batten et al. [22] and the code has been tested with much stronger waves.

Run Time. The computing time required for a simulation of duration 0.002 s after the wave has passed the first transducer location, in a domain containing 280 triangles, and using no grid refinement, is 14.0 seconds on a Silicon Graphics O2 workstation (180 MHz, 64 MB RAM). When adaptive grid refinement is used, producing a maximum of 646 triangles, the computing time increases to 52.2 s. In both cases quoted second-order spatial accuracy was used.

On the same computer 106.9 s CPU time was required to model five cycles of operation of a naturally aspirated four-cylinder spark-ignition engine using a comprehensive engine simulation program with a one-dimensional calculation of the manifold gas dynamics (using a centred-difference scheme with a flux limiter and 220 computational cells). Since the engine speed for this case was 3000 rev/min this represents a duration of 0.2 seconds. Hence the two-dimensional model of a three-pipe junction (no adaptive grid refinement) requires about 13 times as much computational effort as a typical simulation of a complete engine using a one-dimensional program with a simple two-zone combustion model.

Conclusions

It has been established that a two-dimensional inviscid model can predict the correct transmitted pressure levels when a shock wave encounters a simple three-pipe junction. Figures 5 and 6 show that it is not necessary to use a fine mesh in order to predict the mean pressure levels in the ducts. Indeed this can be achieved with a much coarser mesh than is required to produce well resolved two-dimensional images of the wave front. Hence, the pressure-loss characteristics of the junction can be modelled with a very simple representation of the boundary. It is therefore anticipated that the use of such a model as a local multi-dimensional region in a one-dimensional simulation of gas dynamics in engine manifolds will not require unacceptably large computing resources.

Acknowledgments

The authors are grateful for financial support for this project from EPSRC and the Ford Motor Company. The authors are indebted to Mr. E. Clough, Dr. H. Frost, and Mr. R. Lever for assistance with the experimental work undertaken in this project.

Nomenclature

e = specific internal energy
e_0 = specific stagnation internal energy
$\mathbf{F}$ = vector of flux terms
h_0 = specific stagnation internal energy
p = pressure
R = specific gas constant
t = time
T = temperature
u = velocity
$\mathbf{W}$ = state vector
x = distance
ρ = density

References

[1] Bensler, H. P., and Oppermann, R., 1996, ''CFD Optimization of Powertrain Components,'' *I. Mech. E. Third International Conference on Computers in Reciprocating Engines and Gas Turbines*, 9–10 January.

[2] Wren, C. S., and Johnson, O., 1995, ''Gas Dynamic Simulation for the Design of Intake and Exhaust Systems—Latest Techniques,'' SAE Paper 951367.

[3] Bazari, Z., Smith, L. A., Banisoleiman, K., and French, B., 1996, ''An Engineering Building Block Approach to Engine Simulation With Special Reference to New Application Areas,'' *Third International Conference on Computers in Reciprocating Engines and Gas Turbines*, 9–10 January.

[4] Ferrari, G., and Onorati, A., 1994, ''Determination of Silencer Performances and Radiated Noise Spectrum by 1-D Gas Dynamic Modelling,'' Paper no. 945135, XXV FISITA Congress, Beijing, China.

[5] Payri, F., Torregrosa, A. J., and Broatch, A., 1997, ''A Numerical Study of the Study of a Turbocharged Diesel Engine as a Noise Source,'' SAE Paper 970836.

[6] Benson, R. S., Woollatt, D., and Woods, W. A., 1963–64, ''Unsteady Flow in Simple Branch Systems,'' *Proc. I. Mech. E.*, **178**, pp. 3–28.

[7] Watson, N., and Janota, M. S., 1971, ''Non-Steady Flow in an Exhaust System With a Pulse Converter,'' *Proc. I. Mech. E., Fluid Mechanics Conference*, Salford.

[8] Winterbone, D. E., Nichols, J. R., and Alexander, G. I., 1985, ''The Evaluation of the Performance of Exhaust Systems Equipped With Integral Pulse Converters,'' *16th Int. CIMAC*, Oslo, June.

[9] Chan, C. L., Winterbone, D. E., Nichols, J. R., and Alexander, G. I., 1986, ''A Detailed Study of Compact Exhaust Manifolds Applied to Automotive Diesel Engines,'' *Proc. Instn. Mech. Engrs. Conf.: Turbocharging and Turbochargers*, Paper No. C113/86, pp. 269–281.

[10] Tosa, Y., Shimoda, K., and Oikawa, H., 1985, ''Calculation of 2-Dimensional Unsteady Flows in Inlet Pipe System and Its Application for V-8 Resonant Intake System'', *ASME Conf. on Flows in Internal Combustion Engines—III*, Miami, pp. 63–70.

[11] Zhao, Y., and Winterbone, D. E., 1991, ''Numerical Simulation of Multi-Dimensional Flow and Pressure Dynamics in Engine Intake Manifolds,'' *Instn. Mech. Engrs. International Conf., Computers in Engine Technology*, Cambridge, Sept. 10–12.

[12] Zhao, Y., and Winterbone, D. E., 1994, ''A Study of Multi-Dimensional Gas Flow in Engine Manifolds,'' *Proc. Instn. Mech. Engrs.*, Part D, **208**, pp. 139–145.

[13] Flamang, P., and Sierens, R., 1989, ''Experimental and Theoretical Analysis of the Flow in Exhaust Pipe Junctions,'' *Proc. Instn. Mech. Engrs.*, Paper No. C382/082, pp. 461–468.

[14] Toro, E. F., 1997, *Riemann Solvers and Numerical Methods for Fluid Dynamics*, Springer-Verlag, New York.

[15] Godunov, S. K., 1959, ''A Finite Difference Method for the Numerical Computation of Discontinuous Solutions of the Equations of Fluid Dynamics,'' Math. Sbornik, **47**, pp. 271–306.

[16] Sod G. A., 1978, ''A Survey of Several Finite Difference Methods for Systems of Non-Linear Conservation Laws,'' J. Comput. Phys., **27**, pp. 1–31.

[17] Hirsch, C., 1990, *Numerical Computation of Internal and External Flows*, **2**. Wiley, Chichester.

[18] Toro, E. F. Spruce, M., and Speares, W., 1994, ''Restoration of the Contact Surface in the HLL-Riemann Solver,'' Shock Waves, **4**, pp. 25–34.

[19] Harten, A., Lax, P. D., and van Leer, B., 1983, ''On Upstream Differencing and Godunov-Type Schemes for Hyperbolic Conservation Laws,'' SIAM Rev., **25**, No. 1, pp. 35–61.

[20] van Leer, B., 1979, ''Towards the Ultimate Conservative Difference Scheme V. A Second-Order Sequel to Godunov's Method,'' J. Comput. Phys., **32**, pp. 101–136.

[21] Harten, A., 1983, ''High Resolution Schemes for Hyperbolic Conservation Laws,'' J. Comput. Phys., **49**, pp. 357–393.

[22] Batten, P., Lambert, C., and Causon, D., 1996, ''Positively Conservative High-Resolution Convection Schemes for Unstructured Elements,'' Int. J. Numer. Methods Eng., **39**, pp. 1821–1838.

[23] Pearson, R. J., Bassett, M. D., Batten, P., Winterbone, D. E., and Weaver, N. W. E., 1999, ''Multi-Dimensional Wave Propagation in Pipe Junctions,'' SAE Paper 1999-01-1186.

Influence of the Exhaust System Design on Scavenging Characteristic and Emissions of a Four-Cylinder Supercharged Engine

Ferdinand Trenc
e-mail: ferdinand.trenc@fs.uni-lj.si

Frančišek Bizjan

Brane Širok

Department of Mechanical Engineering,
University of Ljubljana,
Aškerčeva 6,
SI-1000 Ljubljana,
Slovenia

Aleš Hribernik
e-mail: ales.hribernik@uni.mb.si
Department of Mechanical Engineering,
University of Maribor,
Smetanova 17,
SI-2000 Maribor,
Slovenia

A four-stroke four-cylinder turbocharged engine can be fitted with two different types exhaust system: a simple common manifold fed by all cylinders, or a twin-branch manifold, where two selected cylinders, directed by the firing order, feed two separate turbine entries. In this case good utilization of the exhaust pressure pulse energy can be achieved at higher loads and lower engine speeds, leading to good overall turbocharger efficiency and favorable pressure distribution during the gas-exchange period. Improved engine scavenging capability affects quality and quantity of the fresh charge and consequently influences the exhaust gas emissions. If, in addition, valve overlap period is increased the benefit of this system is still more evident. Common manifold exhaust system shows its advantage through lower pumping losses at higher engine speeds and lower loads. Both systems were optimized and the results of numerical and experimental work are presented in the paper. [S0742-4795(00)00404-X]

Introduction

A four-cylinder turbocharged Diesel engine can be supplied by two different exhaust systems. Exhaust gases can feed the gas turbine at nearly constant pressure if fed through one single manifold by selected cylinders and if mixed before they enter the turbine inlet scroll. Relatively constant mass-flow ensures good efficiency of the turbine, whereas mixing of the exhaust flow results in friction losses that in turn decreases the available kinetic energy of the exhaust pulses and prevents its further conversion into pressure.

Better utilization of the kinetic energy of an exhaust pulse can be achieved by means of a short exhaust double-pipe system where two selected pairs of the engine cylinders, having exhaust periods shifted by 360 deg CA and called ''two-pulse system'', feed two separate scrolls of a twin-entry radial turbine. The above mentioned two exhaust systems have been described in details by Trenc et al. and others [1–7]. Differences and features of constant and two-pulse assisted turbocharging with a four-cylinder Diesel engine were analyzed numerically and supported by experimental work. Results of previously performed numerical investigations and experiments were unfortunately, and due to lack of adequate turbo-equipment, performed on a non-optimized engine. All comparisons were based on the same Air/Fuel ratio base at diverse engine running conditions and gave only a good general survey of both exhaust systems. The results encouraged the authors of this paper to continue their research work; the baseline 7.11 liter Diesel engine was later optimized to give the best performance with both exhaust systems. Two different new turbochargers (compressors and turbines) were applied for this reason. Fueling system of the engine was a conventional one and was kept unchanged.

The main objective was to find out the scavenging and the emission capability of the newly equipped engine and to determine the role of the applied exhaust system.

Engine Equipment, Applied Methods and Results

Engine Equipment and Experimental Hardware. A four-cylinder, 7.11 liter, four-stroke, air-cooled, turbocharged and aftercooled Diesel engine was used for the experiments. Combustion system, valve timing and turbocharging system of the baseline engine were previously optimized for industrial application. A Holset E1 family turbocharger with a twin-entry turbine scroll was initially applied. A front-mounted air-to-air aftercooler was cooled by a thermally controlled and common engine cooling fan. The main aim of the presented investigations was, as mentioned before, to find out the influence of the exhaust system configuration and of the suitable turbocharging system on the scavenging quality of the engine and its exhaust emission.

The two-pulse and constant pressure exhaust systems, that were explained in detail by Trenc et al. [4,5] and used for the here presented investigations, are schematically shown in Fig. 1. A twin-entry waste-gated radial turbine with the 19 cm^2 turbine housing was connected to a two-branch exhaust manifold and drove an enhanced-map compressor (Fig. 1, left) in the case of the two-pulse exhaust system. On the other hand a different-profile turbine wheel together with the substantially smaller 13 cm^2 size single entry turbine housing, as proposed by Trenc et al. [4], was connected to a common exhaust manifold of the constant pressure exhaust system. Compressor geometry remained unchanged. Total engine air-fuel ratio can be the first measure of a successful turbo match. Figure 2 represents relative A/F ratio for both exhaust versions and different engine running conditions. Generally similar results were obtained and made possible better comparison of other engine data. Slightly higher relative A/F values by the two-pulse system and engine lower-speed range are the consequence of more effective scavenging process, as described later. As the consequence of the waste-gate operation, there is a pronounced lack of the boost-air for the two-pulse system in the region of the engine rated conditions. Total mean indicated pressure, mean indicated pressure of the high pressure as well as the mean indicated pressure of the gas exchange period (low-pressure cycle) were measured and statistically analyzed by a fast computerized,

---

Contributed by the Internal Combustion Engine Division of THE AMERICAN SOCIETY OF MECHANICAL ENGINEERS for publication in the ASME JOURNAL OF ENGINEERING FOR GAS TURBINES AND POWER. Manuscript received by the ICE Division December 2, 1999; final revision received by the ASME Headquarters May 9, 2000. Technical Editor: D. Assanis.

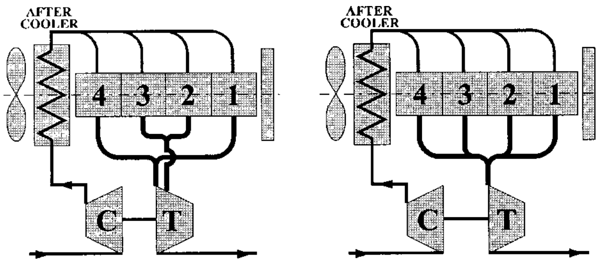

Fig. 1 2-Pulse (left) and constant pressure (right) exhaust systems

special-purpose data logger—PI meter. Through the results obtained engine pumping losses could be evaluated.

Pressure to time histories in the cylinder, in the intake and exhaust port and at the turbine inlet flange were measured by the piezo-electric technique and analyzed by computer. A one-dimensional computer program developed by Hribernik [1,2] was used to determine flow phenomena during the intake and exhaust engine stroke and specially during the valve overlap period. It was also used to predict the influence of the changed (prolonged) valve timing on the engine scavenging and emission for both observed exhaust systems, and not finally for comparison with the experimentally obtained data.

Very accurate laminar flow-meters were used to determine air mass-flow through the engine.

Exhaust gas emissions of the engine were determined by the TECHNOTEST—Multigas Type 488 tester. NDIR based CO, CO_2, and HC analyzers and chemically operated O_2 and NOx analyzers were applied. Accuracy of the absolute individual measurements was not extremely important; comparison of the two exhaust systems was the main purpose of the presented work.

Smoke density of the exhaust gases was established by an accurate Bosch smoke meter.

Results of Numerical and Experimental Investigations and Discussion. Two different types and sizes of exhaust turbines were applied to obtain optimum engine performance for the two above mentioned different exhaust systems.

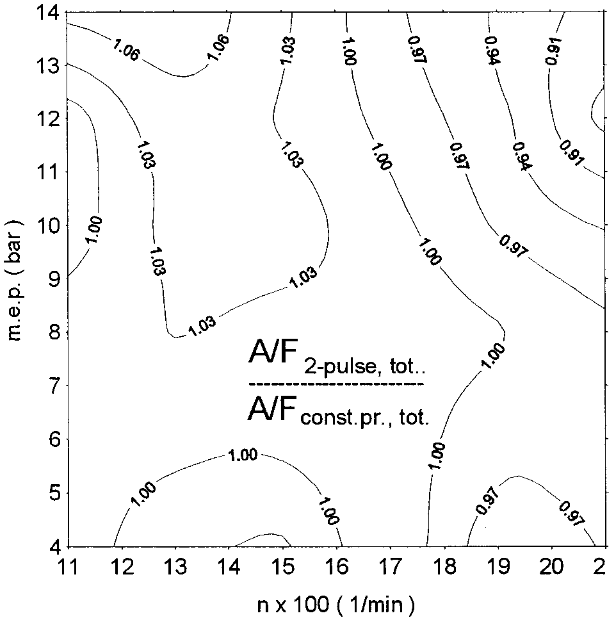

Fig. 2 Relative *A*/*F* ratio for both exhaust systems

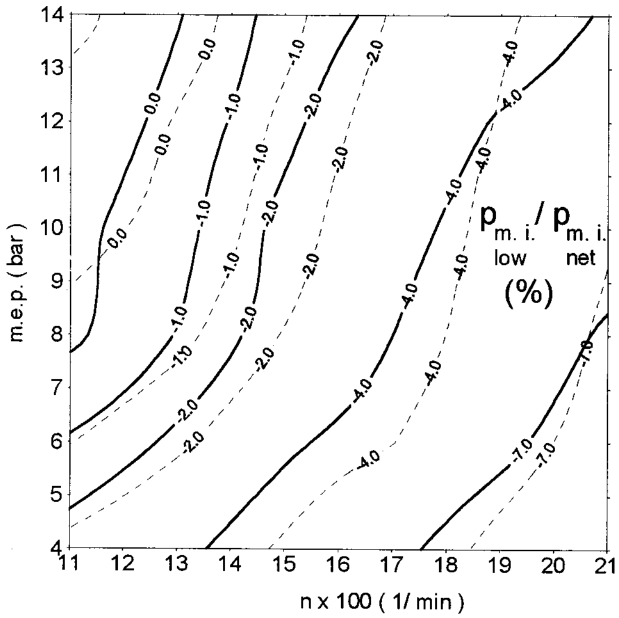

Fig. 3 Ratio of relative pumping losses for: (—) a two-pulse, and (---) a constant pressure exhaust system

Influence of the Exhaust System on the Engine Scavenging Capability. Exhaust system configuration together with pressure pulses from the neighbor engine cylinders, valve timing and the turbocharger efficiency can affect the scavenging process, engine performance and its emission. Dynamic pressure situation in the cylinder, in the exhaust and in the inlet port together rules the filling and emptying procedure and simultaneously defines engine pumping losses—i.e., work consumed to perform gas exchange in the engine. Ratio of the pumping cycle $(m.i.p)_{low}$ and the complete-net $(m.i.p)_{net}$ is one criterion to determine the effectiveness of the gas exchange period. Necessary work to perform the gas exchange in the cylinder is generally negative; however, positive values can be expected by very efficient turbocharged engines. Relative portion of the low-pressure cycle mean indicated pressure—m.i. compared to the net engine cycle m.i.p. for both exhaust systems is presented in Fig. 3. Positive gas-exchange work is limited to a restricted zone of lower speeds and higher engine loads. Lower pumping losses, especially at lower loads and higher engine speeds, are again typical for the optimized constant pressure exhaust system; the reasons have already been explained by Trenc et al. [4]. On the other hand, this advantage diminishes with the two-pulse system and the top engine torque region. Engine pumping losses and gas exchange quality are mostly affected by the pressure history in the cylinder inlet and exhaust port. Pressure history for both exhaust systems and engine peak torque conditions is presented in Fig. 4. Deviation between measured and computed pressure values was in the range of ±0.05 bar as previously explained by Trenc et al. [4,5]. Negative sign denotes influence of the negative pumping work; better scavenging can therefore be obtained by the constant-pressure system at higher engine speeds and lower engine loads.

Very similar amplitudes of the exhaust pressure waves is typical for the constant pressure system (exhaust port, Fig. 4, below), while in the two-pulse system (exhaust port, Fig. 4 above) there is one substantially weakened (damped and from the turbine scroll reflected) pressure wave that reaches the exhaust port of the cylinder No. 2 during the valve overlap sequence. At the same time a huge reflected exhaust pressure wave reaches the exhaust port of the same cylinder and the constant pressure system and prevents good scavenging of the observed cylinder. Final sequence of the exhaust period is interrupted and the exhaust gases are consequently flowing back to the observed cylinder. Furthermore, it can

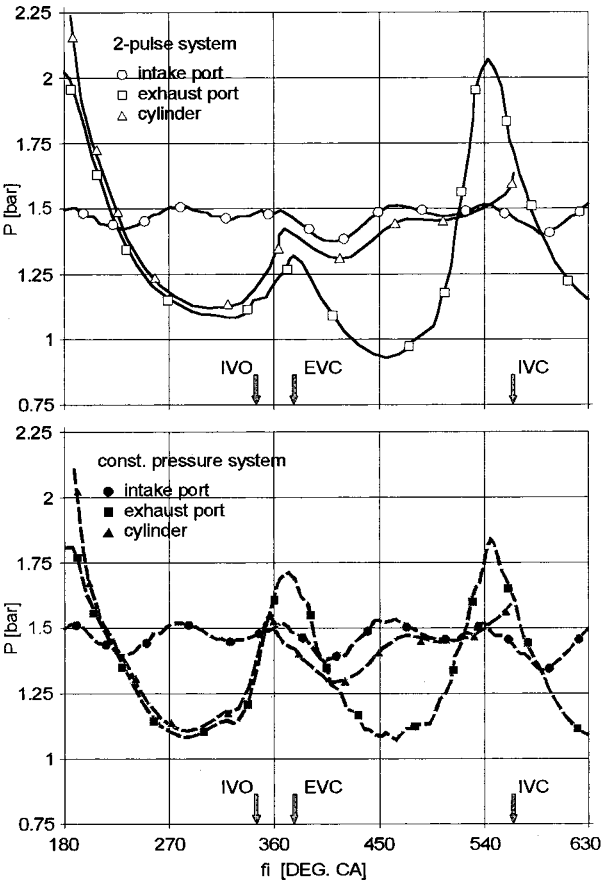

Fig. 4 Torque engine conditions and two-pulse (above), and constant-pressure (below) exhaust system

be concluded from the pressure diagram (Fig. 4 below) and from the results of the numerical simulations (Fig. 5—constant pressure exhaust system) that there is an inflow of the residual gases back into the intake manifold at the beginning of the fresh charge intake sequence. Corresponding pressure history measurements and numerical computations performed on the two-pulse system (Fig. 4 above, and Fig. 5 two-pulse system) do not predict any disturbances and back-flows for the two-pulse system and for the same engine operating conditions. Velocity distribution of the boost-air in the intake port and of the exhaust gases in the exhaust port were computed for both exhaust systems and are also presented in Fig. 5. Fuel-to-air equivalence ratio distribution during the valve overlap period is also presented in the same figure. From the results in Fig. 5 it can be concluded that the original valve timing permits a rather modest scavenging ability of the engine during the existing valve overlap. Gas flow during the valve overlap period (period expressed in deg. C.A. between the opening of intake valve and the closing of the exhaust valve) was computed on the basis of experimentally determined effective flow area through the valves of the warmed-up engine. The intention was therefore to find out the influence of changed valve timing (extended valve overlap sequence) on the scavenging capability of the engine and both exhaust configurations. ''New'' overlap sequence was doubled: from 30 (''old'') to 61 (''new'') deg. C.A. Diagrams in Fig. 5 show again a pronounced back-flow of the residual gases into the cylinder of the common exhaust manifold engine. The portion of the entering residual gases into the charging channel was also increased and covered approximately 40 percent of the available valve overlap period. Again there was no reversed exhaust gas flow noticed with the changed valve timing and the two-pulse exhaust system. As it has been previously stated and reported by Hribernik [3], performance of the constant pressure system could be improved (especially at lower engine speeds) by: (1) change of the valve timing—*reduction* of the valve overlap period, by shifting of the closure of the exhaust valve, and/or (2) by change of the exhaust manifold geometry (longer manifold branches between the neighbor cylinders would delay the arrival of reflected waves in the cylinder during the valve overlap period), and (3) by the introduction of the pulse converter in the exhaust manifold.

As mentioned before, larger negative gas-exchange loop associated with larger pumping losses is noticed by the two-pulse system when higher engine speeds and especially lower engine loads are considered—see Fig. 3. Appropriate measured and computed pressure and velocity curves in Fig. 6 and in Fig. 7 ($n_{\text{engine}}=2100$ l/min, and m.e.p.=6.0 bar) have led to the following conclusions:

- pressure history in the intake port and in the cylinder is very similar for both observed systems
- there is a modest reverse-flow of the residual gases into the intake manifold of the common exhaust manifold engine as the consequence of the locally and relatively higher cylinder pressure (Fig. 6). In the case of the two-pulse exhaust system, the reversed

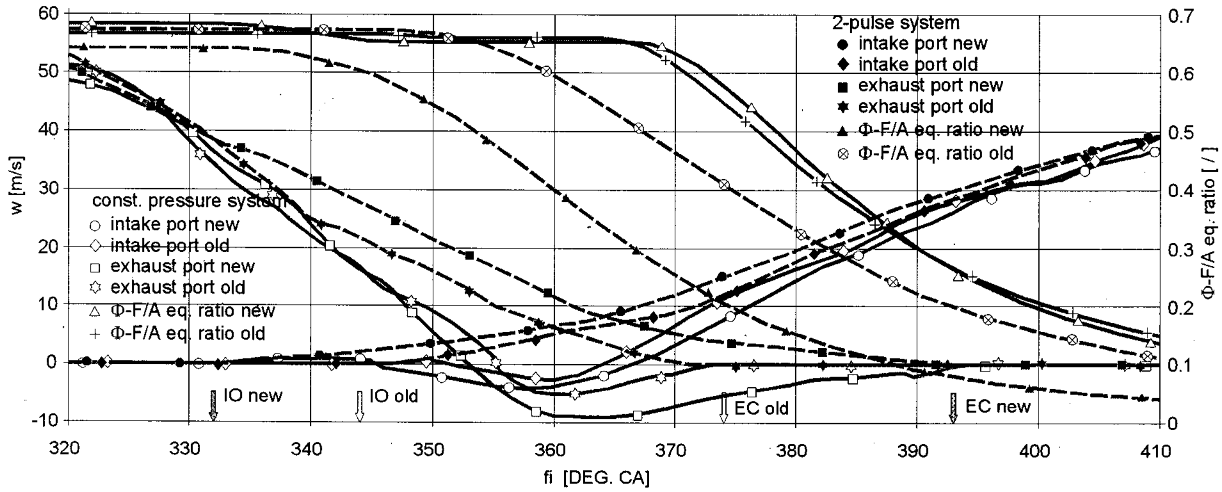

Fig. 5 Computed gas velocity distribution in the intake and exhaust port, relative *F/A* equivalence ratios for both exhaust systems, peak engine torque conditions and two different valve timings

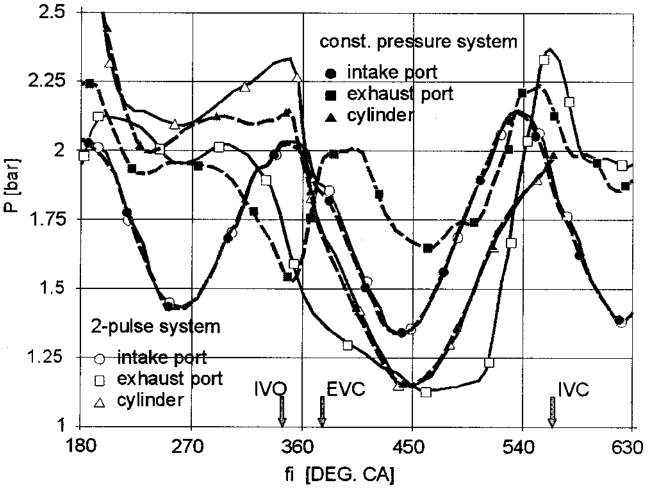

Fig. 6 Pressure distribution in the intake, exhaust port and cylinder for engine rated speed, lower load, and both exhaust systems

gas-flow from the cylinder into the intake manifold is more noticeable (Fig. 7—intake port velocity distribution) for the valve overlap period

- there is practically no reverse flow of the exhaust gases from the exhaust manifold back to the cylinder during the valve overlap period (Fig. 7)

Influence of the Exhaust System on Engine Emission. Emission of the applied engine is also affected by the thermodynamic state of the fresh charge in the cylinder at the beginning of the compression stroke. This state is influenced by the engine volumetric efficiency, by the content of the residual gases, etc., that are consequently depending on the applied exhaust system.

Figure 8 represents the ratio of the measured total volumetric efficiency for the applied exhaust systems and for different engine running conditions. Higher values are, as expected from the previous pressure and velocity diagrams, obtained with the two-pulse system almost all over the engine operation map. The situation is changed only in a limited zone of higher engine speeds, where due to the exhaust waste-gate with the two-pulse system (lower turbocharger efficiencies), the influence of lower turbocharger efficiencies and higher pumping losses prevent optimum scavenging of the (two-pulse exhaust system) cylinder. Residual gases are the consequence of an omitted scavenging process; in our case they were defined as the ratio of the exhaust gas mass compared to the mass of the total fresh charge at the end of the intake stroke. The values presented in Fig. 9 were calculated with the assumption of the perfect gas mixing (of the exhaust gases and the fresh air). The content of the residual gases by the constant pressure system is twice as large as that in the two-pulse exhaust system. A small deterioration—an increase of the γ value—can be observed by the engine rated conditions and the two-pulse system as the consequence of the applied turbine waste-gate. Higher content of the hot residual gases together with relatively lower mass of the trapped fresh air result in lower in-cylinder A/F ratio, higher temperatures at the end of the compression stroke, and therefore shorter ignition delay in the combustion with the constant pressure exhaust system. We must point out, that the quantity of the injected fuel did not vary too much for both observed systems and the entire engine map and that the combustion A/F ratio was generally the function of the in-cylinder trapped air. As the result of lower combustion A/F ratio, higher content of the residual gases and higher in-cylinder temperatures, higher smoke values were obtained by the constant pressure system. Smoke density ratio distribution for the observed two-pulse and constant pressure system is presented in Fig. 10. Cleaner exhaust is typical for the two-pulse system at lower engine speeds all over the load range. This system indicates the possibility of cleaner exhaust even when further increase of the engine peak torque were considered. The results of the two-pulse system at the rated engine condition deteriorate again when the waste-gate is used; corresponding smoke values are approximately 10 percent higher than the values of the constant pressure system. In the same time we must be aware that the absolute smoke density (in Bosch units) is far below 1.0 and therefore the change is relatively small.

Gaseous pollution of a Diesel engine exhaust is characterized by the CO_2, O_2, HC, and NOx emissions. CO_2 emission depends on the quantity of burned fuel only and did not change significantly for the observed exhaust versions: slightly lower values were measured for the two-pulse system, with the exception of the engine rated output and according to Fig. 11, that in term mean lower effective fuel consumption. CO_2 emission values were also successfully used to control the accuracy of the measured air and fuel mass-flow.

HC emission was low for both exhaust versions, although larger values correspond to the two-pulse system, lower engine speeds and loads, where there were larger portions of excess-air, significantly lower rate of the hot residual gases, and therefore lower

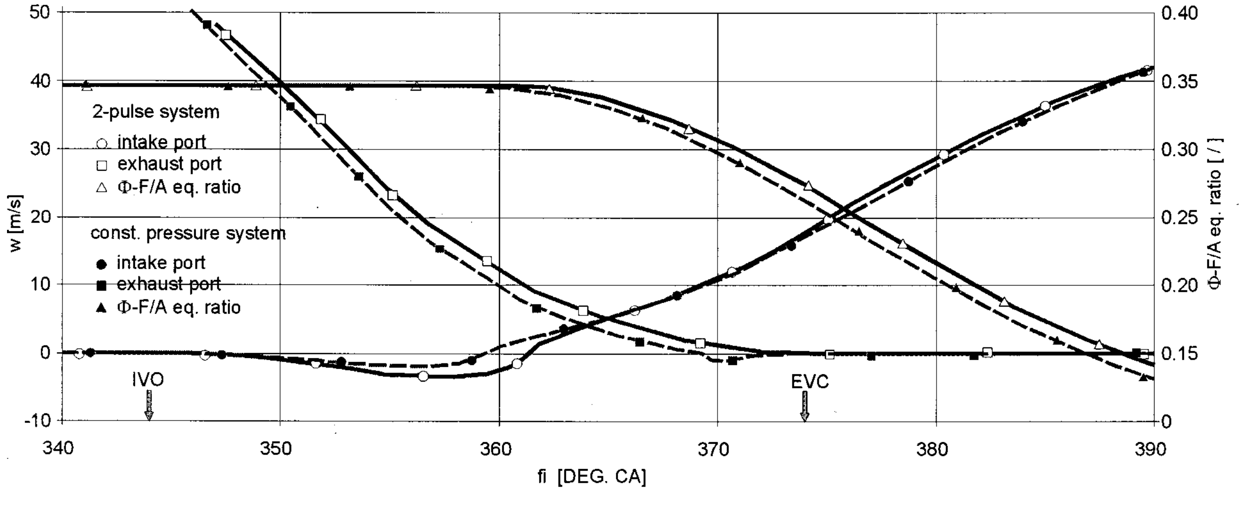

Fig. 7 Gas velocity distribution for the engine rated speed, low loads and both exhaust systems

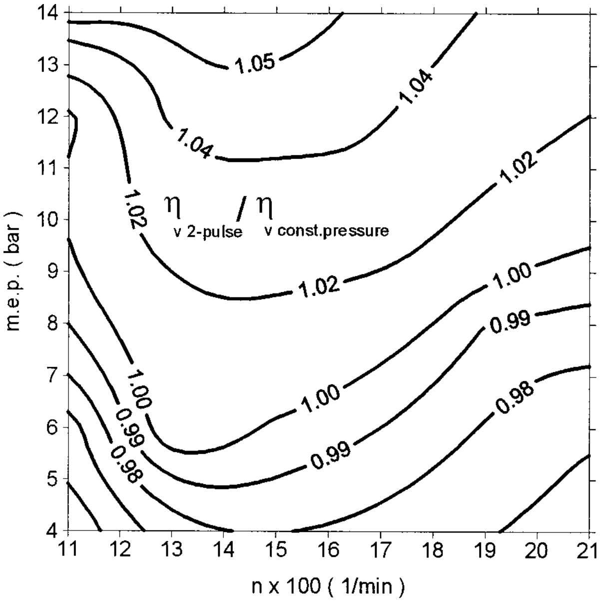

Fig. 8 Ratio of the engine volumetric efficiency for both exhaust systems

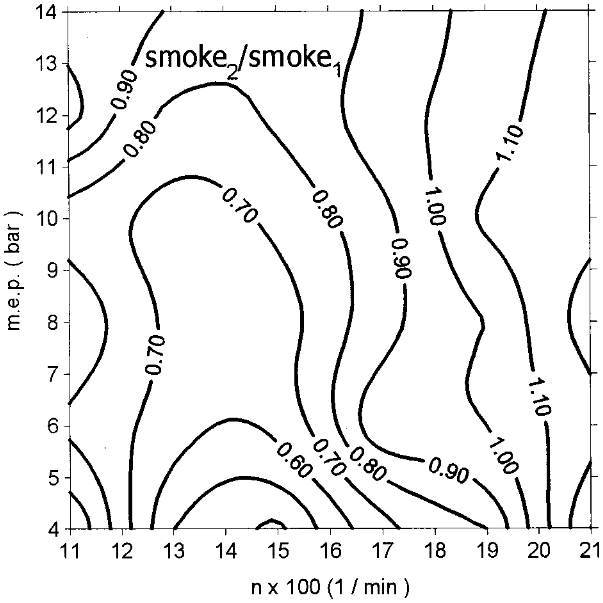

Fig. 10 Smoke density ratio of the two-pulse and constant pressure exhaust system

temperatures during the first phase of the (delayed) combustion. Mass specific HC emission was calculated from the measured values and is presented in Fig. 12.

O_2 emission distribution follows the rules of combustion: higher values correspond to lower engine loads—i.e., to larger *A*/*F* ratios. Total *A*/*F* ratio was presented in Fig. 2. In-cylinder (trapped) *A*/*F* ratio was relatively larger for the two-pulse system due to higher volumetric efficiency and lower rate of the residual gases. As the consequence larger O_2 emission values were measured for the two-pulse system especially at intermittent engine speeds and loads.

NOx emission is crucially important for the engine emission suitability. It was again better to convert individual measured concentrations (ppm by volume) into mass-specific NOx values for better comparison of the data. NOx emission is generally governed by the temperature and local *A*/*F* distribution during combustion process. As mentioned before, higher temperatures of the fresh charge (at the beginning of the combustion process) in the cylinder of the constant pressure system are the consequence of a lower in-cylinder *A*/*F* ratio and higher content of hot residual gases. Residual gases influence increase of soot formation, whereas lower local concentration of O_2 through mixing process with the residual gases simultaneously decreases formation of nitric oxides. Higher effective overall *A*/*F* ratio (Fig. 2), higher in-cylinder excess air with minimum concentration of residual gases (Fig. 9), better cylinder scavenging (Fig. 4 and Fig. 5) increase NOx mass emission of the two-pulse system at lower engine speeds and loads, where ignition delay plays an inferior role. On the other hand, increased temperature at the end of compression stroke reduces ignition delay (especially at higher engine speeds), and as the consequence higher combustion temperatures during the first part of the combustion process provoke increase of the NOx emission. One can conclude from the Fig. 13, that there

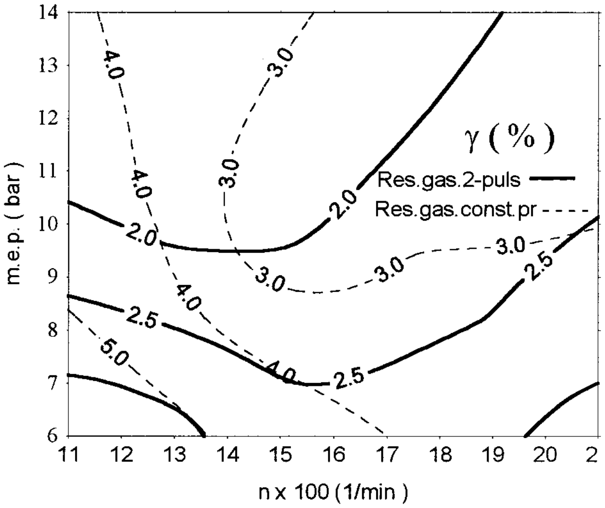

Fig. 9 Residual gases in the cylinder for two exhaust systems

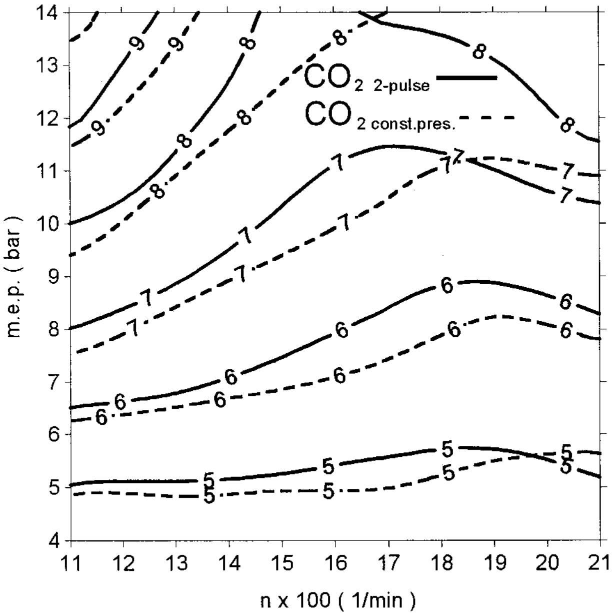

Fig. 11 CO_2 emission for both exhaust systems

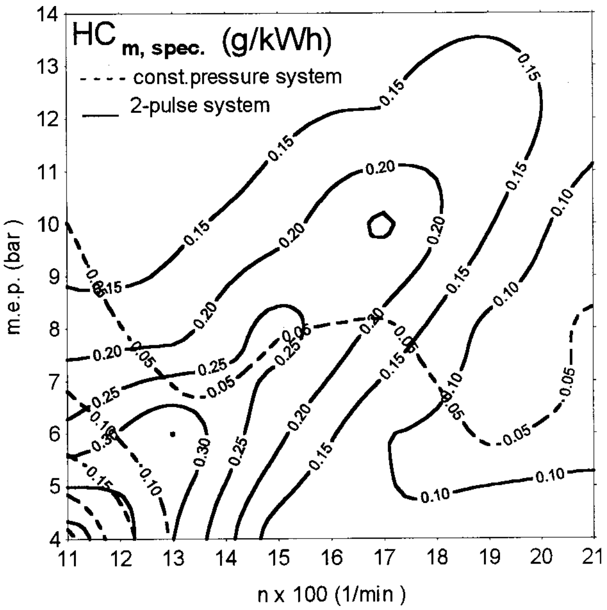

Fig. 12 Specific mass-emission of the hydrocarbons

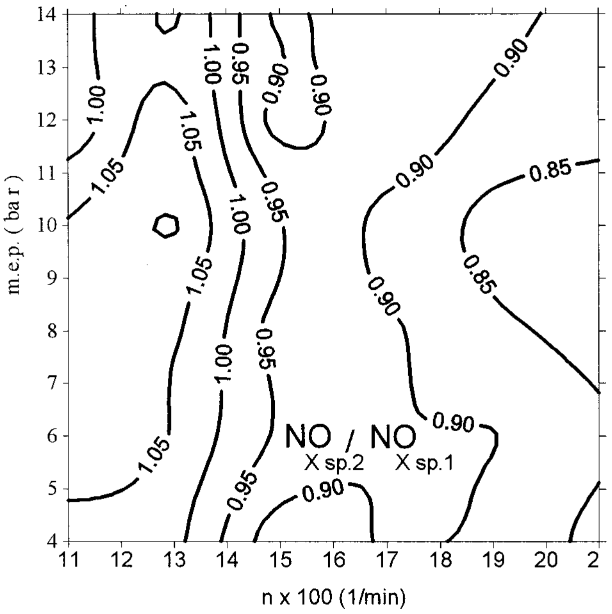

Fig. 13 Ratio of mass-specific NOx emission for two different exhaust systems

is a certain NOx emission advantage in the two-pulse exhaust system, when further increase of the engine output (torque) is concerned.

Conclusion

A Diesel four cylinder and four-stroke engine was optimized by means of two different exhaust systems: one with a common exhaust manifold and another with a double-manifold exhaust system. The main aim was to determine the influence of the exhaust system especially on the scavenging characteristic and emission properties of the observed engine.

It was found out that higher pumping losses of the two-pulse system are the consequence of higher pressure differences during the gas exchange period, caused by higher exhaust amplitudes in the exhaust system. This disadvantage diminishes at lower engine speeds and higher engine loads.

Higher volumetric efficiency and better scavenging of the engine cylinder by the two-pulse system is the consequence of suitable pressure distribution in the exhaust port; there is practically no omission of the cylinder outflow by the reflecting pressure waves and the increase of the valve overlap period can be applied for further increase of the cylinder charge quality and quantity. Reflected pressure waves of neighbor cylinders of a common-exhaust manifold system seriously disturb the exhaust sequence; as the result less fresh air remains in the cylinder and there is a certain amount of residual gases left in the cylinder. Increased valve overlap period additionally deteriorates the situation. Constant pressure exhaust system therefore requires different valve timing, longer exhaust branches or introduction of a pulse converter.

As the consequence of inadequate cylinder scavenging there is an increase of the soot content in the exhaust gases met by the constant pressure system. Higher combustion temperatures of the constant pressure system and sufficient air ensure better combustion of hydrocarbons even at lower engine speeds and loads.

Higher ignition delay by the two-pulse system ensures lower critical peak temperatures in the cylinder and NOx emission is generally lower compared to the constant pressure system. This advantage disappears at lower engine speeds and moderate loads: the ''advantage'' of mixed residual gases and constant pressure exhaust system prevails over the advantage of the delayed ignition.

The overall emission characteristic of the two-pulse exhaust system brings some advantage over the constant pressure system especially for the new-design, higher specific output engines, where more stringent future emission standards can be met with the highest efforts.

References

[1] Hribernik, A., Dobovisek, Z., and Sams, T., 1993, ''Determination of the Equivalent Nozzle Area of a Small Radial Twin-Entry Gas Turbine,'' *Proc. Conference IAT'93*, No. IAT93-M9, Ljubljana, pp. 163–172.

[2] Hribernik, A., 1995, ''Comparison of Zero and One-Dimensional Methods for Simulation of the Process in a Turbocharged Diesel Engine,'' *Proc. Conference IAT'95*, No. 952204, Radenci, pp. 165–173.

[3] Hribernik, A., 1997, ''Comparison of Performances of a 4-Cylinder Supercharged Diesel Engine with Single or Twin Entry Turbine.'' *Proc. Conference IAT'97*, No. 971104, Otocec, pp. 29–36.

[4] Trenc, F., Bizjan, F., and Hribernik, A., 1998, ''Influence of the Exhaust System on Performance of a 4-Cylinder Supercharged Engine,'' ASME J. Eng. Gas Turbines Power, **120**, pp. 855–860.

[5] Trenc, F., Čer, M., Bizjan, F., and Hribernik, A., 1998. ''Determination of the Realistic Turbocharger Efficiency With Pulsating Gas-Flow compared on a 4-Cylinder Engine,'' *ASME Gas Turbine Congress* 98-GT-358.

[6] Watson, N., and Janota, M. S., 1984, *Turbocharging the Internal Combustion Engine*, Macmillan Publishers, London.

[7] Zinner, K., 1980, *Aufladung von Verbrennungsmotoren*, Springer-Verlag, Berlin.

Pascal Chesse
Jean-François Hetet
Xavier Tauzia

Laboratory of Fluid Mechanics,
U.M.R. 6598 C.N.R.S.,
Ecole Centrale de Nantes,
BP 92101,
44321 Nantes Cedex 3, France

Philippe Roy
Bahadir Inozu

School of Naval Architecture
and Marine Engineering,
University of New Orleans,
911, Engineering Building,
New Orleans, LA 70148

Performance Simulation of Sequentially Turbocharged Marine Diesel Engines With Applications to Compressor Surge

This paper presents the SELENDIA code designed for the simulation of marine diesel engines. Various measured and simulated results are compared for the performance of a sequentially turbocharged marine diesel engine during a switch from one to two turbochargers. The results show a good agreement between measured and simulated data. Surge loops that are experimentally observed in case of an anomaly are analyzed using simulated results. Finally, the predictive capabilities of the simulation code are utilized to investigate the influence of the inlet manifold volume on the engine and air charging system performance with a special focus on compressor surge. [S0742-4795(00)01104-2]

1 Introduction

Turbocharger matching is a rather difficult challenge for the design of high output diesel engines, particularly for naval applications. Test-bed measurements are usually tedious and expensive due to the size of the power plant. As a result, engine simulation can be a valuable tool when used in parallel to actual testing for the objective of guiding experimental investigations and improving the global understanding of various aspects of the internal combustion engine. In previous publications, we reported the development of a simulation code that was used to investigate compressor surge and the resulting engine operation limits [1,2]. In this paper, a new version of this code designed for the optimization of turbocharging systems under transient conditions is presented. Various measured and simulated results are shown for a sequentially turbocharged marine diesel engine.

2 The SEMT Pielstick System Applied to the PA6 STC Engine

S.E.M.T. Pielstick has been designing sequentially turbocharged diesel engines since the early eighties. Commercialization started in 1990 for high speed and medium speed engines [3–5]. The system used for the PA6-STC (Sequentially TurboCharged) engine is presented in this section. The engine is equipped with two turbochargers in parallel as shown in Fig. 1. At low and medium loads, one turbocharger is in use. At high loads, valves *G* and *A* are opened allowing the use of both turbochargers. Due to a better air supply, the engine operating range at low speed and high torque is significantly enlarged in comparison with a classic single stage turbocharging system.

The advantages of a sequential turbocharging system are obvious at steady state. However, transient performance needs to be thoroughly investigated, especially with respect to the system switch from one to two turbochargers. This phase is critical due to the large inertia of the turbochargers. The system switch, triggered by a turbocharger speed threshold, is a two step procedure. The *G* valve located on the exhaust gas line shown in Fig. 1 is opened. Subsequently, the turbine drives the second turbocharger whose speed progressively increases. After a certain delay, the *A* valve located on the inlet air line is also opened and the second turbocharger starts supplying air to the engine.

3 The Selendia Simulation Code

3.1 Main Characteristics. The first version of the SELENDIA simulation code was designed for the steady state performance of marine diesel engines [6]. The code is based on the ''filling and emptying'' method which conceives the engine as a succession of control volumes such as the cylinders and manifolds for which mass and energy balance equations are applied [7]. Despite the variations of the gas composition, the gas is assumed to be homogeneously distributed inside the entire control volume. Furthermore, fresh air and exhaust gases are assumed to be perfect. The First Law of Thermodynamics in open systems applied to the various control volumes allows the determination of the gas temperature and pressure as shown in Fig. 2.

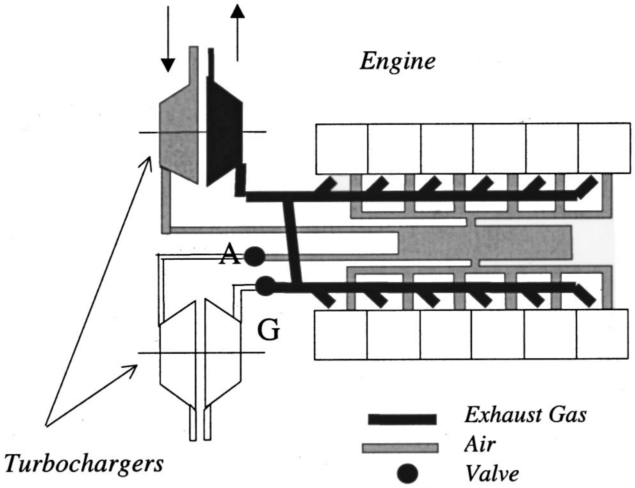

Fig. 1 Sequential turbocharging system developed by S.E.M.T. Pielstick for the PA6 STC

Contributed by the Internal Combustion Engine Division of THE AMERICAN SOCIETY OF MECHANICAL ENGINEERS for publication in the ASME JOURNAL OF ENGINEERING FOR GAS TURBINES AND POWER. Manuscript received by the ICE Division March 27, 2000; final revision received by the ASME Headquarters April 17, 2000. Technical Editor: D. Assanis.

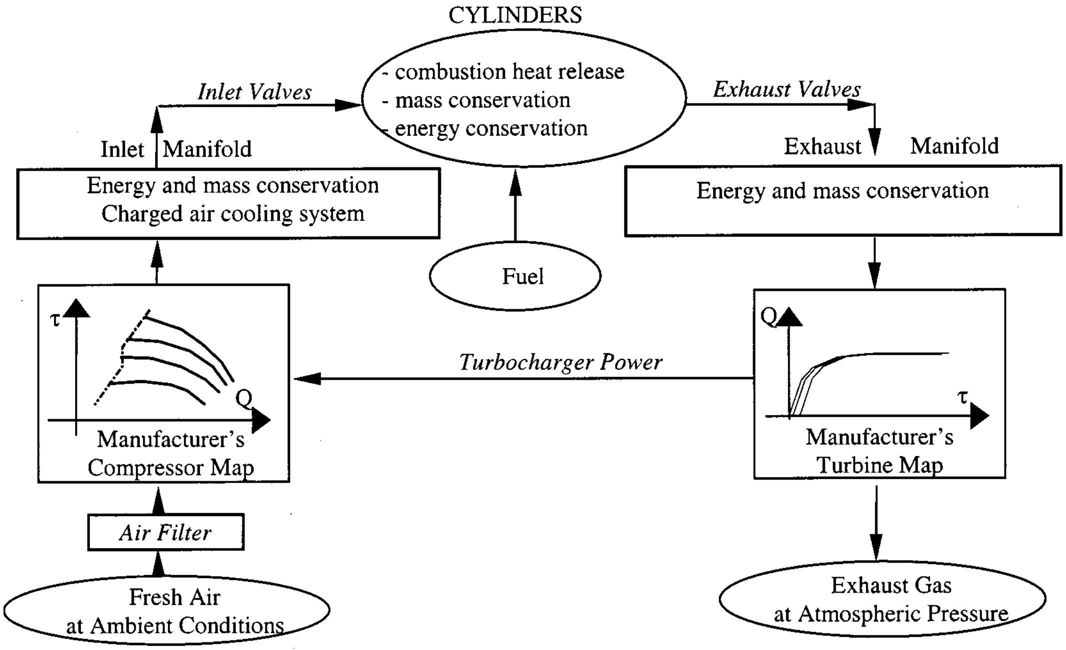

Fig. 2 Structure of the SELENDIA Code

The cylinder volume as a function of the engine crank angle is derived from simple geometry considerations. The Keenan and Kayes tables provide the thermodynamic properties of the exhaust gas and fresh air as a function of temperature and excess air [8]. The combustion heat release and all of the parameters related to the combustion and injection processes are modeled using two Wiebe's laws associated with Gaudart's parameters [9,10]. The heat transfer at the cylinder wall is evaluated using Woschni's model [11]. Friction losses are evaluated with a modified Chen and Flynn's model [12]. Mass flows are derived using Barre de Saint Venant's laws. The inlet and exhaust valve effective areas are either calculated based on geometry consideration or interpolated from test bed data. Finally, the various parameters of the air charging system are evaluated based on the compressor and turbine maps provided by the turbocharger manufacturer [13].

The SELENDIA simulation code makes use of a specific simulation language called A.C.S.L. (Advanced Continuous Simulation Language) [14]. This language provides pre-programmed integration routines among other specific simulation programming tools as well as extensive graphic capabilities for interactive run-time sessions.

After numerous validations for the simulation of steady state performance, the code was modified to allow the transient response simulation of highly rated marine diesel engines as shown in Fig. 3. The governor model is a Proportional Integrator (PI) model. The fuel rack position is provided by the following differential equation:

$$\frac{d\mathrm{Rack}}{dt}=\mathrm{Rack}_n\left(Kp.\frac{d(\mathrm{diff})}{dt}+Ki.\mathrm{diff}\right),$$

$$\mathrm{diff}=\frac{N_{\mathrm{eng}}-N_{\mathrm{requested}}}{N_{\mathrm{eng}}} \tag{1}$$

where *Kp* and *Ki* are provided by the governor's manufacturer as a function of the engine speed. In addition, the model includes

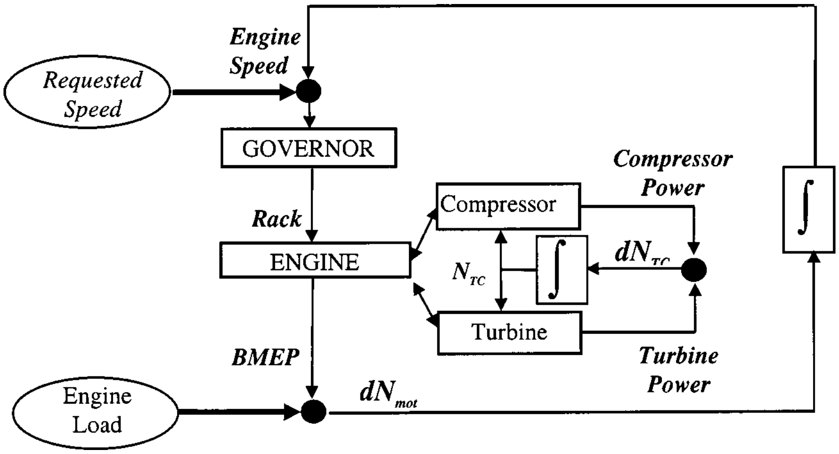

Fig. 3 Engine block diagram for the simulation of marine diesel engine transient response

various fuel rack position limits based on engine speed and boost pressure and aimed at preventing engine over-speed and insufficient excess air. The code was validated and utilized for different projects such as the performance simulation of marine diesel engines under extreme conditions [15,16].

3.2 Additional Models for Sequential Turbocharging. Sequential turbocharging is a rather new technique. Publications regarding this topic are extremely limited. Swain published some results for the simulation of turbocharger switches with a special focus on the turbocharger performance which was modeled in detail [17]. However, the engine model was extremely simplified. The study focused on sequential turbocharging system switches assuming that the engine operation was quasi-constant.

The study presented in this paper includes an engine thermodynamic model to simulate significant variations of the engine speed and torque. In addition to the switch phases, the simulation of the turbocharger performance is based on two major criteria which are the turbocharger speed evaluated with Newton's Second Law and the pressure ratios derived from the First Law of Thermodynamics applied to the inlet and exhaust manifolds. Mass flows and isentropic efficiencies are obtained using a two-dimensional interpolation of the compressor and turbine maps in matrix form.

The switch phases are triggered by a pre-determined turbocharger speed threshold. The model includes the opening characteristics of the two valves mentioned in the previous section in terms of timing and duration. An ''opening coefficient'' *OV* is defined for each valve as the ratio between the current section and the fully opened section, as follows:

$$OV=\frac{S}{S_{fo}}. \tag{2}$$

The turbine mass flow during the exhaust line valve (valve *G*) opening and closing is obtained by multiplying the turbine mass flow when the valve is fully opened and the opening coefficient *OV* as shown in Eq. 3.

$$\frac{dm_{\text{tur}}}{dt}=OV_{\text{exh}}\left(\frac{dm_{\text{tur}}}{dt}\right)_{fo}. \tag{3}$$

When the exhaust gas valve is open and the inlet air valve is closed, the compressor operates with a certain speed and no mass flow. As a result, the development of a new compressor model was necessary. The operating point is located in the surge area of the compressor map. Due to insufficient information in this region of the compressor map, the power consumed by the compressor is derived from the following simplified equation:

$$W_{\text{comp}}=K_{\text{comp}}.N_{TC}^2. \tag{4}$$

The K_{comp} coefficient is specific to the compressor being used. However, it may be extrapolated from a known value for a given type of compressor since it seems to be proportional to the square of the compressor wheel diameter according to our tests. When the inlet air valve is being opened, the compressor power is calculated using an equation which combines the formula of the compressor power under normal operating conditions given by Eqs. 5 and 6 and the simplified compressor power law given by Eq. 4.

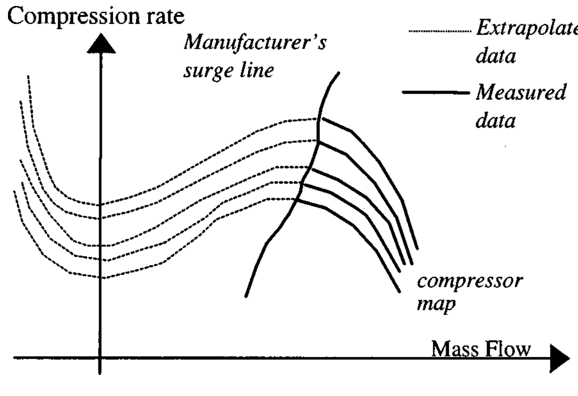

Fig. 4 Extrapolated compressor map

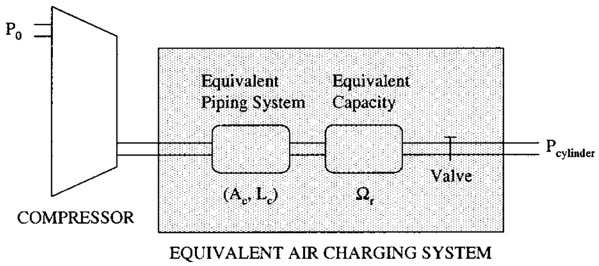

Fig. 5 Equivalent air charging system

$$W_{\text{comp}}=\frac{dm_{\text{comp}}}{dt}\left(\frac{Cp_o+Cp_i}{2}\right)(T_o-T_i), \tag{5}$$

where

$$T_o=\frac{T_i}{\eta_{\text{comp}}}(\eta_{\text{comp}}-1+\tau_{\text{comp}}^{(\gamma_i-1)/\gamma_i}). \tag{6}$$

The compressor map is extrapolated to include negative mass flows as shown in Fig. 4. The objective is to determine the effect of inadequate valve opening timings, including compressor surge [18]. The extrapolation is based on the modeling of the various losses occurring when the compressor operates beyond the adaptation line. The relevant equations are presented in Appendix 1.

As shown in Fig. 5, the combination of the ''filling and emptying'' equations and those associated with the inertia of the fluid between the compressor and the inlet manifold allows the calculation of surge loops [19,20]. The mathematical model is presented in Appendix 2. It provides the boost pressure and the compressor mass flow during surge as a function of time. The compressor power is evaluated using Eq. 5 when the compressor mass flow is positive and Eq. 4 when the compressor mass flow is null or negative.

4 Validation

The validation phase was performed for the SEMT Pielstick PA6-STC engine for which measured data were available. The main characteristics of the PA6-STC engine are shown in Table 1.

Figure 6 shows the measured and simulated boost pressure and turbocharger speeds for the 12PA6 STC (12 cylinders) engine during a switch from one turbocharger to two turbochargers at constant engine speed (1010 rpm). The turbocharger switch is induced by a slight load increase. For this specific test, the delay between the exhaust line valve and inlet line valve openings is two seconds. This delay was adjusted to avoid compressor surge by allowing a sufficient turbocharger speed at the inlet line valve opening as well as to sustain the engine air supply by maintaining the boost pressure. Indeed, when the *A* valve is closed and the *G*

Table 1 Main characteristics of the Pielstick PA6 STC engine

Number of cylinders:	12 or 16
Type:	Vee (60°)
Bore:	280 mm
Stroke:	290 mm
MCR Speed:	1050 rpm
MCR Power:	325 kw/cyl
Turbocharging system:	sequential (axial turbine and centrifugal compressor)

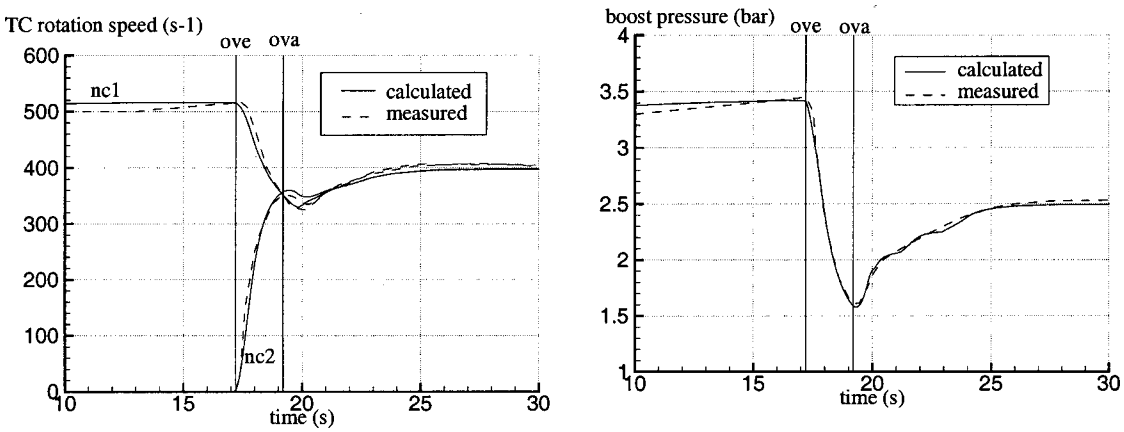

Fig. 6 Engine and air charging system performance during a 1TC/2TC switch at 1010 rpm for the 12PA6STC engine

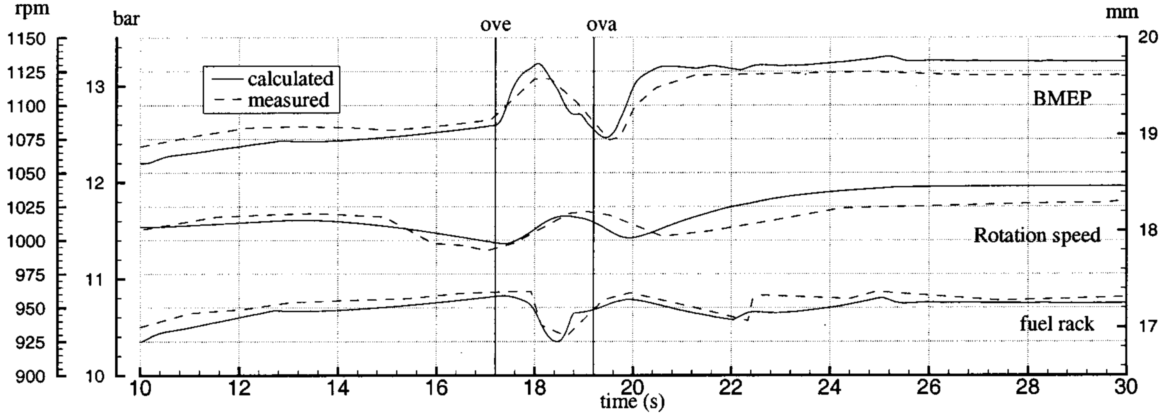

Fig. 7 Engine performance during a 1TC/2TC switch at 1010 rpm for the 12PA6STC engine

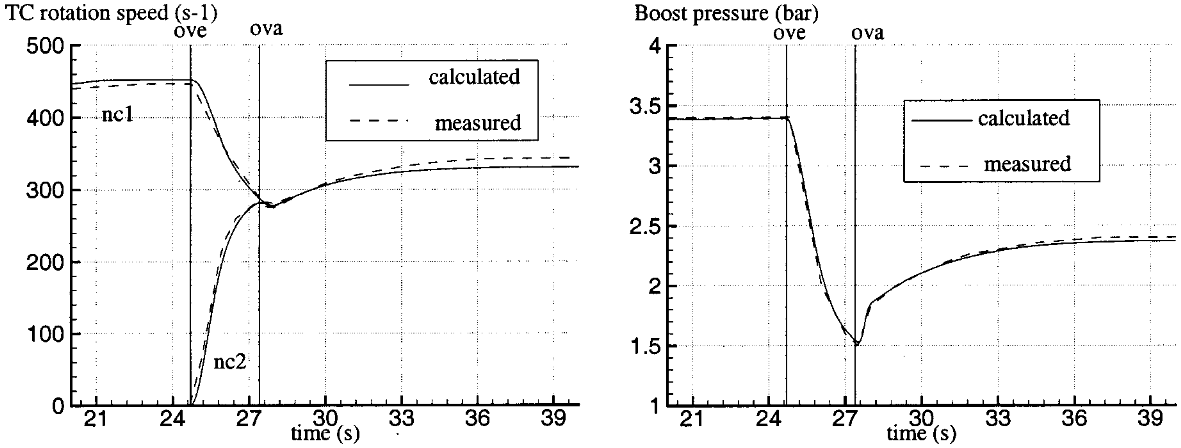

Fig. 8 Air charging system performance during a 1TC/2TC switch at 900 rpm for the 16PA6STC engine

valve is open, the single turbocharger which supplies air to the engine no longer uses the full energy flow of the exhaust gas since the exhaust gas flow is shared by the two turbines. As a result, the boost pressure significantly decreases. It is thus critical to adjust the timing of the *G* and *A* valve opening to avoid penalizing the engine performance when the engine loading process includes a turbocharger switch.

Figure 6 shows that both turbochargers reach the same speed after 1.8 s. The ''OVE'' and ''OVA'' vertical lines correspond to the beginning of the exhaust and inlet line valve opening, respectively. The boost pressure decreases from 3.5 to 2.2 bar during the turbocharger switch with an absolute minimum of 1.8 bar two seconds after the exhaust line valve opening. The results show a satisfactory agreement between measured and simulated data. The error margin for the extreme values of the turbocharger speed and boost pressure is within 8 percent. The duration of each phase is predicted with sufficient accuracy.

Figure 7 also shows a good agreement between measured and calculated results for the engine. The exhaust line valve opening initially results in a pressure drop in the exhaust manifold, which temporarily improves the engine performance. Consequently, the engine scavenging improves, resulting in a slight increase of the

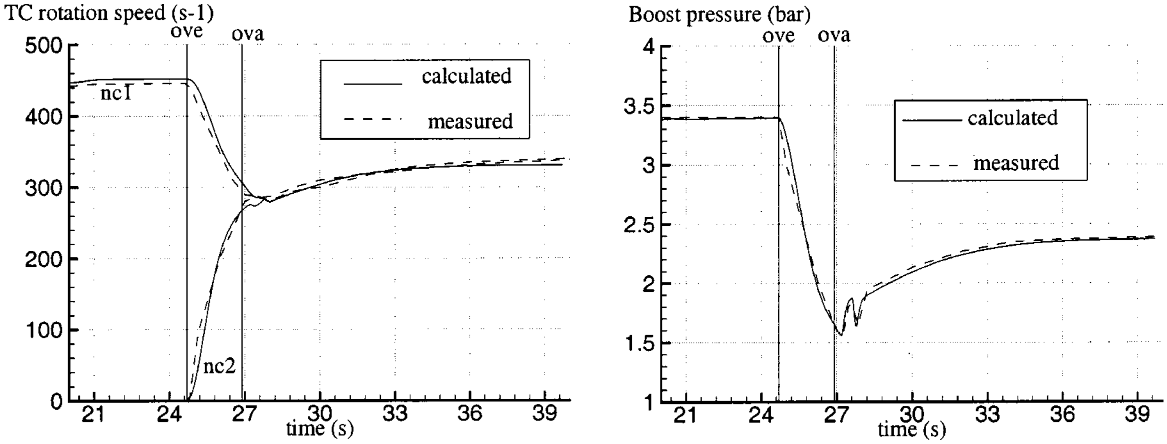

Fig. 9 Air charging system performance during a ITC/2TC switch at 900 rpm in case of a reduced valve opening timing—16PA6STC engine

engine BMEP as well as the engine speed. The actual engine speed exceeds the requested speed and the governor orders a decrease of the fuel rack position. However, the boost pressure drops after approximately one second since the air is supplied by a single turbocharger which receives only half of the exhaust gas flow. As a result, the inlet air flow decreases as well as the engine speed. The rack reaches its higher limit and the governor cannot compensate the speed decrease. After the inlet air line valve opening, the boost pressure augmentation allows a slight increase of the engine speed. However, the engine BMEP does not increase significantly due to the higher limit of the fuel rack position. After approximately five seconds since the beginning of the switching process, the fuel rack limit associated with the use of one turbocharger is replaced with the much higher fuel rack limit associated with the use of two turbochargers. As a result, the fuel rack position slightly increases for a few seconds allowing the engine to stabilize at the requested speed.

The validation process was continued with the 16PA6 STC (16 cylinders) engine, which is equipped with bigger turbochargers than the 12PA6 STC engine. The simulation is again at constant speed (900 rpm). The delay between the exhaust and inlet line valve openings is 2.7 s for this engine instead of 2 s for the previous engine due to higher turbocharger inertia. Figure 8 shows a satisfactory agreement between measured and simulated results. The error margin on the turbocharger speeds, boost pressure and duration of the various phases remains quite low.

5 Predicted Results

The SELENDIA code was utilized to simulate the 16PA6-STC engine performance in case of an anomaly. Figure 9 shows the performance of the air charging system when the delay between the exhaust and inlet line valve openings is reduced from 2.7 s to 2.2 s. In such a case, the speed of the second turbocharger is insufficient when the inlet line valve is opened. This results in compressor surge as shown by the turbocharger speed curve and especially the boost pressure curve for which a sudden drop is observed, indicating a negative compressor mass flow. Figure 9 shows that the simulated results are satisfactory. The results show that there is only one surge ''loop'' whose amplitude and duration are predicted with good accuracy. The trajectory of the compressor operating point on the compressor map contributes to a better understanding of the air charging system performance. This trajectory can be plotted using the simulated inlet manifold pressure and compressor mass flow. Figure 10 shows the operating point of the compressor that is being started during a switch from one turbocharger to two turbochargers. In this figure, ''*A*'' is the compressor operating point at the inlet line valve opening. The corresponding compressor speed is 270 revolutions per sec (rps). The compressor mass flow quickly increases to reach ''*B*.'' Then, the boost pressure increases at constant speed and the compressor operating point reaches ''*C*.'' However, the compressor speed is insufficient and the operating point goes to the surge area to eventually reach ''*D*'' while the compressor mass flow significantly decreases.

Due to a reversed compressor flow, the inlet manifold pressure decreases and the compressor operating point reaches ''*A*'' which corresponds to the minimum of the 270 rps speed line. Subsequently, the compressor mass flow quickly increases to reach ''*E*.'' The ''*A-B-C-D-E*'' surge loop lasted approximately .5 s and the compressor speed reached 280 rps. Since the compressor mass flow is again positive, the inlet manifold pressure progressively increases. The turbocharger speed is now sufficient and the operating point is no longer in the surge area of the compressor map. The inlet manifold pressure stabilizes around ''*F*.''

The SELENDIA code showed good predictive capabilities in case of anomalies. These predictive capabilities were utilized to determine the effect of geometry modifications on the engine performance during a turbocharger switch. The effect of the inlet manifold volume was investigated. The inlet manifold volume of the test engine is 1.3 m^3. Figure 11 shows the performance prediction of the SELENDIA code for an inlet manifold volume of .8 m^3, which was chosen arbitrarily.

The simulated results indicate the occurrence of two surge loops before the stabilization of the engine operation. Figure 12 shows the compressor operating point on the compressor map.

The initial operation of the compressor illustrated by the curve labeled ''*A*'' corresponds to the previously described compressor

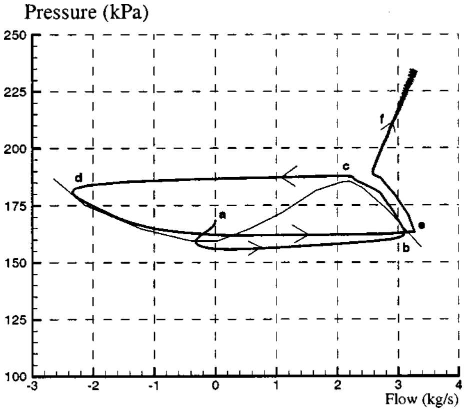

Fig. 10 Surge loop on the compressor map

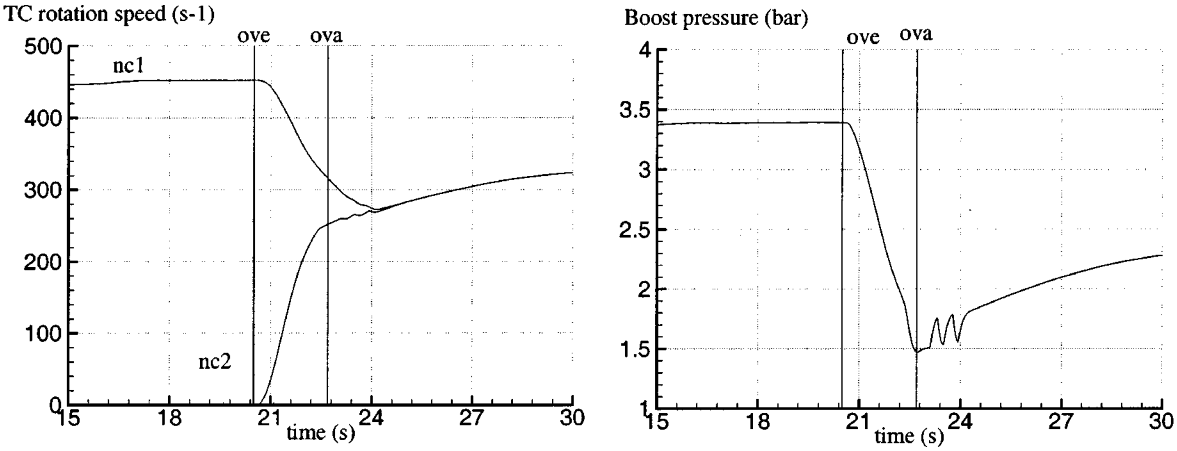

Fig. 11 Engine and air charging system performance during a 1TC/2TC switch at 1010 rpm for the 16PA6STC with an inlet manifold volume of .8 m^3

performance when the inlet line valve is opened. When the compressor mass flow is again positive, the inlet manifold pressure is approximately 1.75 bar. During the first surge loop labeled ''*B*,'' the compressor did not reach a sufficient speed that would prevent surge. As a result, another surge loop labeled ''*C*'' is observed. The first loop corresponds to a compressor speed of 275 rps and the second surge loop corresponds to a compressor speed of 278 rps. The compressor speed after the second surge loop is 280 rps, which is sufficient to prevent a third surge loop. The compressor operating point leaves the surge area of the compressor map and the boost pressure stabilizes around ''*D*.''

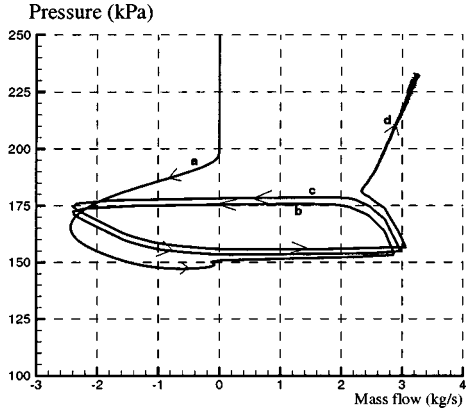

Fig. 12 Performance of the compressor being started during a 1TC/2TC switch with an inlet manifold volume of .8 m^3

Figure 13 shows the engine and air charging system performance for a switch from one to two turbochargers with an inlet manifold volume of 2 m^3. This figure shows that the turbocharger switch does not induce surge when the inlet manifold volume is 2 m^3.

A larger exhaust manifold volume results in a larger inertia of the engine/turbocharger assembly. The amplitude of the inlet manifold pressure drop is thus smaller with a large manifold than with a small manifold. This may appear as a penalizing factor for the engine performance since a higher boost pressure puts the compressor operation closer to the surge area. However, a higher boost pressure increases the engine power. This power increase provides a better energy flow to the turbine which is being started during the one to two turbocharger switch. Consequently, the turbocharger speed increases faster and reaches a higher value when the inlet line valve is opened. This significantly diminishes the risk of surge as predicted by the simulated results.

6 Conclusion

The steady state performance and transient response of high output marine diesel engines must be thoroughly investigated. As

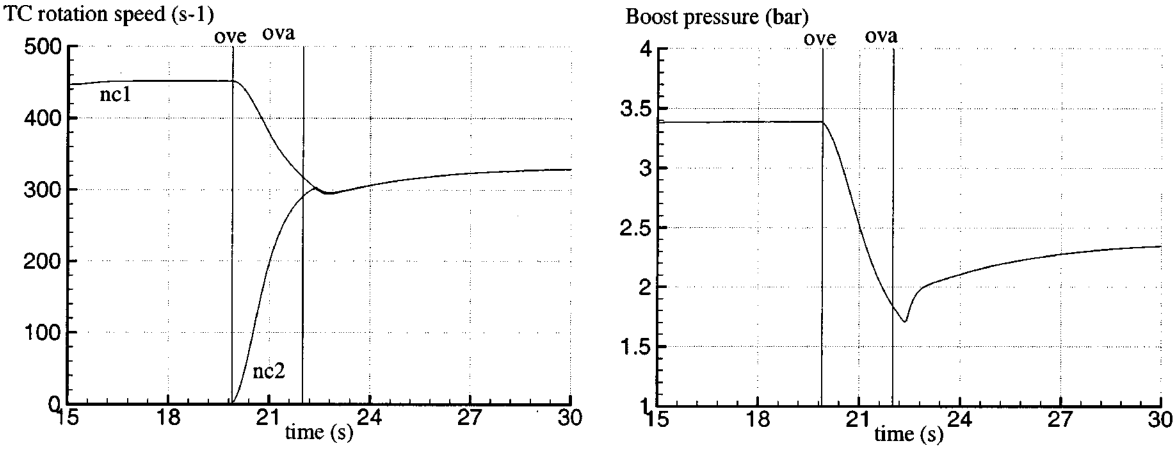

Fig. 13 Engine and air charging system performance during a 1TC/2TC switch at 1010 rpm for the 16PA6STC with an inlet manifold volume of 2 m^3

shown in this paper, the SELENDIA simulation code allows a comprehensive investigation of the engine/turbocharger assembly under transient conditions in the case of sequentially turbocharged engines. The various results show a good agreement between measured and simulated data. As an added advantage, simulation can be used to investigate the influence of specific engine parameters. In parallel to test bed measurements, it may be useful for the design, development and optimization of turbocharged marine diesel engines for both healthy and faulty operations.

Acknowledgments

We would like to thank the Center d'Etude des Machines Thermiques of SEMT Pielstick and especially M. G. Grosshans for his contribution.

Nomenclature

N = rotation speed [rpm]
n = number of cylinders
BMEP = Brake Mean Effective Pressure [bar]
W = power [W]
P = cylinder pressure [bar]
diff = difference between requested & actual speed [-]
m = mass [kg]
S = area [m^2]
Cp = specific heat at constant pressure [J/kg/K]
η = efficiency [-]
γ = specific heat ratio [-]
V = volume [m^3]
I = inertia [kgm^2]
t = time [s]
rack = fuel rack position [mm]
K = coefficients [-]
τ = compression rate [-]
OV = opening coefficient [-]
T = temperature [K]

Subscripts

eng = engine
cyl = cylinder
comp = compressor
tot = total
exh = exhaust
TC = turbocharger
tur = turbine
max = maximum
n = nominal
i = inlet
o = outlet
fo = full opening

Appendix I: Elements for the Extrapolation of the Constant Speed Lines of a Compressor

A single equation cannot characterize the compressor pressure-flow diagram across its complete range. Figure 14 identifies the following 4 distinct sections:

- Section 1 is obtained by the experiment and usually provided by the manufacturer
- Sections 2 and 4 may be obtained by the experiment [18]
- Section 3 does not seem to be accessible by the experiment

The parametric expressions of the compressor's characteristics presented in this appendix are derived from a combination of the classical equations and those related to the main losses experienced in sections 1, 2, 3 and 4. The following assumptions were made:

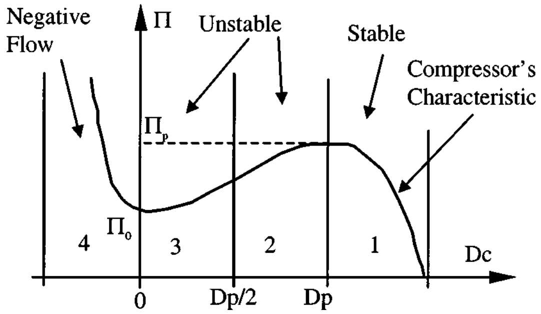

Fig. 14 Schematic of compressor operating map

- A compressor characteristic is unique, independently of the steady or dynamic (during surge) nature of the compressor operation.
- A compressor characteristic is represented by a function that is continuous and derivable across the complete mass flow range.
- The minimum of a compressor characteristic occurs when the mass flow is equal to zero.
- Section 4 can be assimilated as the parabolic curve of a pressure loss.

Using the various notations defined in the general nomenclature as well as the appendix nomenclature, the compressor characteristics are modeled as follows:

Section 2: $D>D_p/2$

The following equations are based on energy conservation, Euler's theorem and experimental data. They include the effect of slip factor σ, friction and incidence losses as well as the previously listed assumptions.

$$\text{si } D_c>D_{\text{ad}}\Pi=\left(a_1-a_2.D_c-K_f.D_c^2-a_3\left(1-\frac{D_{\text{ad}}}{D_c}\right)^2\right)^{\gamma/(\gamma-1)}$$

$$\text{si } D_c<D_{\text{ad}}\Pi=\left(a_1-a_2.D_c-K_f.D_c^2-a_3\left(1-\frac{D_c}{D_{\text{ad}}}\right)^2\right)^{\gamma/(\gamma-1)}$$

where $a_1=1+\sigma(4\pi^2r_2^2)/(Cp.T_1^*)N^2$

$$a_2=\frac{\sigma.N}{Cp.T_1.\rho_1(\Pi_p)^\gamma.l_2.tg(\beta_2)}$$

$$a_3=\frac{2\pi^2(r_1^2+r_2^2)}{Cp.T_1}N^2\text{et}$$

$$D_{\text{ad}}=\frac{a_3.D_p}{(\Pi_p)^{(\gamma-1)/\gamma}-a_1+a_3+\dfrac{a_2.D_p}{2}}$$

$$K_f=a_3\left(\frac{1}{D_{\text{ad}}.D_p}-\frac{1}{D_p^2}\right)-\frac{a_2}{2.D_p}$$

Section 3: $0<D_c<D_p/2$

The formulation of this section was arbitrarily selected to link section 2 and 4. K is fitted to ensure continuity and derivability. $\Pi=K.D_c^2+\Pi_0$ where:

$$K=\frac{\gamma}{\gamma-1}\left[-\frac{a_2}{D_p}-Kf+\frac{2a_3}{D_{\text{ad}}}\left(\frac{1}{D_p}-\frac{1}{2D_{\text{ad}}}\right)\right]$$
$$\times\left[a_1-\frac{a_2.D_p}{2}-\frac{K_f.D_p^2}{4}+a_3\left(1-\frac{D_p}{2D_{\text{ad}}}\right)^2\right]^{1/(\gamma-1)}$$

$$\Pi_0=\left[a_1-\frac{a_2.D_p}{2}-\frac{K_f.D_p^2}{4}+a_3\left(1-\frac{D_p}{2D_{\mathrm{ad}}}\right)^2\right]^{\gamma/(\gamma-1)}-\frac{K.D_p^2}{2}$$

Section 4: $D_c<0$

$$\Pi=K'.D_c^2+\Pi_0 \quad \text{where} \quad K'=(\Pi_p-\Pi_0)/D_p^2$$

Appendix II: Equations Resulting from the Air Charging System Model Shown in Figure 5

- Valve: Barre de Saint Venant's equation for subsonic flows
- Pipe: Newton's First Law

$$\frac{dD_c}{dt}=\frac{A_c}{L_c}(P_c-P_r)$$

- Manifold: Mass and energy conservation

$$\frac{dP_r}{dt}=\frac{r.\gamma.T_r}{\Omega_r}\left(D_c\frac{T_c}{T_r}-D_v\right)$$

$$\frac{dT_r}{dt}=\frac{r.T_r^2}{P_r.\Omega_r}\left[\gamma\left(D_c\frac{T_c}{T_r}-D_v\right)-(D_c-D_v)\right]$$

- Compressor:

$$T_c=T_0\left(\frac{P_c}{P_0}\right)^{(\varepsilon-1)/\varepsilon}$$

$$D_c=f\left(\frac{P_c}{P_0}\right)$$

Appendix Nomenclature

A_c = Pipe cross section
D_c = Compressor mass flow
D_{ad} = Compressor mass flow at adaptation
D_p = Compressor mass flow during surge
D_v = Valve mass flow
l_2 = Width of the wheel outlet
L_c = Pipe length
N = Compressor speed
P_r = Manifold pressure
P_c = Compressor outlet pressure
P_0 = Compressor inlet pressure
r_1 = Radius of the wheel inlet
r_2 = Radius of the wheel outlet
r = Mayer's constant
T_r = Manifold temperature
T_c = Compressor outlet temperature
T_0 = Compressor inlet temperature
t = Time
β_2 = Angle of the wheel outlet
ε = Polytropic coefficient
Π = Compressor pressure ratio
Π_p = Pressure ratio at surge occurrence
Π_0 = Pressure ratio at compressor zero mass flow
ρ_1 = Air density at the compressor inlet
σ = Slip factor
Ω_r = Manifold volume

References

[1] Chessé, P., Hetet, J. F., Tauzia, X., and Frayret, J. P., 1995, ''Influence of the Alteration of the Compressor Surge Line on the Operation Limit of a Marine Turbocharged Diesel Engine,'' Internal Combustion Engine Division of the ASME—Fall Technical Conference 24–27 Sept., Milwaukee.

[2] Chessé, P., Tauzia, X., Hetet, J. F., Inozu, B., and Roy, P. 1996, ''Study by Simulation of the Behavior of a Two Stage Turbocharged System During Surge,'' ASME Spring Technical Conference, *Engine Simulation Cession, Proceedings*, **27-4**, pp. 107–113, October 20–23, Fairborn OH (USA).

[3] Herrmann, R., 1989, ''Sequential Turbocharging for PA6 Engine,'' IMechE seminar, Sprint Rated Engines, London Nov. 28 1989.

[4] Herrmann, R., 1990, ''Sequential Turbocharging for PA 6 Engines,'' ISME Kobe.

[5] Grosshans, G., 1995, ''The Marine Version of SEMT Pielstick's New Generation of Medium Speed Engines,'' Fall Technical Conference, (Milwaukee), ASME 95, I.C.E. Vol. 25-1.

[6] Hetet, J. F., Chessé, P., and Inozu, B., 1994, ''An ACSL Simulation for Optimum Operation of Turbocharged Marine Diesel Engines,'' ASME Paper 94-ICE-7.

[7] Heywood, J. B., 1988, *Internal Combustion Engine Fundamentals*, Mc Graw Hill, New York.

[8] Keenan, J. H., and Kayes, J., 1948, *Gas Tables*, John Willey, New York.

[9] Wiebe, 1967, ''Halbempirische Formel für die Verbre nungsggeschwindigkeit,'' Verlag der Akademie der Wissenchaft der UdssR (Moscow).

[10] Gaudart, L., 1987, ''Incidence des configurations de fonctionnement de navires militaires sur la suralimentation à deux étages de leurs moteurs diesel de propulsion PA6-BTC,'' Thèse de doctorat ENSM.

[11] Woschni, G., 1967, ''An Universally Applicable Equation for the Tinstantaneous Heat Ransfert Coefficient in the Internal Combustion Engine,'' SAE Paper 670931.

[12] Chen, S. K., and Flynn P. F., 1965, ''Development of a Single Cylinder Compression Ignition Research Engine,'' SAE Paper 650773.

[13] Watson, N., and Janota, M. S., 1982, ''Turbocharging the Internal Combustion Engine,'' Mac Millan, New York.

[14] Mitchell, G., ''A.C.S.L.: Advanced Continuous Simulation Language,'' Concord, MA, USA.

[15] Inozu, B., Gervaise, H., Roy, P., and Hetet, J. F., 1995, ''Performance Simulation of Marine Diesel Engines Under Extreme Conditions.'' ASME Fall Technical Conference, Milwaukee, WI.

[16] Inozu, B., 1996, ''Performance Simulation of Marine Propulsion Systems Under Extreme Conditions,'' final report, Gulf Coast Region Maritime Technology Center (GCRMTC) research project no. AMTC95-020A.

[17] Swain, E., 1993, ''Diesel Engine Transient Performance Prediction During Sequential Turbocharging Operations,'' Imech 93, C465/012/93 pp. 123–131.

[18] Chessé, P., 1995, ''Détermination des limites d'exploitation des Diesel de forte puissance. Incidence des circuits de liaison moteur-turbocompresseur. Instabilités et pompage des compresseurs,'' Ph.D. thesis, Université de Nantes and Ecole Centrale de Nantes.

[19] Greitzer, E. M., 1976, ''Surge and Rotating Stall in Axial Flow Compressors: I—Theoretical Compression Model,'' ASME J. Eng. Power, **98**, pp. 190–198.

[20] Yano, T., and Nagata, B. I., 1971, ''A Study on Surging Phenomena in Diesel Engine Air Charging System,'' J.S.M.E., **14**, No. 70.

Intake Flow Structure and Swirl Generation in a Four-Valve Heavy-Duty Diesel Engine

Kern Y. Kang
Senior Researcher,
Engine R&D Dept.,
Korea Institute of Machinery and Materials,
P.O. Box 101,
Yusung, Taejon, Korea
e-mail: kykang@mailgw.kimm.re.kr

Rolf D. Reitz
Professor,
Engine Research Center,
University of Wisconsin-Madison,
Madison, WI 53706
e-mail: reitz@engr.wisc.edu

Intake flow structure was studied using various port geometries in a four-valve heavy-duty diesel engine. Swirl ratio, LDV measurements of bulk flow and turbulence, and flow visualization experiments were conducted on a steady-state bench rig. In addition to the standard production port, archetypal intake port flows (swirl, anti-swirl and tumble) were created using intake valve shrouds. These flow types are not usually found in heavy-duty engines, which typically employ quiescent combustion chamber designs. However, recent CFD analyses have indicated that intake flow structures can significantly influence engine pollutant emissions (Fuchs and Rutland, 1998). Thus, it was of interest to characterize these flows in a heavy-duty engine. The measured swirl and axial velocity components were analyzed to reveal the swirl and tumble generation mechanisms, and the LDV data compared favorably with the swirl meter results. The flow visualization confirmed the existence of flow recirculation regions under the intake valves also seen in the LDV data. These flow structures help to explain the origins of the overall swirl and tumble flow fields. The results were also compared with available CFD predictions made using the same port configurations. The measured swirl levels were found to agree with the CFD trends. However, in some cases quantitative differences were found, presumably due to the effect of piston motion in the actual engine. These differences need to be accounted for when evaluating port designs from steady-flow measurements, especially in cases with high tumble flow components. [S0742-4795(00)00804-8]

Introduction

The design of the intake ports of an internal combustion engine plays an important role in modern low emission engines. In small-bore DI (direct injection) diesel engines, which have a very short duration for the mixture formation and combustion, a rule of thumb is that the fuel system requires that swirl should sweep through the intersection angle between two adjacent sprays [1,2]. Large-bore diesel engines have relatively low swirl, and they rely upon multi-hole injection nozzles and high injection pressures to promote a uniform distribution of fuel within the combustion chamber [3]. It is known that the swirl should be controlled at an optimum level, since a higher swirl increases NOx emissions but reduces soot emissions [4,5]. However, there are relatively few studies available that document the nature of the flow in heavy-duty engines, since most previous studies have considered high-speed diesel or spark-ignition engines. The present work addresses this need and presents results for a modern 4-valve heavy-duty engine. The work also helps validate recent CFD intake flow predictions made for the same engine by Fuchs and Rutland [6]. That work showed that intake flow structures can have a significant effect on heavy-duty diesel engine emissions.

Much work has focused on high-speed engines, and there are two basic methods for generating intake swirl [7–9]; the directed intake port that has good performance at high valve lifts, and the helical intake port that can produce higher swirl at low and middle valve lifts. Previous measurements and flow visualizations made under steady conditions include; comparisons between swirl meter and HWA (hot wire anemometer) [10,11], LDV measurements [12–14], flow visualization using water flow analogs [15–17], and detailed flow visualization coupled with CFD modeling [18,19]. These studies have revealed that HWA has difficulty detecting reverse flow regions in the cylinder and that water analogs can miss small vortices due to flow incompressibility effects. However, there is relatively good agreement between swirl meter results and LDV measurements.

Analyses of the swirl characteristics and the intake flow conditions have been carried out with various methods including; the precession of the swirl center in the cylinder [20,21], and suggestions of appropriate non-dimensional parameters to identify the swirl and flow performance have been made [22,7,9,14,15]. The effect of cylinder wall friction on the swirl decay have been discussed by Uzkan et al. [17].

In spite of the above studies on swirl characteristics, more systematic and analytic studies are still required due to the complexity of the flows. The present study analyzes intake flow structures in detail and reveals the swirl generation mechanism in a modern four-valve heavy-duty diesel engine. Measurements of the swirl flow in four different intake port geometries were accomplished with a swirl meter and an LDV system. The details of the intake flow fields were further revealed using flow visualization where a laser sheet served to illuminate tracer particles. The swirl levels were also compared with available transient results of a three-dimensional computational code (KIVA-3V) for the same intake port geometries. This comparison also serves to examine the validity of the common assumption that steady-state flow measurements can be used to characterize engine intake flows for the present class of engine.

Experimental System and Methods

Steady-State Flow Rig. The flow rig consisted of a rigid stand with an acrylic cylinder, a Caterpillar 3401 DI diesel engine cylinder head, and a flow control system with a blower, as shown schematically in Fig. 1. The air suction through the cylinder was provided by a variable speed blower (SuperFlow Flowbench 600, SuperFlow Co.). Inlet room air for the blower was drawn through a set of calibrated nozzles into a settling chamber preceding the blower. The pressure drop across the nozzles was used to deter-

---

Contributed by the Internal Combustion Engine Division of THE AMERICAN SOCIETY OF MECHANICAL ENGINEERS for publication in the ASME JOURNAL OF ENGINEERING FOR GAS TURBINES AND POWER. Manuscript received by the ICE Division November 23, 1998; final revision received by the ASME Headquarters May 9, 2000. Technical Editor: D. Assanis.

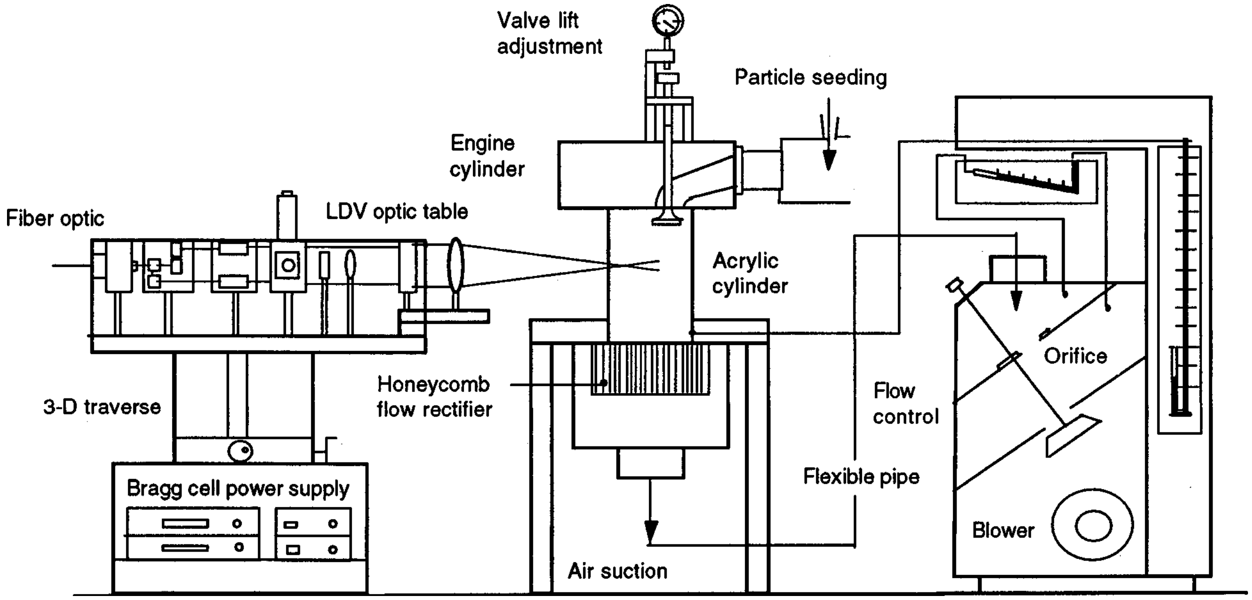

Fig. 1 Schematics of experimental setup for LDV measurements using a flow bench

mine the mass flow rate, while the blower speed was adjusted to provide a desired pressure difference between the port inlet and the cylinder.

Two pressure difference conditions of 221 mm H_2O and 462 mm H_2O were selected to simulate the actual engine operating conditions of 1000 rev/min and 1600 rev/min in the naturally aspirated condition, respectively. The general specifications of the engine are as follows: 141 mm bore, 160 mm stroke, 11 mm maximum valve lift. Four different intake port configurations were selected to effectively change the swirl generation mechanism, as shown in Fig. 2; an appropriate geometry for swirl (swirl port), an anti-swirl geometry (anti-swirl port), and a tumble port and the standard port [6]. These various intake ports were implemented by adding sheet metal shrouds on the intake valves of the standard port.

Swirl Meter Measurement. The swirl measuring system was built as an easily removable part of the steady-flow rig. It consists of an aluminum honeycomb with small cells of large aspect ratio capable of straightening the swirling flow. The angular momentum flux of the flow applies a torque on the honeycomb, which is supported by a very low friction ball bearing. The rotation of the honeycomb, as shown in Fig. 3, is restrained by two spring bars positioned at each corner of the container box, and its rotation angle was detected by the distance between an incoming laser beam (0.9 mW) and the reflected beam on a mirror mounted the honeycomb shaft. The system was calibrated by a dead weight method. The honeycomb size was larger than the cylinder diameter, preventing the air from bypassing the honeycomb.

LDV Measurement. The LDV system consisted of a 5-watt Argon-ion laser, a fiber optic transmitter and optics bed, and a burst signal processor, as shown in Fig. 1. The single-component laser was operated at the green wavelength of 514 nm. The laser power during the experiment was adjusted between 0.3–0.4W. The LDV optical arrangement of back scattering was used to measure the swirl and axial velocity components in the cylinder. Two Bragg cells of 45 and 37 MHz were used to eliminate the directional ambiguity. The fringe spacing of the measuring volume was 3.04 μm. The optical bed could be moved on a three-dimensional traversing system with 0.5 mm resolution. The LDV signal was processed by an FFT type signal processor (TSI Co.). The flow was seeded with atomized silicon oil droplets of 1 to 3 μm mean diameter which were introduced through the upstream end of the ports. The droplets were produced using an air-assist atomizer.

The tangential velocity components for the swirling motion in the cylinder were obtained at 13 points with a 10 mm interval between points along a diameter on four axial stations; $z = 15$, 60, 130, 180 mm. The axial velocity components were obtained at 13

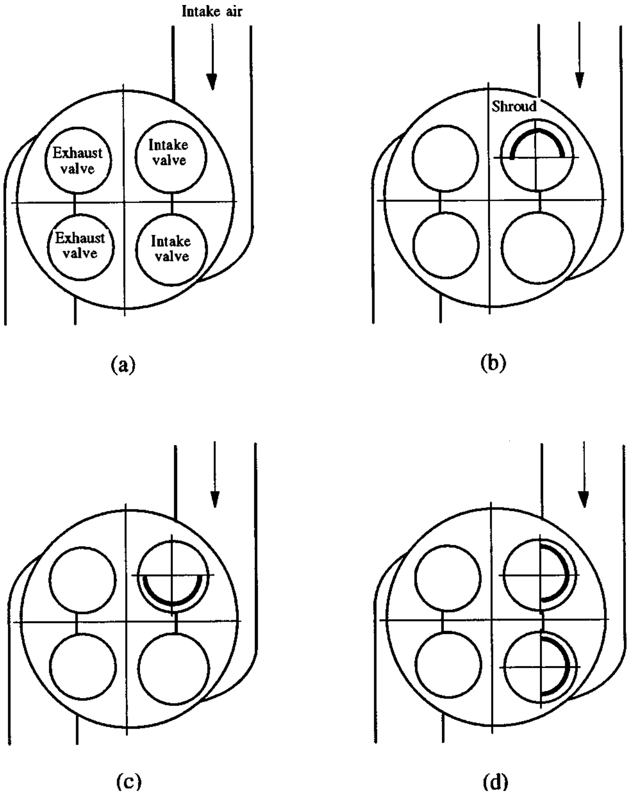

Fig. 2 Four different intake port configurations of a four-valve engine: (*a*) standard port; (*b*) swirl port; (*c*) anti-swirl port; (*d*) tumble port.

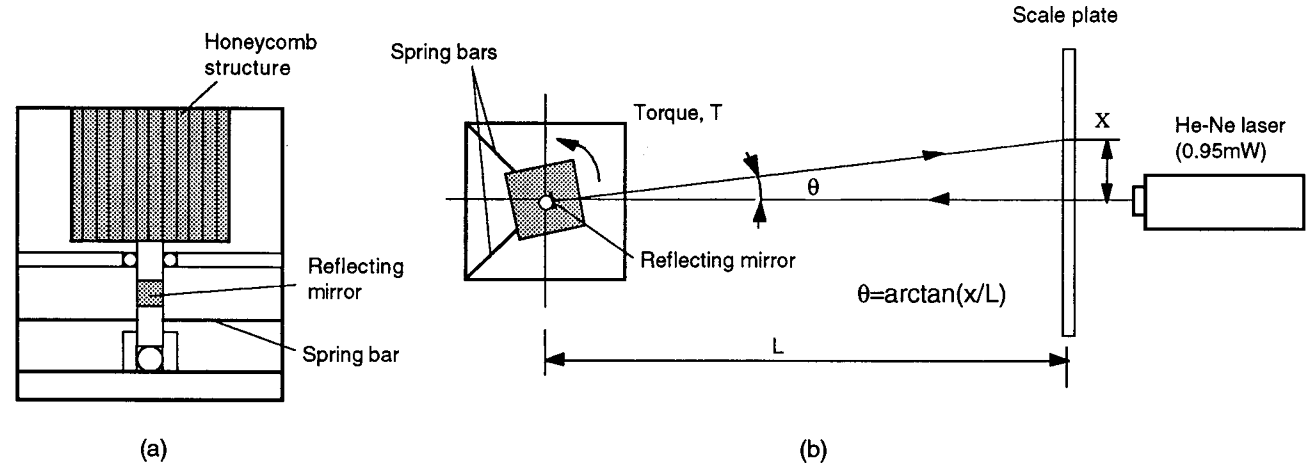

Fig. 3 Swirl meter and measurement principle using laser light: (*a*) layout of swirl meter; (*b*) principle of rotation angle measurement using a deflected laser beam.

points at $z=15$, 60, 130, and 165 mm (165 mm was the closest possible proximity to the swirl meter station). Typically 200 samples were collected at each measurement point and the data rate was normally 0.1 to 0.5 kHz, resulting in maximum uncertainties of 3.6 percent and 10.0 percent for the mean velocities and the turbulence intensities, respectively, which include the Doppler burst bias error of 0.7 percent with a downmixer.

Flow Visualization. A copper vapor laser (1.5 mJ/pulse, 10 kHz repetition rate, Oxford Laser Co.) was used to make a laser sheet with a negative cylindrical lens ($f=-30\,\text{mm}$) and a long focal distance plano-convex lens ($f=700\,\text{mm}$) and three reflecting mirrors on the optical table. The laser sheet was 1 mm thick in the cylinder (from a vertical slit plate [23]). This slit was helpful to reduce background light noise reflecting on the cylinder, as well as black paint on the back of the cylinder surface. Neutrally buoyant micro balloons of 30 to 50 μm mean diameter, as tracers, were seeded into the intake air to create streak lines in the laser sheet. A still camera (Nikon 72) with a micro zoom lens (200 mm f/4) was used with a shutter speed of 1/250s and aperture size 5.6, resulting in about 80 laser pulses in each picture.

Swirl Parameter Definitions. The results of the steady flow rig tests were expressed in non-dimensional terms, in such a way that they are independent of the engine size and of the pressure difference across the port. The flow coefficient, C_f, the breathing capacity of the port, is defined as

$$C_f=\frac{Q}{AV_0}, \tag{1}$$

where Q is volume flow rate, A is area at the valve seat, and the reference velocity, V_0, is calculated from an isentropic relation for a flow in a converging nozzle emptying into a plenum

$$V_0=\left\{\frac{2\gamma}{\gamma-1}\,\frac{P_0}{\rho_0}\left[1-\left(\frac{P_d}{P_0}\right)^{\gamma-1/\gamma}\right]\right\}^{1/2},$$

where P_0, ρ_0, and T_0 are atmospheric pressure, density, and temperature, respectively, and P_d is cylinder pressure.

The swirl coefficient, C_s, as a ratio of the flow angular to axial momentum at each valve lift, is defined as

$$C_s=\frac{8G}{m\dot{Y}V_0B}, \tag{2}$$

where G is impulse meter torque, $m\dot{Y}$ is air mass flow rate through port, and B is cylinder bore.

The swirl ratio, R_s, as a global swirl generation parameter during the entire intake process [9], is defined as

$$R_s=\frac{BS}{D^2}\,\frac{\int_{\alpha_1}^{\alpha_2}C_fC_s\,d\alpha}{\left[\int_{\alpha_1}^{\alpha_2}C_f\,d\alpha\right]^2}, \tag{3}$$

where S is the engine stroke, D the valve inner seat diameter, α the crank angle, and the subscript 1 refers to intake valve opening and 2 the closing crank angle. The varying values of C_f and C_s are evaluated at the appropriate valve lift corresponding to the crank angle, α.

In order to correlate the LDV results with the swirl meter directly, a swirl moment was defined with the swirl velocities obtained from the LDV experiments. The swirl moment (G) is defined by combining the angular momentum produced by the swirl velocity with the axial mass flux, that is,

$$G=2\pi\int_0^R\rho VWr^2dr, \tag{4}$$

where V and W are the swirl and axial velocity components at a distance r from the cylinder center, and R is the cylinder radius ($R=D/2$). Therefore, the swirl moment has the units of torque (Nm), as in the swirl meter measurement.

In practical calculations, several assumptions are needed due to the restricted number of LDV measuring points. Linear interpolation was used and swirl velocities near the cylinder wall were assumed to be the same as the value nearest the wall. The axial velocity was obtained by averaging the measured mass flow rate over the cylinder cross-sectional area, assuming a constant density.

Results and Discussion

Swirl Meter Results. Figure 4 shows the swirl and flow coefficient variations with intake valve lift for the different intake ports. In the case of the standard port, the flow coefficients are higher than those in the other ports at all valve lifts. Because the flow resistance tends to increase with the blockage by the shrouds, the flow coefficient of the tumble port shows the lowest values, while the swirl port and anti-swirl port have nearly a same values. For all the intake ports flow saturation does not appear until the maximum valve lift, $L/D=0.25$.

The swirl port generates the highest swirl. Especially at high valve lifts, the swirl coefficients are high, which is consistent with previous studies that show that the directed intake port can generate higher swirl at high valve lifts [8,24]. In the standard port the swirl coefficient increases monotonically with the intake valve

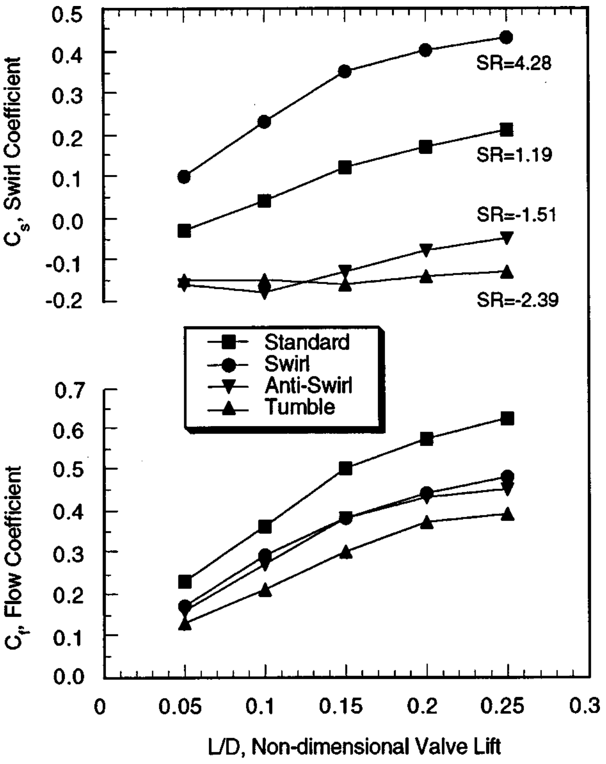

Fig. 4 Swirl and flow coefficients for the different intake ports

lift, even though it has a negative value (i.e., opposite to the swirl direction) at the lowest lift ($L/D=0.05$). In the anti-swirl and tumble ports, the swirl coefficients show negative values at all valve lifts. Moreover, in the anti-swirl port the swirl generation tends to decrease with valve lift, contrary to the trend of the swirl port. This is due to small vortices being generated in the cylinder without any dominant swirl source, as will be explained in the LDV and flow visualization results. In the tumble port, the swirl coefficient tends to decrease slightly with valve lift.

Global swirl generation is expressed in terms of the swirl ratio (SR) in Fig. 4. The swirl ratios are 4.28, 1.19, −1.51, and −2.39 for the swirl port, standard port, anti-swirl port and tumble port, respectively. These are consistent with the trends from the transient three-dimensional KIVA code predictions for the same intake ports, as listed in Table 1. The details of the computational study are described by Fuchs and Rutland [6] and Hessel [25]. The reason why the experimental results are higher than the computational results for all intake ports could be due to the effect of the piston motion which was considered in modeling the intake process in the computations. Clearly, in the actual engine the flow field would be expected to be influenced by the proximity of the piston to the head and by the piston bowl at early times during the intake stroke. This would be most noticeable for the tumble and standard ports which have significant tumble (axial) flow components, and show the largest differences between the measured and computed results. Thus, the present study suggests that caution should be exercised when interpreting swirl meter results for use in port design in cases where tumble flows are significant.

Table 1 Swirl ratio comparison between experiment and CFD computation

Swirl ratio	Standard port	Swirl port	Anti-swirl port	Tumble port
Experiment	1.19	4.28	−1.51	2.39
Computation	0.70	3.70	−1.20	1.40
Difference (%)	40	13	20	41

Intake Flow Structure

Standard Port. Figures 5(*a*) and (*b*) show the LDV axial and swirl velocity distributions at each cross section for the standard port at $dP=221$ mm H_2O. Due to the inertia of the intake air through the intake port which is eccentric to the cylinder center, larger swirl velocities occur around the rear intake valve region (which has a relatively long port runner) than in the front intake valve (which has a relatively short port). This is seen in the upper cylinder section (e.g., at $z=15$ mm), which is the source of the clockwise swirl motion in the entire cylinder. This confirms that the eccentricity of the intake port (which is 57 mm in this engine) strongly influences swirl formation by combining with the inertia of the intake air. This kind of swirl generation method is known as the directed port design [7–9] and it is commonly used in small-bore, high-speed diesel engines.

At axial locations downstream of the head, the uneven distribution of the swirl velocity develops into a large scale swirl vortex. The figure shows that the organized swirl motion is rapidly made starting at $z=60$ mm just after the two intake jet flows of reverse directions, which come from the two intake valves are formed. Note that the stroke of the actual engine is 160 mm, so this swirl flow would be expected to be established in the engine. The velocity profile in the swirl vortex tends to be linear with cylinder radius (solid body) further downstream, while the angular momentum of the swirl vortex decreases. The center of the swirl vortex still stays near the cylinder center irrespective of the cylinder position, which means that the swirl vortex is stably located in the cylinder.

The turbulence intensity distribution reveals relatively even profiles at each cross section, in spite of the uneven distribution of the mean flows. This is because turbulence is not only produced by the high shear in the high gradient regions of the mean velocities, but it can be also generated in high mean flow regimes. The turbulence intensity tends to decrease and its distribution becomes uniform along the diameter with increasing distance from the head.

The axial velocity distribution in the upper part of the cylinder is concentrated in the intake valve region, while only small axial flows exist on the exhaust valve side of the engine. This large axial flow on one side of the cylinder moves toward the other side as the flow develops downstream. The axial velocities on the exhaust valve side become higher than those on the intake valve side because of the flow rearrangement. Eventually, the velocity distribution becomes uniform across the cylinder diameter at the downstream locations.

Turbulence is generated in the high jet axial velocity region just under the intake valves, but the turbulence profile become more uniform at each cross section, while its magnitude progressively decreases with downstream distance from the head.

Swirl Port. Figures 6(*a*) and (*b*) show the LDV axial and swirl velocity distributions at each cross sections for the swirl port at $dP=221$ mm H_2O. Due to the blocking of the inner side of the front intake valve, most of the swirl velocity appears both on the exhaust valve side and in the central region at the top of the cylinder (see $z=15$ mm), while negative swirl velocities occur on the intake valve side. This strongly uneven velocity distribution makes for a well-organized clockwise swirl motion across the entire cylinder. This implies that blocking the inner side of the front intake valve can prevent it from generating negative swirl flows by matching with the intake port geometry. Namely, the intake port geometry makes a clockwise swirl motion with respect to the cylinder axis, while the shrouding leads to further clockwise swirl motion with respect to the front intake valve.

Because these two swirl sources have the same clockwise rotation direction, they combine and an organized swirl vortex can be produced more effectively than that in the standard port. The velocity profile in the swirl vortex tends to be linear with cylinder radius (i.e., solid body swirl) at the downstream locations. The

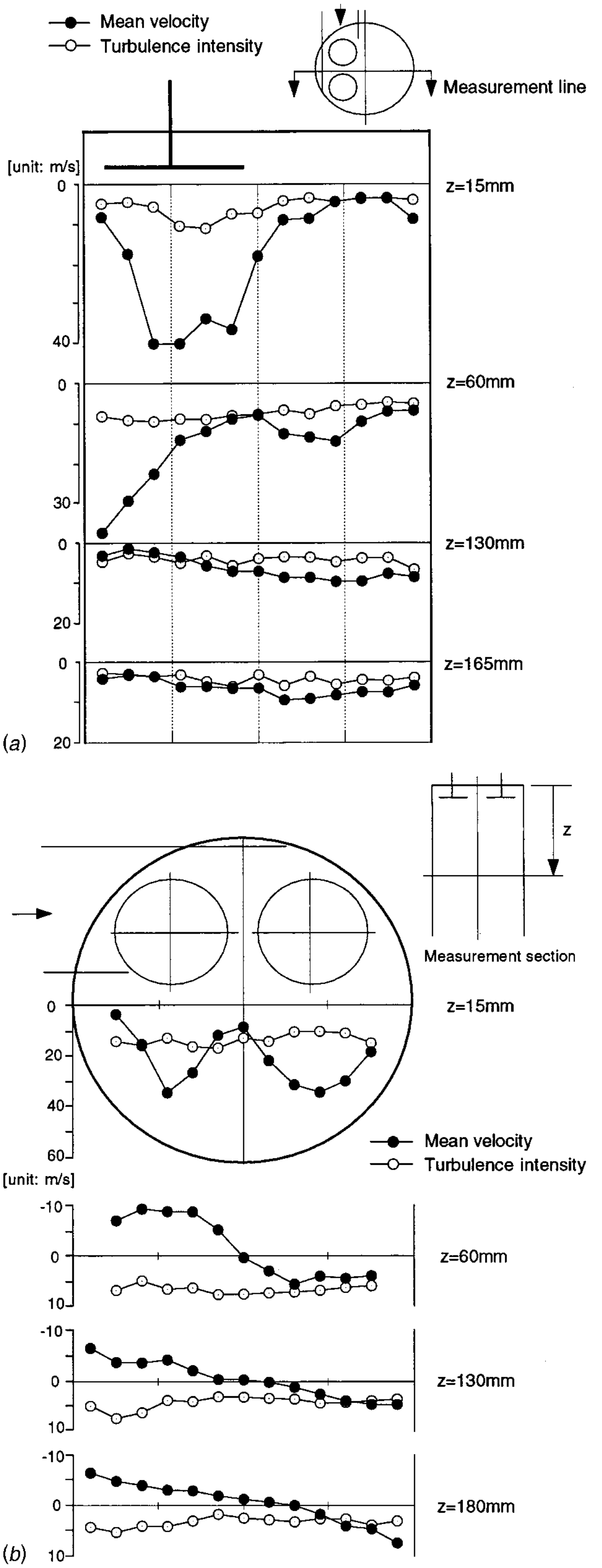

Fig. 5 (*a*) Axial velocities and turbulence intensities in the standard engine (intake valve lift 11 mm, $dP = 221\,\mathrm{mm\,H_2O}$, mean velocity 8.7 m/s); (*b*) swirl velocities and turbulence intensities in the standard engine (intake valve lift 11 mm, $dP = 221\,\mathrm{mm\,H_2O}$).

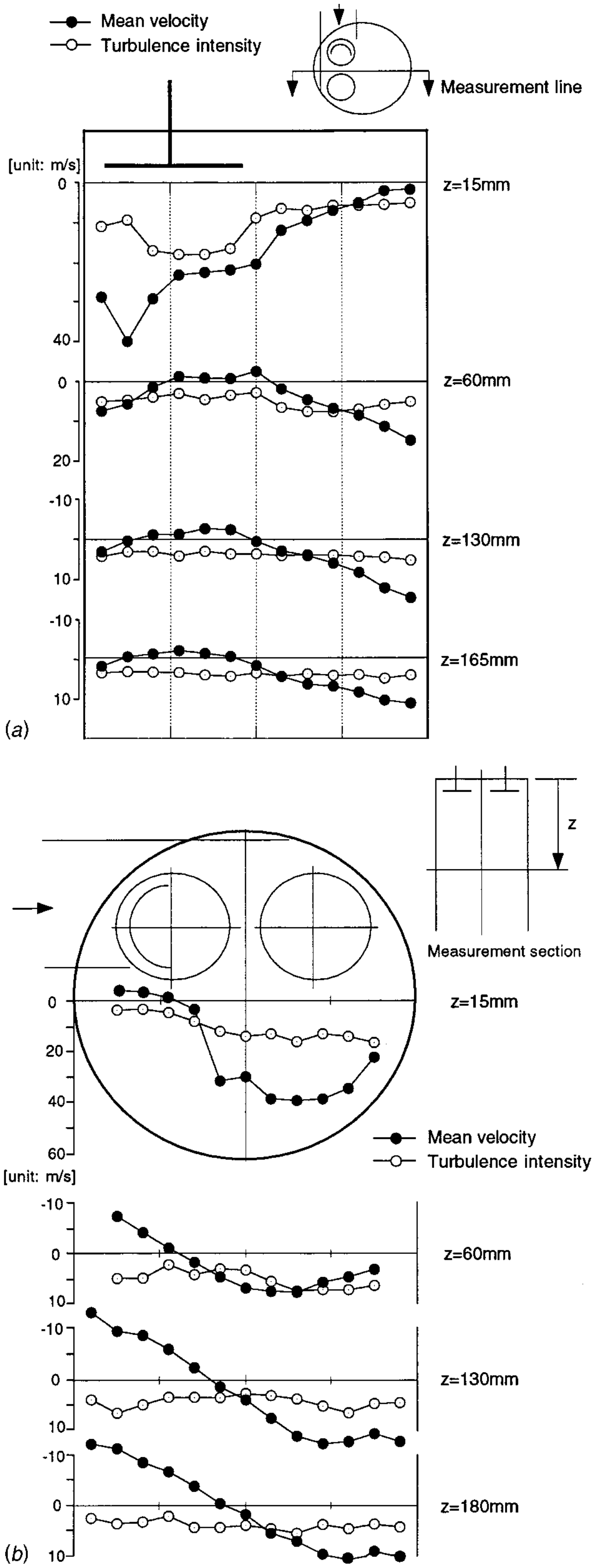

Fig. 6 (*a*) Axial velocities and turbulence intensities in the swirl port engine (intake valve lift 11 mm, $dP = 221\,\mathrm{mm\,H_2O}$, mean velocity 7.8 m/s); (*b*) swirl velocities and turbulence intensities in the swirl port engine (intake valve lift 11 mm, $dP = 221\,\mathrm{mm\,H_2O}$).

center of the swirl vortex is located on the intake valve side at the top of the cylinder and it moves to the cylinder center down in the cylinder, which means the swirl vortex becomes stable with increased distance along the cylinder.

High turbulence is generated on the exhaust valve side of the upper region where high swirl velocities and shearing flows exist. Further down in the cylinder, high turbulence intensity occurs near the cylinder wall region due to high shear gradients of the mean velocities, but it becomes nearly uniform at the bottom of the cylinder (e.g., at $z=180$ mm).

Axial velocities in the upper regions of the cylinder show a sharply uneven distribution along the diameter that occurs due to the high velocities on the intake valve side wall. This eccentric velocity distribution makes a longitudinal recirculation zone in the middle of the cylinder, which tends to weaken and move toward the cylinder wall of the intake valve side down in the cylinder. Due to the weak recirculation flow downstream of the head, the axial velocity distribution is relatively even across the diameter in the lower cylinder region (e.g., at $z=165$ mm).

High turbulence is also produced on the intake valve side of the upper region where high axial mean flow gradients exist, and it becomes uniform with increased distance down the cylinder.

Anti-Swirl Port. Figures 7(*a*) and (*b*) show the LDV axial and swirl velocity distributions at each cross section for the anti-swirl port at $dP=221$ mm H_2O. Due to the opposite orientation of the shroud direction compared to that of the swirl port, the intake flows appear weaker in the front intake valve region of the upper cylinder, while large flows exist both near the rear intake valve and in the cylinder wall region of the front intake valve side. In contrast to the swirl generation mechanism in the swirl port, these two large incoming flows with reverse swirl directions are not effective to make an organized large scale swirl vortex. This is why the counter-clockwise swirl source produced by the valve shrouding attenuates the other clockwise source due to the tangential effect of the intake port. This is confirmed by the fact that two small side vortices with reverse rotation directions appear in both the cylinder wall regions in the middle of the cylinder.

These two small side vortices lead to a negative peak velocity when the flows collide with each other. This negative velocity occurs on the rear valve side in the upper middle region (e.g., at $z=60$ mm). It also exists in the front intake valve side at $z=130$ mm, and finally it is shown also in the central region in the lower part of the cylinder (e.g., at $z=180$ mm) but with decreased magnitude.

The turbulence intensity is as high as 15 m/s in the high gradient region of the mean swirl velocity in the upper part of the chamber (e.g., at $z=15$ mm), and it becomes homogeneous along the diameter with increased distance down the cylinder.

The axial velocity under the intake valve region in the upper cylinder is shown to be smaller than those of the other ports. At $z=60$ mm, a recirculation zone is formed on the intake valve side, which is due to the high axial velocity coming from the front intake valve. In the downstream region, this recirculation disappears and the axial velocity distribution becomes uniform while it still remains slightly higher on the exhaust valve side.

The turbulence intensity is high in the region of the intake valve below the head, and it is still high in the region of the recirculation zone at $z=130$ mm. With increased distance down the cylinder it becomes more homogeneous across the cylinder cross-section.

Tumble Port. Figures 8(*a*) and (*b*) show the LDV axial and swirl velocity distributions at each cross sections for the tumble port at $dP=221$ mm H_2O. Due to the blocking of the upper sides of both intake valves, all swirl velocities are directed toward the exhaust valve side at the top of the cylinder, while a weak flow region occurs between the front intake valve and the cylinder center which might be due to the effect of the intake air inertia. These large uni-directional swirl velocities collide with the cylinder wall and reflect in the other direction. This is confirmed by the fact that all velocity components down stream of the head (e.g., at $z=180$ mm, Fig. 8(*b*)) reveal the opposite swirl flow direction to those in the upper cylinder region (e.g., at $z=15$ mm). Before turning the flow, a small uniform velocity distribution appears at $z=60$ mm because most of the swirl velocities are directed down the cylinder. At $z=130$ mm, a weak swirl vortex is generated by the unbalance of the two intake jet flows in the upper region.

High turbulence is generated in the weak mean flow region where the two intake jets collide. With increased distance down the cylinder, the turbulence intensity becomes uniform along the diameter, the same as with the other intake ports.

The axial velocity distribution in the upper cylinder region shows high velocities only in the unblocked intake valve regions, while trivial velocities (even negative velocities) occur under the blocked intake valves. This uneven axial velocity distribution makes for a large scale vertical swirl (tumble) vortex across the entire cylinder in the downstream direction. With increased distance down the cylinder, the tumble vortex tends to be weakened slightly and its velocity profile becomes linear with distance across the cylinder radius.

High turbulence is generated in the region of high axial mean flow in the upper cylinder, and it becomes uniform across the diameter with increased distance down the cylinder, the same as those of the other intake ports.

Correlation Between Swirl Meter and LDV Results. Figures 9(*a*) and 9(*b*) show the correlation between the LDV and swirl meter results. Due to physical constraints, the LDV data sets were obtained at $z=130$ and 180 mm, while the swirl data were measured at $z=210$ mm. Figure 9(*a*) shows the results for the 221 mm H_2O case while Fig. 9(*b*) shows results for the 462 mm H_2O case, where the LDV data showed similar features to those shown in Figs. 5 to 8. The trends and magnitudes of the swirl moment show good agreement with each other. In the case of relatively stabilized swirl generation ports, such as the swirl port and the standard port, the swirl moment tends to decrease with downstream distance in the cylinder, which is mainly due to wall friction effects, as described by Uzkan et al. [17].

In the case of the anti-swirl port, the swirl moment varies somewhat with position in the cylinder, since a large scale air motion is not established. Therefore the swirl moment for this kind of intake port should be measured far from the cylinder head, after the swirl flow has been stabilized. In this case, a swirl moment obtained on the steady flow bench will not correlate with the actual engine swirl levels because of the important role on the swirl of the piston motion. In the tumble port, the same trend occurs, since tumble flow is still dominant at the further downstream location (e.g., at $z=210$ mm).

Intake Flow Visualization. Figure 10 shows flow visualization results for the different intake ports. The pictures were taken under the same experimental conditions as in the LDV experiments. In the case of the standard port, a dominant downward axial flow is seen under the intake valves, while relatively quiescent flow appears downstream in the cylinder. This is consistent with the LDV measurements shown in Fig. 5(*a*). In the case of the swirl port, a strong swirl flow pattern appears in the central part of the cylinder. This swirl flow creates negative axial velocity regions in the middle of the cylinder, which is also confirmed by the negative flows in the LDV data shown in Fig. 6(*a*). On the exhaust valve side, a consistent downward axial flow is seen, and just under the intake valves strong intake jet flows make high axial velocities, as shown in the LDV measurement.

In the case of the anti-swirl port, many small vortices appear in the flow visualization. The upper region vortex under the exhaust valve side and strong vortices below the intake valves prevent a dominant large-scale flow from occurring in the upper region of the cylinder. This is consistent with the low axial velocities of relatively even distribution shown in Fig. 7(*a*). A cross-flow from

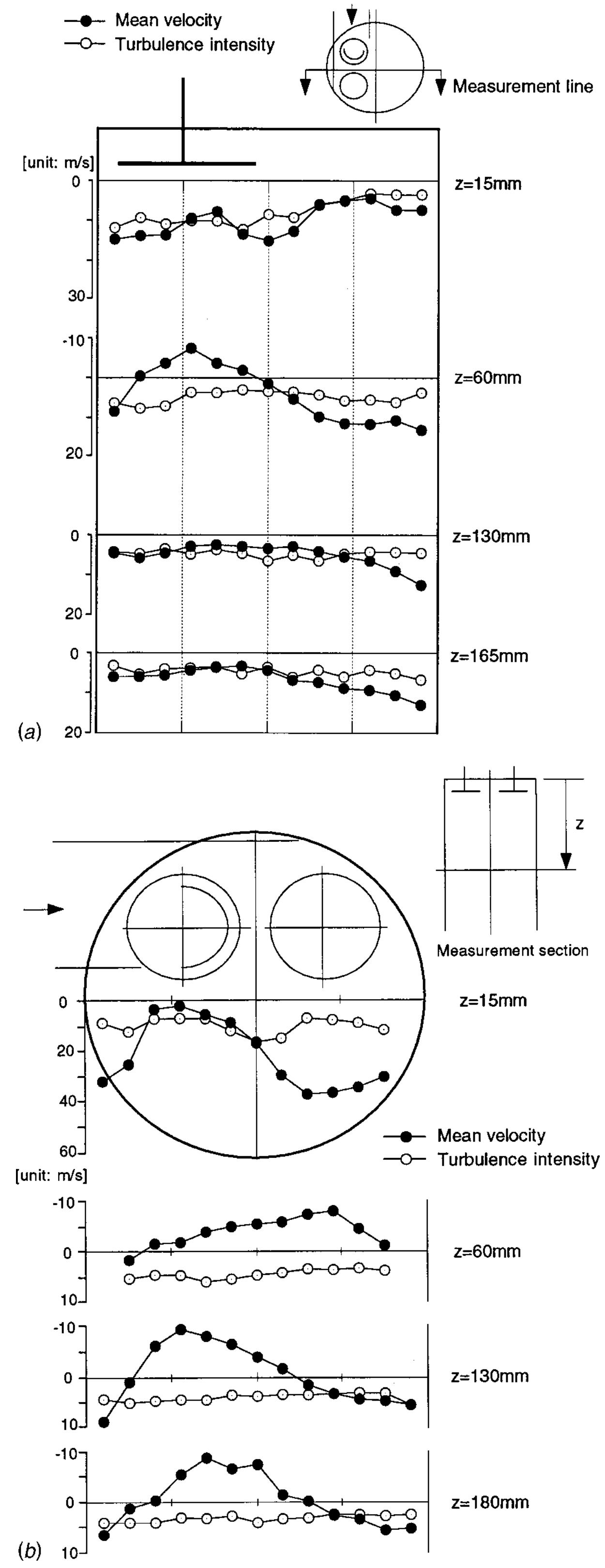

Fig. 7 (*a*) Axial velocities and turbulence intensities in the anti-swirl port engine (intake valve lift 11 mm, *dP* = 221 mm H_2O, mean velocity 7.6 m/s); (*b*) swirl velocities and turbulence intensities in the anti-swirl port engine (intake valve lift 11 mm, *dP* = 221 mm H_2O).

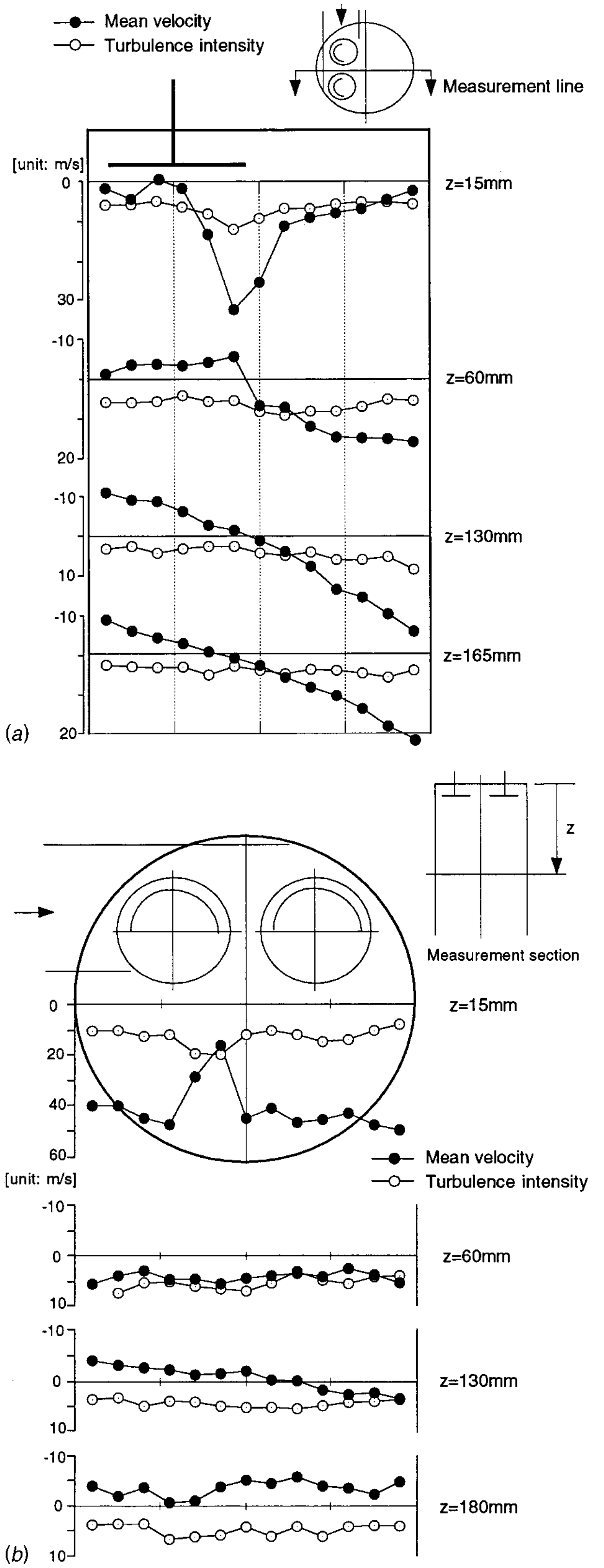

Fig. 8 (*a*) Axial velocities and turbulence intensities in the tumble port engine (intake valve lift 11 mm, *dP* = 221 mm H_2O, mean velocity 6.7 m/s); (*b*) swirl velocities and turbulence intensities in the tumble port engine (intake valve lift 11 mm, *dP* = 221 mm H_2O).

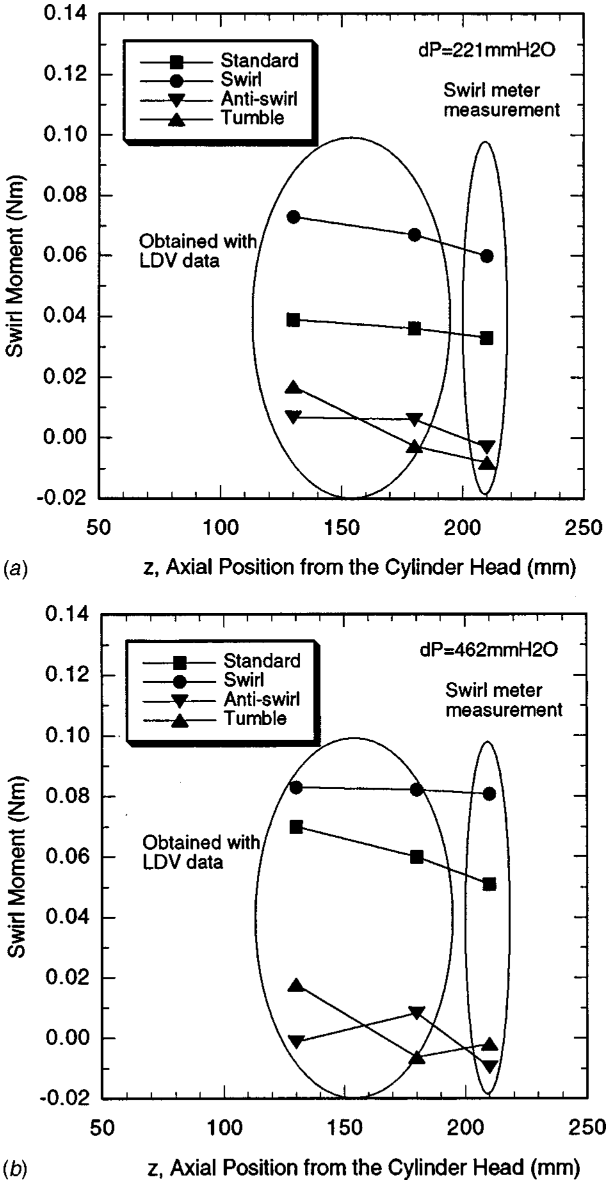

Fig. 9 (*a*) **Swirl moment comparison with those obtained by LDV data** ($dP = 221\ \mathrm{mm\ H_2O}$); (*b*) **swirl moment comparison with those obtained by LDV data** ($dP = 462\ \mathrm{mm\ H_2O}$).

the intake valve side toward the exhaust valve side appears in the middle of the cylinder, which leads to a downward axial flow on the exhaust valve side, as in the LDV results.

In the case of the tumble port, an apparent large-scale tumble flow appears throughout the entire cylinder, and its center stays on the cylinder center. On the exhaust valve side, a consistent downward axial flow and a strong intake air jet from the intake valve are seen clearly in the visualization. These are also confirmed with the LDV results, as shown in Fig. 8(*a*).

Conclusions

A thorough study of the intake flow structure and swirl generation in a modern four-valve heavy-duty diesel engine was performed using a swirl meter, LDV measurements and flow visualization, and the results were also compared with previous detailed CFD predictions in the same engine. The important results can be summarized as follows:

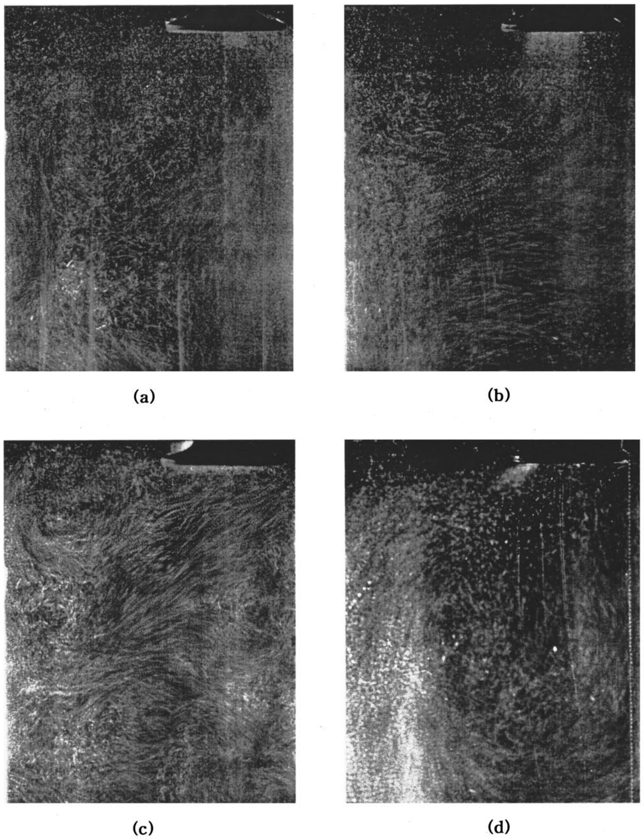

Fig. 10 Photographs of intake flow visualization for the different intake ports: (*a*) standard port; (*b*) swirl port; (*c*) anti-swirl port; (*d*) tumble port.

1 The swirl moment calculated from the measured tangential and axial LDV velocity components using the present algorithms showed good agreement with the swirl meter results. The measured swirl levels were also found to be consistent with available CFD predictions with the same intake port geometries. However, quantitative differences were found that could be due to the effect of piston motion and the influence of the piston bowl in the computations. The differences were most notable for cases with high tumble flow components. These results suggest that care should be taken in interpreting steady-state swirl meter results for use in engine intake port design.

2 In cases with appropriate swirl-producing geometries, a dominant swirl source was found to be formed in the upper region of the cylinder, which generated a stable swirl flow with a near solid-body velocity distribution further downstream in the cylinder. On the other hand, in the case of the anti-swirl port, many small vortices are generated in the cylinder instead of an organized large-scale air motion for swirl formation. The difference of the swirl generation mechanisms in these two cases is due to the inertia of the intake air through the port and the effect of the blockage due to the valve shrouds.

3 Even though the turbulence intensities in the upper regions of the cylinder were distributed differently for the different intake port geometries, their differences became small, tending toward a homogeneous distribution downstream in the cylinder in all cases.

4 The flow visualization studies effectively revealed where the small vortices were located in the cylinder and helped to explain the quantitative details of the LDV measurements.

Acknowledgments

This work was supported by DOE/Sandia labs, the Army Research Office and the Korea Science and Engineering Foundation. The authors thank K. Richards, C. Gherke, and Prof. P. Farrell for helpful comments.

Nomenclature

A = area in valve inner seat
B = cylinder bore
C_f = flow coefficient
C_s = swirl coefficient
D = valve inner seat diameter
G = swirl moment, torque
$m\dot{Y}$ = mass flow rate through the port
P_0 = ambient pressure
P_d = cylinder pressure
Q = volume flow rate through the port
S = engine stroke
T_0 = ambient temperature
ρ_0 = ambient density
r = distance of a measuring point from the cylinder center
R_s = swirl ratio
R = cylinder radius
V_0 = reference velocity
V = swirl velocity component
W = axial velocity component

Greek

α = crank angle
α_1 = intake valve opening angle
α_2 = intake valve closing angle

References

[1] Weaving, J. H., 1990, *Internal Combustion Engineering*, Elsevier Science, New York, pp. 333–384.
[2] Qi, G., Zhou, J., Liu, Z., and Chen, J., 1995, ‘‘The Study of an Optimum Method for Inlet Port Performance in a D.I. Diesel Engine,’’ SAE Paper 952056.
[3] Stone, C. R., and Ladommatos, R., 1992, ‘‘The Measurement and Analysis of Swirl in Steady Flow,’’ SAE Paper 921642.
[4] Ogawa, H., Matsui, Y., Kimura, S., and Kawashima, J., 1996, ‘‘Three-Dimensional Computation of the Effects of the Swirl Ratio in Direct-Injection Diesel Engines on NOx and Soot Emissions,’’ SAE Paper 961125.
[5] Espey, C., Pinson, J. A., and Litzinger, T. A., 1990, ‘‘Swirl Effects on Mixing and Flame Evolution in a Research DI Diesel Engine,’’ SAE Paper 902076.
[6] Fuchs, T. R., and Rutland, C. J., 1998, ‘‘Intake Flow Effects on Combustion and Emissions in a Diesel Engine,’’ SAE Paper 980508.
[7] Ladommatos, N., Balian, R. A., and Stone, R., 1992, ‘‘Analysis of Swirl in Unsteady Flow and its Effect on Diesel Combustion,’’ SAE Paper 921643.
[8] Gale, N. F., 1990, ‘‘Diesel Engine Cylinder Head Design: The Compromises and Techniques,’’ SAE Paper 900133.
[9] Monaghan, M. L., and Pettifer, H. F., 1981, ‘‘Air Motion and Its Effect on Diesel Performance and Emissions,’’ SAE Paper 810255.
[10] Tippelmann, G., 1977, ‘‘A New Method of Investigation of Swirl Ports,’’ SAE Paper 770404.
[11] Tindal, M. J., and Williams, T. J., 1977, ‘‘An Investigation of Cylinder Gas Motion in the Direct Injection Diesel Engine,’’ SAE Paper 770405.
[12] Snauwaert, P., and Sievens, R., 1986, ‘‘Experimental Study of the Swirl Motion in DI Diesel Engines Under Steady State Flow Conditions,’’ SAE Paper 860026.
[13] Zhu, Y., Evers, D., Huigen, G., and Hommersom, G., 1990, ‘‘LDA Measurements of Steady and Unsteady Flow through the Induction System of a Heavy Duty Diesel Engine,’’ SAE Paper 901576.
[14] Arcoumanis, C., and Tanabe, S., 1989, ‘‘Swirl Generation by Helical Ports,’’ SAE Paper 890790.
[15] Stier, B., and Falco, R., 1995, ‘‘An Investigation of Fluid Flow During Induction Stroke of a Water Analog Model of an IC Engine Employing LIPA,’’ SAE Paper 950726.
[16] Kent, J. C., Mikulec, A., Rlmal, L., Adamczyk, A. A., Mueller, S. R., Stein, R. A., and Warren, C. C., 1989, ‘‘Observations on the Effects of Intake-Generated Swirl and Tumble on Combustion Duration,’’ SAE Paper 982096.
[17] Uzkan, T., Borgnakke, C., and Morel, T., 1983, ‘‘Characterization of Flow Produced by a High-Swirl Inlet Port,’’ SAE Paper 830266.
[18] Khalighi, B., Haworth, D. C., and Huebler, M. S., 1994, ‘‘Multi-Dimensional Port and In-Cylinder Flow Calculations and Flow Visualization Study in an Internal Combustion Engine with Different Intake Configurations,’’ SAE Paper 941871.
[19] Khalighi, B., Tahry, S. H. E., Haworth, D. C., and Huebler, M. S., 1995, ‘‘Computational and Measurement of Flow and Combustion in a Four-Valve Engine with Intake Variations,’’ SAE Paper 950287.
[20] Arcoumanis, C., Hadjiapostolou, A., and Whitelaw, J. H., 1987, ‘‘Swirl Center Precession in Engine Flows,’’ SAE Paper 870370.
[21] Baker, P., Benjamin, S. F., Girgis, N. G., Newman, A. W., and Seeley, W. A., 1995, ‘‘Characterization of Barrel Swirl Motion Under Steady Flow Conditions,’’ SAE Paper 950729.
[22] Qi, G., Zhou, J., Liu, Z., and Chen, J., 1995, ‘‘The Study of an Optimum Method for Inlet Port Performance in a D.I. Diesel Engine,’’ SAE Paper 952056.
[23] Durao, D. F. G., Heitor, M. V., Whitelaw, J. H., and Witze, P. O., 1990, *Combustion Flow Diagnostics*, NATO ASI Series, Kluwer Academic, Boston, MA.
[24] Wigley, G., and Hawkins, M. G., 1978, ‘‘Three Dimensional Velocity Measurements by Laser Anemometry in a Diesel Engine Cylinder Under Steady State Inlet Flow Conditions,’’ SAE Paper 780060.
[25] Hessel, R. P., 1993, ‘‘Numerical Simulation of Valved Intake Port and In-Cylinder Flows Using KIVA3,’’ Ph.D. thesis, University of Wisconsin-Madison.

The Separation Between Turbulence and Mean Flow in ICE LDV Data: The Complementary Point-of-View of Different Investigation Tools

Mario Amelio
e-mail: amelio@unical.it

Sergio Bova
e-mail: s.bova@unical.it

Dipartimento di Meccanica,
Università della Calabria,
87030 Rende (Cosenza), Italy

Carmine De Bartolo
Dipartimento di Ingegneria Idraulica ed
Ambientale Università di Pavia,
Via Abbiategrasso, 213
27100 Pavia, Italy
e-mail: debarto@ipv36.unipv.it

LDV measurements have been taken in a disc chamber four-stroke reciprocating engine under motoring conditions. Two non-simultaneous velocity components have been recorded at three different locations on the mid-plane of the TDC clearance during the intake and compression strokes for three different speeds (600, 800, 1000 rpm). The locations are characterized by different flow conditions (near the intake valves; on the cylinder axis; near the exhaust valves). The combination of different engine speeds and different chamber locations enables one to look both at the global behavior of the flow and at the details of the turbulence time-evolution. The aim of the research is to identify the frequency which can be considered a separation between ''true'' turbulence and cycle-by-cycle variation of the mean flow and to analyze the variation of such a frequency with the measuring location and with the engine speed. The analysis has been carried out by using different tools: the non-stationary velocity autocorrelation function, the power spectrum and the cycle-resolved analysis based on the frequency filter. The various approaches offer complementary perspectives of the same phenomenon, which give a clear perception of the physical meaning of the most frequently used investigation tools. The results show that the cut-off frequency increases as the engine speed increases and as the measuring point moves away from the ordered jet coming out of the intake valves. [S0742-4795(00)01204-7]

Introduction

The study of gas motion within the engine cylinder has received continuous attention during the last twenty years, as it has been recognized as one of the major factors for controlling the combustion rate both in spark ignition and in diesel engines.

Beside the development of the experimental techniques (Hot Wire Anemometry and Laser Doppler Velocimetry [1] and, more recently, Particle Image Velocimetry [2]) the effort of researchers has been concentrated on the analysis of the measured velocity data. The question addressed is how to extract information about turbulence intensity and turbulence scales from the velocity data. References [3–13] are a limited, incomplete, sample of papers dealing with the subject.

One of the central issues is how to separate in the measured velocity fluctuations, the contribution of the large-scale, low-frequency, cycle-by-cycle variations of the mean flow from the small-scale, high-frequency, pure random, ''true'' turbulent fluctuations. The topic has practical interest, as different turbulence scales influence the mixing and combustion processes in different ways. In the course of separating the different components of the gas velocity, a crucial step is the calculation of the mean velocity in every single cycle. This is achieved by a sort of smoothing of the in-cycle measured velocity, either by averaging in the time domain over a certain time interval or by filtering the frequency content above a certain cut-off frequency. The selection of both the width of the averaging time interval and of the cut-off frequency is arbitrary: it is based on physical considerations and checked later on by means of the obtained results.

In the present work, different investigation tools will be used to analyze the turbulence data. The various approaches look at the same phenomenon from different points of view and the different perspectives lead to coherent interpretations, thus giving an original perception of the physical meaning of the most frequently used statistical functions. The point focused on will be the definition of an operational procedure to identify the cut-off frequency and to analyze the variation of this frequency with the measuring location and with the engine speed. One could not care such a method in the case of turbulence analysis is carried out at the same engine speed or at the same cylinder location. Nevertheless, as soon as one wants to look at the turbulence behavior by varying both the measuring location and the engine speed, one realizes that such a method is very useful.

Experimental Apparatus

The Engine With Optical Access. The engine with optical access was built on the engine block of a commercial FIAT engine. It has a disk chamber, with 80 mm stroke and an 80 mm bore and the compression ratio is 7:1. A window (87 mm diameter) is located in the head of the engine thus allowing optical access to the entire combustion chamber. Six radial, small diameter, intake valves and six exhaust valves are located in the liner, and open in the clearance volume. They are operated by solenoids, driven by a computer on the basis of an ON-OFF logic. Figure 1 presents a drawing of the engine; more details can be found in [14].

The LDV System. The LDV system used in this project is a one-color system (i.e., capable of measuring one component of the velocity) in a back-scattering configuration, with Bragg-cell and

---

Contributed by the Internal Combustion Engine Division of THE AMERICAN SOCIETY OF MECHANICAL ENGINEERS for publication in the ASME JOURNAL OF ENGINEERING FOR GAS TURBINES AND POWER. Manuscript received by the ICE Division March 2, 2000; final revision received by the ASME Headquarters June 8, 2000. Technical Editor: D. Assanis.

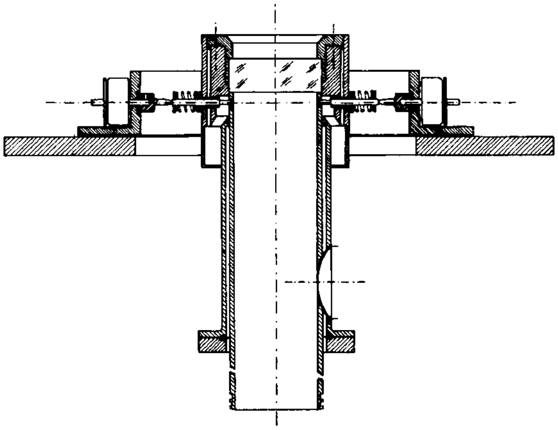

Fig. 1 Schematic drawing of LDV test engine

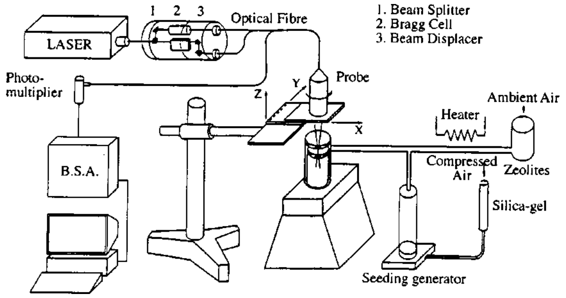

Fig. 2 Schematic of the LDV set-up

frequency shifter for velocity versus discrimination purposes. The system uses a 4 W Argon-Ion Laser as light source and optic fibers for both transmitting and collecting optical paths. The movement of the LDV probe is obtained by using a micrometer X-Y traversing system. The probe can also be rotated around its axis and moved vertically (Z-axis).

A Burst Spectrum Analyzer (BSA), which performs the FFT of the original signal, in order to extract the Doppler frequency, is used for the analysis of the Doppler signal. The BSA is linked to a computer in order to store and analyze the data.

For the seeding system a fluidized bed-like scheme has been adopted [15]. A fraction of the dried inlet air passes through a horizontal porous diaphragm on the top of which is deposited a layer of TiO_2 particles. The air stream then carries the particles and is subsequently mixed with the main intake air, which is also dried. Figure 2 shows a schematic of the LDV set-up; more details have been given in [14].

LDV Measurements

The engine is characterized by a moderate swirl (swirl ratio of about four), which is due to the shape of the intake manifold. Three measuring locations have been selected on the mid-plane of the TDC clearance, which are characterized by different flow conditions: the first point is located near the intake valves and is therefore directly exposed to the jet of the entering flow; the second point is on the cylinder axis, where the flow is subjected to the motion irregularity of the center of the swirling vortex; the third point is located near the exhaust valves (Fig. 3).

At each measuring location two non-simultaneous velocity components have been recorded during the intake and compression strokes at three different speeds (600, 800, 1000 rpm) for about 500 consecutive cycles, at a rate of $2 \div 3$ samples per crank angle degree.

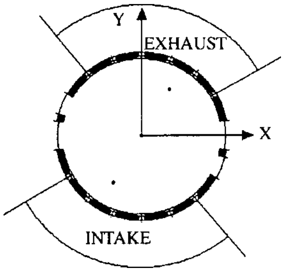

Fig. 3 Measuring location

Data Analysis and Results

Data has been preliminarily examined in the ensemble domain. Subsequently, the power spectra analysis, the autocorrelation function and the cycle-resolved technique based on the frequency filter have been employed in order to investigate the separation between ''true'' turbulence and cycleby-cycle variation of the mean flow and the dependency of such a separation on engine speed and measurement location.

The Ensemble Domain Analysis. The ensemble domain analysis is based on the fact that an engine operates in a cyclical way and, as a consequence, the in-cylinder flow can be considered quasi-periodic. The velocity measurements are therefore repeated at the same location within the engine cylinder over many engine cycles (N_c) at the same crank angular position (θ). The ensemble mean—or Ensemble-Average (EA)—velocity at that crank angle θ is then obtained as the average of values measured, at that specific crank angle position, in the various cycles. In the case of LDV measurements the arrival time of the data is random, so it is necessary to fix a crank angular window ($\overline{\theta}$), rather than a crank angular position, and to average also over the N_i data arrived at the fixed crank angle window of the ith cycle, so that

$$U_{\mathrm{EA}}(\overline{\theta}) = \frac{1}{N_t} \sum_{i=1}^{N_c} \sum_{j=1}^{N_i} U_j(\overline{\theta}, i), \tag{1}$$

where

$$N_t = \sum_{i=1}^{N_c} N_i . \tag{2}$$

The velocity fluctuation intensity around the mean is then determined as the rms value

$$u'_{\mathrm{rms}}(\overline{\theta}) = \sqrt{\frac{1}{N_t} \sum_{i=1}^{N_c} \sum_{j=1}^{N_i} u_j(\overline{\theta}, i)^2}, \tag{3}$$

where

$$u_j(\overline{\theta}, i) = U_j(\overline{\theta}, i) - U_{\mathrm{EA}}(\overline{\theta}). \tag{4}$$

The ''instantaneous'' velocity at a given crank angle window within a single engine cycle is therefore expressed as the sum of the mean velocity (which depends on $\overline{\theta}$ only) and of a fluctuation around this mean

$$U_j(\overline{\theta}, i) = U_{\mathrm{EA}}(\overline{\theta}) + u_j(\overline{\theta}, i). \tag{5}$$

This fluctuation of course includes both high-frequency random fluctuations (''true'' turbulence) and low-frequency cycle-by-cycle variations of the mean flow [16].

The obtained values can be used, first of all, to estimate the measurement uncertainty of the data. As for U_{EA}, the relative uncertainty, calculated as $N_t^{-1/2} \cdot u'_{\mathrm{rms}}/U_{\mathrm{EA}}$ resulted ≈ 3 percent, while the relative uncertainty in u'_{rms} calculated as $\sqrt{2/(N_t - 1)}$ resulted ≈ 7 percent [17].

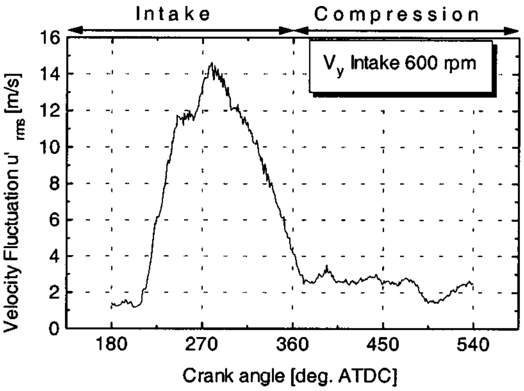

Fig. 4 Velocity fluctuation peaks around the middle of the intake stroke

A detailed characterization of the in-cylinder mean flow, obtained with an ensemble domain analysis of previous measurements, has been presented by Amelio et al. [14]. In the present work, as for the velocity fluctuations around the EA-velocity, a typical result is presented in Fig. 4, which shows that the velocity fluctuation peaks around the middle of the intake stroke and then diminishes substantially toward the end of compression. This agrees with similar measurements taken in disc chambers, where no turbulence-production mechanism exists around TDC of compression.

The Cycle-Resolved Analysis. The cycle-resolved analysis has the aim of separating the contribution of the cycle-by-cycle variation of the mean flow u_{LF} from the turbulence fluctuations $u_{j\mathrm{HF}}$ [16]. The first step is to determine the mean velocity in every single cycle i or *in-cycle mean velocity* $\overline{U}(\overline{\theta},i)$. The ensemble average of this velocity is then computed

$$\overline{U}_{\mathrm{EA}}(\overline{\theta})=\frac{1}{N_c}\sum_{i=1}^{N_C}\overline{U}(\overline{\theta},i) \tag{6}$$

and the instantaneous velocity is decomposed in three terms

$$U_j(\overline{\theta},i)=\overline{U}_{\mathrm{EA}}(\overline{\theta})+u_{\mathrm{LF}}(\overline{\theta},i)+u_{j\mathrm{HF}}(\overline{\theta},i). \tag{7}$$

More details can be found, for example, in [8,10,12,18].

A crucial step in this analysis is the calculation of the above *in-cycle mean velocity* $\overline{U}(\overline{\theta},i)$. This is achieved by a sort of smoothing of the in-cycle measured velocity, either by averaging in the time domain over a certain time interval or by filtering the frequency content above a certain cut-off frequency. The selection of both the width of the averaging time interval and of the cut-off frequency is arbitrary: it is based on physical considerations and checked later on by means of the obtained results.

In this paper the frequency filtering method will be used and different operational methods will be employed to identify the cut-off frequency f_{co}, which can be considered a separation between ''true'' turbulence $u_{j\mathrm{HF}}(\overline{\theta},i)$ and cycle-by-cycle variation of the mean flow $u_{\mathrm{LF}}(\overline{\theta},i)$.

Once this frequency has been identified, the variations of this frequency with the measuring location and with the engine speed will be analyzed. It is worth pointing out, that such an f_{co} can only be within reasonable limits: no exact determination can be pursued. Any proposed method will therefore be based on some degree of arbitrariness. Nevertheless, such an operational method should avoid exercising a subjective judgment for any different measuring condition.

Different approaches have been used in literature for identifying this f_{co}.

The classic and also more fundamental approach is to compute the non-stationary autocorrelation function (ACF) to identify the life or coherence-time τ_{co} of the turbulent structures. Here, once the maximum life-time of the vortex has been identified, it has been assumed that $f_{co}=1/\tau_{co}$.

An analogous approach is to consider the power spectrum, which actually is the Fourier transform of the autocorrelation function. The knee-frequency, which identifies the beginning of the $f^{-5/3}$ slope in the power spectrum can be regarded as proportional to f_{co} [12].

An alternative method has been proposed by Liou and Santavicca [8], which uses the frequency analysis applied to the EA-velocity: the FFT of this velocity is computed and the cut-off frequency f_{co} is selected as the one above which the amplitudes of the harmonics are negligible.

In the following the three techniques will be applied to the collected data.

Autocorrelation Function (ACF). The ACF of the velocity fluctuation has been computed for different points in the intake and compression strokes, for the various engine speeds and in the three measuring locations, as

$$R(\theta_{\mathrm{ref}},\tau)=\frac{\dfrac{1}{N_t}\displaystyle\sum_{i=1}^{N_c}\sum_{j=1}^{N_i}u_j(\theta_{\mathrm{ref}},i)u_j(\theta_{\mathrm{ref}}+\tau,i)}{u'_{\mathrm{rms}}(\theta_{\mathrm{ref}})u'_{\mathrm{rms}}(\theta_{\mathrm{ref}}+\tau)}. \tag{8}$$

The velocity fluctuation, $u_j(\theta_{\mathrm{ref}},i)$, is determined by subtracting the EA-velocity from the instantaneous velocity $u_j(\theta_{\mathrm{ref}},i)=U_j(\theta_{\mathrm{ref}},i)-U_{\mathrm{EA}}(\theta_{\mathrm{ref}})$. In order to improve the statistical quality of the ACF, it has been calculated for 12 different adjacent crank angle values and then averaged [12]. The center of the used angular window is then indicated as the reference angle.

Figure 5 shows results which are typical of the intake and the early compression strokes at the point near the intake valves and at the center of the chamber: the shape of the ACF is characteristic of a flow with chaotic velocity fluctuations, which dissipate very early. No correlation exists between the velocity at the reference angle and the one a few degrees later or a few degrees before. At this stage the lifetime of the vortexes is very short ($\approx$1 ms @ 1000 rpm).

Later on, in the compression stroke, the ACF decays much more slowly, however, thus indicating a more structured, ordered flow (Fig. 6). At this stage the ACF decays in the order of tens of degrees, corresponding to a life time of the order of several milliseconds at 1000 rpm. As a consequence, the frequency content of the vortex motion extends in the lower frequency down to about a few hundred Hz. In addition, at this stage, a persistent oscillatory character of the ACF is clearly visible, which indicates the presence of low-frequency, quasi-deterministic fluctuations in the flow. Unlike the points near the intake valves and at the center, at the point near the exhaust valves the behavior of the ACF does not change very much as the reference angle moves from the middle of the intake to the middle of compression or when the engine speed changes (Fig. 7).

The different character of the flow is clearly visible in Fig. 8 [14], which shows the result of EA-velocity and rms value of previous detailed measurements in the same engine, at the same engine speed. At 270 deg crank angle the center of the chamber is occupied by the center of a still quite disordered vortex. The motion of the center of the vortex is chaotic ($u'_{\mathrm{rms}}\approx 6$ m/s), and this corresponds to the ACF given in Fig. 5. On the contrary, at 450 deg the center of the vortex is now quite far from the cylinder axis, near the exhaust valves. At the center of the chamber and near the intake valves the flow becomes more deterministic ($u'_{\mathrm{rms}}\approx 2\div 3$ m/s), as Fig. 6 suggests, while near the exhaust valves the motion is still quite random, as Fig. 7 confirms. Moreover, this figure also suggests that the distinct, persistent background structure in Fig. 6, derives from the precession motion of the center of the vortex.

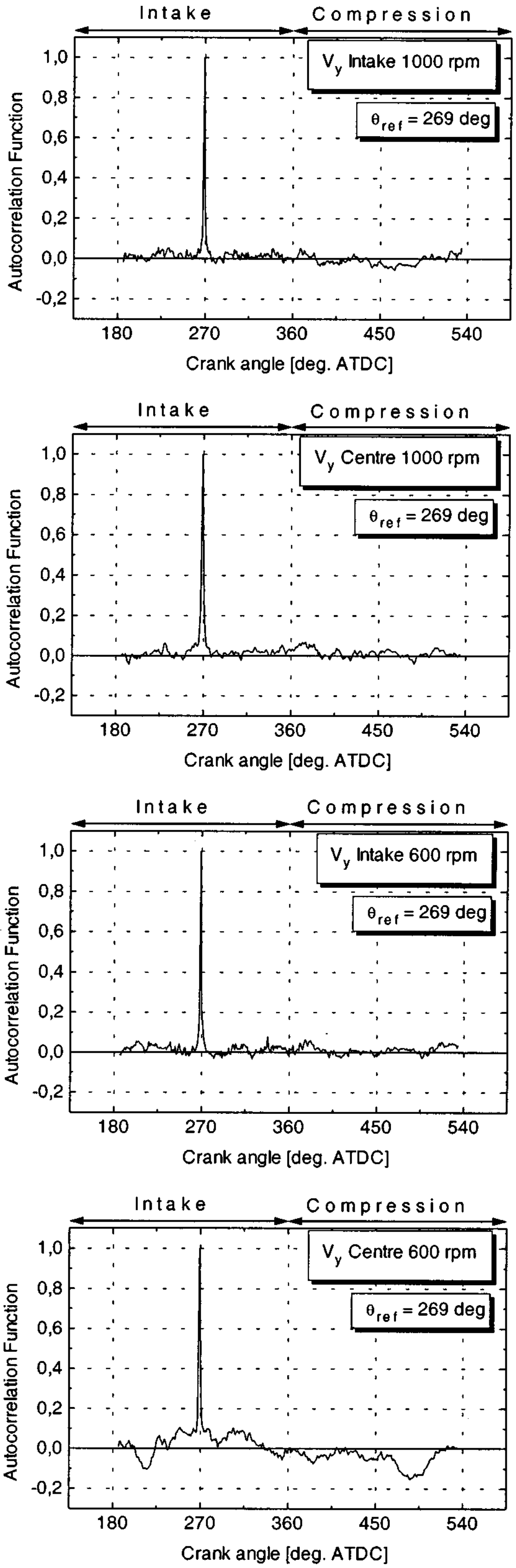

Fig. 5 Autocorrelation function. The reference point is at the middle of the intake stroke.

The actual determination of the coherence time involves some form or arbitrariness. Here the linear decaying zone following the maximum of the ACF has been interpolated over 3 deg both right and left of the maximum, and the intercept of the linear interpolation with the zero level has been determined.

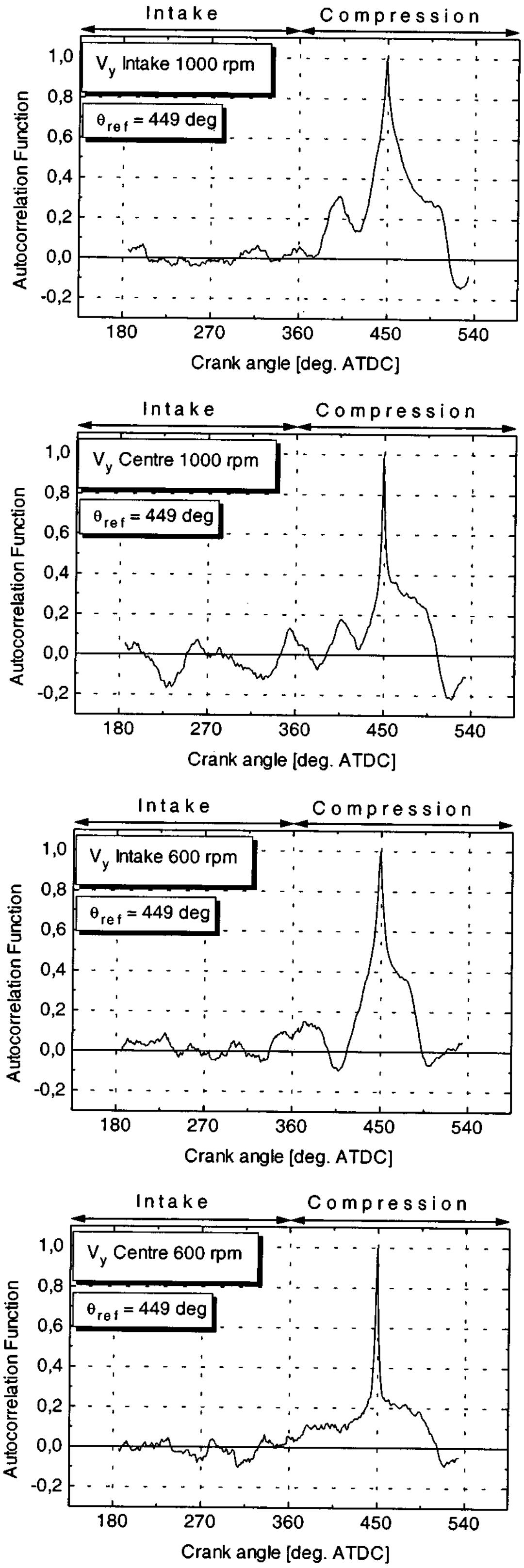

Fig. 6 Autocorrelation function. The reference point is at the middle of the compression stroke.

Figure 9 shows the resulting coherence time in the various measuring conditions for the different reference angles. The longer coherence time is obtained at the measuring point near the intake valves, toward the end of compression, for the lowest engines speed.

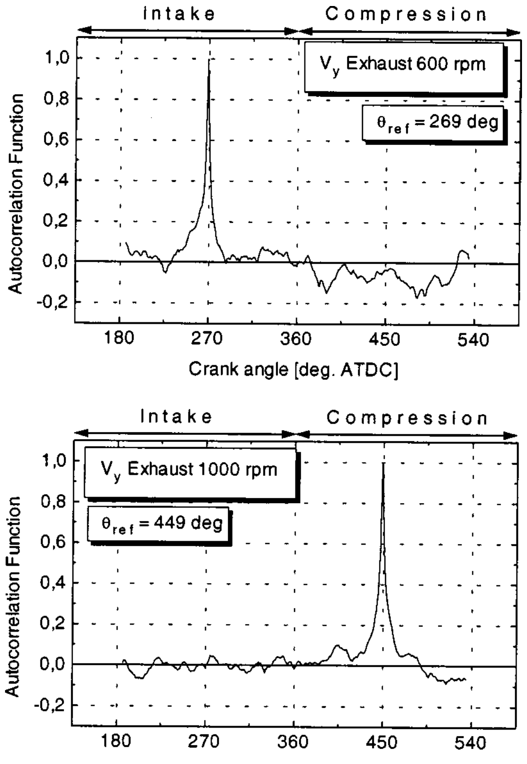

Fig. 7 ACF computed for velocity measured near the exhaust valves

It is generally thought that the small eddies, which are characterized by short coherence time, dissipate much more rapidly than large vortexes [4]. Therefore, it is interesting to plot the rate of dissipation of the turbulence energy $|du'^2/dt|$, calculated from the late intake to the end of compression, as a function of the obtained coherence time. The result is shown in Fig. 10 and confirms that the decay of the turbulence energy is very fast for short coherence times (small eddies), while it vanishes as the coherence time becomes longer. The scatter of the points is well fitted by a first-order exponential decay.

As for the reference angle in the engine cycle where to compute the ACF, the middle of the compression stroke has been selected (449 deg ATDC). At this crank angle the coherence time is longer and the cut-off frequency is therefore shorter. We are in fact looking for the lower limit of the velocity fluctuation frequency as the separation between turbulence and mean flow.

The results are shown in Fig. 11. The cut-off frequency increases as the engine speed increases and as the measuring point moves from the region of the more ordered flow, near the intake valves, to the region of more chaotic flow, at the center of the chamber or near the exhaust valves.

Power Spectrum. For analyzing the frequency distribution of the velocity fluctuations, the observation field has been divided in crank angle windows of 90 deg, centered around the reference angle used for computing ACF. For every single cycle the EA-velocity has been subtracted from the non-filtered instantaneous velocity, the frequency distribution has been computed for every single cycle and then ensemble-averaged. Results are shown in Fig. 12(*a*) for the measurements taken near the intake valves at 600 rpm. The area under each curve is proportional to the overall kinetic energy, so the spectra reach the maximum level in the crank angle interval 225–360 (middle and late intake), then their level decreases; this agrees with the results of Fig. 4. Moreover Fig. 12(*a*) shows that the kinetic energy of the velocity fluctuation is quite uniformly distributed in the frequency range during the intake, so that frequencies up to 1 kHz are present with a significant energy level, while during compression the energy content

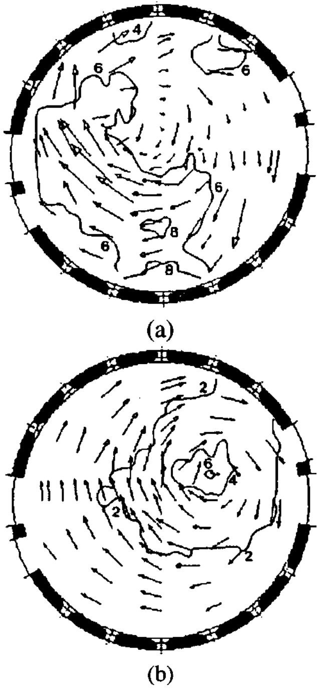

(a)

(b)

Fig. 8 Velocity field at 270 (*a*) and at 450 (*b*) deg ABDC

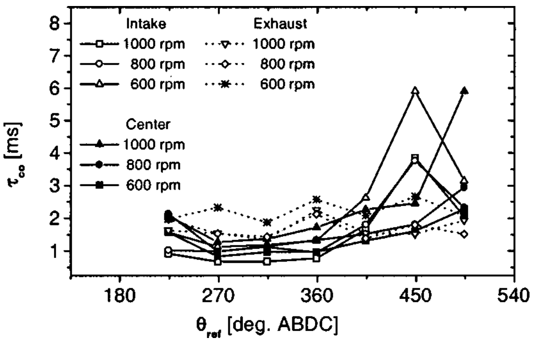

Fig. 9 Time coherence versus degree

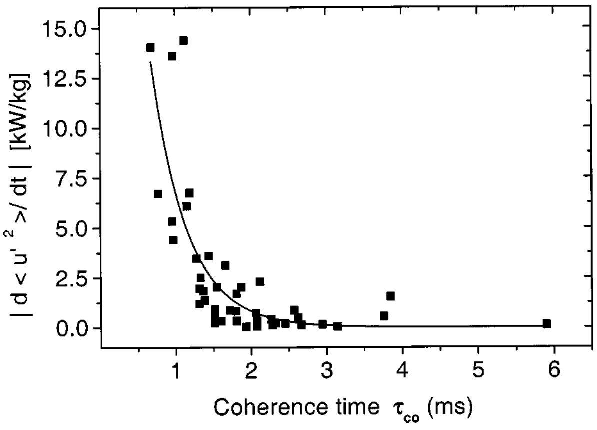

Fig. 10 Turbulence decay

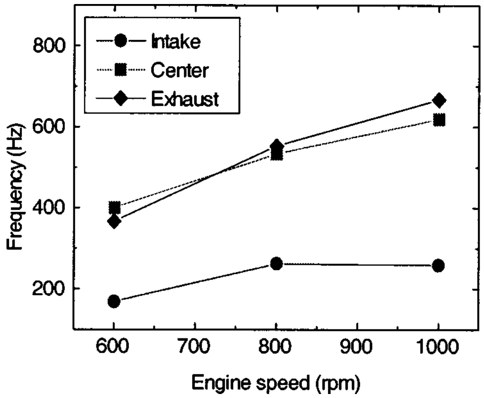

Fig. 11 Cut-off frequency obtained from the coherence-time of the autocorrelation function

decreases substantially as the frequency increases. At this stage, the power spectrum approaches the canonical $f^{-5/3}$ slope, which characterizes the stationary, isotropic turbulence. This observation agrees with results obtained in open chamber engines [4,12]. As the engine speed is increased to 800 rpm (Fig. 12(*b*)) at the same measurement location, the character of the power spectrum for frequencies higher than ≈ 200 Hz is almost the same, but it is shifted to higher frequencies. In addition, during the intake stroke, a distinct knee appears at frequencies of ≈ 200 Hz. Fansler [12] suggests that this knee-frequency is proportional to the coherence time given by the autocorrelation function. As the measuring point moves to the center of the chamber (Fig. 12(*c*)) or near the exhaust valves (Fig. 12(*d*)) the slope of the power spectrum for frequency higher than a few hundred Hz is almost the same for each crank angle interval, and is slightly lower ($\approx f^{-1.4}$) than the canonical $f^{-5/3}$ (Fig. 12(*d*)).

In addition, at these measuring points, the energy content at the end of compression is much lower than the energy content near the intake valves. It is also interesting to observe in Fig. 12(*a*) that the energy decay between the crank angle intervals 315–405 (end of intake) and 450–540 (late compression) is much larger at high frequency than at low frequency, as Lancaster [4] explains. Furthermore, in the plot of Fig. 12(*a*) this decay looks to increase almost linearly with the frequency, and, because of the Log-Log scale, this is in excellent agreement with the exponential decay shown in Fig. 10. Finally, the quasi constant decay as the frequency varies, which can be observed in Fig. 12(*d*) (measuring point near the exhaust valves) is also in agreement with the persistent character of the turbulence shown in Fig. 7.

As for the determination of f_{co} by detecting the knee, which identifies the beginning of the $f^{-5/3}$ region, this knee is not always very evident in the examined power spectra. The power spectrum has been therefore only used to investigate the general character of the turbulent flow, but not to estimate f_{co}.

Frequency Analysis of the EA-Velocity. Because LDV provides an intermittent signal, data is collected as velocity-crank angle pairs, which need to be preliminarily worked out in order to obtain equally spaced data, suitable for frequency analysis. Therefore, the intake and compression strokes have been divided in crank angle intervals of 1 deg. For each single cycle, if more than one measurement was present in one crank angle window, the measurements have been averaged; if a window had no data in it, a value has been calculated for that window by interpolating between adjacent windows. This process introduces a first low-pass filter.

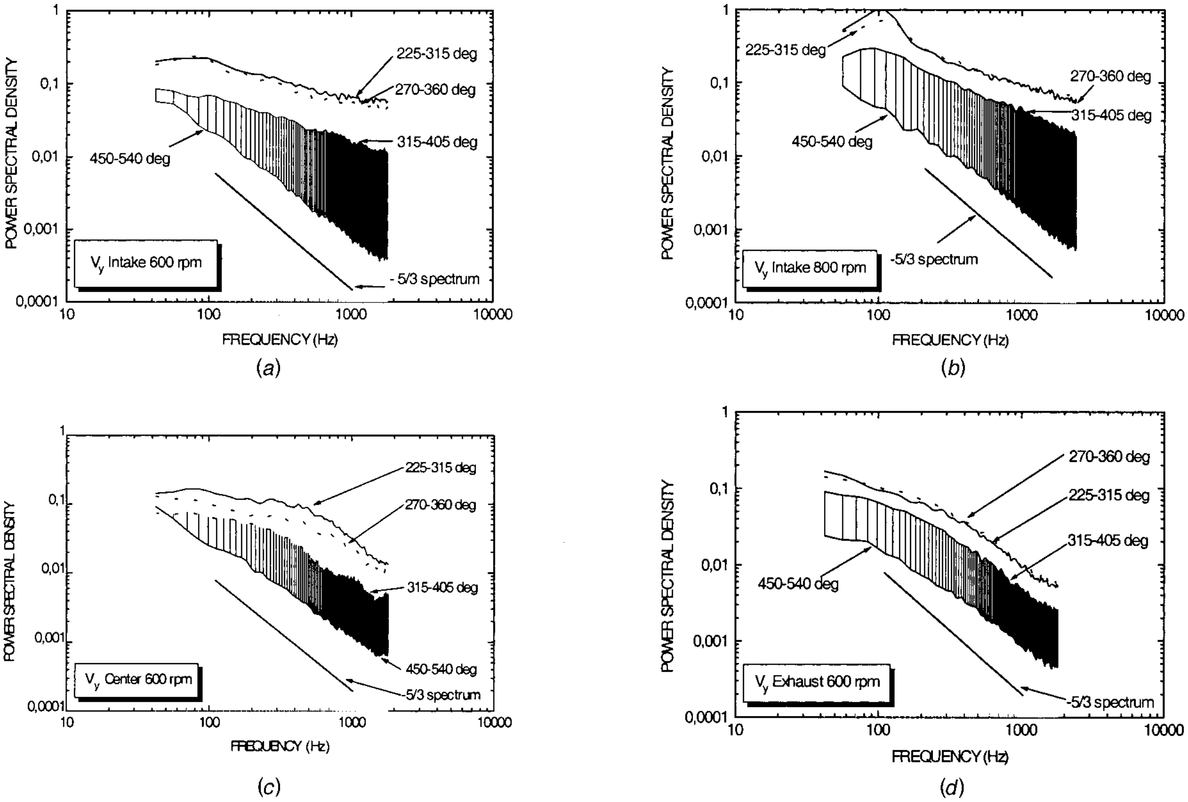

(*a*) (*b*)

(*c*) (*d*)

Fig. 12 Power spectra (*a*) near the intake valves at 600 rpm; (*b*) near the intake valves at 800 rpm; (*c*) center of the chamber at 600 rpm; (*d*) near the exhaust valves at 600 rpm.

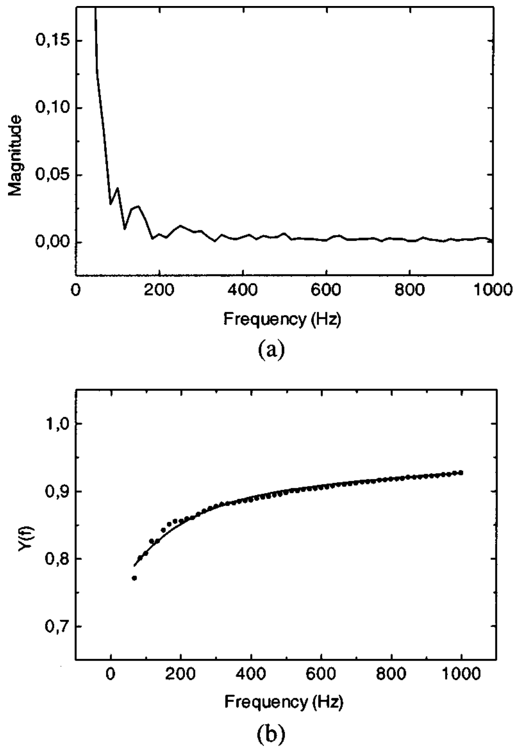

Fig. 13 Frequency spectrum (*a*) integrated spectrum (dots) and interpolating function $Y(f)$ (*b*)

The EA-velocity is then computed and Fourier-transformed. The cut-off frequency f_{co} is selected as the one above which the amplitudes of the harmonics are negligible [8].

The justification for this choice is the following. As the number of collected cycles used to compute the EA-velocity approaches the infinite, the frequency content due to pure random fluctuations vanishes in the mean velocity. In practice, because the number of used cycles is only *large enough*, then the frequency content of the pure random or turbulent fluctuations can only be expected to be *small enough*. The matter is further complicated by the fact that there is enough evidence that a superimposition exists between pure random and quasi-deterministic fluctuations associated with precessing swirl [12]. As a consequence, because of the shape of the frequency spectrum (Fig. 13(*a*)), the selection of the cut-off frequency is the result of a time consuming trial-and-error process, based on subjective judgments.

Here, as an operational method for selecting this frequency, the spectrum has been integrated, so that the fluctuations in the high-frequency region of the spectrum are transformed into a linear trend. The beginning of this linear region has been identified by interpolating the obtained integral with a function

$$Y(f)=C_1+C_2e^{-c_3f}+C_4f \qquad (9)$$

and by looking for the frequency which makes the slope of the exponential term equal to the linear one (Fig. 13(*b*)). For frequencies higher than this one, in fact, the interpolating function approaches the straight line which corresponds to the region of vanishing amplitudes in the frequency spectrum and hence to the region of the turbulence-related frequencies.

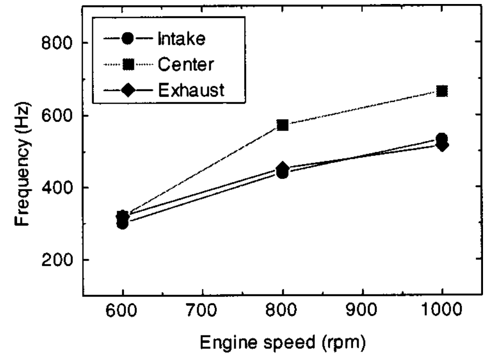

Fig. 14 Cut-off frequency obtained from the frequency spectrum of the ensemble-averaged velocity

The cut-off frequencies obtained by applying this method are reported in Fig. 14 and confirm the trend shown in Fig. 11.

Discussion of the Results

The cut-off frequency f_{co}, as calculated by means of the ACF (Fig. 11) or by means of the frequency analysis of the EA-velocity (Fig. 14), increases as the engine speed increases. This is due to the fact that, as the engine speed rises, the turbulent energy and hence f_{co} moves toward the higher frequencies. Lancaster [4] suggests two reasons for this. The first is that an increment in the engine speed causes an increase in the intake air velocity. This produces higher velocity gradients, which generate smaller eddies, which are characterized by higher frequencies. The second reason is that if the engine speed rises there is less time available for turbulence decay; as the higher-frequency eddies decay faster than the low-frequency vortexes, only with higher engine speeds will the first survive until the end of compression, therefore producing a shift of the frequency spectrum toward the high-frequencies region. Moreover, as the engine speed increases, the large scale swirl or tumble vortexes will also show higher frequencies.

The f_{co} also depends on the measuring location. Its values are lower where the flow is more organized and exhibits less cycle-by-cycle variation, as near the intake valves [19]. At the center of the chamber, on the contrary, the flow is more chaotic, with large-scale cycle-by-cycle variations, which are mainly due to the precession motion of the center of the swirl motion, and, as a consequence, f_{co} reaches the highest values.

The above stated trends are similar both when f_{co} is calculated from the ACF and when it is evaluated from the frequency spectrum of the EA-velocity. The absolute values, however, are obviously different, as they are derived on the basis of criteria which are reasonable but arbitrary. The actual value of f_{co} would in fact change if one, for instance, interpolates the ACF over 5 points instead of 3 or if one considers as the decaying level $1/e$ instead of zero. The same holds for the f_{co} values calculated from the frequency spectrum of the EA velocity.

An additional difference exists between the two sets of results. The f_{co} values near the intake valves are the lowest and at the center are the highest. However, near the exhaust valves they are similar to the ones near the intake in the case of Fig. 11 while they are more like the one at the center in Fig. 14.

For the actual cycle-resolved analysis, the results obtained from the frequency spectrum (Fig. 14) have been used. The conditions to be checked for validating the results of the analysis are that

$$U_{\mathrm{EA}}(\overline{\theta})=\overline{U}_{\mathrm{EA}}(\overline{\theta}) \qquad (10)$$

and

$$u'_{\mathrm{rms}}(\overline{\theta})=\sqrt{u'^{2}_{\mathrm{LF}}(\overline{\theta})+u'^{2}_{\mathrm{HF}}(\overline{\theta})}, \qquad (11)$$

where $u'_{\mathrm{LF}}(\overline{\theta})$ and $u'_{\mathrm{HF}}(\overline{\theta})$ are the rms values of $u_{\mathrm{LF}}(\overline{\theta},i)$ and $u_{j\mathrm{HF}}(\theta,i)$, respectively.

Figures 15 and 16 show that these conditions are verified quite well during the compression, while there is a small difference during the intake. It is evident that the results obtained with the ensemble average method contain higher frequency than the ones given by the cycle-resolved technique. This is due to the fact that the interpolating technique used to obtain equally-spaced measurements introduces a low-pass filter.

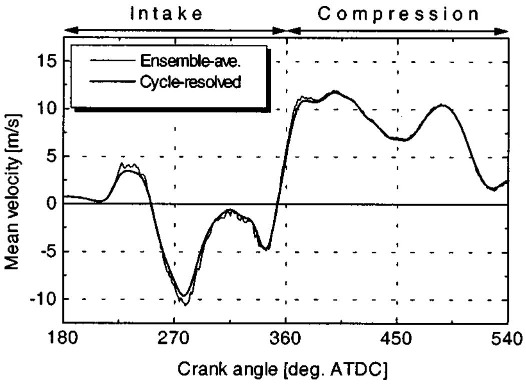

Fig. 15 Mean velocity obtained with the ensemble average and with the cycle-resolved methods.

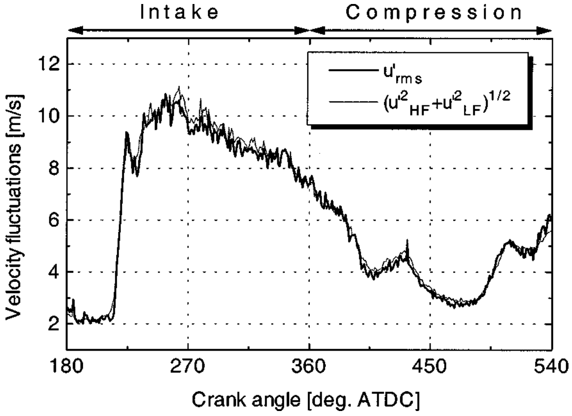

Fig. 16 Comparison of velocity fluctuation intensity (ensemble-average) and $\sqrt{u'^2_{LF}(\theta)+u'^2_{HF}(\theta)}$ quantity (cycle-resolved)

A final remark concerns the influence of the f_{co} value on the turbulence intensity as calculated by the cycle-resolved analysis. During this work it has been observed that variations of $50 \div 100$ Hz in f_{co} have a negligible effect on the resulting turbulence intensity, while a difference of $200 \div 250$ Hz produces a variation of $10 \div 15$ percent. This influence is not linear: because of the spectrum shape, an overestimate of f_{co} has a much smaller effect than an undervalue.

Conclusions

LDV data have been taken at three different engine speeds in three measuring locations within the combustion chamber, which are characterized by different flow conditions. Data has been analyzed by means of different methods in order to identify the cut-off frequency which can be used to separate ''true'' turbulence from cycle-by-cycle variations of the mean flow. The different investigation tools have given complementary, coherent perspectives of the different turbulence regimes.

Both the non-stationary autocorrelation function and the frequency analysis of the ensemble-averaged velocity was suitable for defining operational procedures for identifying such a frequency.

This separation frequency was dependent both on the engine speed and on the measuring location: it increases as the engine speed increases and as the measuring point moves from the more ordered jet exiting the intake valves toward the more chaotic region near the center of the chamber or near the exhaust valves.

The value of the cut-off frequency is not very critical for determining the turbulence intensity by the cycle-resolved analysis: differences of $50 \div 100$ Hz do not have a big impact. Nevertheless, the same cut-off frequency cannot be used for every measuring condition. The use of an operational procedure to identify such a cut-off frequency is therefore less time-consuming and less dependent on subjective judgment than any trial-and-error process.

Nomenclature

ACF = autocorrelation function: $R(\theta_{\text{ref}},\tau)$
C_1,C_2,C_3,C_4 = coefficients defining the interpolating function
f = frequency
f_{co} = cut-off frequency
N_c = number of sampled engine cycles
N_i = data arrived at the fixed crank angle window $\bar{\theta}$ of the i^{th} cycle
N_t = data arrived at the fixed crank angle window $\bar{\theta}$ of all the N_c cycles
$R(\theta_{\text{ref}},\tau)$ = autocorrelation function (ACF)
$U_{\text{EA}}(\bar{\theta})$ = ensemble average velocity
$U(\bar{\theta},i)$ = in-cycle velocity
$U_{\text{EA}}(\bar{\theta})$ = ensemble average of the *in-cycle velocity*
$U_j(\bar{\theta},i)$ = j^{th} velocity datum at the fixed crank angle window $\bar{\theta}$ during the i^{th} cycle.
$u_j(\bar{\theta},i)$ = velocity fluctuation
$u_{j\text{HF}}(\bar{\theta},i)$ = high frequency velocity fluctuation, ''true'' turbulence
$u_{\text{LF}}(\bar{\theta},i)$ = low frequency velocity fluctuation, cycle by cycle variation of mean flow
$u'_{\text{rms}}(\bar{\theta})$ = root mean square of velocity fluctuation
$Y(f)$ = interpolating function of the integrated spectrum
θ = crank angular position
$\bar{\theta}$ = crank angular window
θ_{ref} = reference angle in the ACF computation
τ = angular separation in the ACF computation
τ_{co} = coherence-time of the turbulent structures

References

[1] Witze, P. O., 1980, ''A Critical Comparison of Hot-Wire Anemometry and Laser Doppler Velocimetry for I.C. Engine Applications,'' SAE Paper 800132.
[2] Reuss, D. L., Adrian, R. J., Landreth, C. C., French, D., and Fansler, T. D., 1989, ''Instantaneous Planar Measurements of Velocity and Large-Scale Vorticity Stain Rate in an Engine Using Particle-Image Velocimetry,'' SAE Paper 890616.
[3] Witze, P. O., 1976, ''Hot-Wire Measurements of the Turbulence Structure in a Motored Spark-Ignition Engine,'' AIAA 14th Aerospace Sciences Meeting, Washington, D.C.
[4] Lancaster, D. R., 1976, ''Effects of Engine Variables on Turbulence in a Spark-Ignition Engine,'' SAE Paper 760159.
[5] Lancaster, D. R., Krieger, R. B., Sorenson, S. C., and Hull, W. L., 1976, ''Effects of Turbulence on Spark-Ignition Engine Combustion,'' SAE Paper 760160.
[6] Rask R. B., 1984, ''Laser Doppler Anemometer Measurements of Mean Velocity and Turbulence in Internal Combustion Engines,'' ICALEO '84 Conference Proceedings, Laser Institute of America, Boston.
[7] Rask, R. B., 1985, ''Comparison of Window, Smoothed-Ensemble, and Cycle-by-Cycle Data Reduction Techniques for Laser Doppler Anemometer Measurements in a Motored IC Engine,'' ASME J. Fluids Eng., **107**, pp. 232–240.
[8] Liou, T. M., and Santavicca, D. A., 1985, ''Cycle Resolved LDV Measurements in a Motored IC Engine,'' ASME J. Fluids Eng., **107**, pp. 232–240.
[9] Fansler, T. D., and French, D. T., 1988, ''Cycle-Resolved Laser-Velocimetry Measurements in a Reentrant-Bowl-in-Piston Engine,'' SAE Paper 880377.
[10] Catania, A. E., and Mittica, A., 1989, ''Extraction Techniques and Analysis of Turbulence Quantities From In-Cylinder Velocity Data,'' ASME J. Eng. Gas Turbines Power, **111**, pp. 466–478.
[11] Fraser, R. A., and Bracco, F. V., 1989, ''Cycle-Resolved LDV Integral Length Scale Measurements Investigating Clearance Height Scaling, Isotropy, and Homogeneity in an I.C. Engine,'' SAE Paper 890615.
[12] Fansler, T. D., 1993, ''Turbulence Production and Relaxation in Bowl-in-Piston Engines,'' SAE Paper 930479.
[13] Catania, A. E., Dongiovanni, C., Mittica, A., Molina, G., and Spessa, E., 1995, ''A New Test Bench for HWA Fluid-Dynamic Characterization of a Two-Valved In-Piston-Bowl Production Engine,'' SAE Paper 952467.
[14] Amelio, M., Belli, M., Bova, S., and Florio, G., 1994, ''LDA Flow Field Characterization in a Motored Reciprocating Engine,'' in *PD-Vol. 64-8.3, En-*

gineering Systems Design and Analysis (ESDA) Conference, ASME PD, **8**, Part C, pp. 597–604.

[15] Lorenz, M., and Presher, K., 1990, ''Cycle Resolved LDV Measurements on a Fired SI-Engine at High Data Rates Using a Conventional Modular LDV-System,'' SAE Paper 900054.

[16] Bracco, F. V., 1985, ''Modeling and Diagnostics of Combustion in Spark-Ignition Engines,'' *Proc. of International Symposium on Diagnostics and Modeling of Combustion in Reciprocating Engines*, (COMODIA 85), Tokyo, pp. 1–13.

[17] Bendat, J. S., and Piersol, A. G., 1986, *Random Data Analysis and Measurement Procedures*, 2nd ed., Wiley, New York.

[18] Heywood, J. B., 1988, *Internal Combustion Engine Fundamentals*, McGraw-Hill, New York.

[19] Rask, R. B., 1981, ''Comparison of Window, Smoothed-Ensemble, and Cycle-by-Cycle Data Reduction Techniques for Laser Doppler Anemometer Measurements of In-Cylinder Velocity,'' in Morel, T., Lohman, R. P., and Racklay, J. M., eds., *Fluid Mechanics of Combustion Systems*, pp. 11–20, ASME, New York.

Comparisons of Diesel Spray Liquid Penetration and Vapor Fuel Distributions With In-Cylinder Optical Measurements

Laura M. Ricart

Rolf D. Reitz

Engine Research Center,
University of Wisconsin-Madison,
Madison, WI 53706

John E. Dec

Combustion Research Facility,
Sandia National Laboratories,
Livermore, CA 94550

The performance of two spray models for predicting liquid and vapor fuel distribution, combustion and emissions is investigated. The model predictions are compared with extensive data from in-cylinder laser diagnostics carried out in an optically accessible heavy-duty, D. I. diesel engine over a wide range of operating conditions. Top-dead-center temperature and density were varied between 800 K and 1100 K and 11.1 and $33.2\,kg/m^3$*, respectively. Two spray breakup mechanisms were considered: due to Kelvin-Helmholtz (KH) instabilities and to Rayleigh-Taylor (RT) instabilities. Comparisons of a wide range of parameters, which include in-cylinder pressure, apparent heat release rate, liquid fuel penetration, vapor distribution and soot distribution, have shown that a combination of the KH and the RT mechanisms gives realistic predictions. In particular, the limited liquid fuel penetration observed experimentally was captured by including these two competing mechanisms in the spray model. Furthermore, the penetration of the vapor fuel ahead of the liquid spray was also captured. A region of high soot concentration at the spray tip was observed experimentally and also predicted by the KH-RT spray breakup model.* [S0742-4795(00)01504-0]

1 Introduction

Environmental concerns are resulting in more stringent pollutant emissions and fuel consumption standards for engine manufacturers. To meet these standards a better understanding of the physical processes occurring within internal combustion engines and/or new technologies are needed. Optical diagnostic techniques and multidimensional codes are potential tools to meet these requirements. Optical diagnostic techniques provide needed insight into the physical and chemical processes governing diesel combustion, and also data for development and validation of models in multidimensional codes.

Fuel atomization and droplet dispersion are very complex physical phenomenon that influence the distribution, vaporization, and combustion of the injected fuel, having a major impact on the ignition behavior, emissions level and power output of an engine. Hence, adequately predicting the spray is critical in effectively predicting the combustion process and emissions formation. Even though computational power has increased dramatically since the beginning of engine modeling efforts, it is still not possible to resolve the smallest length and time scales present in diesel sprays, which control the combustion process and the engine flow details. Hence, submodels are introduced to model sub-grid scale physics. These submodels, in particular the spray models, need improvement and validation.

A new spray model has been recently developed for the KIVA codes [1], and has been tested for some operating conditions [2]. A wide variety of experiments [3–7] with a wide range of operating conditions have been carried out in the Sandia National Lab (SNL)/Cummins optical-access engine, making this engine of interest for numerical model verification and development. In the present work, the liquid-fuel penetration and vapor-fuel distribution measurements have been used to test new spray models [2]. In the following sections a brief description of the experimental setup and diagnostics will be given. This is followed by a short description of the relevant models and the comparison of experimental and numerical results.

2 Experimental Setup

In this section, a brief description will be given of the engine and the optical-diagnostic experiments that were used to validate the models. A more complete description of the engine may be found in Espey and Dec [3]. The optical engine used in the liquid-fuel penetration and the vapor-fuel distribution measurements is a single-cylinder, direct-injection, diesel engine based on a Cummins N-series, heavy-duty production engine. The engine was modified to obtain substantial optical access into the combustion chamber. Cut outs have been made in the piston rim to allow laser sheet access along the spray-jet axis. Optical access is possible through a piston-crown window, as first introduced by Bowditch [8], and a window in the cylinder head that replaces one of the exhaust valves to obtain a view of the squish region and the outer portion of the combustion bowl. Additional windows near the top of the cylinder wall allow the introduction of the laser sheets used for the two-dimensional (planar) laser diagnostics imaging. A schematic of the optical-access engine is shown in Fig. 1, and the engine specifications are given in Table 1. The engine is equipped with the Cummins CELECT electronic fuel injector. This closed-nozzle unit injector uses camshaft actuation to build injection pressures. A solenoid valve in the injector body controls the amount of fuel injected and the injection timing. Table 2 summarizes the specifications of the fuel injector.

In the experiments discussed here, the engine was operated at 1200 rpm. Before conducting the experiments the engine was heated to 95°C by means of electrical heaters on the ''cooling'' water and lubricating oil systems. To minimize the rate of window fouling and to avoid overheating, the engine was fired every 20th engine cycle, at which time the data were acquired. The fuel used in the studies was a 42.5 cetane number mixture of the diesel reference fuels, heptamethylnonane and n-hexadecane. The mixture was 67.6 percent heptamethylnonane and 32.4 percent

---

Contributed by the Internal Combustion Engine Division of THE AMERICAN SOCIETY OF MECHANICAL ENGINEERS for publication in the ASME JOURNAL OF ENGINEERING FOR GAS TURBINES AND POWER. Manuscript received by the ICE Division October 15, 1998; final revision received by the ASME Headquarters August 31, 1999. Technical Editor: D. Assanis.

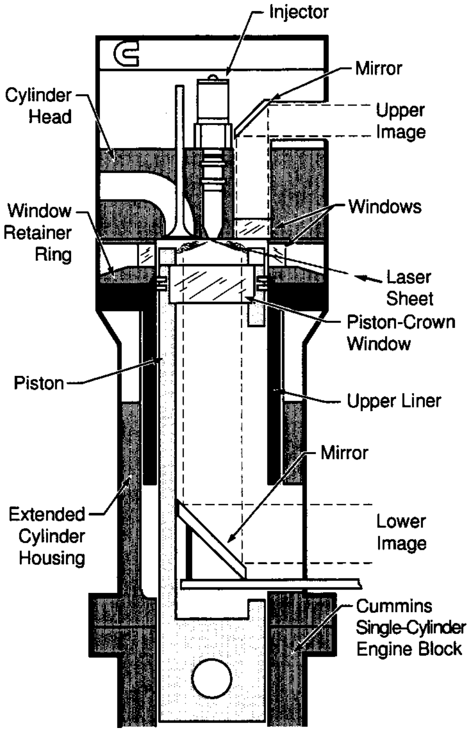

Fig. 1 Schematic of optical-access diesel engine showing the laser sheet along the fuel jet axis. Images were obtained from both the cylinder-head window and the piston-crown window.

n-hexadecane by volume, with a specific gravity of 0.7865. A low-sooting fuel mixture was used for soot imaging and is described in detail by Dec and Espey [9].

Liquid-fuel penetration measurements were made at a base operating condition that is representative of diesel engine operating conditions, and at various other TDC temperatures and densities covering the typical operating range of diesel engines. Due to modifications for the optical access, the engine had a lower compression ratio than the production engine. Hence, intake air temperature and pressures were increased so that the motored TDC conditions were representative of typical diesel engine operating conditions. For the base condition, the intake air temperature and pressure were set to 433 K and 206 kPa (abs.), respectively, to obtain an ignition delay, premixed burn fraction and TDC air density typical of a naturally aspirated diesel engine. A summary of the base engine operating condition is given in Table 3. The effect of TDC temperature and density on the penetration of the liquid-phase fuel was studied by Espey and Dec [4] by systematically varying the intake air temperature and density around the base values. The intake and the estimated TDC conditions for the cases studied are given in Table 4.

Table 1 Specifications of the optical-access engine

Engine type	Cummins N-14, DI Diesel
Bore	139.7 mm
Stroke	152.4 mm
Connecting rod length	304.8 mm
Displacement	2.34 liters
Combustion chamber	Quiescent
Combustion bowl diameter	97.8 mm
Intake valve opening	17° BTDC (Exhaust)
Intake valve closure	195° ATDC (Exhaust)
Exhaust valve opening	235° BTDC (Exhaust)
Exhaust valve closure	27° ATDC (Exhaust)

Table 2 Specifications of the fuel injector

Type	Cummins CELECT
Design	Closed-nozzle,unit injector
Number of holes	8, uniformly spaced
Hole diameter	0.194 mm
Length/diameter of the holes (l/d)	4:1
Angle of fuel-jet axis (from horizontal)	14°

Table 3 Base engine-operating conditions

Engine speed	1200 rpm
Intake air temperature	433 K
Intake air pressure	206 kPa (absolute)
Water temperature	95°C
Oil temperature	95°C
Start of injection	11.5° BTDC
Fuel injected per cycle	0.0535 g
Peak injection pressure	68 MPa

Table 4 Cases studied

Case	T_{TDC} (K)	ρ_{TDC} (kg/m^3)	T_{int} (K)	P_{int} (kPa)
T1	800	16.6	349	166
T2	900	16.6	393	187
BASE	992	16.6	433	206
T3	1100	16.6	480	229
P1	992	11.1	433	138
P2	992	24.9	433	309
P3	992	33.2	433	413

Measurements of the liquid fuel penetration were made via the elastic scattering of laser light, introduced as a sheet along the axis of the spray [4]. A frequency-doubled (532 nm) Nd:YAG laser beam was used and formed into a sheet with a combination of cylindrical and spherical lenses. The sheet was introduced through the cylinder wall window along the axis of the fuel jet. The images of the elastically scattered light were collected through the piston-crown window by a gated, intensified, CCD video camera. Fuel vapor concentration and temperature measurements were made using planar laser Rayleigh scattering [6]. For these experiments, the intake air was carefully filtered to reduce background noise and images were acquired through the cylinder-head window. For detailed description of the assumptions and data processing necessary to obtain both fuel-vapor and temperature distributions from the Rayleigh scattered light refer to Espey et al. [6]. Early soot formation has been studied through simultaneous laser-induced incandescence and elastic-scatter imaging as discussed in Dec and Espey [9]. The results of these and other experimental investigations are summarized and discussed in Dec [7].

3 Numerical Models

The numerical calculations were carried out with an improved version of the KIVA-II code [1]. The most recent improvements are in the turbulence, gas/wall heat transfer, ignition, combustion, NOx and soot models, as described by Han and Reitz [10]. The standard k-ϵ model has been replaced by an RNG k-ϵ model with modification for gas compressibility [10]. The ignition model is based on the multistep Shell model and combustion is achieved through a laminar-turbulent characteristic-time model, as implemented by Kong et al. [11]. Currently, two mechanisms are used to characterize the breakup of the fuel droplets: Kelvin-Helmholtz (KH) and Rayleigh-Taylor (RT) instabilities. More recently, the concept of a breakup length to account for the dense spray region near the nozzle has been used in conjunction with the KH and RT mechanisms [2,12]. The use of a core region has shown improvement in the liquid length penetration predictions and in the computational time requirements for the calculations.

3.1 Ignition and Combustion Models. In a previous study by Kong and Reitz [11], the Shell autoignition model [13] was implemented to model the ignition process. The model uses eight reactions with five generic species representing the hydrocarbon, the fuel radicals, the oxidized products, a branching agent and the labile intermediate species. The formation rate of the labile intermediate species was found to be the rate-limiting step in the kinetic path [13], and the total ignition delay was found to be sensitive to the pre-exponential factor for that step. For the engine operating conditions simulated in the present study (see Table 4), it was found necessary to adjust the pre-exponential, A_{f04}, for the rate of formation of the labile species as follows,

$$A_{f,04}=\frac{(85.5-0.07857T_{in})\times 10^{6}}{P_{in}}, \tag{1}$$

where T_{in} is the intake temperature in K and P_{in} is the intake pressure (absolute) in kPa.

A characteristic-time combustion model, which was initially developed for spark ignition engines by Abraham et al. [14], was used to model combustion. Similar to the SI engine combustion model, the rate of change of the partial density of species m is written as

$$\frac{\partial\rho_m}{\partial t}=-\frac{\rho_m-\rho_m^*}{\tau_{c,m}}, \tag{2}$$

where ρ_m^* is the local and instantaneous thermodynamic equilibrium value of the partial density, and $\tau_{c,m}$ is the characteristic time to achieve such equilibrium for each species. In the computations, only the major chemical species, whose inclusion is required for accurate predictions of combustion energy release, are considered [15]. The characteristic time, $\tau_{c,m}$, is composed of a turbulent-mixing time, τ_t, and a laminar chemical-kinetics time, τ_l, and the coefficient f that characterizes the degree of turbulent combustion [11] as follows,

$$\tau_{c,m}=\tau_l+f\tau_t. \tag{3}$$

The laminar time scale is derived from an Arrhenius-type reaction rate, and the turbulent time scale is proportional to the eddy turnover time, which is calculated from the kinetic energy and the dissipation rate. Hence, in this model, the laminar time scale dominates the combustion during the early stages of combustion, and then, the effect of turbulence on combustion becomes more important once the combustion has proceeded to a certain extent. For further details refer to Kong et al. [11].

3.2 Spray Model. Spray atomization is a complicated physical phenomenon, which is critical in diesel engine combustion. The spray characteristics depend on fluid properties, ambient conditions, the fuel-injector nozzle design specifications and operating conditions. The breakup of the injected liquid is caused by the aerodynamic liquid-gas interactions and nozzle flow effects and/or nozzle effects.

The spray breakup models currently used in engine modeling calculate liquid breakup by using some form of stability analysis [16]. The model sets a limit of stability and if droplets have existed long enough to become unstable, breakup occurs and the characteristics of the new droplets are based on the wavelength or frequency of the instability that brought about the breakup. Two mechanisms are currently used to characterize the breakup of fuel droplets. The wave breakup model of Reitz [17] considers the shearing-off of droplets due to the growth of KH instabilities on the droplet surface resulting from the relative velocity between the gas and liquid phases. Breakup due to the growth of RT instabilities, resulting from the deceleration of the injected droplets, has been implemented [16]. In previous studies, only the KH instabilities were considered [11], or the KH and RT instabilities were applied to the whole spray [16,18]. In this study, both KH and RT instabilities are considered, but within the dense core region near the nozzle exit only KH instabilities are assumed to occur. In this study, the dense core region refers to the region close to the nozzle where the droplets are so densely packed that their penetration rate is different than further downstream.

Conditions of the liquid at the nozzle exit, for example size distribution of the droplets, are generally unknown for a given injector, unless extensive diagnostics are carried out. Hence, the liquid injection is simulated using the ''blob'' injection method of Reitz and Diwakar [19], where droplets are injected with a diameter equal to the nozzle hole diameter. Furthermore, experimental results have shown that diesel spray penetrates at different rates within and beyond the breakup length [20]. This may be attributed to the existence of a dense core region or ''churning'' flow regime close to the nozzle. Hence, to model the spray dynamics near the nozzle, it is assumed that only the KH instabilities occur in this dense core or churning flow region, where accelerative effects are thought to be negligible. The breakup length, L_b, is define to be the limit of the core region and is determined from the Levich theory [21] as

$$L_b=C\sqrt{\frac{\rho_l}{\rho_g}}\,d_0, \tag{4}$$

where C is a constant that can be correlated to nozzle geometry parameters [20] and d_0 is the nozzle hole diameter. The constant for the injector used in this study was found to be 14.5.

Based on KH instabilities, the breakup time, τ, accounts for two conditions: bag breakup at low Weber numbers, and stripping breakup at high Weber numbers [19] and is given by

$$\tau=\frac{3.788B_1 r}{\Omega\Lambda}, \tag{5}$$

where r is the radius of the droplet, Ω and Λ are the frequency and wavelength of the fastest growing wave, and B_1 is a model constant, which accounts for nozzle effects, and is set to 60 in this study as recommended by Han and Reitz [10]. The frequency and wavelength of the fastest growing wave are given by Reitz [17] as

$$\Omega=\frac{0.34+0.38We^{1.5}}{(1+Z)(1.4T^{0.6})}\sqrt{\frac{\sigma}{\rho_l r^3}} \tag{6}$$

$$\Lambda=\frac{9.02r(1+0.45\sqrt{Z})(1+0.4T^{0.7})}{(1+0.865We^{1.67})^{0.6}}, \tag{7}$$

where $We=(\rho_g u_r^2 r)/\sigma$, is the Weber number for the gas, $Z=\sqrt{We_l}/\mathrm{Re}_l$, the Ohnesorge number, and $T=ZWe^{1/2}$, the Taylor number. u_r is the magnitude of the relative velocity, We_l is the liquid Weber number similar to We except the liquid density is used, Re_l, is the liquid Reynolds number.

The breakup was modeled by postulating that new drops are formed (with drop radius, r_c) from a parent drop or blob (with radius, r) with

$$r_c=B_0\Lambda, \tag{8}$$

where B_0 is 0.61 [17]. Hence, the rate of change of drop radius in a parent parcel due to drop breakup is given by

$$\frac{dr}{dt}=\frac{r-r_c}{\tau}, \tag{9}$$

where τ is the breakup time defined in Eq. (5) for the KH case.

In the formulation of the RT breakup model, the breakup time is given by

$$\tau_{\mathrm{RT}}=C_\tau/\Omega_{\mathrm{RT}}, \tag{10}$$

where C_τ is a constant set to 0.5 and Ω_{RT} is the frequency of the fastest growing wave, given by Bellman and Pennington [22] as

$$\Omega_{\mathrm{RT}}=\sqrt{\frac{2}{3\sqrt{3\sigma}}\frac{[-g_t(\rho_l-\rho_g)]^{3/2}}{\rho_l+\rho_g}} \tag{11}$$

when considering surface tension and neglecting viscosity. Sensitivity studies by Ricart [23] found that the spray prediction was not very sensitive to the RT breakup time constant. The corresponding wavelength, Λ_{RT}, is

$$\Lambda_{\mathrm{RT}}=2\pi\sqrt{-\frac{3\sigma}{g_t(\rho_l-\rho_g)}}. \tag{12}$$

In Eqs. 11 and 12, $g_t=\vec{g}\cdot\vec{j}+\vec{a}\cdot\vec{j}$ is the acceleration in the direction of travel, $\vec{g}$ is the acceleration due to gravity, $\vec{a}$ represents the droplet acceleration, and $\vec{j}$ is the unit vector tangential to the droplet trajectory. Ricart et al. [2] found that for typical diesel fuels, the effect of viscosity on the fastest growing frequency and the wave number is negligible; hence, it is not considered in the present implementation.

Hence, if RT instabilities are found to be growing on a droplet and the breakup time is exceeded, the droplet breaks up into droplet with the radius given by

$$r=C_{3,\mathrm{RT}}\Lambda_{\mathrm{RT}}/2,$$

where $C_{3,RT}$ is taken to be 0.1, since it was found to result in the shortened penetration observed in the engine. In the implementation by Patterson [16], new droplets have the same velocity as the parent droplet. However, in this study, the new droplets are given a velocity normal to the path of the parent drop as given by the TAB model [24]. The effects of model constants on the spray characteristics and behavior are studied in detail by Patterson [16] and Xin et al. [12] and Ricart [23].

In the current implementation, once the breakup length has been reached, both models are considered. The model that predicts the fastest onset of instability results in the breakup event. That is, when the disturbances have grown for enough time to exceed the breakup time, regardless of the breakup model, the droplet experiences breakup. In the KH model, this implies shedding-off smaller droplets and creating a new computational parcel, and, in the RT model, it indicates complete break up into smaller droplets. In both cases the size of the new droplet is proportional to the size of the disturbances.

Collisions resulting in coalescence are a competing mechanism for the breakup of the droplets. The collision and coalescence model used in this study is that of Patterson [16]. In this model, collisions only occur within droplets which are physically approaching one another. This is different from the model of O'Rourke [25], where the probability of collision between droplets in a given computational cell is calculated based on the size, number density and their relative velocity. Ricart [17] studied the effect of the collision model and found improved spray predictions with the model of Patterson [16], particularly due to the reduced number of collisions with the new model.

4 Results

The liquid fuel penetration experiments of Espey and Dec [4] were modeled using the improved version of KIVA-II described in the previous section. Two spray breakup models were tested. The first model (KH) assumes that liquid breakup occurs only through Kevin-Helmholtz instabilities. The second model (KH-RT) included the RT instabilities and the breakup length concept. The numerical grid used to model the optical access engine is shown in Fig. 2. The mesh resolution used was found to give adequate grid-independent results [10]. Based on symmetry assumption between the eight sprays, only a 45 deg sector of the combustion chamber was used in the computations. Asymmetries from cut outs in the rim of the piston bowl, which allow for laser-sheet access, have not been considered in this study for simplicity. The volume of the cut outs, however, has been accounted for by increasing the TDC clearance, or squish height. In this study, the fuel mixture was modeled as n-hexadecane for fuel properties. However, the cetane number of the mixture was used. Comparisons between computed and measured pressures and heat release rates will be presented to assess the accuracy of the models in predicting global parameters. Then comparison of liquid fuel penetration, fuel-vapor, temperature and soot distributions will provide more localized validation.

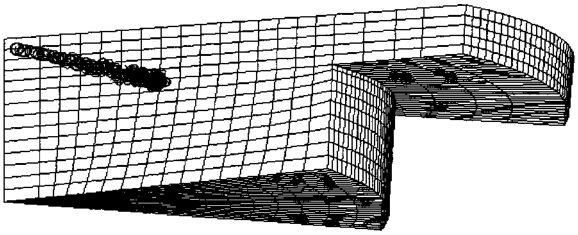

Fig. 2 Perspective view of the computational grid for the Cummins optical-access engine (at TDC) with the computational spray

4.1 Base Condition.

The measured and predicted in-cylinder pressures, and the apparent heat release rate, as derived from the measured and predicted pressure through a first law analysis [26], are shown in Fig. 3. Ignition delay is predicted within 0.5 crank angle degree, regardless of the spray model used. The pressure predicted by the KH-RT model is within 2.5 percent of the measured pressure. Whereas, the KH model under predicts the peak cylinder pressure by 10 percent, indicating that the fuel is not vaporizing and burning effectively when the KH model is used. This is also evident from the apparent heat release rate where the combustion is seen to be slower and continues beyond what is seen experimentally, implying a low vaporization rate. The ignition delay is under-predicted somewhat by both models, resulting in a lower premixed burn spike and a longer mixing

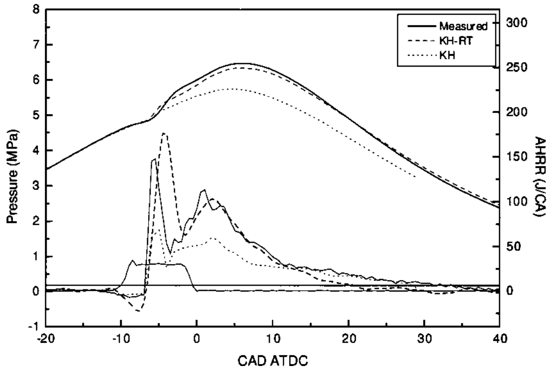

Fig. 3 Measured and predicted cylinder pressure for the base operating condition

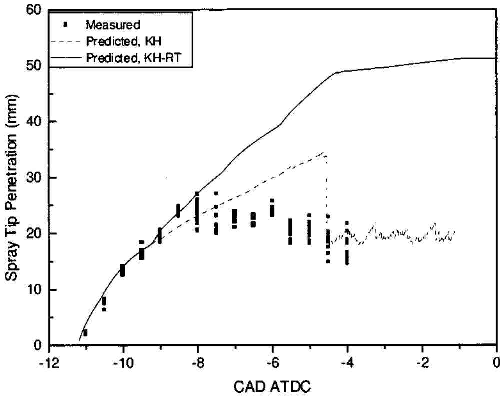

Fig. 4 Liquid fuel penetration as predicted by KH and KH-RT model and measured for the base operating condition

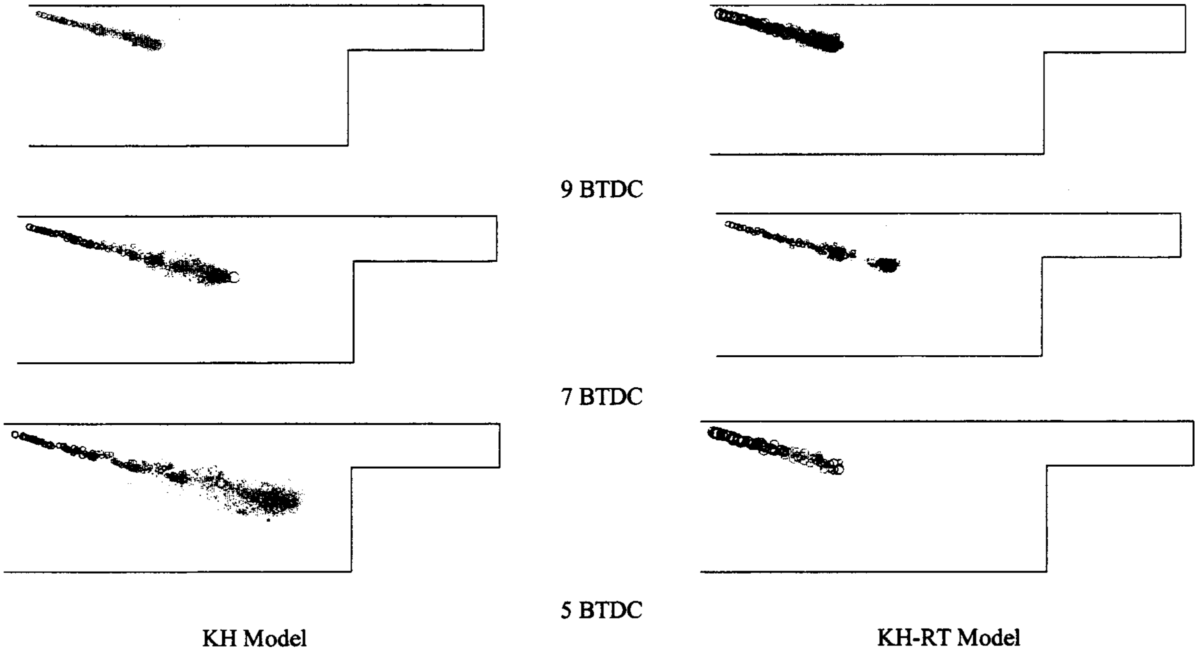

Fig. 5 Spray profiles as predicted by the KH and the KH-RT spray models

controlled burn. However, the KH-RT model does predict the phasing of the end of the energy release correctly. The slower fuel vaporization rate predicted by the KH model is also evident before ignition, where the apparent heat release rate predicted by the KH-RT model drops significantly below its value prior to injection due to the evaporation of the fuel, and its magnitude is comparable to the experimental value. In the prediction by the KH model this drop is barely perceptible.

Liquid fuel penetration as a function of crank angle degree for the baseline operating condition (see Table 4) is presented in Fig. 4. The symbols show the experimental data for 12 engine cycles at half-crank-angle degree increments. The spray tip penetration as

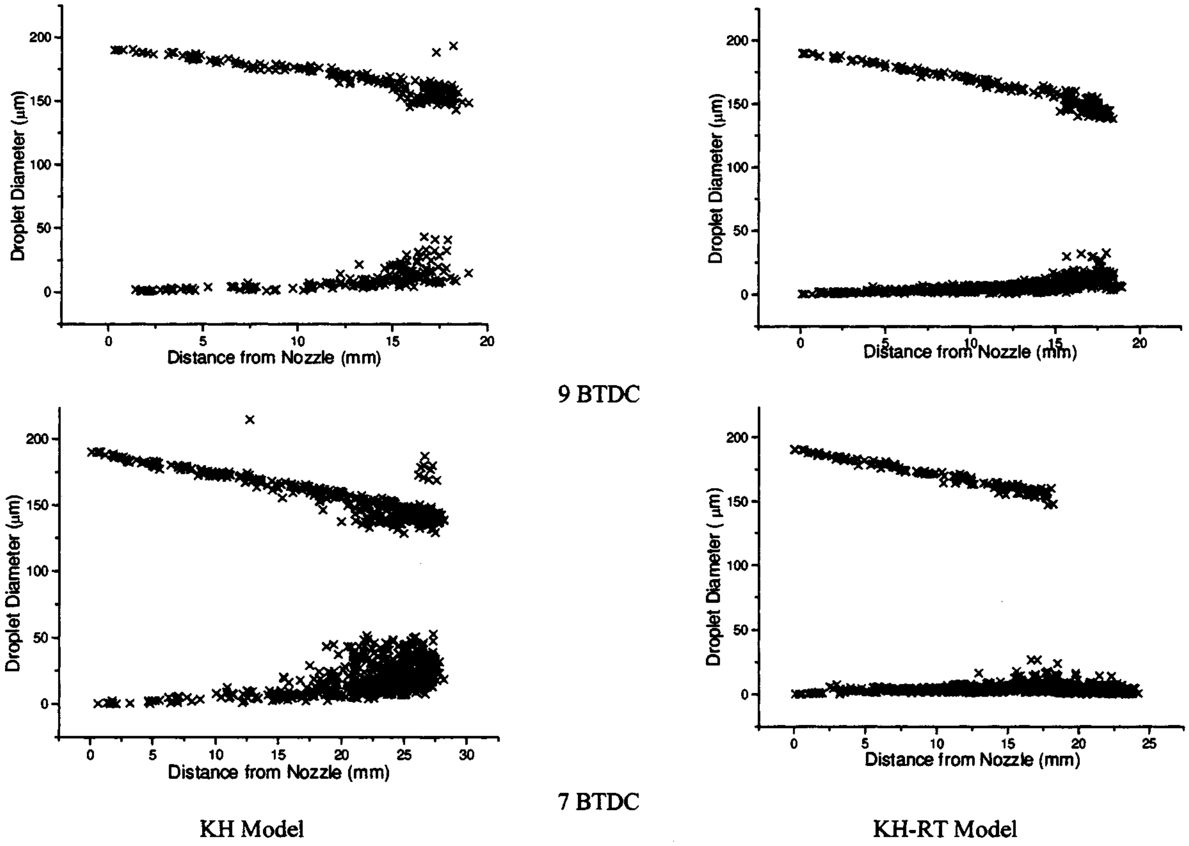

Fig. 6 Droplet size distributions as predicted by the KH and the KH-RT spray models

a) Vapor-fuel mass fraction

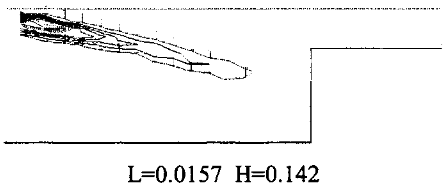

b) Equivalence ratio

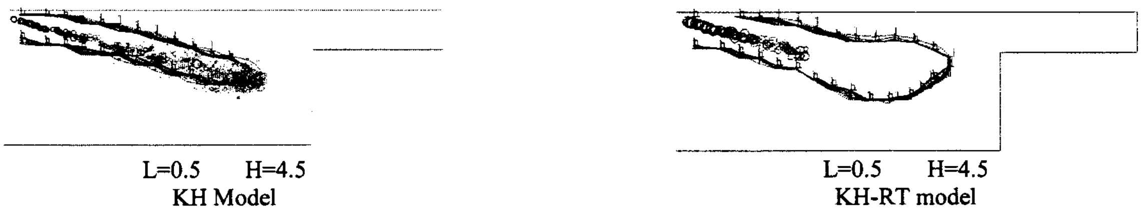

Fig. 7 Vapor-fuel mass fraction (*a*) and equivalence ratio (*b*) as predicted by the KH and the KH-RT spray breakup models

predicted with the KH and KH-RT models and based on the location of the farthest droplet from the nozzle is also shown. The experimental data shows that initially the spray penetrates almost linearly with crank angle (time). However, by about 8 or 8 1/2 deg BTDC (3 deg after the start of injection) the spray ceases to penetrate, reaching a maximum liquid penetration length of about 24 mm. Both the KH and KH-RT model predict the correct initial penetration of the spray. However, the KH model does not predict the limited penetration of the liquid fuel, with this model the spray penetrates all the way to the piston bowl edge (~50 mm). The KH-RT model predicts a slower penetration after 9 deg BTDC, and captures the limited liquid penetration observed experimentally. However, the KH-RT model initially over predicts the penetration, which then drops down closer to the measured values as combustion ensues.

Figure 5 shows the predicted spray profiles and Fig. 6 shows the cross sectionally averaged droplet size distribution with distance from the nozzle for the KH and the KH-RT spray models. Initially, at 9 deg BTDC, there is no significant difference between the predictions from the two different spray models, as was also observed in Fig. 4. The penetration and droplet size distributions are almost the same. This similarity at early times is not unexpected since only the KH mechanism acts on the large injected spray ''blobs'' before the breakup length is reached. By 7 deg BTDC, the predicted sprays start exhibiting significant differences. The KH spray has penetrated farther into the combustion chamber than the KH-RT spray. Also, the KH-RT spray is characterized by smaller droplets beyond the breakup length due to the RT mechanism. These smaller droplets evaporate more effectively creating a break in the main spray (i.e., it appears as if a small group of droplets are penetrating ahead of the main spray). Soon after ignition occurs these droplets are vaporized and a shortened liquid penetration is observed, even though injection continues through to top-dead-center. At 5 deg BTDC, the penetration predicted by the KH model is seen to be significantly longer than that for the KH-RT model, and droplets are much larger than those predicted by the KH-RT model, which were efficiently vaporized.

Figure 7 shows the predicted equivalence ratio and vapor-fuel concentration in the fuel-jet axis plane at 5 deg BTDC. In the KH prediction, high equivalence ratios exist only along the path of the spray, and the highest vapor concentration is located close to the injector nozzle. However, for the KH-RT prediction, the high equivalence ratio region extends far beyond the tip of the spray, and high vapor-fuel concentrations are ahead of the spray in agreement with the experiments [5,6]. Figure 8 shows the measured temperature distribution in a plane 9 mm below the cylinder head, and that predicted by the KH-RT model. The predicted temperatures are seen to be in the same range as the measured values. The predicted distribution, however, does not have the detailed structures and sharp gradients observed experimentally. This is an artifact of the k-ϵ turbulence model's time-averaging as opposed to the single realization in the experiment.

Comparisons of soot distribution in the combustion chamber are shown in Fig. 9. Experimentally, it was found that the early formation of soot occurs in the high vapor-fuel concentration region in the leading portion of the jet [7,9]. This same trend is also observed in the predictions using the KH-RT model. Hence, another improvement resulting from the implementation of the KH-RT model is in the prediction of the distribution of fuel vapor and emissions in the combustion chamber, indicating that the correct spray model is a critical input for the combustion and emissions models.

Hence, the KH-RT model has been found to capture the limited liquid fuel penetration, the penetration of the vapor fuel ahead of the spray, and the location of emission formation observed experimentally. The performance of the KH-RT model is summarized next for the rest of the running conditions studied by Espey and Dec [4].

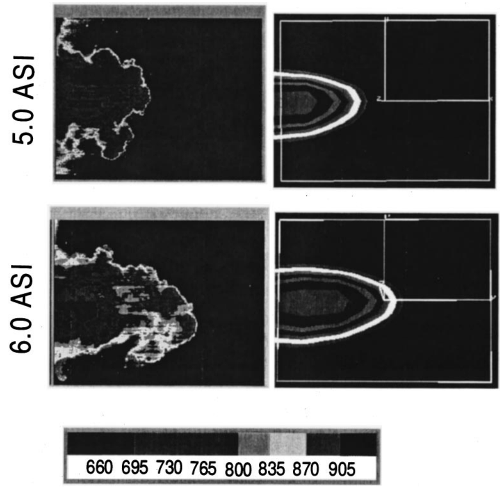

Fig. 8 Measured (left) and predicted (right) temperature distribution in a plane 9 mm below the cylinder head and 27 mm from the injector nozzle. The field of view is 18 mm ×12.5 mm.

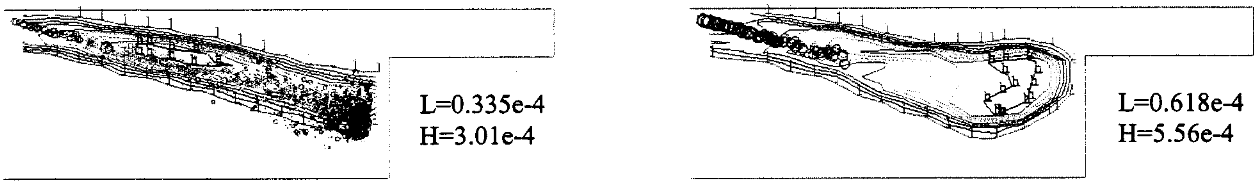

KH Model KH-RT Model

Fig. 9 Soot mass fraction distribution in the plane of the spray axis as predicted by the KH and the KH-RT models at 3 deg BTDC. The spray profile has been superimposed for reference.

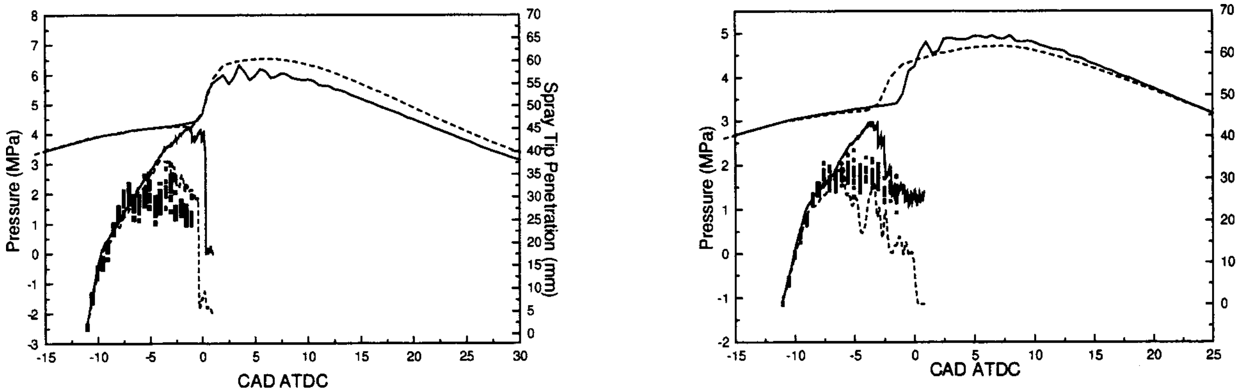

(a) Case T1 (T_{TDC}= 800 K, ρ_{TDC}= 16.6 kg/m^3) (b) Case P1 (T_{TDC}= 992 K, ρ_{TDC}= 11.1 kg/m^3)

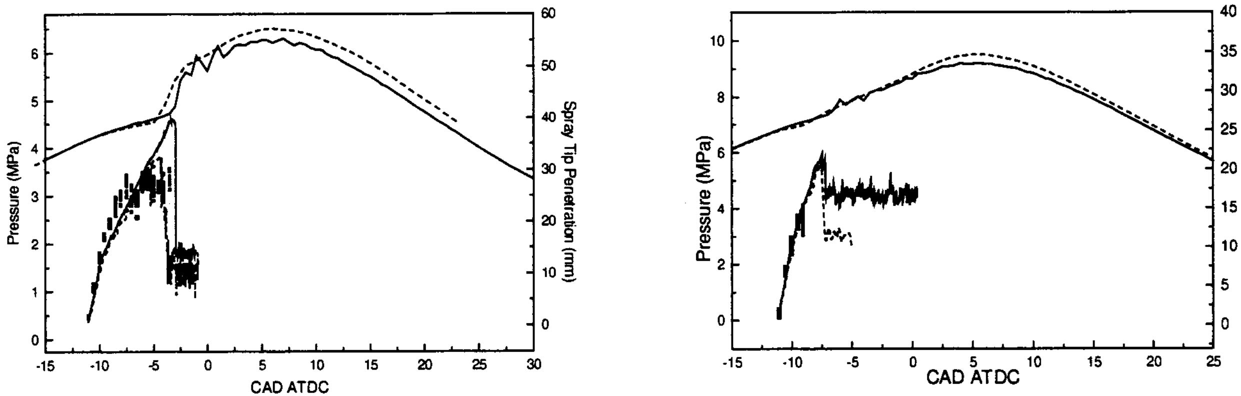

(c) Case T2 (T_{TDC}= 900 K, ρ_{TDC}= 16.6 kg/m^3) (d) Case P2 (T_{TDC}= 992 K, ρ_{TDC}= 24.9 kg/m^3)

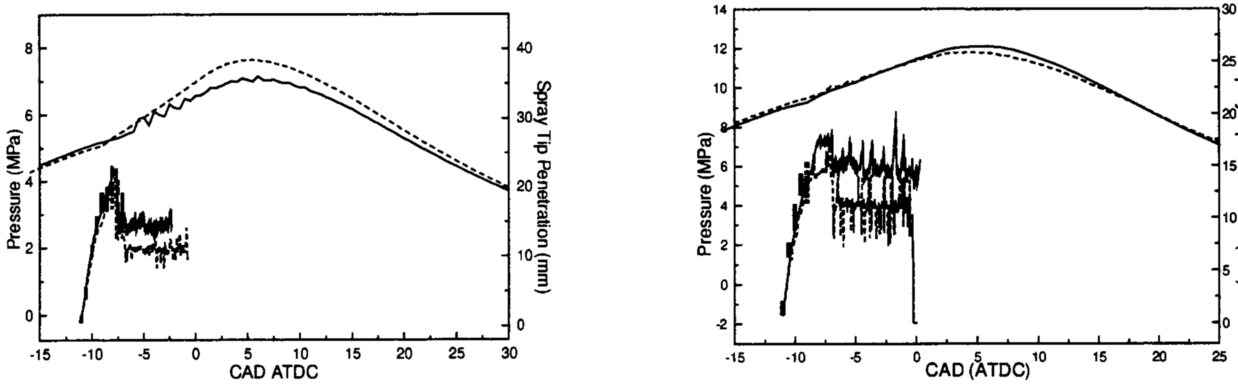

(e) Case T3 (T_{TDC}= 1100 K, ρ_{TDC}= 16.6 kg/m^3) (f) Case P3 (T_{TDC}= 992 K, ρ_{TDC}= 33.2 kg/m^3)

Fig. 10 Predicted (dashed line) and measured (solid line) cylinder pressure and spray tip penetration for the range of operating conditions studied by Espey and Dec [4]. Predictions are for the KH-RT model. For the spray tip penetration, the measured values are shown by the solid squares, the penetration of the farthest droplet is in the solid line and the penetration of 90 percent of the liquid mass is shown by the dashed line.

4.2 Parametric Study.

A model needs to be tested over a wide range of conditions to ensure its validity and universality. In their investigation, Espey and Dec [4] studied the effect of TDC temperature and density on the liquid-fuel penetration. Predictions of liquid length and cylinder pressure for all the cases studied by Espey and Dec (Table 5) are shown in Fig. 10. In general, cylinder pressures are seen to be predicted well and the ignition delay is predicted to within 2 crank angle degrees throughout the range of operating conditions studied.

The spray tip penetration results include the measured values and predicted penetration based on the farthest droplet from the nozzle and penetration based on the penetration of 90 percent of the liquid mass (90 percent mass). These two numerical definitions of the spray penetration should give an upper and lower bound for comparisons with the experimental values, since small droplets ahead of the spray might not be resolved in the experiments. Recent experiments carried out with very high camera gain, indicate that the farthest droplets do penetrate 1 to 2 mm farther than reported in this paper.

Experimental results show a decrease in the maximum liquid-fuel penetration with increasing temperature and/or density. As the TDC temperature was increased from 800 K to 1100 K in the experiments, the liquid fuel penetration decreased from 30 mm to 18 mm. The same trend is predicted by the KH-RT model, where the penetration of the farthest droplet decreased from 42 mm to 21 mm and the 90 percent penetration decreased from 35 mm to 20 mm over the same range of TDC temperature (Cases T1, T2, and T3). Similar trends were observed as the TDC density was varied. The maximum liquid penetration lengths varied from about 30 mm for the $11.1\ \mathrm{kg/m^3}$ to about 13 mm for $33.2\ \mathrm{kg/m^3}$ experimentally, and numerically from 40 mm to 17 mm for the farthest droplet and from 31 mm to 14 mm for the 90 percent penetration (Cases P1, P2, and P3).

The initial liquid penetration rate is predicted accurately for all the conditions studied. Hence, the spray model captures the slightly reduced initial penetration rate observed experimentally as the density was increased. The maximum liquid penetration, however, seems to be over predicted when the penetration is determined by the location of the farthest droplet. But the droplets that appear to over penetrate are quickly consumed once ignition occurs. The penetration of 90 percent mass is consistently in better agreement with the experimental values. Since these two definitions offer an upper and lower bound for the liquid fuel penetration, the KH-RT model predictions are considered to be in good agreement with the experimental values over the range of operating conditions studied.

5 Summary and Conclusions

Two spray models that account for different breakup mechanisms have been tested and compared with in-cylinder liquid-fuel penetration measurements. Comparisons of predicted and measured liquid penetration and vapor-fuel distributions have shown that it is necessary to consider the effect of RT instabilities in the breakup of the diesel fuel spray. The KH-RT model showed reduced, more realistic maximum liquid-fuel penetration lengths, which can be attributed to an improved vaporization rate due to the smaller predicted droplet size. The KH-RT model with the breakup length concept was used over a wide range of operating conditions to further test the validity of the model and its universality. All trends with TDC temperature and density variations are correctly predicted, and the maximum liquid lengths agree with the experimental data to within 15 percent, for the 90 percent mass penetration, across the range of conditions investigated.

Another significant improvement with the KH-RT model is that the fuel vapor penetrates ahead of the liquid as was observed experimentally. Previously with the KH model, the fuel vapor only penetrated as far as the liquid fuel. The range and distribution of equivalence ratio and temperatures ahead of the spray is also in very good agreement with the experimental results. The highest soot concentrations at early times were also predicted ahead of the spray by the KH-RT model as has been observed experimentally.

Acknowledgments

This work was supported by Cummins Engine Co., Caterpillar Inc., the Army Research Office, and the Department of Energy Sandia Laboratories. The authors thank the sponsors sincerely.

References

[1] Amsden, A. A., O'Rourke, P. J., and Butler, T. D., 1989, ''KIVA-II—A Computer Program for Chemically Reactive Flows With Sprays,'' Los Alamos National Laboratory Report No. LA-11560-MS.
[2] Ricart, L. M., Xin, J., Bower, G. E., and Reitz, R. D., 1997, ''In-Cylinder Measurement and Modeling of Liquid Fuel Spray Penetration in a Heavy-Duty Diesel Engine,'' SAE 971591.
[3] Espey, C., and Dec, J. E., 1993, ''Diesel Engine Combustion Studies in a Newly Designed Optical Access Engine Using High Speed Visualization and 2-D Laser Imaging,'' SAE Paper 930971.
[4] Espey, C., and Dec, J. E., 1995, ''The Effect of TDC Temperature and Density on the Liquid-Phase Fuel Penetration in a D.I. Diesel Engine,'' SAE Paper 952456.
[5] Espey, C., Dec, J. E., Litzinger, T. A., and Santavicca, D. A., 1994, ''Quantitative 2-D Fuel Vapor Concentration Imaging in a Firing D.I. Diesel Engine Using Planar Laser-Induced Rayleigh Scattering,'' SAE Paper 940682.
[6] Espey, C., Dec, J. E., Litzinger, T. A., and Santavicca, D. A., 1997, ''Planar Laser-Induced Rayleigh Scattering for Quantitative Vapor-Fuel Imaging in a Diesel Jet,'' Combust. Flame, **109**, pp. 65–86.
[7] Dec, J. E., 1997, ''A Conceptual Model of D.I. Diesel Combustion Based on Laser-Sheet Imaging,'' SAE Paper 970873.
[8] Bowditch, F. W., 1961, ''A New Tool for Combustion Research—A Quartz Piston Engine,'' SAE Trans., **69**, pp. 17–23.
[9] Dec, J. E., and Espey, C., 1995, ''Ignition and Early Soot Formation in a D.I. Diesel Engine Using Multiple 2-D Imaging Diagnostics,'' SAE Transactions, **104**, SAE Paper 950456, pp. 853–875.
[10] Han, Z., and Reitz, R. D., 1995, ''Turbulence Modeling of Internal Combustion Engines Using RNG k-ε Models,'' Combust. Sci. Technol., **106**, pp. 267–280.
[11] Kong, S.-C., Han, Z., and Reitz, R. D., 1995, ''The Development and Application of a Diesel Ignition and Combustion Model for Multidimensional Engine Simulation,'' SAE Paper 950278.
[12] Xin, J., Ricart, L. M., and Reitz, R. D., 1998, ''Computer Modeling of Diesel Spray Atomization and Combustion,'' Combust. Sci. Technol., **137**, Nos. 1–6, p. 171.
[13] Halstead, M., Kirsch, L., and Quinn, C., 1977, ''The Autoignition of Hydrocarbon Fuels at Temperatures and Pressures—Fitting a Mathematical Model,'' Combust. Flame **30**, pp. 45–60.
[14] Abraham, J., Bracco, F. V., and Reitz, R. D., 1985, ''Comparisons of Computed and Measured Premixed Charged Engine Combustion,'' Combust. Flame, **60**, pp. 309–322.
[15] Reitz, R. D., and Bracco, F. V., 1983, ''Global Kinetics and Lack of Thermodynamic Equilibrium,'' Combust. and Flame, **53**, pp. 141–143.
[16] Patterson, M. A., and Reitz, R. D., 1998, ''Modeling the Effects of Fuel Spray Characteristics on Diesel Engine Combustion and Emissions,'' SAE Paper 980131, SAE Transactions, **107**, Section 3, Journal of Engines, pp. 27–43.
[17] Reitz, R. D., 1987, ''Modeling Atomization Process in High-Pressure Vaporizing Sprays,'' Atom. Spray Technol., **3**, pp. 309–337.
[18] Su, T. F., Patterson, M., Reitz, R. D., and Farrell, P. V., 1996, ''Experimental and Numerical Studies of High Pressure Multiple Injection Sprays,'' SAE 960861.
[19] Reitz, R. D., and Diwakar, R., 1987, ''Structure of High Pressure Sprays,'' SAE Paper 870598.
[20] Hiroyasu, H., Arai, M., and Shimizu, M., 1991, ''Experimental and Theoretical Studies on the Structure of Fuel Sprays in Diesel Engines,'' *Proceeding of ICLASS-91*, Paper 26, Gaithersburg, MD.
[21] Levich, V. G., 1962, *Physicochemical Hydrodynamics*, Prentice-Hall, New Jersey.
[22] Bellman, R., and Pennington, R. H., 1954, ''Effects of Surface Tension and Viscosity on Taylor Instability,'' Quarterly Appl. Math., **12**, pp. 151–162.
[23] Ricart, L. M., 1998, Ph.D. thesis, ''An Experimental and Computational Study of Fuel Injection, Mixing and Combustion in Diesel Engines,'' Department of Mechanical Engineering, University of Wisconsin-Madison, WI.
[24] O'Rourke, P. J., and Amsden, A. A., 1987, ''The TAB Method for Numerical Calculation of Spray Droplet Breakup,'' SAE Paper 872089.
[25] O'Rourke, P. J., 1981, ''Collective Drop Effects in Vaporizing Liquid Sprays,'' Ph.D. thesis 1532-T, Princeton University, New Jersey.
[26] Heywood, J. B., 1988, *Internal Combustion Engine Fundamentals*, McGraw-Hill.

Relationship Between Visible Spray Observations and DI Diesel Engine Performance

Takashi Watanabe

Susumu Daidoji

Kurume Institute of Technology,
Kurume 830-0052, Japan

Keshav S. Varde

University of Michigan-Dearborn,
School of Engineering,
Dearborn, MI 48128-1491

This investigation was conducted to enhance understanding of combustion in a direct injection (DI) diesel engine with square combustion chamber. The investigation included a bench study of spray and its interaction with the chamber and correlation with engine performance. The bench study was conducted by using a liquid injection technique (LIT). The technique relies on the use of instantaneous photo images of emulsified fuel spray patterns to deduce spray behavior. It captures spray images in forced swirling flow on a positive film, which was used to deduce fuel-air mixing by scattering radiation technique. Three different chamber configurations, with different ratios of arc radius (r) to inscribed circle radius (R), and several spray deflecting angles were used in the study. The best parameters were found to be a deflecting angle of about 30 deg and a ratio of r/R of about 0.65. The results of the bench test were used to compare engine performance at similar design parameters. The engine performance was found to be superior at the above values of r/R and the deflecting angle. Engine exhaust of NOx and exhaust smoke were found to be lower at these design parameters. The experimental technique of using emulsified spray with LIT can be used qualitatively to evaluate effects of combustion chamber and fuel system design variables on engine performance. [S0742-4795(00)00104-6]

Introduction

The quality of combustion process in a DI diesel engine is highly dependent on the fuel-air mixing in the combustion chamber. This, in turn, depends on three major elements: aerodynamics of the inducted air, characteristics of the injected fuel, and the design of the combustion chamber. To improve the combustion process and exhaust emissions in a DI diesel engine it is important to understand mixing of fuel and air and mixture formation in the cylinder. Several investigations have been carried out to understand the mixing process and its relationships to engine performance.

Bardslay et al. [1] utilized a laser technique to study induced swirl, fuel atomization, droplet distribution, and droplet evaporation. Several studies dealing with combustion chamber configuration and engine performance have recognized the importance of fuel-air mixing on engine performance [2,3]. Recently, Kihara et al. [3] used a square shaped combustion chamber to reduce fuel consumption, exhaust smoke and NOx emissions from a DI diesel engine. However, the study did not investigate the relationship between the combustion chamber shape and engine performance parameters. The potential of the combustion chamber shape to improve engine performance and the lack of understanding between the square combustion chamber shape and the engine performance necessitated the investigation described in this paper.

In the present investigation a liquid injection technique was used to observe the visible aspects of emulsified spray. The information obtained from the technique was used to evaluate mixing characteristics of the spray in different combustion chamber shapes. The results were then used to justify the engine performance parameters in a qualitative manner. The technique used in the study relies on getting positive images of the spray patterns. These are then used to deduce fuel-air mixing by using intensity of the scattered light. The information was used to design combustion chambers of square geometry.

Experimental Apparatus

A The Single Cylinder DI Diesel Engine. The DI diesel engine used in the experiments had a MAN ''M-System'' combustion chamber. It was modified to accommodate combustion chambers of different geometrical configurations, as described later. The intake port of the engine was replaced by a helical port that produced a swirl ratio of 3.15. Table 1 shows the specifications of the test engine. The original injector of the fuel injection system had a single orifice throttling nozzle. It was replaced by a four-hole nozzle. The injector was located in the cylinder head such that it was inclined 35 deg to the cylinder axis against the anti-thrust side and offset by 12 mm. The injection tip protruded 5 mm below the surface of the cylinder head.

The combustion chambers were designed in the form of interchangeable attachments that can be assembled on top of the piston, as shown in Fig. 1. Four combustion chambers of dish (F-type) and square (S-type) shapes, with different geometrical dimensions as shown in Table 2, were used in the study. The ratio of the cavity diameter ''*d*'' and the cylinder bore ''*D*'', d/D, was varied between 0.459 and 0.50, a range that was limited by design considerations. The injector utilized in the tests had a four hole 4×0.25 mm nozzle, with an orifice $1/d=2.4$, injection spray angle between 110 and 120 deg, and nozzle opening pressure of 20 MPa. These values were determined by running tests with different injector parameters. The deflecting angle θ_e, shown in Fig. 2, is defined as the angle with respect to the perpendicular to

Table 1 Specifications of test engine

Combustion Chamber	D.I. (MAN-M)
Cycle	4
Number of Cylinders	1
Bore x Stroke	ϕ 100 x 150 mm
Displacement Volume	1.178×10^{-3} mm^3
Compression Ratio	17.0/1
Output Power	6.62 kW/900 rpm
Nozzle Opening Pressure	20.0 Mpa
Injection Timing	18.0° BTDC

Contributed by the Internal Combustion Engine Division of THE AMERICAN SOCIETY OF MECHANICAL ENGINEERS for publication in the ASME JOURNAL OF ENGINEERING FOR GAS TURBINES AND POWER. Manuscript received by the ICE Division March 8, 2000; final revision received by the ASME Headquarters April 17, 2000. Technical Editor: D. Assanis.

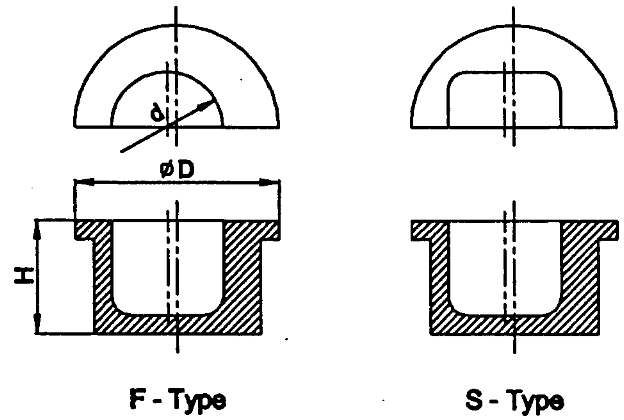

Fig. 1 Dish (F-Type) and Square (S-Type) combustion chambers

Table 2 Specifications of interchangeable piston cavities for test engine

Cavity Configurations		F (Dish)	S (Square)		
			S-1	S-2	S-3
Cavity Diameter	d (mm)	50.0	48.0	45.9	46.7
Cavity Height	H (mm)	30.6	32.3	35.4	32.0
Cavity Ratio	d/H	1.63	1.49	1.30	1.46
Diameter Ratio	d/D	0.500	0.480	0.459	0.467
Injection Hole Angle	θ (deg)	120	120	110	110
Geometric Factor	r/R	1.00	0.60	0.62	0.30

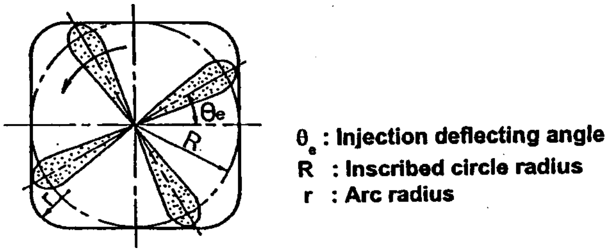

Fig. 2 Definition of geometric factor r/R

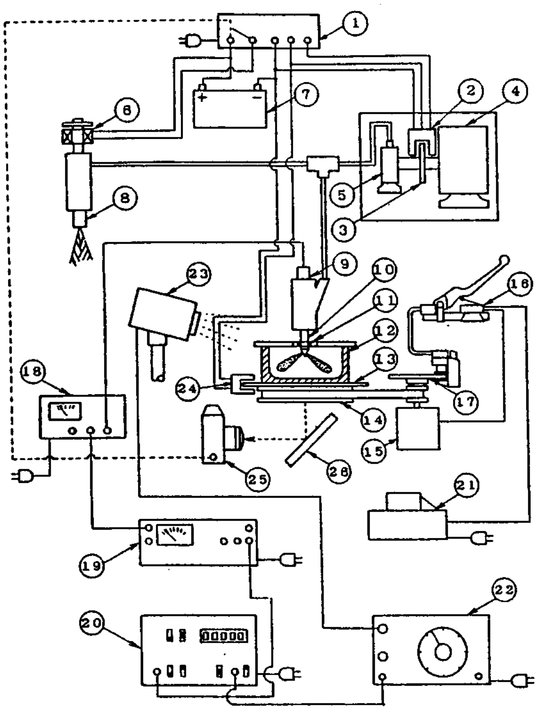

① Single Shot Injection Control Unit
② Photo Micro Sensor
③ Slit Disk
④ AC Motor
⑤ Injection Pump
⑥ Push/Pull Solenoid
⑦ Battery
⑧ Dummy Injection Nozzle
⑨ Needle Lift Sensor
⑩ Main Injection Nozzle
⑪ Oil Seal
⑫ Combustion Chamber Model
⑬ Pulse Detecting Disk
⑭ Pulley
⑮ AC Commutator Motor
⑯ Micro Swich
⑰ Brake Disk
⑱ Displacement Meter
⑲ DC Amplifier
⑳ Digital Retarder
㉑ Transformer
㉒ Pulse Generator
㉓ Microflash
㉔ Photo Micro Sensor
㉕ Camera
㉖ Plane Mirror

Fig. 3 Schematic diagram of liquid injection system

the side wall of the square combustion chamber. The counter clockwise rotation of the swirl is defined as the positive direction.

The deflecting angle of the injector was varied from 0 to 60 deg since earlier studies indicated influence of the angle on engine performance [4].

B Spray Evaluation Set Up. The evaluation was conducted to ascertain mixing and fuel spray dispersion in the combustion chamber of the single-cylinder engine. The experimental investigation was carried out in a model chamber that duplicated the geometry of the engine combustion chamber and some of its operating parameters. Except for the thermal environment, the simulated fluid dynamic conditions in the model chamber and the injection system operating parameters were such that they duplicated, as much as possible, mixing conditions in the engine combustion chamber. The engine performance was then related to the combustion chamber design parameters via spray mixing and dispersion study. Figure 3 shows a schematic diagram of the liquid injection system designed to observe the behavior of the fuel spray. The apparatus consists of a single injection control unit, a mechanism for rotating the model chamber and a rapid stop mechanism to generate relative motion between the liquid and the chamber, and an electronic delay integrated with the operation of the strobe and the photographic equipment. The liquid injection technique (LIT) utilized piston models which were made of acrylic plastic. All model pistons used in the study had 59 ml cavities corresponding to the engine compression ratio of 17.0:1. The cavities were filled with water at ambient temperature and the piston models were rotated to simulate swirl motion in the cylinder of the experimental diesel engine. The rotational speed of the model chambers was such that it provided an equivalent swirl number of 3.15. The method of estimating the swirl number in a model chamber has been described earlier [4]. In addition, the spray was also studied under quiescent conditions in the piston models. Three distinct cavities were used in the model chamber: a circular cavity of 60 mm diameter (geometric factor, $r/R=1.0$), a square cavity with 55.2 mm side and a corner radius 18 mm (geometric factor$=0.65$), and a square cavity with 53 mm side and a corner radius 8 mm (geometric factor$=0.30$). To facilitate swirl generation the injector was located vertically with the injection tip 4 mm below the top surface of the model chamber. Three orifices of the nozzle were closed to avoid interference of the spray plume under examination with the other three plumes. The fuel injection pressure of the modified nozzle was maintained at the same level as the original 4×0.25 mm nozzle.

A xenon type strobe light, with color temperature 6500 K, flash duration of 4 μs, and power output of 4 W, was used to illuminate the spray, as shown in Fig. 3. A monochrome ASA 400 positive film was used to photograph images of the emulsified spray. The photographs were developed at constant fluid temperature (20°C)

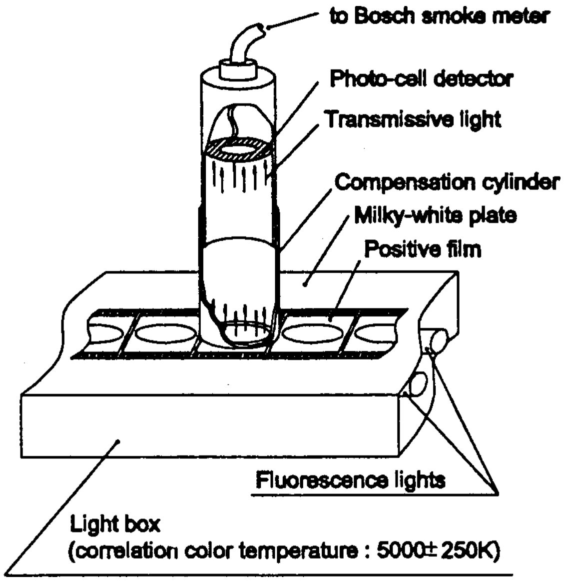

Fig. 4 Optional transmissivity measurement system

and constant processing time. The spray was photographed at intervals of 10, 20, and 30 ms from the start of injection. Several deflecting angles, ranging from 0 to 60 deg as viewed from the top, were used in the investigation. An optical method, based on optical transmissivity described in an earlier paper [4], was used to evaluate spray dispersion. The transmissivity, α, is a measure of transmission of the visible radiation through positive images of the spray. A lower value of α represents a well-dispersed spray and better mixing. A modified Bosch smokemeter set up, attached to a photocell detector and shown in Fig. 4, was used to estimate transmissivity of spray patterns. In order to measure transmissivity positive images of the spray were set between the detector and the light source keeping preset distance between the source and the detector. The value of α was 0 percent for completely shielded light and 100 percent when the developed film was perfect without any images. Only two-dimensional studies were conducted in this investigation. It is difficult to consider the influence of the depth of the square chamber on spray patterns and other results due to distortion of spray images that occur in the chamber [4]. Hence, the investigation was limited to two-dimensional spray images.

Experimental Results

1 Results of Engine Performance with S-type Chamber. Preliminary tests were conducted to assess general effects of the combustion chamber shape and the deflecting angle. The purpose of the tests was to evaluate if variations in deflecting angle and combustion chamber shape affected the engine performance significantly. The performance of the DI diesel engine with one of the combustion chambers, S-2, is shown in Fig. 5. Of all the combustion chambers shown in Table 2 the S-2 chamber showed better overall engine performance in terms of thermal efficiency and exhaust emissions. The engine performance with the S-2 chamber shows minimum specific fuel consumption at bmep $=0.6$ MPa and a deflecting angle $\theta_e=30$. Furthermore, for any given value of bmep the specific fuel consumption was found to be the lowest at $\theta_e=30$ deg. The emissions of oxides of nitrogen (NOx) were generally at their low value when the deflecting angle was set at 30 deg, as shown in the figure. The smoke density, *Sm*, was not affected much by the deflecting angle but it did increase with increasing brake mean effective pressure. Total hydrocarbons (THC) in the engine exhaust varied with deflecting angle and load, with the minimum appearing at $\theta_e=45$. The overall best performance of the test engine in terms of fuel consumption, NOx and exhaust smoke was achieved when the deflecting angle was 30 deg. This value of θ_e also allows simultaneous reduction of fuel consumption, NOx and THC. It is believed that spray dispersion and microturbulence occurring at the corners of the square combustion chamber help to achieve these results, as postulated in reference [4]. Through this study it was concluded that $\theta_e=30$ deg would provide relatively better engine performance with square chambers.

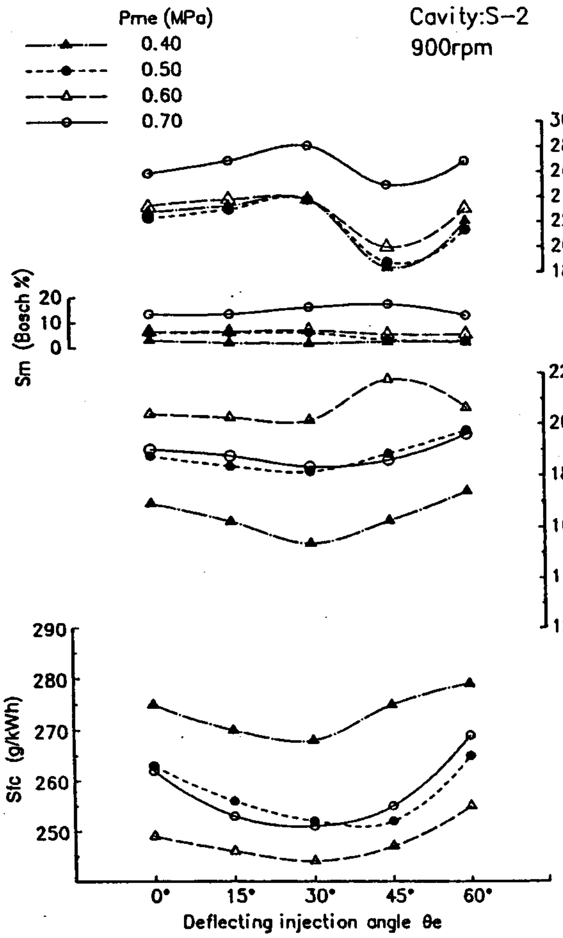

Fig. 5 Engine performance at 900 rpm with S-2 chamber

2 Results of Spray Behavior in Square Chamber. Studies of spray behavior were conducted to understand plausible relationships between the engine performance and spray dispersion in the combustion chambers. Several model chambers were used for the purpose.

Effect of Deflecting Angle θ_e. Figure 6 shows the simulated spray behavior in a square combustion chamber with geometric factor$=0.65$, a value very close to the geometric factor of chamber S-2. The simulated patterns were deduced from photographic images and transmissivity data of the dispersed spray in the model chamber. The swirl ratio for the swirling condition was 3.15, the same as in the actual engine, and the deflecting angle, θ_e, was varied from 0 to 60 deg. At $\theta_e=0$ the spray dispersed symmetrically under non swirling condition but it dispersed over a larger area, in somewhat asymmetrical fashion, under swirling condition, as shown in the figure. As the deflecting angle is increased to 15 deg the spray impinges on the wall and disperses asymmetrically under non-swirling condition. With swirl the spray dispersion is even further enhanced in the direction of the swirl. As the deflect-

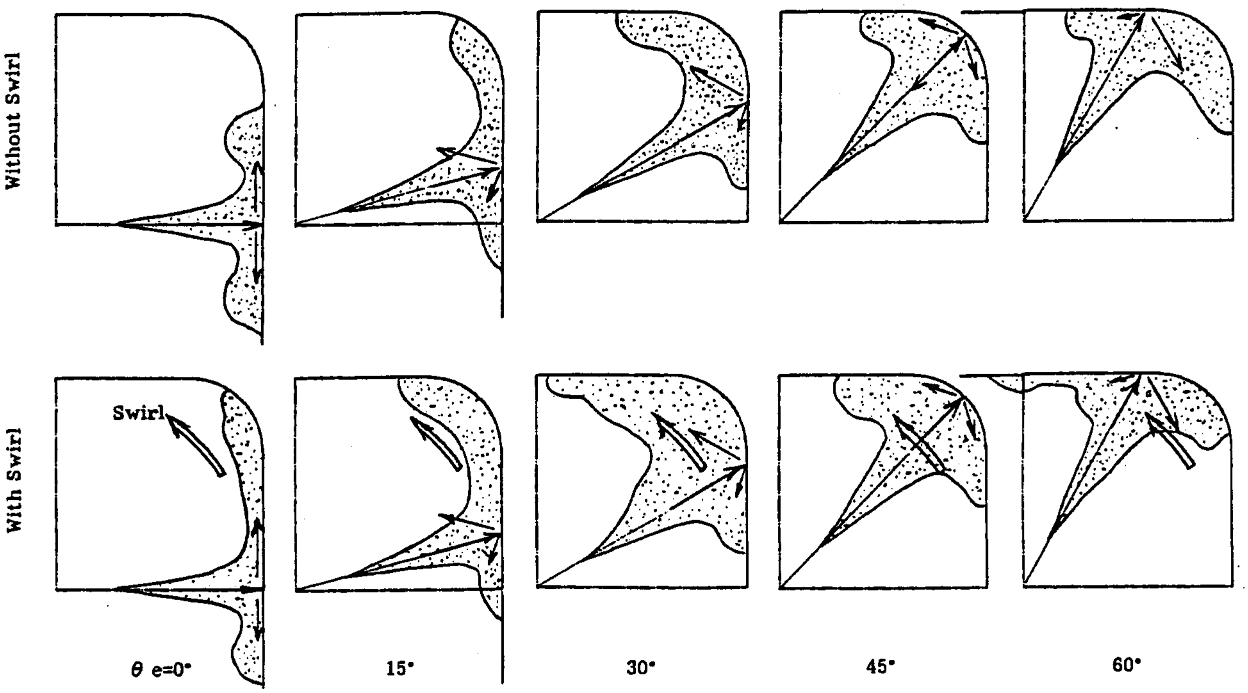

Fig. 6 Characterization of spray profile for various angles (time from the start of injection: 10 ms)

ing angle is increased it can be observed from Fig. 6 that maximum spray dispersion is achieved when $\theta_e = 30$ deg. As the spray penetrates the medium it impinges on the opposite wall and disperses over a wide area under non-swirling condition. With the presence of the swirl the downward flow gains velocity and achieves dispersion over a much wider area in the direction of the swirl.

Further increasing deflecting angle did not improve spray dispersion, as can be observed in Fig. 6. Increasing θ_e to 45 deg reduces the total area over which the spray is dispersed in non-

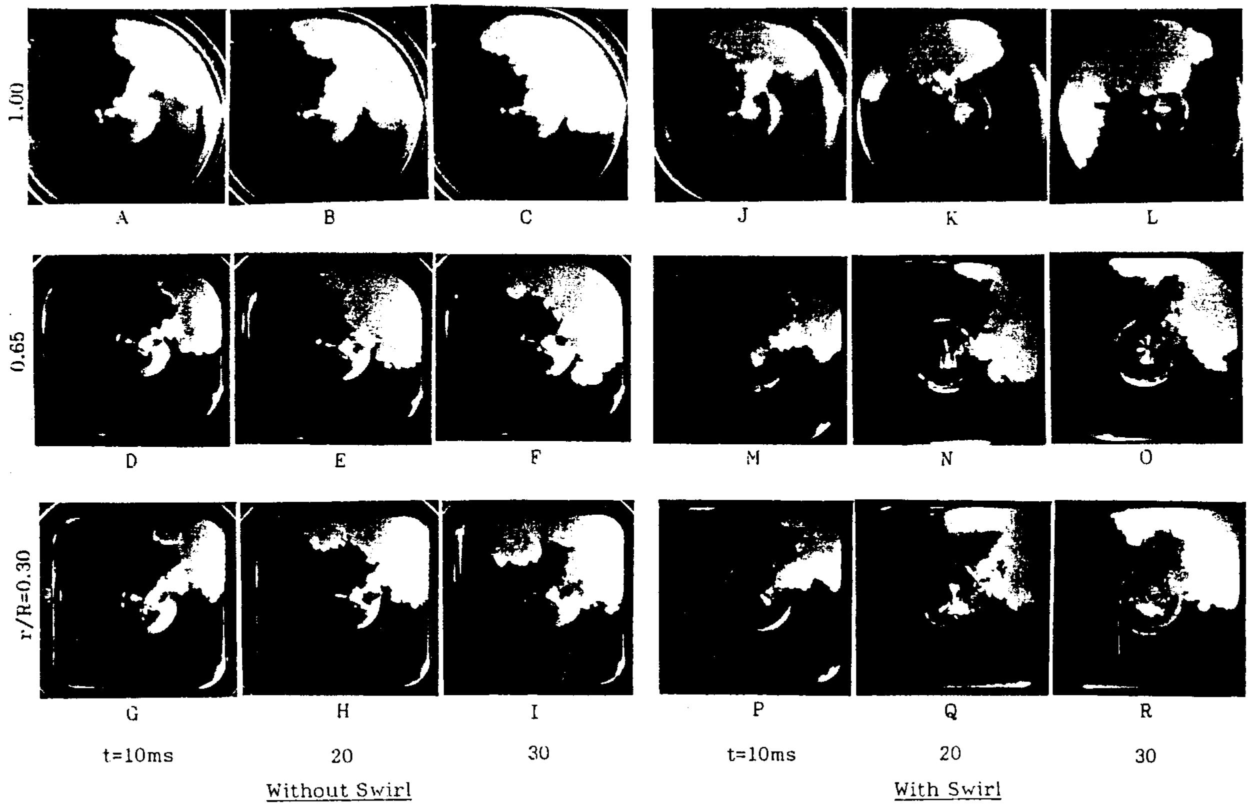

Fig. 7 Effect of geometric factor on emulsified spray patterns (deflecting angle=30 deg, t=time from the start of injection)

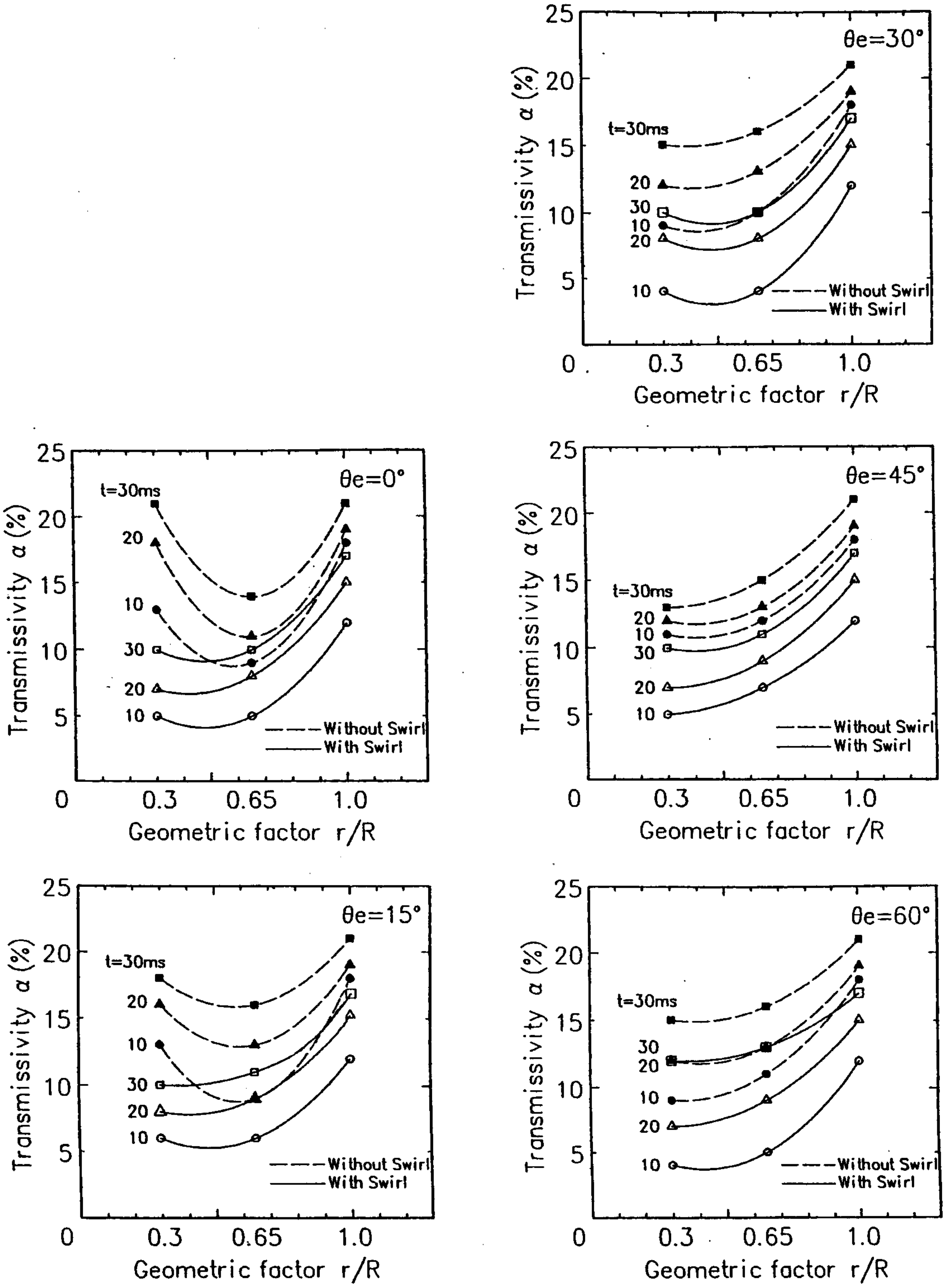

Fig. 8 Effects of geometric factor on optical transmissivity

swirling as well as in swirling environment. Similar trends can be observed when the deflecting angle was increased to 60 deg. The study shows qualitatively the influence of deflecting angle on spray dispersion in the model chamber of square geometry. In the present chamber configuration the best position of the spray trajectory was such that the deflecting angle was about 30 deg with the side of the square chamber.

Effect of Geometric Factor r/R. The configuration of the square combustion chamber, with the inscribed radius ''*R*'' consisted of four sides with rounded corners of radius ''*r*'', as shown in Fig. 2. The geometric factor, r/R, is expected to influence fuel and air mixing, and, hence, the combustion process in the engine. The geometric factor of the model chambers ranged from 1.0 (dish type chamber) to 0.30 (square chamber), the lower value being a limitation in square chamber design, as identified in an earlier publication [5]. The deflecting angle, θ_e, was maintained at 30 deg for the square chamber geometry. The effects of geometric factor on spray dispersion are shown in photographs in Fig. 7 under swirling and non-swirling conditions.

Table 3 Specifications of interchangeable piston cavities at geometric factor (r/R)

Combustion Configurations		F	S-1	S-4
Geometric Factor	r/R	1.0	0.6	0.3
Arc Radius	r (mm)	25	13	6.5
Inscribed Circle Radius	R (mm)	25	22	21.5
Cavity Height	H (mm)	30.6	32.3	32.0
Diameter Ratio	d/D	0.500	0.480	0.467

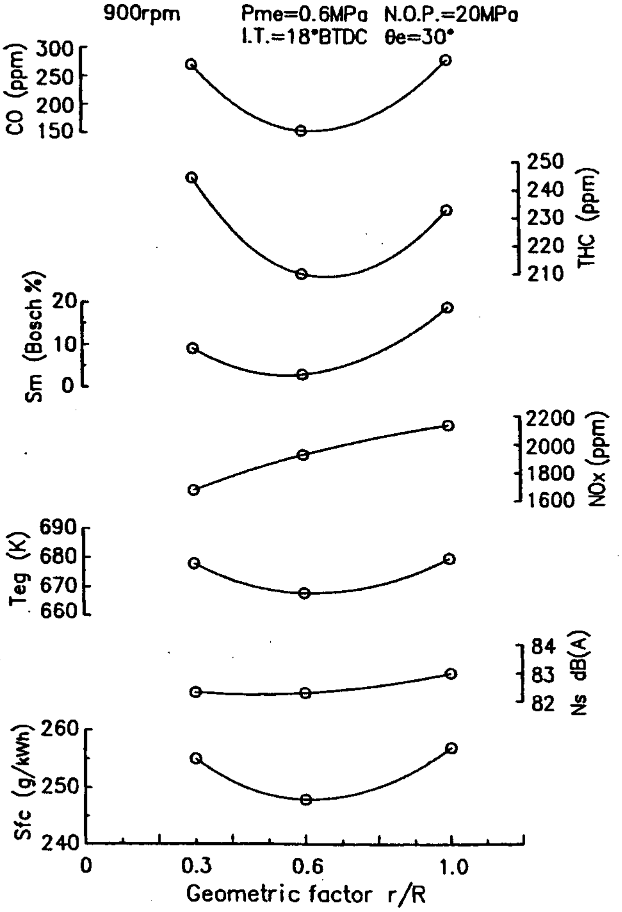

Fig. 9 Effects of geometric factor on engine performance (square combustion chamber, 900 rpm, Pme=0.6 Mpa)

Without swirl, the spray disperses along the side-wall and the lower surface of the dish shaped chamber with $r/R=1.0$. The spray disperses over a wider area with increasing time. When the spray was subjected to swirl, similar situation is observed. However, with swirl, the spray is dispersed much further along the direction of the swirl, as shown in images *J* to *L*. Comparison of images under swirling condition in dish and square shaped chambers show the spray being dispersed over a larger area in former than in the latter chamber. This may appear to enhance spray dispersion and fuel distribution. However, when multiple orifices of the nozzle are used dispersed sprays from orifices would interfere with one another causing nonuniform fuel distribution.

In the square chamber with a geometric factor$=0.65$, the spray impinges on the side wall and has a long residence time at the corner. It is then gradually dispersed with increasing time along the direction of the swirl, as shown in images *M* to *O*. With a lower value of geometric factor ($r/R=0.30$) the spray tends to disperse in somewhat nonuniform fashion. Under swirling flow the spray tip has almost uniform area and clings to side wall (image *Q*) well after the start of injection. Comparison of spray images at subsequent time after the start of injection exhibits somewhat restricted dispersion for the square chamber with larger geometric factor than for the smaller one. The spray dispersion for $r/R=0.65$ is expected to enhance fuel distribution and mixing when multiple orifices of the nozzle are used, as in the case of the single cylinder test engine.

It was observed from spray images at $\theta_e=30$ that the spray disperses along the straight side wall and is most affected by the side wall, the corner of the chamber and the swirl. At $\theta_e=45$ deg, the centerline of the spray plume has to travel the longest distance and the flow residence time at the corner is prolonged resulting in inadequate dispersion. When the deflection angle was increased to 60 deg, the trailing part of the spray plume moves upstream, as shown in the schematic patterns in Fig. 6. Of the five deflecting angles used in the study $\theta_e=30$ deg shows better spray dispersion in the chamber when all four orifices are functioning.

Relationship Between the Geometric Factor and Optical Transmissivity. Figure 8 shows the relationships between the optical transmissivity of the emulsified diesel spray and the geometric factor in quiescent and swirling water flow. The value of α increases very rapidly as the geometric factor increases beyond 0.65. As expected, for all values of deflecting angle, α is higher under quiescent flow than under swirling flow. However, the variation in α increases almost exponentially with an increase in geometric factor for deflecting angles of 45 and 60 deg, as shown in the figure. α does not vary much between geometric factors of 0.3 and 0.65 and small values of deflecting angle but increases rapidly for the dish type chamber ($r/R=1.0$). In this work it was difficult to evaluate absolute dispersion since no consideration of the dispersion area ratio was taken into account. Careful measurements of α at different values of θ_e and r/R show that the minimum was achieved when the deflecting angle was 30 deg at all time intervals considered in the study. A value of $r/R=0.65$ was preferred because it exhibited lower transmissivity at most of the time after the start of injection.

Based on spray images and optical transmissivity it appears that the square combustion chamber would improve spray dispersion in the DI diesel engine if the deflecting angle and the geometric factor are at 30 deg and 0.65, respectively. This would provide adequate good fuel and air mixing when a 4×0.25 mm injection nozzle is used in the engine.

3 Results on Engine Performance. Three different combustion chambers were used to evaluate the influence of geometric factors on engine performance. Table 3 shows dimensions of the interchangeable combustion chambers used in the experiments. The engine was operated at steady state at the following conditions: speed$=900$ rpm, injection nozzle opening pressure $=20$ MPa, injection timing$=18$ deg BTDC, deflecting angle $\theta_e=30$, and break mean effective pressure$=0.6$ MPa. At this value of bmep the engine fuel consumption was generally lower and it represented high load condition.

Figure 9 shows the effects of geometric factor on the engine performance parameters. The specific fuel consumption and emissions of carbon monoxide and total hydrocarbons were at minimum when the geometric factor was 0.60. The exhaust smoke level, measured with Bosch smoke meter, was also the lowest at $r/R=0.60$. Reducing the value of geometric factor from 0.60 to 0.30 increased fuel consumption and exhaust smoke. Comparison of engine performance with the two S-type chambers shows marginal improvement in NOx emissions and engine noise with the S-4 chamber (geometric factor$=0.30$) over the S-1 chamber (geometric factor$=0.60$).

Analysis of combustion process from the pressure-time data, shown in Table 4, exhibits a shorter delay and reduced burn duration with the S-1 combustion chamber than with the S-4 chamber. Furthermore, the time for maximum heat release rate in the S-1 chamber is earlier than in the cylindrical chamber by 0.3 deg and by over 4 deg in S-4 chamber. It appears that the square

Table 4 Combustion analysis value at geometric factor (r/R), ($N=900$ rpm, ∅ $e=30$ deg)

Combustion Configurations		F	S-1	S-4
Geometric Factor	r/R	1.0	0.6	0.3
Break Mean Effective Pressure	Pme (MPa)	0.60	0.60	0.60
Equivalence Ratio	ϕ	0.614	0.587	0.599
Indicated Mean Effective Pressure	Pmi (Mpa)	0.775	0.788	0.775
Maximum Cylinder Pressure	Pmax (MPa)	8.07	7.94	7.66
Rate of Pressure Rise	dP/d θ (Mpa/deg)	0.458	0.432	0.382
Crank Angle at Max. Heat Release	(deg)	7.3	7.0	11.4
Crank Angle at 10 % Mass Burning	(deg)	-5	-5	-4
Crank Angle at 90 % Mass Burning	(deg)	25	24	35

combustion chamber with $r/R=0.6$ provides rapid diffusion and afterburning of the mixture due to enhanced mixing created by moderate turbulence and swirling flow at the corners of the chamber. The S-4 chamber produced lower peak cylinder pressure and had higher exhaust gas temperature than the other two chambers. This indicates that the burn duration in S-4 chamber was longer due to inadequate mixing in the chamber cavity. The engine performance with cylindrical chamber with $r/R=1.0$ did not perform as well as the square chamber in terms of fuel consumption and emissions, as seen in Fig. 9.

The improvement in engine performance with square combustion chamber of $r/R=0.6$ is supported by spray dispersion investigation using LIT. The square chamber with $r/R=0.65$ qualitatively produced better spray dispersion and lower α (more dispersed spray with finer particles) than the chamber with $r/R=0.30$. The square shaped combustion chamber can improve engine performance of a DI diesel engine using a fuel injection system similar to the one utilized in the present study, provided its shape and geometric factors are optimized.

Conclusions

A liquid injection technique was used to evaluate diesel fuel spray dispersion in square combustion chambers. The spray distribution was evaluated qualitatively by visible observations and using intensity of scattered radiation through positive images of the spray. The results of the study can be summarized as follows:

1 The deflecting angle $\theta_e=30$ deg was found to produce spray distribution that resulted in good fuel and air mixing in the cylinder in a swirling flow.

2 The square combustion chamber, with geometric factor value between 0.60 and 0.65, helped to achieve adequate spray dispersion in swirling flow. This was supported by investigation of emulsified aspects of spray through analyses of positive images and by optical transmissivity technique.

3 Tests conducted on a single cylinder diesel engine showed improved engine performance when a square combustion chamber with spray deflecting angle and geometric factor, as identified in the above investigation, was employed. The engine fuel consumption was improved and the design provided overall reduction of smoke and other exhaust pollutants.

4 The experimental technique of using emulsified spray with LIT can qualitatively be used to evaluate effects of combustion chamber geometry and fuel systems design. It allows qualitative evaluation of model testing without extensive experimental facility.

Nomenclature

d = chamber cavity diameter, mm
D = cylinder bore diameter, mm
l/d = injection nozzle orifice length to diameter ratio
r/R = geometric factor, defined as the ratio of arc radius to inscribed circle radius
α = transmissivity (percent)
θ_e = deflecting angle, degrees

References

[1] Bardslay, M. E. A., Felton, P. G., and Bracco, F. V., 1988, ''2-D Visualization of Liquid and Vapor in an I. C. Engine,'' SAE Paper 880521.

[2] Nagaoka, M., and Osawa, K., 1990, ''Numerical Analysis of In-Cylinder Flow and Spray Motion in New DI Diesel Combustion Chamber,'' Trans. Jpn. Soc. Mech. Eng., **44**, pp. 3–8.

[3] Kahira, R., Mikami, Y., and Kinbara, M., 1983, ''The Advantages of the Isuzu Square Combustion Chamber for DI Engine,'' SAE Paper 830372.

[4] Watanabe, T., 1991, ''Visual Study of Influence of Combustion Chamber Configurations on Fuel-Air Mixing Process in DI Engine,'' SAE Trans., **99**, Sec 3, pp. 1826–1835.

[5] Watanabe, T., and Daidoji, S., 1993, ''A Few Experimental Considerations on the Spray Behavior for the Open Combustion Chamber of Square Type by the Liquid-Liquid Injection Technique,'' Proc. JSME, **930-9**, pp. 734–736.

Charles E. Mitchell

Daniel B. Olsen

Engines and Energy Conversion Laboratory,
Department of Mechanical Engineering,
Colorado State University,
Fort Collins, CO 80523

Formaldehyde Formation in Large Bore Natural Gas Engines Part 1: Formation Mechanisms

Recent testing of exhaust emissions from large bore natural gas engines has indicated that formaldehyde (CH_2O) is present in amounts that are significant relative to hazardous air pollutant standards. In consequence, a detailed literature review has been carried out at Colorado State University to assess the current state of knowledge about formaldehyde formation mechanisms and evaluate its applicability to gas engines. In this paper the following topics from that review, which bear directly on formaldehyde formation in natural gas engines, are discussed: (1) post combustion equilibrium concentrations; (2) chemical kinetics; (3) flame propagation and structure; (4) partial oxidation possibilities; and (5) potential paths for engine out formaldehyde. Relevant data taken from the literature on equilibrium concentrations and in-flame temperatures and concentrations are presented in graphical form. A map of possible paths for engine out formaldehyde is used to summarize results of the review, and conclusions relative to formation and destruction mechanisms are presented. [S0742-4795(00)00904-2]

Introduction and Problem Identification

As declared in the 1990 Clean Air Act Amendments, the US Environmental Protection Agency (EPA) is developing air toxic regulations for oil and gas production. The EPA is also scheduled to publish air toxic regulations for internal combustion (IC) engines by the year 2000. In addition, the gas industry is faced with Title V—Operating Permit regulations, with fast approaching deadlines for compliance. A stationary source that emits more than 10 tons per year of any single hazardous air pollutant (HAP), or cumulative HAP emissions in excess of 25 tons per year is deemed a major source under Title III, the ''HAPs Rule.'' HAPs do not include the primary pollutants, CO, NO_X, and total hydrocarbons (THC). They include a variety of aldehydes, volatile organic compounds, semi-volatile organic compounds, sulfur compounds, and metals. Formaldehyde and many of the other aldehydes are known contributors to photochemical smog [1] and irritants of the skin, eyes and nasopharyngeal membranes [2]. Formaldehyde is postulated to react with ionic chloride compounds in the air to produce bischloromethyl ether [3,4], a suspected carcinogen. Studies performed at the Chemical Industry Institute of Toxicology indicate an increased incidence of nasal cancer in rats exposed to high concentrations (15 ppm) of formaldehyde [5]. The current Occupational Safety and Health Administration (OSHA) 8-hour time weighted average permissible exposure limit for formaldehyde is 1 ppm (Title 29, CFR) and is expected to be reduced to 0.75 ppm in the coming years.

As discussed in Part 2 of this paper (see also Olsen and Mitchell, [6]) recent data from stationary large bore engine sites indicate that in some cases formaldehyde emissions would have to be reduced by 90 percent in order to avoid being designated a major source under Title III. To obtain reductions of this magnitude, a clear understanding of how formaldehyde is formed in large-bore natural gas engines is needed.

In this work, a thorough literature search and review was carried out on formaldehyde emission and related topics. Of particular interest was the identification of locations, events and operating conditions in large-bore engines which favor formaldehyde formation or, equally important, its destruction. Formaldehyde is known to be a critical intermediate specie in the chemical mechanism through which natural gas burns in air. Thus, the potential for having some quantity of formaldehyde in the products of combustion always exists. It is crucial that those physical and chemical phenomena which affect whether and to what extent this potential is realized in an operating engine be determined. In this paper the following topics bearing on formaldehyde formation are reviewed:

- equilibrium (thermodynamic) considerations
- chemical kinetics (including reduced mechanisms)
- flame propagation (laminar flame structure and turbulence effects)
- partial oxidation possibilities (locations outside of flames)
    1. end gas reactions
    2. bulk quenching
    3. mixing effects
    4. partial oxidation during the compression stroke
    5. wall quenching
    6. crevices and crevice outflow
    7. protection in oil layers and solid deposits
    8. exhaust flow reactions
- paths for engine out formaldehyde (a map of possible paths)

A list of conclusions based on the review completes the presentation. In a companion paper [6] the present authors use the results of this review to interpret measured emissions from large bore natural gas engines.

Equilibrium Considerations

A fundamental question is whether and to what extent formaldehyde is favored as a combustion product thermodynamically. That is, if the chemical reactions consuming natural gas and air at some equivalence ratio are allowed to reach the equilibrium composition predicted by thermodynamics, how much CH_2O would be present? Calculations of this type can be performed using standard thermochemical databases [7,8]. Results of such calculations for methane in air have been presented by Vlachos et al. [9]. A plot of some of the data presented in that work is displayed in Fig. 1. Shown in the figure are adiabatic equilibrium temperatures

---

Contributed by the Internal Combustion Engine Division of THE AMERICAN SOCIETY OF MECHANICAL ENGINEERS for publication in the ASME JOURNAL OF ENGINEERING FOR GAS TURBINES AND POWER. Manuscript received by the ICE Division November 6, 1998; final revision received by the ASME Headquarters December 29, 1999. Technical Editor: D. Assanis.

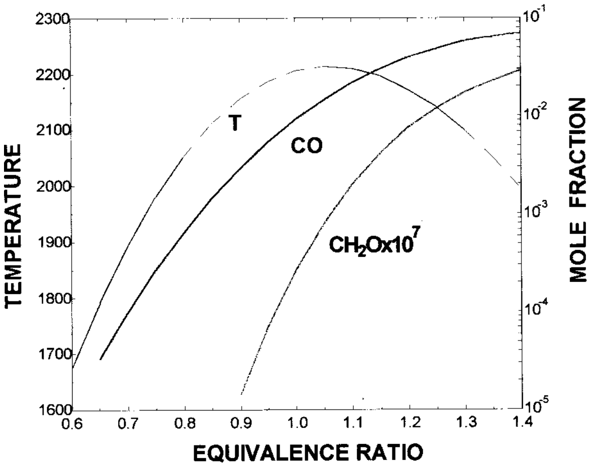

Fig. 1 Equilibrium temperature and composition: methane/air

(flame temperatures) and the equilibrium mole fractions of CO and CH_2O for a range of equivalence ratios. Note that the curve for CH_2O represents its calculated value times 10^7. It is apparent that the equilibrium quantities of formaldehyde are predicted to be very small indeed. For stoichiometric and lean mixtures the amount is in all cases less than 0.1 ppb. The predicted mole fractions for both CO and CH_2O decrease with increasing mixture leanness, though the rate of decrease is more rapid for CH_2O. Additional calculations performed by Vlachos et al. for lower temperatures (due to heat transfer losses) and fixed mixture equivalence ratios further indicate a rapid decrease of CH_2O concentration with decreasing flame temperature. Measured engine exhaust mole fractions of formaldehyde can exceed 50 ppm in large bore engines burning natural gas [10]. It is clear then, that super-equilibrium (by a factor of 5×10^5) amounts of CH_2O are formed somewhere in the engine combustion process and survive into the exhaust stream. Thus, partial oxidation and incomplete combustion must be instrumental in the formation of significant amounts of formaldehyde. In consequence of this, the time and space dependent physical and chemical mechanisms comprising the overall engine combustion process must play critical roles in CH_2O generation in large bore engines.

Chemical Kinetics

Detailed kinetic schemes for the combustion of methane are readily available in the literature [11–13]. These mechanisms are hugely complex and typically involve more than one hundred elementary reaction steps and thirty chemical species. Their validity for a wide range of combustion phenomena such as ignition and flame propagation has been established experimentally [14,15]. A schematic representation of the main kinetic steps, which includes only the most important C_1 and C_2 pathways, is summarized in Fig. 2, adapted from Crawford and Wallace [16]. The importance of CH_2O as an intermediate specie in the scheme is apparent. The primary C_1 path leading to the intermediate product CO goes directly through formaldehyde. The secondary path passing through C_2H_6, C_2H_4, etc. complicates the mechanism considerably but can play a significant role under some situations, particularly for rich and low temperature mixtures, as discussed by Glassman [17]. This path also includes CH_2O as a basic intermediate specie. The so-called C_2 path has been neglected in some modeling work (see for example Vlachos [9], or Peters and Rogg [18]) but the validity of doing this must be examined carefully for the particular physical situation being treated.

Reduced Kinetic Mechanisms. The detailed kinetic mechanisms just discussed are extremely complex and time consuming computationally. A great deal of effort has been expended since the early 1980s to simplify the overall kinetics to a few reaction steps suitable for engineering calculations in particular combustion situations such as flame propagation and ignition. The early work of Westbrook and Dryer [13] was particularly important. The philosophy and methodology used to effect the required simplifications is well explained and summarized by Dryer [15]. A monograph devoted entirely to reduced kinetic schemes for methane air flames became available in 1991 [19]. The collection of papers edited by Peters and Rogg [18] emphasizes applications of reduced kinetic mechanisms to both premixed and diffusion controlled combustion problems. In all of this work the importance of testing any reduced scheme against the predictions of the complete detailed mechanism or (preferably) against experimental measurements is emphasized. Using only part of any detailed mechanism is not advised and any reduction should be pursued with great caution. This said, it is also true that for some applications, notably laminar flame propagation, reduced kinetic schemes can work well.

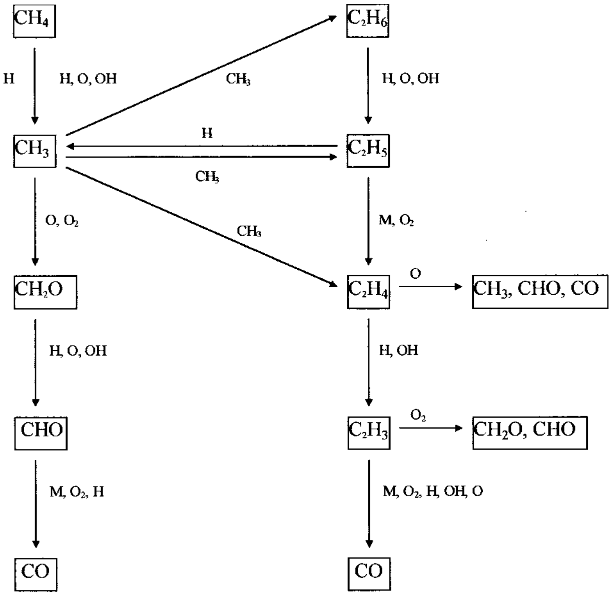

Fig. 2 Methane combustion mechanism

Flame Propagation

The chemical mechanism by which natural gas is burned to products is of fundamental importance in understanding how CH_2O is formed in engines. However, the engine combustion environment is not homogeneous in space or time and chemical kinetics consequently can give only part of the picture. Physical phenomena including heat transfer, diffusion, and fluid mechanics also play critical roles in the combustion process and thus in the formation and destruction of formaldehyde in real engines. For example, a flame of some kind is generally agreed to propagate through the premixed charge in the engine. The flame structure and speed depend not only on chemistry but also on the rate of diffusion of heat and species in the flame and on the level of turbulence in the gases. Though flame propagation in a real engine is certainly turbulent, examining laminar flame structure gives some insight on how and where CH_2O may be formed. Calculations using a complete kinetics scheme for methane-air mixtures and standard one dimensional equations for laminar flame propagation including diffusion of heat and species have been completed by Ruy [20]. Results plotted from his data are presented in Figures 3 and 4 for an equivalence ratio of 0.89.

Shown in Fig. 3 are the mole fractions of CH_2O, CO, and OH as a function of distance through the laminar flame (note that the mole fraction of CH_2O is in ppm while the other species are not).

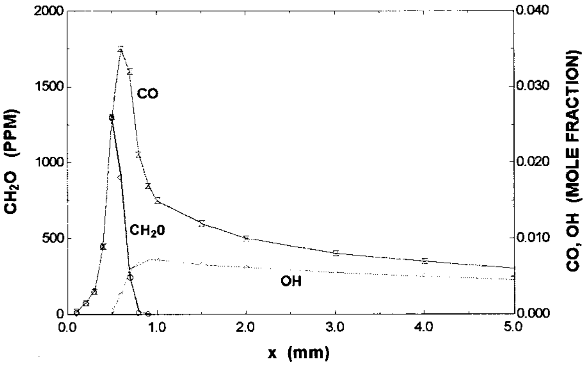

Fig. 3 Laminar flame mole fractions

Physically, the figure may be thought of as representing composition results for a stationary flame with reactants at $x=0$ and final (equilibrium) products to the right at large values of x. Both CH_2O and CO are seen to peak early in the flame, with the peak in CH_2O (at about 1300 ppm) occurring noticeably before that of CO. After peaking the amount of CH_2O falls rapidly to a negligible quantity about one mm through the flame.

In Fig. 4 temperature and mole fraction of NO (in ppm) are displayed for the same flame. The temperature rises steeply to approximately 80 percent of its equilibrium value at 1 mm through the flame and then continues a slow increase as additional CO is burned to CO_2 further through the reaction zone. Comparison of the temperature and CH_2O curves indicates that the peak in formaldehyde concentration occurs at a temperature near 1100 K in the flame and that almost all the CH_2O is gone by the time the temperature reaches 1500 K. Predictions related to formaldehyde formation in laminar flames can be summarized as follows:

1 CH_2O is formed and peaks in concentration very early in the flame.

2 It is consumed rapidly as the primary radical pool of OH, H, and O develops and disappears almost entirely before this pool reaches its maximum concentration.

3 Though both CO and CH_2O peak early in the flame, the CH_2O peak occurs first, at a distinctly lower temperature.

4 Essentially no CH_2O survives into the downstream post flame region. This is in contrast with results for CO and NO concentrations, which have significant values there.

The conclusion is that CH_2O is not likely to be found in products of combustion formed as the result of a self-propagating flame in an engine burning natural gas. The formaldehyde that is born in a propagating flame dies there as well. Moreover, because of the rapidity with which CH_2O is destroyed in the presence of free radicals such as O, H, and OH (recall observations no. 1 and 2 above), any unburned CH_2O/air mixed with the products of combustion at temperatures which are above about 1200 K also should be consumed very quickly indeed.

Effects of Turbulence on Flame Propagation. The mixture of natural gas and air, into which the flame propagates in a large bore engine, exists as a turbulent flowfield which affects both the speed of the flame and its character. The intensity and scale of the turbulent flow depends in a complex and not yet well understood way on such factors as piston speed, cylinder clearance volume and residual turbulence from the gas exchange process. Following Williams [21] it is possible to make predictions about the qualitative nature of the turbulent combustion process using a map dependent on two non dimensional parameters, the Damkohler number (Da) and the turbulent Reynolds number. The Damkohler number is the ratio of a characteristic flow time to a characteristic chemical reaction time. The turbulent Reynolds number compares turbulent to molecular transport. Da and Re were calculated for a Cooper-Bessemer large bore engine, assuming that the fuel was methane and the equivalence ratio 0.73, using approximate techniques suggested in the literature [12]. The resulting operating point was then placed on a Da versus Re map, as indicated in Fig. 5.

Shown in the figure is a rectangle, which represents the approximate domain of spark ignition engines as described by Turns [12]. The calculated point for the Cooper-Bessemer engine can be seen to fall near the upper right hand boundary of the rectangle. About two thirds of the spark ignition engine domain, including the calculated large bore engine point, lie above the line separating the reaction sheet region from the flamelets in eddies region. In the flame sheet regime the turbulent flame is characterized as a laminar flame distorted by turbulence to the extent that its reaction area and consequently its flame speed are increased substantially. As far as the generation and destruction of CH_2O are concerned, the conclusions reached for laminar flames should hold for the turbulent flame sheet structure as well. Formaldehyde is formed early in the (thin) flame sheet and is consumed by reaction before the flame temperature is reached. The products of combustion behind the turbulent flame sheet should contain essentially no formaldehyde. In the flamelets in eddies region, turbulent mixing becomes increasingly important with decreasing laminar flame

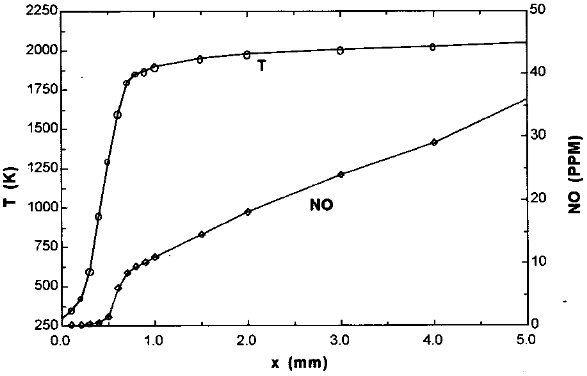

Fig. 4 Laminar flame temperature and NO

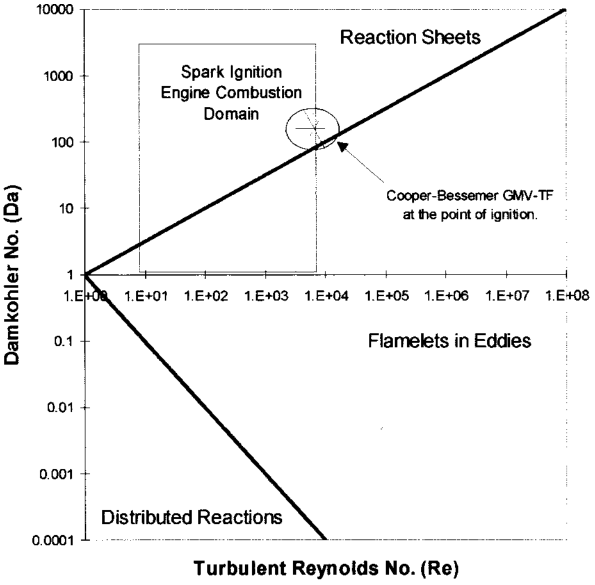

Fig. 5 Engine Damkohler map

speed or increasing turbulent intensity. Eventually the flame structure is broken into eddies where predictions based on combustion models for laminar flames will not be accurate.

Photographic evidence of flame sheet type behavior in a large bore two cycle gas engine of the same type as the one in Fig. 5 was presented decades ago by Boyer and co-workers [22]. Both the original motion picture along with the still photographs made from it [22] show a clearly identifiable wrinkled flame front propagating through the combustion chamber away from the spark ignition source.

Formaldehyde Formation Outside of Flames

According to the kinetic scheme for methane combustion discussed above, it should be possible for CH_2O to form in regions of an engine outside of a propagating flame, as long as the temperature and mixture ratio are in the correct range and there is adequate time. Possible locations in the engine where this might occur include the bulk of the unburned charge (end gas) during flame propagation, the unburned mixture during the compression stroke, protected regions such as crevices and walls, rich or lean regions of the charge caused by poor or incomplete mixing, and portions of the exhaust flow, especially near exhaust ports.

End Gas Reactions. The rate of reaction in the premixed combustible gases in front of the propagating flame in an engine has long been of interest because of its importance in auto-ignition and knocking. Computational studies of the chemical kinetics and ignition time of natural gas mixtures in air under conditions typical of those found in the unburned end gas of engines have been carried out extensively by Westbrook and co-workers [23,24,25]. One prediction of practical significance from this work is the sensitivity of the ignition delay to natural gas composition. Small amounts of ethane or higher hydrocarbons added to pure methane are found to substantially reduce the predicted ignition time. For example, in one calculation the reported ignition time for a stoichiometric pure CH_4 air mixture was 100 ms. In contrast, a 95 percent CH_4, 5 percent C_2H_6 fuel mixture in stoichiometric proportion with air had a predicted ignition time of 8.3 ms. An increase in the amount of ethane in the fuel to 10 percent further reduced the ignition time to 3.2 ms, while further increasing the amount of ethane to 20 percent only reduced the ignition time to 1.7 ms. The conclusion is that the kinetics are very sensitive to small additions of ethane to pure methane, but that the impact is not linear and decreases rapidly with increasing amounts of ethane. These predictions are supported by subsequent experimental work at least in a qualitative way [24,25].

In none of this work was the amount of formaldehyde produced during the pre-ignition period reported, though its importance as a specie in the kinetic mechanism at the relevant temperatures and pressures was discussed [23]. Nevertheless, the work does have an implication as far as formaldehyde formation in large gas engines is concerned. This is that, because of the important role that higher hydrocarbons play in the pre-ignition regime, computations or experiments attempting to quantify formaldehyde production in gas engines should not use or be based on pure methane-air mixtures, but rather should include at least a small amount of a higher hydrocarbon. It is unlikely that kinetic models including only the C_1 path, which ignores higher hydrocarbons completely, can predict the rate of formaldehyde production adequately.

Bulk Quenching During Expansion. If a vigorous turbulent flame eventually propagates through the reacting end gases just discussed then any CH_2O formed in front of the flame will be consumed completely. However, if the temperature and pressure drop rapidly because of piston motion then the flame propagation may be slowed and weakened to the extent that complete consumption of all the end gas volume does not occur. Partial oxidation products, including formaldehyde, as well as unburned fuel may survive through the expansion stroke and into the exhaust. This type of bulk quenching is known to occur to some extent in gasoline engines, especially for lean mixtures [26]. It has also been blamed for a significant fraction of the formaldehyde emissions from methanol engines [27,28]. Because of the increased volume and consequent increased flame propagation distance typical of large bore gas engines, it might seem that this type of bulk quenching could be more important in them. However, the high level of residual turbulence in the cylinder resulting from the scavenging process, along with low engine speeds conspire to enable the completion of flame propagation before significant drops in pressure and temperature can occur due to piston motion. Examination of the flame propagation films in a large bore engine and the photographs taken from them mentioned above [22] indicate that the flame requires only about 13 deg of crank angle to complete its propagation starting from spark discharge. Pressure data taken CSU on a similar engine also indicate that 90 percent charge consumption takes well under 20 deg of crank angle. This means that the flame propagation event takes approximately half the crank angle typical of many automotive gasoline engines [26]. Thus, bulk quenching because of a long flame propagation time may be *less* likely in large bore two cycle engines.

Mixing Effects. To this point it has been assumed that the mixing of fuel and air in the engine is adequate so that premixed flame propagation controlled by chemical kinetic and turbulent mechanisms occurs and that, outside of flames, homogeneous chemical reactions dominate as well. Direct injection lean burn two stroke engines and clean burn two stroke engines make up a significant percentage of operating gas engines [10]. Both types of engines are designed to reduce NO_x production by burning at overall air/fuel ratios that are very lean. Moreover, both designs require substantial in-cylinder mixing since fuel and air enter the cylinder non-premixed or only partially premixed. If the mixture ratio in some parts of the chamber is too lean to support a self-propagating flame, then these components of the gas charge must burn through mechanisms dominated by turbulent diffusion and mixing. In some cases they may not burn at all, but only react to the extent that partial oxidation products such as formaldehyde are produced. Note that if the rate of diffusive reaction is slow enough that the bulk temperature in the cylinder falls to low values before these unburned fractions are burned, then there is no subsequent mechanism for their complete combustion. In these engines, modeling the combustion event by turbulent premixed flame propagation combined with homogeneous chemical kinetics would be seriously in error. Bulk quenching caused by inadequate mixing could be a major source of formaldehyde in this case.

Considerable experimental work is needed to define and describe the state of the gas at the time of ignition as it relates to the mixing of fuel and air. It is not clear at all that lean burn and clean burn engines used today can be described adequately as premixed combustion engines.

Partial Oxidation During the Compression Stroke. During the compression stroke in engines, high pressures and temperatures close to those necessary for rapid formaldehyde formation can occur. Thus, the question of whether any significant CH_2O can really be generated during this compression process arises. Karim and co-workers [11] modeled the pre-ignition reactions which occur during the compression stroke in a dual fuel engine. They used a comprehensive kinetic mechanism for methane-air combustion and carried out computations that tracked temperature and the important pre-ignition species as a function of time (or crank angle). Results indicated that under some conditions very large amounts of formaldehyde were predicted near the end of the compression stroke as the piston approached top dead center. For example, at an equivalence ratio of about 0.6, a maximum CH_2O concentration of approximately 1 percent by volume (10,000 ppm) was predicted at 10 deg BTDC. After this point the formaldehyde was consumed rapidly and was essentially absent by 5 deg BTDC. For the given mixture ratio this means that at 10 deg BTDC approximately 20 percent of the methane initially present at the start of the compression stroke had been converted to formaldehyde. In considering the applicability of these results to large gas engines it must be pointed out that the compression ratio in the work cited was 14.2 to 1 and that the predictions were based on a kinetic scheme for pure methane which did not include any higher hydrocarbons as part of the fuel. Still, this work suggests that significant quantities of formaldehyde may be formed during the compression stroke because of the relatively long compression times typical of large gas engines. Westbrook, in his work on the effect of gas composition on knocking in gas engines [23], also speculated that pre-ignition reactions might advance to some considerable extent during compression, though no calculations were reported.

Wall Quenching. Because of heat transfer losses, flames in an engine cannot propagate all the way to wall surfaces nor penetrate crevices with wall spacings that are sufficiently small (less than the quenching distance). Within these protected volumes partial oxidation of natural gas-air mixtures may occur and result in the generation of significant amounts of formaldehyde. The phenomenon of wall quenching, particularly as a source of unburned hydrocarbons, has long been the focus of considerable computational and experimental work [26,29–31]. The general consensus from these efforts has been that the flame does not propagate to the wall but reaches a standoff distance that depends on the fuel and operating conditions. Subsequently, the fuel-air mixture between the flame and the wall diffuses into the flame and is converted to products in times that are on the order of a few milliseconds. Thus, even if formaldehyde is created in the region between the wall and the flame, most of it will be destroyed in the hot products of combustion in times that are short compared with the residence time of the gas in the engine. For reference, in typical automotive gasoline engines the amount of fuel that is protected from combustion by wall quenching is small, estimated as being on the order of 0.5 percent. About 2/3 of this is eventually burned completely before leaving the engine [26]. Wall quenching has been identified as a significant source of formaldehyde in methanol engines, particularly at low loads with cold walls [27,28]. The effect is probably exaggerated compared with natural gas engines because of the impingement of liquid methanol on the walls of the chamber.

More recent computational work by Vlachos et al. [9] has extended the earlier work to include some flow effects near a wall. In this model a combustible mixture of methane and air impinges on a planar hot wall in a stagnation point flow. This might represent, in a general way, a flow of unburned gases fed by a local vortex near the wall into hot products of combustion. Calculations for a wide range of wall temperatures and flow rates were carried out using a detailed kinetic model coupled with a fluid dynamics code. Results included predictions of formaldehyde concentration as a function of distance from the wall. Multiple solutions were found to exist for many equivalence ratios and wall temperatures, indicating the existence of both ignited and extinguished branches for the flow. For extinguished branch solutions (in which ignition did not occur), the concentration of CH_2O at the hot wall was predicted to be several orders of magnitude higher than for the ignited (flame) solution branch. For example, at a wall temperature of 1700 K and an equivalence ratio of about 0.6, CH_2O concentration was predicted to be more than 2000 ppm. An implication of this work is that turbulent flows near the wall may exhibit multiple extinctions and ignitions and result in the production of locally high levels of formaldehyde.

Crevices and Formaldehyde. The crevice volumes into which flames do not propagate may serve as sources of formaldehyde. The question of whether flames can propagate into a given crevice is determined by calculating the quenching distance for the given fuel air mixture and comparing it with the wall separation distance for the cavity. If the wall separation distance exceeds the quenching distance, then the flame may propagate into the crevice. Quenching distance depends inversely on the laminar flame speed and pressure, neither of which is size dependent [12]. For the larger crevices of large bore engines then, flame propagation into the crevices becomes more likely and crevice protection less likely.

If the temperature is in the right range and the residence time in the crevice is long enough, then partial oxidation to CH_2O may occur to some appreciable extent in the cavity itself. However, given the high surface volume ratios for crevices and the cold walls available for heat transfer it is unlikely that the temperature is high enough (above about 650 K [27]) for significant reaction to occur. Indeed, if the wall temperature is used to estimate the crevice gas temperature as has been done previously by Cheng et al. [26], then no reaction is possible.

Even when little or no formaldehyde is produced in the cavity, a combustible mixture from the crevices may be mixed with the oxygen rich products of combustion in the engine cylinder and react to form CH_2O and other partial oxidation products during the blowdown, exhaust and gas exchange process. If the combustion product gases are at too high a temperature, above about 1300 K, then the unburned gases from crevice volumes will themselves burn very rapidly when mixed with them [32–34]. In this case none of the formaldehyde which is formed can subsequently survive, since it is destroyed at temperatures below those necessary for complete combustion. After the expansion stroke, however, bulk gas temperatures seldom exceed 1000 K, and partial reaction to formaldehyde should be possible. For gasoline engines it is estimated that, overall, approximately 1/3 of the gas mixture protected in crevices is not consumed and leaves the cylinder [26]. A much lower estimate is given for the survival of fuel that is stored in crevices for an engine burning propane [34]. In that work only about 10 percent to 15 percent of the stored fuel survived and was measured in the exhaust. Formaldehyde formed from crevice gases during the exhaust stroke has also been the mechanism used to explain qualitatively the measured time resolved CH_2O concentrations emitted from methanol fueled engines [27,28].

Formaldehyde From Oil Layers and Solid Deposits. For conventional gasoline four stroke engines it is estimated that about 1/3 of the unburned fuel in the exhaust comes from fuel absorbed and later desorbed in oil layers and solid deposits on engine surfaces [26]. If a similar fraction were protected in natural gas engines these layers could be a significant source of formaldehyde. However, the amount of methane that can be absorbed in oil is much smaller than for gasoline. Engine tests run with and without oil layers present indicate that no measurable change in HC emissions occurs when propane is used as the fuel. In contrast, HC emissions increase substantially (of the order of 35 percent) for gasoline when oil layers are present [35]. Since the solubility of methane in oil is about ten times smaller than for propane in oil, the amount of methane that can be stored in oil layers in gas engines is almost certainly negligible. The solubility of ethane in oil is somewhat greater than that of methane but still less than that of propane, so none of the major components of natural gas should be absorbed to any significant extent in engine oil layers.

For typical gasoline engines it is estimated that about the same amount of fuel is stored in solid deposits as in liquid oil layers, that is about 1 percent of the fuel supplied [26]. However, since the saturation pressure for methane is about 100 times that of gasoline at engine wall temperatures, it is to be expected that the amount of methane absorbed in solid deposits in gas engines should be very small in comparison. Laboratory experiments [36] using activated carbon at room temperature tend to support this. Finally, it should also be noted that the surface to volume ratio for large bore engines is smaller than for typical gasoline engines by a factor of four or so, making the importance of both solid deposits and oil layers even less consequential.

Formation of Formaldehyde in the Exhaust Flow. Depending on temperature and composition of the exhaust gases it is possible for formaldehyde to be formed or destroyed during the flow out of the exhaust port and through the rest of the exhaust system. For low enough temperatures, kinetic rates will be so slow that essentially no reactions either forming or destroying CH_2O occur. At higher temperatures pre-ignition fuel-air reactions may dominate and result in the net production of formaldehyde, as long as unburned fuel and oxygen are present in the exhaust gases. At higher temperatures than this, the quantities of both unburned fuel and formaldehyde entering the exhaust system will probably be diminished as they are burned to products such as CO, CO_2, and H_2O. In this last case formaldehyde will be formed as an intermediate specie, but subsequently it will be consumed rapidly and completely, as it is in a laminar flame. Thus, a temperature window for net formaldehyde production in the exhaust may well exist. Based on existing kinetic calculations and experiments it is possible to make rough estimates of the temperature limits for the formation window.

Kinetic calculations and experiments applicable to methanol-air combustion and formaldehyde formation in exhaust flows were reviewed by Kim and Foster [27]. They cite results of isothermal flow reactor calculations indicating that above 890 K methanol oxidation and formaldehyde destruction are very fast. Indeed, the complete disappearance of both formaldehyde and unburned fuel in 50 msec of reactor time was predicted at this temperature. On the other hand, at 700 K methanol oxidation and formaldehyde formation were found to be very slow. Composition became completely frozen at a temperature of 643 K. The oxidation kinetics of methane and methanol have some overall similarity, though differences in chain initiation and H atom abstraction make methane kinetics somewhat slower, particularly at low temperatures. In view of this, it seems reasonable to accept a low temperature limit for formaldehyde formation in the exhaust of about 700 K, and a high temperature threshold for rapid formaldehyde destruction of about 900 K.

Average exhaust gas temperatures were measured for all of the large bore engine tests reported in the Radian work [10]. For all of the two-stroke engines the measured temperature was less than 620 K. This value is well below the estimated minimum temperature required for formaldehyde formation. The temperature measurements were taken at unspecified locations in the exhaust duct. Thus, higher temperatures in and just downstream of the exhaust port are to be expected. For almost all of the two-stroke engines, however, the maximum temperatures measured *in the engine* at locations near the exhaust port were less than 690 K. This value is still below the low temperature limit for formaldehyde formation.

The exhaust temperatures for the lean-burn and rich-burn four-stroke engines were considerably higher, reaching in excess of 790 K in several of the tests and usually above 700 K. Clearly, formation of formaldehyde in the exhaust is a distinct possibility for this engine class.

Paths for Engine Out Formaldehyde

The main formation and destruction possibilities for formaldehyde are summarized in the simple qualitative diagram presented in Fig. 6. It is necessary to track both unburned fuel (represented by HC in the figure) and formaldehyde since CH_2O forms directly from the surviving fuel. The HC path is represented by solid lines and arrows; the CH_2O path is dashed.

The trapped fuel-air mixture is both compressed and heated during the compression stroke. As discussed above, depending on such factors as the compression ratio, initial temperature and mixture ratio, it is possible for some fraction of the fuel to be partially

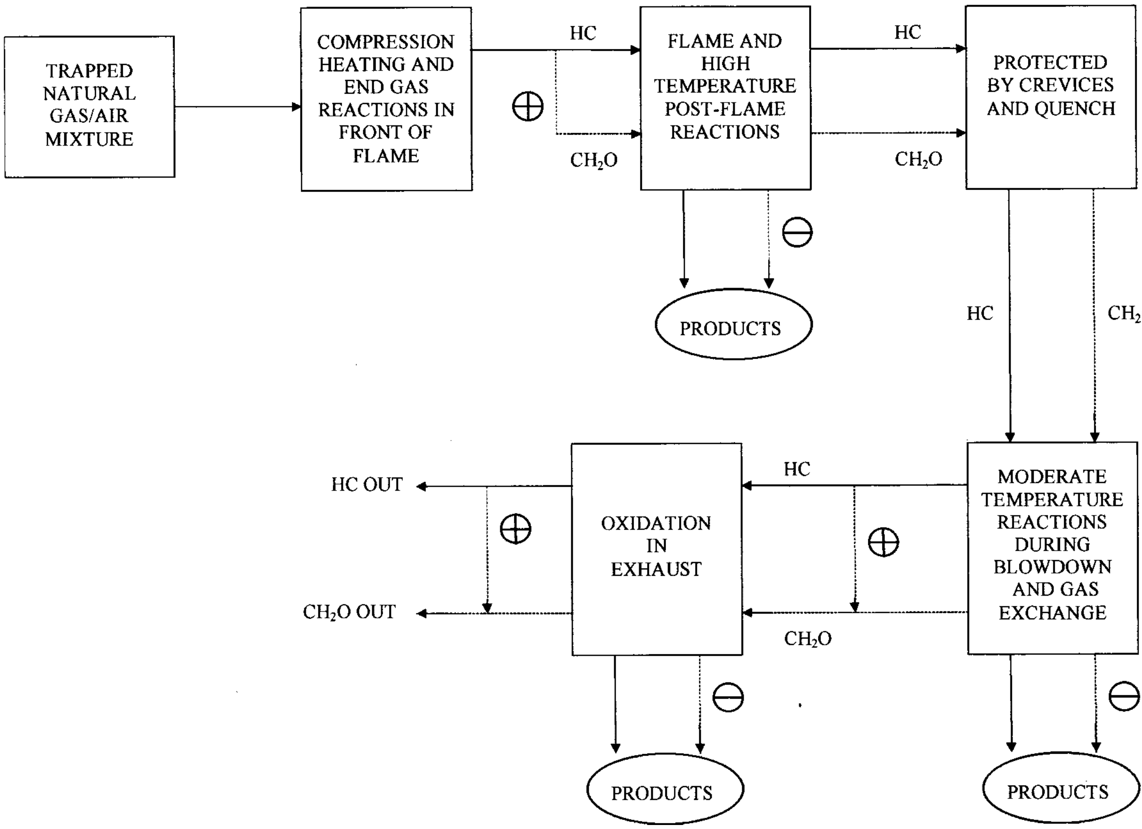

Fig. 6 Paths for engine out formaldehyde

oxidized to formaldehyde as this occurs. After ignition and during flame propagation, the end gases in front of the flame are further heated and compressed. Partial oxidation reactions can continue and additional CH_2O may be formed. These events are represented by the splitting of the HC arrow leaving the second box in the figure and the + sign indicating a formaldehyde source.

Most of the fuel and formaldehyde are subsequently burned to products of combustion such as CO_2 and H_2O in the propagating flame and the high-temperature, oxygen-rich gases behind the flame. The ''−'' sign on the formaldehyde path leading to the products oval represents a sink for CH_2O. None of the formaldehyde formed as an intermediate specie inside the flame structure survives. Some finite fraction of the fuel, and possibly some of the formaldehyde already formed, is protected by crevices and in quench zones or poorly mixed regions into which the flame does not propagate. If this protected fuel and formaldehyde is subsequently mixed with the high temperature products it will oxidize rapidly and be consumed.

However, some of the protected mixture will survive until the bulk gas temperature has been reduced by piston motion during the expansion stroke. At this point the temperature can be low enough that only a part of the protected fuel and formaldehyde are oxidized completely to products as they leave the cylinder. This may occur, even if the bulk temperature is high, if mixing is incomplete. Also, during the flow to the exhaust port, a fraction of the surviving fuel may be partially oxidized to form additional formaldehyde. After entering the exhaust port formaldehyde formation reactions may continue into the exhaust manifold and ducting, depending on engine operating conditions and design. Eventually, the temperature will decrease to the point that the gas composition is effectively frozen. It is also possible, especially for high flame temperature engine designs, for the temperature to remain high enough downstream of the exhaust port that some additional complete combustion of fuel and formaldehyde occurs in the exhaust flow.

Conclusions

1 Equilibrium Formaldehyde. There appears to be no complete combustion regime for which formaldehyde is favored thermodynamically in the amounts approaching those measured in the exhausts of operating gas engines. For the possible ranges of temperature and mixture ratio the equilibrium fraction is always less than one ppb. Formaldehyde exhaust emissions must be the result of chemical kinetic and fluid dynamic mechanisms which result in partial oxidation. This is in direct contrast to other emissions such as CO and NO_x for which post flame equilibrium fractions are generally of the same order of magnitude as exhaust fractions.

2 Chemical Kinetics. The overall mechanism for the oxidation of methane has been studied extensively and substantiated by experiments. The role of formaldehyde in the overall mechanism is also well understood. Kinetic mechanisms for fuels including ethane, propane and some other light hydrocarbons are also fairly well established. Relatively small amounts of these higher hydrocarbons can have a very strong impact on the low temperature kinetic regime where formaldehyde is formed. Unfortunately, all these mechanisms are complex and reduced mechanisms suitable for rapid prediction of formaldehyde formation are not currently available.

3 Formaldehyde and Flames. Self-propagating flames are not a likely source of formaldehyde. Composition and temperature profiles inside methane-air laminar flames show that super-equilibrium amounts of formaldehyde, in excess of 1000 ppm, form in the upstream part of the flame structure. However, virtually all of this is subsequently consumed in the flame, well before the final flame temperature is reached. By the time the flame temperature is approached, formaldehyde levels have dropped below one ppb. Thus, though formaldehyde necessarily is formed inside the flame, it does not survive to the post flame region. This is probably true for the turbulent flames which propagate in large bore gas engines as well, since estimates of the turbulence levels and Damkohler numbers indicate that wrinkled laminar flames are their likely form.

4 Formaldehyde Formation by Partial Oxidation. Since formaldehyde is not favored at equilibrium and does not survive in flames, it must be produced by partial oxidation events in the engine. Several possibilities have been identified. All require that the temperature be in the correct range: high enough for formaldehyde formation reactions to occur, but not so high that the follow-on destruction reactions take place. Potential locations for partial oxidation include:

- pre-flame reactions (compression stroke, end gases in front of flame)
- bulk quenching zones (incomplete mixing, local intense turbulence)
- walls (quenching by heat transfer—possibly enhanced by turbulent flows)
- crevice outflows (bulk product gases must be at low enough temperature)
- exhaust flow (but temperature probably too low for most two-stroke designs)

5 Fuel Protection in Crevices. This is likely to be a very significant source of unburned and partially burned fuel (possibly including formaldehyde), as it is for both gasoline and methanol engines reported in the literature. If the outflow from these crevices is exposed to the correct range of temperature, it could be a major source of formaldehyde for large gas engines. Note that if the outflow temperature is too low, no formaldehyde will be formed and only unburned fuel will show up in the exhaust from this source. If the outflow temperature is too high, on the other hand, most of the formaldehyde formed will be consumed by subsequent reactions (some could be protected by the walls and incomplete mixing).

6 Fuel Protection in Oil Layers and Deposits. The extremely low rate of absorption for methane as compared to either gasoline or methanol makes any significant storage of this type highly unlikely [35,36].

References

[1] Bailey, R. A., Clark, H. M., Ferris, J. P., Krause, S., and Strong, R. L., 1978, *Chemistry of the Environment*, Academic Press, New York, p. 268.

[2] Sittig, M., 1974, *Pollution Detection and Monitoring Handbook*, Noyes Data Corp., Park Ridge, NJ.

[3] Yao, C. C., and Miller, G. C., 1969, Publication No. 79-118, Department of Health Education and Welfare, National Institute for Occupational Safety and Health, Cincinnati, OH, p. 73.

[4] Klim, W. S., Geraci, C. L., and Kupel, R. E., 1980, Am. Ind. Hyg. Assoc. J., **41**, Akron, OH, p. 334.

[5] Gunby, P. J., 1980, Amer. Med. Ass., **243**, p. 1697.

[6] Olsen, D. B., and Mitchell, C. E., 1998, ''Factors Affecting Measured CH_2O in Large Bore Engines,'' ASME-ICE Conference.

[7] JANAF Thermochemical Tables, 1986, 3rd ed., NSRDS-NBS37, U.S. Government Printing Office, Washington, DC.

[8] Kee, R. J., Rupley, F. M., and Miller, J. A., 1991, ''The CHEMKIN Thermodynamic Data Base,'' Sandia National Laboratory Report SAND87-8215B.

[9] Vlachos, D. G., Schmidt, L. D., and Aris, R., 1994, ''Products in Methane Combustion Near Surface,'' AIChE J., **40**, No. 6, pp. 1018–1025.

[10] Shareef, G. S., Ferry, K. R., Gundappa, M., Leatherwood, C. A., Ogle, L. D., and Campbell, L. M., 1996, Gas Research Institute, GRI-96/0009.1, ''Measurement of Air Toxic Emissions from Natural Gas-Fired Internal Combustion Engines at Natural Gas Transmission and Storage Facilities, Volume I.''

[11] Karim, G. A., Ito, K., Abraham, M., and Jensen, L., 1991, ''An Examination of the Role of Formaldehyde in the Ignition Process of a Dual Fuel Engine,'' SAE Paper 912367.

[12] Turns, S. R., 1996, *An Introduction to Combustion*, McGraw-Hill, New York.

[13] Westbrook, C. K., and Dryer, F. L., 1984, ''Chemical Kinetic Modeling of Hydrocarbon Combustion,'' Prog. Energy Combust. Sci., **10**, pp. 1–57.

[14] Westbrook, C. K., and Pitz, W. J., 1993, ''A Chemical Kinetic Mechanism for the Oxidation of Paraffinic Hydrocarbons Needed for Primary Reference Fuels,'' The Combustion Institute, Western States Section Meeting.

[15] Dryer, F. L., 1991, ''The Phenomenology of Modeling Combustion Chemis-

try,'' *Fossil Fuel Combustion*, Chap. 3, John Wiley, New York.

[16] Crawford, J. G., and Wallace, J. S., 1995, ''Engine Operating Parameter Effects on the Speciated Aldehyde and Ketone Emissions from a Natural Gas Fuelled Engine,'' SAE Paper 952500.

[17] Glassman, I., 1987, *Combustion*, 2nd ed., Chap. 3, Academic Press, New York, pp. 81–84.

[18] Peters, N., and Rogg, B., eds., 1993, *Reduced Kinetic Mechanisms for Applications in Combustion Systems*, Springer-Verlag, Berlin.

[19] Smooke, M. D., ed., 1991, *Reduced Kinetic Mechanisms and Asymptotic Expansions for Methane-Air Flames*, Springer-Verlag, Berlin.

[20] Ruy, C., March 1994, ''Zur Reactionkinetik bei der Erdgas/Methan-Verbrennung im Hinblick auf das Zwischenprodukt Formaldehyd,'' *GASWARME International*, **43**, No. 3, pp. 102–109.

[21] Abraham, J., Williams, F. A., and Bracco, F. V., 1985, ''A Discussion of Turbulent Flame Structures in Premixed Charges,'' SAE Paper 850345.

[22] Boyer, R. L., Craig, D. R., and Miller, C. D., 1954, ''A Photographic Study of Events in a 14-In. Two-Cycle Gas-Engine Cylinder,'' Trans. ASME, ASME Paper No. 53-S-45, pp. 97–108.

[23] Westbrook, C. K., and Pitz, W. J., 1987, ''High Pressure Autoignition of Natural Gas/Air Mixtures and the Problem of Knock,'' GRI Topical Report GRI-87/0264.

[24] Griffiths, J. F., Coppersthwaite, D., Phillips, C. H., Westbrook, C. K., and Pitz, W. J., 1990, ''Auto-Ignition Temperatures of Binary Mixtures of Alkanes in a Closed Vessel: Comparisons Between Experimental Measurements and Numerical Predictions,'' *Twenty-Third Symposium (International) on Combustion*, pp. 1745–1752.

[25] Naber, J. D., Siebers, D. L., Di Julio, S. S., and Westbrook, C. K., 1994, ''Effects of Natural Gas Composition on Ignition Delay under Diesel Conditions,'' Combust. Flame, **99**, pp. 192–200.

[26] Cheng, W. K., Hamrin, D., Heywood, J. B., Hochgrieb, S., Min, K., and Norris, M., 1993, ''An Overview of Hydrocarbon Emission Mechanisms in Spark-Ignition Engines,'' SAE Paper 932708.

[27] Kim, C., and Foster, E. F., 1985, ''Aldehyde and Unburned Fuel Emission Measurements from a Methanol-Fueled Texaco Stratified Charge Engine,'' SAE Paper 852120.

[28] Ribeiro, J. C. M., Ohta, T., and Aoyama, T., 1992, ''Study on Formaldehyde Generation Mechanism and Formaldehyde Reducing Items,'' SAE Paper 921435.

[29] Westbrook, C. K., and Adamczyk, A. A., 1981, ''A Numerical Study of Laminar Flame Wall Quenching,'' Combust. Flame, **40**, pp. 81–99.

[30] LoRusso, J. A., Kaiser, E. W., and Lavoie, G. A., 1983, ''In-Cylinder Measurements of Wall Layer Hydrocarbons in a Spark Ignited Engine,'' Combust. Sci. Technol., **33**, pp. 75–112.

[31] Adamczyk, A. A., Kaiser, E. W., Cavolowsky, J. A., and Lovoie, G. A., 1981, ''An Experimental Study of Hydrocarbon Emissions from Closed Vessel Explosions,'' *Eighteenth Symposium (International) on Combustion*.

[32] Weiss, P., and Keck, J. C., 1981, ''Fast Sampling Valve Measurements of Hydrocarbons in the Cylinder of a CFR Engine,'' SAE Paper 810149.

[33] Lee, G. R., and Morley, C., 1994, ''Chemical Modelling of Hydrocarbon Exhaust Emissions,'' SAE Paper 941958.

[34] Min, K., Cheng, W. K., and Heywood, J. B., 1994, ''The Effects of Crevices on the Engine-Out Hydrocarbon Emissions in SI Engines,'' SAE Paper 940306.

[35] Gatellier, B., Trapy, J., Herrier, D., Quelin, J. M., and Galliot, F., 1992, ''Hydrocarbon Emissions of SI Engines as Influenced by Fuel Absorption-Desorption In Oil Films,'' SAE Paper 920095.

[36] Calgon Carbon Corp., 1987, ''Heavy Hydrocarbon Removal or Recovery from Gas Streams,'' Bulletin No. 23-66b.

Formaldehyde Formation in Large Bore Engines Part 2: Factors Affecting Measured CH_2O

Daniel B. Olsen
Charles E. Mitchell

Engines and Energy Conversion Laboratory,
Department of Mechanical Engineering,
Colorado State University,
Fort Collins, CO 80523

Current research shows that the only hazardous air pollutant of significance emitted from large bore natural gas engines is formaldehyde (CH_2O). A literature review on formaldehyde formation is presented focusing on the interpretation of published test data and its applicability to large bore natural gas engines. The relationship of formaldehyde emissions to that of other pollutants is described. Formaldehyde is seen to have a strong correlation to total hydrocarbon (THC) level in the exhaust. It is observed that the ratio of formaldehyde to THC concentration is roughly 1.0–2.5 percent for a very wide range of large bore engines and operating conditions. The impact of engine operating parameters, load, rpm, spark timing, and equivalence ratio, on formaldehyde emissions is also evaluated. [S0742-4795(00)01004-8]

Introduction and Problem Identification

As discussed in Part 1 of this work, the gas industry is faced with new air toxic regulations being developed by the EPA, as declared by the 1990 Clean Air Act Amendments. A stationary source that emits more than 10 tons per year of any single hazardous air pollutant (HAP), or cumulative HAP emissions in excess of 25 tons per year is deemed a major source under Title III.

An extensive GRI funded test program was recently carried out by Radian Corporation on large-bore natural gas engines [1]. Radian found that the only HAP present at levels of possible significance is formaldehyde. Large-bore natural gas engines are generally classified as two-stroke lean-burn, two-stroke clean-burn (low-NOx), four-stroke lean-burn, four-stroke rich-burn, or four-stroke clean-burn (low-NOx). The average formaldehyde emissions for each engine family is shown in Table 1, which was generated from the Radian data. Continuous engine operation was assumed and engines where the emissions were measured downstream of catalysts were not considered. An average engine size of 1800 hp was used for all classes. There is no problem with a single engine, no matter what family it is in, meeting the Title III limitation. However, an emission source is generally not just one engine. An emission source, or site, typically houses numerous engines. Site horsepower ranges from about 10,000 to 40,000. The formaldehyde emissions for these power levels are also shown in Table 1 for each engine family. The result is that the only engine family that complies is the four-stroke rich burn family, but only for a small site. This is a simplified analysis, but it gives a rough idea of the kind of reduction in formaldehyde emissions that may be necessary. The estimate indicates that, in some cases, formaldehyde emissions will need to be reduced by as much as 90 percent of the current value to avoid ''major source'' designation. A clear understanding of how formaldehyde is formed and destroyed in large bore natural gas engines is needed.

Measurement Techniques

There are numerous techniques available for detecting formaldehyde. Some techniques which have been used are Fourier Transform Infrared (FTIR) Spectroscopy, 2,4-dinitrophenylhydrazine (DNPH)/high performance liquid chromatography (HPLC), Laser-induced Fluorescence (LIF), Gas Chromatography (GC), and Electrochemical sensors. FTIR Spectroscopy [2] is a way of analyzing gases using species infrared radiation absorption spectra. The instrument response time for an FTIR spectrometer is generally on the order of a few seconds or less. The primary advantages of the FTIR are that the exhaust can be continuously monitored and a wide range of constituents can be detected, including formaldehyde. Because the measurement is made in ''real time,'' it is possible to see changes in exhaust constituent concentrations with time, as long as the duration of the changes is within the response time of the instrument. The accuracy of the FTIR spectrometer depends on the calibration technique, the purity of the calibration gas, and the software method used to distinguish between species, typically from 1 to 5 percent.

DNPH/HPLC has been used extensively for detecting formaldehyde in engine exhaust. In this method, exhaust gas is bubbled through an acetonitrile solution of the DNPH reagent where aldehydes react to make DNPH-aldehyde derivatives (hydrazone). The solution is then injected directly into the HPLC to quantify the concentrations of the derivatives. The technique is described in detail by Lipari and Swarin [3]. Recent testing indicates that nitrogen dioxide in the exhaust can react with hydrazone and skew the results of DNPH-based methods [4]. Field data show that the difference between FTIR and DNPH-based method measurements goes up with nitrous oxide concentration in the exhaust. The disadvantage of this technique, besides the apparent error described above, is that it is not a ''real time'' measurement. The sample is collected over some length of time, resulting in an average concentration value.

Laser-induced Fluorescence is generally used to study the mixing and combustion processes rather than measure constituents in the exhaust. It is possible to utilize LIF to measure formaldehyde concentrations throughout an engine cycle to determine when and where formaldehyde is formed in the cylinder. LIF has been used extensively to map concentration in fuel jets [5–8]. Formaldehyde spectral emission has been observed in flames [9–11] and in an

Table 1 Engine family comparison of formaldehyde emissions

Engine Family	Single Engine CH_2O (tons/year) 1800 hp	CH_2O (tons/year) 10,000 hp/site	CH_2O (tons/year) 40,000 hp/site
2-S lean-burn	3.7	21	82
2-S clean-burn	3.1	17	70
4-S lean-burn	2.3	13	52
4-S rich-burn	1.5	8.2	33
4-S clean-burn	4.7	26	100

Contributed by the Internal Combustion Engine Division of THE AMERICAN SOCIETY OF MECHANICAL ENGINEERS for publication in the ASME JOURNAL OF ENGINEERING FOR GAS TURBINES AND POWER. Manuscript received by the ICE Division November 6, 1998; final revision received by the ASME Headquarters December 29, 1999. Technical Editor: D. Assanis.

internal combustion engine [12]. Formaldehyde is well suited for LIF because it has been well studied spectroscopically and the spacing between rotational energy levels is relatively large.

Gas Chromatography has been used for formaldehyde detection with some success at Sandia National Laboratories [13]. A packed column followed by a methanizing catalyst (powdered nickel) and a Flame Ionization Detector (FID) are implemented. The formaldehyde is converted to methane via the catalyst, and then methane is detected with GC. The FID is inadequate to detect formaldehyde directly because of the strong carbon-oxygen bond. The accuracy is estimated to be within 25 percent. Like the DNPH/HPLC method, this is not a ''real time'' measurement. With GC a small volume of sample gas is injected into an inert carrier gas flow to begin the measurement so it is effectively a ''snap shot'' of what is going on in the exhaust. With the DNPH/HPLC method the sample represents an average over time, which is in most cases an advantage over the GC. The GC method measures formaldehyde concentration by way of conversion to methane. This presents a problem in natural gas engines, since the unburned hydrocarbons are largely methane, making it difficult to detect the additional methane from formaldehyde conversion.

Electrochemical sensor arrays have been used to detect formaldehyde [14]; however, this technique at present does not seem to be developed enough for practical application to engine research.

Of the techniques reviewed, FTIR spectroscopy appears to be optimal for measuring formaldehyde concentration in engine exhaust. It provides a ''real time'' measurement of many exhaust constituents, including formaldehyde. They are available commercially as benchtop units and the accuracy is very good when compared with other techniques. The CSU Engines and Energy Conversion Laboratory (EECL) is equipped with a Nicolet REGA 7000 FTIR Exhaust Gas Analyzer. The formaldehyde emissions data from the EECL cited herein was measured with this instrument.

Relationship to Other Pollutants: CO, THC, and NOx

The mechanisms through which the major pollutants, CO, THC, and NOx, are formed and eventually emitted from engines of many kinds have been well studied. Comparison of formaldehyde emissions to those of these major pollutants therefore may produce some insight into the way formaldehyde is formed and emitted from large bore gas engines. Certainly if CH_2O emissions show a strong correlation to one of the other pollutants, then the mechanisms of formation are likely to be related. In this section both the Radian data [1] (field engines) and data from CSU's large-bore test engine will be discussed. The Radian data includes measurements from the five different engine classifications, two-stroke lean-burn, two-stroke clean-burn (low-NOx), four-stroke lean-burn, four-stroke rich-burn, and four-stroke clean-burn (low-NOx). Data from engines where the measurements were taken downstream of catalysts were not included in the results discussed here. All formaldehyde measurements for both the CSU and Radian data were made with an FTIR spectrometer.

Most of the engines in the Radian report are slow speed, large bore engines, operating between 250 and 330 rpm with piston diameters between 35 cm (14″) and 46 cm (18″). The only exception is a Waukesha L7042GU, four-stroke rich-burn, medium bore, high speed engine. This engine operates at 1000 rpm and has a 24 cm (9.4″) bore. Brake power for engines in the Radian report range between 670 kW (900 hp) and 3200 kW (4200 hp). Radian lumps the engines that they test into five engine classifications, which are listed above. The two-stroke lean-burn engines are fuel injected and operate with overall A/F ratios between 20:1 and 60:1. Although much of the excess air is for scavenging, the trapped A/F ratio is generally lean. The two-stroke clean-burn engines contain combustion modifications to reduce NOx, such as turbochargers and precombustion chambers. The combustion modifications generally allow them to operate with a leaner trapped A/F ratio to reduce NOx. The four-stroke rich-burn engines burn a ''rich'' A/F mixture, relative to other large bore engines. They actually burn a mixture that is stoichiometric, or just lean of stoichiometric. Leaner A/F ratios are characteristic of four-stroke lean-burn engines. The four-stroke clean-burn engines, like the two-stroke clean-burn engines, are designed to operate at leaner A/F ratios to reduce NOx. This is accomplished through the use of turbochargers and precombustion chambers.

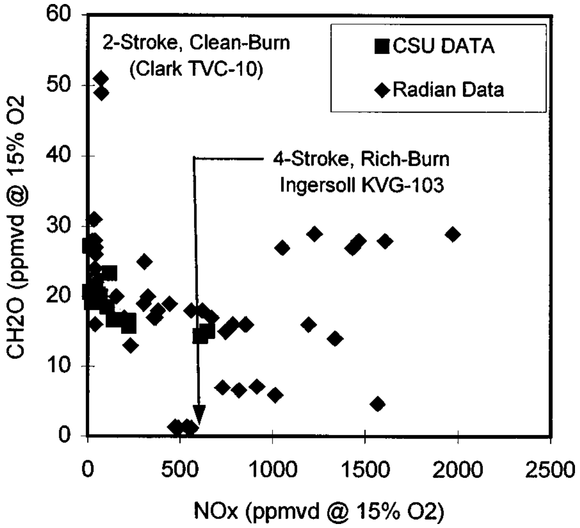

Fig. 1 Formaldehyde versus NOx

The CSU data is from a four-cylinder Cooper-Bessemer two-stroke GMV-4TF test engine with a 35 cm (14″) bore and 35 cm stroke. The sea level brake power rating is 330 kW (440 hp) at 300 rpm. Unlike engines tested in the field, the CSU test engine has much latitude in varying engine operating conditions. Operating parameters which can be varied include boost pressure, equivalence ratio, load, ignition timing, intake air temperature, fuel injection timing, and coolant temperature. The test bed accommodates a variety of ignition and fuel injection systems and control methodology as well. The CSU engine, depending on the operating conditions, can fall into either of the two-stroke engine classifications mentioned earlier, lean-burn or clean-burn.

NOx. Figure 1 is a plot of formaldehyde versus oxides of nitrogen for a wide range of different engine designs and operating conditions. It can be seen from the plot that formaldehyde does not correlate well with NOx. For example, at a formaldehyde level of 20 ppm, NOx could be anywhere from near zero to 2000 ppm. There are two different groups of points which are separated from the majority of the points, Clark TVC-10 engines (two-stroke clean burn) and Ingersoll KVG-103 engines (four-stroke rich-burn). The Clarks are very high in formaldehyde emissions and relatively low in NOx emissions. These engines were running extremely lean, 17 percent O_2 in the exhaust, which is the highest of any of the engines Radian tested. At the other extreme, the Ingersoll engines were very low in formaldehyde emissions and about average in NOx emissions. These engines had high exhaust temperatures, approximately 780 K. A definitive relationship between CH_2O and NOx emissions does not seem to exist. This is not surprising since NOx is formed mainly at high temperatures near the adiabatic flame temperature, while CH_2O is formed at low temperatures and is destroyed very rapidly at temperatures above 1300 K [15]. In terms of flame propagation, CH_2O is formed very early in the flame structure and is subsequently destroyed rapidly. NOx is formed late in the flame, after all CH_2O is consumed, and continues to form in the post flame region as long as the temperature remains high and O_2 is present. The mechanisms of formation are completely different for NOx and CH_2O and no correlation between their emissions should be expected.

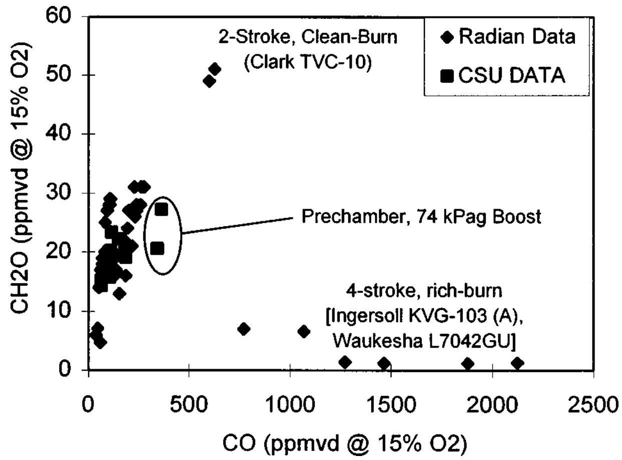

Fig. 2 Formaldehyde versus CO

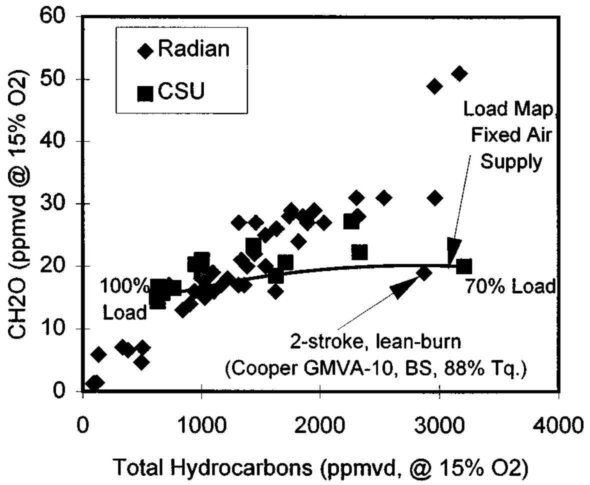

Fig. 3 Formaldehyde versus THC

CO. Figure 2 shows the relationship between formaldehyde and CO. For four-stroke rich-burn engines, there appears to be no correlation. No matter how high CO gets, formaldehyde is only present in quantities of less than 10 ppm. The other engine classes, those that in general run leaner, do show some correlation. For those engine classes, formaldehyde emissions tend to increase with increasing CO. Therefore, CO appears to correlate to some extent with formaldehyde, but only under certain conditions and for certain engine designs. Even for the lean burn engines the range of CO concentration for which the correlation is observed is small, 0 to 600 ppm, and may be sensitive to experimental error if one were to try and use CO to predict formaldehyde emissions.

In trying to understand these data it is helpful to remember that CO has a significant equilibrium mole fraction in the products of natural gas [15]. This fraction of equilibrium CO changes very rapidly with equivalence ratio, increasing by approximately an order of magnitude as ϕ increases from 0.8 to 1.0. As far as the mechanisms by which CO is produced, two general paths can be identified. First, CO is generated in the propagating flame. It reaches a peak early in the flame structure and subsequently decreases in concentration as it is converted to CO_2. If enough time is available and if the temperature remains high enough behind the flame, the concentration will eventually approach the equilibrium value. If the temperature drops, for example because of gas expansion in the power stroke, then the CO concentration can be frozen at super-equilibrium values. It is also possible to generate CO away from the flame by the same low temperature kinetics which form CH_2O, in regions such as at the walls, in crevice outflows and possibly the exhaust port: locations where the temperature is in the right range. Considering this, the part of the CO in the exhaust that is formed away from the flame should correlate well with the exhaust concentration of CH_2O, since both are formed the same way. On the other hand, the CO that is formed in the flame has a completely different history from that of CH_2O and no correlation should be expected. Rich burn engines have high concentrations of flame produced CO (as predicted by equilibrium calculations), vigorous flame propagation and high post flame product gas temperatures. Because of this, it is to be expected that the production of both CH_2O and CO from the protected regions outside the flame propagation zone should be relatively small and no correlation between exhaust CO and CH_2O should exist. For engines operating at lower equivalence ratios (lean burn and clean burn engines) the part of the exhaust CO formed away from the flame is much more likely to form a considerable fraction of the total and *this fraction* should correlate well with CH_2O emissions. Since varying amounts of the total CO would still be formed in the flame for these lean burning engines, the degree of correlation of CH_2O to *total* CO may not be strong, and will vary among different engine designs and operating conditions.

THC. Total hydrocarbon emissions show the best overall correlation with formaldehyde of any of the three primary pollutants. Figure 3 is a plot of formaldehyde concentration versus total hydrocarbon concentration. With the exception of two outlying points (discussed below) there is a generally good correlation between THC and CH_2O regardless of engine type and operating condition. Excluding these two points the rest of the Radian and CSU data show values of CH_2O concentration to lie generally between 1 and 2.5 percent that of THC. The average value for all the Radian data was 1.5 percent while for the CSU data 1.8 percent. Shown on the figure is a line representing fixed air supply load map results for GMV-4TF two stroke engine tests run at CSU. As dynamometer load was decreased in these tests, the fuel flow rate was also decreased so as to maintain a constant engine speed. With the air supply fixed, the trapped air/fuel ratio at ignition continued to increase with decreasing load, leading to an increasing number of misfires and consequent substantial increases in unburned hydrocarbons far out of line with normal efficient operation. Indeed, the THC concentration increased by over a factor of four as the load was reduced from full load to 70 percent. For this reason the 70 percent load point was eliminated when the data were replotted in Fig. 4. Also eliminated was the point for the GMVA-10 engine operating at 88 percent torque, from the Radian data. This blower-scavenged engine showed an increase of over 100 percent in THC as the torque was reduced from full load to 88 percent load. It is likely that erratic or incomplete bulk combustion was occurring for this operating point as well. An increase in the number of misfires resulting in a lower CH_2O/THC ratio suggests that CH_2O formation during compression is not likely to be a major source. Figure 4 is the same plot as Fig. 3 except that the two low load points and the load map line are removed.

For the engines operating normally without low load misfires, the ratio of CH_2O concentration to THC concentration was always in a fairly narrow range, 1 to 2.5 percent. This was true for a very wide range of engine designs and operating conditions including rich burn, clean burn and lean burn four stroke engines, and lean burn and clean burn two stroke engines, both turbocharged and blower scavenged. Direct fuel injection, port injection, and precombustion chamber designs were all included. The implication appears to be that regardless of bulk combustion temperature, degree of mixing, level of turbulence, engine size and shape, equivalence ratio and engine speed, about 1.5 percent of the total hydro-

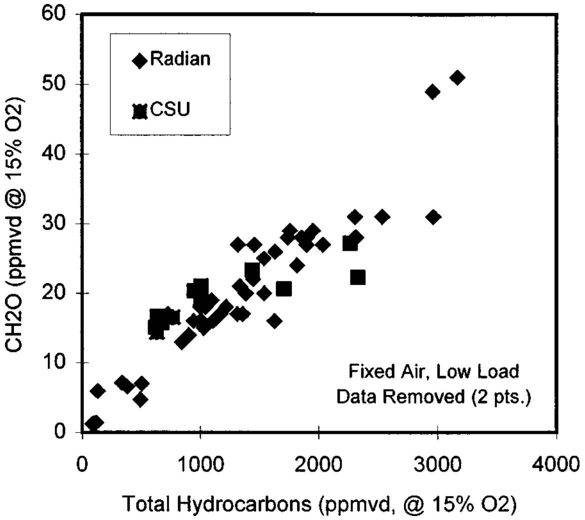

Fig. 4 Formaldehyde versus THC

carbons which escape combustion in the engine or exhaust are partially oxidized to CH_2O. The fact that a rich burn four stroke engine producing about 100 ppm THC and a two stroke clean burn prechamber engine running extremely lean and producing about 3000 ppm THC, both have essentially the same CH_2O to THC ratio is somewhat surprising and may have significance as far as how and where CH_2O is formed. Of course, a change in the ratio from 1 percent to 2.5 percent is important and knowing why it varies between these limits is critical in limiting engine formaldehyde emissions. A study of the effect of natural gas composition on engine emissions [16] showed that substantial variation of the gas composition had very little impact on THC levels, but could change the mix of partially reacted species substantially. Formaldehyde was not measured in this study but variations in ethylene, which could only appear by partial reaction, changed as much as a factor of two for different fuel compositions. For comparison with a somewhat similar fuel, two engines running on methanol [17,18] had CH_2O to unburned fuel ratios which ranged between about 1.5 percent and 9 percent depending on operating conditions, a substantially larger variation than that observed in the gas engines.

Some possible interpretation of the results for gas engines can be given in terms of the formation mechanisms presented by Mitchell and Olsen [15]. As discussed there, it is likely that substantial formaldehyde may be formed in the outflow from protected regions such as crevice volumes and quench zones during blowdown and later stages of the gas exchange process in the engine. At the end of the expansion stroke the bulk (burned gas) temperature in the cylinder has decreased to the neighborhood of 1000 K, depending on maximum flame temperature, compression ratio, heat transfer and other design and operating variables. The fuel/air mixture from the protected regions would reasonably have a temperature somewhere between the wall temperature and the bulk gas temperature depending on the degree of mixing. This places the temperature in the active range for the formation of formaldehyde (approximately 700–1200 K) and also for its further conversion to products as the temperature approaches 1000 K. As the reacting gas flows out of the engine through the exhaust port, its temperature decreases and production of formaldehyde stops when the temperature reaches about 700 K. The time taken for these reacting gases to leave the engine and be quenched, their temperature history and their degree of mixing with the bulk product gases (and their associated free radicals) will all affect the degree of conversion and thus the final ratio of CH_2O to THC. From the data presented above, the indication is that the degree of conversion which actually occurs in large bore gas engines is approximately 1.5 percent and varies by about a factor of two depending on engine design and operating conditions. For rich burn designs, the temperature is high and the formaldehyde that is formed along with the other hydrocarbons tends to be converted to products at a higher rate. Lower levels of both CH_2O and THC in the exhaust result, but their ratio remains around 1.5 percent. For lean burn and clean burn engines the temperature is lower and less formaldehyde and THC are burned out to products, though formaldehyde is *formed* at about the same rate. Higher levels of both CH_2O and THC in the exhaust result while their ratio remains about the same. When very lean mixture ratios, poor mixing, or misfires occur, the temperature of some significant fraction of the unburned gases exhausting the main chamber may never reach a level high enough for reaction to formaldehyde to occur. In this case the ratio of CH_2O to THC can be substantially lower than 1.5 percent.

The value 1.5 percent for the ratio between formaldehyde and THC is of the same order of magnitude as predicted indirectly in the kinetic and flame calculations carried out by Ruy [19]. In that work it can be seen that at an equivalence ratio of 0.89, CH_2O concentration peaks in the flame structure at a value of approximately 1200 ppm. At this location in the flame the unburned CH_4 mole fraction has a value of approximately 0.05. This gives a ratio between these two species of approximately 3 percent. Though CH_4 is not an exact measure of THC and the low temperature part of a laminar flame may not model the reactions occurring in the cylinder very well, the value is at least generally in the right range, especially considering that less than peak values for CH_2O concentration are likely in an engine. The compression stroke calculations performed for a dual fuel engine [20] also give CH_2O to CH_4 ratios just before ignition of around 2 to 5 percent for equivalence ratios near 0.8. Finally, the stagnation point flow calculations by Vlachos et al. [21] give values for the ratio at the wall on the ''extinguished branch'' (no ignition) of roughly 5 percent. These last calculations did not include the C_2 kinetics branch and may give a high value of the ratio for that reason. Certainly all of these calculations, though incomplete and not intended for the problem at hand, show enough correspondence with engine results to encourage additional and more extensive computational work.

Relationship of Formaldehyde to Engine Operating Parameters: Load, RPM, Spark Timing and Equivalence Ratio

Engine operating parameters affect the physical and chemical mechanisms that result in the production of formaldehyde emissions in ways which are indirect, complicated, and often interrelated. For example, increasing load typically increases the captured fuel/air ratio, average bulk and exhaust temperatures, and peak pressure. It also affects mixing, level of turbulence, and flame propagation in unknown ways. This makes any evaluation of the effects of engine operation on formaldehyde both difficult and speculative given the present state of understanding. However, since data on the gross results of varying these parameters is available to a limited extent, a brief attempt to interpret and understand these results in terms of the formaldehyde formation mechanisms described by Mitchell and Olsen [15] will be made.

Load. A conclusion in the Radian report on toxic emissions from large bore engines [1] was that the operating parameter which affected formaldehyde emissions most was load, or torque. Formaldehyde emissions were found to decrease with increasing torque. This decrease was attributed to an increase in bulk temperature that resulted in the consumption of CH_2O at an increased rate. This is likely to be true, at least indirectly. A critical time for formaldehyde formation and destruction is probably during the exhaust blowdown and gas exchange process. The higher peak flame and bulk temperatures that result from the increased load cause the temperature after expansion has occurred also to be higher. A consequent higher rate of destruction of CH_2O during this critical time is the result. An additional effect may be that a more vigorous and complete flame propagation and primary combustion process occurs at high load. This can reduce the amount of unburned fuel and air mixture that survives to the start of the exhaust and gas exchange process. Less unburned fuel means that less formaldehyde will be formed as this process proceeds. Recall that the amount of unburned fuel converted to formaldehyde is observed to be approximately 1.5 percent under most conditions. A higher rate of destruction of CH_2O means a higher rate of destruction of THC as well. It should be mentioned that for constant speed engines, such as those tested by Radian, an increase in load is accompanied by an increase in overall equivalence ratio.

RPM. Large bore natural gas engines are primarily constant speed engines. RPM is a parameter that was not varied even in the engine performance tests run at CSU. A comparison of engines which operate at different speeds is possible, but would probably be inconclusive since other engine operating parameters vary so much among these engine designs. Increased engine speeds might lead to an incomplete combustion process if flame propagation is not finished before the piston moves a significant distance in the power stroke. This could result in increased unburned fuel and an associated increase in formaldehyde. High turbulence levels and low piston speeds of large bore engines combine to cause the completion of flame travel very close to TDC, which was shown by Boyer et al. [22] decades ago. In some recent work by Crawford and Wallace [23] the effect of RPM on formaldehyde emissions was examined for a four-cylinder, automotive size, four-stroke, natural gas engine. The engine speed was varied from 1000 to 4500 rpm. The difference in formaldehyde emissions between the lowest and highest rpm points was negligible (less than 10 percent). However, the data followed a see-saw profile rather than showing an increasing or decreasing trend. The most significant variation was an increase in formaldehyde emissions from 50 to 80 ppm for a corresponding increase in rpm of 2800 to 3900. The see-saw behavior was attributed by them to the competing effects of increasing temperature and decreasing residence time as engine speed was increased. It is worthwhile noting that the rising temperature in the engine with increasing rpm did not reduce formaldehyde levels, in contrast with the general trend of higher engine temperatures resulting in less formaldehyde.

Spark Timing. In general, for the large bore natural gas engines tested by Radian [1], spark timing did not appear to have a strong influence of formaldehyde emissions. In particular, spark timing on a single Ingersoll-Rand KVS-412 (four-stroke, clean burn) engine was varied 3 degrees on both sides of the nominal timing and only slight changes in formaldehyde concentration, about 1–3 ppm were observed. In contrast, results from Crawford and Wallace [23] showed an approximate doubling of formaldehyde as timing was advanced from 20 degrees before MBT (maximum brake torque) timing to 15 degrees after MBT timing. Over this same range of spark timing, the exhaust gas temperature (measured in the exhaust port) decreased by about 150 K. In consequence of this, the authors attributed the increased CH_2O emissions to decreased destruction of formaldehyde caused by lower bulk engine temperatures. For timing advanced past MBT a flattening of the rate of increase was observed. This could be due to temperatures being reduced to the point that the rate of *formation* of CH_2O as well as its rate of destruction is diminished. A consequence of this would be that, for over advanced timing, low temperatures and incomplete combustion lead to steadily increasing levels of THC while CH_2O concentrations level off. This is, indeed, shown in the Crawford and Wallace data.

Equivalence Ratio. The equivalence ratio was not measured directly for any of the engines tested by Radian [1]. Instead, this ratio was assumed to be inversely proportional to the oxygen concentration in the exhaust. Certainly, the overall air/fuel ratio is likely to be proportional to exhaust oxygen concentration. However for two stroke designs the overall air/fuel ratio includes scavenging air. The trapped air/fuel ratio, on the other hand, is likely to be the quantity of interest, since it influences the flame propagation and combustion processes directly. Currently there is no standardized method for measuring the trapped equivalence ratio on two stroke large-bore natural gas engines. Because of this, the data on the relationship between formaldehyde and equivalence ratio presented in the Radian report are hard to interpret. This is particularly true since air/fuel variations on individual engines were not large and variations in scavenging efficiency among engine designs were not given. For the four-stroke lean burn engines and four-stroke rich burn engines, a trend of increasing formaldehyde with exhaust O_2 was shown at high exhaust O_2 levels (>7 percent). This is in agreement with the fact that the maximum temperature and the consequent temperature during blowdown and exhaust would be lower at higher air/fuel ratios. Lower temperatures at this point in the cycle are likely to mean that less of the formaldehyde formed during this period is later destroyed by subsequent higher temperature reactions. Data for the four-stroke rich burn engines, the only engine class tested at near stoichiometric conditions, showed a decrease in formaldehyde emissions as the exhaust O_2 level decreased from 10 to 4 percent. However an increase in formaldehyde emission was seen as the exhaust O_2 level decreased from 4 to 1 percent, with a minimum at 4 percent. This indicates that there is a formation mechanism dominating at near stoichiometric conditions which is unaffected or possibly enhanced by the increase in bulk temperature. A minimum in formaldehyde emissions for very lean equivalence ratios was also observed by Jones and Heaton [24]. This testing was on a 3.9 liter four-stroke single cylinder research engine running on natural gas at 1800 rpm.

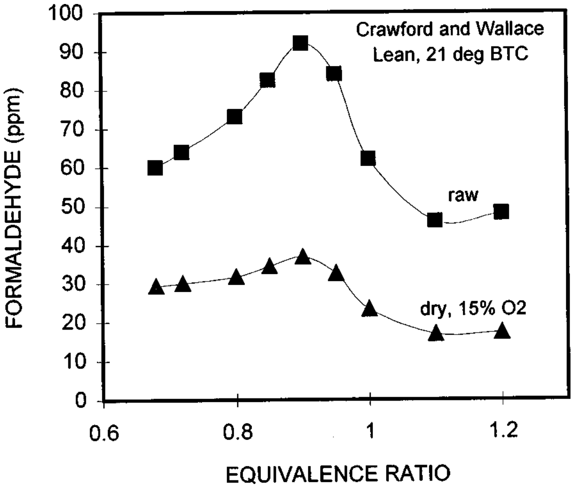

Fig. 5 Formaldehyde versus equivalence ratio

In the work of Crawford and Wallace [23] the effect of equivalence ratio on formaldehyde emissions was tested directly using the four stroke natural gas engine mentioned above. In these tests spark timing and rpm were fixed. Results from their work are replotted in Fig. 5 as the raw curve. This data is on a wet basis and uncorrected for dilution, which tends to make the peak at $\phi = 0.9$ more pronounced. The lower curve, expressed on a dry basis and corrected to 15 percent O_2, shows a more gradual decrease in CH_2O with decreasing equivalence ratio and appears to be approaching a constant value. The decrease in CH_2O with decreasing equivalence ratio from 0.9 to 0.7 does not support the general rule of CH_2O emissions increasing with decreased bulk temperature. This trend was also observed in the Radian data for a four-stroke rich burn engine. The data also show a decrease in CH_2O with increasing equivalence ratio after $\phi = 0.9$. Crawford and Wallace relate this decrease to kinetic calculations by Warantz [25] which show an increase in the importance of methyl-methyl recombination to form ethene, ethane, and acetylene (the C_2 path) as compared to the reaction of methyl with oxygen to form formaldehyde as the mixtures enriched beyond $\phi = 0.9$.

Conclusions

It appears that formaldehyde exhaust fractions follow THC fractions most closely. For a wide range of engine designs (two-stroke, four-stroke, clean burn, lean burn, rich burn) and operating conditions, about 1.5 percent (range was 1–2.5 percent) of the fuel that was not burned completely (and thus showed up in the exhaust as THC) was partially oxidized to formaldehyde. This ratio of formaldehyde to fuel is close to that observed in laminar methane-air flames in the early part of the flame structure where formaldehyde reaches its peak concentration. Correlations with CO are not as good, though a general trend of increasing formaldehyde with CO does exist. The correlation with CO is not as strong because considerable CO can survive in the high temperature post-flame region while formaldehyde cannot exist there. No correlation between NOx and formaldehyde emissions was found. This is because NOx is formed mainly in post-flame regions at high temperatures, not in the low temperature partial oxidation zones where formaldehyde is generated.

In general the operating parameters, load, rpm, spark timing, and equivalence ratio, can significantly affect formaldehyde emissions. A trend of decreasing formaldehyde emissions with increasing load is seen in large bore engine data. Large variations in engine speed can result in changes in formaldehyde emissions in either direction. This is inconsequential for large bore engines since they are generally operated at a constant speed. Formaldehyde emissions increase with increasing spark advance, due to the decrease in bulk temperature. Changes in equivalence ratio, like rpm, can bring about increases or decreases in formaldehyde. It appears that a minimum formaldehyde level exists near stoichiometric equivalence ratios. The data suggest that as equivalence ratio gets lean from stoichiometric, a general trend of increasing formaldehyde exists.

References

[1] Shareef, G. S., Ferry, K. R., Gundappa, M., Leatherwood, C. A., Ogle, L. D., and Campbell, L. M., 1996, ''Measurement of Air Toxic Emissions from Natural Gas-Fired Internal Combustion Engines at Natural Gas Transmission and Storage Facilities, Volume I,'' Gas Research Institute, GRI-96/0009.1.
[2] Skoog, D. A., and Leary, J. J., 1992, *Principles of Instrumental Analysis*, 4th ed., Saunders College Publishing.
[3] Lipari, F., and Swarin, S. J., 1982, ''Determination of Formaldehyde and Other Aldehydes in Automobile Exhaust with an Improved 2,4-Dinitrophenylhydrazine Method,'' J. Chromatogr., **247**, pp. 297–206.
[4] Ogle, et al., 1995, ''Measurement of Aldehydes in Internal Combustion Engine Exhaust,'' GRI Air Toxics Conference, Denver, CO.
[5] Dahm, W. J. A., and Dimotakis, P. E., 1986, ''Measurements of Entrainment and Mixing in Turbulent Jets,'' AIAA J., **24**, No. 9.
[6] Bardsley, M. E. A., Felton, P. G., and Bracco, F. V., 1989, ''2-D Visualization of a Hollow-Cone Spray in a Cup-in-Head, Ported, I.C. Engine,'' Paper SAE 890315.
[7] Kido, A., Ogawa, H., and Miyamo, N., 1993, ''Quantitative Measurements and Analysis of Ambient Gas Entrainment Into Intermittent Gas Jets by Laser-Induced Fluorescence of Ambient Gas (LIFA),'' Paper SAE 930970.
[8] Baritaud, T. A., and Heinze, T. A., 1992, ''Gasoline Distribution Measurements with PLIF in a SI Engine,'' SAE Paper 922355.
[9] Harrington, J. E., and Smyth, K. C., 1993, ''Laser-Induced Fluorescence Measurements of Formaldehyde in a Methane/Air Diffusion Flame,'' Chem. Phys. Lett., **202**, No. 3, p. 4.
[10] Pearce, R. W. B., and Gaydon, A. G., 1976, *The Identification of Molecular Spectra*, 4th ed., Chapman and Hall, London.
[11] Garland, N. L., 1984, SRI International Report, MP 84-033.
[12] Smith, J. R., Green, R. M., Westbrook, C. K., and Pitz, W. J., 1984, 20th International Symposium on Combustion, The Combustion Institute, Pittsburgh, PA, p. 91.
[13] Green, R. M., and Rychnovsky, R. E., 1994, ''Exhaust Emissions of Alternative Fuels in Spark-Ignition Engines,'' Final Report, Sandia National Laboratories, Livermore, CA.
[14] Stetter, J. R., Findlay, M. W., Maclay, G. J., Zhang, J., Vaihinger, S., and Gopel, W., 1990, ''Sensor Array and Catalytic Filament for Chemical Analysis of Vapors and Mixtures,'' Sensors and Actuators, Neuchâtel, Switzerland, pp. 43–47.
[15] Mitchell, C. E., and Olsen, D. B., 1998, ''Mechanisms Affecting Formation of Formaldehyde in Large Bore Natural Gas Engines,'' ASME-ICE Conference.
[16] Ryan, III, T. W., and Callahan, T. J., 1991, ''Effects of Gas Composition on Engine Performance and Emissions,'' Topical Report GETA 91-13, GRI-92-0054.
[17] Kim, C., and Foster, E. F., 1985, ''Aldehyde and Unburned Fuel Emission Measurements from a Methanol-Fueled Texaco Stratified Charge Engine,'' SAE Paper 852120.
[18] Ribeiro, J. C. M., Ohta, T., and Aoyama, T., 1992, ''Study on Formaldehyde Generation Mechanism and Formaldehyde Reducing Items,'' SAE Paper 921435.
[19] Ruy, C., 1994, ''Zur Reactionkinetik bei der Erdgas/MethanVerbrennung im Hinblick auf das Zwishchenprodukt Formaldehyd,'' *GASWARME International*, **43**, No. 3, pp. 102–109.
[20] Karim, G. A., Ito, K., Abraham, M., and Jensen, L., 1991, ''An Examination of the Role of Formaldehyde in the Ignition Process of a Dual Fuel Engine,'' SAE Paper 912367.
[21] Vlachos, D. G., Schmidt, L. D., and Aris, R., 1994, ''Products in Methane Combustion Near Surfaces,'' AIChE J., **40**, No. 6, pp. 1018–1025.
[22] Boyer, R. L., Craig, D. R., and Miller, C. D., 1954, ''A Photographic Study of Events in a 14-in. Two-Cycle Gas-Engine Cylinder,'' Trans. ASME, Paper No. 53-S-45, pp. 97–108.
[23] Crawford, J. G., and Wallace, J. S., 1995, ''Engine Operating Parameter Effects on the Speciated Aldehyde and Kettone Emissions from a Natural Gas Fueled Engine,'' SAE Paper 952500.
[24] Jones, M. G. K., and Heaton, D. M., 1989, ''Nebula Combustion System for Lean Burn Spark Ignited Gas Engines,'' SAE Paper 890211.
[25] Warnatz, J., 1979, ''Flame Velocity and Structure of Laminar Hydrocarbon-Air Flames,'' Prog. Astronaut. Aeronaut., **76**, pp. 501–521.

Stoichiometric Operation of a Gas Engine Utilizing Synthesis Gas and EGR for NO*x* Control

Jack A. Smith
Department of Engine Research,
Engine and Vehicle Research Division,
Southwest Research Institute,
6220 Culebra Road,
San Antonio, TX 78226-0510

Gordon J. J. Bartley
Department of Emissions Research,
Automotive Products
and Emission Research Division,
Southwest Research Institute,
6220 Culebra Road,
San Antonio, TX 78226-0510

This paper presents the results from an internal research study conducted at the Southwest Research Institute (SwRI) on the effects of stoichiometric mixtures of natural gas and synthesis gas with exhaust gas recirculation (EGR) on engine performance and exhaust emissions. Constant load performance and emissions tests were conducted on a modified, single-cylinder, Caterpillar 1Y540 research engine at 11.0 bar (160 psi) bmep. Engine performance and emissions comparisons between natural gas with EGR, and natural gas with syngas and EGR are presented. In addition, the performance characteristics of the fuel reforming catalyst are presented. Results show that thermal efficiency increases with increasing EGR for both natural gas operation and natural gas with syngas operation at constant load. The use of syngas with natural gas extended the EGR tolerance by 44.4 percent on a mass basis compared to natural gas only, leading to a 77 percent reduction in raw NOx emissions over the lowest natural gas with EGR NOx emissions.
[S0742-4795(00)00504-4]

Introduction

This paper is a companion paper to a recently published ASME paper (ASME Paper No. 97-ICE-64) describing the effects of natural gas/syngas mixtures on engine performance and emissions during lean-burn operation. As a result, parts of the Introduction and catalyst-testing results are duplicated here to maintain the focus and ideas of using syngas in an internal combustion engine.

Increased sensitivity to internal combustion engine emissions and the accompanying regulations in municipalities, in particular non-attainment zones, has led to the conceptualization and testing of advanced, low-emissions combustion technologies. Many of these concepts utilize irregular piston bowls, exhaust gas recirculation (EGR), complex control algorithms, alternative fuels (or combinations thereof), high-power ignition systems, and even unconventional engine configurations such as the hybrid rich-burn/lean-burn (HRBLB) engine to meet present and future emissions regulations [1–13]. Greenhouse gases and NO*x* are currently the focal point of many emissions regulations. At the present, compliance with NO*x* emissions regulations is the most difficult because NO*x* is, in the simplest of terms, a byproduct of good and efficient combustion. Hence, reducing NO*x* typically results in an undesirable power derate and an increase in operating costs. Therefore, a need exists to develop a low-emissions, high-efficiency engine or combustion concept.

Stoichiometric engines have had the greatest success in reducing NO*x* emissions by using three-way catalysts (TWCs). However, engine brake thermal efficiency (BTE) is compromised by knock-induced compression ratio limitations and high rates of heat transfer through the combustion chamber, ultimately reducing component life. Furthermore, the error margin for air-fuel mixture control to maintain a high TWC conversion efficiency across the TWC is small [14].

Natural gas-fueled, lean-burn engine BTE can exceed stoichiometric engine BTE by more than 20 percent. However, NO*x* emissions are typically greater than 100 ppm (corrected to 15 percent exhaust O_2). Newer combustion technologies like the HRBLB have demonstrated the potential to reduce NO*x* emissions to near stoichiometric/TWC levels by using H_2 enriched EGR to extend the EGR tolerance and lean limit of lean burning cylinders. The HRBLB engine demonstrated NO*x* emissions below 25 ppm (@ 15 percent exhaust O_2) at greater than 35 percent BTE without catalytic aftertreatment (0.5 g/bhp-hr) [1,2]. However, NO*x* emissions still remain above the 0.15 g/bhp-hr level required for new engine installations in the South Coast Air Basin of California; presently the lowest level in the United States.

SwRI has developed a new combustion concept that utilizes syngas to extend the EGR tolerance of a stoichiometric engine to reduce engine out NO*x* emissions and increase BTE. The concept centers on S̲toichiometric, S̲yngas, E̲GR, N̲atural G̲as, C̲ombustion (SSENGC). The objective is to obtain lean-burn engine efficiency in a stoichiometric engine by using excessive levels of EGR in the same manner as excess air in lean-burn engines. The engine operates stoichiometrically, therefore, a conventional TWC can be used to reduce emissions to below regulated levels.

The SSENGC concept requires EGR in excess of levels currently tolerable by stoichiometric engines to inhibit knock and reduce in-cylinder gas temperatures at the high boost pressures required to achieve lean-burn engine efficiency. Therefore, syngas is used to enhance the ignitability of the high EGR natural gas/air charge. Syngas can be created by partially oxidizing natural gas and is a mixture of H_2, CO, CO_2, H_2O, and N_2 when air is the oxidizer, hence no external H_2 gas supply is required. The global syngas reaction is shown in Eq. (1) when CH_4 is the feed gas. Syngas itself is a H_2 rich EGR much like the exhaust gas generated by the rich-burn cylinder of the HRBLB engine [1,2]. Hence, SSENGC is a blend of stoichiometric engine technology, lean-burn engine technology, and the HRBLB engine technology. This paper presents the results of an internally-funded SwRI research study conducted to determine the effects of the SSENGC concept on raw exhaust emissions and engine performance.

$$CH_4+\frac{1}{2}[O_2+3.77N_2]-2H_2+CO+1.54N_2+\text{Heat} \qquad (1)$$

Test Bed and Experimental Setup

A spark-ignited single-cylinder Caterpillar 1Y-540 research engine modified for natural gas operation was used as the test bed. Engine specifications are listed in Table 1. A schematic of the instrumented engine/catalyst system is shown in Fig. 1. An electronically controlled dynamometer provided speed control while

---

Contributed by the Internal Combustion Engine Division of THE AMERICAN SOCIETY OF MECHANICAL ENGINEERS for publication in the ASME JOURNAL OF ENGINEERING FOR GAS TURBINES AND POWER. Manuscript received by the ICE Division March 20, 2000; final revision received by the ASME Headquarters April 2, 2000. Technical Editor: D. Assanis.

an auxiliary roots type blower and heat exchanger modulated intake manifold air pressure to simulate turbocharged operation. The work of compression by the external roots blower is not included in the efficiency values presented in this paper.

A heated plenum chamber with a volume greater than 50 times the cylinder volume was located upstream of the intake manifold to dampen pressure pulsations. Varying amounts of water in a fine mist spray were added to the intake air through an air-assisted water injection system installed in the bottom of the plenum chamber to control the intake air specific humidity to 0.012 lbm H_2O per lbm of dry air. This provided a datum for comparing data since syngas contains water vapor and affects the effective specific humidity of the intake mixture.

The engine fuel system consisted of an injector block and a fuel mixer located upstream of the throttle. A similar arrangement was used in the catalyst *leg* upstream of the catalyst. The natural gas fuel composition was on average 95.4 percent CH_4, 1.8 percent C_2H_6, 0.2 percent C_3H_6, 1.45 percent CO_2, and 1.15 percent N_2. Shop air provided air flow to the catalyst via another injector block. A 110 volt electric heater was placed upstream of the catalyst to heat the air/fuel mixture to promote light off in the syngas catalyst.

EGR was routed through a heat exchanger to reduce the EGR temperature to 82.2°C (180°F) before mixing with fresh intake air. The gas mixture in the intake manifold was maintained at 51.7°C (125°F) for all tests.

An SwRI-developed, PC-based Rapid Prototyping Engine Control System (RPECS) was used to control equivalence ratio, spark timing, and the syngas fraction. A manually-controlled pneumatic valve was used to modulate the EGR flow rate while a universal exhaust gas oxygen (UEGO) sensor in the engine exhaust stream allowed closed-loop equivalence ratio control. All NO*x* emissions are presented as measured on a dry basis in ppm. CO emissions are also presented on a dry basis, and HCs are presented on a wet basis as measured.

Table 1 Test engine specifications

Displacement	2.44 L (148.9 in^3)
Bore	137.2 mm (5.4 in)
Stroke	165.1 mm (6.5 in)
Combustion Chamber	Open chamber w/ spherical piston bowl
Compression Ratio	11.9:1
Number of Valves	2 intake, 2 exhaust

POM Catalyst Testing

The syngas used in this study was generated by a partial oxidation of methane catalyst; sometimes called a syngas catalyst. A moderate test program was conducted on potential POM catalysts and is described in ASME Paper No. 97-ICE-64 [15]. Therefore, only a brief description of the POM catalyst used during the SSENGC testing and its performance are presented here.

The POM catalyst was composed of a ceramic monolithic substrate with 300 cpsi and a 10.5-mil wall thickness coated with a gamma alumina (140 m^2/g) washcoat. Rhodium was loaded onto the washcoat at 10 weight percent. Figure 2 shows the performance of the POM catalyst in terms of the syngas composition as a function of the catalyst fuel-air equivalence ratio, ϕ_{cat}. The objective of generating syngas in this study was to maximize the H_2 yield while minimizing CH_4 and O_2 breakthrough. Figure 2 shows that the H_2 mole fraction is maximized at a ϕ_{cat} of 2.8. In addition, at 2.8 and richer conditions CH_4 begins to appear in the syngas composition. Therefore, the POM catalyst was operated at 2.8 for all SSENGC engine testing and controlled by the RPECS. The complete syngas composition at a ϕ_{cat} of 2.8 is shown in Table 2. Although the soot threshold equivalence ratio for CH_4 is about 2.0, no soot was found in the POM catalyst or intake system.

Engine/Catalyst System Tests

The engine was operated at 1800 rpm and a constant 11.0 bar (160 psi) bmep load at wide open throttle. Sweeps were made with the engine/catalyst system overall equivalence ratio maintained stoichiometric (1.0) for syngas fractions of 0 (baseline), 30 percent, and 40 percent. The overall equivalence ratio is shown in Eq. (2) and is the stoichiometric air to fuel ratio of the base fuel, natural gas in this case, divided by the air to fuel ratio of system;

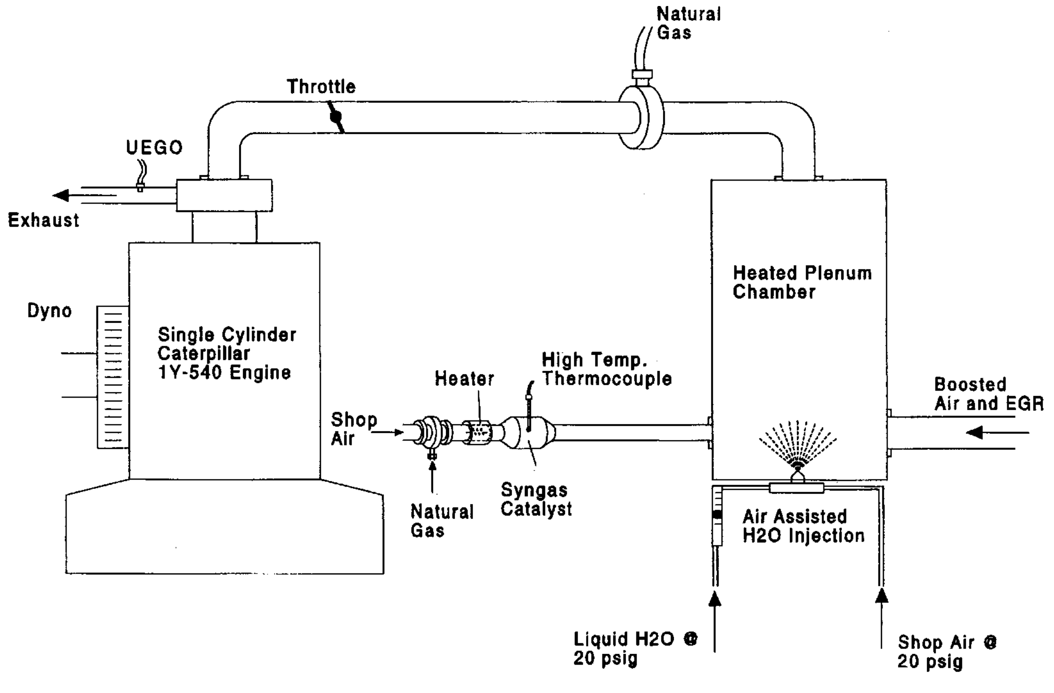

Fig. 1 Schematic of test engine setup

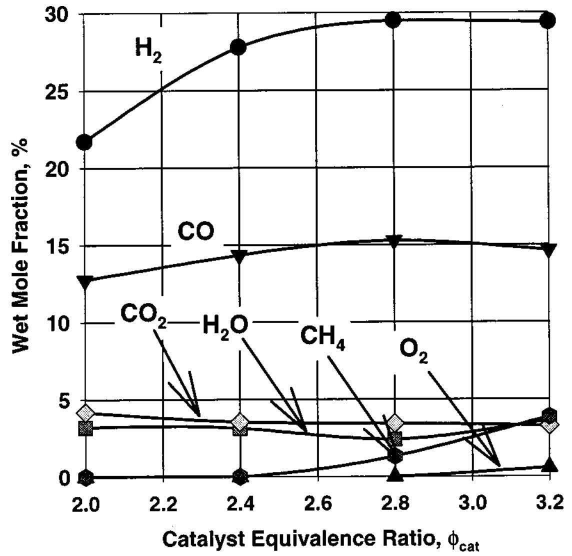

Fig. 2 Syngas composition as a function of catalyst equivalence ratio

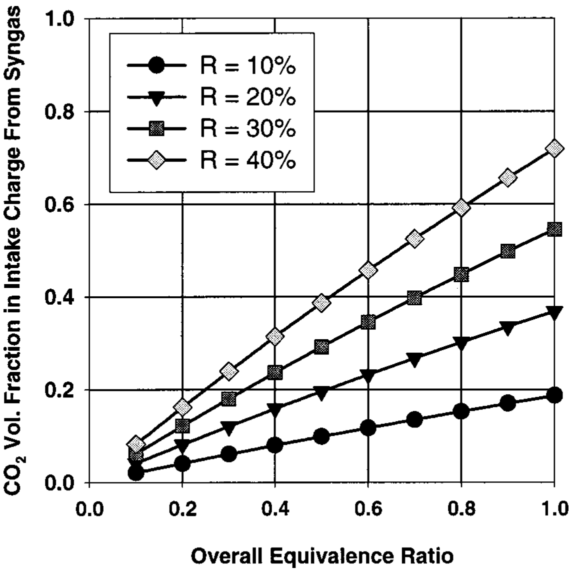

Fig. 3 CO_2 mole fraction in intake charge as a function of overall system equivalence ratio

Table 2 Syngas composition at a catalyst equivalence ratio of 2.8

Gas	Wet Mole, Fraction, %	Wet Mass, Fraction, %
H_2	29.7	2.9
CO	15.1	20.8
H_2O	3.4	3.0
CO_2	3.3	7.1
CH_4	1.2	0.9
O_2	0.0	0.0
N_2	47.3	65.2

syngas catalyst and engine. The syngas fraction, R, is defined as the fraction of natural gas routed into the syngas catalyst relative to the total amount of natural gas used by the engine/catalyst system as shown in Eq. (3). At each syngas fraction/EGR combination, spark timing was adjusted to maintain the constant 11.0 bar load at the minimum boost pressure.

$$\phi_{\text{sys}}=\frac{\left.\frac{A}{F}\right|_s}{\frac{\dot{m}_{A,e}+\dot{m}_{A,c}}{\dot{m}_{\text{NG},e}+\dot{m}_{\text{NG},c}}} \tag{2}$$

$$R=\frac{\dot{m}_{\text{NG,cat}}}{\dot{m}_{\text{NG},e}+\dot{m}_{\text{NG,cat}}} \tag{3}$$

A brief analysis of how the EGR fraction was determined in this study will be presented before results of the engine/catalyst system tests are presented. A classical method for determining the EGR fraction is to measure the volume fractions of CO_2 in the intake and exhaust gas. Equation (4) is then used to deduce the EGR fraction.

$$\text{EGR}=\frac{\text{CO}_{2,\text{intk}}-\text{CO}_{2,\text{bkgnd}}}{\text{CO}_{2,\text{exh}}-\text{CO}_{2,\text{bkgnd}}}\times 100 \tag{4}$$

Although Eq. (4) provides a quick and relatively easy method for defining an EGR fraction, erroneous EGR fractions can be computed if the fuel contains CO_2. For example, Fig. 3 shows how the CO_2 mole fraction in the intake charge varies with the overall system equivalence ratio and the syngas fraction. At a syngas fraction of 40 percent and a ϕ equal to 1.0 there is about 0.73 percent CO_2 in the intake air/fuel charge from syngas alone. If Eq. (4) is used with an exhaust gas composed of 11.5 percent CO_2, typical of stoichiometric gas engines, the EGR fraction would be computed as 6.35 percent. This result is misleading because no true engine EGR was assumed in the calculation. In addition, EGR fractions computed with Eq. (4) provide no scale for the amount of EGR mass actually inducted by the engine. Hence, another method should be employed.

In this study a few simple equations were derived to determine the mass flow rate of EGR given the measured molar CO_2 concentrations in the syngas, the intake charge, and the exhaust stream. We start by defining a mass-based EGR ratio as shown in Eq. (5).

$$\text{EGR}=\frac{\dot{m}_{\text{EGR}}}{\dot{m}_{A,e}+\dot{m}_{\text{NG},e}+\dot{m}_{\text{EGR}}+\dot{m}_{\text{SG}}}\times 100 \tag{5}$$

The unknown in Eq. (5) is the EGR mass flow rate. It can be determined from Eq. (6) which relates the measured CO_2 mole fraction in the intake charge to the total intake molar flow rate.

$$x_{\text{CO}_2,\text{intk}}=\frac{\dot{n}_{\text{CO}_2,\text{EGR}}+\dot{n}_{\text{CO}_2,\text{SG}}}{\dot{n}_{A,e}+\dot{n}_{\text{NG},e}+\dot{n}_{\text{EGR}}+\dot{n}_{\text{SG}}} \tag{6}$$

Equation (6) can be recast in terms of appropriate mole fractions, molecular weights, and mass flow rates as shown in Eq. (7) where all mole fractions, X_i, are assumed dry. $X_{\text{CO2,EGR}}$ is the mole fraction of CO_2 in the exhaust gas, $X_{\text{CO2,SG}}$ is the measured CO_2 mole fraction in the syngas, and $X_{\text{CO2,intk}}$ is the measured CO_2 mole fraction in the total intake charge.

$$x_{\text{CO}_2,\text{intk}}=\frac{x_{\text{CO}_2,\text{EGR}}\frac{\dot{m}_{\text{EGR}}}{\text{MWT}_{\text{EGR}}}+x_{\text{CO}_2,\text{SG}}\frac{\dot{m}_{\text{SG}}}{\text{MWT}_{\text{SG}}}}{\frac{\dot{m}_{A,e}}{\text{MWT}_A}+\frac{\dot{m}_{\text{NG},e}}{\text{MWT}_{\text{NG}}}+\frac{\dot{m}_{\text{EGR}}}{\text{MWT}_{\text{EGR}}}+\frac{\dot{m}_{\text{SG}}}{\text{MWT}_{\text{SG}}}} \tag{7}$$

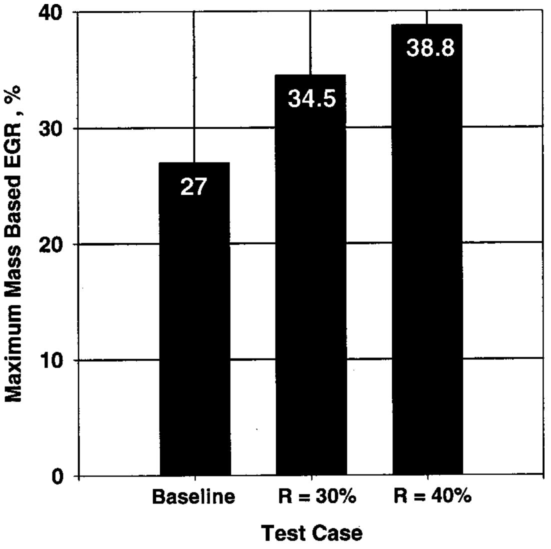

Fig. 4 Maximum EGR fractions for syngas fractions of 0, 30, and 40 percent

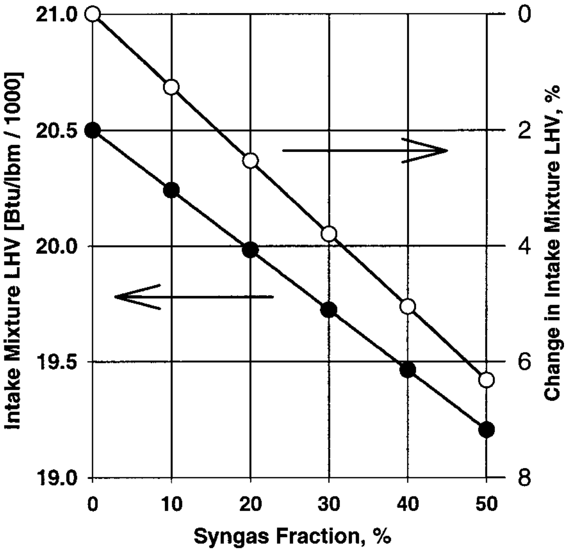

Fig. 6 Effect of syngas on lower heating value of fuel mixture at intake port

A few algebraic manipulations yield the desired mass flow rate of EGR as shown in Eq. (8). Hence, the mass-based EGR flow rate is then easily determined from Eq. (5), which is in terms of known constants and measurable quantities.

$$\dot{m}_{\mathrm{EGR}}=\frac{\mathrm{MWT}_{\mathrm{EGR}}}{x_{\mathrm{CO}_2,\mathrm{intk}}-x_{\mathrm{CO}_2,\mathrm{EGR}}}\times(\alpha-\beta) \tag{8}$$

where,

$$\alpha=\frac{\dot{m}_{\mathrm{SG}}}{\mathrm{MWT}_{\mathrm{SG}}}\times(x_{\mathrm{CO}_2,\mathrm{SG}}-x_{\mathrm{CO}_2,\mathrm{intk}})$$

$$\beta=x_{\mathrm{CO}_2,\mathrm{intk}}\left(\frac{\dot{m}_{A,e}}{\mathrm{MWT}_A}+\frac{\dot{m}_{\mathrm{NG},e}}{\mathrm{MWT}_{\mathrm{NG}}}\right)$$

Figure 4 shows the extension in the mass based EGR fraction. At an *R* of 40 percent, the maximum EGR fraction was 38.8 percent compared to 27 percent with no syngas. Hence, the EGR tolerance of the engine was extended by 44.4 percent.

BTE as a function of the EGR fraction is shown in Fig. 5. At EGR fractions less than 10 percent, the baseline (no syngas) condition was bracketed between the 30 and 40 percent syngas fractions. However, as the EGR fraction increased, all data nearly collapse onto a single curve up to about 30 percent EGR. Above 30 percent EGR, the 40 percent syngas fraction curve reaches a maximum of 38.2 percent, while the 30 percent syngas curve peaks at 39.1 percent.

The increase in BTE with EGR is a well documented trend similar to the use of excess air in lean-burn engines. However, the most important feature in Fig. 5 is that comparable BTE was obtained while operating on syngas. This is somewhat surprising since the heating value of the intake fuel mixture is reduced by about 5 percent as the syngas fraction increases to 40 percent as shown in Fig. 6. It must be noted that to maintain 11.0 bar bmep, the manifold pressure had to be increased as *R* increased for a

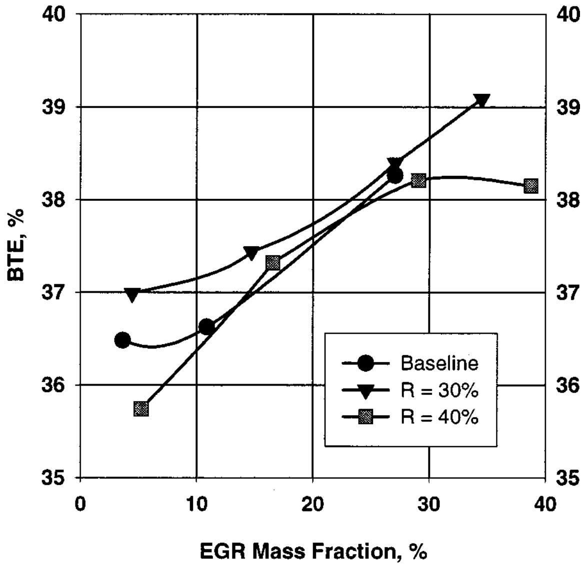

Fig. 5 Brake thermal efficiency versus the EGR fraction

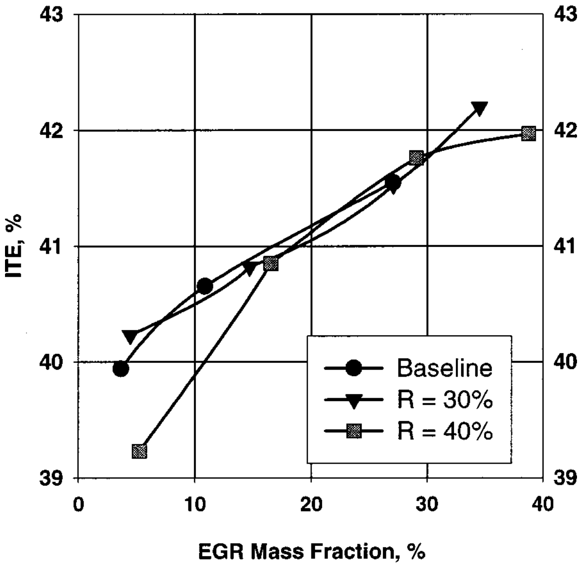

Fig. 7 Indicated thermal efficiency versus the EGR fraction

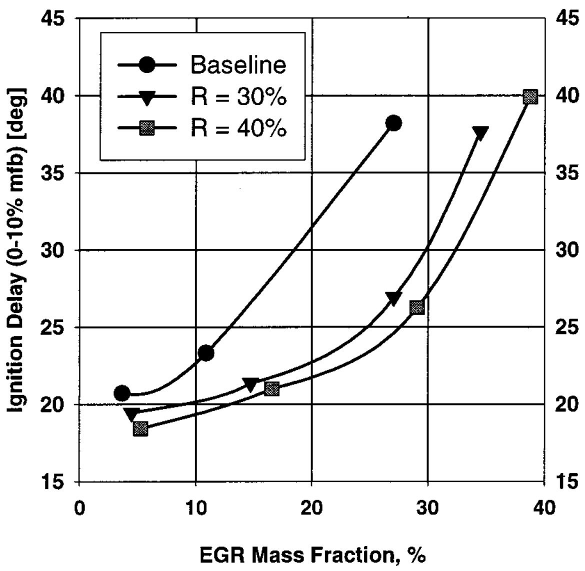

Fig. 8 Ignition delay versus the EGR fraction

given EGR fraction. Therefore, a better indicator of performance for this single-cylinder engine is the indicated thermal efficiency (ITE). Figure 7 shows the ITE as function of the EGR fraction. The syngas curves lie nearly on top of each other beyond an EGR fraction of 20 percent. Hence, the syngas/natural gas fuel mixture is being used as efficiently as natural gas alone.

The reasons for the comparable ITEs in Fig. 7 can be partially explained by examining the ignition delay and the 10 to 90 percent mass fraction burn duration plots in Figs. 8 and 9. In Fig. 8 it can be seen that the ignition delay decreases with increasing syngas fraction for any given EGR fraction. A similar trend is shown in Fig. 9 as the EGR fraction increase beyond 10 percent. This is most probably due to the low ignition energy requirements of H_2 and the fast flame speed of H_2 relative to natural gas.

The primary focus of the use of syngas with EGR is its effects on NO*x*. It has already been shown that syngas can extend the EGR tolerance significantly. Therefore, we now present the effects of syngas/EGR mixtures on NO*x*, HC, and CO emissions.

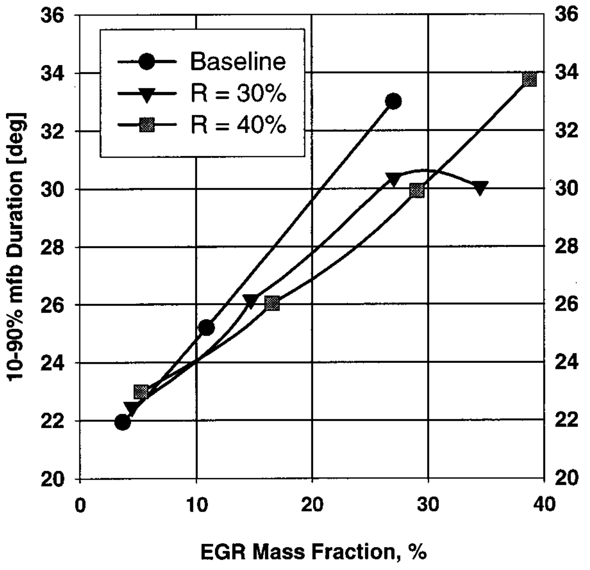

Fig. 9 10–90 percent MFB duration versus the EGR fraction

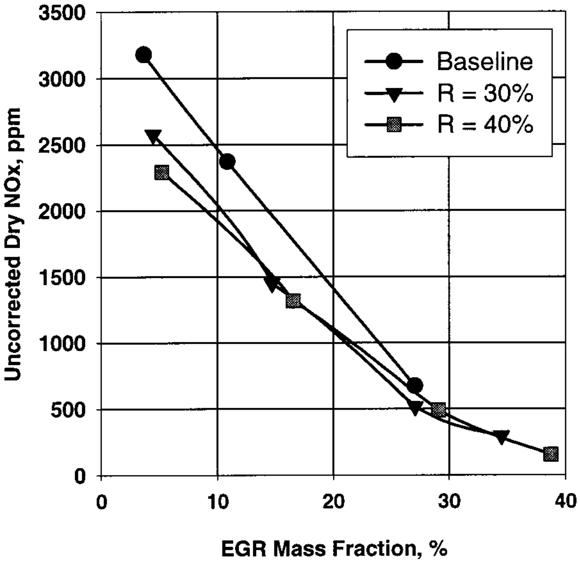

Fig. 10 Effects of syngas and EGR on raw, uncorrected, NO*x* emissions

Figure 10 shows how raw, uncorrected, NO*x* varies with the syngas and EGR fractions. At low EGR fractions the baseline case always generated more NO*x* than the syngas cases. This occurs because syngas itself provides a ‘‘dilution’’ effect in the sense that it contains CO_2, as well as other non-combustible gases. As the EGR fraction approaches 30 percent, the effect of CO_2 becomes more apparent in the baseline case as NO*x* nears NO*x* values for the syngas cases.

The minimum NO*x* at the corresponding maximum EGR fractions are shown in Fig. 11. The minimum NO*x* for the baseline condition was 680 ppm while the minimum NO*x* for a syngas fraction of 40 percent was 156 ppm. Hence, syngas reduced NO*x* emissions by 77 percent relative to baseline.

Unburned HCs and CO are plotted in Figs. 12 and 13, respectively. HCs decreased with increasing syngas fraction for a given EGR fraction. This decrease in HC emissions is an effect of reforming the natural gas into syngas that has also been observed

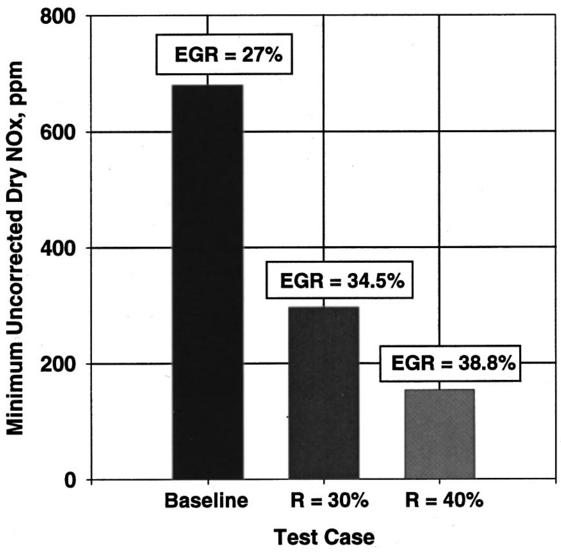

Fig. 11 Minimum NO*x* for the baseline and syngas cases at the corresponding maximum EGR fraction

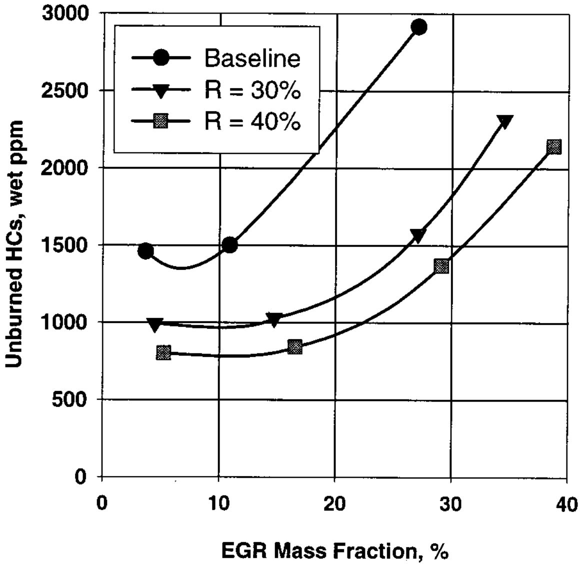

Fig. 12 Wet unburned HC emissions versus the EGR fraction

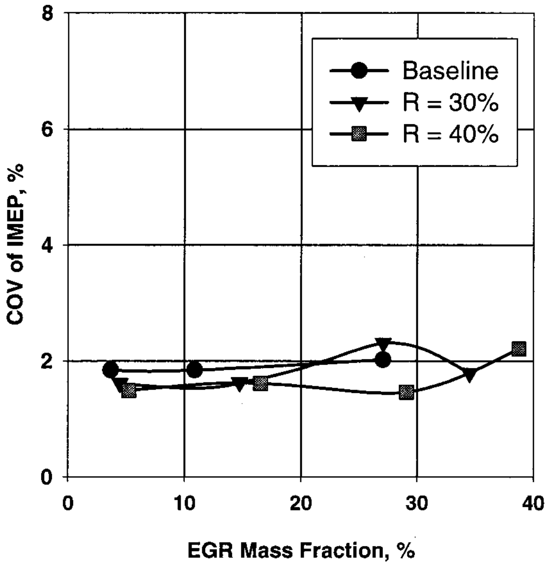

Fig. 14 The COV of IMEP versus the EGR fraction

when operating engines on air-reformed gasoline and the lean-burn syngas concept discussed in reference [15]. Figure 13 shows that CO emissions do not change as *R* increases relative to baseline CO emissions at low EGR fractions. However, the CO trends at EGR fractions greater than 20 percent increase and exhibit a trend typically observed in ultra-lean-burn engines. Increases in CO emissions might be expected since the fuel charge itself contains CO due to the syngas.

Combustion stability, as measured by the coefficient of variation of the indicated mean effective pressure (COV of IMEP), is also a concern when developing low emissions combustion systems. Figure 14 shows that the COV of IMEP was less than 2 percent except at one point. Intuitively one would expect the COV of IMEP to increase with increasing EGR fraction. Figure 14 does show a slight increase as the EGR fraction increases for all three curves, but not at the expected rate. Setting the EGR fraction and maintaining a prescribed syngas fraction proved to be a cumbersome task during testing. The engine would either run, or not run. Changes in EGR appeared to be very dramatic near the EGR tolerance limit. Therefore, the maximum attainable EGR fractions for baseline and syngas operation more than likely lie slightly beyond the maximum EGR fractions presented. It is likely that the combustion stability degrades dramatically at EGR fractions just beyond the maximum values presented.

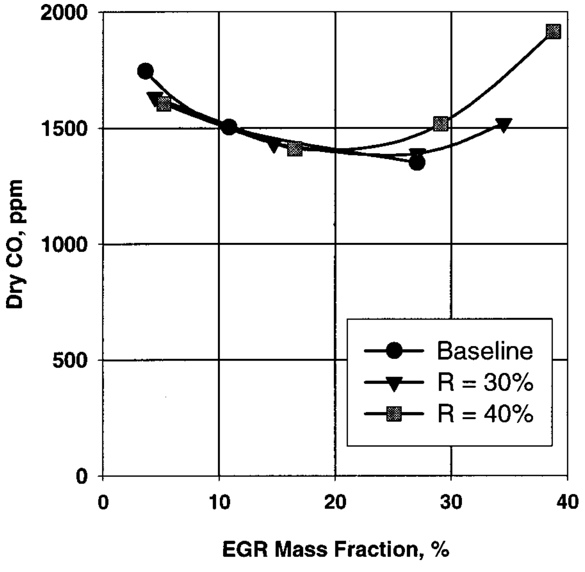

Fig. 13 Dry CO emissions versus the EGR fraction

Conclusions and Recommendations

A ceramic monolithic catalyst loaded with 10 percent by weight rhodium was installed in the intake system of a single cylinder Caterpillar 1Y-540 natural gas fueled engine and generated syngas with a H_2 mole fraction of 29.7 percent. The engine/catalyst system was operated at a constant load of 11.0 bar (160 psi) bmep. The effects of stoichiometric mixtures of syngas and natural gas with EGR on engine performance and emissions was determined. Testing showed that:

1 Use of syngas extended the EGR tolerance of the engine by 44 percent compared to the baseline, no syngas condition.

2 Extensions of the EGR tolerance resulted in a decrease in raw engine out NO*x* emissions from 680 ppm during baseline operation with maximum EGR down to 156 ppm at a syngas fraction of 40 percent and at maximum EGR.

3 HC emissions decrease at a given EGR fraction when operating on natural gas/syngas mixtures as *R* increases.

4 At low EGR fractions there was no difference in CO emissions while operating on natural gas and EGR or natural gas/syngas and EGR. Above an EGR fraction of 20 percent, however, CO emissions increased as the syngas fraction increased.

5 At a given EGR fraction, both the ignition delay and 10 to 90 percent mass fraction burn duration decrease relative to baseline when operating on natural gas/syngas mixtures as the syngas fraction increased.

The SSENGC concept has several significant implications on the conversion requirements and life of a TWC, as well as the complexity of the control system required for closed-loop equivalence ratio control. First, since the conversion efficiency of a TWC decreases with use, a TWC can possibly be utilized for a longer period of time in an SSENGC application because the NO*x* conversion efficiency requirements are significantly reduced compared to a conventional stoichiometric engine. For example, 0.15 g/bhp-hr NO*x* is equivalent to approximately 47 ppm for a stoichiometric engine operating at 38 percent BTE (47 ppm is equivalent to 14 ppm corrected to 15 percent exhaust O_2). A TWC has to be 93.1 percent efficient to convert 680 ppm down to 47 ppm. In comparison, a TWC in an SSENGC system only has to be 69.4 percent efficient to convert 156 ppm down to 47 ppm. Hence, the conversion efficiency requirements are reduced by 25.5 percent.

Second, it is difficult to maintain the equivalence ratio within the very narrow control window required for maximum TWC conversion efficiency to meet 0.15 g/bhp-hr NOx. The SSENGC concept may allow equivalence ratio excursions to be tolerated while still maintaining NOx to 0.15 g/bhp-hr or below. Hence, the control system algorithms can possibly be relaxed and small shifts in the exhaust gas oxygen sensor output, used for control feedback on these systems, may be tolerable.

The tests described in this paper were conducted on an engine with a compression ratio typical of lean-burn engines. In addition, the air flow and exhaust temperature characteristics of the SSENGC concept are typical of lean-burn engines. Therefore, although the focus of SSENGC appears to be directed at increasing stoichiometric engine performance and emissions, lean burn engines may be more suitable for SSENGC retrofits since most lean-burn engines have turbochargers and compression ratios near 11:1. In either case, the SSENGC concept can be applied to stoichiometric or lean-burn engines. The benefits of the SSENGC concept, however, can only be determined by performing baseline tests on a stoichiometric engine that can be certified in Southern California, and then subsequently retesting the same engine modified with the SSENGC concept. This task is currently being considered for future work.

Acknowledgments

The authors would like to thank Paul Kunkel for graciously accepting the challenging task of modifying and operating the test engine in just about every conceivable manner. In addition, John Kubesh and Dan Podnar, both of SwRI, deserve special thanks for their assistance in interpreting the results and help with the control system. Finally, the authors wish to thank the Advisory Committee for Research at SwRI for granting approval to conduct this work.

Nomenclature

BTE = system brake thermal efficiency
LHV = lower heating value
POM = partial oxidation of methane
R = syngas fraction
SG = syngas from POM catalyst
TWC = three-way catalyst
WOT = wide open throttle
ϕ = fuel/air equivalence ratio
$\mathbf{A/F}|_s$ = stoichiometric air-to-fuel ratio

Subscripts

A = air
bkgrnd = system value
cat = syngas catalyst
e = engine
exh = exhaust
intk = intake
NG = natural gas
sys = system value

References

[1] Meyers, D. P., and Kubesh, J. T., 1995, ''The Hybrid Rich-Burn/Lean-Burn Engine,'' *Natural Gas and Alternative Fuels for Engines*, Book No. H0093 ASME, New York.

[2] Smith, J. A., et al., 1996, ''The Hybrid Rich-Burn/Lean-Burn Engine, Part 2,'' *Natural Gas Engine, Combustion, Emission and Simulation*, ASME, New York.

[3] Houseman, J., and Hoehn, F. W., 1974, ''A Two-Charge Engine Concept: Hydrogen Enrichment,'' SAE Paper No. 741169.

[4] Parks, F. B., 1976, ''A Single-Cylinder Engine Study of Hydrogen Rich Fuels,'' SAE Paper No. 760099.

[5] MacDonald, J. S., 1976, ''Evaluation of the Hydrogen-Supplemented Fuel Concept with an Experimental Multicylinder Engine,'' SAE Paper No. 760101.

[6] Andreatta, D., 1996, ''An Experimental Study of Air-Reformed Natural Gas in Spark-Ignited Engines,'' SAE Paper No. 960852.

[7] Transamerica Delaval, Inc., 1982, ''Emulsified Fuel Testing in a Medium Speed Diesel Engine,'' Final Report, Prepared for the United States Department of Transportation Maritime Administration, MARAD Report No. MA-RD-920-82069.

[8] Pearce, K. R., et al., ''Emission Characteristics of a Medium Speed Diesel Using Water-Emulsified Residual Fuels,'' Final Report, Prepared for the United States Department of Transportation Maritime Administration, MA-RAD Contract No. MA-80-SAC-01859.

[9] Harbach, J. A., and Agosta, V., 1991, ''Effects of Emulsified Fuel on Combustion in a Four-Stroke Diesel Engine,'' J. Ship Res., **35**, No. 4, pp. 356–363.

[10] Kuroda, H., et al., 1978, ''The Fast Burn with Heavy EGR, New Approach for Low NOx and Improved Fuel Economy,'' SAE Paper No. 780006.

[11] Sato, Y., et al., 1993, ''Effect of EGR on NOx and Thermal Efficiency Improvement in a D.I. Methanol Engine for Light Duty Vehicles,'' SAE Paper No. 930758.

[12] Noble, A. D., and Beaumont, A. J. 1991, ''Control System for a Low Emissions Natural Gas Engine for Urban Vehicles,'' SAE Paper No. 910255.

[13] Podnar, D. J., et al., 1978, ''Development and Application of Advanced Control Techniques to Heavy-Duty Natural Gas Engines,'' presented at the Society of Automotive Engineers Conference.

[14] Heywood, J. B., 1988, *Internal Combustion Engine Fundamentals*, McGraw-Hill, New York, New York, pp. 567–586.

[15] Smith, J. A., and Bartley, G. J. J., 1997, ''Using Syngas in a Heavy-Duty, Lean-Burn Natural Gas Engine as a Means of NOx Reduction,'' *Engine Combustion Performance and Emissions*, ASME, New York.

Impact of Using Biodiesels of Different Origin and Additives on the Performance of a Stationary Diesel Engine

A. Serdari
K. Fragioudakis
S. Kalligeros
S. Stournas
E. Lois
e-mail: elois@orfeas.chemeng.ntua.gr

Laboratory of Fuel Technology and Lubricants,
Department of Chemical Engineering,
National Technical University of Athens,
Iroon Polytechniou 9, Zografou Campus 15700,
Athens, Greece

With the exception of rape seed oil which is the principal raw material for biodiesel Fatty Acid Methyl Esters, (FAME) production, sunflower oil, corn oil, and olive oil, which are abundant in Southern Europe, along with some wastes, such as used frying oils, appear to be attractive candidates for biodiesel production. In this paper fuel consumption and exhaust emission measurements from a single cylinder, stationary diesel engine are described. The engine was fueled with fuel blends containing four different types of biodiesel, at proportions up to 100 percent; the further impact of the usage of two specific additives was also investigated. The four types of biodiesel appeared to have equal performance and irrespective of the raw material used for their production, their addition to the traditional diesel fuel improved the particulate matter emissions. The results improve further when specific additive combinations are used. [S0742-4795(00)00604-9]

Introduction

The necessity to cope with environmental pollution problems, the changes in petroleum distillate demands, and the strict requirements of modern diesel engines lead to the need to improve diesel fuel quality. The development of biomass derived substitutes for diesel fuel is a possible attractive outlet, as it could help improve diesel fuel quality.

The substitution of conventional diesel fuel with rape seed oil methylesters comprises already a commercial activity in many countries of Central Europe [1]. However, the use of biodiesel has not expanded into Greece and other Southern European countries, due to the lack of adequate rape seed cultivation. Some other types of vegetable oils, such as sunflower oil, corn oil and olive oil, that are abundant in many Mediterranean areas, along with some wastes, such as used frying oils, appear to be attractive candidates for biodiesel production [2]. It must be stressed that the warranty of a product of extra high quality through the application of adequate relevant specifications is of the greatest importance and a key to scientifically proving its performance.

It is well known that biodiesel is non-toxic, contains no aromatics, has higher biodegradability than fossil diesel, is less pollutant to water and soil and does not contain sulphur [3,4]. It offers safer handling in the neat form and shows reduced oral and dermal toxicity, mutagenic and carcinogenic compounds. It is the most suitable fuel in environmentally sensitive areas (national parks, lakes, rivers) or in confined areas where environmental conditions and worker protection must meet high standards (underground mines, quarries) [5–7].

In this paper exhaust emission and fuel consumption measurements from a single cylinder, stationary diesel engine are described. The engine was fueled with fuel blends containing four different types of biodiesel, at proportions up to 100 percent. For two types of biodiesel, the further impact of the addition of two specific additives was investigated. In general, according to our results, the substitution of mineral diesel with biodiesels produced from sunflower oil, corn oil, olive oil and used frying oils leads to a combination of positive and negative outcomes; the four types of biodiesel tested performed in a similar way; they decreased exhaust emission of particulate matter, resulted in a limited change of nitrogen oxide emissions and in slightly increasing the volumetric fuel consumption.

The strong advantage of the use of fatty acid methyl esters (biodiesel) is the fact that independently on the raw material used for their production, the addition of biodiesel in the traditional diesel fuel improves the emissions of particulate matter [8] which comprise a serious disadvantage of the diesel engine, especially in seriously polluted areas like Athens.

Experimental Procedure

For this study, a stationary diesel powered Petter engine, model AV1-LAB was employed. The engine characteristics are cited in Table 1. The engine was fueled with four types of pure biodiesels, pure traditional road diesel and mixtures containing 10 percent, 30 percent, and 50 percent of each type of biodiesel. The four types of biodiesel were methyl esters produced from sunflower oil, corn oil, olive oil and used frying oil. The emission tests included HC, CO, CO_2, NO_x and particulate matter emission measurements under various loads up to 5 HP, the load being measured by shaft output. Volumetric fuel consumption was checked as well.

Similar tests on the stationary diesel engine investigated the effect of using a combination of two specific additives, on exhaust emissions from fuel mixtures containing corn oil and used frying

Table 1 Stationary, Petter AV1-LAB engine

Engine type: single cylinder, indirect injection

Speed: 1500 rpm

Compression ratio: 19/1

Total displacement: 553 cc

Maximum output: 5 HP (3.8 kW)

Contributed by the Internal Combustion Engine Division of THE AMERICAN SOCIETY OF MECHANICAL ENGINEERS for publication in the ASME JOURNAL OF ENGINEERING FOR GAS TURBINES AND POWER. Manuscript received by the ICE Division September 20, 1999; final revision received by the ASME Headquarters May 8, 2000. Technical Editor: D. Assanis.

Table 2 Specifications of the exhaust emission analyzers

	Thermo Environmental Instruments Inc NOx analyzer	Horiba MEXA 574-GE		
Emission	NO_x, ppm	HC, ppm	CO, % vol.	CO_2, % vol.
Method	Chemiluminencence	NDIR	NDIR	NDIR
Operation Range	0 – 5000	0 – 10000	0-10.00	0-20.00
Accuracy	0.050	2	0.01	0.02
Precision	±1%	±20	±0.05	±0.1

oil biodiesel at various proportions. The two additives (additive H1 and H2) are commercially available; H1 is a common diesel cetane improver (iso-octyl nitrate), while H2 is a combustion improver. The additive H1 was used in a concentration of 200 ppm in the fuel mixture and the additive H2 was used in a concentration of 500 ppm. These two additives have already been used in previous experiments in our Laboratory; the two additives were used in various concentrations for diesel evaluation, and the combination of 200 ppm H1 and 500 ppm H2 seems to be a very good proportion, since it resulted in the reduction of both particulate and nitrogen oxide emissions [9].

Two exhaust emission analyzers were used: a Horiba instrument (type MEXA 574-GE, that gauges HC, CO and CO_2 exhaust emissions) and a NOx analyzer (42C $NO\text{-}NO_2\text{-}NO_x$ Analyzer High Level, Thermo Environmental Instruments Inc.). The specifications of the emissions analyzers are cited in Table 2. The above analyzers were supported by Exhaust Gases Transportation Heated Lines, (Signal Instruments Co, model 530/540), and a Prefilter (Signal Instruments Co, Prefilter Unit 333) that restrains the emitted particulates from entering the Horiba and Thermo Environmental analyzers.

To measure particulate matter emitted from the stationary diesel Petter engine, equipment recommended by the Western Precipitation Division Joy Manufacturing Company was used. According to this method, exhaust gases pass through a fiber glass filter, while the flue gas volume is recorded by using a gas meter. Particulate matter weight results were obtained by subtracting the weight of the clean fiberglass filter from its weight at the end of the experiment, after drying. The procedure followed is depicted in Fig. 1. The filters used were glass microfiber by Whatman, Grade 934-AH. The filter face velocity of the exhaust gases was measured to be 1.3 m/sec, whereas, at the filter face, the average temperature was 150°C and the pressure drop 4×10^3 N/m^2.

Fuel was supplied to the Petter engine by an outside tank of about three-liter capacity, which could easily be drained for fuel changes; a glass burette of known volume was also attached in parallel to this tank and was used for fuel consumption measurements. For every fuel change, the fuel lines were cleaned, and the engine was left to run for at least 60 minutes to stabilize on the new conditions. No fuel filter was used.

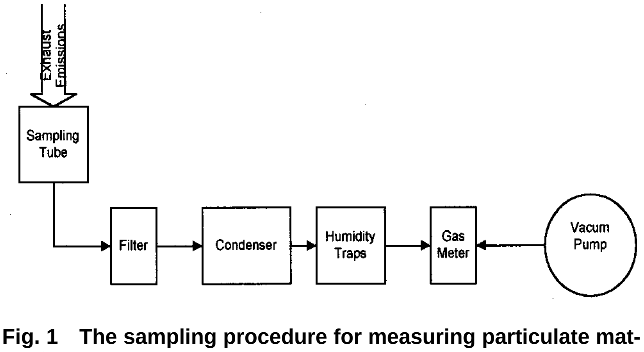

Fig. 1 The sampling procedure for measuring particulate matter (PM)

Test Fuels

The conventional diesel fuel was supplied by Hellenic Aspropyrgos Refinery and the values of its fuel properties are presented in Table 3. All types of biodiesel used in the currently described tests were supplied by the Italian company Florys Spa and their properties were in complete accordance with the Italian specifications for biodiesel (CUNA specifications). The fuel properties of the four types of biodiesel are given in Table 4.

Discussion and Results

The experiments in the stationary Petter engine included emission and consumption measurements, under various loads. The engine was fueled with five different fuels containing biodiesels, at various proportions. The fuels tested were low sulphur typical Greek road diesel and mixtures of the typical Greek road diesel containing 10 percent, 30 percent, and 50 percent by volume sunflower oil, corn oil, olive oil and used frying oil biodiesel. The pure (100 percent) biodiesels were also examined. Also, the impact of the additive combination (200 ppm of the additive H1 and 500 ppm of the additive H2) on the performance of fuel mixtures containing corn oil and used frying oil biodiesel at various proportions was examined.

The use of biodiesel fuels results in the reduction of unburned hydrocarbons and carbon monoxide [10–12]. However, in the course of our experiments, both of these pollutants were practically unaffected by the addition of every type of biodiesel; their emission levels were very low even when mineral diesel fuel was used. Moreover, their emission levels were much lower than the measuring accuracy of the Horiba Analyzer. The same performance was observed when the additive combination was examined. This behavior is attributed to the technology of the specific engine.

The emission levels of the base fuel without and with the addition of additives are cited in Table 5; the mean values of 4 indi-

Table 3 Greek road diesel properties

Properties	*unit*	*value*	*test method*
Density at 15 °C	kg/l	0.8371	ASTM D 1298
Distillation curve	% v/v		ASTM D 86
- recovered at 250°C		32	
- recovered at 350°C		88	
- recovered at 370°C		95	
Sulphur	% wt	0.035	ASTM D 4294
Copper strip corrosion		1A	ASTM D 130
Flash point	°C	68	ASTM D 93
Kin. Viscosity at 40°C	cSt	3.0	ASTM D 445
Water	mg/kg	80	ASTM D 1744
Cetane Index		54.8	ASTM D 4737
Ash	% wt	0.005	ASTM D 482
Conradson Carbon Residue	% wt	0.02	ISO 10370
CFPP	°C	-11	IP 309
Suspended matter	mg/kg	< 24	DIN 51419
Oxidation Stability	g/m^3	< 25	ASTM D 2274
Low Heating Value	kcal/kg	10204	ASTM D 2015

Table 4 Characteristic properties of the pure (100 percent) biodiesels

Properties	*Sunflower oil*	*Corn oil*	*Olive oil*	*Used frying oil*	*Test method*
Density at 15°C (gr/m^3)	0.8853	0.8858	0.8801	0.8829	ASTM D 1298
Copper Strip Corrosion	1A	1A	1A	1A	ASTM D 130
Sulphur (% wt)	0.0047	0.0047	0.0010	0.0010	ASTM D 4294
Flash Point (°C)	110	111	>110	>110	ASTM D 93
Kin. Viscosity at 40°C (cSt)	4.391	4.515	4.700	4.500	ASTM D 445
CFPP (°C)	-2	-7	-6	-4	IP 309
Cloud Point (°C)	1.5	-3.4	-2.0	1	ASTM D 2500
Pour Point (°C)	-3	-3	-3	-3	ASTM D 97
Cetane Number	58	65	61	59	DIN 51773
Ash (% wt)	0.0007	0.005	0.0054	0.0091	ASTM D 482
Water (mg/Kg)	518	528	243	320	ASTM D 1744
Conradson Carbon Residue (% wt)	0.98	1.20	0.22	0.51	ISO 10370
Oxidation Stability (g/m^3)	36	83	16	24	ASTM D 2274
Low Heating Value (kcal/kg)	9189	9191	8906	8918	ASTM D 2015

vidual measurements along with their standard deviations at the 95 percent confidence level are included. In Tables 6 and 7 the effect, on the NOx emissions and the particulate matter (PM), respectively, of adding the four investigated types of biodiesel and the additives to mineral diesel fuel, at various proportions and under various loads up to 5 HP (full load), are presented along with their standard deviations at the 95 percent confidence. More specifically,

1 Regarding the impact of the four biodiesel containing fuels on total nitrogen oxide emissions, it seems that at low concentrations of biodiesel (10 percent and 30 percent), total nitrogen oxide emissions are reduced in most cases, Table 6 and Figures 2–5. At high concentrations of biodiesel (50 percent and 100 percent), in most of the cases total nitrogen oxide emissions are increased. This becomes more apparent at high loads (75 percent and 100 percent), almost in all mixtures and for every type of biodiesel. These results are in agreement with the relevant literature [13–16] which shows, in most of the cases, a trend to increase NO and NOx emissions. This increase is due to the oxygen content of the biodiesel, which leads to better oxidation of the nitrogen available, thus increasing the nitrogeneous emissions, although engine technology also plays an important role [17].

2 As for the impact on particulate matter emissions of adding

Table 5 Emission measurements from the stationary Petter engine, when Greek diesel fuel was used (base fuel measurements)

	0.1 HP	1.25 HP	2.5 HP	3.75 HP	5HP
NOx emissions of the diesel base fuel (ppm)					
Mean Value	355	538	700	701	883
Strd Deviation	22.6	8.6	8.7	36.1	28.5
NOx emissions of the diesel base fuel + additives (ppm)					
Mean Value	342	505	680	695	833
Strd Deviation	27.8	6.6	6.7	27.9	35.0
Particulate Matter emissions of the diesel base fuel (mg/m^3)					
Mean Value	12	19	37	53	82
Strd Deviation	0.9	0.8	4.7	1.0	2.8
Particulate Matter emissions of the diesel base fuel + additives (mg/m^3)					
Mean Value	11	17	33	47	72
Strd Deviation	1.0	0.7	4.2	0.9	3.1

Table 6 Emission measurements of total nitrogen oxide (ppm) due to the addition of biodiesels and additives

		NOx EMISSIONS (ppm)				
	Concentration in the fuel blends	0.1 HP	1.25 HP	2.5 HP	3.75 HP	5HP
Sunflower oil biodiesel						
	10%	351±22.4	522±8.3	690±8.6	667±34.4	905±29.2
	30%	353±22.5	529±8.4	671±8.3	677±34.9	913±29.5
	50%	362±23.0	554±8.8	729±9.1	743±38.3	945±30.5
	100%	373±23.7	554±8.8	735±9.1	757±39.0	971±31.4
Corn oil biodiesel						
	10%	337±21.5	494±7.9	665±8.3	651±33.5	843±27.2
	30%	340±21.6	516±8.2	669±8.3	677±34.9	865±28.0
	50%	349±22.2	520±8.3	707±8.8	712±36.6	901±29.1
	100%	355±22.6	533±8.5	714±8.9	717±36.9	953±30.8
Olive oil biodiesel						
	10%	327±20.8	506±8.1	662±8.2	653±33.6	847±27.3
	30%	334±21.3	510±8.2	668±8.3	659±33.9	849±27.4
	50%	344±21.9	527±8.4	694±8.7	711±36.6	898±29.0
	100%	353±22.5	541±8.6	707±8.8	720±37.1	909±29.4
Used frying oil biodiesel						
	10%	334±21.2	520±8.3	685±8.5	715±36.8	925±29.9
	30%	336±21.4	522±8.4	704±8.8	716±36.9	933±30.1
	50%	341±21.7	533±8.5	712±8.8	729±37.5	937±30.2
	100%	351±22.4	537±8.8	720±9.0	743±38.3	946±30.5
Corn oil biodiesel + additives						
	10%	335±21.4	503±8.0	652±8.1	650±33.5	817±26.4
	30%	338±21.5	514±8.2	666±8.3	667±34.3	839±27.1
	50%	348±22.2	516±8.2	686±8.5	672±34.6	872±28.1
	100%	354±22.5	532±8.5	691±8.6	692±35.6	901±29.1
Used frying oil biodiesel + additives						
	10%	330±21.0	516±8.2	678±8.4	694±35.7	902±29.1
	30%	335±21.3	519±8.3	693±8.6	699±36.0	908±29.3
	50%	339±21.6	529±8.5	698±8.7	708±36.5	911±29.4
	100%	328±22.1	536±8.6	707±8.8	723±37.2	923±29.8

Table 7 Emission measurements of particulate matter (mg/m^3) due to the addition of biodiesels and additives

	PARTICULATE MATTER EMISSIONS (mg/m^3)					
	Concentration in the fuel blends	0.1 HP	1.25 HP	2.5 HP	3.75 HP	5HP
Sunflower oil biodiesel						
	10%	11±0.8	18±0.7	34±4.3	47±0.9	68±2.3
	30%	11±0.8	17±0.7	33±4.2	46±0.9	67±2.3
	50%	11±0.8	17±0.7	33±4.2	45±0.8	59±2.0
	100%	11±0.8	17±0.7	32±4.1	44±0.8	49±1.7
Corn oil biodiesel						
	10%	11±0.9	18±0.8	34±4.4	48±0.9	71±2.4
	30%	11±0.8	18±0.8	35±4.4	47±0.9	69±2.3
	50%	11±0.8	18±0.8	34±4.4	47±0.9	66±2.2
	100%	11±0.8	17±0.7	32±4.0	43±0.8	57±2.0
Olive oil biodiesel						
	10%	11±0.8	18±0.8	34±4.3	46±0.9	66±2.2
	30%	11±0.8	18±0.7	34±4.3	44±0.8	64±2.2
	50%	11±0.8	17±0.7	33±4.2	43±0.8	57±2.0
	100%	11±0.8	17±0.7	32±4.1	42±0.8	50±1.7
Used frying oil biodiesel						
	10%	12±0.9	19±0.8	36±4.5	48±0.9	73±2.5
	30%	12±0.9	19±0.8	35±4.5	47±0.9	71±2.4
	50%	12±0.9	19±0.8	35±4.5	45±0.8	68±2.3
	100%	12±0.9	18±0.8	35±4.5	44±0.8	61±2.1
Corn oil biodiesel + additives						
	10%	11±0.8	18±0.8	34±4.4	47±0.9	69±2.4
	30%	11±0.8	18±0.7	34±4.3	45±0.8	67±2.3
	50%	11±0.8	18±0.7	34±4.3	45±0.8	65±2.2
	100%	11±0.8	17±0.7	31±3.9	42±0.8	55±1.9
Used frying oil biodiesel + additives						
	10%	12±0.9	19±0.8	35±4.5	47±0.9	72±2.5
	30%	12±0.9	19±0.8	35±4.5	46±0.7	69±2.4
	50%	12±0.9	18±0.8	35±4.4	45±0.8	66±2.3
	100%	12±0.9	18±0.8	34±4.4	43±0.8	60±2.0

different types of biodiesel to mineral diesel fuel, the literature review [16–19] shows that particulate matter emissions are generally reduced by the addition of biodiesel in the traditional diesel fuel, due to the oxygen contained in the biodiesel molecules and the abscence of sulphur. Some studies however, showed a big increase in particulate emissions in transient cycles [17]. In this study biodiesel appears to reduce particulate emissions almost in

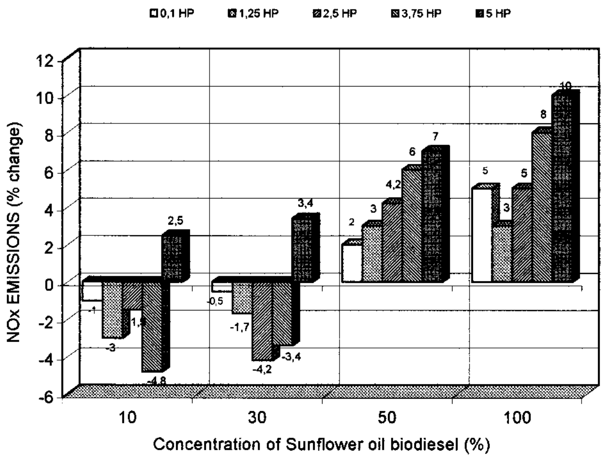

Fig. 2 Percentage change of the total nitrogen oxide emissions (ppm), due to the addition of sunflower oil biodiesel

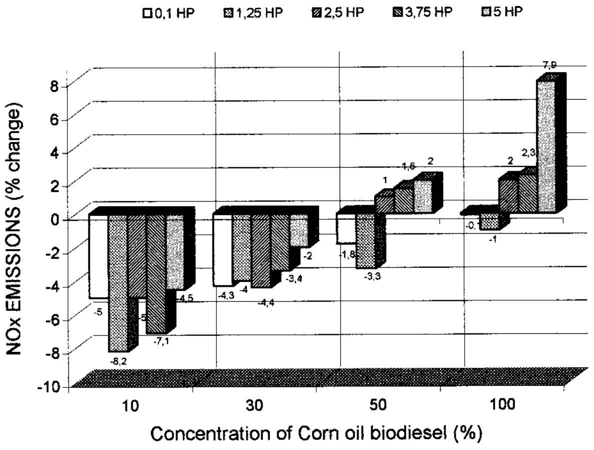

Fig. 3 Percentage change of the total nitrogen oxide emissions (ppm) due to the addition of corn oil biodiesel

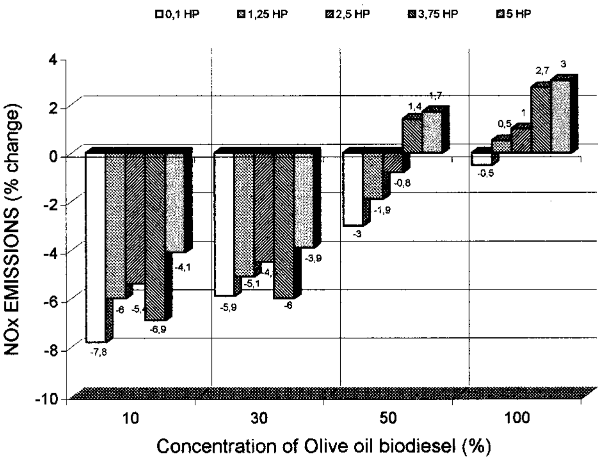

Fig. 4 Percentage change of the total nitrogen oxide emissions (ppm) due to the addition of olive oil biodiesel

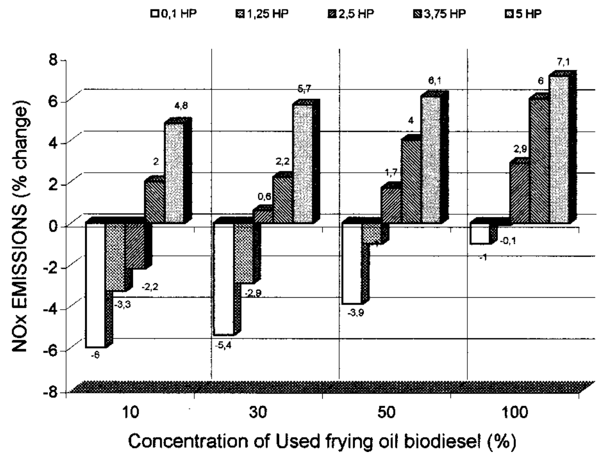

Fig. 5 Percentage change of the total nitrogen oxide emissions (ppm) due to the addition of used frying oil biodiesel

all cases, Table 7 and Figs. 6–9. At low concentrations and loads the reduction is marginal, especially at 10 percent mixtures, whereas the most beneficial reductions appear at higher concentrations and loads. Although it is an important aspect of the particulate matter emitted from compression ignition engines, no further treatment was carried out to establish the soluble organic fraction (SOF).

The study of the impact of adding the specific combination of H1 and H2 additives (200 ppm H1 and 500 ppm H2) to some of the above fuel blends included emissions (NOx, particulates) and volumetric fuel consumption measurements in the same engine. For these experiments, fuel blends with corn oil biodiesel and used frying oil biodiesel were used.

Table 5 shows the effect of the additives on the base fuel. It can be seen that for all loads there is a systematic decrease of the NOx emitted from the engine. This is to be expected, since the iso-octyl nitrate (H1) is a Cetane Number improver which, at the concentration used, increases the base fuel Cetane Number by 1 unit. However, any increase in Cetane Number usually leads to lower NOx emissions [17]. The additive H2 is a combustion improver and, being an organometallic compound, it has a catalytic effect on the combustion process in the diesel engine [17]. Addition of 10 percent corn oil biodiesel into the base fuel plus additives, initially reduces NOx emissions for all loads, but this tendency is reversed for higher concentrations, the exceptions being at 30 per-

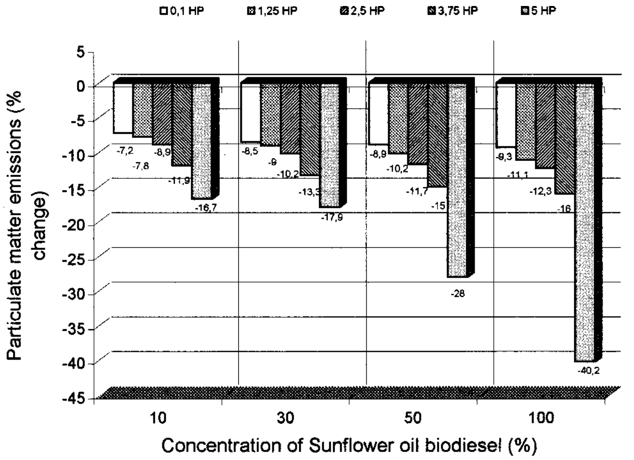

Fig. 6 Percentage change of particulate matter emissions (mg/m^3) due to the addition of sunflower oil biodiesel

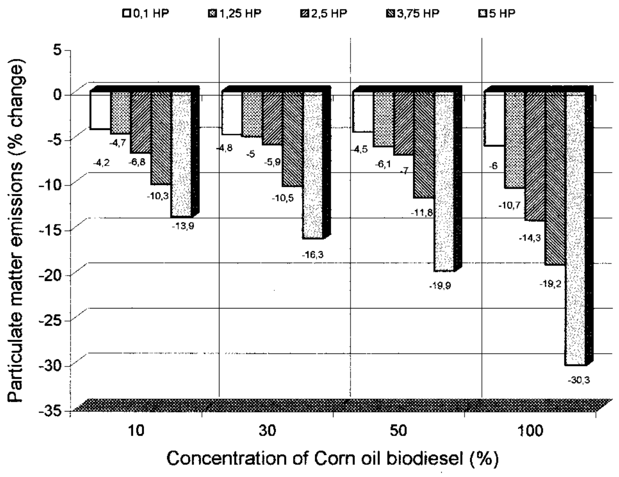

Fig. 7 Percentage change of particulate matter emissions (mg/m^3) due to the addition of corn oil biodiesel

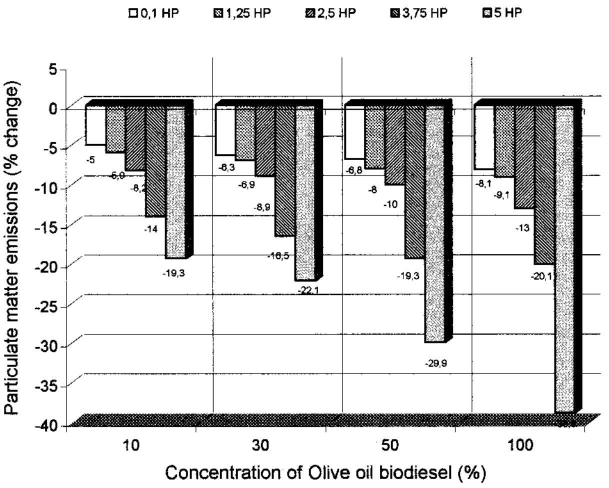

Fig. 8 Percentage change of particulate matter emissions (mg/m^3) due to the addition of olive oil biodiesel

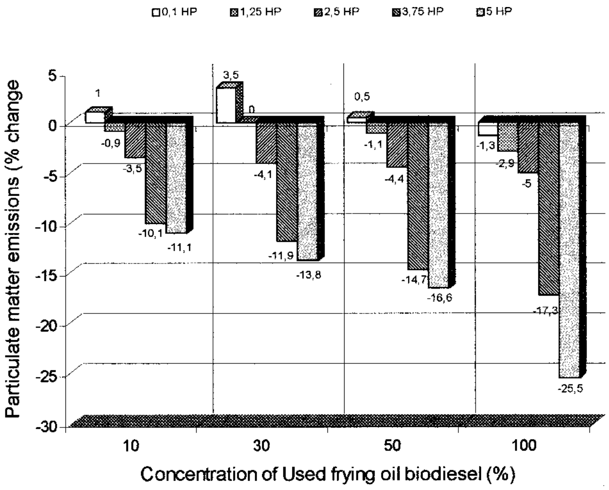

Fig. 9 Percentage change of particulate matter emissions (mg/m^3) due to the addition of used frying oil biodiesel

cent addition of corn oil and loads up to 3.75 HP, Table 6. When used frying oil is added to the base fuel plus additives, there is a further decrease of NOx emissions at 0.1 HP irrespective of the biodiesel concentration, but this tendency again is reversed for higher loads. The notable result is that the use of the two additives into the mixture of the base fuel plus biodiesel, reduces NOx emissions further, practically for all loads and concentrations, irrespective of the type of the biodiesel used, Table 6 and Figs. 10–11.

Table 5 shows that the addition of the additives H1 and H2 into the base fuel, reduces the particulate matter (PM) emitted for all loads. Again, as explained earlier this behavior is expected given the nature of the additives [17]. Table 7 and Figs. 12–13 illustrate the impact of the addition of H1 and H2 additives, on particulate matter emissions, into fuel blends containing various concentrations of corn oil and used frying oil biodiesel, under various loads up to 5 HP. This combination, almost under any load, either did not affect or reduced the particulate matter emissions.

The influence of the addition of the corn oil and used frying oil into the base fuel at various concentrations up to 100 percent, plus the additives H1 and H2, on the fuel consumption is presented in Figs. 14–17. All mixtures, under any load, resulted in slight increases of fuel consumption. Due to the oxygen content and, consequently, to the lower calorific value of the fuels which contain biodiesel, this behavior was expected. No significant impact was observed owing to the use of the additive combination.

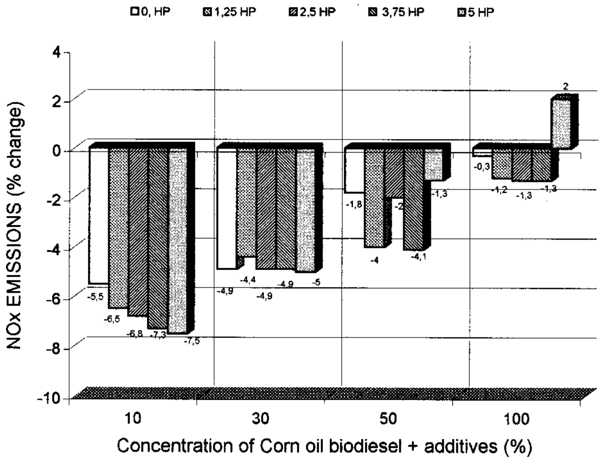

Fig. 10 Percentage change of the total nitrogen oxide emissions (ppm) due to the addition of corn oil biodiesel+additives

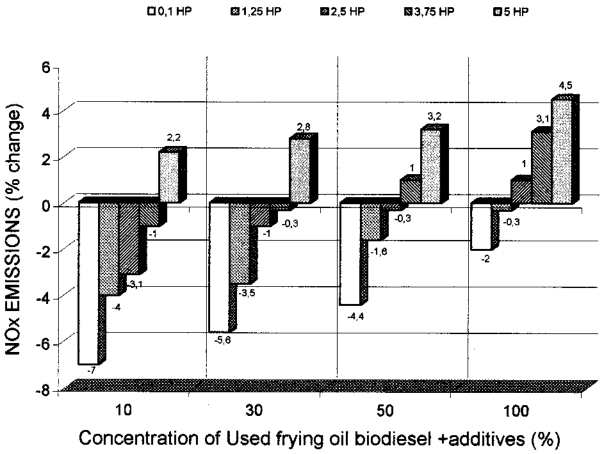

Fig. 11 Percentage change of the total nitrogen oxide emissions (ppm) due to the addition of used frying oil biodiesel+additives

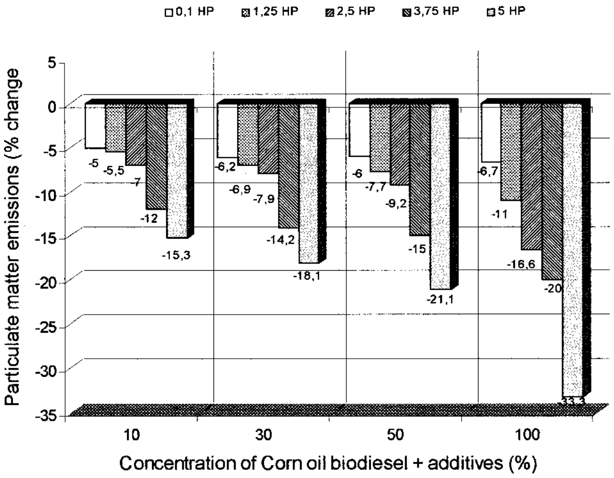

Fig. 12 Percentage change of particulate matter emissions (mg/m^3) due to the addition of corn oil biodiesel+additives

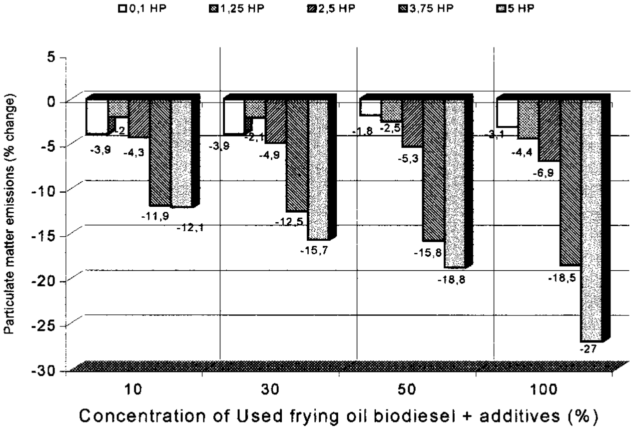

Fig. 13 Percentage change of particulate matter emissions (mg/m^3) due to the addition of used frying oil biodiesel+additives

Conclusions

The substitution of mineral diesel with biodiesels produced from sunflower oil, corn oil, olive oil and used frying oils leads to a combination of positive and negative outcomes. The four types of biodiesel examined performed in a similar way; they clearly decreased particulate matter emissions, and resulted in a limited change of nitrogen oxide emissions and slightly increased the volumetric fuel consumption.

The strong advantage of the use of fatty acid methyl esters (biodiesel) seems to be the fact that independently on the raw material used for their production, the addition of biodiesel in the traditional diesel fuel improves the emissions of particulate matter which comprise a serious disadvantage of the diesel engine, especially in polluted areas.

The specific combination of two additives does not affect exhaust emissions negatively; however, the additives may act as a drawback in some cases where biodiesel blends had achieved sig-

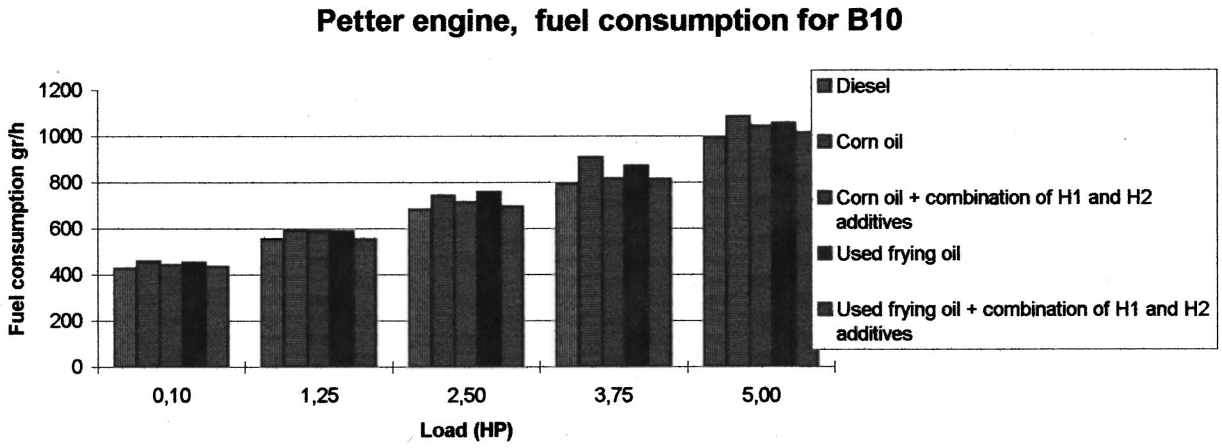

Fig. 14 Fuel consumption for conventional diesel fuel and fuel blends containing 10 percent biodiesel with/without the combination of H1 and H2 additives

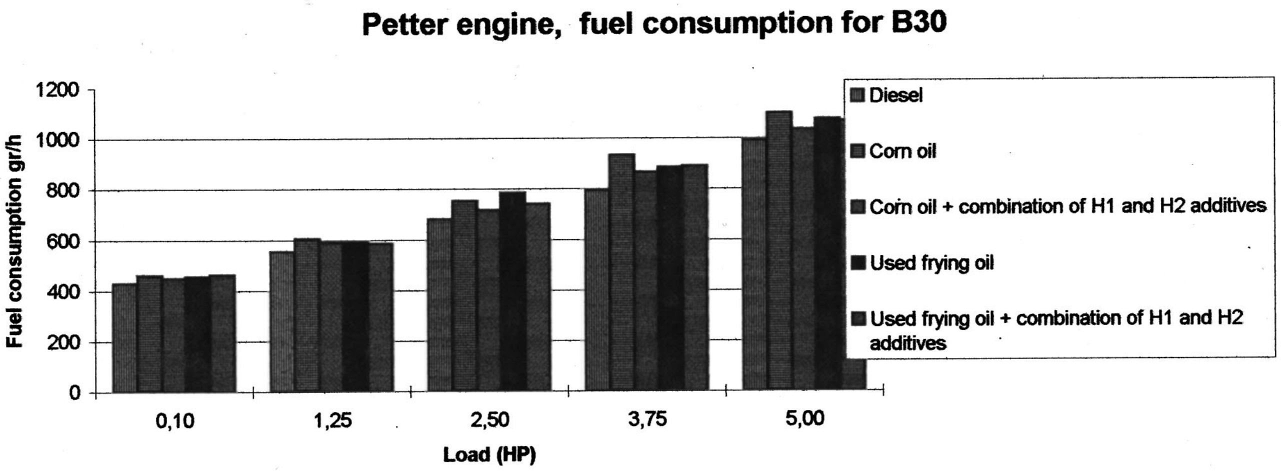

Fig. 15 Fuel consumption for conventional diesel fuel and fuel blends containing 30 percent biodiesel with/without the combination of H1 and H2 additives

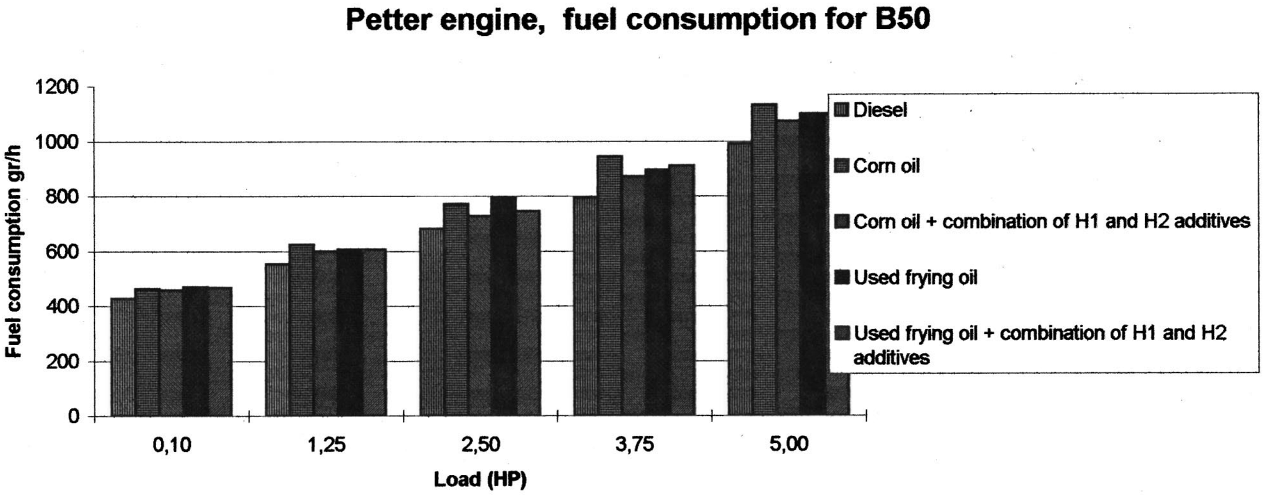

Fig. 16 Fuel consumption for conventional diesel fuel and fuel blends containing 50 percent biodiesel with/without the combination of H1 and H2 additives

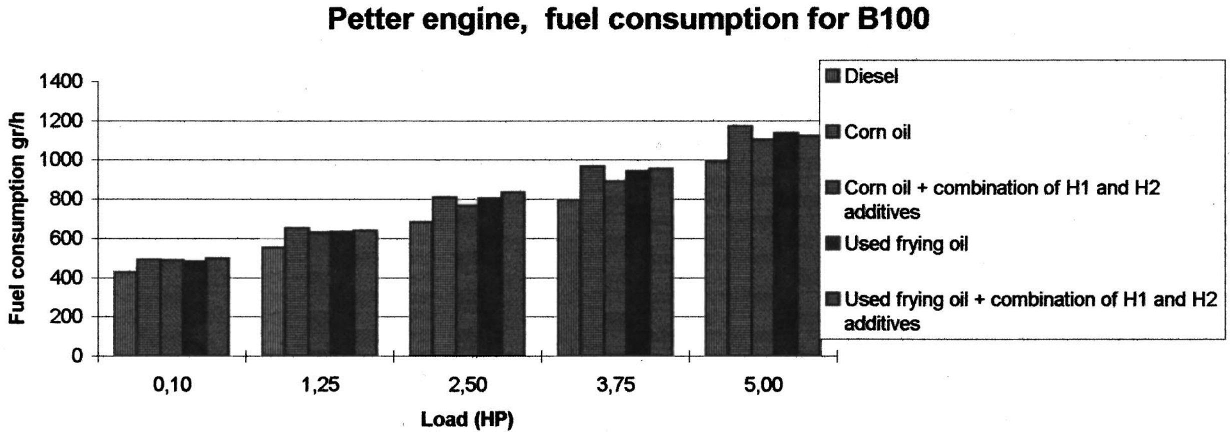

Fig. 17 Fuel consumption for conventional diesel fuel and 100 percent biodiesel with/without the combination of H1 and H2 additives

nificant reduction in exhaust emissions. It was observed that the combination of the two additives was more effective in the cases when the biodiesel blends had not offered a notable reduction in particulate emissions and in the cases where the biodiesel blends had a negative or neutral effect on NOx emissions.

Acknowledgments

Thanks are due to the European Commission, DG XVII, for their financial support in the frame of ALTENER 1995 Program. The authors wish to express their gratitude to Hellenic Aspropyrgos Refinery for supplying typical road diesel and to the Italian company Florys SPA for supplying the sunflower oil, corn oil, olive oil and used frying oil biodiesel.

Nomenclature

B10 = diesel fuel containing 10 percent biodiesel and 90 percent diesel fuel
B30 = diesel fuel containing 30 percent biodiesel and 70 percent diesel fuel
B50 = diesel fuel containing 50 percent biodiesel and 50 percent diesel fuel
B100 = 100 percent biodiesel
CO = carbon monoxide
CO_2 = carbon dioxide
FAME = fatty acid methyl esters
HC = hydrocarbons
HP = horse power
NDIR = non-dispersive infra-red
NOx = nitrogen oxides
ppm = parts per million

References

[1] *Biodiesel, Documentation of the World-Wide Status 1997*, 1997, Austrian Biofuels Institute, ABI, Austria.

[2] Korizi, A., 1995, ''The Perspectives of Biodiesel Development in Greece,'' Diploma thesis, Laboratory of Fuel Technology and Lubricants, National Technical University of Athens, Greece.

[3] ''*Acute Toxicity of Biodiesel to Freshwater and Marine Organisms*,'' 1996, Development of Rapeseed Biodiesel for Use in High-Speed Diesel Engines, Progress Report, University of Idaho, Dept. Biol. Ag. Eng., Moscow, ID, pp. 117–131.

[4] ''*Biodegradability of Biodiesel in the Aquatic Environment*,'' 1996, Development of Rapeseed Biodiesel for Use in High-Speed Diesel Engines, Progress Report, University of Idaho, Dept. Biol. Ag. Eng., Moscow, ID, pp. 96–116.

[5] Howell, S., and Weber, A. J., 1997, ''*Biodiesel Use in Underground Metal and Non-Metal Mines*,'' MARC-IV, LLC, Consulting, ⟨http://www.dieselnet.com/papers/9705howell.html⟩.

[6] ''Field Trials of Soy Methyl Esters as a Fuel for Diesel Powered Equipment in Underground Mines,'' 1995, U.S. Bureau Of Mines/Air Quality Division, ⟨http://www.biodiesel.org/cgi-local/search⟩.

[7] ''Summary results from NBB/USEPA TIER I Health and Environmental Effects Testing for Biodiesel Under the Requirements for USEPA Registration of Fuels and Fuel Additives,'' 1998, Final Report, NBB/USEPA TIER I, ⟨http://www.biodiesel.org/cgi-local/search⟩.

[8] Neeft, J., Makeem, P., and Moulijn, J., 1996, ''Diesel Particulate Emission Control, Review Article,'' Fuel Process. Technol., **47**, pp. 1–69.

[9] ''Development of a Double Treatment Package for Automotive Diesel Fuel—Stages I, II,'' 1995, Final Report, Laboratory of Fuel Technology and Lubricants, National Technical University of Athens, Athens, Greece.

[10] Sharp, C., 1998, ''Exhaust Emissions and Performance of Diesel Engines With Biodiesel Blends,'' Southwest Research Institute, San Antonio, TX, ⟨http://www.biodiesel.org/cgi-local/search⟩.

[11] Marshall, W., Schumacher, L., and Howell, S., 1995, ''Engine Exhaust Emissions: Evaluation of a Cummins L10E When Fueled With a Biodiesel Blend,'' SAE Paper 952363.

[12] ''Biodiesel First Alternative Fuel to Meet EPA Health Effects Requirements,'' 1998, Biodiesel Report, National Biodiesel Board.

[13] Serdari, S., Fragioudakis, K., Teas, C., Sakellaropoulos, F., Zannikos, F., Stournas, S., and Lois, E., 1998, ''Adding Biodiesel Corn Oil and Sunflower Oil to Diesel Fuel: The Impact on the Performance of Conventional Road Vehicles,'' J. Inst. Energy, **71**, pp. 126–136.

[14] ''Alternative Fuel Transit Buses,'' First Report, 1995, U.S. Department of Energy, National Renewable Energy Laboratory Vehicle Evaluation Program.

[15] Ademe, E. U., 1995, ''The Non-Technical Barriers 'Liquid Biofuels' European Network (Used in Engines and Boilers),'' DG XVII (Altener Programme), Information Leaflet, Ademe, Paris.

[16] Akasaka, Y., Suzuki, T., and Sakurai, Y., 1997, ''Exhaust Emissions of a DI Diesel Engine Fueled With Blends of Biodiesel and Low Sulfur Diesel Fuel,'' SAE Paper 972998.

[17] Owen, K., and Coley, T., 1995, *Automotive Fuels Reference Book*, Society of Automotive Engineers, USA.

[18] ''The Biodiesel Industry in the United States: An Industry on the Move. An Update,'' 1995, American Biofuels Association, Arlington, VA.

[19] ''Comprehensive Emissions and Chemical Characterization of Rapeseed Oil-Derived Biodiesel,'' 1996, Montana Project, Biodiesel and Biolubricants Project, Bioenergy Program, Pacific Northwest and Alaska Regional Bioenergy Program.

Key Durability Issues With Mullite-Based Environmental Barrier Coatings for Si-Based Ceramics

Kang N. Lee[1]
Chemical Engineering Department,
Cleveland State University,
Cleveland, OH 44115

Plasma-sprayed mullite ($3Al_2O_3 \cdot 2SiO_2$) and mullite/yttria-stabilized-zirconia (YSZ) dual layer coatings have been developed to protect silicon-based ceramics from environmental attack. Mullite-based coating systems show excellent durability in air. However, in combustion environments, corrosive species such as molten salt or water vapor penetrate through cracks in the coating and attack the Si-based ceramics along the interface. Thus the modification of the coating system for enhanced crack-resistance is necessary for long-term durability in combustion environments. Other key durability issues include interfacial contamination and coating/substrate bonding. Interfacial contamination leads to enhanced oxidation and interfacial pore formation, while a weak coating/substrate bonding leads to rapid attack of the interface by corrosive species, both of which can cause a premature failure of the coating. Interfacial contamination can be minimized by limiting impurities in coating and substrate materials. The interface may be modified to improve the coating/substrate bond. [S0742-4795(00)03203-8]

Introduction

Silicon-based ceramics are promising candidates for hot section structural components of heat engines and heat exchanger tubes for industrial furnaces. One potential barrier to such applications is their environmental durability. The excellent oxidation resistance of silicon-based ceramics at high temperatures in clean, dry oxygen is due to the formation of a solid, protective external silica scale. However, the normally protective silica scale can be degraded by reacting with impurities, such as alkali salts [1,2] or water vapor [3–5].

Molten Na_2SO_4 can deposit in gas turbine engines operating near marine environments or from contaminants in the fuel [6]. The Na_2SO_4 then reacts with the silica to form liquid sodium silicate, leading to accelerated degradation of Si-based ceramics [1]. In coal-fired combustion environments, combustion gases contain low levels of alkali salts because of naturally occurring minor alkali components in the coal. These alkali salts can dissolve in the silica scale and enhance the transport of oxygen, leading to drastically enhanced oxidation [2]. In heat engines, substantial amounts of water vapor, typically about 10 percent, is produced from burning hydrocarbon fuels in air [7]. The water vapor reacts with silica, forming gaseous hydroxide species, such as $Si(OH)_4$ [3–5]. In high-pressure combustion environments, the higher water vapor pressure generates even higher levels of gaseous hydroxide species, resulting in linear volatilization of silica. The linear volatilization of silica coupled with the parabolic oxidation of Si-based ceramics results in overall paralinear kinetics [4], causing rapid degradation of Si-based ceramics. Therefore, the realization of the full potential of silicon-based ceramics in high temperature structural applications depends on the development of environmental protection schemes.

An external environmental barrier coating is a promising approach to protect Si-based ceramics from environmental attack. Mullite is a promising candidate coating material because of its close coefficient of thermal expansion (CTE) match and good chemical compatibility with Si-based ceramics. Researchers at Solar Turbines, Inc., San Diego, CA, and Oak Ridge National Laboratory, Oak Ridge, TN, have done pioneering work on applying refractory oxide coatings such as alumina, zirconia, yttria, mullite, cordierite, etc., on SiC [8,9]. In those studies, mullite was found to be adherent and offer the best protection of all the refractory coatings tested. However, those plasma-sprayed mullite coatings tended to crack on thermal cycling. Researchers at NASA Glenn Research Center, Cleveland, OH, identified the crystallization of amorphous phase mullite, which accompanies a volumetric contraction, as the main source for the cracking of plasma-sprayed mullite coatings [10]. Based on this finding, researchers at NASA GRC successfully eliminated most of the amorphous phase mullite from the coating by spraying the mullite while heating the SiC substrate above the crystallization temperature of amorphous mullite (~1000 °C) [10].

These second-generation mullite coatings provide excellent protection in air and molten salt environment [10–14]. Mullite coatings, however, suffer selective vaporization of silica in the presence of water vapor because of its high silica activity (0.3~0.4) [11,15,16]. Thus, an environmental overlay coating is required when protection from water vapor is needed. Yttria-stabilized zirconia (YSZ) was selected as a baseline overlay coating because of its proven performance as a thermal barrier coating (TBC) in combustion environments. The mullite coating in the mullite/YSZ coating system is somewhat analogous to the bond coat in conventional TBC's, in the sense that it provides bonding as well as oxidation protection. This paper will discuss the current durability issues of second generation mullite-based environmental coatings on Si-based ceramics and future research directions in this area.

Experimental

Mullite and YSZ coatings were applied by atmospheric pressure plasma spraying onto 2.5×0.6×0.15 cm sintered α-SiC coupons (Hexoloy™, Carborundum, Niagara Falls, NY) and reaction bonded silicon nitride (RBSN R. Bhatt, NASA GRC). The SiC

---

[1] Resident Research Associate at NASA Glenn Research Center.

Contributed by the International Gas Turbine Institute (IGTI) of THE AMERICAN SOCIETY OF MECHANICAL ENGINEERS for publication in the ASME JOURNAL OF ENGINEERING FOR GAS TURBINES AND POWER. Paper presented at the International Gas Turbine and Aeroengine Congress and Exhibition, Indianapolis, IN, June 7–10, 1999; ASME Paper 99-GT-443. Manuscript received by IGTI March 9, 1999; final revision received by the ASME Headquarters May 15, 2000. Associate Technical Editor: D. Wisler.

substrates were roughened ($R_a{}^2$=5–6 μm) by etching in Na_2CO_3 to achieve a good mechanical bond [10], whereas RBSN was used as processed. Fused mullite powder with the particle size of 44–74 μm was used (Cerac, Inc., Milwaukee, WI). Typical coating thickness was 100–200 μm for the mullite coating and 50 μm for the YSZ coating. Details of the coating parameters are described elsewhere [10].

Coated coupons were annealed in air at 1300 °C for 100 h, prior to the environmental exposure. Environmental exposures were thermal cycling in air, thermal cycling in 90 percent H_2O/O_2 at 1 atm (simulated lean combustion environments) or isothermal exposure in high-pressure burner rigs with or without molten salt. Thermal cycling tests in water vapor were to evaluate the long-term behavior of coatings in lean combustion environments because high-pressure burner rigs are not suitable for long-term tests due to their high operating cost. Thermal cycling was performed using an automated thermal cycling furnace. Each thermal cycle consisted of 2 h at temperature, rapid cooling to room temperature, and 20 min at room temperature. Typically, samples reached the high temperature within 2 min and the low temperature within 5 min in each cycle. Molten salt environments were generated using a high-pressure burner rig with Jet A fuel containing 2 ppm Na at 4 atm.

Tested samples were mounted in epoxy, polished to 1 μm using diamond suspension, and examined using Scanning Electron Microscopy (SEM) and Energy Dispersive Spectroscopy (EDS).

Environmental Durability

Air. Mullite/YSZ-coated SiC was exposed to a 2 h thermal cycling exposure in air at 1300 °C. Figure 1 shows the cross-section after 500h exposure. Mullite coatings typically developed through-thickness cracks, however, they maintained excellent adhesion and provided excellent oxidation protection. Mullite-coated SiC exhibited a similar behavior under the same exposure, indicating that the presence of YSZ overlay coating did not affect the coating durability despite the large CTE mismatch between the two layers.

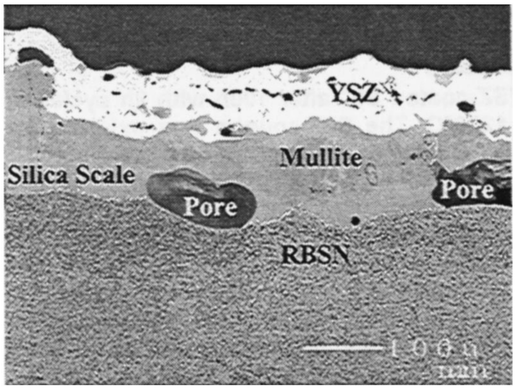

Fig. 2 Mullite/YSZ-coated RBSN after 50 h at 1300 °C in air

Mullite/YSZ-coated RBSN was exposed to an isothermal oxidation at 1300 °C in air for 50 h. A thick oxide scale and large pores developed at the mullite/RBSN interface (Fig. 2). EDS showed a significant amount of Mg in the scale. This contamination by MgO, which is from the RBSN, is responsible for the enhanced oxidation and pore formation. Similar enhanced oxidation and pore formation of mullite-coated SiC was observed when the system was contaminated by Na_2O or K_2O from the coating processed with a low purity mullite powder [17]. Alkali and alkaline earth metal oxides are known to degrade the oxidation resistance of Si-based ceramics by enhancing the oxygen transport through silica by altering the silica network [18].

Combustion Environments

High Pressure Burner Rig. Uncoated, mullite-coated, and mullite/YSZ-coated SiC was exposed to high-pressure burner rig (HPBR) under a rich burn condition (equivalence ratio=1.9) at 6 atm and 1230 °C. Figure 3 shows the plot of weight change vs. time. Uncoated and mullite-coated SiC showed weight loss due to the volatilization of silica. The lack of weight change in the mullite/YSZ-coated SiC indicated that the YSZ overlay coating provided the protection from water vapor. Figure 4(*a*) shows the cross-section of mullite-coated SiC after the high-pressure burner rig exposure. Pores are observed at the interface where cracks intersected the SiC interface. Enhanced oxidation was observed around pores, indicating that water vapor penetrated through the cracks and reacted with SiC. The pore formation is attributed to the generation of gaseous silicon hydroxide species. The selective volatilization of silica from mullite left a porous layer of alumina on the surface of mullite (Fig. 4(*b*)).

Water Vapor Cyclic Furnace. Mullite-coated SiC/SiC (Dupont Lanxide, Newark, DE) exposed to 2 h cycle exposure in 50 percent H_2O/O_2 at 1300 °C showed weight loss, whereas mullite/YSZ-coated SiC/SiC exhibited parabolic oxidation [19]. The weight loss of mullite-coated SiC/SiC was attributed to the selective volatilization of silica from the mullite. This result is consistent with the weight change behavior of mullite and mullite/YSZ coatings in high pressure burner rig (Fig. 3). A similar weight

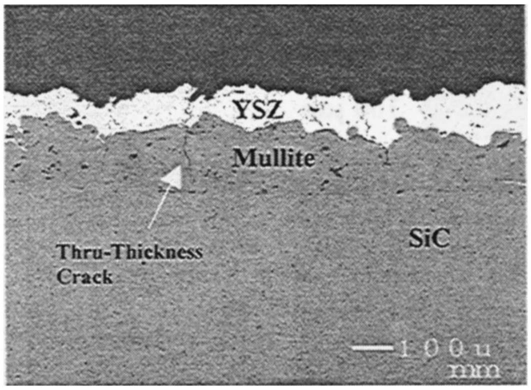

Fig. 1 Mullite/YSZ-coated SiC after 500 h with 2 h cycles at 1300 °C in air

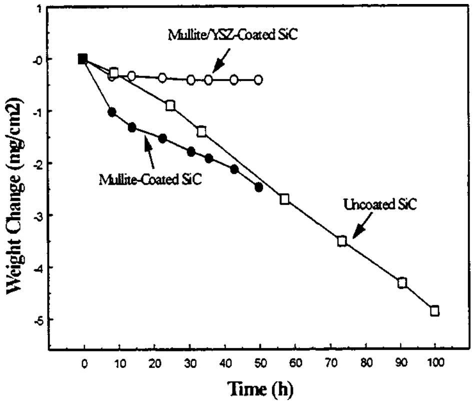

Fig. 3 Weight change versus time for coated and uncoated SiC in HPBR (6 atm, 1230 °C)

---

[2] Average distance from the roughness profile to the mean line

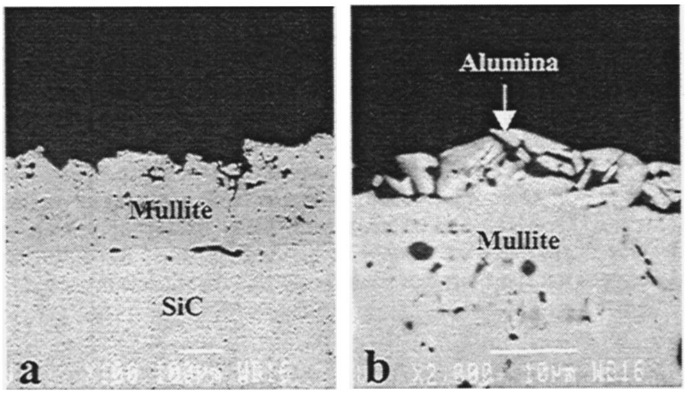

Fig. 4 Mullite-coated SiC after 50 h in HPBR (6 atm, 1230 °C)

change behavior is expected for these coatings on sintered SiC in water vapor cyclic furnace because the reaction at the surface should not be affected by the type of substrates.

Mullite/YSZ-coated SiC was exposed to 2 h cycle exposure in 90 percent H_2O/O_2 at 1300 °C to evaluate the long-term durability in lean combustion environments. Most interfacial areas showed excellent adherence with limited oxidation after 100 h. However, at some interfacial areas, where through-thickness-cracks intersected the SiC interface, accelerated oxidation initiated (Fig. 5(*a*)). After 200 h, accelerated oxidation propagated along the entire mullite/SiC interface, forming a thick porous silica scale (Fig. 5(*b*)). Water vapor, the predominant oxidant in a H_2O/O_2 environment, is known to enhance the oxidation of SiC. The silica scale formed in high water vapor is porous, allowing the oxidation to propagate readily along the interface. The porous scale is attributed to the generation of gaseous silicon hydroxide species. This is in contrast to the scale formed in dry air where the scale is dense and thus prevents the rapid propagation of oxidation.

The effect of preoxidation on the coating adherence was evaluated by preoxidizing a SiC coupon at 1300 °C for 100 h in air, prior to the application of mullite/YSZ coating. The coated coupon was exposed to 90 percent H_2O/O_2 at 1250 °C with 2 h cycles. The cross-section after 100 h showed that the entire interface was attacked by water vapor, forming a thick porous silica scale (Fig. 6). It is believed that the silica scale from preoxidation weakened the mullite/SiC bonding, leading to more rapid penetration by water vapor than in the coupon without preoxidation. Preoxidation did not affect the durability of the system when exposed in air.

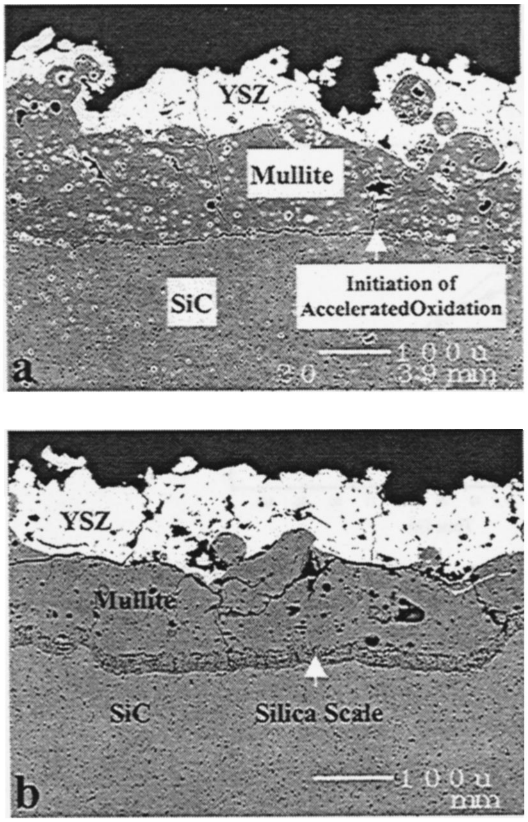

Fig. 5 Mullite/YSZ-coated SiC exposed to 2 h cycle exposure in 90 percent H_2O/O_2 at 1300 °C; (*a*) 100 h; (*b*) 200 h.

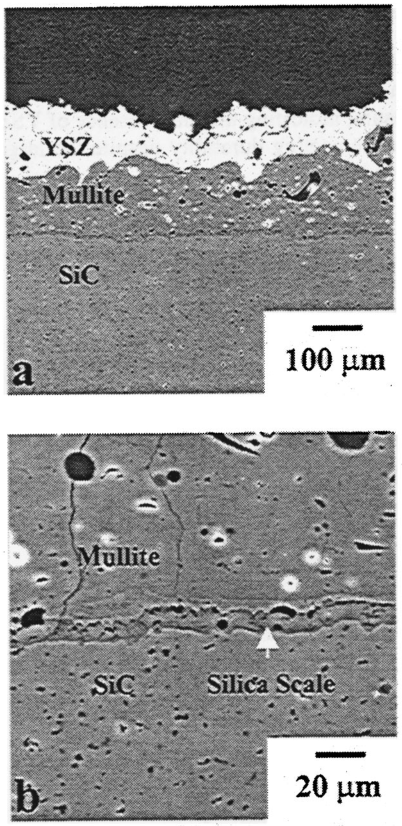

Fig. 6 Mullite/YSZ-coated SiC after 100 h with 2 h cycles in 90 percent H_2O/O_2 at 1250 °C. The SiC coupon was oxidized for 100 h in air at 1300 °C prior to the application of coating.

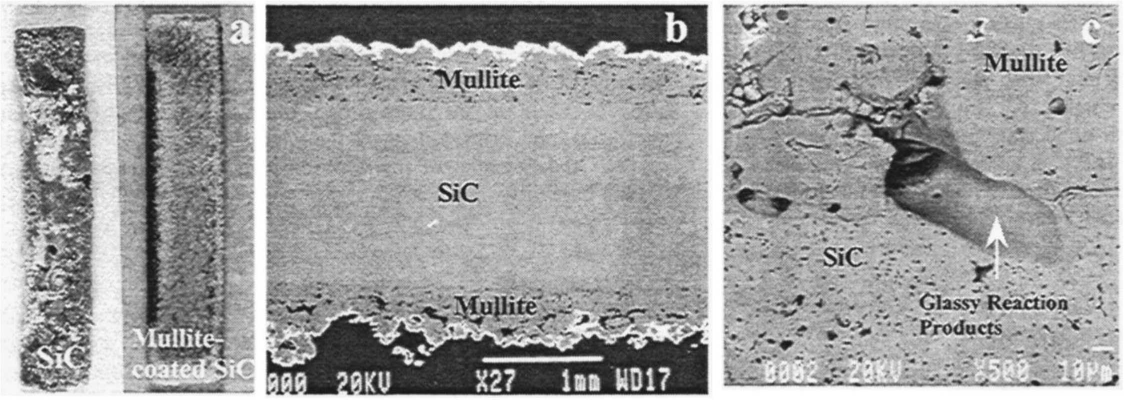

Fig. 7 Mullite-coated SiC coupon after 50 h in hot corrosion rig at 1000 °C

Hot Corrosion Rig. Uncoated and mullite-coated SiC coupons were exposed in a hot corrosion burner rig at 1000 °C for 50 h. Prior to the hot corrosion exposure, the coated coupon underwent 600 one hour thermal cycles at 1200 °C in air to let cracks form. Uncoated SiC was severely deformed due to the attack by the molten salt, whereas mullite-coated SiC was well preserved (Fig. 7(*a*)). Cross-section of the mullite-coated SiC showed that mullite/SiC interface was fairly intact (Fig. 7(*b*)). Only a limited attack with glassy reaction products, presumably sodium silicates, was observed at the interface where cracks intersected the SiC interface (Fig. 7(*d*)). This is an indication of the penetration of salt through some cracks.

Key Issues

Several key durability issues are identified from the environmental durability test results. They include through-thickness-cracking, bonding of mullite to the Si-based ceramic, and interface contamination. These key issues will be discussed in this section to help elucidate the future research directions to improve the coating durability.

Through-Thickness-Cracking. As-sprayed mullite coatings are free of macrocracks (crack width >1 μm). However, on thermal exposure, they develop macrocracks, the size of which can be as wide as 5–10 μm. It has been shown in the foregoing section that corrosive species, such as molten salt or water vapor, can penetrate through these cracks and attack the SiC, leading to accelerated degradation of the system.

It is believed that the development of through-thickness-cracks is due to stresses in the coating. The most likely source for stresses is the precipitation of various second phases in the mullite coating. Amorphous phase mullite precipitates in the coating due to the rapid cooling of molten mullite [10]. Even in the second generation mullite coating, it is likely that some residual amorphous phase mullite still remains in the coating. Volumetric shrinkage results during the crystallization of the residual amorphous phase mullite in subsequent thermal exposures. A significant amount of alumina also precipitates in the plasma-sprayed mullite coating [10]. Plasma-sprayed alumina typically contains substantial amount of metastable alumina phases such as γ-alumina [20]. Volumetric shrinkage results when the metastable alumina phases transform to stable α-alumina in subsequent thermal exposures. The precipitation of alumina phase is also accompanied by the precipitation of silica-rich phases to maintain the chemical balance [10]. Both the alumina and silica-rich phases cause CTE mismatch stresses. Thus the precipitation of second phases in the mullite coating and the resulting volumetric shrinkage and CTE mismatch are suggested to be the major sources for the stresses in the coating.

Mullite/Substrate Bond. Mullite does not form a strong chemical bond with SiC according to our diffusion couple study [21]. Thus the mullite/SiC bond of as-sprayed coatings is mainly due to mechanical interlocking. The lack of chemical bond may be why the oxidation propagates readily along the interface in water vapor. Silica scale from preoxidation presumably further weakens the interfacial bond, leading to more rapid attack by the water vapor.

Contamination. Interfacial contamination can degrade the coating durability by altering the physical or chemical properties of silica scale. Contaminants, such as alkali or alkaline earth metal oxides, are known to be most detrimental to the oxidation resistance of Si-based ceramics [7]. They enhance the oxygen transport through silica by altering the silica network [18]. They also reduce the scale viscosity by forming silicates [22]. Pores develop at the interface when gases generated as a result of oxidation bubble through the low viscosity silica scale [17]. High interfacial porosity can eventually lead to coating delamination. Contamination from coating materials can be minimized by using high purity mullite powder or by limiting the addition of alkali or alkaline earth metal oxides in the processing of Si-based ceramics [17].

Future Research Directions

Modification of Mullite Coating for Improved Crack Resistance. Second phases that cause cracking may be reduced through process optimization. However, it may be impossible to completely eliminate all second phases. For example, melt grown mullite is always alumina-rich and thus some silica-rich phases will always be present to maintain the chemical balance [23,24]. The free alumina phase is likely due to the incongruent melting of mullite and thus may not be completely eliminated by process optimization. Other approaches to improve the crack resistance include modifying the physical properties of mullite coating or sealing the cracks by applying an overlay coating with good crack resistance. Figure 8 shows mullite/cordierite-coated SiC after 600 h with 20 h cycles at 1200 °C in air. Note that the crack stopped at the cordierite/mullite interface. Plasma-sprayed cordierite seems to be more resistant to cracking than plasma-sprayed mullite.

Interface Modification for Improved Bonding. The mullite/Si-based ceramic interface may be modified to enhance the coating/substrate bonding. One example is Mo flash layer. A Mo flash layer (1∼5 μm) was applied on SiC by sputtering and annealed in Ar-5 percent H_2 at 1200–1300 °C for 20–100h, prior to the application of mullite/YSZ coating. Silicon diffused into the molybdenum during the annealing, forming molybdenum silicide with varying composition through the thickness [16]. Similar results were reported in a Mo/SiC diffusion couple study [25,26].

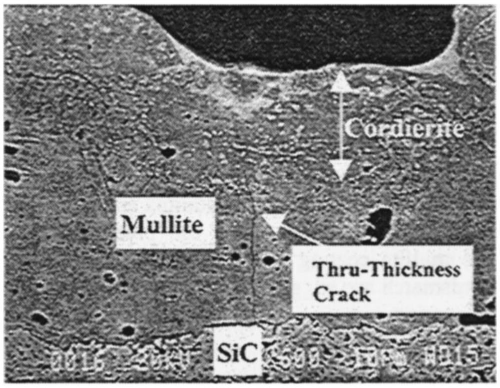

Fig. 8 Mullite/Cordierite-coated SiC after 600 h with 20 h cycles at 1200 °C in air

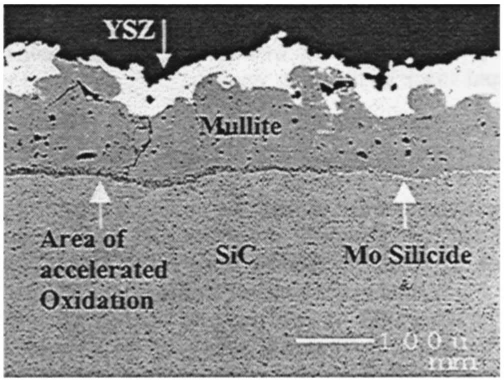

Fig. 9 Mullite/Mo Silicide/YSZ-coated SiC after 500 h with 2 h cycles at 1300 °C in 90 percent H_2O/O_2

The annealed flash layer was thicker and partially delaminated, presumably due to the volume expansion as the silicon diffused into the molybdenum. Figure 9 shows the mullite/molybdenum silicide/SiC system after 500 h at 1300 °C with 2 h cycles in 90 percent H_2O/O_2. Excellent durability was observed at some areas of the coating where the molybdenum silicide layer remained intact. Even the silica scale at the interface attacked by water vapor was thinner than the scale at the unmodified interface, indicating that the interfacial modification delayed the water vapor attack. This result suggests the potential of interface modification for improving the coating durability.

Conclusions

A mullite-based coating system is promising as an environmental barrier for Si-based ceramics in combustion environments. Key durability issues are through-thickness cracking in the mullite coating, a weak mullite/Si-based ceramic bond, and interfacial contamination. Improvement of the crack resistance through the modification of mullite or the application of an overlay coating is suggested. Improved bonding may be achieved through the modification of interface. Interfacial contamination can be minimized by limiting impurities in coating and substrate materials.

Acknowledgments

The author would like to thank R.A. Miller (NASA-Glenn Research Center) for many helpful discussions. The author is also grateful to G.W. Leissler (Dynacs, NASA Glenn Group) for the preparation of plasma-sprayed coatings, M. D. Cuy (Dynacs, NASA Glenn Group) for the hot corrosion test, R. C. Robinson (Dynacs, NASA Glenn Group) for the HPBR test, and R. Bhatt (Army) for the supply of RBSN coupons

References

[1] Jacobson, N. S., Smialek, I. L., and Fox, D. S., 1990, ''Molten Salt Corrosion of SiC and Si_3N_4,'' in *Handbook of Ceramics and Composites*, Vol. 1, Cheremisinoff, N. S., ed., Marcel Dekker, New York, pp. 99–135.
[2] Pareek, V., and Shores, D. A., 1993, ''Oxidation of Silicon Carbide in Environments Containing Potassium Salt Vapor,'' J. Am. Ceram. Soc., **74**, No. 3, pp. 556–563.
[3] Hashimoto, A., 1992, ''The Effect of H_2O Gas on Volatilities of Planet-Forming Major Elements: I—Experimental Determination of Thermodynamic Properties of Ca-, Al-, and Si-hydroxide Gas Molecules and Its Application to the Solar Nebula,'' Geochim. Cosmochim. Acta, **56**, pp. 511–532.
[4] Opila, E. J., and Hann, R., 1997, ''Paralinear Oxidation of CVD SiC in Water Vapor,'' J. Am. Ceram. Soc., **80**, No. 1, pp. 197–205.
[5] Opila, E. J., Fox, D. S., and Jacobson, N. S., 1997, ''Mass Spectrometric Identification of $Si(OH)_4$ from the Reaction of Silica and Water Vapor,'' J. Am. Ceram. Soc., **80**, No. 4, pp 1009–1012.
[6] Pettit, F. S., and Giggins, C. S., 1987, *Superalloys II*, C. T. Sims, N. S. Stoloff, and W. C. Hage, eds., Wiley, New York, p. 327.
[7] Jacobson, N. S., 1993, ''Corrosion of Silicon-Based Ceramics in Combustion Environments,'' J. Am. Ceram. Soc., **76**, No. 1, pp. 3–28.
[8] Price, J. R., van Roode, M., and Stala, C., 1992, ''Ceramic Oxide-Coated Silicon Carbide for High-Temperature Corrosive Environments,'' Key Eng. Mater., **72–74**, pp. 71–84.
[9] Federer, J. I., 1990, ''Alumina Base Coatings for Protection of SiC Ceramics,'' J. Mater. Eng., **12**, No. 2, pp. 141–149.
[10] Lee, K. N., Miller, R. A., and Jacobson, N. S., 1995, ''New Generation of Plasma-Sprayed Mullite Coatings on Silicon-Carbide,'' J. Am. Ceram. Soc., **78**, No. 3, pp. 705–710.
[11] Lee, K. N., Jacobson, N. S., and Miller, R. A., 1994, ''Refractory Oxide Coatings on SiC Ceramics,'' MRS Bull., **XIX**, No. 10, pp. 35–38.
[12] Lee, K. N., and Miller, R. A., 1996, ''Oxidation Behavior of Mullite-Coated SiC and SiC/SiC Composites Under Thermal Cycling between Room Temperature and 1200–1400 °C,'' J. Am. Ceram. Soc., **79**, No. 3, pp. 620–626.
[13] Lee, K. N., and Miller, R. A., 1996, ''Development and Environmental Durability of Mullite and Mullite/YSZ Dual Layer Coatings for SiC and Si_3N_4 Ceramics,'' Surf. Coat. Technol., **86–87**, pp. 142–148.
[14] Jacobson, N. S., Lee, K. N., and Yoshio, T. Y., 1996, ''Corrosion of Mullite By Molten Salts,'' J. Am. Ceram. Soc., **79**, No. 8, pp. 2161–2167.
[15] Lee, K. N., Miller, R. A., Jacobson, N. S., and Opila, E. J., 1995, ''Environmental Durability of Mullite Coating/SiC and Mullite-YSZ Coating/SiC Systems,'' Ceram. Eng. Sci. Proc., September–October, pp. 1037–1044.
[16] Lee, K. N., and Miller, R. A., 2000, ''Durability of Mullite/YSZ-Coated SiC in 90 percent H_2O/O_2,'' Adv. Ceram. Matrix Compos., IV, pp. 17–25.
[17] Lee, K. N., 1998, ''Contamination Effects on Interfacial Porosity During Cyclic Oxidation of Mullite-Coated SiC,'' J. Am. Ceram. Soc., **81**, No. 12, pp. 3329–3339.
[18] Lamkin, M. A., Riley, F. L., and Fordham, R. L., 1992, ''Oxygen Mobility in Silicon Dioxide and Silicate Glasses,'' J. Eur. Ceram. Soc., **10**, pp. 347–367.
[19] Lee, K. N., and Miller, R. A., 1997, ''Modification of Mullite-Based Coatings on Si-Based Ceramics for Enhanced Durability,'' *HITEMP Review*, **III**, NASA Lewis Research Center, Cleveland, OH, p. 45.
[20] Heintz, G. N., and Uematsu, U., 1992, ''Preparation and Structures of Plasma-Sprayed γ and α-alumina Coatings,'' Surf. Coat. Technol., **50**, pp. 213–222.
[21] Lee, K. N., 1998, NASA Glenn Research Center, unpublished research.
[22] Holloway, D. G., 1973, *The Physical Properties of Glass*, Wykeham Publications, London, U.K.
[23] Aksay, I. A., and Pask, J. A., 1975, ''Stable and Metastable Equilibria in the System SiO_2-Al_2O_3,'' J. Am. Ceram. Soc., **58**, Nos. 11–12, pp. 507–512.
[24] Kriven, W. M., and Pask, J. A., 1983, ''Solid Solution Range and Microstructure of Melt-Grown Mullite,'' J. Am. Ceram. Soc., **66**, No. 9, pp. 649–654.
[25] Martinelli, A. E., and Drew, R. A. L., 1995, ''Microstructure Development During Diffusion Bonding of α-Silicon Carbide to Molybdenum,'' Mater. Sci. Eng., A, **191**, pp. 239–247.
[26] Martinelli, A. E., Drew, R. A. L., and Berriche, R., 1996, ''Correlation Between the Strength of SiC-Mo Diffusion Couples and the Mechanical Properties of the Interfacial Reaction Products,'' J. Mater. Sci. Lett., **15**, pp. 307–310.

Bjoern Schenk

Peggy J. Brehm

M. N. Menon

Honeywell Engines & Systems,
P.O. Box 52181,
Phoenix, AZ 85072-2181

William T. Tucker

General Electric Corporation,
Corporate Research and Development Center,
Schenectady, NY 12301

Alonso D. Peralta

State University of New York,
Mechanical Engineering Department,
Stony Brook, NY 11794-2300

A New Probabilistic Approach for Accurate Fatigue Data Analysis of Ceramic Materials

Statistical methods for the design of ceramic components for time-dependent failure modes have been developed that can significantly enhance component reliability, reduce baseline data generation costs, and lead to more accurate estimates of slow crack growth (SCG) parameters. These methods are incorporated into the Honeywell Engines & Systems CERAMIC and ERICA computer codes. Use of the codes facilitates generation of material strength parameters and SCG parameters simultaneously, by pooling fast fracture data from specimens that are of different sizes, or stressed by different loading conditions, with data derived from static fatigue experiments. The codes also include approaches to calculation of confidence bounds for the Weibull and SCG parameters of censored data and for the predicted reliability of ceramic components. This paper presents a summary of this new fatigue data analysis technique and an example demonstrating the capabilities of the codes with respect to time-dependent failure modes. This work was sponsored by the U.S. Department of Energy/Oak Ridge National Laboratory (DoE/ORNL) under Contract No. DE-AC05-84OR21400. [S0742-4795(00)02103-7]

1.0 Introduction

The design of ceramic components for structural applications can be very challenging. Often ceramic components are expected to exceed reliability standards which the metallic components they are replacing could not meet. In the process of assessing the reliability of ceramic components, two issues must be addressed: (1) generation of the Weibull and fatigue parameters of the material; and (2) risk integration of the component to determine the reliability. The basic theories that address these two issues are well developed [1–3], but in order to produce reliable designs with the typically small material properties databases and large extrapolations, more advanced statistical methods are required.

To this effect, Honeywell Engines & Systems has been pursuing the development of probabilistic and statistical methods for extracting the most information out of a given set of data. These efforts have been performed under the Life Prediction Methodologies for Ceramic Components of Advanced Heat Engines program, Phase I and Phase II, funded by the Department of Energy/Oak Ridge National Laboratory (DoE/ORNL) under Contract No. De-AC05-84OR21400. The result has been the development of two computer codes, CERAMIC and ERICA, that are intended to be used in tandem [4]. These codes incorporate state-of-the-art methodologies for the design and life prediction of ceramic components, as follows.

First, the statistical methodologies consist of approaches that use censored data analysis techniques for the pooling of material data. By pooling, it is meant that data from specimens of different sizes that are loaded under different conditions (including proof testing) and at different temperatures can be analyzed together, in a single analysis, to generate the required Weibull parameters. The material parameters generated in this way are more accurate than those obtained from the individual analysis of each data set. The pooling of specimens of different sizes and loading conditions can be used to provide an indication as to how well the chosen failure theory fits the given material. This approach has been extended to allow the pooling of fast fracture and static fatigue data in order to generate more accurate estimates of the slow crack growth parameters of the ceramic material.

Second, the methodology of calculating confidence bounds using the likelihood ratio technique has been expanded to allow the computation of confidence bounds for the slow crack growth parameters.

Third, the methodology includes approaches for the calculation of confidence bounds for the reliability prediction of a component. This is particularly important, because actual components are generally much larger and are loaded at significantly lower stress levels than test specimens, resulting in sizable extrapolations of the material properties. For actual components, the ratio of failures that originate from volume and surface flaws may also be much different than the ratio observed in the database specimens. Extrapolation away from the bulk of the stress levels where the data are generated results in significantly wide confidence bounds. One should, therefore, design ceramic components to a desired level of reliability using the upper-bound confidence limit. This methodology has been expanded to the extent of calculation of confidence bounds for the reliability of a specimen (or component) for a given lifetime and multiple, independent (but concurrently acting), flaw populations.

Therefore, the risk integration approach has been modified to facilitate confidence bound calculations for components. The procedure consists of the evaluation of the effective size of a component as a function of the Weibull slope, slow crack growth parameters, and time. This information is then used to compute confidence bounds for the given component.

The motivation for the development of this fatigue data analysis methodology has been the shortfalls seen in ordinary statistical treatment of fatigue data with respect to runouts and failures on loading (which are especially typical during fatigue testing of ceramic materials). A runout is defined as a test which is interrupted before the specimen fails. Runouts do not contain the same information about the placement on the stress versus time curve as failures do, and ignoring this fact leads to serious errors in the estimated materials response.

To illustrate this, consider the following thought experiment: a test is performed very near the runout strength of a material and it does not fail before *x* hours. A similar test, performed at 100 MPa below ''runout'', is also stopped after *x* hours. An ordinary least

---

Contributed by the International Gas Turbine Institute (IGTI) of THE AMERICAN SOCIETY OF MECHANICAL ENGINEERS for publication in the ASME JOURNAL OF ENGINEERING FOR GAS TURBINES AND POWER. Paper presented at the International Gas Turbine and Aeroengine Congress and Exhibition, Indianapolis, IN, June 7–10, 1999; ASME Paper 99-GT-319. Manuscript received by IGTI March 9, 1999; final revision received by the ASME Headquarters May 15, 2000. Associate Technical Editor: D. Wisler.

a. Only Static Fatigue Failures

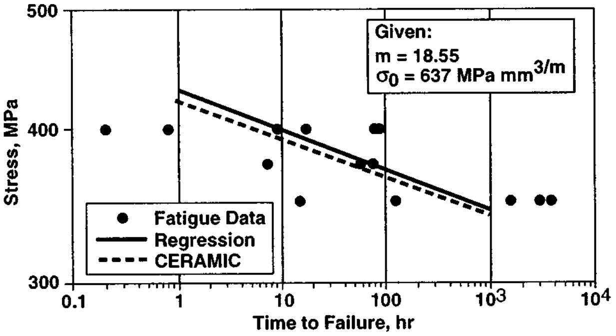

b. Static Fatigue Failures Plus Some Runouts

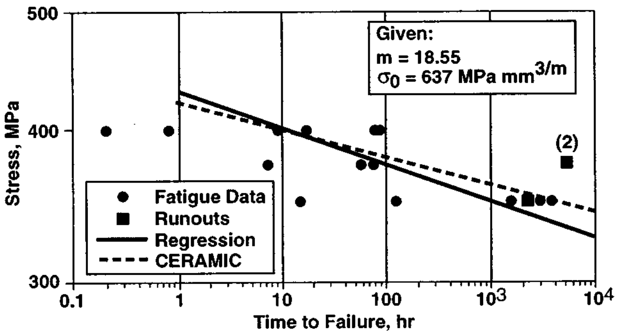

c. Static Fatigue Failures Plus All Runouts

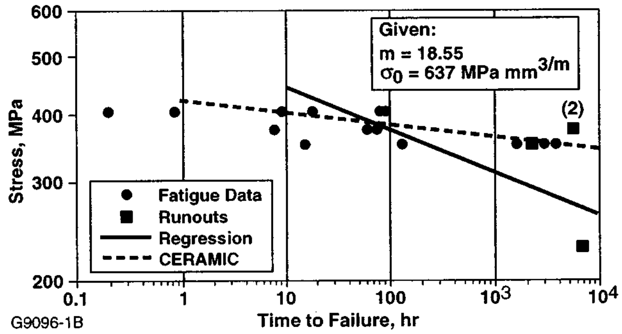

Fig. 1 Conventional fatigue data analysis is not capable of accounting for runouts correctly: (*a*) only static fatigue failures; (*b*) static fatigue failures plus some runouts; and (*c*) static fatigue failures plus all runouts

squares regression of all the data, including the first example, but not the second, would have little effect on the final position of the curve. But including the very low point—as if it were a failure—will greatly lower the resulting curve.

Conventional least squares regression is the accepted method for estimating fatigue parameters of the stress-time curve only when all fatigue specimens really do fail. If runouts (and failures on loading) have to be included in the data analysis, censored data analysis using the maximum likelihood approach should be used to extract the most information out of the data available. This short introduction is illustrated in Fig. 1, comparing fatigue curves derived from conventional least squares regression and the newly-developed censored maximum likelihood data analyses.

2.0 Derivation of the Statistical Method

If stress rupture failures are a consequence of subcritical crack growth (SCG), and if SCG and fast fracture both occur from the same flaw population, fast fracture strength, and stress rupture data may be pooled to perform a combined likelihood analysis of the complete fast fracture and stress rupture data. One implication from such an analysis is that the number of observations is significantly increased which in turn greatly increases the confidence of subsequent predictions.

2.1 Development of the Likelihood Function. Development of the likelihood function that forms the basis of the analysis method requires the distribution function for the observations. The solution for the distribution of observations having strength degradation in the presence of slow crack growth under static loading and competing flaw populations is derived for the situation in which each specimen is tested to failure or the test is terminated. In this case, an observation is either the strength value at failure (observation or censored observation), or either the time at which failure occurs (observation or censored observation) or the runout time. The former situation happens when failure occurs during loading to the static value, and the latter occurs when the static load has been safely reached and failure occurs after sufficient subcritical crack growth has taken place or the test is terminated with a time runout. The development is based on the multiaxial Weibull setup with assumed coplanar crack growth. This setup and assumptions give a first step in the development of analysis procedures including likelihood ratio confidence bounds that allow for subcritical crack growth in the presence of competing failure modes.

2.1.1 Transformation of Strength Due to Slow Crack Growth. The multiaxial setup was first presented by Batdorf and Heinisch [2] and Lamon and Evans [3]. This approach has been strengthened and generalized by Cuccio et al. [5], Nemeth et al. [6], Johnson and Tucker [7,8], and Schenk et al. [4]. Also, Tucker and Johnson [9] have shown that the Batdorf and Heinisch, and Lamon and Evans approaches are equivalent (cf. references in Tucker and Johnson). In the multiaxial setup, the probability of fast fracture failure is given by Eq. (1):

$$P_f(\sigma_{\max}) = 1 - \exp\left\{ -IV\left(\frac{\sigma_{\max}}{\sigma_0}\right)^m \right\}, \tag{1}$$

where $\sigma_{\max}$ typically is the maximum principal stress in the component, and is strictly used for normalization purposes; m is the first Weibull parameter or Weibull modulus; σ_0 is the second Weibull parameter or characteristic strength; V is the physical size of a specimen; and I is the multiaxial stress factor (for a volume flaw population in this case), as defined by Eq. (2):

$$I = \frac{1}{4\pi V} \iiint_V \int_0^{2\pi} \int_{-\pi/2}^{\pi/2} \left(\frac{\sigma_e(x,y,z,\phi,\psi)}{\sigma_{\max}}\right)^m \cos\phi \, d\phi \, d\psi \, dV, \tag{2}$$

where σ_e is the equivalent stress determined by a suitable fracture criterion and is a value of σ_c, the critical stress, i.e., the remote stress applied normal to the crack plane that would produce failure. Similar expressions have been derived for surface and chamfer flaw populations (see [4]). Note that $\sigma_{\max}$ is independent of any specific failure mode with its associated σ_e. Moreover, for a fixed loading geometry, $\sigma_e/\sigma_{\max}$ is not a function of the failure stress. Indeed, σ_e can be expressed as Eq. (3):

$$\sigma_e = \sigma_1 F[\cdot], \tag{3}$$

where (cf. Lamon and Evans and Tucker and Johnson), $F[\cdot]$ is not a function of σ_1, the maximum principal stress. Thus, $\sigma_{\max}$ (the failure stress) is just the maximum value of σ_1 in the specimen. In treating time-dependent phenomena, the distribution of σ_c must be generalized to cover the change of strength that occurs over time.

The following discussion will demonstrate the approach, using the simplest form of the fracture mechanics description of SCG (the power law), Eq. (4):

$$da/dt = A(K)^n, \tag{4}$$

where A and n are constants, and (Eq. (5)):

$$K = Y\sigma\sqrt{a}, \tag{5}$$

and where Y denotes a geometry factor, σ is the applied load (stress), and a is the crack length. Then, as shown in Trantina and Johnson [10], under uniform loading Eq. (5) can be substituted into Eq. (4), and Eq. (4) can be integrated and rearranged to yield Eq. (6):

$$(\sqrt{a_f})^{2-n} = (\sqrt{a_i})^{2-n} + \left(\frac{2-n}{2}\right) A (Y\sigma)^n t, \tag{6}$$

where $n \neq 2$, a_f denotes the final crack length ($\geqslant a_i$), a_i denotes the initial crack length, and t is the time span over which the constant load, σ, is applied.

In view of the assumptions and the fact that the setup leading to Eq. (6) is essentially uniaxial, Eq. (6) can be used to transform an initial strength to a final strength at which failure occurs after the time span, t. In order to do this so as to determine the distribution that results from SCG, a substitution in Eq. (6) for the crack lengths is made in terms of the critical stress via the relationship to K_{Ic} given by $K_{Ic} = Y\sigma_c\sqrt{a}$, where σ_c is the critical stress that will just produce failure for the length a. When this substitution is carried out and some rearrangement made, we obtain Eq. (7):

$$(\sigma_f)^{n-2} = (\sigma_i)^{n-2} + \left(\frac{2-n}{2}\right)\left(\frac{K_{Ic}}{Y}\right)^{n-2} A (Y\sigma)^n t, \tag{7}$$

where $n > 2$ and the f and i subscripts denote the final and initial critical stresses, respectively. Equation (7) gives the degradation in strength for a particular flaw population, since σ_f and σ_i are values of σ_c: it is obvious that $\sigma_f < \sigma_i$ when t is greater than zero. Thus, the difference between σ_f and σ_i produces the amount of time for SCG. Also, SCG can occur if and only if $\sigma < \sigma_i$, otherwise failure occurs on applying the load, σ.

Sturmer et al. [11] generalize the results of Eqs. (4)–(7) to the multiaxial case by rewriting Eq. (5) as follows (Eq. (8)):

$$K_{Ic} = Y\sigma_e(t)\sqrt{a(t)}, \tag{8}$$

where $\sigma_e(t)$ is the load at time t expressed as an equivalent stress that would just produce failure for the length $a(t)$, which is changing over time. This implies, among other things, that $\sigma_e(t)$ accounts for any initial non-coplanar crack growth. Since a crack must grow in order to have fracture failure, the implication is very reasonable. Eq. (8) is then substituted into Eq. (4) and the integration of Eq. (6) is carried out to yield Eq. (9), upon the substitution of Eq. (5):

$$(\sigma_{ef})^{n-2} = (\sigma_{ei})^{n-2} + \left(\frac{2-n}{2}\right)\left(\frac{K_{Ic}}{Y}\right)^{n-2} AY^n \int_{t=0}^{t_f} (\sigma_e(t))^n dt, \tag{9}$$

where $\sigma_e(t)$ is such that Eqs. (8) and (5) are first met at t_f, and σ_{ef}, and σ_{ei} are the final and initial equivalent stresses, respectively. When the load is constant as in stress rupture tests, the integration on the right-hand side of Eq. (9) can be carried out to yield Eq. (10):

$$(\sigma_{ef})^{n-2} = (\sigma_{ei})^{n-2} + \left(\frac{2-n}{2}\right)\left(\frac{K_{Ic}}{Y}\right)^{n-2} AY^n \sigma_L^n t, \tag{10}$$

where σ_L is the equivalent stress resulting from the constant load. Now, on failure σ_{ef} equals σ_L. Taking this into account and solving Eq. (10) for σ_{ei} yields Eq. (11) (dropping the subscript i and in what follows, understanding that σ_e is the initial equivalent stress):

$$\begin{aligned}\sigma_e &= \sigma_L\left[1 + \left(\frac{n-2}{2}\right)(K_{Ic})^{n-2} AY^2 \sigma_L^2 t\right]^{1/(n-2)} \\ &= \sigma_L\left[1 + \frac{\sigma_L^2}{B} t\right]^{1/(n-2)},\end{aligned} \tag{11}$$

where

$$B = \left[\left(\frac{n-2}{2}\right)(K_{Ic})^{n-2} AY^2\right]^{-1}. \tag{11a}$$

Equation (10) also can be solved for t, yielding the time that is required for the initial strength to be degraded to the load and hence failure then occurs, which is (Eq. (12)):

$$t = \frac{B}{\sigma_L^2}\left[\left(\frac{\sigma_e}{\sigma_L}\right)^{n-2} - 1\right]. \tag{12}$$

It is clear that Eqs. (11) and (12) are in a one-to-one and onto relationship and, hence, inverses of each other. Equation (12) has other important properties; in view of Eq. (3), the ratio inside the brackets in Eq. (12) is a scalar ratio of the initial failure stress to that of the load failure stress and is just proportional to σ_c. Thus, except for the σ_L^2 term, t is independent of location and angle and, hence, of any element. Moreover, for a given location and angle, Eq. (12) is a strictly monotonically increasing function of the scalar ratio.

Equations (11) and (12) form the basis for the development of the distribution of an observed time for a specific failure mode. Using Eq. (11), Eq. (2) can be rewritten to define a multiaxial stress factor, I_t for time-dependent flaw populations as in Eq. (13):

$$\begin{aligned} I_t(m,t,n,B) &= \frac{1}{4\pi V}\iiint_V \int_0^{2\pi}\int_{-\pi/2}^{\pi/2}\left(\frac{\sigma_e(x,y,z,\phi,\psi,n,B,t)}{\sigma_{\max}}\right)^m \\ &\quad \cdot \cos\phi\, d\phi\, d\psi\, dV \\ &= \frac{1}{4\pi V}\iiint_V \int_0^{2\pi}\int_{-\pi/2}^{\pi/2}\left[\frac{\sigma_L(x,y,z,\phi,\psi)}{\sigma_{\max}}\right. \\ &\quad \left. \cdot \left(1 + \frac{t}{B}\sigma_L^2(x,y,z,\phi,\psi)\right)^{1/(n-2)}\right]^m \cos\phi\, d\phi\, d\psi\, dV, \end{aligned} \tag{13}$$

which is computed by the ERICA code using the multiaxial stress distribution in the specimen or component calculated by a finite element code (in this case, ANSYS).

2.1.2 Distributions of Actual Observations. In developing the likelihood function, actual failure events need to be considered. For a given specimen with a single flaw population that is tested to failure, either a strength or time is observed. Thus, the events of observing a strength or a time are mutually exclusive and exhaustive. Therefore, the probability of observing any strength ($<\sigma_{\max L}$) plus the probability of observing any time (>0 and $<\infty$) is one. The term $\sigma_{\max L}$ denotes the maximum equivalent stress in the specimen when loaded to the static test load.

The development of the likelihood needs to cover these two joint, exhaustive events. The development will be given in steps, beginning with the derivation for time distributions first.

The event of observing a time (denoted by $t < T < \infty$) occurs if and only if a time is observed for all elements of a specimen. Following the argument of Eq. (1) in Batdorf and Heinisch [2], Eqs. (1) and (2) of this paper can be used to express the probability of this, as (Eq. (14)):

$$P(0<T<\infty)=\exp\left\{-\frac{1}{4\pi V}\iiint_V\int_0^{2\pi}\int_{-\pi/2}^{\pi/2}\left(\frac{\sigma_L(x,y,z,\phi,\psi)}{\sigma_0}\right)^m\cos\phi d\phi d\psi dV\right\}=\exp\left\{-IV\left(\frac{\sigma_{\max}}{\sigma_0}\right)^m\right\}. \tag{14}$$

The event of observing a time that is greater than t (denoted by $t<T<\infty$) occurs if and only if this occurs for all elements of a specimen. Arguing as for Eq. (14), this can be expressed formally as (Eq. (15)):

$$P(t<T<\infty)=\exp\left\{-\frac{1}{4\pi V}\iiint_V\int_0^{2\pi}\int_{-\pi/2}^{\pi/2}\left(\frac{\dfrac{\sigma_L(x,y,z,\phi,\psi)}{\sigma_0}\cdot}{\left(1+\dfrac{t}{B}\sigma_L^2(x,y,z,\phi,\psi)\right)^{1/(n-2)}}\right)^m\cos\phi d\phi d\psi dV\right\}=\exp\left\{-I_tV\left(\frac{\sigma_{\max}}{\sigma_0}\right)^m\right\}. \tag{15}$$

The monotonic nature of Eq. (12) and hence Eq. (11) implies that there can be no value of the equivalent stress less than $\sigma_L[1+(\sigma_L^2/B)t]^{1/(n-2)}$ for any element (σ_L is a function of location and angle) for which it is true that an observed time would be between t and infinity. Thus Eq. (15) is valid. Since $\sigma_L[1+(\sigma_L^2/B)t]^{1/(n-2)}$ is continuous in t (for any element), Eq. (15) reduces to Eq. (14) when $t=0$. Therefore, Eq. (14) can be employed to obtain the probability of a strength failure or that $T=0$, as in Eq. (16).

$$P(T=0)=1-\exp\left\{-\frac{1}{4\pi V}\iiint_V\int_0^{2\pi}\int_{-\pi/2}^{\pi/2}\left(\frac{\sigma_L(x,y,z,\phi,\psi)}{\sigma_0}\right)^m\cos\phi d\phi d\psi dV\right\}=1-\exp\left\{-IV\left(\frac{\sigma_{\max}}{\sigma_0}\right)^m\right\}. \tag{16}$$

Since the events $(0<T\leq t)$ and $(t<T<\infty)$ are mutually exclusive and exhaustive of the event $(0<T<\infty)$, the joint probability that ($0<T\leq t$ and a time is observed) is given by Eq. (15) minus Eq. (16) as Eq. (17):

$$\begin{aligned}P(0<T\leq t\text{ and a time is observed})&=\exp\left\{-\frac{1}{4\pi V}\iiint_V\int_0^{2\pi}\int_{-\pi/2}^{\pi/2}\left(\frac{\sigma_L(x,y,z,\phi,\psi)}{\sigma_0}\right)^m\cos\phi d\phi d\psi dV\right\}\\&\quad-\exp\left\{-\frac{1}{4\pi V}\iiint_V\int_0^{2\pi}\int_{-\pi/2}^{\pi/2}\left(\frac{\dfrac{\sigma_L(x,y,z,\phi,\psi)}{\sigma_0}\cdot}{\left(1+\dfrac{t}{B}\sigma_L^2(x,y,z,\phi,\psi)\right)^{1/(n-2)}}\right)^m\cos\phi d\phi d\psi dV\right\}\\&=\exp\left\{-IV\left(\frac{\sigma_{\max}}{\sigma_0}\right)^m\right\}-\exp\left\{-I_tV\left(\frac{\sigma_{\max}}{\sigma_0}\right)^m\right\}.\end{aligned} \tag{17}$$

The cumulative (marginal) distribution for an observed time of t is given by Eq. (18):

$$\begin{aligned}P(T\leq t)&=P(T=0)+P(0<T\leq t),\quad &t>0\\&=P(T=0),&t=0.\end{aligned} \tag{18}$$

In view of Eq. (16), Equation (18) reduces to Eq. (19):

$$\begin{aligned}P(T\leq t)&=1-\exp\left\{-\frac{1}{4\pi V}\iiint_V\int_0^{2\pi}\int_{-\pi/2}^{\pi/2}\left(\frac{\dfrac{\sigma_L(x,y,z,\phi,\psi)}{\sigma_0}\cdot}{\left(1+\dfrac{t}{B}\sigma_L^2(x,y,z,\phi,\psi)\right)^{1/(n-2)}}\right)^m\cos\phi d\phi d\psi dV\right\}\\&=1-\exp\left\{-I_tV\left(\frac{\sigma_{\max}}{\sigma_0}\right)^m\right\},\quad t\geq 0.\end{aligned} \tag{19}$$

It is noted for reference, by employing Eqs. (14) and (17) and the definition of conditional probability (or Bayes Theorem) that (Eq. (20)):

$$P(T\leq t|A\text{ time is observed})=1-\exp\left\{\begin{aligned}&-\frac{1}{4\pi V}\iiint_V\int_0^{2\pi}\int_{-\pi/2}^{\pi/2}\left(\frac{\dfrac{\sigma_L(x,y,z,\phi,\psi)}{\sigma_0}\cdot}{\left(1+\dfrac{t}{B}\sigma_L^2(x,y,z,\phi,\psi)\right)^{1/(n-2)}}\right)^m\cos\phi d\phi d\psi dV\\&+\frac{1}{4\pi V}\iiint_V\int_0^{2\pi}\int_{-\pi/2}^{\pi/2}\left(\frac{\sigma_L(x,y,z,\phi,\psi)}{\sigma_0}\right)^m\cos\phi d\phi d\psi dV\end{aligned}\right\}. \tag{20}$$

Equation (20) is analogous to the distribution of ''customer'' observed times after a proof test has been carried out (in this case at σ_L). Equation (20) will not be used in our derivations, since it does not employ the strengths of specimens that fail on load-up.

The event of observing a strength (denoted by $\sigma_{\max e} \leqslant \sigma_{\max L}$, where $\sigma_{\max e}$ denotes the maximum value of σ_e in the specimen) occurs if and only if the strength for at least one element is less than the σ_L for that element. Now the events ($0 \leqslant$ strength $\leqslant \sigma_{\max e}$) and ($\sigma_{\max e} <$ strength $\leqslant \sigma_{\max L}$) are mutually exclusive and exhaustive of the event ($0 \leqslant$ strength $\leqslant \sigma_{\max L}$). Thus, the joint probability that ($0 \leqslant$ strength $\leqslant \sigma_{\max e}$ and a strength is observed) follows from the Batdorf element argument using Eqs. (1) and (2) as (Eq. (21)):

$$
\begin{aligned}
&P(0 \leqslant \text{strength} \leqslant \sigma_{\max e} \ \text{ and a strength is observed}) \\
&\quad = 1 - \exp\left\{ -\frac{1}{4\pi V} \iiint_V \int_0^{2\pi} \int_{-\pi/2}^{\pi/2} \left(\frac{\sigma_e(x,y,z,\phi,\psi)}{\sigma_0} \right)^m \cdot \cos\phi \, d\phi \, d\psi \, dV \right\} \\
&\quad = 1 - \exp\left\{ -IV \left(\frac{\sigma_{\max}}{\sigma_0} \right)^m \right\}. \qquad (21)
\end{aligned}
$$

where $\sigma_{\max e} \leqslant \sigma_{\max L}$.

A specimen has a censored strength observation (analogous to a time runout) if and only if the specimen strength is greater than the censored load. Clearly, the complement of Eq. (21) (1—Eq. (21)) can be employed to evaluate this probability, with σ_e taking on the censored load value. Also, Eq. (16) gives the probability that a strength is observed.

2.1.3 Distributions of Censored Observations Due to Competing Flaw Populations. We now consider the censoring that occurs when competing flaw populations are present in a specimen. The subscript *i* (now) denotes the *i*th observation and the subscript *j* denotes the *j*th flaw population. A time is observed if and only if $\min_j\{\sigma_{ej}\} > \sigma_L$, for all elements, and thus all flaw populations undergo subcritical growth. In this case, the time that is observed is the minimum of the times computed by Eq. (12) for each of the failure modes. Otherwise, a critical strength for at least one flaw population is less than or equal to σ_L for at least one element, and failure will occur on initial loading.

The distribution for a specimen strength observation is derived by employing the probability of having a strength of less than or equal to x_i that is observed. Since at least one flaw population must have a critical strength less than or equal to σ_L for at least one element (in order to observe a strength upon failure), this probability is given by Eq. (22):

$$F(x_i) = 1 - S_1(x_i) S_2(x_i), \quad 0 \leqslant x_i \leqslant \sigma_{\max L}, \qquad (22)$$

where, for simplicity, the setup is given for two competing flaw populations, S denotes the survivor function based on Eq. (21) (the probability that the critical strength is greater than x_i, i.e., the complement of Eq. (21) evaluated at x_i), and it is assumed that the flaw populations act independently of each other. Differentiation of Eq. (22) yields the probability density for a strength observation of x_i, which is (Eq. (23)):

$$f(x_i) = f_1(x_i) S_2(x_i) + S_1(x_i) f_2(x_i). \qquad (23)$$

From Eq. (23) it follows that the joint probability density of a specimen failing from the first flaw population *and* at strength x_i is (Eq. (24)):

$$g_1(x_i) = f_1(x_i) S_2(x_i). \qquad (24)$$

For an observed strength of flaw population 1 (standard fast fracture data point or failure on loading) the probability density function f_1 is given by the derivative of Eq. (21) with respect to strength, while for S_2 the complement of Eq. (21) is employed, since it is a censored strength observation with respect to flaw population 1.

A similar expression for g_2 holds for the second flaw population. Since Eq. (23) conditioned on ($0 \leqslant x_i \leqslant \sigma_{\max L}$) must integrate to unity and the flaw populations are independent of each other, the event of failure by one is mutually exclusive of the other. Also, both events are exhaustive. Thus, the likelihood for an observed strength and observed flaw population is given by either g_1 or g_2.

The distribution for a specimen time observation is built on the development of Eqs. (14), (15), (17), and (19). Since all flaw populations must have critical strengths greater than $\sigma_{\max L}$ for all elements (in order to observe a time upon failure), and the observed time, y_i, is the minimum of all possible times, this probability, $\mathbf{F}$, is given formally by Eq. (25):

$$
\begin{aligned}
\mathbf{F}(y_i) &= S_1(\sigma_{\max L}) S_2(\sigma_{\max L}) - S_1(\sigma_{\max e1i}) S_2(\sigma_{\max e2i}) \\
&= S_1(\sigma_{\max L}) S_2(\sigma_{\max L}) - \mathbf{S}_1(y_i) \mathbf{S}_2(y_i), \quad y_i > 0, \qquad (25)
\end{aligned}
$$

where the dependency on y_i is given from Eq. (11) by Eq. (26):

$$\sigma_{eji} = \sigma_L \left[1 + \frac{\sigma_L^2}{B_j} y_i \right]^{1/(n_j - 2)}, \qquad (26)$$

and where the survivor function S_j for strengths is given by Eq. (14) and the survivor function $\mathbf{S_j}$ for times is given by Eq. (15) for each flaw population. The monotonic nature of Eq. (26) implies that there can be no value of the equivalent stress less than the value of Eq. (26) for any element such that an observed time would be greater than y_i. This also implies that a y_i censored by another flaw population, j, could not have an equivalent stress less than σ_{eji}, otherwise by the monotonicity of Eq. (26) t would have been observed. Thus, Eq. (25) is valid. Differentiation of Eq. (25) yields the probability density $\mathbf{f}$ for a time observation of y_i, which is (Eq. (27)):

$$\mathbf{f}(y_i) = \mathbf{f}_1(y_i) \mathbf{S}_2(y_i) + \mathbf{S}_1(y_i) \mathbf{f}_2(y_i) \qquad (27)$$

The first term on the right-hand side of Eq. (27) covers the situation in which the observed time is due to flaw population 1, and the second term covers the situation due to flaw population 2. From Eq. (27) it follows that the joint probability density of a specimen failing from the first flaw population and at time y_i is (Eq. (28)):

$$h_1(y_i) = \mathbf{f}_1(y_i) \mathbf{S}_2(y_i). \qquad (28)$$

For a time observed for flaw population 1, the probability density function $\mathbf{f}_1$ is given by the derivative of Eq. (17) with respect to time, while Eq. (15) (or the complement of Eq. (19)) is used, with t equal to the time to failure for $\mathbf{S}_2$, since it is a censored time observation with respect to flaw population 1.

A similar expression for h_2 holds for the second flaw population. As in the case for a strength observation, since Eq. (27) conditioned on $y_i > 0$ must integrate to unity and the flaw populations are independent of each other, the event of failure by one is mutually exclusive of the other, and both events are exhaustive. Thus, the likelihood for an observed time and observed flaw population is given by either h_1 or h_2.

2.1.4 The Complete Likelihood Function. The likelihood of an individual observation is defined approximately as the probability $[F(x+\Delta) - F(x)]$, where F is the cumulative distribution function and Δ is sufficiently small.

Dividing by Δ and taking the limit as Δ approaches zero gives the density function (when it exists). Since Δ is a constant scalar, the likelihood can be defined as the density evaluated at an observation. In the case of censoring or runouts, the probability of the event is used as the likelihood (see Schenk et al., [4]). For computational reasons, the natural logarithm of the likelihood is usually taken [12].

Now, for observed failures each observation is either a failure strength or a time at which failure occurred. Thus Eq. (24) multiplied by dx_i gives the probability of an observed failure strength due to flaw population 1 in the interval from x_i to x_i+dx_i. Likewise, Eq. (28) multiplied by dy_i gives the probability of an observed time due to flaw population 1 in the interval from y_i to y_i+dy_i. This forms the basis for developing the likelihood function for observed failures. Let:

$$\begin{aligned}\delta_{ji}&=1, \quad \text{if the } i\text{th specimen fails from flaw population } j \\ &\qquad \text{with a strength observation} \\ &=0, \quad \text{otherwise}\end{aligned} \tag{29}$$

$$\begin{aligned}\gamma_{ji}&=1, \quad \text{if the } i\text{th specimen fails from flaw population } j \\ &\qquad \text{with a time observation} \\ &=0, \quad \text{otherwise,}\end{aligned} \tag{30}$$

where

$$\delta_{1i}+\delta_{2i}+\gamma_{1i}+\gamma_{2i}=1. \tag{31}$$

Then the likelihood for an observed strength x_i and observed flaw population, or an observed time y_i and observed flaw population is (Eq. (32)) from Eqs. (24) and (28), the similar expressions for g_2 and h_2, and the definitions of Eqs. (29), (30), and (31):

$$\begin{aligned}L_i&=[f_1(x_i)S_2(x_i)]^{\delta_{1i}}[S_1(x_i)f_2(x_i)]^{\delta_{2i}}[\mathbf{f}_1(y_i)\mathbf{S}_2(y_i)]^{\gamma_{1i}} \\ &\quad\cdot[\mathbf{S}_1(y_i)\mathbf{f}_2(y_i)]^{\gamma_{2i}} \\ &=[f_1(x_i)^{\delta_{1i}}S_1(x_i)^{\delta_{2i}}\mathbf{f}_1(y_i)^{\gamma_{1i}}\mathbf{S}_1(y_i)^{\gamma_{2i}}] \\ &\quad\cdot[S_2(x_i)^{\delta_{1i}}f_2(x_i)^{\delta_{2i}}\mathbf{S}_2(y_i)^{\gamma_{1i}}\mathbf{f}_2(y_i)^{\gamma_{2i}}].\end{aligned} \tag{32}$$

For future reference, note that the bracketed terms in the last line of Eq. (32) each only involve flaw population 1 or flaw population 2. The log likelihood is, by definition, the logarithm of the likelihood of the complete data set, which under independence is the product of the L_i. This yields Eq. (33):

$$\begin{aligned}l=\sum_{l=1}^{n}\ln L_i=\sum_{i=1}^{n}\ &\ln[f_1(x_i)^{\delta_{1i}}S_1(x_i)^{\delta_{2i}}\mathbf{f}_1(y_i)^{\gamma_{1i}}\mathbf{S}_1(y_i)^{\gamma_{2i}}] \\ &+\ln[S_2(x_i)^{\delta_{1i}}f_2(x_i)^{\delta_{2i}}\mathbf{S}_2(y_i)^{\gamma_{1i}}\mathbf{f}_2(y_i)^{\gamma_{2i}}]\end{aligned} \tag{33}$$

as the log likelihood of the observed strengths or times and flaw populations for the data set of actual failure observations.

Any terms accounting for censored observations due to test termination must be added to Eq. (33). These type of observations censor all flaw populations, and, hence, the appropriate survivor term needs to be entered in Eq. (33) in each bracket. Then since the bracketed terms of the completed Eq. (33) only involve a single mode, the maximum of Eq. (33) is obtained by maximizing individually each of the summed bracketed terms. But, due to the nature of the δ_{ji} and γ_{ji} for the observed strengths and times (i.e., within a bracket, one and only one is unity and the others are zero), the maximization of an individual sum of brackets is obtained from a standard censored data analysis.

In order to obtain the complete log likelihood function that will also account for runout observations, let:

$$\begin{aligned}\alpha_{ji}&=1, \quad \text{if the } i\text{th specimen is a censored strength} \\ &\qquad \text{observation (unknown failure mode)} \\ &=0, \quad \text{otherwise}\end{aligned} \tag{34}$$

$$\begin{aligned}\beta_{ji}&=1, \quad \text{if the } i\text{th specimen is a time runout} \\ &\qquad \text{(unknown failure mode)} \\ &=0, \quad \text{otherwise,}\end{aligned} \tag{35}$$

where (Eq. (36))

$$\begin{aligned}\delta_{1i}+\delta_{2i}+\gamma_{1i}+\gamma_{2i}+\alpha_{1i}+\alpha_{2i}+\beta_{1i}+\beta_{2i}&=2, \quad \text{if the} \\ i\text{th specimen is a censored observation}& \\ &=1, \quad \text{otherwise}\end{aligned} \tag{36}$$

or for j concurrent flaw populations

$$\begin{aligned}\sum_{j}(\delta_{ji}+\gamma_{ji}+\alpha_{ji}+\beta_{ji})&=j, \quad \text{if the } i\text{th specimen} \\ &\qquad \text{is a censored observation} \\ &=1, \quad \text{otherwise}\end{aligned}$$

Then the complete log likelihood function for x_i and observed flaw population, or an observed time y_i and observed flaw population, or an observed censored strength at x_i, or an observed runout at y_i is

$$\begin{aligned}l&=\sum_{l=1}^{n}\ln L_i \\ &=\sum_{i=1}^{n}\ln[f_1(x_i)^{\delta_{1i}}S_1(x_i)^{\delta_{2i}}\mathbf{f}_1(y_i)^{\gamma_{1i}}\mathbf{S}_1(y_i)^{\gamma_{2i}}S_1(x_i)^{\alpha_{1i}}\mathbf{S}_1(y_i)^{\beta_{1i}}] \\ &\quad+\ln[S_2(x_i)^{\delta_{1i}}f_2(x_i)^{\delta_{2i}}\mathbf{S}_2(y_i)^{\gamma_{1i}}\mathbf{f}_2(y_i)^{\gamma_{2i}}S_2(x_i)^{\alpha_{2i}}\mathbf{S}_2(y_i)^{\beta_{2i}}],\end{aligned} \tag{37}$$

where $S_j(x_i)^{\alpha_{ji}}$ is defined by the complement of Eq. (21), while $\mathbf{S}_j(y_i)^{\beta_{ji}}$ is defined by Eq. (15). A generic data set is provided in the Appendix to further explain the computation of the individual likelihood for a specific flaw population.

2.2 Development of Confidence Bounds. Methods for obtaining likelihood ratio confidence bounds of parameters for individual flaw populations and reliabilities at a fixed stress and/or strengths at a fixed probability of failure are given in Cuccio et al. [5]. The likelihood ratio method [13] is based on the direct use of the likelihood ratio statistic, Eq. (38)

$$W(\beta)=2[\hat{l}-\hat{l}_\beta], \tag{38}$$

where l is the appropriate bracketed term(s) of Eq. (37), $\hat{l}$ is the value of the log likelihood function evaluated at the joint maximum likelihood estimate of all parameters, β is any parameter, and $\hat{l}_\beta$ is the value of the log likelihood function evaluated at a fixed value of β and the maximum likelihood estimates of all other parameters conditional on the given value of β. $W(\beta)$ has, approximately, a chi-squared distribution with one degree of freedom. This yields a $1-\alpha$ confidence region, on the parameter β as (Eq. (39)):

$$\{\beta : W(\beta)\leqslant\chi^2_{1,\alpha}\}. \tag{39}$$

Obtaining confidence limits on a quantity such as a reliability

Table 1 Pooled fast fracture and static fatigue data set from NT154 Silicon Nitride—ORNL tensile buttonhead specimens [14]

Fast Fracture Data at 2200°F (1204°C)		Static Fatigue Data at 2200°F (1204°C) and 54.4 ksi (375 MPa)	
Failure Strength, ksi (MPa)	**Failure Mode**	**Time to Failure, hours**	**Failure Mode**
52.80 (364.1)	Internal	0.40	Internal
60.30 (415.8)	Internal	0.50	Internal
61.40 (423.4)	Internal	0.84	Internal
61.80 (426.1)	Internal	6.00	Surface
65.30 (450.2)	Internal	7.00	Surface
66.30 (457.1)	Internal	12.00	Internal
67.50 (465.4)	Internal	19.00	Internal
69.50 (479.2)	Internal	24.00	Surface
71.20 (490.0)	Internal	40.00	Internal
71.80 (495.1)	Censored	43.00	Surface
72.00 (496.4)	Surface	66.00	Internal
73.40 (506.1)	Internal	80.00	Surface
74.30 (512.3)	Internal	120.00	Surface
76.20 (525.4)	Internal	141.00	Internal
78.30 (539.9)	Internal	153.00	Internal
79.30 (546.8)	Internal	252.00	Surface
80.10 (552.3)	Internal	253.00	Surface
85.00 (586.1)	Internal	266.00	Internal
86.90 (599.2)	Internal	525.00	Runout
96.40 (664.7)	Internal	528.00	Runout

requires substitution for, and elimination of, one of the distribution parameters, e.g., σ_0, for a particular flaw population. If only one failure mode is involved, then this can be carried out in a straightforward manner, maximizing the conditional likelihood function in terms of the introduced quantity. However, a much simpler approach, is to recognize that making the substitution is equivalent to imposing a constraint on the conditional likelihood, an observation that applies equally well to the situation of competing failure modes (cf. Cuccio, et al. [5]). Thus, we have a constrained optimization problem comprised of the log likelihood function given in Eq. (37) with a constraint equation defining the particular conditions for which the confidence limits are desired.

2.2.1 Likelihood Ratio Confidence Bounds for a Specimen or Component Probability at a Specified Time. For a specified service time, *t*, the reliability of a component (again with two independent flaw populations) is given by Eq. (40):

$$R(t)=S_1(t)S_2(t). \tag{40}$$

where from Eq. (19):

$$S_j=\exp\left\{-\frac{1}{4\pi V_c}\int\!\!\int_{V_c}\!\!\int\int_0^{2\pi}\int_{-\pi/2}^{\pi/2}\left(\frac{\sigma_{Lc}(x,y,z,\phi,\psi)}{\sigma_{0_j}}\cdot\left(1+\frac{t}{B_j}\sigma_{Lc}^2(x,y,z,\phi,\psi)\right)^{1/(n_j-2)}\right)^{m_j}\cos\phi\, d\phi\, d\psi\, dV\right\}, \tag{41}$$

and the subscript *c* refers to a reference component (possibly a specimen type). Taking the logarithm of Eq. (40) yields:

$$\gamma=\ln\left(\frac{1}{R(t)}\right)=\ln\left(\frac{1}{S_1(t)}\right)+\ln\left(\frac{1}{S_2(t)}\right). \tag{42}$$

Noting that Eq. (42) imposes a constraint on the optimization of *l*, given by the complete Eq. (37), $\hat{l}_\beta$ can be obtained by a constrained optimization as the solution of Eq. (43):

$$\text{Maximize } l, \quad \text{subject to: } \gamma=\ln\left(\frac{1}{S_1(t)}\right)+\ln\left(\frac{1}{S_2(t)}\right). \tag{43}$$

This setup produces a nice division between the specimen data through *l* and the component characteristics through the constraint in Eq. (43). The capability for this type of analysis is given by use of the codes ERICA and CERAMIC developed by Honeywell Engines & Systems. Note that the solution given by Eq. (43) is employed to find the value of γ that meets the bounds of Eq. (39). γ is then inverted to obtain $R(t)$ for specified values of *t*.

For illustration purposes, this procedure has been applied to data on tensile specimens of a common size tested at 2200°F (1204°C) for fast fracture strengths and stress rupture lives with a stress rupture loading of 54.4 ksi (375 MPa); see Table 1 [14]. There are two competing failure modes: internal and surface; one censored strength observation having an unidentified fracture origin; two time runouts; and 20 strength and 20 time observations.

Analyses were performed using the CERAMIC/ERICA probabilistic life prediction codes. The maximum likelihood parameter estimates for the internal flaw population are $\hat{\sigma}_0=926.7$ $MPamm^{3/\hat{m}}$, $\hat{m}=8.19$, $\hat{B}=21{,}230$ MPa^2h, and $\hat{n}=22.5$; while the estimates for the surface flaw population yield values of $\hat{\sigma}_0=1{,}338.4$ $MPamm^{2/\hat{m}}$, $\hat{m}=10.79$, $\hat{B}=2{,}000$ MPa^2h, and

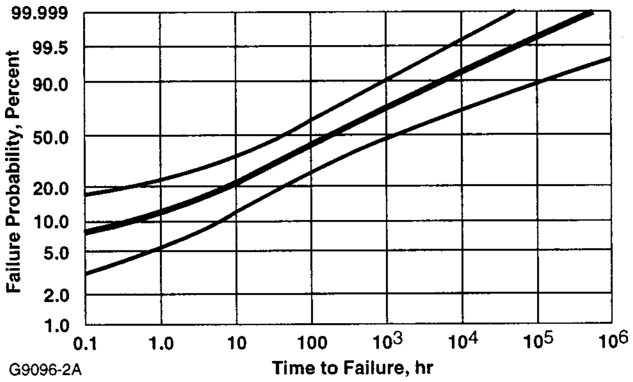

Fig. 2 Resulting Weibull plot for specimen or component life prediction including likelihood ratio confidence bounds

$\hat{n} = 18.1$. While conventional fatigue data analysis is not even able to compute fatigue parameters from a static fatigue data set generated only at a single stress level, the method suggested by Fett and Munz [15], does allow the computation of slow crack growth parameters for a single flaw population using fast fracture data and such a fatigue data set. Wu et al. [14], used this method to analyze the data set given in Table 1. The resulting parameters for the volume flaw population were $\hat{m} = 7.45$, $\hat{\sigma}_0 = 976.3\ MPa^2h$, $\hat{n} = 16.33$, and $\hat{B} = 216{,}250\ MPa^2h$.

The likelihood ratio confidence bounds that result from solving Eq. (39) for selected values of t for the internal flaw population are shown in Fig. 2. The curve flattens for ''small'' times due to the jump at $t = 0$ in the time distribution. This phenomenon generally holds in the time domain.

Summary and Conclusions

The methodology presented in this paper is generic enough to be applied to cyclic fatigue data analysis and life prediction as well, simply by changing the underlying stress-time transformation (Eq. (12)) appropriately. The methodology is implemented into the CERAMIC/ERICA probabilistic life prediction codes [16], and currently allows the computation of maximum likelihood best estimates for all material parameters (Weibull modulus m, characteristic strength σ_0, slow crack growth parameters B and n), including the likelihood ratio confidence bounds of all concurrently acting (competing) flaw populations in a single run using a pooled set of fast fracture and static fatigue data, even if the static fatigue data are generated at a single stress level.

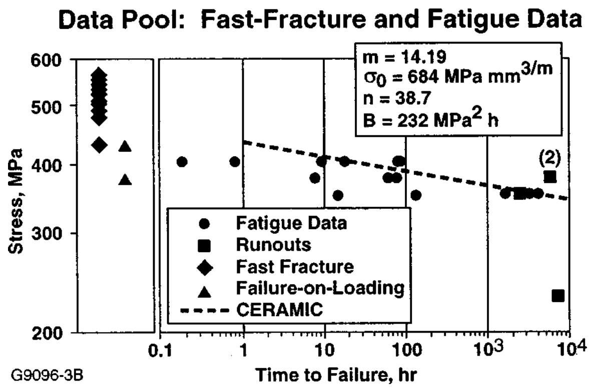

Fig. 3 Pooled data analysis of AS-800 Silicon Nitride fast fracture and static fatigue data (1204°C/2200°F)

By doing so, this approach also reveals whether slow crack growth has been the only time-dependent failure mode acting during the static fatigue experiments. Consider Fig. 1, for example. The analysis of the fast fracture data alone resulted in a Weibull modulus m of 18.55. One would expect that by pooling the fast fracture data with the static fatigue data, a higher Weibull modulus should be computed, due to the increased amount of data available for parameter estimation.

Again, this is only true if the underlying assumption that slow crack growth is the only time-dependent flaw population acting on the specimens during the static fatigue experiments is correct. In this case, the pooled data analysis resulted in a lower Weibull modulus m of 14.19, and a fairly low slow crack growth exponent n of 38.7 (see Fig. 3).

On the other hand, dynamic fatigue experiments resulted in a very high n parameter value of 185. In the case of the static fatigue experiments, it could be shown that creep damage accumulation contributed to comparatively low times to failure, and, therefore, to this artificially low slow crack growth exponent. Since the static fatigue data have been heavily biased by creep, larger scattering resulted for the pooled data set, which in turn is expressed by the decreased Weibull modulus.

Nomenclature

A = slow crack growth parameter
a = crack length
ANSYS = finite element modeling computer code
ASME = American Society of Mechanical Engineers
ASTM = American Society for Testing and Materials
B = slow crack growth parameter
°C = degrees Celsius
CERAMIC = AlliedSignal ceramic life prediction code
DoE = U.S. Dept. of Energy
ERICA = AlliedSignal ceramic life prediction code
$\mathbf{F}$,F = probability
f = probability density for strength observation
$\mathbf{f}$ = probability density for time observation
°F = degrees Fahrenheit
I = multiaxial stress factors for fast fracture
I_t = multiaxial stress factors for slow crack growth
K = stress intensity factor
K_{Ic} = critical mode I stress intensity factor
ksi = thousands of pounds per square inch
$m,\hat{m}$ = first Weibull parameter or Weibull slope
MPa = MegaPascals
n = slow crack growth parameter
ORNL = Oak Ridge National Laboratory
P = probability
P_f = probability of failure
R = reliability or probability of success
S = probability of survival for strength observation
$\mathbf{S}$ = probability of survival for time observation
SCG = subcritical crack growth
t = time
t_f = time to failure
U.S., USA = United States of America
V = physical size of a specimen or component
$W(\cdot)$ = likelihood ratio statistic
x_i = observed strength
Y = crack geometry factor
y_i = observed time
σ_e,σ_L = effective stress levels
$\sigma_{\max}$ = maximum applied principal stress on the component
$\sigma_o,\hat{\sigma}_o$ = second Weibull parameter
ϕ,ψ = angles used in integration of unit radius sphere

Appendix

Table A1 Computation of the individual likelihoods of an example data set

stress	time to failure	flaw population	component of the volume likelihood	component of the surface likelihood
σ_{L1}	t_1	*volume*	*d/dt of Eq. [17]*	*Eq. [15]**
σ_2	*fast fracture or failure on loading*	*surface*	*1 - Eq. [21]*	*d/dσ of Eq. [21]**
σ_{L3}	t_3	*runout*	*Eq. [15]*	*Eq. [15]**
σ_4	*fast fracture or failure on loading*	*volume*	*d/dσ of [21]*	*1 - Eq. [21]**
σ_{L5}	t_5	*unknown*	*Eq. [15]*	*Eq. [15]**
σ_6	*fast fracture or failure on loading*	*unknown*	*1 - Eq. [21]*	*1 - Eq. [21]**
σ_{L7}	t_7	*surface*	*Eq. [15]*	*d/dt of Eq. [17]**
$\vdots$	$\vdots$	$\vdots$	$\vdots$	$\vdots$
			$\prod = L(volume)$	$\prod = L(surface)$

*Equivalent definition for surface flaw population has to be used

Maximization of L(flaw population) yields the best estimates $\hat{m}$, $\hat{\sigma}_0$, $\hat{B}$, and $\hat{n}$ for this specific flaw population.

References

[1] Weibull, W., 1939, ''A Statistical Theory of the Strength of Materials,'' R. Swedish Acad. Eng. Proc., **151**, 1–45.

[2] Batdorf, S. B., and Heinisch, H. L., 1978, ''Weakest Link Theory Reformulated for Arbitrary Failure Criterion,'' ASME J. Appl. Mech., **61**, pp. 355–358.

[3] Lamon, J., and Evans, A. G., 1983, ''Statistical Analysis of Bending Strengths for Brittle Solids: A Multiaxial Fracture Problem,'' J. Am. Ceram. Soc., **66**, No. 3, pp. 177–182.

[4] Schenk, B., Peralta, A. D., Brehm, P., and Menon, M. N., 1998, ''CERAMIC/ERICA: AlliedSignal Engines' Life Prediction Codes for Structural Ceramic Applications,'' *Proceedings of the World Ceramics Congress CIMTEC 1998*, Florence, Italy.

[5] Cuccio, J., Peralta, A. D., Song, J., Brehm, P., Johnson, C. A., Tucker, W. T., and Fang, H., 1994, ''Probabilistic Methods for Ceramic Component Design and Implications for Standards,'' in *Life Prediction Methodologies and Data for Ceramic Materials*, C. R. Brinkman and S. F. Duffy, eds., ASTM STP1201, pp. 291–308.

[6] Nemeth, N. N., Powers, L. M., Janosik, L. A., and Gyekenyesi, J. P., 1994, ''Time-Dependent Reliability Analysis of Monolithic Ceramic Components Using The CARES/Life Integrated Design Program,'' in *Life Prediction Methodologies and Data for Ceramic Materials*, C. R. Brinkman and S. F. Duffy, eds., ASTM STP1201, pp. 390–408.

[7] Johnson, C. A., and Tucker, W. T., 1992, ''Advanced Statistical Concepts of Fracture in Brittle Materials,'' in *Engineered Materials Handbook—Volume 4; Ceramics and Glasses*, S. J. Schneider, Chairman, ASM International, pp. 709–715.

[8] Johnson, C. A., and Tucker, W. T., 1994, ''Weibull Estimators for Pooled Fracture Data,'' in *Life Prediction Methodologies and Data for Ceramic Materials*, C. R. Brinkman and S. F. Duffy, eds., ASTM STP1201, pp. 250–288.

[9] Tucker, W. T., and Johnson, C. A., 1994, ''The Multiaxial Equivalent of Stressed Volume,'' in *Life Prediction Methodologies and Data for Ceramic Materials*, C. R. Brinkman and S. F. Duffy, eds., ASTM STP1201, pp. 265–279.

[10] Trantina, G. G., and Johnson, C. A., 1983, ''Probabilistic Defect Size Analysis Using Fatigue and Cyclic Crack Growth Rate Data,'' in *Probabilistic Fracture Mechanics and Fatigue Methods: Applications for Structural Design and Maintenance*, J. M. Bloom and J. C. Ekvall, eds., ASTM STP798, pp. 67–78.

[11] Sturmer, G., Schulz, A., and Wittig, S., 1993, ''Lifetime Prediction for Ceramic Gas Turbine Components,'' ASME J. of Gas Turbines and Pwr., **115**, No. 1, pp. 70–75.

[12] Nelson, W., *Applied Life Data Analysis*, Wiley, New York.

[13] Cox, D. R., and Oakes, D., 1984, *Analysis of Survival Data*, Chapman and Hall, New York.

[14] Wu, D. C., Peralta, A. D., Menon, M. N., and Cuccio, J. C., 1995, ''Subcritical Crack Growth Life Prediction For Ceramic Components Of Advanced Heat Engines,'' ASME Paper 95-GT-236.

[15] Fett, T., and Munz, D., 1991, ''Methods of Determining Subcritical Crack Growth by Static Lifetime Tests With Natural and Artificial Flaws,'' J. Test Eval., **19**, No. 6, pp. 461–466.

[16] Schenk, B., Brehm, P. J., Menon, N. M., Tucker, W. T., and Peralta, A. D., 1999, ''Status of the CERAMIC/ERICA Probabilistic Life Prediction Codes Development for Structural Ceramic Applications,'' ASME Paper 99-GT-318.

Patrick T. Scarborough
e-mail: ptscarbo@southernco.com

Howard L. Hendrix
e-mail: hlhendri@southernco.com

Matthew D. Davidson
e-mail: mddavids@southernco.com

Xiaofeng Guan
e-mail: xguan@southernco.com

Southern Company Services,
P.O. Box 1069,
Wilsonville, AL 35186

Robert S. Dahlin
e-mail: rsdahlin@southernco.com

E. Carl Landham
e-mail: eclandha@southernco.com

Southern Research Institute,
P.O. Box 1069,
Wilsonville, AL 35186

Power Systems Development Facility: High Temperature, High Pressure Filter System Operations in a Combustion Gas[1]

The Power Systems Development Facility (PSDF) is a Department of Energy (DOE) sponsored engineering scale demonstration of two advanced coal-fired power systems. Particulate cleanup is achieved by several High Temperature, High Pressure (HTHP) gas filtration systems. The PSDF was designed at sufficient scale so that advanced power systems and components could be tested in an integrated fashion to provide confidence and data for commercial scale-up. This paper provides an operations summary of a Siemens-Westinghouse Particulate Control Device (PCD) filtering combustion gas from a Kellogg, Brown, and Root (KBR) transport reactor located at the PSDF. The transport reactor is an advanced circulating fluidized bed reactor designed to operate as either a combustor or a gasifier. Particulate cleanup is achieved by using one of two PCDs, located downstream of the transport reactor. As of the end of 1998, the transport reactor has operated on coal as a combustor for over 3500 h. To date, filter elements from 3M, Blasch, Coors, Allied Signal (DuPont), IF&P, McDermott, Pall, Schumacher, and Specific Surface have been tested up to 1400 °F in the Siemens-Westinghouse PCD. The PSDF has a unique capability for the collection of samples of suspended dust entering and exiting the PCD with Southern Research Institute's (SRI) in-situ particulate sampling systems. These systems have operated successfully and have proven to be invaluable assets. Isokinetic samples using a batch sampler, a cascade impactor and a cyclone manifold have provided valuable data to support the operation of the transport reactor and the PCD. Southern Research Institute has also supported the PSDF by conducting filter element material testing. [S0742-4795(00)02203-1]

Introduction

Hot gas filtration technology is becoming increasingly more important in the development of advanced power technologies. With the highly competitive natural gas market, major improvements in the discovery and extraction of natural gas and the relatively low capital cost of the technology to burn gas for power generation; coal is facing serious challenges in the industry. The PSDF is dedicated to the development of advanced coal-based generation technologies. Through coal gasification, PSDF hopes to demonstrate that coal can remain competitive with natural gas as a viable energy alternative. The PCD will play the most crucial role in filtering out particulates from the gas stream and protecting the downstream turbines. The most critical components in the PCD are the filter elements themselves. The PSDF is challenged with testing elements for their viability in commercial operation. Commercial viability of filter elements relies heavily on resistance to thermal shock (material properties), filter performance and filter life.

Project Description

The PSDF is configured into two separate trains. The transport reactor train is used to produce a particulate-laden gas for testing two of the PCDs. The Advanced Pressurized Fluidized Bed Combustor (APFBC) train will be integrated with a topping combustor and gas turbine for long term testing of two additional PCDs in an integrated system and assessment of the control and integration issues associated with the APFBC system.

Transport Reactor. The KBR transport reactor technology, under development at the PSDF at a scale of about 2 tons/h (1800 kg/hr) of coal feed, can operate either as a gasifier or combustor. Tests will be conducted in both configurations. In the gasifier mode, coal is introduced and fired sub-stoichiometrically. The coal devolatilizes, the volatiles pyrolyze and the residual char is steam gasified. This staging of the gasification reaction forces oxygen to react with char rather than volatiles, as is characteristic in fluid bed gasifiers. As a result, the size of the gasifier is reduced because the amount of char to be gasified by reaction with steam is reduced substantially. Operation in the combustion mode is similar, but the reactor is fired with excess air, and a fluidized bed heat exchanger is included in the reactor loop to remove heat.

Advanced PFBC. First generation PFBC technology offers the advantages of being more compact and efficient than pulverized coal units. The PFBC design is simpler than most advanced power generation systems. However, first generation PFBC systems have limited efficiency, due to low temperature operation and the use of ruggedized turbines. To improve efficiency, PFBC systems must employ hot particulate removal and a topping cycle in order to use advanced turbine designs. These second-generation APFBC designs are expected to be capable of achieving 50 percent net plant efficiency. Advancing the development of APFBC systems is one of the primary goals of the PSDF.

At a scale of 3 tons/h (2700 kg/hr), the Foster Wheeler APFBC system under development at the PSDF utilizes a topping cycle.

---

[1] The PSDF is supported by the U.S. Department of Energy's Federal Enegy Technology Center (FETC), under Contract DE-FC21-90MC25140 with Southern Company Services, Inc, P.O. Box 1069, Wilsonville, AL 35186-1069, telefax: 205-670-5843. The FETC Contracting Officer's Representative is James Longanbach.

Contributed by the International Gas Turbine Institute (IGTI) of THE AMERICAN SOCIETY OF MECHANICAL ENGINEERS for publication in the ASME JOURNAL OF ENGINEERING FOR GAS TURBINES AND POWER. Paper presented at the International Gas Turbine and Aeroengine Congress and Exhibition, Indianapolis, IN, June 7–10, 1999; ASME Paper 99-GT-343. Manuscript received by IGTI March 9, 1999; final revision received by the ASME Headquarters May 15, 2000. Associate Technical Editor: D. Wisler.

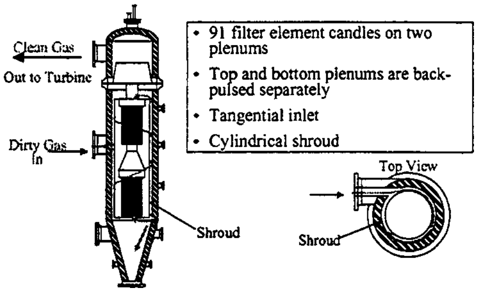

Fig. 1 Siemens-Westinghouse PCD

The process is a hybrid system that combines partial gasification with PFBC. Coal is first fed to a pressurized carbonizer, where it is converted to a low-Btu fuel gas and char. The char produced in the carbonizer is transferred to a circulating PFBC (CPFBC) where it is subsequently burned. Sulfur is removed in the process by the addition of limestone into the carbonizer and CPFBC. The carbonizer fuel gas and CPFBC flue gas are cleaned of particulates in separate ceramic filters, after which the fuel gas is fired in a specially designed topping combustor before entering a high-temperature gas turbine using the CPFBC flue gas as the oxidant.

Particulate Control Devices. At the PSDF, three PCDs have been installed in the process structure. Siemens-Westinghouse has provided two of the PCDs. The smaller Siemens-Westinghouse PCD can test up to 91 candle filter elements and is installed on the KBR transport reactor process. The larger Siemens-Westinghouse PCD contains up to 273 candle filter elements and will be used to remove particulate from the vitiated air leaving the combustor in the FW APFBC system. In addition to the Siemens-Westinghouse systems, a Combustion Power Company (CPC) moving granular bed filter is installed and will be tested on the KBR transport reactor.

Siemens-Westinghouse PCD Design. Dirty gas from the transport reactor enters the PCD through a tangential inlet nozzle, then flows in an annulus between the vessel wall and a shroud. The gas flows both over the top and under the bottom of the shround into the central filtration zone of the vessel. Dirty gas flows through the filter elements, depositing the particulate on the filter surface. Figure 1 shows a schematic of the system operation.

The filter elements are attached to one of two plenums, or levels, which support filter elements, collect the clean gas and distribute the pulse flow. There are 55 filter elements attached to the lower plenum and 36 filter elements attached to the upper plenum. Each filter element has a series of gaskets to provide a dust tight seal, and there is a Siemens-Westinghouse fail-safe device located above each filter element. The fail-safe is designed to limit ash penetration in the event of a filter element failure.

The clean gas flows from the plenum to the outlet of the filter vessel through the support tube, which is attached to the vessel tubesheet, and eventually downstream to a gas turbine (while in gasification mode). The tubesheet provides a physical barrier separating the ''dirty'' and ''clean'' sides of the PCD. The Siemens-Westinghouse tubesheet is designed with a double cone expansion joint, to provide a positive seal at a variety of operating temperatures.

As the particulate accumulates on the outside of the filter surface, the differential pressure will continually rise. Periodically, a pulse of high pressure gas generated by the back-pulse skid removes the filter cake. This gas flows into the filter vessel through the pulse piping and is channeled to the individual plenums via the support tube. The filter cake removed from the filter elements falls to the bottom of the vessel, where it is removed and cooled by a screw cooler and lockhopper system.

Results

Operationing Conditions. Typical operating conditions of the Siemens-Westinghouse PCD for the KBR process are summarized in Table 1.

To date, the PCD has been exposed to coal combustion particulate-laden gas from the KBR transport reactor for over 3500 h since initial start-up with about 1400 h in 1998 (See Fig. 2). Initial operations were conducted at ~600 °F (320 °C) by flowing all of the gas from the transport reactor through a gas cooler. The primary reason for this approach was to operate the PCD as conservatively as possible while gaining familiarity with the transport reactor. As operation of both the reactor and the PCD were better understood, the temperature in the PCD was increased to ~1000 °F (540 °C) by partially bypassing the gas cooler. Operation at this temperature went quite well, so shortly afterwards the PCD inlet temperature was increased to its present operating temperature of ~1400 °F (760 °C) where it has been for all of 1998.

Permeance. For a given face velocity the baseline pressure drop just after cleaning with a back-pulse changes with time as a residual cake forms on the filter surface. If the face velocity remains constant, the rate of change in the baseline pressure drop should approach zero as the filter system reaches steady state. Since face velocity is changed fairly often in test facilities, such as the PSDF the change in pressure drop is monitored by plotting the system *permeance* versus time. Permeance is defined as the face velocity, divided by the pressure drop and corrected for gas temperature. The equation for permeance is

$$\text{Permeance} = \frac{(\text{FaceVelocity})\mu}{(\Delta P)\mu_{20}}. \tag{1}$$

Table 1 Typical operating conditions in the Siemens-Westinghouse PCD

Temperature	1350-1400°F (732-760°C)
Pressure	200 psig (13.8 bar, g)
Face Velocity	5.0 ft/min (91 m/hr)
Baseline Pressure Drop	80 INWG (200 mbar)
Baseline Permeance	0.154 ft/(min*INW) (1.13 m/(hr*mbar))
Back-pulse Pressure	400-500 psig (27.6-34.5 bar, g)
Back-pulse Duration	0.2 seconds
Back-pulse Interval	40 minutes
Particulate Loading	11,000 ppm
Particle Size MMD	18-25 micron

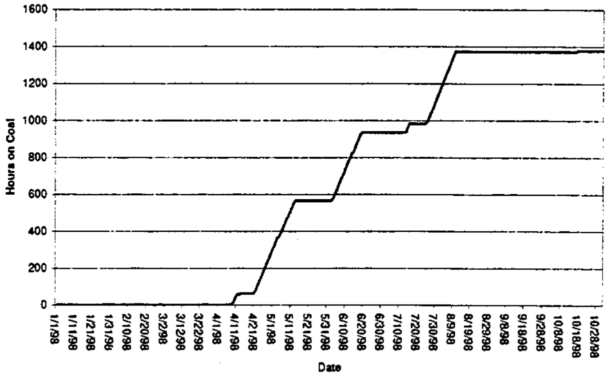

Fig. 2 1998 KBR cumulative hours on coal

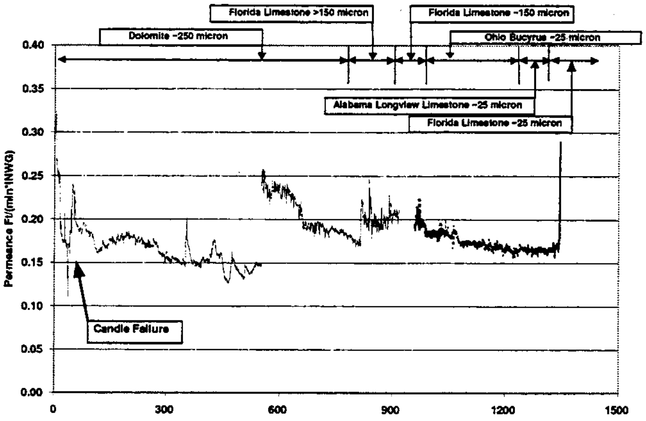

Fig. 3 1998 PCD permeance versus hours on coal

Under ideal conditions, the permeance will decrease as the residual cake forms until a steady-state value is reached. If the permeance fails to reach a steady state, operations may eventually be affected, due to higher than acceptable pressure drops. Eventually, the plant may have to shut down to avoid compromising the mechanical integrity of the PCD.

The permeance of the Siemens-Westinghouse PCD for the nearly 1400 h of testing in 1998 is shown in Fig. 3. There are several items of interest shown on the graph.

An element failure occurred in early April 1998, while transitioning to coal. This resulted in a shut down. During this time a significant number of filter elements were cleaned and/or replaced with new filter elements. New elements were installed after 500 h of operation resulting in the large step change in permeance as the newer/clean elements began operation. During the year, dolomite as well as limestone sorbents were used in the operation of the transport reactor. Changes in these sorbents, type as well as grind size, are indicated on the graph. Several ''breaks'' are shown in the curve. These are primarily due to rapid changes in gas flow, temperature, pressure, etc. on start-up and shut-down.

Filter Element Materials

Materials Exposed. In light of the critical defense that the PCD provides to the downstream equipment, a variety of filter elements have been tested. The variety in material composition of these elements range from cement-like materials, commonly referred to as Alumina/mullite (monolithic oxides) or monolithic silicon carbide elements (silicon carbide), to many different types of weaves and layered materials, commonly referred to as composite elements (composite oxides, composite silicon carbide). Table 2 below shows the filter elements that have been tested and the maximum number of exposure hours for each type of filter element.

During the 3500 h of combustion testing on the KBR transport reactor, there have been several incidents where filter elements have broken during operation. These incidents can be broadly categorized into two groups: initial operation of a developmental reactor and transition from propane to coal during start-up.

Initial Operation. As with most new facilities, there were start-up challenges with various pieces of equipment throughout the plant, and the PCD was no exception. During this period of learning, the PCD was filled to an ash level high enough to break a significant number of filter elements. Additionally, a significant amount of coal was fed into the transport reactor, while the system was being heated. The transport reactor was at a temperature hot enough to cause the initial combustion of the coal, and the PCD was at a temperature of about 400 °F (200 °C). It is believed that when the smoldering coal reached the filter elements it ignited, causing a rapid increase in the filter element temperature and failure of many of the filter elements. Understanding why the events during start-up occurred was relatively simple and was followed by changes in operating procedures as well as additional training.

Table 2 Filter elements tested at PSDF (as of 12/31/98)

Manufacturer	Type	Material	Exposure Hours on Coal
3M	Oxide	Composite	790
	Type 203	Composite	1250*
Blasch		Alumina/mullite	50
Coors	P-100A-1	Alumina/mullite	810
Allied Signal (Dupont)	PRD66C	Composite	1350
IF&P	REECER	Recrystallized silicon carbide	1350
McDermott		Composite	1350
Pall	326	SiC	3210
	442T	SiC	3210
	FeAl	Iron Aluminide	1350
Schumacher	F40	SiC	620
	TF20	SiC	1350
	T10-20	SiC	2590
Specific Surface	CC-4001	Cordierite	50

* The 3M Type 203 filter elements with 1250 hours have been removed from the PCD.

Transition to Coal. In September 1997, several monolithic oxide filter elements failed during the transition from the start-up burner to coal feed. All but one of these failures occurred during the transition to coal or when there was an upset in the coal feeder. Concurrently, there were monolithic silicon carbide and composite oxide and silicon carbide filter elements installed from a variety of manufacturers that did not fail during these thermal transients.

After in-depth analysis and the installation of thermocouples on the surface of the elements, the cause of the failures is now thought to be determined. It is currently believed that the temperature in the transport reactor was too cool to fully combust the coal prior to the solids entering the PCD. Consequently, coal burned on the surface of the elements thermally stressing the elements to the point of failure. This was not readily evident from plant instrumentation.

As a result, the start-up burner was modified to allow higher temperatures prior to firing coal, and the start-up procedure was modified to require the transport reactor temperature to exceed 1200 °F (650 °C) before coal feed can begin. This procedure was followed during the next start-up and no similar transients were detected. These experiences have shown that the thermal properties of the monolithic silicon carbide elements make them much less susceptible to these types of thermal transients than the monolithic oxide materials.

System Performance

Inlet Mass Loadings. Figure 4 gives a summary of the particulate loadings measured in the gas stream entering the PCD during 1998. The first series of measurements were made during Test Campaign 2 (TC02) which lasted from April 5, 1998, until May 13, 1998. The last series of measurements were made during Test Campaign 3 (TC03) which lasted from May 31, 1998, until August 10, 1998.

During 1998, runs were also completed with the Eastern Kentucky coal that is being considered for the Lakeland Clean Coal Technology Project. Additionally, Gregg mine limestone (Florida limestone), the limestone being considered for the Lakeland CCT Project, was also used during 1998. Various other types of limestone were also used during the year. The differences in loadings

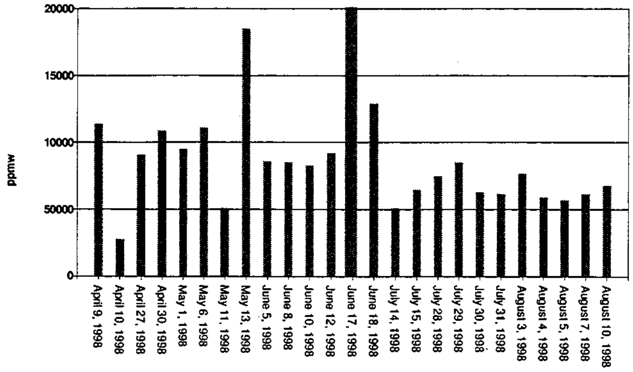

Fig. 4 1998 PCD inlet loadings

are attributed to several factors. Varying flue gas velocities through the primary cyclone from the transport reactor produced varying cyclone collection efficiencies and varying particulate loadings to the PCD. Operational changes in the transport reactor, differing feed requirements for various types of sorbent materials and variations in the compositions of the coal are just a few of the other factors that attributed to some of these variations. Regardless, PCD performance was not negatively affected by varying coal and sorbent material.

Outlet Mass Loadings. Figure 5 gives a summary of the particulate concentrations exiting the PCD (what would be entering the turbine) during 1998. As shown in the figure, the outlet particulate loading varied from 0.03 to just over 10 ppmw. Also included in the table are the corresponding blank values for each run. The blank values indicate the magnitude of the error associated with flue gas interaction with the filter material, weighing errors and any other problems that may have occurred in handling the substrates. In all but one case, the measured loadings were at least 60 percent greater than the corresponding blank values, suggesting that there was a very low, but measurable, concentration of dust in the flue gas. The TC03 outlet loadings were significantly lower than the outlet loadings obtained during TC02 (5 to 12 ppmw), when there was some leakage caused by an inadequate sealing arrangement between the 3M filter elements and the tubesheet. This problem was solved prior to TC03 by the use of a 3M-designed modification.

Collection Efficiency. PCD collection efficiencies, which are shown in Table 3, were calculated using corresponding inlet and outlet loadings. These collection efficiencies are quite high compared to those obtained with control technologies that are currently in service at many conventional coal-fired power plants. Collection efficiencies confirm that there was very little particulate penetration through the PCD during any segment of TC03. Outlet loadings as high as 12 ppmw had been measured during TC02. As mentioned above, the source of this particle penetration was traced to a sealing problem between the 3M filter elements and their fail-safe devices that was allowing particles to penetrate between the tubesheet and the element/fail-safe assembly. To address this problem, 3M modified the element's flange assembly. The outlet loadings measured during TC03 confirm the modifications were effective in eliminating the leakage that had occurred previously.

Table 3 1998 collection efficiencies for the Siemens-Westinghouse PCD

Run	Outlet	Loadings, ppmw		Efficiency	Penetration
	Run Date	Inlet	Outlet	%	%
TC02	4/23/98	10,150[1]	4.56	99.96	0.04
	4/24/98	10,150[1]	4.78	99.95	0.05
	5/5/98	10,150[1]	6.13	99.94	0.06
	5/7/98	10,150[1]	8.19	99.92	0.08
	5/13/98	10,150[1]	11.8	99.88	0.12
TC03	6/05/98	8,600	0.15	99.9982	0.0018
	6/08/98	8,500	0.13	99.9985	0.0015
	6/10/98	8,300	0.17	99.9980	0.0020
	6/12/98	9,200	0.27	99.9971	0.0029
	7/29/98	8,500	0.03	99.9996	0.0004
	7/31/98	6,200	0.18	99.9971	0.0029
	8/03/98	7,700	0.32	99.9959	0.0041
	8/05/98	5,700	0.37	99.9935	0.0065
	8/07/98	6,200	0.21	99.9966	0.0034
	8/10/98	6,800	0.22	99.9968	0.0032

1. Inlet loading used in these calculations is the average value for the four inlet sampling runs performed during stable reactor operation with dolomite addition.

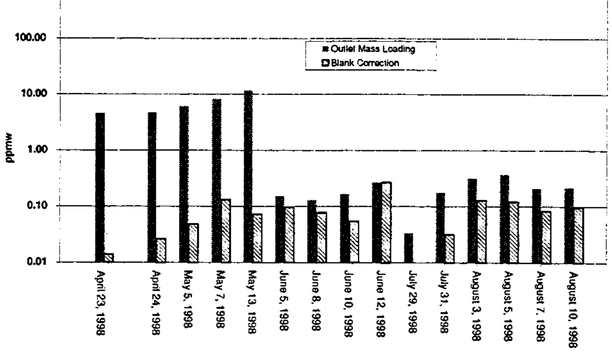

Fig. 5 PCD outlet loadings

Destructive Filter Element Strength Testing. To date, extensive destructive testing has been performed on many of the filter elements. Destructive testing has aided in the understanding of the failure events with the monolithic oxide filters and served as a prediction tool for the performance of elements under thermal stress conditions.

Non-Destructive Filter Testing. The PSDF is working closely with Dr. Roger Chen at West Virginia University (WVU) to evaluate his acoustic technique for non-destructively determining the mechanical properties of filter elements. Under a separate DOE contract,[2] Dr. Chen has evaluated 36 filter elements that are undergoing testing at the PSDF. He obtained a baseline Young's Modulus for each of the filter elements tested and his values closely agree with the values obtained through literature or from the manufacturer.

The 36 filter elements tested have included twelve Coors P-100A-1, twelve Pall type 326 and twelve Schumacher TF20. The Schumacher elements are being tested on the transport reactor train and have been measured after ~1000 h exposure. The results showed a general decrease in Young's Modulus over time. Exposure of these elements will continue and the changes in the mate-

---

[2] Research sponsored by the U.S. Department of Energy's Federal Energy Technology Center (FETC), under contract DE-AP21-95MC05134.

rials monitored over time. Ultimately, the elements will be destructively tested to confirm the results from Dr. Chen's analysis.

Operational Developments and Achievements. Operationally, the PCD has worked well, with few mechanical problems. Consequently, many accomplishments were seen during the last twelve months of operation. The most significant of these are listed below:

- The PCD has operated successfully on coal for over 3500 h. Over 3000 h of this operation has been at a PCD inlet temperature of ~1400 °F (760 °C).
- There have been no incidents of ash bridging (a process by which ash collects between elements and can cause failures).
- There have been no incidents of candle bowing (the elements themselves bending during exposure).
- No measurable elongation (a process by which the element stretches, which compromises strength) of silicon carbide filter elements has occurred after 1000 h exposure at 1350–1400 °F (730–760 °C).
- Filter elements from 3M, Blasch, Coors, Allied Signal (Dupont), IF&P, McDermott, Pall, Schumacher and Specific Surface have been tested.
- Exposure of several clay bonded silicon carbide filter elements has exceeded 3200 h.
- The PCD operated on coal for over 800 h with two broken filter elements to monitor fail-safe performance. The outlet loading measured was no greater than 15 ppm. The PSDF is working with Siemens-Westinghouse and others to improve the fail−safe performance.
- The originally supplied back-pulse valves (the system used to remove the collected ash cake) had a design flaw that limited their performance. This flaw was identified and corrected.
- The collection efficiency of the Siemens-Westinghouse PCD has been demonstrated to be greater than 99.99 percent.
- The ability to isokinetically collect representative ash samples from the process gas stream has been demonstrated.
- The Siemens-Westinghouse PCD has successfully operated continuously with outlet loadings below 1 ppm for 800 h.
- PSDF has successfully demonstrated the operation of the transport reactor and PCD with the design coal and sorbent for the Lakeland CCT project.
- Installation of filter elements in the Siemens-Westinghouse PCD for the Foster Wheeler combustor has been completed.
- The Foster Wheeler APFBC has been pressure tested and solids circulation tests performed.
- A better understanding of what is happening inside the PCD during operation has been developed. This was accomplished through many avenues: on-going FLUENT modeling (which is a cooperative effort between the DOE and PSDF), sampling to determine what fraction of the particulate is being separated *prior* to reaching the filter elements, and pulse system modeling and optimization.
- Worked with the filter element manufacturers such as 3M and Pall to evaluate two-meter filter elements. The use of the longer filter elements should improve the economics of the filter systems.

Future Activities

1999 is shaping up to be a very busy year at the PSDF. The current plans call for combustion-mode operation of the transport reactor with the Siemens-Westinghouse PCD in the first quarter. The unit will then be modified for gasification testing later in 1999. Commissioning of the Foster Wheeler APFBC will resume as operational difficulties with the topping combustor are overcome. During that time there are many objectives related to the filter system:

- Operate the KBR PCD for a minimum of 1000 additional hours at a temperature of 1350–1400 °F (730–760 °C).
- Prepare the transport reactor for gasification trials in the last half of 1999.
- Raise the face velocity for the PCD on the transport reactor train to determine if a reduction in capital cost can be realized by using fewer filter elements.
- Start-up the Foster Wheeler APFBC in a ''first-generation'' PFBC mode.
- Continue to work with the filter element manufacturers to evaluate new materials and two-meter filter elements, as they become available.
- Continue destructive testing of the exposed silicon carbide filter elements to evaluate their property changes with exposure.
- Continue supporting the research of Dr. Chen and others on non-destructive testing techniques for filter elements.

Acknowledgments

The authors wish to acknowledge the contributions and support provided by various project managers: Jim Longanbach (DOE), Marty Fankhanel (KBR), Zal Sanjana (Siemens-Westinghouse) and Duane Pontius (SRI). The U.S. Department of Energy's Federal Energy Technology Center, under contract DE-FC21-90MC25140 sponsored the project.

The authors would also like to especially thank Rich Dennis (DOE), Ted McMahon (DOE) and everyone who has been involved in supporting the PCD testing over the last year. There are well over 100 people who have provided their expertise, support and encouragement to this part of the project. The success of the PCD program at the PSDF is largely due to their input.

Nomenclature

Face Velocity = volumetric flow/filtration area, ft/min
μ = gas viscosity at operating conditions, cP
ΔP = filter pressure drop immediately after the backpulse, INWG
μ_{20} = gas viscosity at 20 °C and 1 atm, cP

Experimental and Numerical Studies of Two-Stage Ethane-Air Flames

M. M. Y. Waly

S. C. Li

F. A. Williams

Center for Energy and Combustion Research,
Department of Applied Mechanical
and Aerospace Engineering,
University of California, San Diego,
La Jolla, CA 92093-0411

This paper reports results of experimental and numerical investigations on ethane-air two-stage combustion in a counterflow burner where the fuel stream, which is partially premixed with air for equivalence ratios from 1.6 to 3.0, flows against a pure air stream. Similar to methane, the two-stage ethane combustion exhibits a green fuel-rich premixed flame and a blue diffusion flame. Flame structures, including concentration profiles of stable intermediate species such as C_2H_4, C_2H_2 *and* CH_4, *are measured by a gas chromatography and are calculated by numerical integrations of the conservation equations employing an updated elementary chemical-kinetic data base. The implications of the results from these experimental measurements and numerical predictions are summarized, the flame chemistry of ethane two-stage combustion at different degrees of premixing (or equivalence ratio) is discussed, and the relationship between NOx formation and the degree of premixing is established. The present work helps to increase understanding of flame chemistry of hydrocarbon fuels, identify important reactions for pollutant formation and suggest means to reduce emissions.* [S0742-4795(00)01303-X]

Introduction

Ethane is the second most important hydrocarbon constituent of natural gas (NG). Variation of ethane concentration is found to influence ignition, combustion and extinction of NG-air mixtures in practical applications such as in gas turbines and internal combustion engines [1]. Trumpy et al. [2] and Leppard [3] studied preknock chemistry of ethane in internal combustion engines and helped to develop understanding of the ethane ignition mechanism at temperatures lower than 1100 K. Laurendeau and co-workers developed an experimental method using laser-saturated fluorescence to measure nitric oxide in laminar $C_2H_6/O_2/N_2$ premixed flames [4] and in laminar counterflow ethane diffusion flames [5]. These nonintrusive optical measurements of NO have advanced our knowledge on NO formation in both premixed and diffusion flames. Lean premixed flames of ethane at pressures ranging from 1 to 10 atm were studied by Drake et al. [6] in a flat-flame burner, providing useful information to better understand NO production at high pressures.

Detailed measurements and computations for flame structures of staged ethane combustion are not available in the literature. Since those measurements and their comparison with theory may improve our understanding of two-stage ethane flame chemistry in gas turbines and other combustors, an experimental and computational study of a two-stage ethane-air flame is performed here to investigate how ethane is oxidized and how the intermediate species such as C_2H_4, C_2H_2, and CH_4 are formed in rich premixed and diffusion flames. As discussed in our previous publications [7,8], staged combustion can be realized in a counterflow burner where, for instance, a fuel-rich mixture flows downward counter to a stream of pure air.

A practical motivation for studying this configuration arises from its possible utility in increasing combustion stability and combustion efficiency and in reducing pollutants. A test rig can be constructed that affords ready access for instrumentation, and complementary theoretical and computational studies are facilitated by reduction of the applicable conservation equations along the centerline to ordinary differential equations.

Experiments

This study employed a laminar counterflow burner which is schematically shown in Fig. 1(*a*). In this burner, coaxial streams issue from two ducts placed one above the other, each with exit inner diameter of 20 mm. The separation distance between the duct exits, L, is 15 mm, and the exit area of each duct, A, is 314 mm^2. The ethane-air mixture flows through the upper duct, and the pure air stream flows through the lower duct. The equivalence ratio of the fuel stream is in the range from 1.6 to 3.0 in the present study while the mean strain rate, a, is adjusted to 90 s^{-1} based on the total flow rates from the upper duct and from the lower duct, that is, $a=2(Q_a+Q_l)/(LA)$, where Q_a and Q_l are the volumetric flow rates from the upper and lower ducts, respectively.

In the experiment, the desired equivalence ratio and strain rate are established first, and then a torch is used to ignite the flame. A typical photograph of such a flame is shown in Fig. 1(*b*). It can be seen that there are two distinguished flame zones: One is thin with green emission, and the other is thicker with blue emission. The former is the premixed flame, where the ethane is consumed to form carbon monoxide and hydrogen along with some carbon dioxide and water, and the latter is the diffusion flame, where the CO and H_2 produced in the first stage burn. It seems likely that the color of the premixed flame is dominated by emissions from C_2 species, while that of the diffusion flame reflects excited CO_2 emissions stemming from the oxidation of CO. These flame colors are the same as those of two-stage methane-air flames [7].

A SRI-8610C gas chromatograph (SRI Instruments), which has Molecular Sieve and Silica Gel columns with a thermal conductivity detector (TCD) and a flame ionization detector (FID), is employed to measure concentrations of stable species. A methanizer accessory is built in the gas chromatograph so that the FID can be used to measure concentrations of CO and CO_2 as well as those of hydrocarbon species. Gas samples in the flame are taken by a quartz microprobe whose tip has an outer diameter around 0.5 mm and an inner diameter around 0.1 mm. In the present ethane flames, the measurable species by the FID are CH_4, CO, CO_2, C_2H_6, C_2H_4, C_2H_2, and C_3H_6. Nitrogen and oxygen are

---

Contributed by the International Gas Turbine Institute (IGTI) of THE AMERICAN SOCIETY OF MECHANICAL ENGINEERS for publication in the ASME JOURNAL OF ENGINEERING FOR GAS TURBINES AND POWER. Paper presented at the International Gas Turbine and Aeroengine Congress and Exhibition, Indianapolis, IN, June 7–10, 1999; ASME Paper 99-GT-108. Manuscript received by IGTI March 9, 1999; final revision received by the ASME Headquarters May 15, 2000. Associate Technical Editor: D. Wisler.

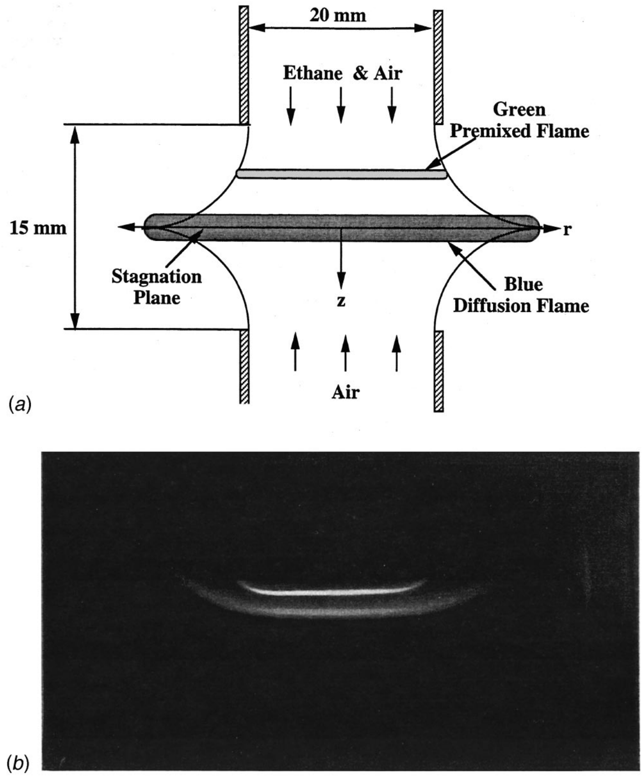

Fig. 1 (*a*) **Schematic diagram of a two-stage flame of ethane in counterflowing streams;** (*b*) **a photograph of the flame sketched above.**

measured by the TCD. Concentrations of water and hydrogen are not measured in the present study. Temperature profiles are measured with a Pt-6% Rh versus Pt-30% Rh thermocouple with a bead diameter of 140 μm; corrections for radiation are made.

Numerical Computations

The computational methods employed here were described previously [7,8]. The numerical integrations concern laminar flames with potential flow in the outer streams. The air-side potential-flow strain rate was taken to be 90 s^{-1}, estimated to be within 10 percent of a for these flames. Radiation from CO_2 and H_2O is taken into account in the energy equation. With these assumptions, the equations of continuity, radial momentum, energy and chemical species reduce to those given previously [9,10]. The present computations employ a numerical code developed at RWTH, Aachen, Germany [11].

The present study employs a detailed chemical mechanism consisting of 186 elementary reactions among 45 species, which are CH_3O, CH_2OH, O_2, H_2, H_2O, HO_2, H_2O_2, H, OH, O, CO, CO_2, CH_4, CH_3, CH_2O, CHO, C_2H_6, C_2H_5, C_2H_4, C_2H_3, C_2H_2, C_2H, singlet $^*CH_2$ and triplet CH_2, CH, HCCO, C_3H_7, C_3H_6, C_3H_5, C_3H_4, C_3H_3, N_2, HCN, N, NH_3, NH_2, NH, HNO, NO, N_2O, N_2H, NO_2, NCO, CN, and HNCO. This reaction mechanism is upgraded from our 177-step reaction mechanism [8] by adding species C_2H and 9 reactions for its production and consumption. These 9 reactions and their rate parameters for C_2H are taken from the paper by Frenklach et al. [12] (reactions 95–101, 107 and 111). With the exception of the rate parameters for $C_2H_4+H \rightarrow C_2H_3+H_2$ and $C_2H_4+OH \rightarrow C_2H_3+H_2O$ as discussed below, all rate parameters listed in Table 1 of [8] are kept unchanged in the present study.

Results of Experimental Measurement and Numerical Computations

The computational results are compared with the measurements in Figs. 2–6, and predicted NO, CH, N, and HCN are shown in Fig. 7. Each one of these figures has four subfigures, labeled (*a*), (*b*), (*c*), and (*d*), which correspond to equivalence ratios, Φ, of 1.65, 1.85, 2.20, and 2.65, respectively, in decreasing degree of

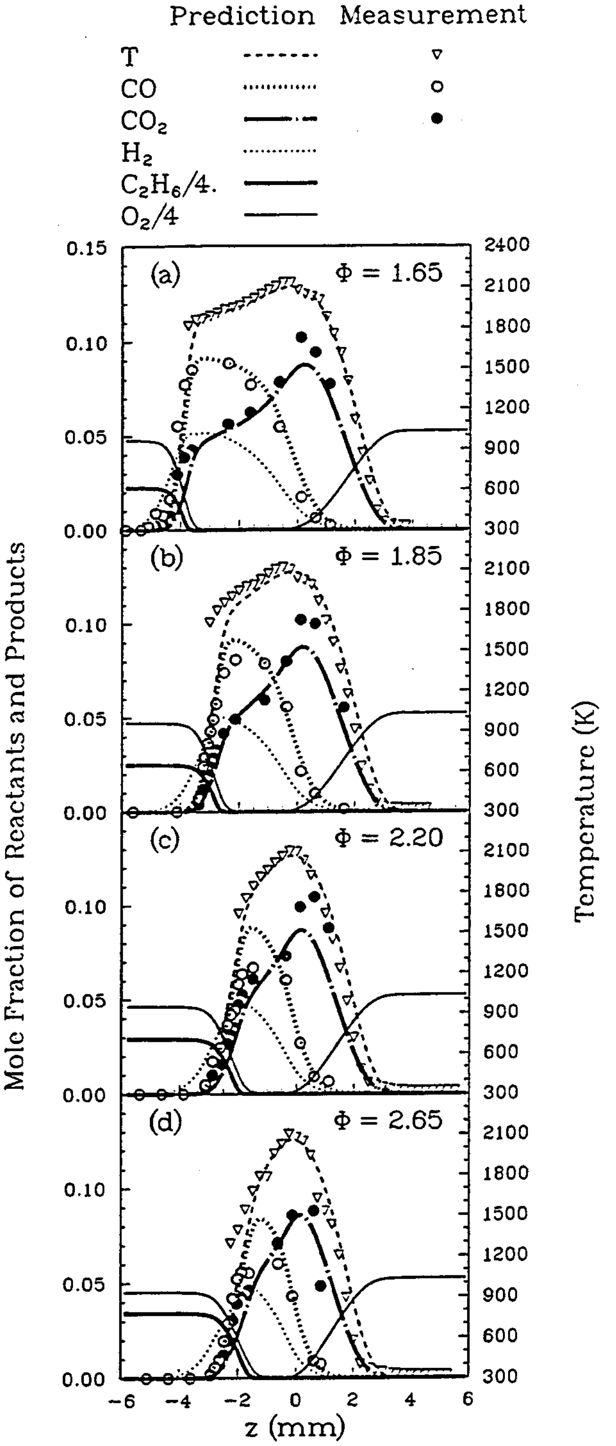

Fig. 2 Comparison between measurement and prediction for profiles of temperature and major species for strain rate $a=90\ s^{-1}$ **at different equivalence ratios:** (*a*) $\Phi=1.65$; (*b*) $\Phi=1.85$; (*c*) $\Phi=2.20$; (*d*) $\Phi=2.65$.

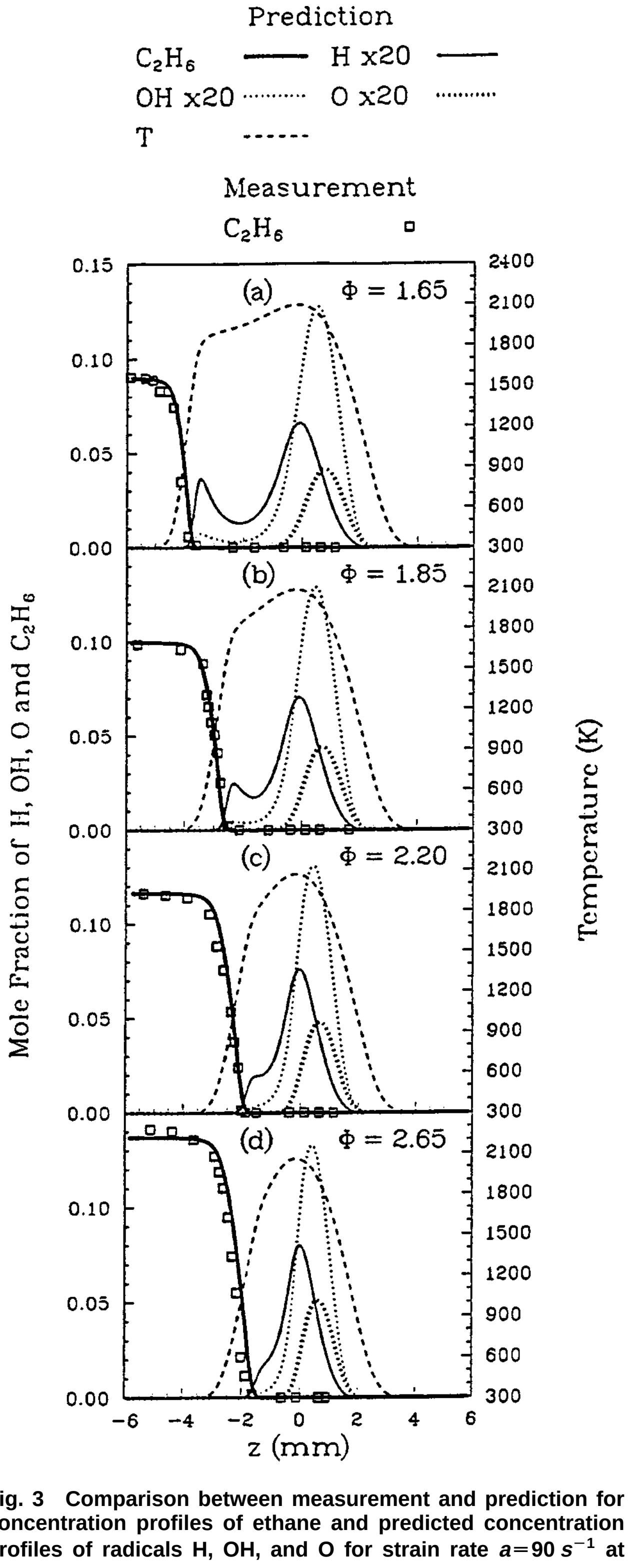

Fig. 3 Comparison between measurement and prediction for concentration profiles of ethane and predicted concentration profiles of radicals H, OH, and O for strain rate $a=90\ s^{-1}$ at different equivalence ratios: (*a*) Φ=1.65; (*b*) Φ=1.85; (*c*) Φ=2.20; (*d*) Φ=2.65.

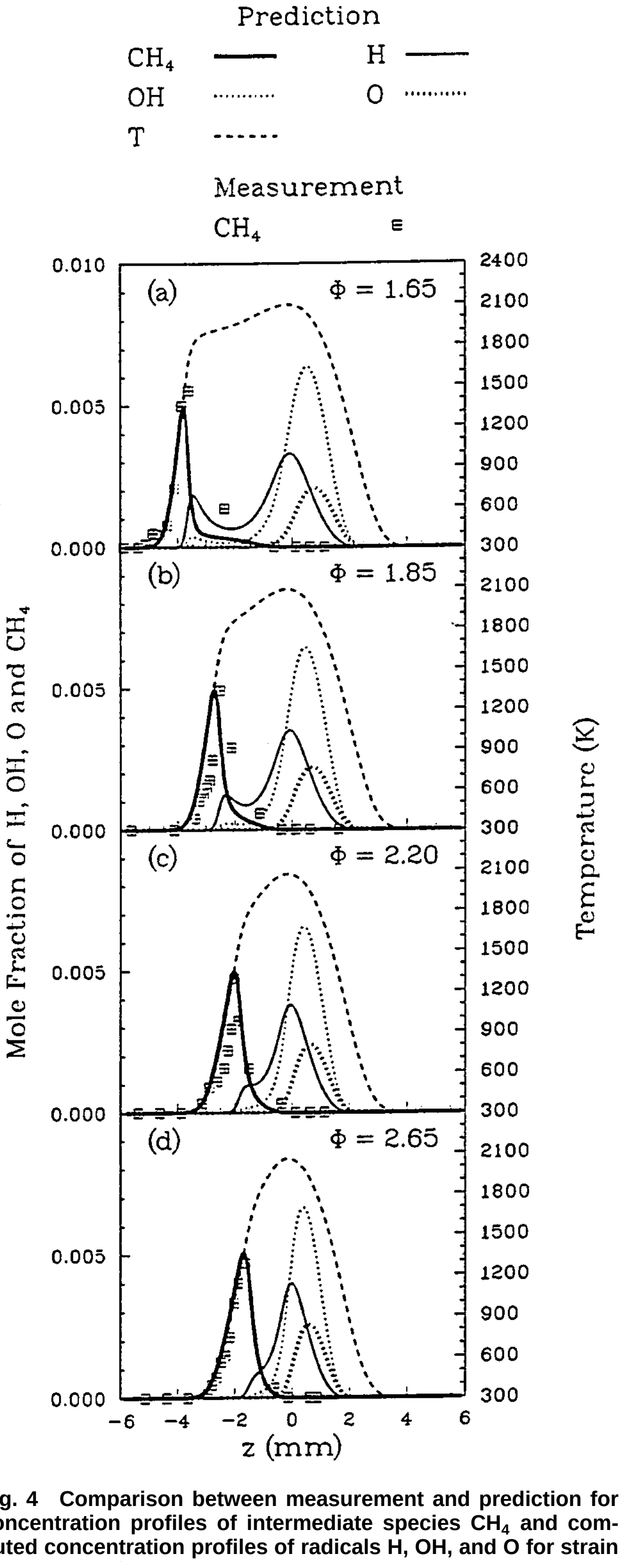

Fig. 4 Comparison between measurement and prediction for concentration profiles of intermediate species CH_4 and computed concentration profiles of radicals H, OH, and O for strain rate $a=90\ s^{-1}$ at different equivalence ratios: (*a*) Φ=1.65; (*b*) Φ=1.85; (*c*) Φ=2.20; (*d*) Φ=2.65.

premixing. Results in these figures show how the equivalence ratios (related to the degree of premixing) influences structures of ethane flames.

General Flame Structure. Figure 2 shows profiles of temperature, *T*, and of concentrations of reactants C_2H_6 and O_2 and products H_2, CO, and CO_2, indicating good agreement of measured and predicted profiles for CO, CO_2 and temperature, differences typically being less than 10 percent, comparable with the previously discussed [7,8] measurement uncertainty. The two-stage structure is very evident at the higher degrees of premixing in Fig. 2(*a*) and (*b*), with the premixed flame on the left, producing CO and H_2, which burn with O_2 from the air in the diffusion flame about 4 mm away. At the lesser premixing in Fig. 2(*c*) and

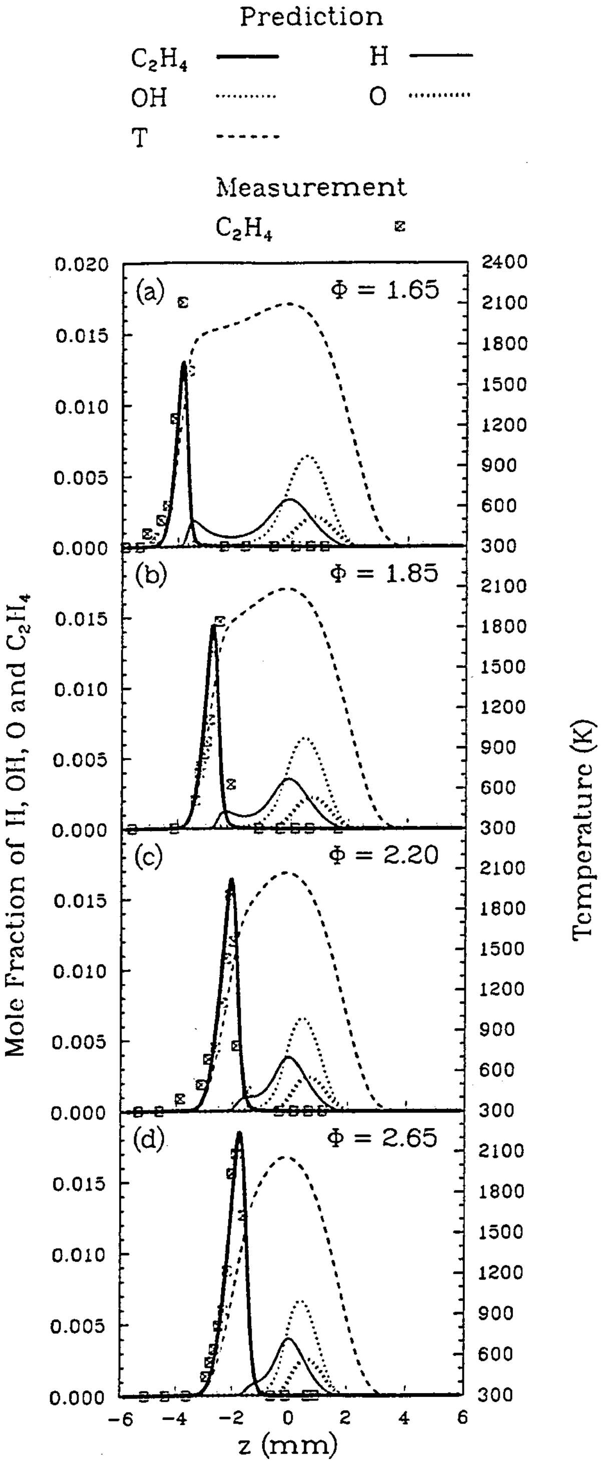

Fig. 5 Comparison between measurement and prediction for concentration profiles of intermediate species C_2H_4 and computed concentration profiles of radicals H, OH, and O for strain rate $a=90\ s^{-1}$ at different equivalence ratios: (*a*) Φ=1.65; (*b*) Φ=1.85; (*c*) Φ=2.20; (*d*) Φ=2.65.

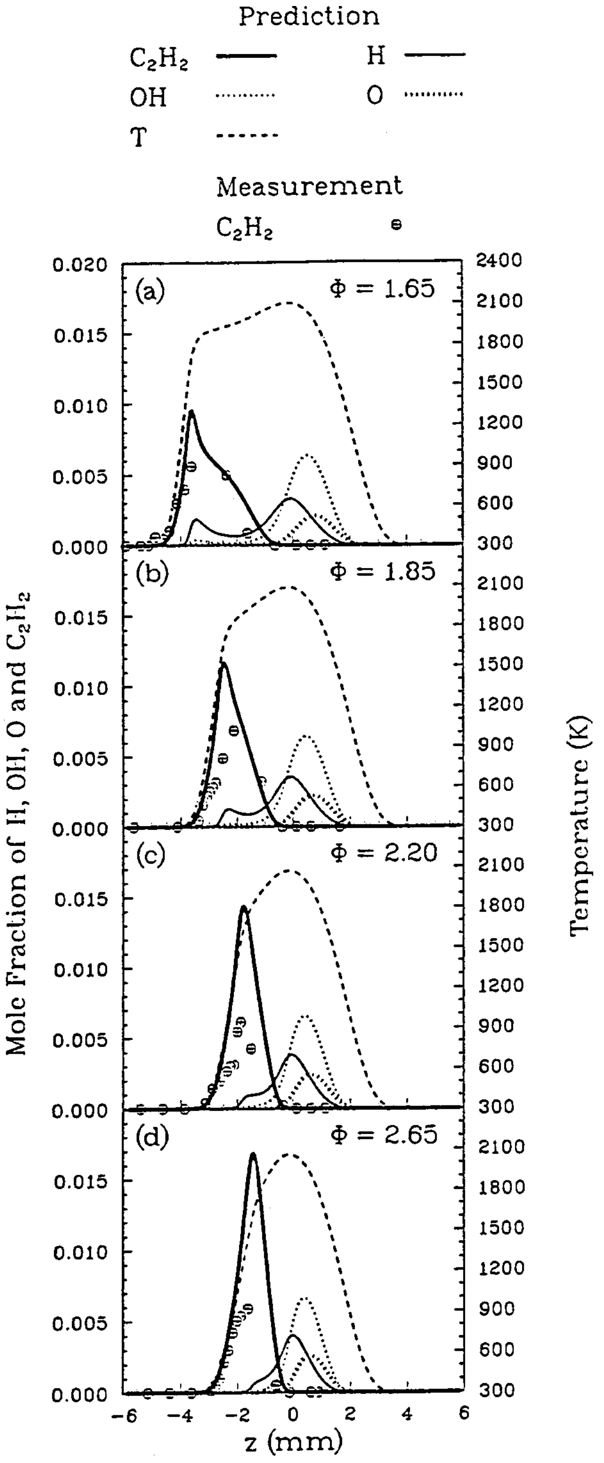

Fig. 6 Comparison between measurement and prediction for concentration profiles of intermediate species C_2H_2 and computed concentration profiles of radicals H, OH, and O for strain rate $a=90\ s^{-1}$ at different equivalence ratios: (*a*) Φ=1.65; (*b*) Φ=1.85; (*c*) Φ=2.20; (*d*) Φ=2.65.

(*d*) the two flames have nearly merged, so that CO peaks only slightly to the left of CO_2. This can be understood by referring to Fig. 1 where the configuration illustrates that the premixed flames with lower equivalence ratios, which have higher burning velocities, will propagate further upstream, producing larger separation distances between the two flames. Increasing the strain rate slightly decreases the separation distance but does not change the flame structure.

The maximum CO concentration occurs in the premixed flame, while the maximum concentration of CO_2 is found in the diffusion flame. As expected, Fig. 2 shows that the maximum concentration of CO decreases with increasing Φ; experiment and computation agree, although spatial resolution difficulties prevent experimental identification of the peak value at higher Φ. The maximum concentration of CO_2 is essentially the same for different premixing

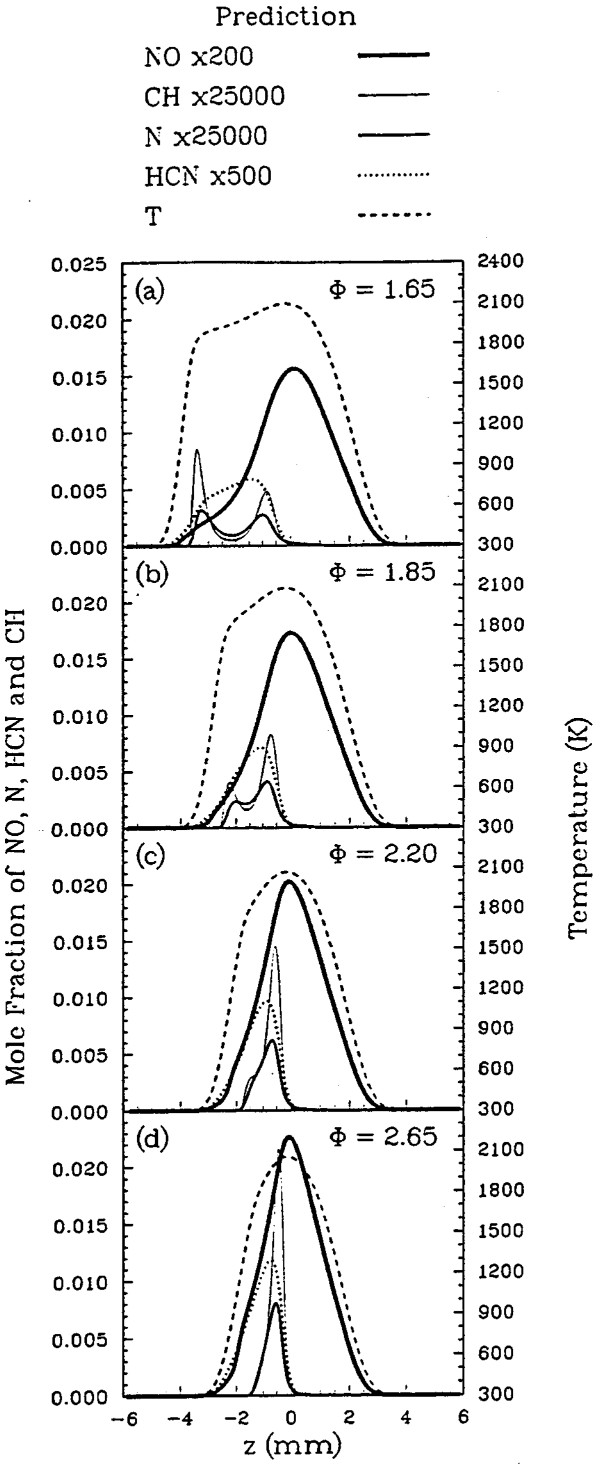

Fig. 7 Predicted concentration profiles of NO, CH, N, and HCN for strain rate $a=90\,s^{-1}$ at different equivalence ratios: (*a*) Φ=1.65; (*b*) Φ=1.85; (*c*) Φ=2.20; (*d*) Φ=2.65.

and, consequently, the maximum flame temperature is about 2100 K for all four cases, regardless of Φ. This is because all of the fuel finally is burned completely in the diffusion flame, and the strain rate is the same in all cases.

The production and consumption of CO are found to occur mainly through the four production reactions

$$CHO+M \rightarrow CO+H+M \qquad (R1)$$

$$CH_2+O_2 \rightarrow CO+OH+H \qquad (R2)$$

$$HCCO+H \rightarrow CO+CH_2 \qquad (R3)$$

$$HCCO+O_2 \rightarrow 2CO+OH \qquad (R4)$$

and the oxidation step

$$CO+OH \rightarrow CO_2+H. \qquad (R5)$$

These reactions are consistent with CO being produced in the premixed flame, since CHO, CH_2 and HCCO are formed and consumed there and do not exist in the diffusion flame according to the computational results. Most of CO_2 is formed, through *R*5, in the diffusion flame, in which the OH concentration peaks and in which the CO concentrations are everywhere much higher than those of OH so that CO is consumed gradually.

Ethane Consumption Chemistry. Figures 3 shows measured and predicted profiles of ethane concentrations. Computed concentrations of the radicals H, OH, and O are also plotted in this figure since these radicals are the dominant species that attack ethane and other hydrocarbons. Predicted profiles of temperature are replotted in Fig. 3 for orientation. It is seen that ethane rapidly disappears in the premixed-flame reaction zone where the temperatures are around 1750 K.

The four principal reactions that consume ethane, identified by the numerical computations, are

$$C_2H_6+H \rightarrow C_2H_5+H_2 \qquad (R6)$$

$$C_2H_6+O \rightarrow C_2H_5+OH \qquad (R7)$$

$$C_2H_6+OH \rightarrow C_2H_5+H_2O \qquad (R8)$$

and

$$C_2H_6+CH_3 \rightarrow C_2H_5+CH_4. \qquad (R9)$$

At low equivalence ratios, two peaks are predicted in the H and OH concentration profiles, a low peak in the premixed flame and a much higher peak in the diffusion flame. Concentrations of OH in the premixed flames are much lower than those of H, and *R*6 is much faster than *R*7, *R*8, and *R*9, based on computational results. Therefore, about 80 percent of ethane is consumed by *R*6. From Fig. 3, it is also seen that the radical H, which is produced in the diffusion flame, diffuses back to attack the reactants at higher Φ but not at lower Φ, where sufficient *H* is produced in the premixed flame.

The ethyl radical C_2H_5, which is unstable, decomposes rapidly to C_2H_4 and CH_3 through reactions

$$C_2H_5+M \rightarrow C_2H_4+H+M, \qquad (R10)$$

$$C_2H_5+H \rightarrow 2CH_3 \qquad (R11)$$

and

$$C_2H_5+O_2 \rightarrow C_2H_4+HO_2. \qquad (R12)$$

Reactions *R*10 and *R*11 consume more than 60 percent and 30 percent of C_2H_5, respectively. It may be noted that reactions *R*1, *R*2, *R*5, and *R*10 are the major sources of H radicals in the premixed flame reaction zone. The main products from reactions *R*6 through *R*12 are H_2O, H_2, C_2H_4, CH_4 and CH_3, with the latter four species being further oxidized.

Formation and Consumption of CH_4. Measured and predicted profiles are plotted in Figs. 4(*a*)–(*d*). These figures indicate that the maximum mole fraction of CH_4 is about 0.5 percent and is insensitive to the equivalence ratio in these flames. It is formed dominantly by

$$CH_3+H+M \rightarrow CH_4+M \qquad (R13)$$

and by reaction *R*9 and is consumed by the three well-known reactions

$$CH_4+H\rightarrow CH_3+H_2, \qquad (R14)$$

$$CH_4+OH\rightarrow CH_3+H_2O \qquad (R15)$$

and

$$CH_4+O\rightarrow CH_3+OH. \qquad (R16)$$

As shown in Fig. 4, good agreement between experiment and prediction is obtained when use is made of the rate parameters for *R*6 through *R*15 listed in the Table 1 of [8]. All of the differences seen in Fig. 4 can be attributed to uncertainties in probe positioning and sampling.

C_2H_4 Chemistry. Ethene is consumed by the reactions

$$C_2H_4+H\rightarrow C_2H_3+H_2, \qquad (R17)$$

$$C_2H_4+O\rightarrow CH_3+CHO \qquad (R18)$$

and

$$C_2H_4+OH\rightarrow C_2H_3+H_2O. \qquad (R19)$$

Among these three reactions, *R*17 removes most of the C_2H_4. This occurs because the concentration of H is much larger than that of the O and OH in the premixed flame, as seen in Fig. 5, and computations show that *R*17 is much faster than *R*18 and *R*19 there.

By neglecting the least important reactions, chemical-kinetic steady-state balances for C_2H_5 and C_2H_4 result approximately in

$$X_{C_2H_4}\approx\frac{k_6X_{C_2H_6}X_H}{(k_{17}X_H+k_{19}X_O)(1+k_{11}X_H/k_{10})}, \qquad (1)$$

where k_i is the rate constant of the reaction *Ri* and X_i denotes the mole fraction of the species *i*. The validity of Eq. 1, within error less than 20 percent at the position of maximum $X_{C_2H_4}$, is supported by the computational results.

It is found that if the rate parameters listed in [8] are used, then the predicted concentration of C_2H_4 is too low by a factor of two, while the predicted sum of the concentrations of C_2H_2 and C_2H_4 is too high in comparison with experimental results. The first of these problems was not encountered in our previous work [8] because C_2H_4 and C_2H_2 were not distinguishable by the Porapak Q column used in the previous gas chromatograph measurements [8]. The second of these problems was encountered [8], but the concentrations of both C_2H_4 and C_2H_2 are much lower in methane flames than in ethane flames.

According to Eq. 1, the concentration of C_2H_4 increases with increasing k_6 and with decreasing k_{17}, k_{19}, and k_{11}/k_{10}. The values of k_6, k_{10}, and k_{11}, however, cannot be changed because these values are less uncertain and have led to the good agreements as shown in Figs. 3 and 4, for example. In order to obtain improved agreements between measured and predicted concentrations of both C_2H_4 and C_2H_2, values of k_{17} and k_{19} are reduced to $k_{17}=2.25\times10^7T^{2.12}\exp(-6727/T)$ and $k_{19}=2.70\times10^5T^{2.31}\exp(-1450/T)$, respectively, which are smaller by a factor of 2 than those given by Bhargava and Westmoreland [13]. These new rate constants are within the reported [13] uncertainties, which are a factor of 2.4 in k_{17} and a factor of 2.75 in k_{19}.

Figures 5(*a*)–(*d*) compare measured concentrations of C_2H_4 with predictions based on these new rate constants k_{17} and k_{19}. It is seen that the agreements are excellent. These figures indicate that the maximum concentration of C_2H_4 increases with increasing equivalence ratio, as the premixed flame, where C_2H_4 disappears, moves closer to the stagnation plane located at $z=0$.

Formation and Consumption of C_2H_2. The radical C_2H_3, which is the main product of reactions *R*17 through *R*19, decomposes to C_2H_2 dominantly by

$$C_2H_3+M\rightarrow C_2H_2+H+M \qquad (R20)$$

and less importantly by

$$C_2H_3+H\rightarrow C_2H_2+H_2 \qquad (R21)$$

and

$$C_2H_3+O_2\rightarrow C_2H_2+HO_2. \qquad (R22)$$

Following these reactions, the C_2H_2 is oxidized mainly by

$$C_2H_2+O\rightarrow HCCO+H \qquad (R23)$$

and

$$C_2H_2+O\rightarrow CH_2+CO. \qquad (R24)$$

Different from CH_4, C_2H_4, and C_2H_6, which are mainly attacked by the H radical, the removal of C_2H_2 is dominantly by the O radical in the current reaction scheme.

In a first approximation, chemical-kinetic steady-state balances for C_2H_3 and C_2H_2 result in

$$X_{C_2H_2}\approx\frac{k_{17}X_{C_2H_4}X_H}{(k_{23}+k_{24})X_O}. \qquad (2)$$

This equation implies that the lower consumption rate of C_2H_4 by *R*17 and *R*19, in comparison with *R*18, leads to a lower concentration of C_2H_2 in the flame, consistent with experimental observations. The previous rate parameters [8] predicted C_2H_2 concentrations in excess of C_2H_2 concentrations in both CH_4 and C_2H_6 flames, contrary to experiment, but the new rates reverse this relationship and also lower the sum of the concentrations of C_2H_2 and C_2H_4, improving agreement with experiment.

Measured and predicted profiles of C_2H_2 are plotted in Figs. 6(*a*) to (*d*). The agreement between experiment and prediction is fair at lower equivalence ratios, but the predicted maximum concentration of C_2H_2 is much higher than the measurement at higher equivalence ratios. This difference is probably due to oversimplified C_2H_2 chemistry employed here. The links of C_2H_2 chemistry to soot inception make it more complicated [14]. In particular, there are indications that additional outlet channels, such as through OH attacks, rate for which are extremely uncertain [14], need to be included. More work is needed to resolve this discrepancy.

NOx Formation. In the present study, concentrations of NOx were not measured by our NOx analyzer because its response to high concentrations of the C_2 species produces false high NOx readings [8]. Work is continuing to enable reliable NOx results to be extracted in the presence of these complications, but that work is not yet completed. Despite the absence of these critical experimental tests, the present computation may give insight into the NOx formation mechanism in ethane flames, since the present nitrogen chemistry is reasonably successful in two-stage methane flames [8].

In two-stage ethane flames, both thermal NO formation

$$O+N_2\rightarrow NO+N \qquad (R25)$$

and the prompt mechanism

$$CH+N_2\rightarrow HCN+N \qquad (R26)$$

are important. Both of these steps are followed by $N+O_2\rightarrow NO+O$. The CH radicals are dominantly formed from triplet methylene by

$$CH_2+H\rightarrow CH+H_2 \qquad (R27)$$

and

$$CH_2+OH\rightarrow CH+H_2O, \qquad (R28)$$

where the CH_2 is from reaction *R*24, isomerization of the singlet and the reaction $CH_3+H\rightarrow CH_2+H_2$. The most important consumption steps for CH species are

$$CH+H_2O\rightarrow CH_2O+H, \qquad (R29)$$

$$CH+CO_2\rightarrow CHO+CO \qquad (R30)$$

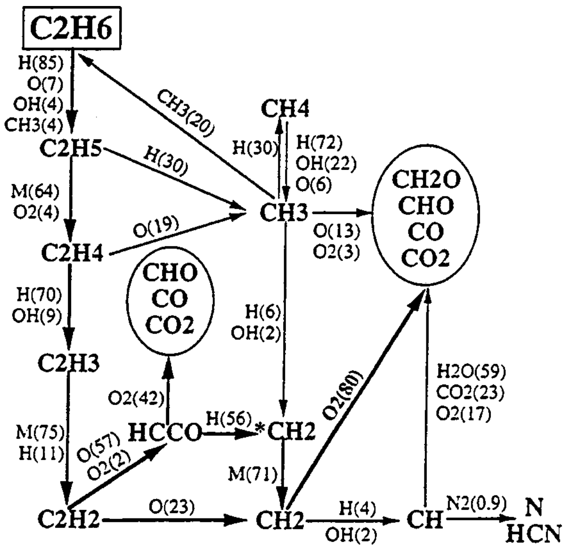

Fig. 8 Reaction path for ethane in a two-stage ethane-air flame with equivalence ratio $\Phi=1.65$ and strain rate $a=90\ s^{-1}$

and

$$CH+O_2\rightarrow CHO+O. \qquad (R31)$$

On the basis of a chemical-kinetic steady-state balance, the CH radical concentration can be approximately calculated from

$$X_{CH}=\frac{(k_{27}X_{H}+k_{28}X_{OH})X_{CH_2}}{k_{29}X_{H_2O}+k_{30}X_{CO_2}+k_{31}X_{O_2}} \qquad (3)$$

if X_{CH_2} is known. It is clear from this equation that increasing the concentrations of CO_2 and H_2O in the region where CH exists reduces X_{CH} and thus decreases NO_x production rates. Concentrations of CH decrease with decreasing Φ, since the higher premixing means higher concentrations of O_2 and leads to a faster consumption rate of CH by *R*31. In lean premixed flames, the prompt path becomes negligible in comparison with the thermal path because X_{CH_2} is smaller and X_{O_2} is larger, giving a much smaller value of X_{CH} in Eq. 3.

Figure 7 shows calculated concentration profiles of NO, N, HCN, and CH. At the lower Φ, as shown in Figs. 7(*a*) and (*b*), two CH peaks are predicted as may be expected from Eq. 3 since the concentration profiles of H and OH have two peaks, shown in Figs. 3(*a*) and (*b*). This same reason applies to the two peaks of the N radical, produced by *R*25 and *R*26 and by reactions of NH with H and OH and consumed in producing NO through reactions of N with OH and O_2. It can be seen from Fig. 7 that the NO concentration reaches its maximum value in the diffusion-flame reaction zone, where the temperature is the highest. Results in Fig. 7 also show that the maximum concentration of NO increases with Φ; greater premixing lowers NOx formation because of the lower concentrations of HCN and N in the flame. This same type of behavior was observed for methane flames [8], but NOx levels are a little higher for ethane through greater contribution of the prompt mechanism.

Concluding Remarks

The present work has studied the flame chemistry of ethane experimentally and numerically. Figure 8 shows the principal reaction pathways of ethane oxidation in two-stage combustion with equivalence ratio $\Phi=1.65$ and strain rate $a=90\,s^{-1}$ at normal atmospheric pressure according to the present results. While specific information in the figure is associated with this condition, the general scheme applies over a wide range of conditions for which two-stage flames exist. In this figure, the heavier arrows represent the main pathways, with the agents and their fractions given in light print. The fractions (in parentheses) are obtained by integrating consumption rates over the entire field, including both flames. Indications of the fates of some of the minor species, such as C_2H, C_3H_3, C_3H_4, and C_3H_6, have been omitted from preceding discussions and the diagram for simplicity, although these generally proceed along mainly to the CO_2 and H_2O products. The diagram is designed to track the carbon atom in ethane rather than the hydrogen atoms. The N and HCN, derived from CH, are the sources of prompt NO_x, through subsequent pathways that are not shown.

It is seen here that H plays the most important role in fuel consumption. The important intermediate species are C_2H_5, C_2H_4, C_2H_3, C_2H_2, CH_4, CH_3, CH_2, HCCO and CH. Because C_2H_4, C_2H_2, and CH_4 are much more stable than other species in flames, their concentrations are high and measurable. The oxidation of radicals CH_2, HCCO, CH_3, CHO, and CH_2O leads to CO and CO_2. The radical CH is derived from CH_2 and proceeds to form N and HCN as well as CO and CO_2. Although only less than 1 percent of the CH is consumed by nitrogen, this is the main source of NO in these flames.

Besides their potential practical interest in increasing combustion stability and reducing pollutant formation, two-stage flames of the kind studied here afford advantages for determining flame chemistry, providing a greater range of reaction-zone conditions and larger distances for easier spatial resolution, thereby aiding in obtaining reliable experimental results. In identifying rate parameters for numerical computations to compare with the present experiments, the previously employed elementary rate data for the reactions $C_2H_4+H\rightarrow C_2H_3+H_2$ and $C_2H_4+OH\rightarrow C_2H_3+H_2O$ have been modified here to obtain better agreement between experimental measurement and numerical computation.

Acknowledgment

This research was supported by the National Science Foundation under Grant No. CTS98-12996.

References

[1] Naber, J. D., Siebers, D. L., Di Julio, S. S., and Westbrook, C. K., 1994, ''Effects of Natural Gas Composition on Ignition Delay Under Diesel Conditions,'' Combust. Flame, **99**, pp. 192–200.

[2] Trumpy, D. K., Uyehara, O. A., and Myers, P. S., 1969, ''The Preknock Kinetics of Ethane in a Spark Ignition Engine,'' SAE Trans., **78**, pp. 1849–1874.

[3] Leppard, W. R., 1985, ''A Detailed Chemical Kinetics Simulation of Engine Knock,'' Combust. Sci. Technol., **43**, pp. 1–20.

[4] Reisel, J. R., Carter, C. D., Laurendeau, N. M., and Drake, M. C., 1993, ''Laser-Saturated Fluorescence Measurements of Nitric Oxide in Laminar, Flat, $C_2H_6/O_2/N_2$ Flames at Atmospheric Pressure,'' Combust. Sci. Technol., **91**, pp. 271–295.

[5] Ravikrishna, R. V., and Laurendeau, N. M., 1998, ''Brief Communication: Laser-Saturated Fluorescence Measurements of Nitric Oxide in Laminar Counterflow Diffusion Flames,'' Combust. Flame, **113**, pp. 473–475.

[6] Drake, M. C., Ratclffe, J. W., Blint, R. J., Carter, A. D., and Laurendeau, N. M., 1990, ''Measurements and Modeling of Flame-Front NO Formation and Superequilibrium Radical Concentrations in Laminar High-Pressure Premixed Flames,'' *Twenty-Third Symposium (International) on Combustion*, The Combustion Institute, Pittsburgh, PA, pp. 387–395.

[7] Li, S. C., Ilincic, N., and Williams, F. A., 1997, ''Reduction of NOx Formation by Water Sprays in Strain Two-Stage Flames,'' ASME J. Eng. Gas Turbines Power, **119**, p. 836.

[8] Li, S. C., and Williams, F. A., 1998, ''Experimental and Numerical Studies of NOx Formation in Two-Stage Methane-Air Flames,'' ASME Paper 98-GT-73.

[9] Smooke, M. D., Seshadri, K., and Puri, I. K., 1988, ''The Structure and Extinction of Partially Premixed Flames Burning Methane in Air,'' *Twenty-Second Symposium (International) on Combustion*, The Combustion Institute, Pittsburgh, PA, pp. 1555–1563.

[10] Smooke, M. D., Crump, J., Seshadri, K., and Giovangigli, V., 1990, ''Comparison between Experimental Measurements and Numerical Calculations of the Structure of Counterflow, Diluted, Methane-Air, Premixed Flames,''

Twenty-Third Symposium (International) on Combustion, The Combustion Institute, Pittsburgh, PA, pp. 463–470.

[11] Pitsch, H., 1993, ''*Entwicklug eines Programmpaketes zur Berechnung eindimensionaler Flammen am Beispiel einer Gegenstomdiffusionsflamme*,'' Master thesis, RWTH Aachen, Germany.

[12] Frenklach, M., Wang, H., and Rabinowitz, M. J., 1995, ''Optimization and Analysis of Large Chemical Kinetic Mechanism Using The Solution Mapping Method-Combustion of Methane,'' Prog. Energy Combust. Sci., **18**, pp. 47–73.

[13] Bhargava, A., and Westmoreland, P. R., 1998, ''Measured Flame Structure and Kinetics in a Fuel-Rich Ethylene Flame,'' Combust. Flame, **113**, pp. 333–347.

[14] Lindstedt, R. P., and Skevis, G., 1997, ''Chemistry of Acetylene Flames,'' Combust. Sci. Technol., **125**, pp. 73–137.

Jeff Jablin
Sensor Engineering Manager,
Thermo Electric Company, Inc.,
Saddle Brook, NJ 07663-6167
e-mail: us-info@thermo-electric-online.com

Michael R. Storar
Instrument Maintenance Master Technician,
Watson Cogeneration Company,
Carson, CA 90749-6203

Phillip L. Gray
Staff Engineer, Electrical Instrument,
Watson Cogeneration Company,
Carson, CA 90749-6203

Improved Operating Efficiency Through the Use of Stabilized Thermocouples

The development of a ''stabilized'' temperature sensor has led to significant increases in turbine operating efficiency by maximizing output when compared with present sensor technology. These stabilized type K and E thermocouples are superior to existing standard non-stabilized thermocouples because they are not prone to the typical aging effects in the 400 to 600°C (752 to 1112°F) temperature range that can result in measurements errors. A complete set of 18 stabilized type K thermocouples were installed on the exhaust of several gas turbines used for power generation. These thermocouples were subjected to normal operating conditions for a period of one year. During that year, the increase in turbine output has ranged from 0.5 percent to almost 2.0 percent. This increase in output also translates into significant cost savings. In addition, the stabilized thermocouples have given the turbine maintenance technicians more confidence in the accuracy of their temperature measurements and resulted in improved troubleshooting and decision making. [S0742-4795(00)02502-3]

Introduction

The purpose of this paper is to first give a brief explanation of why temperature measurement is critical to efficient gas turbine operation. Then discuss the aging phenomenon common to Type K (Chromel-Alumel) and Type E (Chromel-Constantan) thermocouples, the cause and effects and how stabilized thermocouples can eliminate the effects of aging. Next, various data is presented illustrating the improved temperature measurements and increased output and efficiency resulting from the use of stabilized thermocouples versus standard nonstabilized thermocouples when installed on a gas turbine over an extended period of time. Finally, the conclusion and plans for further monitoring are presented.

Temperature Measurement and Turbine Efficiency

Optimizing turbine operating efficiency requires precise control of operating temperatures. In turn, precise control of operating temperatures requires accurate measurement provided by accurate, stable and repeatable temperature sensors. This is critical to optimal turbine efficiency because temperature control is used to limit the turbine firing temperature for gas turbines by regulating fuel flow. The firing temperature in the combustion chamber or ''burner cans'' is the hottest in the turbine and the most difficult to monitor due to the heat and thermal gradients. However, exhaust temperature is measurable and is directly proportional to the firing temperature. Typically, Chromel-Alumel (Type K) thermocouples are mounted in the turbine exhaust duct to provide a temperature feedback proportional to the firing temperature. This temperature feedback is subject to a time lag corresponding to the velocity of the air moving through the turbine and the response time of the thermocouples.

Turbine operating efficiency is directly proportional to the firing temperature of the gas leaving the combustion chamber and entering the turbine. This means that the higher the firing temperature, the greater the operating efficiency will be. However, the maximum firing temperature is limited by the metallurgical constraints of the turbine components. Precise temperature control is critical in preventing under firing or over firing of the turbine. Under firing is the condition where the turbine is being operated at a firing temperature that is lower than the optimal point, therefore sacrificing efficiency and fuel. Over firing is the condition where the turbine is being operated at a firing temperature that is higher than the recommended maximum. This will result in greater stress and wear on the turbine components and will shorten the life of the parts and increase maintenance costs. Therefore precise temperature measurement and control is critical to ensuring that the turbine is operating at optimal efficiency.

Aging Effects of Non-Stabilized Thermocouples

Standard non-stabilized Type K (90 Ni/10 Cr versus 95 Ni/Si, Al) and Type E (90 Ni/10 Cr versus 45 Ni/55 CU) thermocouples are subject to aging effects when exposed to the temperature range of 400 to 600°C (752°F to 1112°F) in which aging occurs [1]. This phenomenon is common and well known within the industry described elsewhere. The effects of aging cause a positive shift in the thermal emf output of the thermocouple which results in a temperature reading that is higher than the actual temperature being measured. This positive shift is typically about 5°C (9°F). Aging can begin to effect the output of a thermocouple in as little as 5 h exposure to the aging temperature range described in [2]. Aging can also be a problem for thermocouples that measure temperatures outside the aging temperature range if the thermocouple/process must pass through the aging range during a heat-up or cool-down period.

The cause of aging can be attributed to the positive thermoelement, Chromel (90 percent nickel, 10 percent chromium), shared by Type K and E thermocouples. In order to understand the aging process of Chromel, the atomic structure must be examined. The atomic lattice structure of Chromel is face-centered cubic (f.c.c.) which is common for other Ni/Cr alloys (reference Fig. 1). In the f.c.c. structure, there are a total of four atomic sites or positions that can be occupied by atoms per unit cube, three face sites and one corner site.

Unaged or fully annealed material is in the ''disordered'' state meaning that the nickel and chromium atoms are randomly distributed throughout the lattice (reference Fig. 1(*a*)). To obtain this structure the material is generally processed at a temperature of about 1000°C (1832°F) and then subjected to rapid cooling. All thermocouple wire is normally supplied in this annealed state.

Upon aging Ni/Cr alloys in the temperature range of 400 to 600°C (752 to 1112°F), diffusion takes place until the atoms have

---

Contributed by the International Gas Turbine Institute (IGTI) of THE AMERICAN SOCIETY OF MECHANICAL ENGINEERS for publication in the ASME JOURNAL OF ENGINEERING FOR GAS TURBINES AND POWER. Paper presented at the International Gas Turbine and Aeroengine Congress and Exhibition, Indianapolis, IN, June 7–10, 1999; ASME Paper 99-GT-401. Manuscript received by IGTI March 9, 1999; final revision received by the ASME Headquarters January 3, 2000. Associate Technical Editor: D. Wisler.

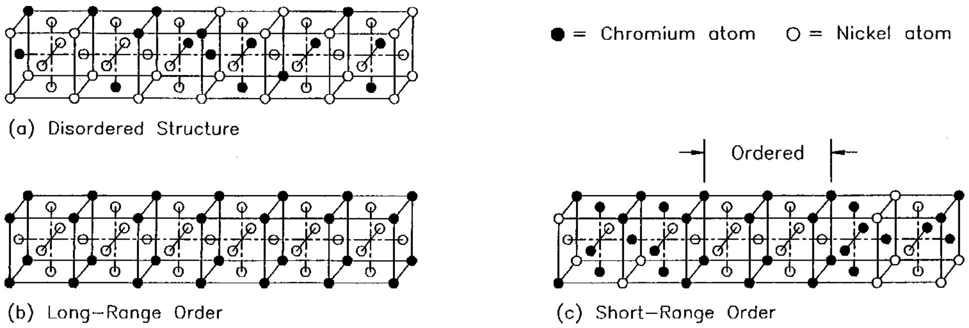

(a) Disordered Structure

(b) Long–Range Order

(c) Short–Range Order

Fig. 1 Face-centered cubic atomic lattice structure

reached equilibrium. When equilibrium is reached, the atoms have arranged themselves in what is termed ''long-range order'' (reference Fig. 1(*b*)). In long-range order all of the nickel atoms occupy the face center sites on the lattice and all of the chromium atoms occupy the corner sites. However, it is not possible for this long-range order to exist for Chromel over the entire lattice because the ratio of nickel atoms to chromium atoms is close to 10:1. In order to achieve a perfect long-range order the required ratio would be 3:1. As a result, part of the structure is ordered and the balance is disordered. This is known as ''short-range order'' (reference Fig. 1(*c*)). When Chromel is aged and the structure becomes short-range ordered, significant changes in the physical properties occur. These changes include an increase in resistivity of approximately 5 percent and a significant positive change in thermal emf.

Stabilizing Thermocouple Manufacturing Process. Thermo Electric developed Stabilized Type K and E thermocouples described elsewhere [3]. Specially selected thermocouple alloy materials is first matched to meet the special limits of error of the thermocouple type after being processed using a proprietary process. After this process the entire thermoelement is in short range ordered state eliminating the future thermal shifts regardless of heating rate from ambient to 1100°C (2000°F). It makes no difference if the heating rate is fast 20 min or slow 16 h [3].

Non-Stabilized Versus Stabilized Thermocouples

The typical construction for both the new stabilized thermocouples supplied and the non-stabilized thermocouples that were replaced on this project is metal sheathed MI (mineral insulated) cable design. This is also the most common construction for most industrial thermocouple applications. MI cable construction consists of an outer metal sheath, usually made of a stainless steel or nickel based alloy, filled with a compacted ceramic insulation that surrounds the thermoelements. The ceramic insulation most commonly used is MgO (magnesium oxide). The advantages of this MI cable construction include superior protection of the thermoelements, vibration resistance and flexibility.

Initially, any new thermocouple whether it is stabilized or non-stabilized should meet the initial calibration tolerance as specified by ASTM E230 shown below [4]:

Type	Range	Standard Tolerance	Special Tolerance
K	0–1260°C	±2.2°C or ±0.75 percent	±1.1°C or ±0.4 percent
E	0–870°C	±1.7°C or ±0.5 percent	±1°C or ±0.4 percent

The advantage of stabilized thermocouples is that they will remain within the special tolerance limits over long periods of time even when used in the aging temperature range. Whereas non-stabilized thermocouples exhibit significant drift over time when

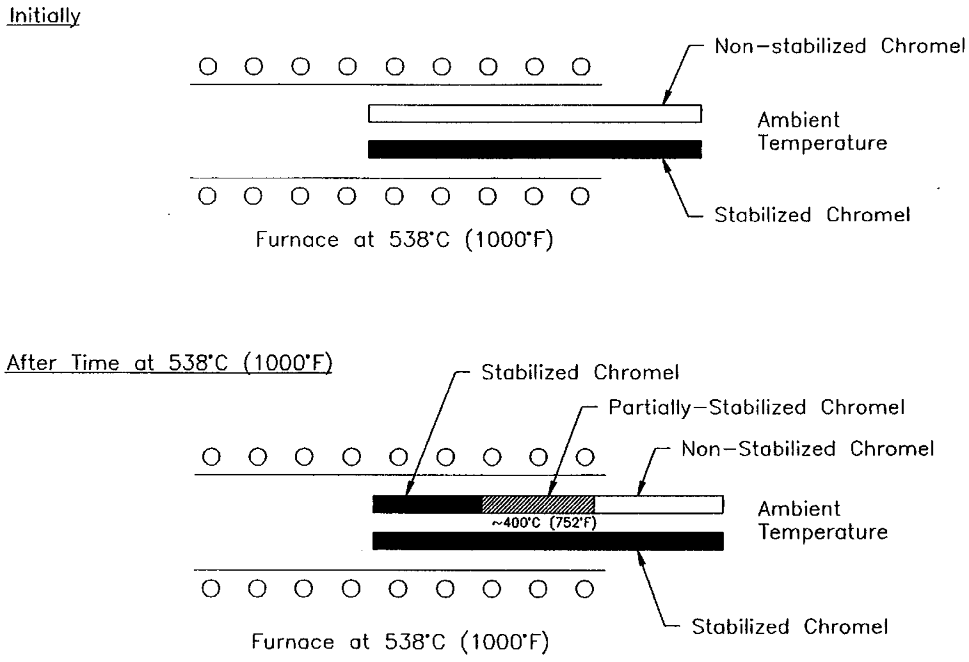

Fig. 2 Non-stabilized versus stabilized chromel exposed to the aging temperature

exposed to the aging temperature range. The typical drift is approximately 5°C (9°F) in the positive direction and can begin to occur in as little as 5 h. As stated previously, the cause of this shift is the change in atomic structure of the Chromel thermoelement.

Examination of the structural differences between a non-stabilized versus a stabilized Chromel thermoelement exposed to the aging temperature range can help give some insight into the changes that occur (reference Fig. 2). Keep in mind that stabilized thermocouple MI cable material is supplied in the short-range ordered state while non-stabilized thermocouple MI cable material is supplied in the fully annealed or disordered state. Initially, both the stabilized and non-stabilized thermoelements are inserted into a furnace (or the process to be measured) at a temperature in the aging range, i.e., 538°C (1000°F). The non-stabilized thermoelement has a uniform disordered structure throughout its length while the stabilized thermoelement has a uniform short-range ordered structure throughout its length. The part of the thermoelement that is where the thermocouple junction would be is heated and the other end where the termination would be is at ambient temperature. After some time at temperature, the stabilized thermoelement retains its initial short-range ordered state uniformly throughout its entire length. However, the non-stabilized thermoelement develops three separate structures along its length. In the hot part of the furnace/process the exposure to the aging temperature range has caused the material to become short-range ordered or stabilized through the diffusion of the atoms. At the mouth of the furnace or where the thermoelement exits the process, the structure has some short-range ordering and is partially stabilized. The material that is outside the furnace or process at ambient temperature retains its original disordered or fully annealed state. This change to three structurally different zones contributes to the positive change phenomenon in non-stabilized Chromel.

Supporting Data—Aging Phenomenon

In order to provide supporting information illustrating the positive shift phenomenon common to non-stabilized type K thermocouples, the following data was collected:

A complete set of 18 non-stabilized type K thermocouples were removed from one gas turbine in October 1997 and calibrated by Thermo Electric at 538°C (1000°F). Thermo Electric maintains a NIST traceable calibration laboratory using reference standards calibrated by NIST. The calibration procedure was as follows: four to five samples were tied together with a base metal reference standard (directly traceable to NIST) in the center so that all junctions were together with no temperature gradient between them. Then the thermocouples and the standard were inserted into the middle of the uniform temperature zone of the furnace (approximately 12 in). The test measurements were taken after the thermocouples and the standard reached a steady-state thermal equilibrium (approximately 50 min).

The data shows that the average deviation of the thermocouples is a positive 4.1°C (7.4°F) which is outside the special tolerance limit of ±2.2°C (±4.0°F) for Type K at this temperature. This is also close to the typical 5°C (9°F) positive shift expected. One of the 18 thermocouples was damaged upon removal and was therefore excluded from the data (reference Table 1).

Table 1 Deviation of used non-stabilized thermocouples at 538°C (1000°F) calibrated by Thermo Electric

T/C No.	Deviation °C (°F)	T/C No.	Deviation °C (°F)
1	4.8 (8.7)	10	5.9 (10.7)
2	4.3 (7.8)	11	n/a (damaged)
3	2.6 (4.6)	12	5.1 (9.1)
4	3.0 (5.4)	13	1.2 (2.2)
5	5.1 (9.2)	14	5.3 (9.6)
6	2.6 (4.6)	15	4.4 (8.0)
7	3.1 (5.6)	16	4.6 (8.2)
8	4.9 (8.8)	17	5.0 (9.0)
9	4.0 (7.2)	18	4.3 (7.8)

Note: Values were recorded in °F; °C values were converted and rounded-off to the nearest 1/10 degree.

Table 2 Deviation of used non-stabilized thermocouples at 538°C (1000°C) calibrated by NIST versus Thermo Electric

T/C No.	NIST Deviation °C (°F)	TE Deviation °C (°F)
2	5.3 (9.6)	4.3 (7.8)
8	4.3 (7.8)	4.9 (8.8)
14	4.7 (8.4)	5.3 (9.6)

Note: Values were recorded in °F; °C values were converted and rounded-off to the nearest 1/10 degree. All calibration data was taken at an immersion depth of approximately 30.5 cm (12.0 inches).

Table 3 Deviation of a non-stabilized thermocouple at 538°C (1000°F) initially and after 16 h at temperature

Initial Dev. °C (°F)	Dev./16 Hrs °C (°F)	Δ°C (°F)
0.4 (0.8)	1.4 (2.6)	1.0 (1.8)

Note: Values were recorded in °F; °C values were converted and rounded-off to the nearest 1/10 degree.

Three of the remaining 17 non-stabilized thermocouples were selected at random and sent to NIST for calibration at the same temperature for a comparison and verification of Thermo Electric's results. NIST found the average positive shift of the three thermocouples to be 4.8°C (8.6°F). The results were within 1°C (1.8°F) for all three thermocouples tested confirming that the agreement between the two laboratories is good (reference Table 2). This is also within the ±1.14°C (±2.06°F) limit of uncertainty for Thermo Electric's calibration. It should be noted that the period of time for which these 18 non-stabilized thermocouples had been installed and operating in the turbine is unknown. Most likely it had been a number of years. Also, the original calibration data for these 18 thermocouples was not available. However, it is reasonable to assume that they were initially supplied within tolerance.

To confirm the aging phenomenon, a new (unused) non-stabilized type K thermocouple was calibrated at 538°C (1000°F) by Thermo Electric. Then it was exposed to 538°C (1000°F) in the laboratory furnace for a period of 16 h and re-calibrated at 538°C (1000°F). The results show that the thermocouple shifted positive by 1°C (1.8°F) after only 16 h at temperature (reference Table 3).

Installation and Performance of New Stabilized Thermocouples

The new stabilized thermocouples were installed at the Cogeneration facility located on the site of a refinery. The facility is capable of producing 385 MW (megawatts) of electricity and 1.2 million pounds per hour of steam from 4 gas turbines. The new stabilized thermocouples were installed on turbine unit #91 in April 1997, unit #92 in October 1997, unit #93 in March 1998, and unit #94 in January 1998. Each turbine requires 18 thermocouples.

A data ''snap-shot'' was taken of unit #91 immediately before and after the installation of the new stabilized thermocouples. No other modifications were made and other operating parameters such as inlet temperature, humidity, fuel composition, etc, remained fairly consistent. The results show that the spread of the 18 thermocouple readings dropped from 40°C (72°F) with the un-stabilized thermocouples to 32.8°C (59°F) for the new stabilized thermocouples. Spread values this low have not been recorded since the entire turbine unit was brand-new. In addition, the output increased from 81.94 MW to 83.50 MW, which repre-

Table 4 Deviation of stabilized thermocouples at 538°C (1000°F) initially and after 1 yr of service

T/C No.	Initial Dev. °C (°F)	Dev./1Yr °C (°F)	Δ°C (°F)
1	-1.2 (-2.1)	n/a	n/a
2	-1.2 (-2.2)	n/a	n/a
3	-1.2 (-2.2)	-1.1 (-1.9)	0.2 (0.3)
4	-1.1 (-2.0)	n/a	n/a
5	-1.3 (-2.4)	n/a	n/a
6	-1.3 (-2.3)	n/a	n/a
7	-0.8 (-1.5)	-1.4 (-2.5)	-0.6 (-1.0)
8	-0.7 (-1.3)	n/a	n/a
9	-1.9 (-3.5)	n/a	n/a
10	-1.2 (-2.2)	n/a	n/a
11	-1.8 (-3.3)	n/a	n/a
12	-1.3 (-2.4)	-1.7 (-3.0)	-0.3 (-0.6)
13	-1.2 (-2.1)	n/a	n/a
14	-1.8 (-3.3)	-1.7 (-3.1)	0.1 (0.2)
15	-1.9 (-3.5)	n/a	n/a
16	-1.6 (-2.9)	-1.7 (-3.1)	-0.1 (-0.2)
17	-1.1 (-2.0)	n/a	n/a
18	-1.2 (-2.2)	-1.7 (-3.1)	-0.5 (-0.9)

Note: Values were recorded in °F; °C values were converted and rounded-off to the nearest 1/10 degree. Only six of the 18 thermocouples were removed for calibration after one year of service.

Uncertainty of Calibration for Thermocouples at Thermo Electric

Test reproducibility for thermocouples in the 538°C (1000°F) to 1093°C (2000°F) temperature range = ± 0.56°C (± 1.0°F)

Uncertainty of calibration by NIST for base metal type K and N standards in the 0°C (32°F) to 1100°C (2012°F) temperature range = ± 1.0°C (± 1.8°F)

Uncertainty of calibration by Thermo Electric:

$$U_{TE} = \pm \sqrt{(U_{NIST})^2 + (R_{TE})^2}$$

U_{TE} = Uncertainty of calibration by Thermo Electric
U_{NIST} = Uncertainty of calibration by NIST
R_{TE} = Reproducibility of test by Thermo Electric

Uncertainty of calibration for type K thermocouples at 538°C (1000°F) by Thermo Electric:

$$U_{TE} = \pm \sqrt{(1.8°F)^2 + (1.0°F)^2} = \pm \sqrt{3.24 + 1.0} = \pm \sqrt{4.24}$$

$$U_{TE} = \pm 1.14°C\ (\pm 2.06°F)$$

sents an increase of 1.9 percent. The increase in output is due to the fact that the old non-stabilized thermocouples had aged during operation and shifted positive by approximately 5°C (9°F). This positive shift means that the thermocouples would be reading higher than the actual temperature, therefore causing the turbine to under fire. Of course these results will vary slightly over time given the changing operating conditions of the turbine, but it is clear that the stabilized thermocouples have a positive effect on the operation and efficiency.

All thermocouples supplied for each unit were calibrated in Thermo Electric's laboratory at 538°C (1000°F) prior to installation. Using the same calibration procedure as previously stated. All were within the special tolerance limits of ±2.2°C (±4.0°F) at 538°C (1000°F). The thermocouples installed on unit #91 were subjected to normal turbine operation for a period of one year. This was almost continuous operation equaling 8137 hours total including 10 start-ups. After one year of operation, the turbine was brought off-line and six of the original 18 thermocouples were removed for calibration by Thermo Electric. The six removed were taken randomly from locations spaced around the circumference of the exhaust. All six thermocouples were still within special tolerance limits at 538°C (1000°F). In addition, the amount of change for each individual thermocouple did not exceed 0.56°C (1.0°F) (reference Table 4).

Data was also taken on unit #92 comparing the new stabilized thermocouples to the non-stabilized thermocouples. Two sets of data were taken for the non-stabilized thermocouples over the week immediately following a water-wash of the turbine in the fall of 1996. The same data was collected immediately after a water-wash in the fall of 1997 after the new stabilized thermocouples were installed. Operating conditions were similar for this off-peak season for 1996 and 1997. It was found that for the week immediately following the water-wash in 1996 the average corrected MW output was 83.97 MW. In 1997 with the new stabilized thermocouples, the average corrected MW output had increased to 85.18 MW. This represents a 1.44 percent increase. The second set of data taken two months after the installation of the new stabilized thermocouples shows that the increased output from the new thermocouples was maintained and did not decrease. The corrected MW is a term used to indicate that the MW output has been normalized to be independent of inlet air temperature and DeNOx steam injection levels. This allows for a fair comparison of gas turbine performance from one time during the year with another time. The corrected MW calculation does not account for all inlet conditions but it is accurate enough for a fair comparison and is commonly used. No other modifications were made to unit #92 over the year that would enhance performance.

Unfortunately, similar performance comparisons cannot be made for units #93 and #94. During the turn-around for these units when the new stabilized thermocouples were installed, other modifications were made that affect turbine performance. Although overall efficiency and output have increased, it is impossible to isolate the portion contributed by the new thermocouples.

Summary

This paper was written to document the results of using stabilized Type K thermocouples in lieu of non-stabilized thermocouples in gas turbines for power generation. It was found that the stabilized thermocouples maintain their calibration tolerance over long periods of normal turbine operation whereas non-stabilized type K thermocouples drift in the positive direction out of tolerance. Increases in turbine output attributable to the stabilized thermocouples have been shown to be in the range of 0.5 percent to almost 2.0 percent.

We believe that a valid comparison can be made among thermocouples tested under identical controlled conditions such as this study. However, it would be difficult to make a quantitative prediction on how much the calibration of these thermocouples will change in actual environment. In this study, temperature, time, composition of the thermocouples and environmental condition common to all the independent variables which affect their calibrations. However, the thermocouples are subject to vibration, moisture, and contaminations in actual turbine engine operations. These factors, which all have adverse effects on the calibration of thermocouples are not encountered in the laboratory testing. The combined effects of these factors on the calibration of the thermocouples, together with those of temperature, time, etc., should be measured in-situ [5].

Future plans for this particular project include periodic monitoring of the stabilized thermocouples in use to determine how long they will remain within tolerance. At this time the proposal is to remove three thermocouples at random from each turbine on an annual basis for re-calibration. This data should give good insight into the expected life of the stabilized thermocouples and how long they remain within tolerance. In addition, a complete metallurgical examination of the turbine components determined that there were no indications of over firing.

Acknowledgments

The authors wish to thank the management of Watson Cogeneration Company and Thermo Electric Company for their encouragement and support of the research and preparation required to write this paper. In addition, we would like to thank all of those individuals who contributed to the testing and data presented.

Nomenclature

ASTM = American Society for Testing and Materials
°C = degrees Celsius
Cr = chromium
emf = electromotive force
°F = degrees Fahrenheit
f.c.c. = face-centered cubic
MgO = magnesium oxide
MI = mineral insulated
MW = megawatt
n/a = not available
Ni = nickel
NIST = National Institute of Standards and Technology
T/C = thermocouple
TE = Thermo Electric Company Inc.
Type E = Chromel-Constantan Thermocouple
Type K = Chromel-Alumel Thermocouple

References

[1] Silbey, F. S., Spooner, N. F., and Hall, B. F., 1968, ‘‘Aging In Type K Couples,’’ Instrum. Technol., **15**, p. 107.

[2] Wang, T. P., and Wells, A., 1989, ‘‘Thermocouple System Technology and Applications for Gas Turbines,’’ *Proceedings, ASME International Gas Turbine Institute Second International Symposium on Turbin Machinery and Generation*, **3**, p. 305.

[3] Wang, T. P., Bediones, D. P., and Allen, M. G., 1995, ‘‘Recent Advances in Temperature Sensors,’’ *Proceedings*, ISA/95, pp. 811–820.

[4] *Temperature Measurement*, 1997, ASTM Standard Vol. 14.03, E230-96.

[5] Wang, T. P., Wells, A., and Bediones, D., 1989, ‘‘Stability Testing of Type K, N, J, and E Thermocouples at 538°C,’’ ASME IGTI-Vol. 4, ASME Cogen-Turbo.

A. F. Massardo
Mem. ASME
e-mail: massardo@unige.it

M. Scialò
Dipartimento di Macchine,
Sistemi Energetici e Trasporti,
Universita' di Genova,
Italia

Thermoeconomic Analysis of Gas Turbine Based Cycles

The thermoeconomic analysis of gas turbine based cycles is presented and discussed in this paper. The thermoeconomic analysis has been performed using the ThermoEconomic Modular Program (TEMP V.5.0) developed by Agazzani and Massardo (1997). The modular structure of the code allows the thermoeconomic analysis for different scenarios (turbine inlet temperature, pressure ratio, fuel cost, installation costs, operating hours per year, etc.) of a large number of advanced gas turbine cycles to be obtained in a fast and reliable way. The simple cycle configuration results have been used to assess the cost functions and coefficient values. The results obtained for advanced gas turbine based cycles (inter-cooled, re-heated, regenerated and their combinations) are presented using new and useful representations: cost versus efficiency, cost versus specific work, and cost versus pressure ratio. The results, including productive diagram configurations, are discussed in detail and compared to one another. [S0742-4795(00)01903-7]

Introduction

In the thermodynamic analysis of energy systems, the study is generally focused on describing processes evolving into the system and deriving relationships between flow rates, energy exchange, sizing design, etc. The various alternatives are usually compared on the basis of purely thermodynamic measures as efficiency, irreversibility or specific work. Gas turbine simple and complex cycles have been analyzed in detail, from the thermodynamic point of view, in a number of publications [1–3]. The results are usually shown on the classic efficiency versus specific work diagram taking into account TIT (Turbine Inlet Temperature) and pressure ratio influence. Only sometimes has the economic analysis been carried-out in a very simplified way, after the thermodynamic investigation.

The rapid development of new cycles based on gas turbine technology in the last years evinces the importance of a complete coupling between the thermodynamic and the economic analysis. This complete analysis shows the influence of the most important cycle parameters and the economic boundary conditions during the design phase of advanced systems.

A thermoeconomic approach maybe used to solve this problem; in fact, thermoeconomics is a technique, which combines thermodynamic analysis directly with economic aspects in order to optimize thermal systems like a gas turbine based cycles. There are essentially two thermoeconomic techniques proposed in literature and analyzed in detail by the authors in previous works [4–6]. The approach here used is similar to Thermoeconomic Functional Analysis (TFA) [7], but employs an original, direct approach to carry out the Direct Thermoeconomic Analysis (DTA) and Optimization (DTO).

Simple steam plants [8] and simple regenerative gas turbine cycle [8] have been studied using the TFA approach, while simple and complex steam plants, simple gas turbine, and combined cycles have been investigated using the DTA/DTO approach [5]. In this work the thermoeconomic analysis has been carried out using an apt tool developed by the Authors (TEMP code): the modular organization of the code makes the DTA of several advanced gas turbine cycles obtainable in a fast and reliable way. Thanks to the use of apt cost functions for the different components that compose the gas turbine based cycles (compressor, expander, combustion chamber, regenerator, inter-cooler, etc.) the analysis is particularly well suited for cost versus efficiency and cost versus specific work evaluation of advanced gas turbine cycles. The different cycle configurations are presented and discussed in detail and compared to one other.

Direct Thermoeconomic Analysis (DTA)

The thermoeconomic approach here utilized is similar to classical TFA but employs an original direct approach to carry out the thermoeconomic analysis (and Optimization—DTO). In DTA, the analyzed plant is subdivided into a set of units, each one including one or more physical components, connected by material flows. The schematization of the plant in single units interconnected by material and mechanical work streams is the ‘‘physical structure of the system,’’ and a new study of the system has been introduced, called ‘‘Functional Productive Analysis.’’ The graphical representation is called ‘‘Functional Productive Diagram,’’ while the productive purpose of each component is defined by introducing functional exergy flows in addition to the physical exergy flows. The complete mathematical formulation of this Functional Productive Analysis has been presented by Agazzani and Massardo [5]. By means of the ‘‘Functional Productive Analysis’’ in which each component has several inputs and one output (product) the ‘‘functional exergy flows’’ among the components to be calculated. In addition, marginal and average unit costs of each functional exergy flow are determined, and therefore the global thermoeconomic performances of the components (internal economy) are defined.

The thermoeconomic analysis of thermal energy systems has been performed using a modular simulator tool called TEMP, described in detail by Agazzani [4]. The tool has been aimed at the following targets: thermodynamic and exergy analysis, thermoeconomic and environomic analysis optimization. The modularity of the code facilitates the study of several cycle configurations. The code has been expanded by means of the introduction of new modules [9,10] and now the 5.0 version is composed of 53 modules. There are three routines for each module included in the code library: the first is used for the thermodynamic analysis; the second for the exergy analysis; and the third for the thermoeconomic analysis. The plant data chart contains all the physical components; how they are physically interconnected among themselves; their fixed thermodynamic values, and, in some cases includes economic data values (i.e., unit fuel price or unit elec-

---

Contributed by the International Gas Turbine Institute (IGTI) of THE AMERICAN SOCIETY OF MECHANICAL ENGINEERS for publication in the ASME JOURNAL OF ENGINEERING FOR GAS TURBINES AND POWER. Paper presented at the International Gas Turbine and Aeroengine Congress and Exhibition, Indianapolis, IN, June 7–10, 1999; ASME Paper 99-GT-312. Manuscript received by IGTI March 9, 1999; final revision received by the ASME Headquarters May 15, 2000. Associate Technical Editor: D. Wisler.

tricity price); fictitious units; environment unit; functional productive diagram; data of some heat exchangers (geometry and metallurgy); etc.

Cost Evaluation

The thermoeconomic technique used here must have reliable and updated cost functions of plant components. Determining these functions is rather complicated since it is difficult to consider every factor that contributes to estimate the final purchase cost of a component to its full extent. They must be related to thermodynamic parameters of the plant and factors covering every type of item. Furthermore, it must be possible to update them by taking into account the progress of both performance improvement and market prices.

In particular for DTA there is a need to evaluate the capital cost for each unit (Purchased Equipment Cost—PEC) as a function of its product and the sizing variables. The following equation has been used to evaluate the capital cost rate of a unit ''r'':

$$Z_r = \frac{\Xi_r \cdot \mathrm{FCR} \cdot \Phi_r}{3.6 \cdot 10^5 \cdot N}, \tag{1}$$

where Φ_r is the maintenance factor; FCR the annual fixed charge rate percent; N the number of operating hours per year, and Ξ is the Purchased Equipment Cost (PEC). The following standard values have been considered: FCR=18.2 percent; $\Phi_r = 1.06$; $N = 8000[h/y]$. These values can be easily modified to take into account different financial scenarios. The purchase costs can be estimated by two types of equations: (i) cost equations: written in terms of geometrical and manufacturing variables: and (ii) costing equations: written in terms of performance and stream variables [4,5]. Every price estimated by the two methods has been escalated to updated prices by means of an escalation index. One such index is the Chemical Engineering Plant Cost Index [11]. The original cost functions for the compressor, combustor, and turbine equations as follows:

$$\text{compressor:} \quad \Xi = \mathbf{c}_1 \cdot \frac{39.5 \cdot \dot{\mathbf{m}}_a}{0.9 - \eta_{is}} \cdot \beta_c \cdot \ln \beta_c \tag{2}$$

$$\text{combustor:} \quad \Xi = \mathbf{c}_1 \cdot \frac{25.6 \cdot \dot{\mathbf{m}}_a}{0.995 - \Delta \mathbf{p}_{\text{percent}}} \cdot [1 + \exp(0.018 \cdot \mathbf{T}_{\max} - 26.4 \cdot \mathbf{c}_2)] \tag{3}$$

$$\text{turbine:} \quad \Xi = \mathbf{c}_1 \cdot \frac{266.3 \cdot \dot{\mathbf{m}}_g}{0.92 - \eta_{is}} \cdot \ln \beta_t \cdot [1 + \exp(0.036 \cdot \mathbf{T}_{\max} - 54.4 \cdot \mathbf{c}_2)] \tag{4}$$

proposed by El-Sayed and Tribus [12] and modified by Frangopoulos [8], have been updated by the Authors as shown by Agazzani and Massardo [5] to take into account the influence of the allowable maximum temperature for the combustor and the expander. The values of the coefficients c_1 and c_2 have been calculated by using, as reference, the gas turbine costs reported by 1995 Gas Turbine World Handbook, and verified using the last available edition [13] of the Handbook as shown by Scialò [10]. The data presented are applicable for industrial and aeroderivative gas turbines in the range of the GTW handbook data (~1 MW–250 MW). The subdivision of a gas turbine into three components is very useful when considering the present thermoeconomic study of advanced complex gas plants, in which the components can be arranged differently than in the simple cycle gas turbine (two ore more compressors, two or more combustion chambers and expanders, etc.).

Estimating the cost of purchased equipment is obviously the first step in any detailed power system cost estimation. However, in the thermoeconomic analysis, one should consider the capital cost necessary to purchase the land, build all the necessary facilities, and install the required machinery and equipment. The sum of these costs and PEC is called Fixed Capital Investment (FCI), and it represents the total system cost assuming a so-called overnight construction [14]. Indeed the Total Capital Investment (TCI) is considered the sum of fixed capital investment and other outlays. A factor method is used for the estimation of FCI, and the cost components of FCI is evaluated in term of a percentage of the PEC as follows: Purchased Equipment Installation=45 percent; Piping=30 percent; Instrumentation and Control=20 percent; Electrical Equipment and Materials=10 percent; Land=5 percent; Civil, Structural and Architectural Work=20 percent; Service Facilities=65 percent; Engineering and Supervision=30 percent; Construction=15 percent of the previous costs; Contingencies =15 percent. The following terms have been considered for other outlays: start-up costs-10 percent FCI; working capital 15 percent TCI; licensing R&D=7 percent FCI; allowance for funds used during construction=8 percent FCI. The results shown in this paper have been obtained using both of the previous approaches: (i) PEC approach: only Purchased Equipment Cost is used as usually presented in literature for Thermoeconomic analysis; and (ii) TCI approach—the thermoeconomic analysis has been carried out using the Total Capital Investment parameter. Obviously, the percentages can be easily modified if necessary.

Simple Cycle Results

The first plant analyzed is a simple gas turbine cycle and the fixed quantities used in the calculation are: ambient conditions: 15°C, 101300 Pa; relative humidity 60 percent; compressor, expander, and combustion chamber efficiencies: 0.86, 0.88, and 0.996; electrical efficiency: 0.985; mechanical efficiency: 0.98; combustor pressure loss: 3 percent; fuel composition: 93 percent CH_4 and 7 percent N_2; power: 60 MWe. The complete set of thermodynamic and thermoeconomic results is reported by Scialò [10]; only the most important results are shown here.

Figure 1 shows the classical efficiency versus specific work diagram for two different TIT values (1200 and 1400°C). In the figure, point A represents the maximum efficiency condition, and point B the maximum specific work condition. The minimum cost conditions are represented by points C′ and C; the first for PEC analysis (only equipment costs are considered) and the second for TCI approach.

The thermoeconomic analysis has been carried out for three different fuel cost values to evaluate the impact of this parameter on the system economy. It is possible to note that point B is very close to points C′ taking into account the fuel cost value, while the effect of TIT is not very evident on the cost point position. When TCI approach is used the minimum cost points move to the

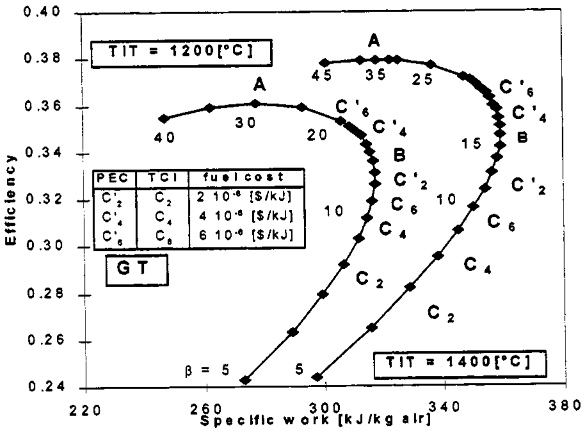

Fig. 1 Efficiency versus specific work a simple cycle gas turbine

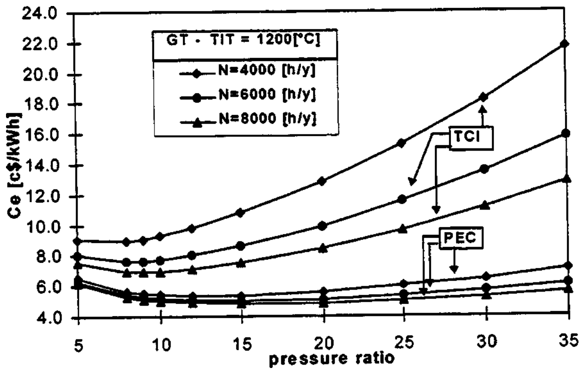

Fig. 2 Simple cycle gas turbine: operating hours per year influence

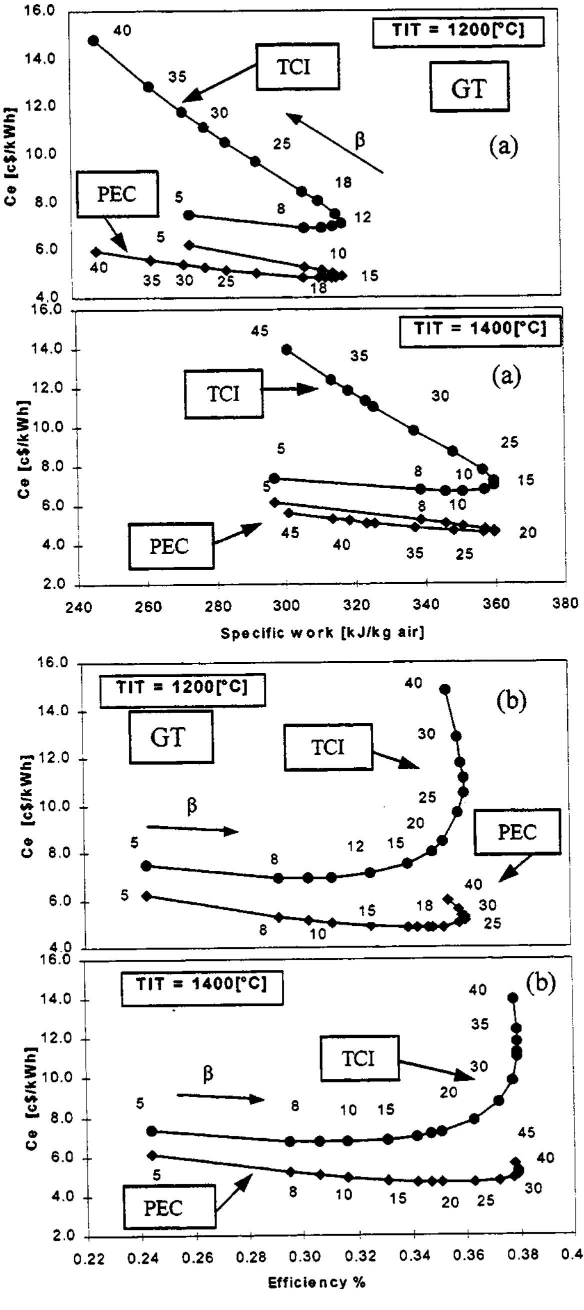

Fig. 3 Simple cycle gas turbine: cost versus specific work (*a*) and cost versus efficiency (*b*)

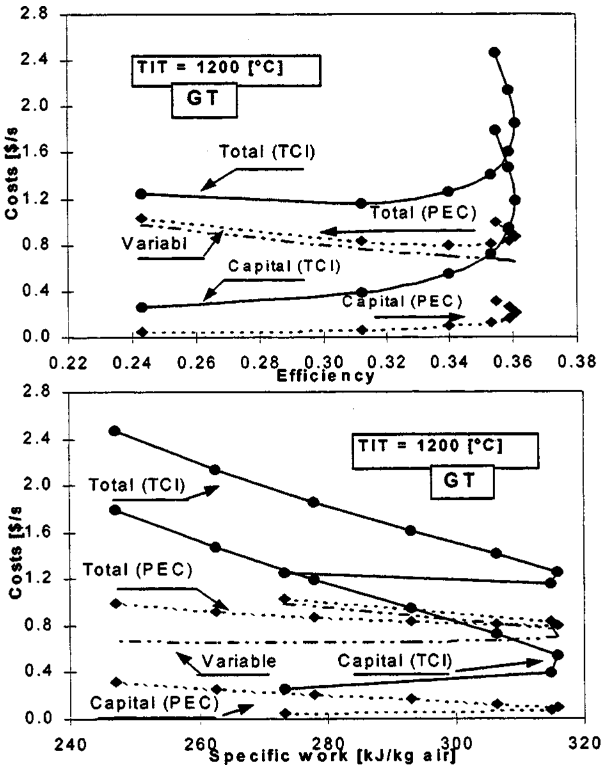

Fig. 4 Simple cycle gas turbine: total and variable cost versus efficiency and specific work

zone where pressure ratio values are low. In this case the influence of the fuel cost is less important since the influence of capital costs has increased.

The effect of an increase of fuel cost is quite evident: the minimum cost position increases the pressure ratio and the efficiency to compensate the energy cost; the opposite when fuel cost is reduced. The proximity of point B to points C′ is compatible with the pressure ratio values published in literature for 60 MW heavy duty gas turbines, where the minimization of the cost is one of the most important goals.

Figure 2 shows the influence of the operating hours per year on the thermoeconomic performance of the plant versus cycle pressure ratio. The difference between PEC and TCI analysis is evident, not only in the level of the costs, but also in the different pressure ratio values that minimize the costs. When PEC is used, the pressure ratio is about 15, and when TIC approach is used, the value is between 8 and 10.

Figure 3 shows a new representation of the thermodynamic and thermoeconomic performance of gas turbine plants. The results are presented using the cost versus efficiency and cost versus specific work diagrams. In this case, both of the results obtained with the PEC and TCI approaches are shown. When the cost versus specific work curves are analyzed (Fig. 3(*a*)), the influence of the compressor pressure ratio is evident and the minimum cost is practically coincident with the maximum specific work condition; the influence of TIT and the type of analysis (PEC or TCI) is evident too. The use of the TCI approach is noteworthy, since an inversion of the curves is present when this approach is used rather than the simplified one (PEC). This inversion is due to the simultaneous influence of installation and fuel costs at low pressure ratio and low efficiency values. Figure 3(*b*) (cost versus efficiency) shows a rapid increase of the cost when the pressure ratio increases without a correspondent increase of efficiency, particularly for TCI analysis. In this case the TIT influence is more evident, particularly in the different shape of the curves. Figure 4 shows the same diagram as in Fig. 3, where both capital and variable costs are reported together with the total cost (for both PEC and TCI analysis). The shape of the total cost is strictly correlated to the capital cost behavior, while the predominant influence of efficiency on variable costs is quite evident.

Advanced Gas Turbine Cycles

In this part, the thermoeconomic analysis of advanced gas turbine based cycles is presented. Figure 5(*a*) shows as an example the layout of a complex plant including three compressors, two inter-coolers, two combustion chambers and two expanders (inter-cooled, regenerated and re-heated cycles ICRRh). Figure 5(*b*) shows the functional productive diagram of the plant. This diagram is an automatic output of the code TEMP, and is analyzed in detail by Scialò [10].

Before presenting the thermoeconomic results for such a complex plant, the analysis has been carried out for simplified cycles such as inter-cooled, regenerated, re-heated, inter-cooled and regenerated, re-heated and regenerated, inter-cooled and re-heated, etc.

Regenerated Cycle. Using the lay-out of Fig. 5 without inter-cooler and second combustion chamber, the cycle coincides with a regenerative one, where the hot gases leaving the expander are used in a regenerator to heat the air at the compressor outlet. This way the efficiency of the system increases, given that a reduced fuel mass flow rate is necessary for the same power output always (60 MWe). The regenerator has been analyzed from the thermoeconomic point of view using the equations suggested by Frangopoulos [8]. The analysis has been performed with a fixed temperature approach value of 30°C, and the effectiveness has been obtained as a result of the calculation [10].

Figure 6 shows the cost versus efficiency and versus specific work diagrams for the regenerated cycle for two TIT values (1200 and 1400°C). It is interesting to note that the minimum cost does not coincide with the maximum specific work condition; in fact, for low-pressure ratio values (4–8) the efficiency is high and the capital cost values decrease. On the other hand, for large specific work values (high-pressure ratio) the influence of capital cost is evident and predominant. When TIT influence is taken into account, it is possible to observe that for TIT = 1400°C, the capital cost influence decreases for low pressure ratio values if compared to TIT = 1200°C results [10]. The cost versus efficiency diagram shows that the pressure ratio influence on the capital cost behavior is predominant. Since the regenerator approach temperature has been considered fixed the calculated regenerator effectiveness is shown in the cited Fig. 6. In the zone of minimum cost, this parameter is about 0.80, and it decreases when the pressure ratio increases together with the capital costs. The use of high regenerator effectiveness value suggested at low-pressure ratio values by the classical thermodynamic analysis is confirmed.

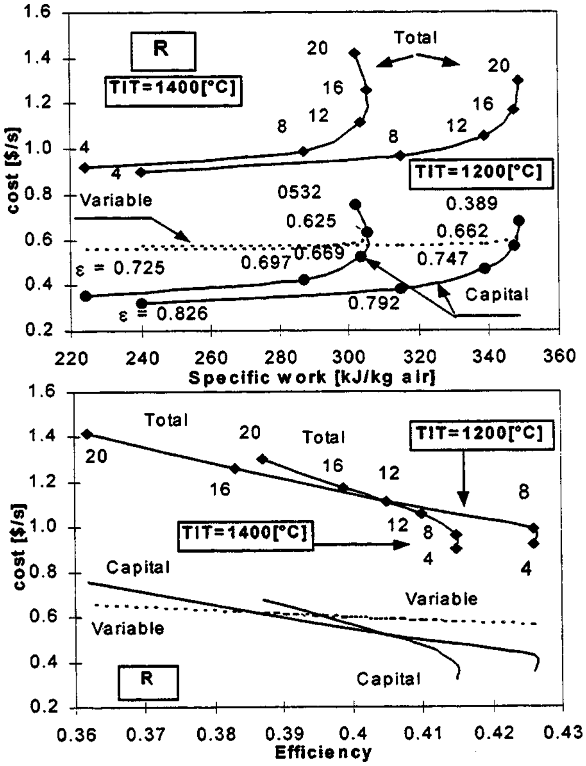

Fig. 6 Regenerated cycle: cost versus specific work and versus efficiency

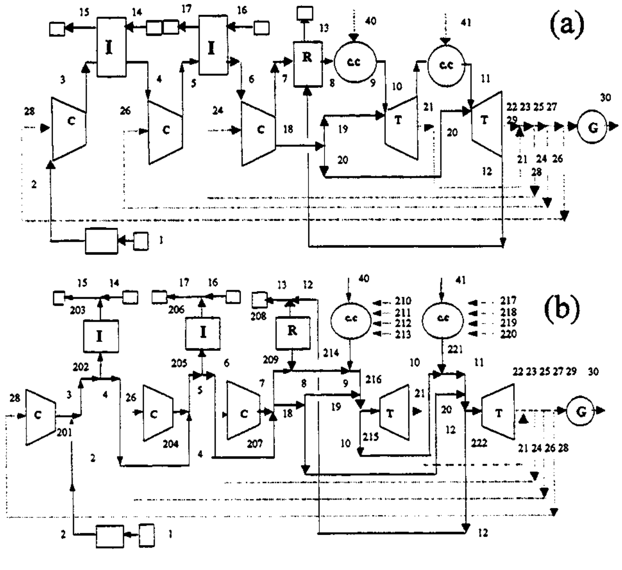

Fig. 5 Inter-cooled, regenerated and re-heated cycle: (*a*) simplified layout; (*b*) functional productive diagram

Inter-Cooled Cycle. In this case the cycle is obtained from the layout of Fig. 5 using only an inter-cooler and two compressors.

The compressor pressure ratio (β_{tot}) is divided in two parts: Low-Pressure Compressor (LPC) and High Pressure Compressor (HPC). First of all, a thermoeconomic analysis to evaluate the influence of pressure ratio distributions has been carried out and Fig. 7 shows the results obtained for three different overall pressure ratios ($\beta_{\mathrm{Tot}}=15$; 30; 65).

For each β_{tot} curve the influence of different β_{LPC} values has been investigated; the classical thermodynamic minimum compression work condition coincident with $\beta_{\mathrm{LPC}}=\beta_{\mathrm{HPC}}=\mathrm{sqrt}\,(\beta_{\mathrm{tot}})$ is also reported in the figure (point B). It is clear that the minimum cost conditions (point C) are considerably dependent on the value of β_{tot} and β_{LPC}. In particular minimum cost condition is always present between maximum work condition and maximum efficiency condition (point A). The cost is influenced by β_{tot} and for its minimum value (15) the costs are lower than for high-pressure ratio values; this aspect is mainly correlated with the compressor capital cost equations, where the influence of pressure ratio is noticeable. Figure 8 shows cost versus specific work and versus efficiency for two different TIT (1200 and 1400°C). The influence of TIT is noteworthy for specific work diagram (Fig. 8(*a*)), while the effect of TCI or PEC approaches is also evident particularly for the cost values and also for the cost curves behavior versus pressure ratio. In this case, minimum cost conditions are near the zone of maximum specific work and maximum efficiency for PEC analysis, while some differences exist when the TCI approach is used.

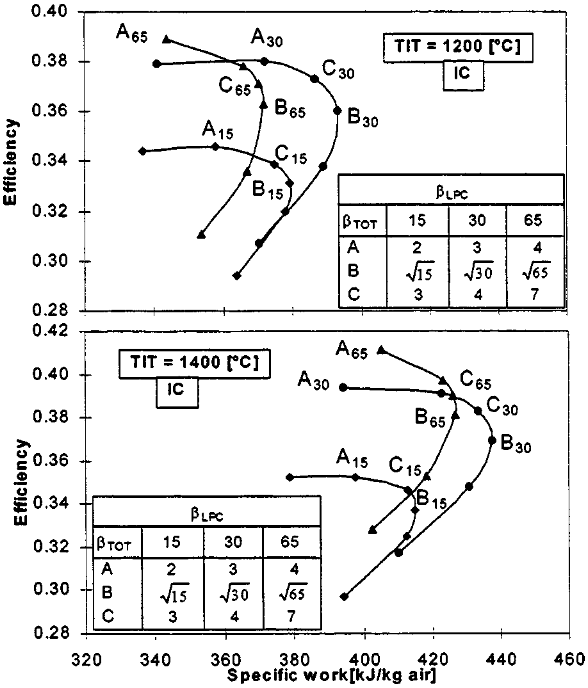

	β_{LPC}		
β_{TOT}	15	30	65
A	2	3	4
B	$\sqrt{15}$	$\sqrt{30}$	$\sqrt{65}$
C	3	4	7

	β_{LPC}		
β_{TOT}	15	30	65
A	2	3	4
B	$\sqrt{15}$	$\sqrt{30}$	$\sqrt{65}$
C	3	4	7

Fig. 7 Inter-cooled cycle: efficiency versus specific work

Re-Heated Cycle. In this case, two combustion chambers and two expanders are used, and the cycle pressure ratio (expansion ratio) is divided in two parts again (HPT and LPT). First of all, the thermoeconomic analysis has been carried out to evaluate the influence of this distribution on the thermodynamic and thermoeconomic performance of the plant.

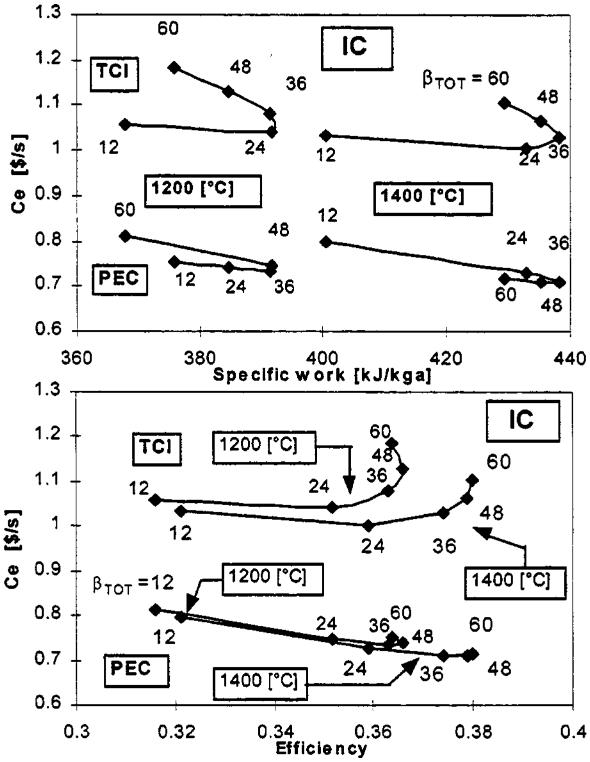

Fig. 8 Inter-cooled cycle: cost versus specific work and versus efficiency

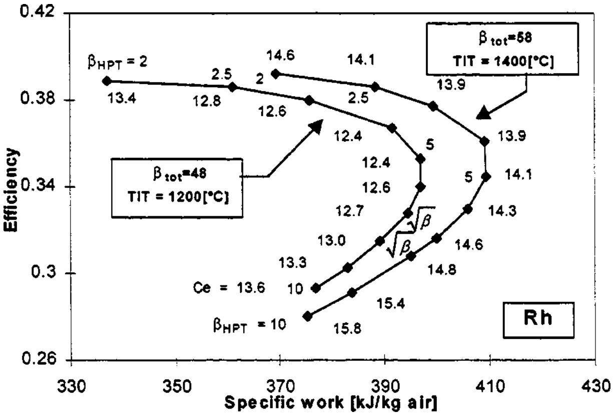

Fig. 9 Re-heated cycle: efficiency versus specific work

Figure 9 shows the efficiency versus specific work diagram for two different total pressure ratios (48 and 58) obtained in the case of maximum efficiency when the expansion ratio is the same for high and low pressure expander ($\beta_{HPT}=\beta_{LPT}$), for two TIT values (1200 and 1400°C). In the diagram the costs indicated are correspondent to the high-pressure turbine expansion ratio conditions shown. It is interesting to observe the great influence of the expansion ratio distribution on the system costs. Cost distributions versus specific work and versus efficiency are presented in Fig. 10 for both TCI and PEC approaches; the TIT influence is also included in the analysis. When TCI analysis has been used, minimum cost condition is in the zone of low total pressure ratios, while for PEC analysis this condition is close to the maximum efficiency zone (high pressure ratio value). In this case, the maximum specific work condition does not coincide with minimum cost zone either, and the effect of pressure ratio on the cost is similar for both of the applied approaches.

Figure 11 shows the plots of nondimensional total cost versus pressure ratio of the previously investigated systems. Two different β_{HPT} solutions are included for the re-heated cycle. It is important to note that for intercooled cycle the costs are weakly influenced by total pressure ratio value; while the minimum cost is obtained for the regenerated cycle when the pressure ratio is particularly low (<6). The β_{HPT} choice is not particularly important for the re-heated solution in the zone of high overall pressure ratio values; while for low values the solution $\beta_{HPT}=2$ is preferable from the cost point of view. The influence of TIT is evident also, particularly for re-heated cycle. In fact, two expanders are used in this case and the cooling mass flow rate increases.

Regenerated and Re-Heated (RRh) Cycle. The thermoeconomic results for this case are shown in Fig. 12. The influence of TIT is noticeable in this case also, and the effect of the increase of cooling mass flow rate with TIT must be carefully considered, since two expanders must be cooled in this case too. The minimum cost condition for this cycle is practically coincident with the maximum efficiency condition and the pressure ratio is about 10(TIT=1200°C). The behavior of the cost versus specific work curves is different. In fact, the specific work remains practically constant when pressure ratio is over 20 and the correspondent cost grows rapidly.

Inter-Cooled and Regenerated (ICR) Cycle. The thermoeconomic results are shown in Fig. 13; in this case the TIT effect is noteworthy, minimum cost condition coincides with maximum efficiency point for TIT=1200°C, while for TIT=1400°C the pressure ratio at minimum cost is lower (9) than its value at maximum efficiency point (14). From the specific work point of view, minimum cost conditions for both TIT values do not coincide with maximum specific work; this condition has been obtained at very high-pressure ratio values.

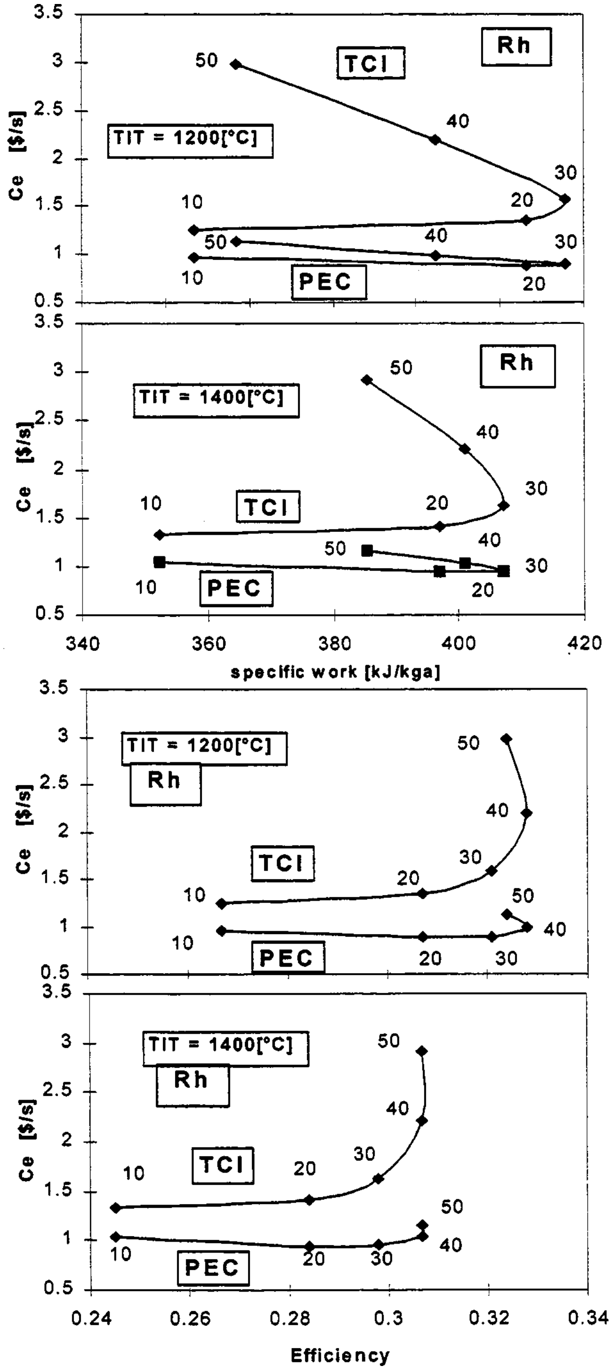

Fig. 10 Re-heated cycle: cost versus efficiency and versus specific work

Inter-Cooled, Regenerated, Re-Heated (ICRRh) Cycle. In this case the number of variables that influences the thermoeconomic analysis is large and also a large number of data, constraints, etc. are used and reported by Scialò [10]. Figure 14 presents efficiency versus specific work diagram at TIT=1400°C and for different β_{tot} and β_{HPT}, while the $\beta_{\mathrm{LPC}}=\beta_{\mathrm{HPC}}$ condition has been used. The maximum efficiency, minimum cost, maximum specific work and sqrt(β_{TOT}) curves are also shown in the figure.

It is interesting to note that increasing the total pressure ratio, the minimum cost curve is close to the maximum efficiency condition, and in this case the β_{HPT} value is very low if compared with β_{TOT}.

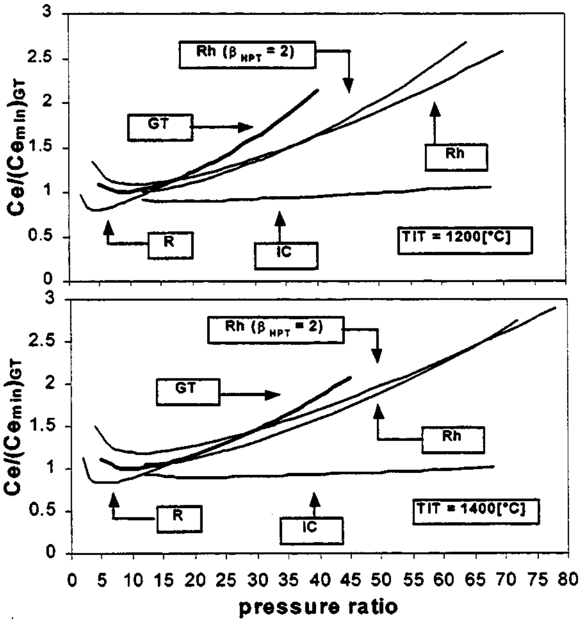

Fig. 11 Cost versus pressure ratio for advanced gas turbine based cycles (TCI approach)

The comparison between nondimensional thermoeconomic performances of the cycles investigated is presented in Fig. 15: cost versus efficiency and cost versus specific work.

All the nondimensional results have been obtained for TIT=1400°C, $N=8000$ hours per year and TCI approach. The best cost performance can be obtained with an inter-cooled regen-

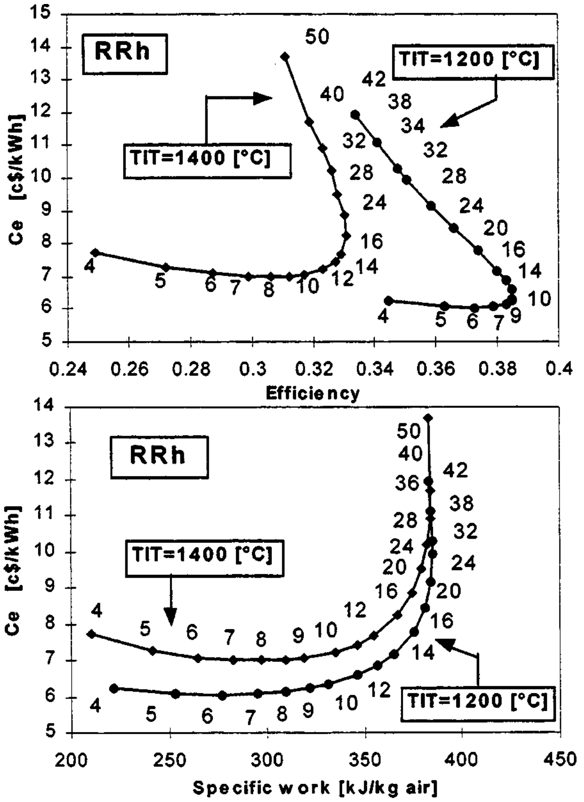

Fig. 12 Regenerated and re-heated cycle: cost versus efficiency and versus specific work (TCI approach)

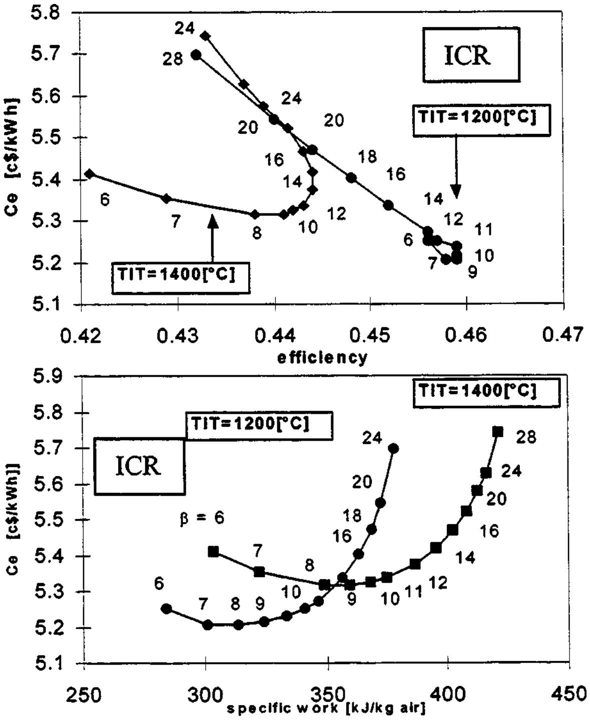

Fig. 13 Inter-cooled and regenerated cycle: cost versus efficiency and versus specific work (TCI approach)

erated cycle, and in this case minimum cost coincides with maximum efficiency zone. Also using regenerated, inter-cooled, regenerated/inter-cooled/re-heated cycles it is possible to obtain good results. In these cases minimum cost conditions do not coincide with maximum efficiency values. A good result from the cost and specific work point of view is shown by the inter-cooled, regenerated and re-heated cycle (in this case the curve is very flat since the pressure ratio influence is weak). It is important to note that re-heated cycles without inter-cooling are not good solutions from the thermoeconomic point of view and that taking into account practicality, reliability, maintenance and the modest differences shown in Fig. 15 the intercooled cycle should be the more attractive, free from the complexity of regeneration and reheat.

It is possible to conclude that, thanks to the thermoeconomic analysis here presented the improvement of thermodynamic performance (efficiency, specific work) from a simple to a complex cycle can be easily associated to an evident improvement of the generated electricity cost.

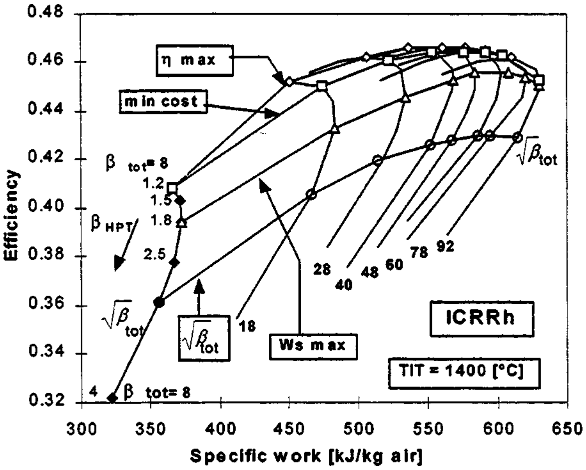

Fig. 14 Re-heated, regenerated and intercooled cycle: efficiency versus specific work (TCI approach)

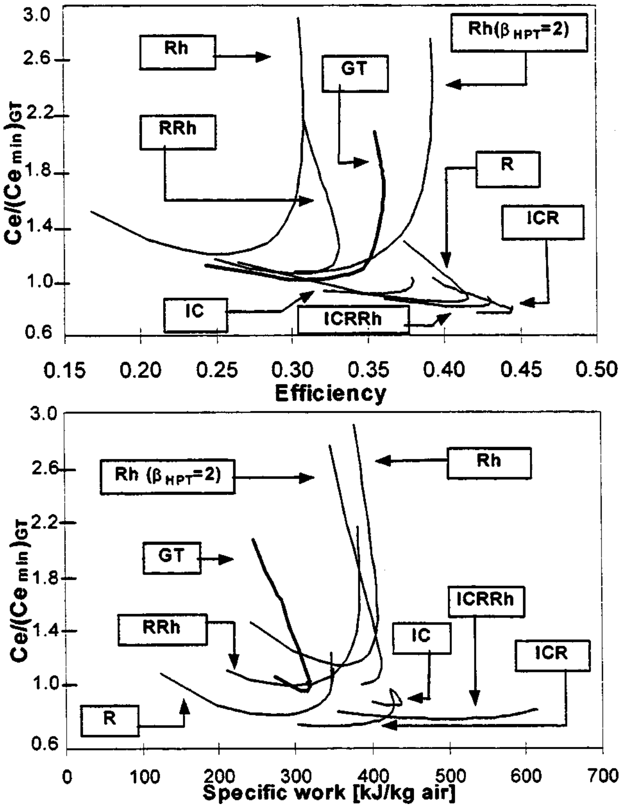

Fig. 15 Cost versus efficiency (*a*) and cost versus specific work (*b*) for advanced gas turbine based cycles (TCI approach)

Conclusions

A computational modular approach for the thermoeconomic simulation of gas turbine based cycles has been presented. Thanks to the use of a robust, efficient and reliable tool (TEMP), the parametric thermoeconomic analysis of a large number of plants has been carried out and the results presented and discussed. The following main conclusions can be stated:

1 For the first time in the thermoeconomic field not only has the purchased equipment costs (PEC) evaluation been considered, but the influence of total capital investment (TCI) has been taken into account also.

2 The thermoeconomic analysis using PEC is more dependent on the fuel cost; the opposite is true for TCI analysis, where the capital costs are more important.

3 The thermoeconomic results have been presented in a new and useful way: cost versus efficiency, cost versus specific work, and cost versus pressure ratio. This original representation enables us to obtain and use a direct evaluation of the best thermoeconomic conditions of the plant.

4 The obtained results for simple cycle gas turbine plants confirm the maximum specific work condition in the range of minimum cost when PEC approach is used, taking also into account the variation of fuel cost. By using the TCI technique, the minimum cost condition moves to very low-pressure ratio value and low efficiency zone.

5 The subdivision of the gas turbine costs into three components has been essential for the thermoeconomic analysis of advanced gas turbine based cycles (inter-cooled; regenerated; re-

heated); the upgrading of the cost equation coefficients has also been carried out to take into account the technological improvement of the components.

6 For advanced cycles, the results of the thermoeconomic analysis have been presented and carefully discussed; in particular, the TIT and pressure ratio (total, low-pressure, high-pressure) influences have been taken into consideration.

7 The new cost representations (versus efficiency, versus specific work, and versus pressure ratio) have been presented and they have shown their importance in defining the best thermoeconomic design of the plant.

8 The technique presented here can be used to analyze combined plants, mixed cycles (STIG, ISTIG, etc.) as reported by Scialò [10], and advanced GT and fuel cell combined plants.

9 Economic results here presented must be considered not as an absolute solution but mainly for the thermoeconomic comparison of different gas turbine based cycles.

Acknowledgments

The authors would like to thank the University of Genoa, the MURST (CoFin 99) for the financial support granted to this research, and Dr. A. Agazzani for his valuable collaboration.

Nomenclature

C_e = electricity cost
FCR = annual fixed charge rate [percent]
GT = simple cycle gas turbine
IC = intercooled gas turbine
N = number of operating hours per year
PEC = purchased equipment cost [\$]
R = regenerated gas turbine
Rh = re-heated gas turbine
TCI = total capital investment [\$]
TIT = turbine inlet temperature [K]
Φ_r = maintenance factor
ε = regenerator effectiveness
β = pressure ratio
η_{is} = isentropic efficiency
Δp percent = pressure loss [percent]
$\dot{\mathbf{m}}$ = mass flow rate [kg/s]

Subscripts

a, g = air, gas
c, t = compressor, turbine
LPC, HPC = low, high pressure compressor
LPT, HPT = low, high pressure turbine
Tot = total

References

[1] Pilidis, P., and Mathieu, P., 1991, ''The Use of Gaseous Fuels on Aeroderivative Gas Turbines,'' ASME Paper 91-GT-44.
[2] Wilson, D. G., and Korakianitis, T., 1997, ''The Design of High Efficiency Turbomachinery and Gas Turbines,'' Prentice-Hall, Inc., Englewood Cliffs, NJ.
[3] Cohen, H., Rogers, G. F., and Saravanamuttoo, H. I. H., 1996, *Gas Turbine Theory*, Longman, UK.
[4] Agazzani, A., 1995, ''Ottimizzazione termodinamica, economica e di impatto ambientale dei sistemi energetici,'' Ph.D. thesis, University of Pisa.
[5] Agazzani, A., and Massardo, A., 1997, ''A Tool for Thermoeconomic Analysis and Optimization of Gas, Steam and Combined Plants,'' ASME J. Eng. Gas Turbines Power, **119**, pp. 885–892.
[6] Agazzani, A., Frangopoulos, C., and Massardo, A., 1998, ''Environmental Influence on the Thermoeconomic Optimization of a Combined Plant with No_x Abatement,'' ASME J. Eng. Gas Turbines Power, **120**, pp. 557–565.
[7] Frangopoulos, C. A., 1983, ''Thermoeconomic Functional Analysis: a Method for Optimal Design or Improvement of Complex Thermal System,'' Ph.D. thesis, Georgia Institute of Technology, Atlanta, GA.
[8] Frangopoulos, C. A., 1994, ''Application of Thermoeconomic Functional Approach to the CGAM problem,'' Energy, **19**, No. 3, pp. 323–342.
[9] Massardo, A., and Lubelli, F., 1998, ''Internal Reforming Solid Oxide Fuel Cell—Gas Turbine Combined Cycles (IRSOFC-GT): Part A—Cell Model and Cycle Thermodynamic Analysis,'' ASME Paper 98-GT-577.
[10] Scialò, M., 1998, ''Thermoeconomic Analysis of Power Plants Based on Gas Turbine Technology,'' (in Italian), Master thesis, University of Genoa, Italy.
[11] *Chemical Engineering*, 1998, McGraw-Hill, New York.
[12] El-Sayed, Y. M., and Tribus, M., 1983, ''Strategic Use of Thermoeconomics for System Improvement,'' in *Efficiency and Costing: Second Law Analysis of Processes*, Gaggioli, R. A., ed., A.C.S. Symposium Series, No. 235, Washington, DC, pp. 215–239.
[13] *Gas Turbine World Handbook*, 1997, Gas Turbine World, **16,17,18**, Pequot Publishing Inc., Fairfield, (USA).
[14] Bejan, A., Tsatsaronis, G., and Moran, M., 1996, *Thermal Design and Optimization*, Wiley, New York.

Detailed Experimental Studies of Flow in Large Scale Brush Seal Model and a Comparison With CFD Predictions

L. H. Chen

P. E. Wood

T. V. Jones

Department of Engineering Science,
University of Oxford,
Parks Road,
Oxford, United Kingdom

J. W. Chew

Mechanical Science Group,
Rolls-Royce plc.
Moor Lane,
Derby, United Kingdom

A five times scale model of an engine brush seal has been manufactured. The bristle stiffness and pressure were chosen to satisfy close similarity of the relevant non-dimensional parameters, and the choice of parameters is described. The comparison of flow characteristics for the model seal and an engine seal confirmed the non-dimensional similarity. Detailed pressure measurements were performed within the bristle pack by employing hollow bristles. This novel measurement allowed insight to be obtained into the operation of both clearance and interference seals. In particular, the measured pressure variation in the region of the bristle tips was significant. The deflection of the bristles was determined by comparing the bristle tip pressures with the static pressures along the shaft. Hence the compaction of the pack in this region was found directly. A numerical modeling of brush seals employing anisotropic flow resistance has been developed. Predictions were compared with the measured pressure distributions within the pack. This enabled sensible selection of the pack resistance distribution to be made. Although uniform anisotropic resistance throughout the pack gave reasonable flow rate characteristics, the pressure distribution was not reproduced. A variation of resistance coefficient consistent with the observed compaction was required to give a solution comparable with the experiments. [S0742-4795(00)01703-8]

Introduction

Brush seals are a form of shaft seal in which fine bristles are closely packed so that they offer relatively high resistance to flow. In manufacture the bristle pack is clamped between a front plate, on the high pressure side, and a backing ring, giving support on the low pressure side. The build clearance seal is designed with a small gap between the relaxed bristles and the static rotor, as shown in Fig. 1, whereas the build interference seal has a negative clearance and is in contact with the shaft and is consequently displaced. In the clearance seal under a pressure differential the bristles move radially inward so as to close the gap. This is referred to as blowdown in the following.

Engine experience has shown that significant improvements in engine performance and efficiency can be obtained by replacing labyrinth seals with brush seals [1]. Considerable efforts have therefore been underway to develop brush seals since the 1980s. However, the design of brush seals for future needs is becoming threatened by a lack of detailed understanding of basic mechanisms of flow and instabilities. There would appear to be little likelihood that this understanding can be derived from industrial development rigs, and it would be prohibitively expensive to attempt fundamental studies in this environment. Because of their dimensions, e.g., bristle length 15 mm, diameter 70 μm, 11 close packed rows giving a pack thickness of approximately 0.70 mm, actual seals are virtually impossible to study in the required detail. A representative large-scale model is therefore a feasible approach to the experimental study of the flow mechanisms.

Braun et al. [2] have investigated the complex flow fields in a simulated brush seal. The pack of rigid lucite bristles was positioned in a water and an oil tunnel. Visualization of the flow field revealed the flow structures. Pressure along the surface of the shaft was also measured.

In this paper, a Large Scale Model (LSM) was designed not only geometricallly similar to the engine seal but also physically similar. Thus the bristles behaved in the same manner as in the engine seal. This aided fundamental understanding of mechanisms in brush seals. In addition, such detailed information was used to examine the numerical modeling, thus enabling the numerical modeling to be improved.

The Dimensionless Groups

The performance of a brush seal may be expressed in functional, form as a relationship of the following 13 physical quantities:

$$f(\Delta p,T,\rho,\mu,R,L,\omega,\rho_b,E,m,f_b,f_s,f_{BR})=0,$$

where Δp is the pressure differential across the seal; T, ρ, μ, and R are the gas total temperature, density, viscosity, and gas constant, respectively; L is a characteristic length; ω is the rotation speed of the shaft; ρ_b and E are the density and Young's modulus of the bristle material; m is the mass flow of the gas through the seal; and f_b, f_s, and f_{BR} are the friction coefficients within the bristle pack, on the shaft surface and on the backing ring face.

Using conventional dimensional analysis the above quantities may be expressed in terms of non-dimensional groups as follows:

$$f\left(\frac{\Delta p}{p_u},\frac{\rho L\sqrt{RT}}{\mu},\frac{\omega L}{\sqrt{RT}},\frac{\rho_b}{\rho},\frac{E}{p_u},\frac{m\sqrt{RT}}{p_u L^2},f_b,f_{BR},f_s\right)=0.$$

The pressure p_u replaced ρRT in some groups due to the perfect gas law. The term $\rho L\sqrt{RT}/\mu$ is Reynolds number. The non-dimensional shaft rotation group $\omega L/\sqrt{RT}$ is neglected since pressure-drop/flow characteristics for single seals are not highly dependent on speed, and simulation of shaft rotation would be difficult in practice in the context of the LSM design. The density

---

Contributed by the International Gas Turbine Institute (IGTI) of THE AMERICAN SOCIETY OF MECHANICAL ENGINEERS for publication in the ASME JOURNAL OF ENGINEERING FOR GAS TURBINES AND POWER. Paper presented at the International Gas Turbine and Aeroengine Congress and Exhibition, Indianapolis, IN, June 7–10, 1999; ASME Paper 99-GT-281. Manuscript received by IGTI March 9, 1999; final revision received by the ASME Headquarters May 15, 2000. Associate Technical Editor: D. Wisler.

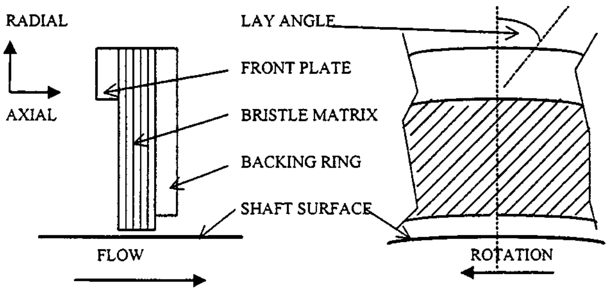

Fig. 1 Schematic of build clearance brush seal

ratio ρ_b/ρ accounts for buoyancy forces. Since the bristle density is three orders of magnitude greater than the gas density, this term is not considered to be important and is ignored. The bristle flexure characteristic is included in the stiffness term E/p_u, which dictates the extent to which applied pressure influences deflection and compaction of the bristle pack. The flow function is $\phi = m\sqrt{RT}/p_uL^2$. The coefficient of friction between neighboring bristles f_b and at the backing ring f_{BR} have a considerable effect on seal performance. The hysteresis in the flow characteristic of a brush seal provides a measure of the extent of the influence of friction. Replication of this hysteresis of an engine seal in the LSM experiments requires matching the frictional term f_b and f_{BR}. Selection of an appropriate backing material may fulfill the friction factor f_{BR}, however, the friction factor between bristles f_b is constrained by the selection of a bristle material that will comply with the criteria of the more influential stiffness term. The other friction term f_s is considered to have a second order effect on bristle displacement and in the absence of rotation is ignored. Taking all of the above into consideration, the seal performance can be reasonably described by the following relationship of six dimensionless quantities:

$$\frac{m\sqrt{RT}}{p_uL^2}=f\left(\frac{\Delta p}{p_u},\frac{\rho L\sqrt{RT}}{\mu},\frac{E}{p_u},f_b,f_{BR}\right).$$

It should be noted at this point that previous workers have employed large models of brush seals to validate and compare with numerical simulations, for example Braun and Kudriavtsev [3].

Test Section

The gas for the large scale model is air. A scale of five in geometry was chosen because it allows representative testing to be performed at close to atmospheric pressure when the Reynolds number is the same as for the engine seal. The high aspect ratio of the seal periphery to height is such that the flow is judged to be essentially two dimensional at any location. Thus a linear model was considered to be sufficient to represent the brush seal flow.

The test section of the large scale model is shown in Fig. 2(*a*). The cross sectional area is a parallelogram with angle of 45 deg, which is the same as the bristle lay angle. The cross section is 200 mm×115 mm. The length of the test section is 190 mm, and the bristle pack was installed in the middle. The overhang radial length of the bristles is 5 mm. Therefore, the backing ring clearance of 4.075 mm corresponds to an interference seal with the build interference of 0.925 mm; and the backing ring clearance of 6.5 mm corresponds to a clearance seal with a clearance of 1.5 mm, as shown in Fig. 2(*b*) and (*c*). There were 4125 bristles within the pack.

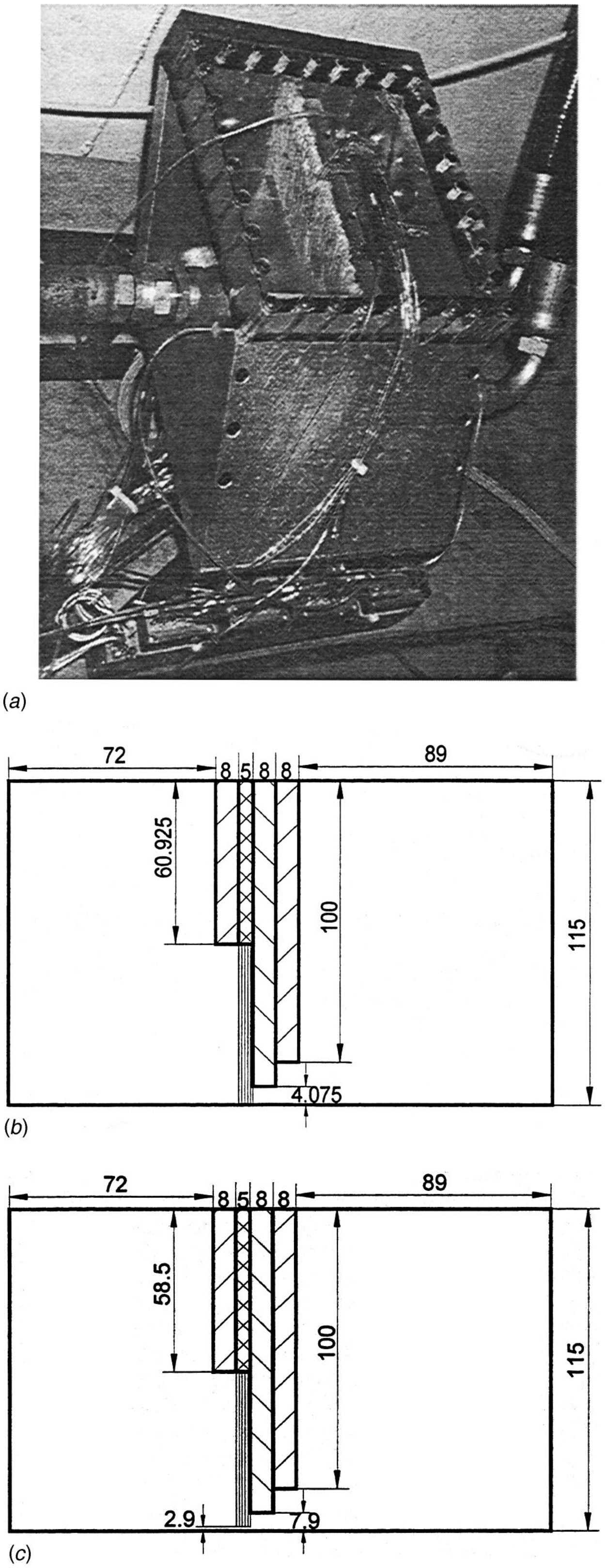

(*a*)

(*b*)

(*c*)

Fig. 2 Large scale model: (*a*) Test section; (*b*) configuration of the interference seal; (*c*) configuration of the clearance seal.

The bristle pack consists of aluminum alloy wires to BS 1471 5251 H8. Table 1 gives the properties of the real engine seal and the large scale model. Aluminum alloy was chosen as the best available compromise to maintain Reynolds number and stiffness term E/P_u, the same in the model and the engine. Also, f_b and f_{BR} were approximately the same for both cases.

The seal housing was constructed from aluminum alloy plate, with the exception of the top plate which is manufactured from perspex to provide optical access.

Table 1 Parameters of the engine seal and large scale model

	Engine Seal Tests		Large Scale Model Tests	
Bristle Length (mm)	15		77.8	
Bristle Diameter d (mm)	0.07112		0.36	
Lay Angle φ (°)	45		45	
Young's modulus E (GN/m^2)	207		60	
Density of Bristle ρ_b (kg/m^3)	7800		2700	
No. of Bristle Rows	11		11	
Packing Density (/inch)*	2600		504	
	Clearance	Interference	Clearance	Interference
Backing Ring Clearance (mm)	1.58	0.725	7.9	4.075
Build Clearance (mm)	0.6	−0.185	2.9	−0.925

*packing density is the number of bristles per circumference length

Measurement System

In order to obtain the details of the flow field, three sets of pressure tappings were installed in the large scale model. Firstly, eight pressure tappings were on the backing ring with the radial distance from the edge of 1.5, 5, 10, 15, 20, 30, 40, and 50 mm. Secondly, 14 tappings were on the top plate with axial distance 1 mm between the tappings. Thirdly, approximately 80 bristles were replaced by tubes of 200 micron bore. A tapping hole of diameter approximately 100 microns was drilled in the bristle. The measurement points were at 0, 5, 10, 15, 20, 35, 50, and 70 mm from the bristle tip. All of these bristle tappings were installed in the middle of the section to eliminate end effects. Tappings on the backing ring and top plate were also installed. The hollow bristles with end tappings measured the static pressure at the tips since the deflection of the bristles is small. For other bristles, the tappings were nominally aligned in the direction of main axial flow; however, this was somewhat indeterminate. Thus, the pressure values measured by these tappings may include a component of dynamic head and hence not give the local static pressure within the pack.

The upstream and downstream pressures were measured from the inlet and outlet walls of the test section. The mass flow was measured by an orifice plate downstream. The pressure instrumentation included 32 Channel Scanivalve ZOC14BNP System (0–35 bar) and 48 Channel Pressure Systems Inc. ESP-48 Scanner (0–10) bar.

Air supply was from a 30 bar tank via a Norbro 40R series electrically controlled actuator and a manual ball valve. A manually operated G4 regulator followed to control the upstream pressure to the test section. The flow passed through the test section and then exited to atmosphere via an orifice plate flow meter. The orifice plate was preceded by a manually operated ball valve which was used to set the downstream pressure. When the ball valve was fully open, the downstream pressure approached atmospheric pressure.

Instrumentation was interfaced to a 386 PC via a CIL Alpha Block interfacing system. The GW-basic code controlling the interfacing system has been used for the calibrations and the measurements.

Numerical Modeling

The model is described in Chen et al. [4] and is based on the model by Turner et al. [5]. For completeness a brief description is given here. For a fuller discussion of porosity modelling readers may refer to Chew and Hogg [6] and papers by Hendricks et al. (e.g., [7]).

Outside the bristle pack, which is assumed to be a rectangular region, the Reynolds-averaged Navier-Stokes equations are used with a Prandtl mixing length model of turbulence. Uniform total temperature of the air is assumed. The conservation equations for mass and momentum are as follows (respectively):

$$\nabla\cdot(\rho\underline{u})=0 \tag{1}$$

$$\rho\underline{u}\cdot\nabla\underline{u}=\nabla\cdot\mu_e\nabla\underline{u}+\nabla\cdot\mu_e\nabla\underline{u}^T-\nabla p. \tag{2}$$

Within the bristle matrix the right hand side of the momentum conservation equation (Eq. 2) is modified with the addition of a anisotropic, non-linear resistance law (Eq. 3). The tensors A and B contain six unknown constants which were chosen to reproduce experimental data. The form of Eq. (3) has been validated against independent tests on well defined anisotropic porous models [8].

$$\underline{F}_r=-\mathbf{A}\mu\underline{u}-\mathbf{B}\rho|\underline{u}|\underline{u} \tag{3}$$

$$\rho\underline{u}\cdot\nabla\underline{u}=\nabla\cdot\mu_e\nabla\underline{u}+\nabla\cdot\mu_e\nabla\underline{u}^T-\nabla p+\underline{F_r}$$

This represents the body force acting on the bristle matrix. **A** and **B** are the viscous and inertial resistance tensors:

$$\mathbf{A}=a_n\underline{e}_n\underline{e}_n+a_s\underline{e}_s\underline{e}_s+a_z\underline{e}_z\underline{e}_z$$

$$\mathbf{B}=b_n\underline{e}_n\underline{e}_n+b_s\underline{e}_s\underline{e}_s+b_z\underline{e}_z\underline{e}_z\,.$$

The resistance coefficients, a_n, a_s, a_z, b_n, b_s, and b_z are defined in the principal directions, which are; normal to the bristles in the r-θ plane ($\underline{e_n}$), aligned with the bristles in the r-θ plane ($\underline{e_s}$), and in the axial direction ($\underline{e_z}$) (see Fig. 1). The boundary conditions are the total pressure and flow angle at inlet, static pressure at outlet, and no-slip, no-penetration at the walls.

In the bending calculation it is assumed that the bristle deflections are much smaller than the bristle length, and, therefore, axial deflections are independent of the forces and deflections in the r-θ plane. Cantilever theory is used to calculate the bristle deflections. Friction between bristle rows and between the bristle pack and the backing ring are included in the modeling. Similar assumptions and calculating have been performed by other workers in the field.

Experimental and Modeling Results

Flow Characteristics. As described in the previous section, the flow function is a function of the pressure drop across the seal, Re, the stiffness term and frictional terms; therefore, if we have identical Reynolds number

$$\left(\frac{\rho L\sqrt{RT}}{\mu}\right),$$

the stiffness term

$$\left(\frac{E}{p_u}\right),$$

and frictional terms, we should have the same relationship between $m\sqrt{RT}/p_uL^2$ and $\Delta p/p_u$ for both engine seal and large scale model. The pressure ratio $p_r=p_u/p_d$ is used as an alternative to $\Delta p/p_u$.

Both engine seal and LSM tests were taken at room temperature. The working gas was air. Therefore, R, T, and μ are almost same for the engine seal tests and the LSM tests. Matching Reynolds number gives $(p_u)_e/(p_u)_l=L_l/L_e=5$. However, if

$$\left(\frac{E}{p_u}\right)_e=\left(\frac{E}{p_u}\right)_l,$$

we have $(p_u)_e/(p_u)_l=E_e/E_l=3.45$. This means that we cannot have the same Re and stiffness term simultaneously. However, the experimental results show little difference between them, as shown in Fig. 3.

The engine seals were tested on the engine rig [9], and the LSM tests were taken on the large scale model described below. The tests were taken when the upstream pressure was regulated at a constant level. The downstream ball valve cycled from closed to

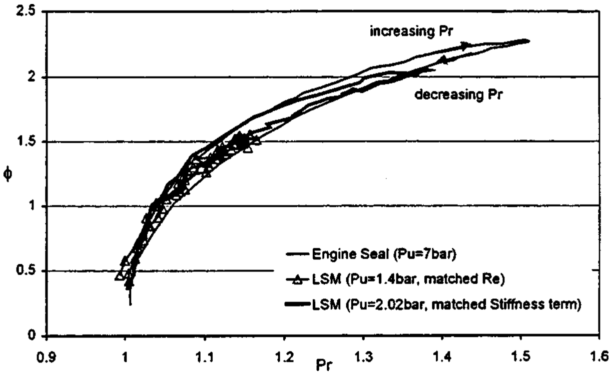

Fig. 3 Flow characteristics for the clearance seals

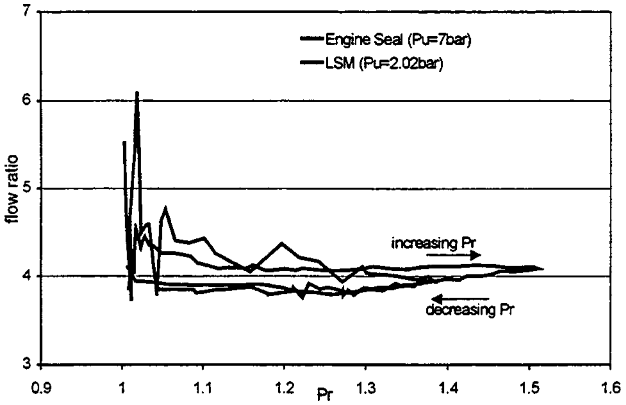

Fig. 4 Ratio of seal flow to orifice flow versus pressure ratio (clearance seals)

fully open to closed so that in the first part of the test the pressure across the seal was increasing and in the second part decreasing. The minimum downstream pressure would be obtained when the valve was fully open.

In Fig. 3, the results for the flow function ϕ versus the pressure ratio p_r are presented for the clearance seal. The engine seal results are from the test under the upstream pressure of 7 bar. Two LSM tests were taken under the upstream pressures of 1.4 bar and 2.02 bar. The upstream pressure of 1.4 bar for the LSM can be considered to represent the engine seal under 7 bar according to the matched Reynolds' number. Similarly, $p_u = 2.02$ bar for the LSM corresponds to $p_u = 7$ bar for the engine seal if the stiffness term matched. The flow characteristics for the LSM are in excellent agreement with that of the engine seal. The experimental results show that all three cases exhibited almost the same flow function/pressure ratio characteristics. This indicates the LSM indeed can represent the engine seal behavior despite the fact that Re and the stiffness could not be exactly matched simultaneously. Hysteresis effects were also very similar indicating that the frictional terms are approximately satisfied.

The flow characteristics can also be presented as the ratio of the flow function to that for inviscid compressible flow through an orifice of constant cross section. This ratio indicates an equivalent flow area, which changes as a consequence of blow down and compaction of the bristle pack.

It can be shown that the ratio of the flow function of a given gas through a brush seal to that through an orifice of constant cross section, ϕ_{ideal}, is proportional to

$$\frac{\phi}{\phi_{\text{ideal}}} \propto \frac{\dfrac{m\sqrt{RT}}{p_u D^2}}{M \dfrac{\rho}{\rho_0}\dfrac{a}{a_0}}$$

In Fig. 4, the flow ratio term

$$\left(\frac{m\sqrt{RT}}{p_u D^2}\right) \bigg/ \left(M \frac{\rho}{\rho_0}\frac{a}{a_0}\right)$$

is plotted against the pressure ratio for the clearance seals. For the engine seal, as the downstream pressure is initially decreased, the flow ratio term decreases, indicating that as a result of blow down and compaction the flow area through the seal is reducing. As downstream pressure is further decreased from a pressure ratio of 1.1, the flow ratio term becomes reasonably constant, indicating that the mean flow area through and bypassing the seal is constant. Increasing the downstream pressure from the maximum pressure, ratio of 1.5 produces a further small reduction in the flow ratio term, and, therefore, indicates a further reduction in flow area. Mechanism for this further small reduction in both the LSM and engine seal are still under consideration at this time. The flow ratio term of the LSM is also plotted in Fig. 4 and is certainly in good agreement with the engine seal data. The greater degree of uncertainty is evident in the LSM results.

Similar tests were taken for the interference seal for the LSM. No engine data were available for a geometrically similar case but a test which was close to that required was used. Thus several points from the static tests [9] were plotted in Fig. 5 for comparison. Two LSM tests were taken for upstream pressures of 2.02 bar and 3.18 bar, which correspond to the upstream pressure of 7 bar and 11 bar for the engine seal according to the matched stiffness term. The engine seal data are from static tests when $p_u = 6$ bar. As shown in Table 1, the interference of the LSM is 5 times that of the engine seal; but the backing ring clearance of the LSM is 56 times that of the engine seal. Thus, the flow function for the LSM is larger than that for the engine seal possibly to this geometry difference.

The level of hysteresis in the lower pressure test is generally negligible whereas that in the higher pressure test is an order of magnitude less than that for the clearance seals. Since compaction of the bristle pack is the only mechanism by which hysteresis can be manifest in the flow function/pressure ratio relationship, generally lower levels of hysteresis would be expected in interference seals which are always in contact with the shaft. The fact that hysteresis is evident in the higher pressure test provides evidence that at above a certain differential pressure, compacting of the bristle pack does produce a reduction in flow area.

Pressure Distribution. The detailed pressure distributions were measured when the upstream pressures were maintained constant and the downstream valve was always fully open. The exact downstream pressure was determined by the flow rate and resistance of the exhaust pipework.

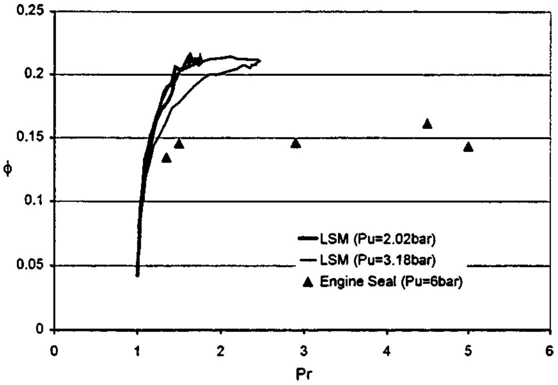

Fig. 5 Flow characteristics for the interference seals

As the CFD code employed was in cylindrical coordinates a 10 deg sector on a radius of 1040 mm was chosen to approximately represent the linear model. The actual large scale seal was somewhat splayed, the thickness being approximately 5 mm at the root and 8 mm at the tip. This is characteristic of engine seals. In the CFD, the seal region was treated as a rectangle with a thickness of 5 mm. The resistance coefficients used in the CFD were chosen as, $a_z = a_n = 1.258\times 10^{10}$, $a_s = a_n/60$, $b_z = b_n = 3.07\times 10^{5}$, $b_s = 0$, to match the mass flow.

The experimental and CFD results for the interference seal are presented in Fig. 6 and Fig. 7 for $p_u = 2.11$ bar and $p_d = 1.28$ bar. Figure 6 shows the experimental and computed pressure fields. The pressure values from the experiments are plotted at the undeflected measurement points, i.e., the deflection of the bristles is neglected. The static pressure predicted by the CFD is given for the same points. The legends identify the bristle rows: the first row is the upstream row, and the 11th row is the downstream row. For plotting purposes a uniform spacing of points was required. The results are plotted on a uniform grid for each row (5 mm between adjacent points). The actual measurement points are less than these. Thus, all the extra points required in the plots were linearly interpolated from the measurement points. This introduced error at some points. Errors are also present in the measurements themselves. Another error arises as measurement points were assumed to be at the undisturbed design points even when pressure was applied. In practice, the bristles may be curved or twisted due to manufacture. Even though the pressure measurements for the whole field are not accurate at all the points, they still can be used to indicate the pressure field within the bristle pack. It is the first time such detailed information has been obtained for brush seals.

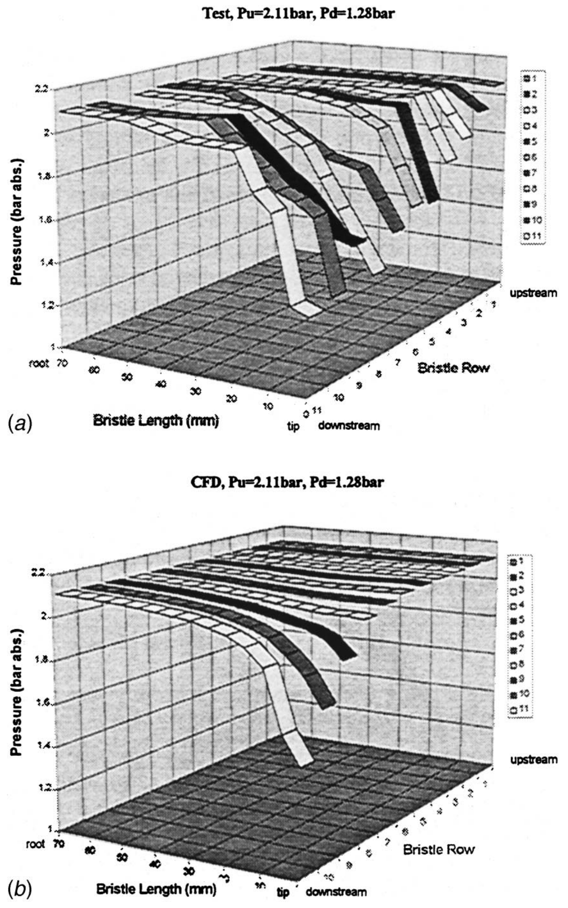

Fig. 6 Pressure distribution within the bristle pack (interference seal: $Pu = 2.11$ bar; $Pd = 1.28$ bar)

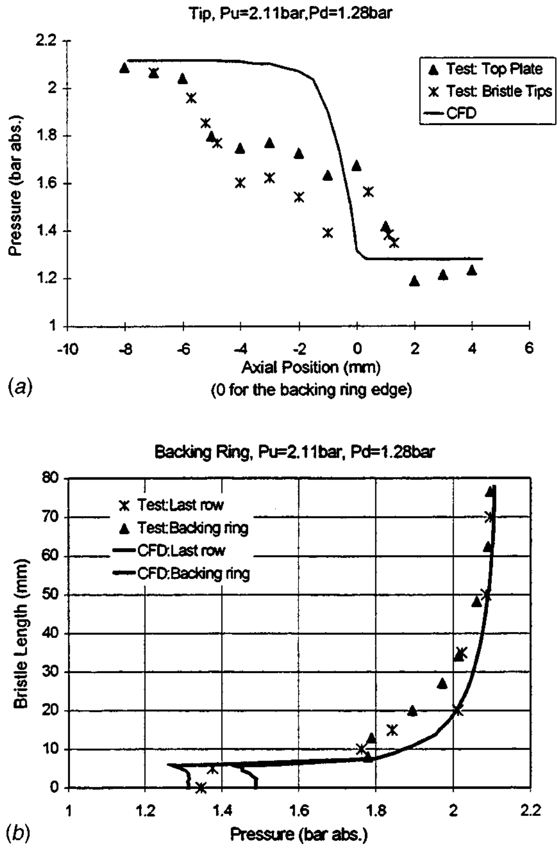

Fig. 7 Pressure distributions for the interference seal: (*a*) pressure distributions in the axial direction; (*b*) pressure distributions in the direction along the bristles.

The experimental results show that the pressure began dropping from the second row, most pressure drop occurring close to the tips. The CFD results show that the pressure drop concentrates in the downstream region, close to the tips.

Figure 7 includes two plots:

(a) A comparison of static pressure along the shaft through the seal. $x = 0$ is the backing ring face; a negative x value is for upstream positions before the backing ring; a positive x value is downstream behind the backing ring face. The points labeled ''Test: Top Plate'' are the measurements on the top plate, corresponding to the shaft surface (1 mm spacing between the measurement points). The points labeled ''Test: Bristle Tips'' are the values from the bristle tip tappings. The line is the result from the CFD.

(b) A comparison of the pressure on the backing ring and for the last row of bristles. The y coordinate is the length along the bristle. $y = 0$ is the bristle tip, and $y = 77.78$ mm is the bristle root. The points labeled ''Test: Backing Ring'' are from the measurements along the backing ring face. The points labeled ''Test: Last Row'' are from the pressure tappings of the last bristle row. The lines are from the CFD. The line labeled ''CFD: Backing Ring'' gives the pressure distribution at $x = 0$, which includes the backing ring face and the gap between the backing ring and the top plate.

Figure 7(*a*) is the pressure distribution along the axis. The values measured by the bristle tip tappings are close to those from the top plate, which confirms the measurement by the hollow bristles. The experimental results show the non-uniform pressure drop along the shaft surface. The pressure drop is in two steps: it drops in a thin upstream region, then remains almost constant pressure in the middle of the pack, and finally drops again near the backing ring. This may be because the pressure differential compacted the upstream bristle rows since the bristles were initially splayed before pressure was applied. The pressure difference was not large enough to compact the whole seal but only the upstream rows. In the middle of the seal, the pack was not dense enough to give a high resistance to the flow so that the pressure did not drop much. At the backing ring, the flow area contraction causes the pressure to decrease rapidly. The CFD gives a different variation of pressure, i.e., the pressure drop concentrates in the downstream region ($x=-2$ to $x=0$). The brush seal in the CFD is a uniform rectangular porous medium and this is not in good agreement with the tests.

Examining the results along the bristles (Fig. 7(*b*)), the following is observed. The experimental results show the pressure of the last bristle row is the same as that on the backing ring face. This is a good check of the measurement by the bristle tappings. The pressure in the upper half of the pack ($y>40$ mm) is the same as the upstream pressure, which indicates little or no leakage flow through the pack in this region. The pressure decreases as the backing ring gap is approached and the air flows downwards along the bristles. The maximum pressure gradient occurs at the backing ring edge since the flow turns into the axial direction at the point. The measurement points for the last bristle row show the pressure rapidly decreasing in the gap between the backing ring and top plate, reaching a pressure of 1.37 bar when $y=5$ mm. The CFD gives reasonable agreement with the test but the pressure drop obtained by the CFD is more concentrated near the edge of the backing ring. The experimental result from the tip of the last row is lower than that of the CFD. This implies the last row had axial bending so it actually measured the pressure further downstream and hence gives a value between the two CFD lines.

The results of pressure distribution for the clearance seal are presented in Fig. 8 and Fig. 9 for $p_u=2.03$ bar and $p_d=1.47$ bar. The situation is more complicated for the clearance seal than for the interference seal since the bristle pack may be partially blown down. From the experimental observations the front rows of the clearance seal blow down to contact the top plate, which is very similar to that observed in the engine seal tests. The blow down is far from uniform. There were gaps between the blown down bristle bundles The smaller resistance coefficients ($a_z=a_n=1.245\times 10^9$, $a_s=a_n/60$; $b_z=b_n=1.3\times 10^4$, $b_s=0$) were used for this blown down region. Also small friction factors (i.e., 0.05) were given for the upstream rows in the modeling to allow the bristles to blow down. This reflected the fact that the bristles were somewhat splayed in the large scale model bristle pack.

Figure 8 gives the pressure field for the clearance seal. Compared to the interference seal (Fig. 6), the pressure drop across the seal is less, i.e., for the clearance seal, the pressure drop across the seal is $p_u-p_d=0.56$ bar, and for the interference seal, the pressure drop is $p_u-p_d=0.83$ bar. The pressure decreases more in the upstream region than that of the interference seal. The pressure drop still concentrates on the region close to the tips. It should be noticed that the figure was still plotted according to the undeflected positions of the measurement points. When the seal was partially blow down, the front rows could bend downstream beyond the following row. The state of blow down of the bristle rows could be seen through the perspex model shaft.

The pressure field predicted by the CFD can be divided into two regions: the region of the upstream two bristle rows (blown down to contact the shaft) and the rest of the pack (at the initial clearance). For the former the pressure drop is confined to the bristle tips whereas elsewhere the pressure decreases gradually in

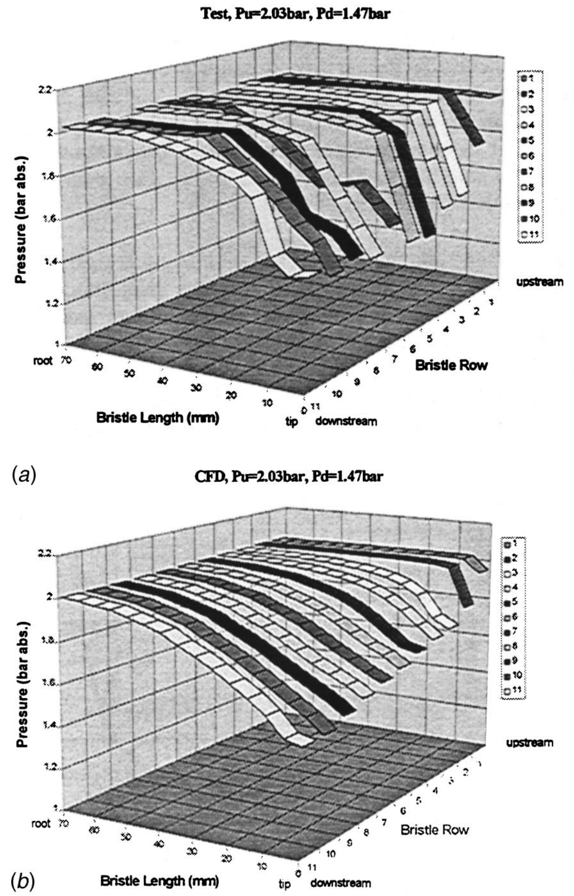

Fig. 8 Pressure distribution within the bristle pack (clearance seal: $Pu=2.03$ bar; $Pd=1.47$ bar)

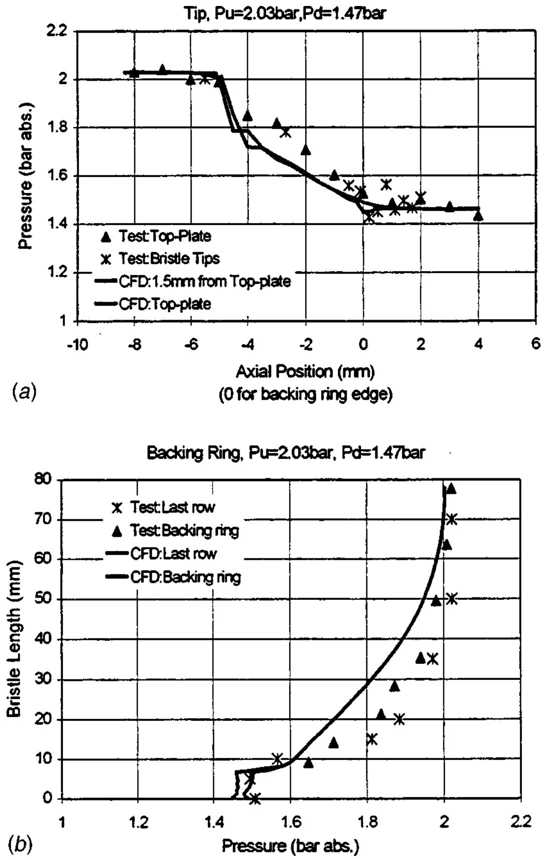

Fig. 9 Pressure distributions for the clearance seal: (*a*) pressure distributions in the axial direction; (*b*) pressure distributions in the direction along the bristles.

both axial and radial directions. Compared with the experiment, the CFD gives a smoother pressure distribution. The pressure decreases along the whole length of the bristles rather than concentrates on the region close to the tips.

Figure 9(*a*) shows the pressure distribution along the axis. The CFD results are presented on two lines along the axial direction: one is on the surface of the top plate; another is 1.5 mm radial distance from the surface of the top plate. The latter are the same points as the bristle tips when these are not blown down. The CFD gives a sharp pressure drop for the first row of the bristles. Then the pressure exhibited a narrow plateau which corresponds to a local weak re-circulating flow after the blown down bristles. From here the pressure decreases gradually until the backing ring face is reached. Behind the backing ring face, the pressure is almost the same as the downstream pressure. There is little difference between the two lines. The experimental pressure distribution is similar to that of the CFD with less pressure drop for the upstream row and hence greater pressure drop for the rest, but the difference is less than 10 percent.

The pressure decreases more evenly along the rear bristle row (Fig. 9(*b*)) compared to the interference seal (Fig. 7(*b*)). The pressure of the upper half of the bristle ($y > 40$ mm) is close to the upstream pressure, which implies little flow exists in that region. The CFD gives a lower pressure, but the difference is less than 10 percent. The experimental pressure value of last row tip is very close to that of the CFD, which indicates the axial bending of the last row is very small, unlike the interference seal.

When using the same resistance coefficient tensors throughout the whole bristle pack, the CFD in general predicts a reasonable pressure distribution throughout the pack. The agreement with the experimental results is better for the clearance seal than for the interference seal. For the interference seal, the predicted pressure gradient is too large along the shaft under the bristle tips, and, hence, is confined to too small a region, as shown in Fig. 7. It is apparent that due to the bristle movement in this region the degree of compaction and hence resistance varies considerably through the pack. This can be taken into account by varying the resistance as shown in the example below.

The porous region was divided into five parts, as shown in Fig. 10. The example which used varying resistance coefficients is given in Fig. 11 for the interference seal with $p_u = 3.11$ bar, $p_d = 1.62$ bar, Since the overhang region dominates the flow, it is reasonable to consider using varied resistance coefficients in this region. Region 1 extends from a position 3.8 mm from the shaft to the bristle roots. The other regions are of the same size with a thickness of 1.25 mm and height of 3.8 mm in the overhang region. Because the downstream bristles bend more in the axial direction, the actual resistance downstream will be less since the resistance falls as the bristles spread. The different coefficients applied in each region are: $a_z = a_n$, $a_s = a_n/60$; $b_z = b_n$, and $b_s = 0$. In regions 1 and 2: $a_z = 1.22\times 10^{11}/\text{m}^2$, $b_z = 1.26\times 10^6/\text{m}$. In region 3: $a_z = 8.24\times 10^{10}/\text{m}^2$, $b_z = 8.6\times 10^5/\text{m}$. In region 4: $a_z = 4.24\times 10^{10}/\text{m}^2$, $b_z = 4.6\times 10^5/\text{m}$. In region 5: $a_z = 2.4\times 10^9/\text{m}^2$, $b_z = 6\times 10^4/\text{m}$. These resistances were chosen such that the overall mass flow remained unaltered from that already calculated with uniform resistance and the experiment.

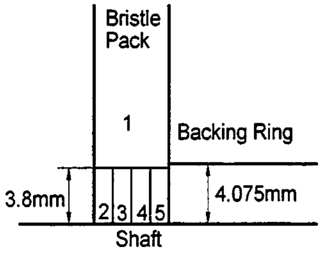

Fig. 10 Divided porous regions with varied resistance coefficients

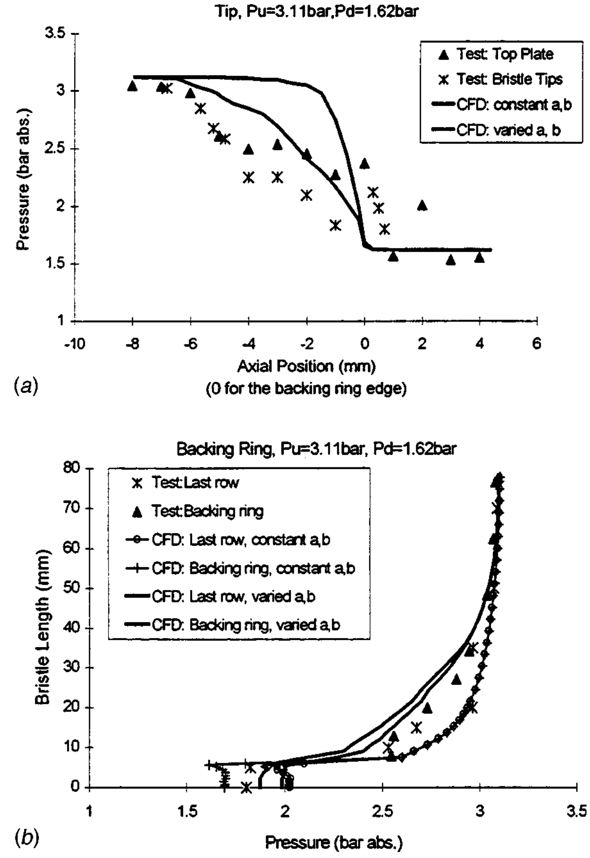

Fig. 11 Pressure distributions with varied resistance coefficients: (*a*) pressure distributions in the axial direction; (*b*) pressure distributions in the direction along the bristles.

The results in Fig. 11 show that the prediction with varied resistance coefficients gives much better agreement with the experiments both on the shaft and backing ring pressure distributions. In practice, the geometry of the bristle pack may vary in a more complex manner than assumed above. This modeling with uniform resistance coefficients can achieve a very good agreement with average flow parameters such as the total mass flow rate, but it is not good enough to predict the detailed pressure distribution. This indicates that the deflections of the bristles play an important role in the pressure distribution of a brush seal.

Conclusions

The following conclusions can be obtained through the experimental and numerical studies on the large scale model of the brush seal.

1 Comparison of flow characteristics of the engine seal and the large scale model has demonstrated that the two systems are not only geometrically similar but also physically similar. Thus, it can be concluded that the assumptions made in the derivation of the relevant non-dimensional groups are satisfactory.

2 The ability to measure the pressure distribution within the bristle pack has provided a valuable insight into the operation of both interference and clearance seals. Detailed flow information has been obtained. In both seals, the form of the pressure drop close to the bristle tips, in the overhang region, is very significant.

3 It has been shown by visual observation and pressure measurement that the bristle pack was compacted under pressure. The bristle bending in the axial direction could be several times the bristle diameter. Together with the numerical prediction the mea-

surements give a clear indication of the way in which the compaction and local resistance varied through the pack.

4 When using the single uniform resistance coefficient tensors to represent the whole bristle pack, the CFD in general does not predict an accurate pressure distribution throughout the pack. The agreement with the experimental results is better for the clearance seal than for the interference seal.

5 The change in geometry of the bristle pack plays an important role in the seal behavior, especially in the pressure distribution through the pack. It is necessary to select varied resistance coefficients in the modeling to give more accurate predictions.

Acknowledgments

The authors would like to thank the EPSRC and Rolls-Royce plc. for their financial support for this work described in this paper.

Nomenclature

$\mathbf{A},\mathbf{B}$ = viscous and inertial resistance tensors
a = speed of sound
a,b = viscous and inertial resistance coefficients
d = bristle diameter
D = shaft diameter
$\underline{e}$ = unit vector
E = modulus of elasticity
f = friction factor
$\underline{F_r}$ = resistance force per unit volume
l = bristle length
L = characteristic length
m = mass flow
M = Mach number
p = static pressure
p_d = downstream pressure
p_r = pressure ratio (p_u/p_d)
p_u = upstream pressure
r = radial co-ordinate
R = gas constant
Re = Reynolds number $\rho L\sqrt{RT}/\mu$
T = gas temperature
$\underline{u}$ = mean velocity vector
z = axial co-ordinate
ϕ = flow function
φ = bristle lay angle (0 deg for radial alignment)
μ = viscosity
θ = tangential co-ordinate
ρ = density
ω = shaft rotation speed

subscripts

0 = total (pressure, temperature etc.)
b = bristle
BR = backing ring
e = effective; engine seal
l = large scale model
n = direction normal to the bristles in the r-θ plane
s = shaft; direction aligned with the bristles in the r-θ plane
t = turbulent
z = axial direction

References

[1] Steinetz, B. M., Hendricks, R. C., and Munson, J., 1998, ‘‘Advanced Seal Technology Role in Meeting Next Generation Turbine Engine Goals,’’ NASA/TM-1998-206961, AVT-PPS Paper No. 11, April 1998.
[2] Braun, M. J., Hendricks, R. C., and Cannaci, V. A., 1990, ‘‘Flow Visualization in a Simulated Brush Seal,’’ ASME Paper 90-GT-217.
[3] Braun, M. J., and Kudriavtsev, V. V., 1995, ‘‘A Numerical Simulation of a Brush Seal Section and Some Experimental Results,’’ ASME J. Turbomach., **117**, pp. 190–202.
[4] Chen, L. H., Wood, P. E., Jones, T. V., and Chew, J. W., 1998, ‘‘An Iterative CFD and Mechanical Brush Seal Model and Comparison with Experimental Results,’’ ASME-98-GT-372.
[5] Turner, M. T., Chew, J. W., and Long, C. A., 1997, ‘‘Experimental Investigation and Mathematical Modelling of Clearance Brush Seals,’’ ASME Paper 97-GT-282.
[6] Chew, J. W., and Hogg, S. I., 1997, ‘‘Porosity Modelling of Brush Seals,’’ ASME J. Tribol., **199**, pp. 769–775.
[7] Hendricks, R. C., Schlumberger, S., Brown, M. J., Choy, F., and Mullen, R. L., 1991, ‘‘A Bulk Flow Model of a Brush Seal System,’’ ASME Paper 91-GT-325.
[8] Chen, L. H., 1998, ‘‘Numerical and Experimental Modelling of Brush Seals,’’ D. Phil thesis, University of Oxford, U.K.
[9] Wood, P. E., and Jones, T. V., 1997, ‘‘A Test Facility for the Measurement of Torques at the Shaft to Seal Interface in Brush Seals,’’ ASME Paper 97-GT-184.

Royal Navy Experience of Propulsion Gas Turbines and How and Why This Experience is Being Incorporated Into Future Designs

James Rand
ME214, In Service Gas Turbines,
Ships Support Agency,
Somerset, United Kingdom

Nigel Wright
ME215, Future Gas Turbines,
Ships Support Agency,
Somerset, United Kingdom

The Royal Navy (RN) has in-service experience of both marinized industrial and aero derivative propulsion gas turbines since the late 1940s. Operating through a Memorandum of Understanding (MOU) between the British, Dutch, French, and Belgian Navies the current in-service propulsion engines are marinized versions of the Rolls Royce Tyne, Olympus, and Spey aero engines. Future gas turbine engines, for the Royal Navy, are expected to be the WR21 (24.5 MW), a 5 to 8 MW engine and a 1 to 2 MW engine in support of the All Electric Ship Project. This paper will detail why the Royal Navy chose gas turbines as prime movers for warships and how Original Equipment Manufacturers (OEM) guidance has been evaluated and developed in order to extend engine life. It will examine how the fleet of engines has historically been provisioned for and how a modular engine concept has allowed less support provisioning. The paper will detail the planned utilization of advanced cycle gas turbines with their inherent higher thermal efficiency and environmental compliance and the case for all electric propulsion utilizing high speed gas turbine alternators. It will examine the need for greater reliability/availability allowing single generator operation at sea and how by using a family of 3 engines a nearly flat Specific Fuel Consumption (SFC) down to harbour loads can be achieved. [S0742-4795(00)01203-5]

Background

Why Gas Turbines Were Chosen. Although a gas turbine first saw service in the Royal Navy in 1947, it was not until 1967 that Naval policy changed so that aero derivative gas turbines became the first choice prime mover for major surface warships. The gas turbine was seen as a simple, compact, nonreciprocating machine that had the potential for development and high reliability. Their high power density allowed smaller engine rooms, larger magazine space or smaller and thus cheaper ships. It was perceived that the potential for higher reliability, availability, and reduced personnel requirement far outweighed the then poor cycle efficiency.

A major factor in the move to aero derivatives was the foreseen rapid exchange times for complete engines. An industrial based G6 engine in HMS Ashanti suffered a partial disc failure which required removal of the complete engine, measured in weeks with full dockyard support. Aero derivatives however, were shown to allow a complete ship re-engine in a few days in theatre.

All the advantages predicted by the change in propulsion policy have now been realized with many of the reservations being not as serious as was first expected. The move from the steam and G6 turbines to Tyne and Olympus brought about a new maintenance philosophy of limited life and upkeep by exchange. The new operating and emergency procedures gave dramatically better availability which paved the way to doubling the time between docking and refit intervals over those common with steam propulsion fit ships. This, with the ability to significantly reduce the marine engineering crew, has given a significant benefit to the defense budget.

Configuration and Operation. The configuration of Royal Navy gas turbines is either CODLAG, COGOG, or COGAG using the principle of cruise/boost. The smaller Tyne engine or an electric motor is used as the cruise engine while the Spey or Olympus is used for sprinting. The majority of the operating time is spent below 15 knots and thus the cruise boost system gives large fuel savings. The disadvantage is that a logistic holding for several different engines is required.

Support Through a Memorandum of Understanding (MOU). The MOU was initiated in 1975 between the Dutch, Belgian and British Navies and was later joined by the French Navy and covers both technical and logistic support. The aim of the MOU is to invest in a pool of gas turbines, support facilities, maintenance policies, technical manuals, practices, component systems, and equipment common to the participating navies and thus reduce expenditure through economies of scale and ensure commonality to maximize benefits. Costs are shared based on engine running hours with the major expenditure being the repair and overhaul bill (fuel and shipborne labor costs play no part in the MOU).

Support Policy

Provisioning. Provisioning of Gas Turbines and spares is on a ''Pool'' basis with equipment being allocated to MOU ships as the need arises. Pool Gas Turbines may be new, reconditioned or part life units. The planned size of the Pool at any given time is determined by a number of factors including population fit, planned life, rates of random failure, and the repair down time of unserviceable units. On removal from ships, life expired or unserviceable Gas Turbines are returned to an overhaul facility for reconditioning, refurbish, or repair and subsequent return to the Pool. When Ships go into refit or reserve, part life Gas Turbines may be removed, preserved, modified or returned to the Pool (as necessary) to ensure their proper care and to supplement Pool stocks.

Contributed by the International Gas Turbine Institute (IGTI) of THE AMERICAN SOCIETY OF MECHANICAL ENGINEERS for publication in the ASME JOURNAL OF ENGINEERING FOR GAS TURBINES AND POWER. Paper presented at the International Gas Turbine and Aeroengine Congress and Exhibition, Indianapolis, IN, June 7–10, 1999; ASME Paper 99-GT-89. Manuscript received by IGTI March 9, 1999; final revision received by the ASME Headquarters May 15, 2000. Associate Technical Editor: D. Wisler.

Table 1 Engine release lives verses achieved lives

Engine	Original OEM Release Life	Current OEM Release Life	Achieved Life
Olympus	3,500hrs / 10 years	5,000 hrs / 10 years	7,500 hrs / 18 years
Tyne	3,000 hrs	5,000 hrs	7,000+hrs
Spey SM1A	3,000 hrs	3,000 hrs	6,000 hrs
Spey SM1C	9,000 hrs	9,000 hrs	Lead engine at 1,500 hrs

Maintenance. Component ''Upkeep by Exchange'' (UXE) is the base philosophy for MOU gas turbines and their ancillary equipment which makes for reduced operational downtime, reduced manpower, increased propulsion system availability and some reduction in ships' staff skills level. In-situ repairs are also conducted on a UXE basis for such items as combustion chambers, auxillary gearboxes, and enclosure mounted equipment. Onboard repair techniques have of course been developed but these skills tend to be retained by the waterfront repair and specialist technical groups.

Fleet Support. As with introduction of any engine into service, engine life was initially taken as that conservatively agreed between the Rolls Royce and the RN following development and endurance trials. By ensuring that development engines accumulated more equivalent hours than those in operational service an understanding of possible modes of operational degradation was gained: hopefully before they occurred in service. Soon operating experience and engine hours grew to such a level that engine life expectations based on development engine testing were exceeded. To gain experience of engine life specialist engine inspection teams were formed and these are currently based in Bath, UK, and Den Helder, The Netherlands. Corporate knowledge is maintained by mixing civilians with uniformed personnel who have operating and maintenance experience on gas turbines.

Life Sampling. Critical components (termed Group A) are those which are subjected to low cycle fatigue whose failure could be non-contained within the engine carcass. Clearly it is of paramount importance that this does not happen. The components are lifed in terms of major cycles; each cycle representing an excursion from zero to maximum speed and back. Whilst an initial assessment of the cyclic usage rate is made, the installation of low cycle fatigue counters (LCFC) in a sample of ships allows for regular evaluation of ship operating profiles and hence cyclic consumption. Engine component Group A life is occasionally recalculated on the basis of the operating profiles gained from the LCFC but due to the consequences of a low cycle fatigue failure (such as a disc failure) it is the MOU's policy to tread very warily and conservatively in this area.

Modification Embodiment. One of the first modifications adopted on the Olympus engine was the installation of endoscope inspection ports to allow internal examination without an engine removal and strip. Endoscope inspection is the primary weapon in extending engine life, based increasingly on condition. This has led to the MOU departing from OEM engine release lives (Table 1). However, the MOU is currently pursuing a life assessment program with the OEM to formally extend the engines release life to that achieved by the MOU Navies.

In the early years of running, as OEM and operator experience grew and novel/unforeseen failure modes became apparent, reliance on OEM and operator proposed modifications was heavy. These modifications often brought with them increases in component and thus engine life. However in the early 1980s the return on expenditure compared to gains was falling and it was decided to cease accepting engine modifications unless there was an overriding cost benefit or for safety.

Interval Between Overhaul Extensions. Operating experience showed that there were significant variations in achieved engine and component life between the same engine type fitted in the same class of ships as well as between different classes and types of ship. Components were declared (against OEM standards) as unserviceable well before and in some cases well after declared life. The declared life of an engine therefore needs to be a sensible compromise. The compromise is the balance of achieving the maximum possible running hours against maintaining high availability.

The reason for vastly differing achieved life was found to be in part due to a combination of fuel, fuel system quality, engine husbandry (especially that of the intake/filtration system) and varying operating profiles. Newer classes of ships were fitted with improved fuel cleaning systems, better air intake filtration systems and ships' staff were educated to give them a better understanding of the need for good husbandry and maintenance of gas turbines and their associated systems. Combined with improved hot end barrier coatings, these measures dramatically improved the premature failure of engines caused by corrosion, induced by salt borne contaminates and fluxing sulphidation at the hot sections.

Modular Benefits. The Olympus and Tyne engines are 1960s vintage aero derivatives and as such are non-modular. The Spey engine is 1970s modular build which needs an overhaul line to break the engine into its six Maintenance Assembly Change Units (MACU).

Engine and Module Provisioning. A modular engine enables the support structure to be targeted at the more vulnerable hot end sections thus reducing procurement costs. Being able to break an engine into separate parts has many benefits and a major one is the reduced costs of engine repair. To illustrate, the average cost of an Olympus repair has been £200K with a turn around time of 3 to 4 months. With the Spey engine, 2 MACUs on average require refurbishment each engine failure which gives a cost of £40K for the strip and 2× £40K for the MACU repair. By breaking the

Table 2 How Olympus and Spey were provisioned for and how Spey and WR21 should be provisioned for (based on a 40 Gas Turbine fleet)

	Non Modular (ie Olympus)	1st Generation Modular (ie Spey)	What We Should Have Done Spey	Fully Modular (ie WR21)
Spares Stock Level	8 x Engines	6 x Engines + 31 x MACU	3 x Engines + 18 x MACU	0 x Engines 18 x MACU
Minimum Holding (War Stock)	3 x Engines	3 x Engines + 7 x MACU	2 x Engines + 6 x MACU	0 x Engines 7 x MACU
Total Engines	8 + 40	15 + 40	9 + 40	4 + 40

engine and exchanging the damaged MACUs for serviceable ones a turn around time of 1 month for the engine is possible. The damaged MACUs can then be repaired at comparative leisure.

Spey engine procurement was based on the experience of non modular Olympus and Tyne engines (Table 2). Using this previous experience failed to anticipate the benefits of a modular engine and to realize the large potential for life extension which resulted in significant over provisioning.

Measuring Success

The MOU and RN use a variety of indicators to measure the performance of engine support. The most useful ones to demonstrate the effects of life extension programmes are the Premature Removal Rate (PRR) and the Demonstrated Mean Achieved Life (DMAL). The PRR is the quotient of the total number of gas turbine failures to total engine hours run (expressed as per 10,000 h). The DMAL is the quotient of the total hours run by engines that have been removed (i.e., life expired or failed engines) to the total number of engines removed over a 12 month rolling average. These indicators are generally moving in the right direction showing the tangible returns on expenditure (Fig. 1).

The rise in Olympus PRR in the early 1990s were due to two failure modes: High Cycle Fatigue failures of turbine blades and Starter Drive Bracket Cracking. These problems were addressed by a calibrated burner campaign and a soft start modification which showed results from the mid 1990s (Fig. 2).

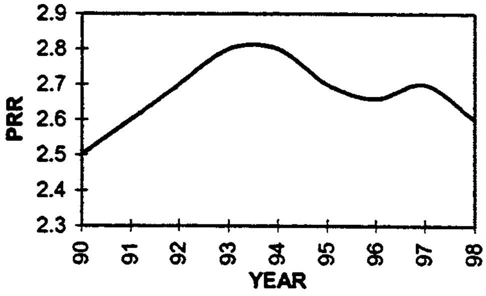

Fig. 1 Olympus premature removal rate

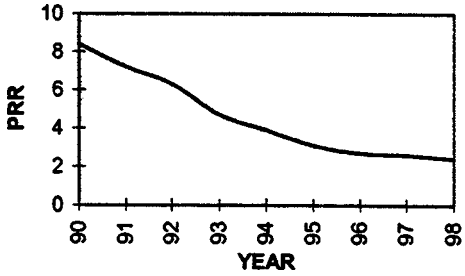

Fig. 2 Spey premature removal rate

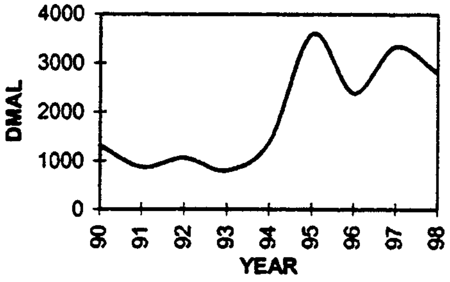

Fig. 3 Olympus demonstrated mean achieved life

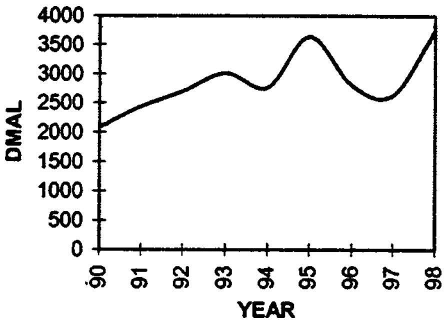

Fig. 4 Spey demonstrated mean achieved life

Since the Spey's introduction in the late 1980s the PRR has improved year on year as early novel failures were overcome and investment into extending engine life paid off (Fig. 3).

The Olympus DMAL is slowly increasing year on year. The peaks and troughs tend to be caused by the Olympus engines on the Aircraft Carriers (which can accumulate 10 times more running hours than a frigate) achieving high life engines and on other occasions suffering early failures (Fig. 4).

The Spey engines DMAL is very sensitive to single events because of the comparatively low hours run but is improving as hours run and number of engines in service increase.

Gas Turbine Progress—Lessons of the Past With an Eye to the Future

With almost 30 years of gas turbine operation experience and with current in service engine aero parents are being phased out, the Royal Navy is at a point where there is a need for another step change. This policy, termed The Royal Navy Marine Engineering Development Strategy (MEDS) is to adopt emerging technology that will give lower through-life cost and comply with future legislation without detriment to the operational capability of the warship. To meet the strategy, the criteria for modern prime movers are as follows:

- meet future emissions legislation to ensure RN ships are welcome in all foreign ports
- low at-sea maintenance requirement and therefore reduced manpower
- high reliability and availability
- high fuel efficiency at part loads as well as full power
- minimum total life cycle costs
- high power density

It has been recognized that to achieve this strategy, if gas turbines are to be used, they must be diesel beaters in terms of physical dimensions and through-life maintenance costs and have good part and full load efficiencies. It is only the advanced cycle gas turbines that can achieve the necessary thermal efficiencies and these have to be fully modular if lessons learned in supporting Spey and Olympus are to be employed. The advanced cycle gas turbine is the cornerstone of the MEDS and thus the Royal Navy has returned, albeit with modern technology, to the intercooled and recuperative technology last used in the 1950s in HMS Gray Goose (Fig. 5).

As the cost of designing and developing an aero or industrial marine or industrial gas turbine from concept onwards is ever increasing, the Royal Navy is in collaboration with the US Navy and the French Navy in the development of the WR21 Intercooled Recuperated gas turbine. The WR21 offers the RN the following:

- improved availability using the lessons learned from the aero world where down time is prohibitive in cost and sales

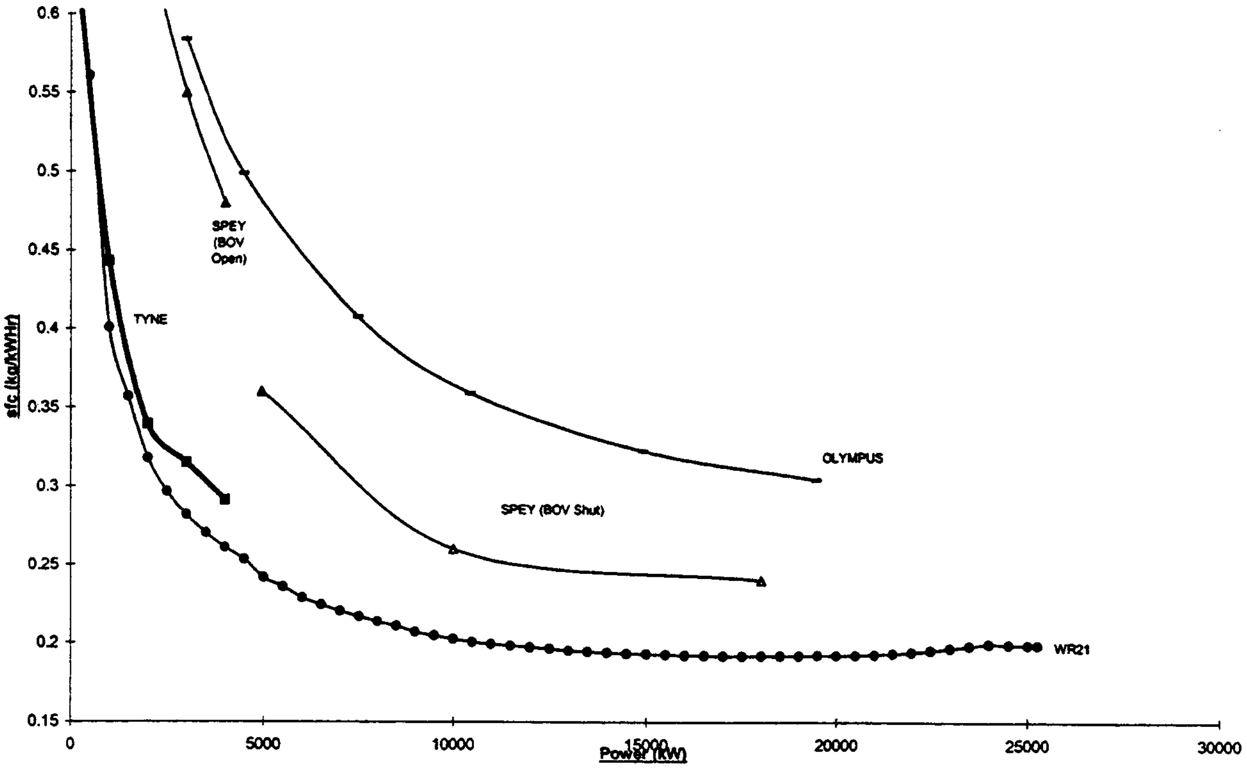

Fig. 5 WR21's near flat specific fuel consumption curves compared to current in service engines

- reduced Unit Production Costs (UPC) with the ability to replace two engines (Cruise/Boost) with one
- reduced through-life cost and the use of a second generation modular gas turbine
- the ability to drive the ship farther, or faster or stay on station for longer for a given fuel capacity
- the prime mover for a high powered gas turbine alternator for an integrated full electric propulsion plant

At present the electrical generation on board RN vessels is conducted by diesel generators. These have been inherently costly in maintenance and will not meet future emission legislation without additional complexity. To overcome this the RN are currently negotiating a MOU with France and The Netherlands for the development of a 1–2MW advanced cycle gas turbine alternator (1–2MW GTA).

The development of the WR21 has enabled a nearly flat SFC curve to be achieved from 24.5 MW to 4 MW, and the 1–2MW GTA is planned to produce a flat SFC curve at the lowest powers. Thus due to different sizes of ship and the need to optimize efficiency and operating cost over their operating spectra, there is a need to complete the family with a mid size engine to fill the 2 to 7 MW power range. The provision of the small, medium, and large (WR21) gas turbine will enable a flat SFC to be achieved for any size of vessel from minesweepers to aircraft carries and fleet support vessels. The selection of engine to meet the small and mid power requirement has yet to be made.

It is not just the change to gas turbines that will meet the MEDS, but it is their use within an Integrated Full Electric Propulsion (IFEP) plant that will ensure maximum savings to be accrued. IFEP enables a single prime mover to meet both propulsive and hotel loads and thus has the following benefits:

- reduced number of prime movers and therefore UPC
- increased availability of electrical and propulsion power
- reduced maintenance
- reduced fuel burn
- increased survivability

Studies have been undertaken to determine the number and size of gas turbines required for the All Electric Ship Architecture (Fig. 6), the objective being for the entire future fleet to run on a single family of advanced cycle gas turbine alternators. The studies undertaken used typical destroyer, frigate and carrier displacements and operating profiles, including electrical loading and propulsion power and showed the optimum family of prime movers would be a WR21 at 24.5 MW, a 5–7 MW and 1–2 MW gas turbine alternator. The 5–7 MW provides cruising power for frigates or destroyers whilst the 1–2 MW provides harbour load or low speed operation (towed array) and acts as an emergency ''get you home'' power plant. A destroyer/frigate is likely to need two WR21 sized engines to achieve its top speed of 30 knots, whilst a carrier will require between 4 and 8 WR21s for top speed operation and a 5–7 MW machine to provide low speed and hotel electrical load. The 1–2 MW GTA also provides the opportunity to consider retro-fit into Type 23 Frigates and the use of the engine in mine hunter sized ships.

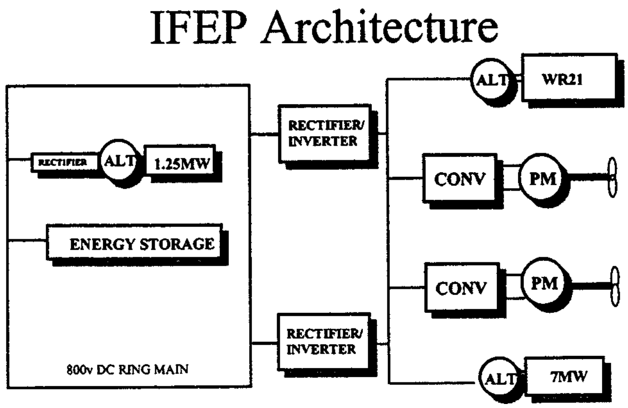

Fig. 6 Typical integrated full electric propulsion architecture

Summary

Past and Present. Many valuable lessons have been learned from past engine development and operation which will be borne in mind for future engine development.

- The benefits of a modular engine are fast repair times, reduced repair costs and greater ship availability.
- Early commitment to the full engine/spares requirement may result in over provisioning. Procure equipment in stages to gain a good understanding of engine and component usage.
- In house teams of specialist engine inspectors can build up a good knowledge base and help drive life extension policy.

The Future. For a single Navy the high development costs of gas turbine alternators do not give a significant reduction in through life costs based on comparison with present simple cycle gas turbines. However, a step change in ship propulsion is needed to give lower through life costs and comply with future environmental legislation without detriment to operational capabilities. Therefore, partnership with industry and other governments is seen as the vehicle to gain the operational benefits at an affordable development cost. To this end future Royal Naval propulsion is being directed towards an All Electric Ship Architecture and key development areas of this program are as follows:

- high speed alternators to allow direct drive without a gearbox
- recuperated cycles to gain the best compromise between power density and economy for ship fit
- a family of three gas turbine alternators to give a near flat SFC for all future platforms in the All Electric Ship Architecture

Conclusions

- The future of Royal Naval ship propulsion is seen in terms of gas turbine alternators in an All Electric Ship Architecture.
- Due to the high development costs industry and other governments will need to co-operate if the required lower through life costs are to be realised. This co-operation with industry may see the present Royal Naval reliance on aero derivative engines for low powers wane.
- A comprehensive understanding of the procurement and life management of the Olympus, Tyne and Spey engines will enable the in service introduction of future gas turbines to be made with minimum pain.

Finally ‘‘The views expressed are those of the authors and do not necessarily represent those of HM Government.’’

Bibliography

Bowers, N. K., 1966, ‘‘Gas Turbines in the Royal Navy,’’ J. Naval Eng., **16**, No. 2.

Morgan, S. J., Lamport, A. W., and Smith, A. J. R., 1970, ‘‘Gas Turbines in the Royal Navy,’’ J. Naval Eng., **19**, No. 1.

Sherwin, D. J., 1973, ‘‘Some Thoughts on the Reliability of Gas Turbines for Warship Propulsion,’’ J. Naval Eng., **21**, No. 1.

Shaw, T. R., 1974, ‘‘Gas Turbines in the Royal Navy, 1970 to 1973,’’ J. Naval Eng., **21**, No. 3.

O’Hara, D., 1975, ‘‘Shore Testing of Gas Turbine Ship Propulsion Machinery,’’ J. Naval Eng., **22**, No. 2.

Pearson, A. D., 1984, ‘‘Gas Turbine Life—Influence on Ship Design and Operation,’’ J. Naval Eng., **28**, No. 3.

Experimental Investigation of Adaptive Control Applied to HSFD Supported Rotors

A. El-Shafei

M. El-Hakim

Department of Mechanical Design
and Production,
Faculty of Engineering,
Cairo University, Giza,
Egypt 12316

This paper describes the experimental application of adaptive control to Hybrid Squeeze Film Damper (HSFD) supported rotors. The HSFD has been shown to be an adaptive damper capable of providing infinite damper configurations between short and long damper configurations. Previously, theoretical investigations of the adaptive control of HSFD concentrated on the development of the model reference adaptive control (MRAC) method, as well as development of a nonlinear reference model. Simulations of the performance of the adaptive controller during run-up and coast-down indicated the superior performance of the adaptive controller. In this paper, the adaptive controller is tested on a multi-mode rotor. A test rig is designed and developed using computer control. A simple reference model is investigated consisting of a second order system. Three forms for adaptation gain are studied. The results of the experimental investigation illustrated the performance capabilities of the adaptive controller applied to the HSFD, and moreover indicated the possibility of simple design for the adaptive controller.
[S0742-4795(00)01603-3]

Introduction

The need for active vibration control of rotors has been established in the last few years. It is particularly desirable to increase rotor speed beyond several criticals and simultaneously minimize the rotor vibration and ensure the engine's proper operation in adverse conditions. Actually, magnetic bearings have found their place in the market, as possible active rotor supports. However, for aircraft engines, several complications arise with magnetic bearings that preclude their use in the foreseeable future. The details of the reasons for such a conclusion are beyond the scope of the current paper; however, this conclusion illustrates the need for the development of more reliable control devices for aircraft engines. This paper is thus concerned with the development of the Hybrid Squeeze Film Damper (HSFD) as an active control device for rotor vibration.

Squeeze film dampers (SFDs) have been used successfully for the last thirty years to passively damp rotating machinery, in particular aircraft engines [1–3]. They provide the primary source of damping in aircraft engines since the rolling element bearings on which these engines are mounted provide very little damping. Because of their reliability, it seems natural to develop SFDs to actively control rotor vibrations. Burrows et al. [4] investigated the possibility of controlling rotating machinery vibration by controlling the pressure in a SFD, and they point out that control of rotors using active SFDs is much cheaper than using magnetic bearings, and is more simple and reliable. Adams and Zahloul [5] studied the control of rotors by controlling the pressure in hydrostatic SFDs. Mu et al. [6] proposed an active SFD by using a movable conical damper ring. El-Shafei [7,8] proposed using Hybrid Squeeze Film Dampers (HSFDs) for active vibration control of rotors. The basic idea is to control the flow in the SFD through movable end seals, thus achieving the ability to change the damper from a short damper to a long damper and vice versa. If the sealing is tight then circumferential flow occurs in the damper, and the long damper is approached, which provides much more damping. If the sealing becomes near open-ended then the flow is axial and the short damper is approached which provides less damping. The performance of HSFDs was verified experimentally, and it was shown that the HSFDs are effective in controlling the amplitude of rotor vibrations and in reducing the force transmitted to the support. Also it was shown that the hybrid damper is much more effective in controlling rotor vibrations than the previous strategies of controlling the pressure in a conventional squeeze film damper.

Later, El-Shafei and Hathout [9] developed a complete mathematical model of the HSFD rotor system for an automatically controlled system. Simulations of the behavior of the open-loop system were presented, and an on-off control algorithm based on the feedback of rotor speed was proposed and was shown by the simulation results to be quite effective in controlling the rotor vibrations. The transient and steady state simulations of the closed-loop system revealed an overall improved behavior of the rotor system, implying that the automatically controlled HSFD can be a very useful device for the active control of rotors.

The success of the HSFD incited several investigations of its control strategies. Hathout and El-Shafei [10] investigated the adaptive control of HSFDs using model reference adaptive control (MRAC) strategy. They later studied the PI control of HSFDs [11]. Also Hathout et al. [12] investigated the on-off control of multi-mode rotors supported on HSFDs.

Experimentally, the authors have developed a computer-controlled test rig [13], have automated the HSFD hydraulic circuit, have statically tested the HSFD, and have experimentally investigated the on-off control of the HSFD.

In this paper, the adaptive control algorithm is applied to the HSFD. The test rig has been modified to accommodate a multi-mode rotor. An MRAC adaptive controller is designed and applied to the computer controlled test rig. A simple reference model is investigated consisting of a second order system. Three forms of adaptation gain are studied. The results illustrate the capabilities of the MRAC controller in controlling HSFD supported rotors, and indicate the possibility of simple design of the adaptive controller.

The Hybrid Squeeze Film Damper

Figure 1 shows a cut-out of the HSFD. Two movable sealing rings (4) with sliding fit both to the end caps and to the housing,

---

Contributed by the International Gas Turbine Institute (IGTI) of THE AMERICAN SOCIETY OF MECHANICAL ENGINEERS for publication in the ASME JOURNAL OF ENGINEERING FOR GAS TURBINES AND POWER. Paper presented at the International Gas Turbine and Aeroengine Congress and Exhibition, Indianapolis, IN, June 7–10, 1999; ASME Paper 99-GT-176. Manuscript received by IGTI March 9, 1999; final revision received by the ASME Headquarters May 15, 2000. Associate Technical Editor: D. Wisler.

one on each end of the damper are used as shown in Fig. 1. The principle of the seals' operation is simple. The damper oil film and the hydraulically actuated seals are supplied from independently variable sources. In order for the damper to operate as a long damper, the pressure to the seal chambers (12) is elevated above the internal pressure of the damper (5). The seal rings (4) will move in axially and seal the oil film inside the damper clearance. In order to return to the short damper configuration, the seal pressure is lowered until it is less than the internal pressure of the damper. This causes the seal rings (4) to return to their original positions.

It may be required to locate the sealing rings in intermediate positions, other than those for the short or long dampers, to provide for the required rotor control. Thus the sealing rings are connected to springs that would act to restrain their motion versus the applied pressure in the sealing chambers. As illustrated by the computer simulations of the system [14], this is quite an effective method of controlling the position of the sealing rings. To physically incorporate the springs in the design of the HSFD, 3 measuring rods (6) were connected to each sealing ring, and would protrude through the sealing chambers and the end caps, as shown in Fig. 1. Springs, resting on the surfaces of the end caps, can be connected to the measuring rods to provide spring action restraining the motion of the sealing rings versus the applied pressure in the sealing chamber. The measuring rods have an additional benefit, they could be directly connected to a position transducer (e.g., an LVDT) to accurately measure the position of the sealing rings.

The spring rods (10) shown in Fig. 1 allow for centering the journal in the damper, in addition to preventing the damper from rotation. The centering spring action provided by the spring rods (10) can be an important factor in the dynamics of the rotor bearing system [15].

The oil feed to the damper is provided by three feed holes distributed circumferentially at the center of the damper. The damper oil drain in the short damper mode is through the end caps. No damper drain is required in the long damper mode. The oil port for the seal chambers is located on the extended housing. This is the port connecting the seal chambers with the pressure control proportional valve (PPCV). This port provides for both the feed and drain to the seal chamber and is the only port required.

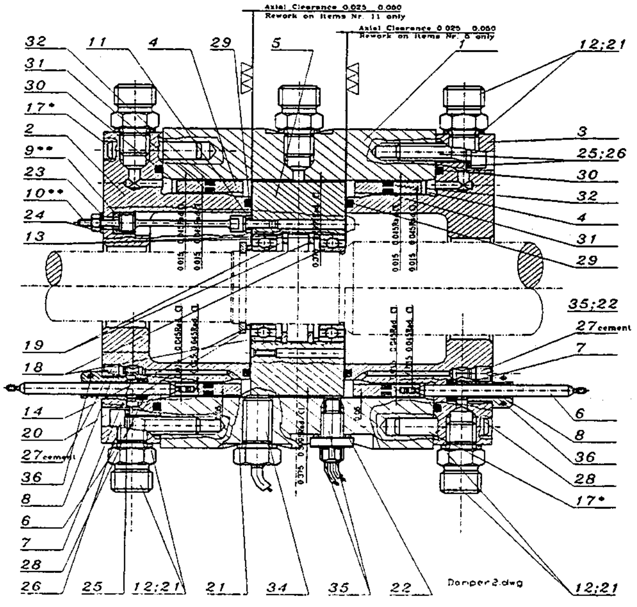

Fig. 1 Cut-out of manufactured HSFD

Test Rotor

The design criteria for the test rotor were set as follows:

1 three critical speeds to be attained in speed range
2 speed range to be up to 15,000 rpm
3 the HSFD to be located at a point of high modal activity

The results of the extensive design effort [16] is illustrated in Fig. 2, where a three mass rotor is selected. The three mass rotor exhibits three critical speeds at 3260 rpm, 5707 rpm, and 11,282 rpm. These critical speeds, as shown in Fig. 2, can be classified as bouncing mode, conical mode, and first bending mode, respectively.

Moreover, all three modes exhibit significant modal activity at the bearing location thus allowing the HSFD to adequately control all three modes. The first two modes can be classified as rigid modes, where most of the deflection (and thus potential energy) occurs in the support, while the third mode represents a flexible mode, where most of the deflection (and thus potential energy) occurs in the shaft.

Figure 3 shows the set-up of the test rotor. A universal motor drives the rotor through a 2:1 belt drive. Two HSFDs, termed D1 and D2 are supporting the rotor. The rotor is 985 mm long and weighs 13 kg. The measurement locations of the rotor vibration are also indicated in Fig. 3.

The HSFDs shown in the test rig of Fig. 3, have the same cut-out as shown in Fig. 1. The dimensions of the dampers are: clearance $c=750\,\mu$m, length $L=7.5$ mm, and radius $R=37.5$ mm. The oil chosen for the test rig is Shell Tellus 46 with viscosity $\mu=0.014$ Ns/m^2 at 70°C and oil density $\rho=875$ kg/m^3.

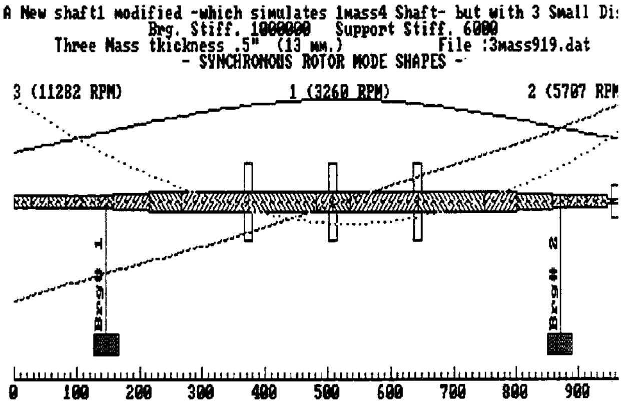

Fig. 2 The test rotor and its mode shapes

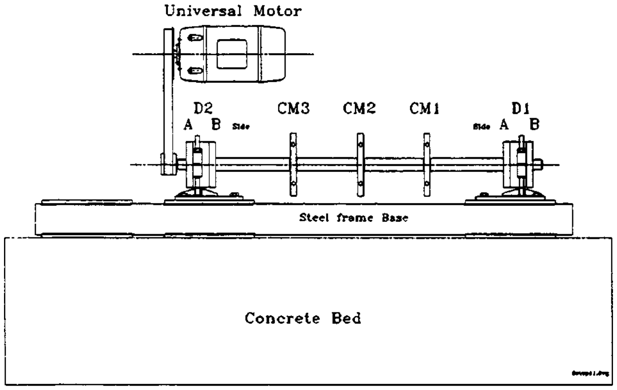

Fig. 3 Setup of test rotor

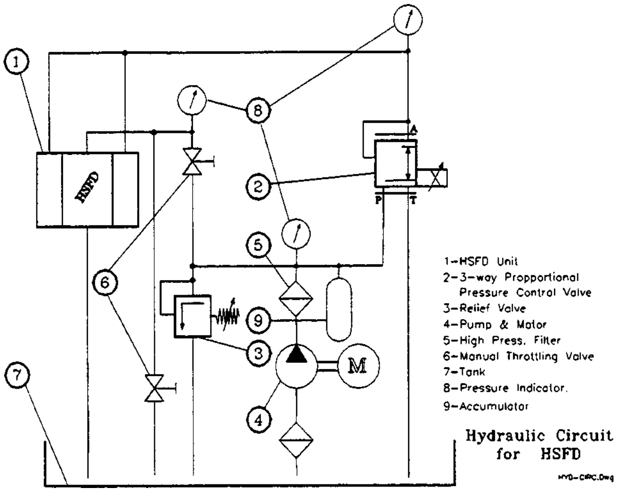

Fig. 4 Automated hydraulic circuit

HSFD Hydraulic Control Circuit

Figure 4 shows the automated hydraulic circuit used to control the HSFD. A three-way proportional pressure control valve (PPCV) 2 is used to control the pressure in the sealing chambers. The control valve is normally closed; however, when it receives a current signal, it connects the supply line, through an orifice, to the sealing chamber, thus increasing the pressure in the sealing chamber. If, on the other hand, a reduction in pressure is required, the PPCV connects the drain, also through an orifice, to the sealing chamber, thus reducing the pressure in the sealing chamber. When the required pressure is achieved the valve is closed.

The pressure control valve was chosen over the more common flow control servovalve, since the associated hydraulic circuit is simpler in this particular application, and in addition continuous flow would be required to maintain a constant pressure with the flow control valve which is an unnecessary energy loss.

Several important features of the automated hydraulic circuit of Fig. 4 need to be discussed. Firstly, the supply to the damper is direct, only a manual throttling valve was added to the circuit to reduce the supply pressure to that required by the damper. The damper drain is also through a needle valve as before. Secondly, the sealing chamber, in this design, has only one port. This port is used to both supply and drain the sealing chamber. Thirdly, the pressure control valve is the only component required to control the pressure in the sealing chambers. The feed and drain of the seal chamber is provided through the pressure control valve. This simple design of the automated pressure control circuit provides for an efficient control loop. Moreover, because of the current control of the valve, it can be easily interfaced to a computer to provide computer control.

Complete Computer-Controlled Test Rig

Figure 5 shows the complete computer controlled test rig. The test rig consists of the rotor of Fig. 2 supported on two HSFDs as shown in Fig. 3 driven by a high speed Universal motor through a belt drive. The oil feed and drain into and out of the dampers were controlled by the hydraulic circuit of Fig. 4. The hydraulic circuit was controlled by the pressure control valve signal which is generated from the computer.

The computer was an IBM compatible PC with 16 MB Ram and 2.1 GB hard disk. Two cards are installed into the computer. A GPIB card based on the IEEE 488.2 standard is used to control the instruments in the test rig. The other card is a 16 channel 12-bit data acquisition card with two channel control used for measurement and control. Both cards are from National Instruments.

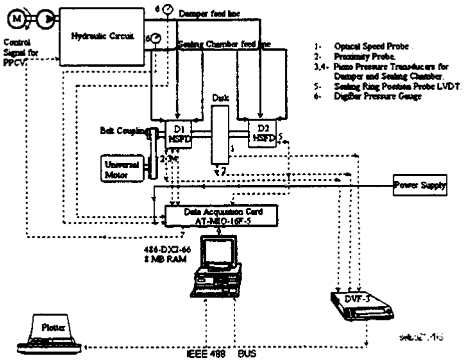

Fig. 5 Computer controlled test rig

The GPIB card is a National Instruments PC II/IIA, and was used to control and acquire data from the Bently Nevada DVF-3 tracking filter and the Brüel and Kjær 2033 single channel spectrum analyzer. The DVF-3 is a two channel tracking filter to which the signal from two of the proximity probes are routed and filtered according to the speed of the shaft, which was also fed into the DVF-3 by another proximity probe monitoring a key-way. The spectrum analyzer was used to view both the time and frequency domain signals from the pressure transducers, or the acceleration signal measured on the damper housing. Both the DVF-3 and the B&K 2033 could either download the data into the computer or directly onto a plotter. Two plotters were available: a Tektronix HC-100 and a Brüel and Kjær 2308.

The data acquisition card is a National Instruments AT-MIO-16F-5 card with 200 KHz sampling rate. The card is 16 channels Analog-to-Digital conversions for data acquisition and 2 channels Digital-to-Analog conversions for control. All channels are 12-bit. Both the GPIB and data acquisition and control cards were controlled by the National Instruments LabView software, which is a versatile and powerful software system that is capable of performing a wealth of functions including a variety of signal processing functions.

In addition to the proximity probe monitoring the key-way for speed information, each of the HSFDs and the central disk are monitored by two proximity probes each, 90 deg apart, for a total of seven eddy current proximity probes (Bently Nevada series 7200, 5 mm) monitoring the rotor. The proximity probes within the dampers were located in a very tight space. In order to avoid interference from adjacent material, and to reduce the possibility of disturbing the flow within the damper, a Teflon adapter was manufactured to isolate the probes and allowing them only to view the journal motion. Figure 6 shows a photograph of the test rig and the instrumentation used.

Fig. 6 Test rig and its instrumentation

Each of the dampers is monitored by two Kulite XT-190 pressure transducers for monitoring the dynamic pressure in the damper and the pressure in the sealing chambers. These signals were either fed to the spectrum analyzer or directly to the computer or both. The hydraulic circuit lines were also monitored by Digital Pressure Gages HBM Digibar type PE200/20 bar and are also fed into the computer. In addition, two thermocouples were inserted within the HSFD to monitor the temperature in the damper, both for viscosity determination and for possible use in feedback.

Uncertainity Analysis

The uncertainity in the proximity probes as provided by the manufacturer is -0.25 percent, while the uncertainity in the DVF3, also as provided by the manufacturer is -0.0008 percent for speed, and -2.4 percent for amplitude. The computer receives a digital signal from the DVF3. A simple calculation reveals that the total uncertainity in the speed measurements is only within 0.35 percent, while the total uncertainity in the amplitude is less than 2.5 percent. These figures are quite acceptable. However, it should be noted that, since we have a closed loop system, the uncertainity in measurement is not as critical as in other experimental exercises.

Critical Speed Testing

Critical speed testing is important before the application of the control algorithms because of the need to verify the behavior of the test rig before controlling it. The procedure for critical speed testing was to run-up the rotor at above the third critical speed, and to manually remove the belt using a special tool, and to collect data (two channels at a time) using the tracking filter DVF3 during coast-down.

The results of the critical speed testing are illustrated in Table 1. The tests were repeatedly performed and the results indicated consistent repeatability of the critical speed data. Analysis of the coast-down data indicate that the critical speeds occur at 2950 rpm, 5400 rpm, and 11,000 rpm. Table 1 represents a comparison between the theoretical critical speed data obtained from the CRITSPD program, and the experimental critical speed data. Acceptable agreement is observed, and this experimental verification confirmed the suitability of the design of the rotor shown in Fig. 2, for the application of the HSFD.

The open-loop system consists of the control valve, the HSFD and the rotor. The system functions as follows: first a volt is chosen from the PC controller and is supplied to the valve conditioning board. The board in turn supplies a current *i* which actuates the valve to output a controlled pressure *p* in the sealing chamber. The amount of pressure *p* positions the sealing ring between the short and long modes, and hence controls the amount of damping supplied to the rotor. Figure 7 shows the block diagram of the open-loop system. This is considered as the plant for the control development.

In the experimental set-up there is a sensor for measuring the vibration amplitude of the output variable to be controlled. In addition, in the work of Hathout et al. [12] it became evident that the feedback on eccentricity is enough for controlling the system and achieving the required objectives. Thus the presented control algorithm aims at damping the vibration amplitude through the feedback of the eccentricity *e*.

Table 1 Comparison between design and experimental critical speeds of new test rotor

Critical Speed	Design Value (RPM)	Experimental Value (RPM)	Difference %
1st Critical	3260	2950	9.5 %
2nd Critical	5707	5400	5.4 %
3rd Critical	11282	11000	2.5 %

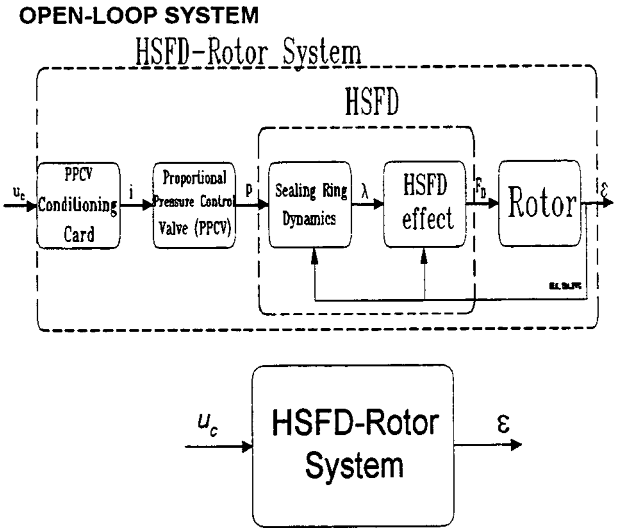

Fig. 7 Block diagram of open-loop system

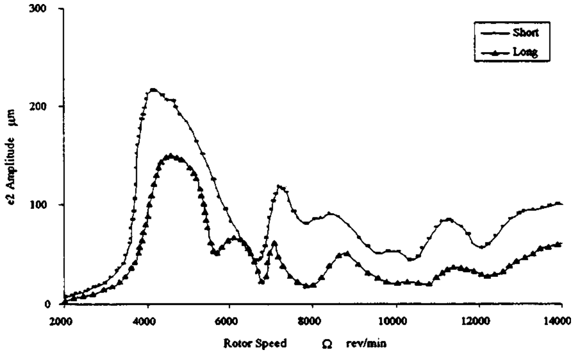

Fig. 8 Short and long modes for the open-loop system

Figure 8 shows the open-loop testing of the test rig in a coast-down test. Two curves are presented: one in the short damper mode where the pressure in the sealing chamber is minimum, and the other in the long damper mode, where the pressure in the sealing chamber is maximum. These tests illustrate the limits of the control of the HSFD on the rotor test rig. That is, any control effort can only locate the rotor in between the two limits illustrated in Fig. 8. The purpose of the controller is to try to reduce the amplitude of vibration along the rotor, and simultaneously reduce the force transmitted to the support. The long bearing consistently shows smaller vibrations at the damper, but this is not necessarily the optimum damping value. Actually, the short bearing also consistently shows smaller vibrations at the center location. This implies that the least deflection occurs with the short bearing. Moreover, the theoretical and experimental results of El-Shafei [8] indicate that the forces are much smaller in the short damper case. However, the long bearing provides much more damping that can be quite useful in crossing critical speeds and providing stability to the rotating machine. The controller thus should try to optimize the damping for varying operating objectives.

Model Reference Adaptive Controller (MRAC)

Adaptive control has a unique feature that distinguishes it from constant linear feedback control. An adaptive controller is usually composed of a controller and an adaptation mechanism. The adaptation mechanism is continuously updating the controller gains or parameters such that a specific performance criterion is maintained or achieved. As a result, the controller is able to perform in a wide range of operating conditions for which a constant gain controller either is unstable or does not perform satisfactorily. Another feature of adaptive control encouraged its application for the rotor system is that it can perform quite exceptionally even when the dynamic model parameters of the plant to be controlled are partially known. This is particularly true for the rotor system, since extensive identification is required to construct the full accurate dynamic model.

The principal of operation of the Model Reference Adaptive Control (MRAC) is that a reference model having the same order and structure of the plant is designed to achieve the desired performance. The adaptation mechanism compares the difference between the output of the plant and the output of the reference model then computes and updates the controller parameters in such a way that in the steady state the regulation error approaches zero. In other words, the output of the controller plant can track the output of the reference model.

Design of the MRAC for the Rotor System

The complete MRAC strategy is based on the basic structure shown in Fig. 9. The output is chosen to be the amplitude of vibration at the bearing center. The desired performance is expressed in terms of the reference model. The three fundamental components that constitute the MRAC are the linear controller, the reference model, and the adaptation mechanism. Once these three components are designed then the MRAC can be tested.

The Controller. The controller is a simple proportional controller that aims at positioning the sealing ring infinitely between the short and long damper mode positions such that the vibration amplitude is regulated to the reference input. The controller is given by

$$u = K_p e, \tag{1}$$

where K_p is a varying proportional gain. This proportional gain is updated according to the adaptation mechanism. The reason a proportional controller is chosen to be the linear regulator is its simplicity and the remarkable enhancement the nonlinear proportional controller achieved over the constant proportional controller. According to the analysis of the proportional controller and the definition of the model reference adaptive controller, one expects that the MRAC is continuously changing the dynamics of the system by changing the proportional gain. Thus, the closed loop response is changing in such a way that the rotor vibration follows the reference model output.

The Reference Model. The choice and design of the reference model reflect the desired performance and the structure of the system. The basic principle that the reference model must satisfy is that it must have the same structure of the plant to be controlled. For the rotor system, the order and structure of the model is dependent on the number of modes represented. In other words, if a single mode of vibration is chosen to model the rotor resonance in a particular speed range then it is sufficient to model the rotor as a second order system. In the speed range of interest, the rotor used has three dominant resonance frequencies and a reasonable model is of order 6. However, since the amplitude of vibration of the first mode is greater than those of the second and third modes, the first mode is of more interest for the control purpose. Thus, the plant during the range containing the first mode can be approximated by a second order system. In fact, one can construct a particular second order model for each mode and the response of the system is the summation of the responses of the second order systems of all modes. Hathout and El-Shafei [10] used the full nonlinear model of the rotor system as the reference model. This is not the usual case in choosing the reference model. It is common to choose the reference model which reflects a desired performance. The reference models for the MRAC are usually linear reduced order models of the true plant. Based on the above discussion and reasoning, the reference model is chosen to be a second order linear system. It is given by

$$\frac{\varepsilon_m}{R} = \frac{\omega_v^2}{s^2 + 2\zeta\omega_v s + \omega_v^2}. \tag{2}$$

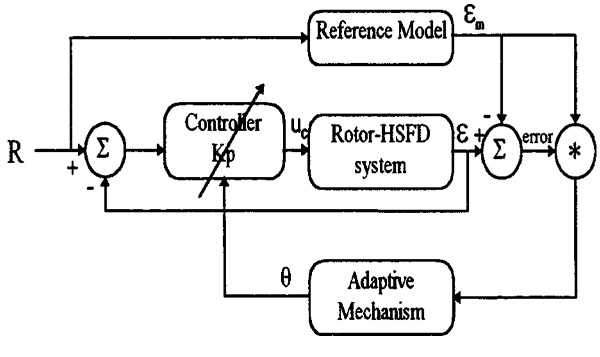

Fig. 9 Block diagram of MRAC

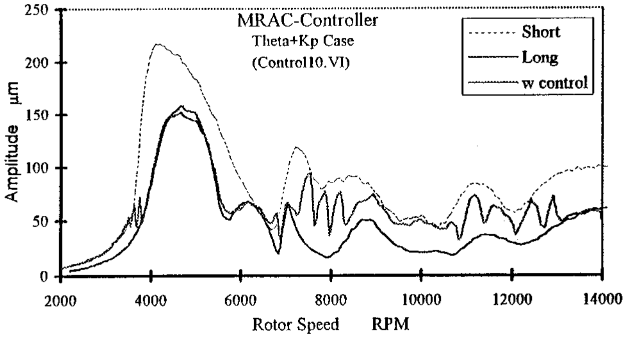

Experimental response of rotor at Damper 2 for MRAC-Controller (Theta + Kp)

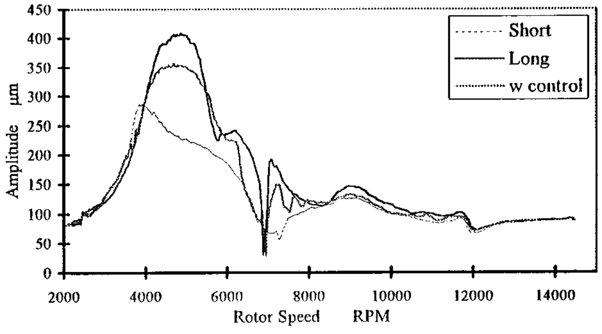

Experimental response of rotor at CM2 for MRAC-Controller (Theta + Kp)

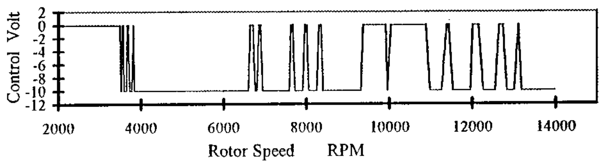

Actuating signal for MRAC-Controller Theta+Kp case

Fig. 10 Experimental results of MRAC controller (θ+Kp Case)

The damping ratio is chosen to be that of a critically damped system. The natural frequency is chosen to be equal to that of the first vibration mode of the rotor. Thus, the reference model is as fast as the first mode. In other words, the desired bandwidth is equal to the bandwidth of a system dominated by the first mode.

The Adaptation Mechanism. A simple adaptation mechanism is chosen to update the controller gain Kp. The adaptation mechanism is based on the gradient search approach that is usually called the MIT rule [17]. The final form of adaptation mechanism is given by

$$\frac{d\theta}{dt}=-\nu(\varepsilon-\varepsilon_m)\varepsilon_m, \qquad (3)$$

where θ is the adaptation parameter and ν is the adaptation gain. The MIT rule can be explained as follows: assume that the parameter θ changes much slower than the other system variables. To make the square of the error smaller, it seems reasonable to change the parameter in the direction of the negative gradient of the error. The parameter adjustment mechanism proposed by the MIT rule can be regarded as composed of a linear filter for computing the sensitivity derivative from the error between the plant and the reference model outputs, a multiplier, and an integrator. The parameter change is then introduced in the control law using a second multiplier. In addition, if the adaptive regulator is chosen such that

$$\frac{d\theta}{dt}=-\nu(\varepsilon-\varepsilon_m)\frac{\partial(\varepsilon-\varepsilon_m)}{\partial\theta},$$

and let the reference model have the transfer function $G_m(s)=\theta^\circ G(s)$, where $G(s)$ is function of the plant transfer function and the relation is through an assumed known constant θ°. Therefore, the sensitivity derivative becomes

$$\frac{d(\varepsilon-\varepsilon_m)}{d\theta}=G(s)u_c=\varepsilon_m/\theta^\circ$$

and Eq. (3) is obtained [17]. Some of the characteristics of the MIT rule stated in the literature are that the MIT rule can be successful with non-linear systems, and can be used to handle partially known systems.

Implementation and Experimental Results

The detailed MRAC is implemented in the time domain. Two main issues enabled accurate implementation of the MRAC. The first issue is related to reference model. The solution of the second order reference model to a step input is chosen to replace its function. This eases implementation and saves execution time. The output of the reference ε_m model for a step input R is given by

$$R(1-e^{-\omega_n t}(1+\omega_n t)). \qquad (4)$$

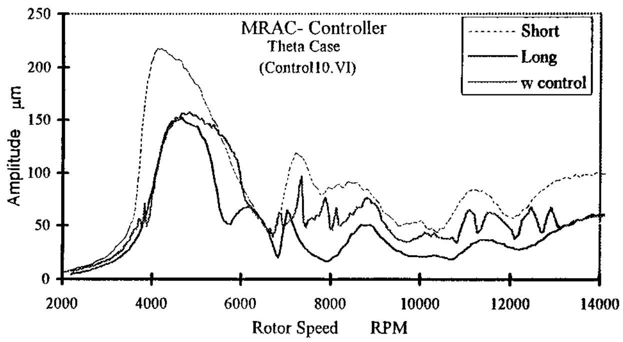

Experimental response of rotor at Damper 2 for MRAC-Controller Theta case

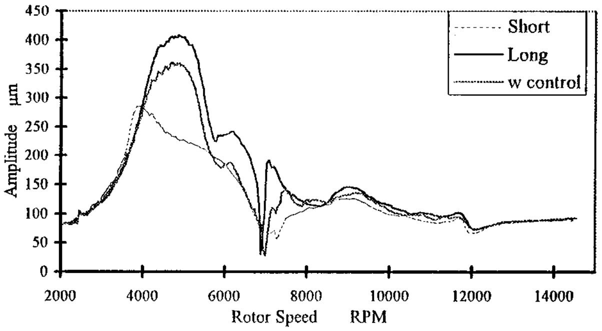

Experimental response of rotor at CM2 for MRAC-Controller Theta case

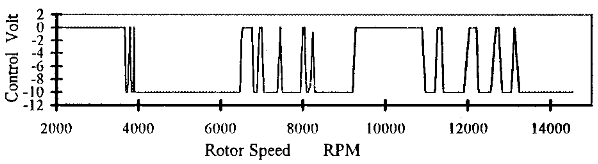

Actuating signal for MRAC-Controller Theta case

Fig. 11 Experimental results of MRAC controller (θ Case)

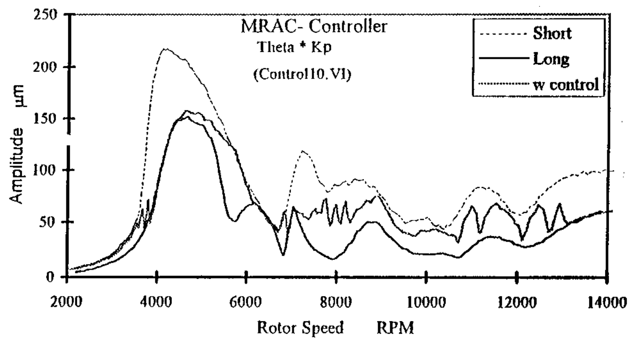

Experimental response of rotor at Damper 2 for MRAC-Controller (Theta * Kp)

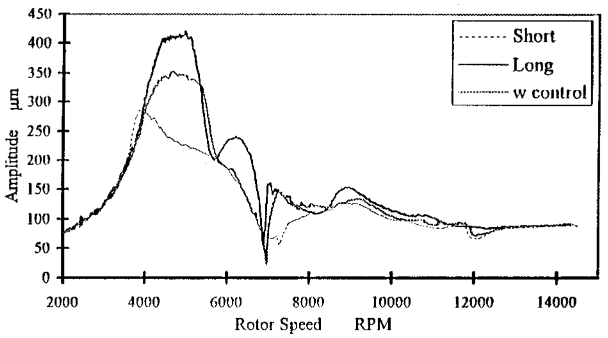

Experimental response of rotor at CM2 for MRAC-Controller (Theta * Kp)

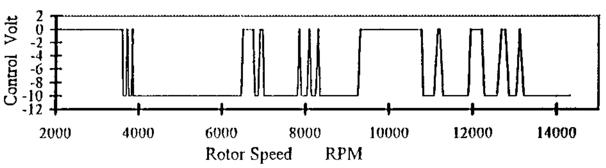

Actuating signal for MRAC-Controller Theta * Kp case

Fig. 12 Experimental results of MRAC controller (θ* Kp Case)

For the adaptation mechanism, integration of the adaptation gain is implemented using the Euler form for its simplicity. Three forms are chosen to update the controller gains once a new value is computed by the adaptation mechanism. These three forms are meant to give conservative action by relying on previously tested proportional gain. The three forms are

$$K_p = \theta \tag{5}$$

$$K_p = K_{p0} + \theta \tag{6}$$

$$K_p = K_{p0}\theta, \tag{7}$$

where K_{p0} is a fixed proportional gain. Hathout and El-Shafei [10] used the form (5). The other two forms were proposed so that the effective proportional gain is not entirely dependent on the adaptation parameter θ. This is a usual approach to avoid vast changes by the adaptation mechanism which might cause instability. In the form (6), however, the effective proportional gain is the summation of a test constant proportional controller and the adaptation gain θ. Thus in the dangerous and/or unexpected regions of operation, the controller can safely be switched to the nonadaptive mode. As a result, a previously tested valid performance can be achieved. Based on experimentation with the proportional control, a value of 0.5 gave the most satisfacting performance. The adaptation gain is tuned experimentally to a value of 0.0008. A satisfactory performance is usually obtained for the summation type (6) over the other multiplicative types (5) and (7). This is due to the fact that the summation type is less aggressive than the multiplicative types in changing the proportional gain.

The experimental results of implementing the MRAC are shown in Fig. 10 for the additive structure. It is clear from Fig. 10(*a*) that the adaptive controller succeeded in regulating the vibration amplitude at the bearing system to the reference value. Passing over the resonance, the adaptive controller preferred the short mode which results in a smaller error in this range. The response of the center mass is shown in Fig. 10(*b*). As the vibration of the center mass is not a directly controlled variable, its response is complementing the regulation of the bearing vibration. During the whole range the center mass amplitude remained between the short and long modes with less chattering than that of the bearing vibration. Investigation of the actuation signal shown in Figure 10(*c*) clearly indicates that the controller saturated the output channel in a wide range.

The experimental results of implementing the MRAC in the multiplicative structures are shown in Figs. 11 and 12, and show similar behavior to those of the additive rule. Experimentally, there is no great difference between the three forms of updating the controller gains.

In all cases, the reference input was set at 50 μm and the controller always tried to achieve the reference value at the damper location. It is clear from Figs. 10, 11, and 12 that the controller away from resonance tried to achieve the reference value of 50 μm at the damper, while it opted to the long damper mode at resonance. This is reasonable since the long damper

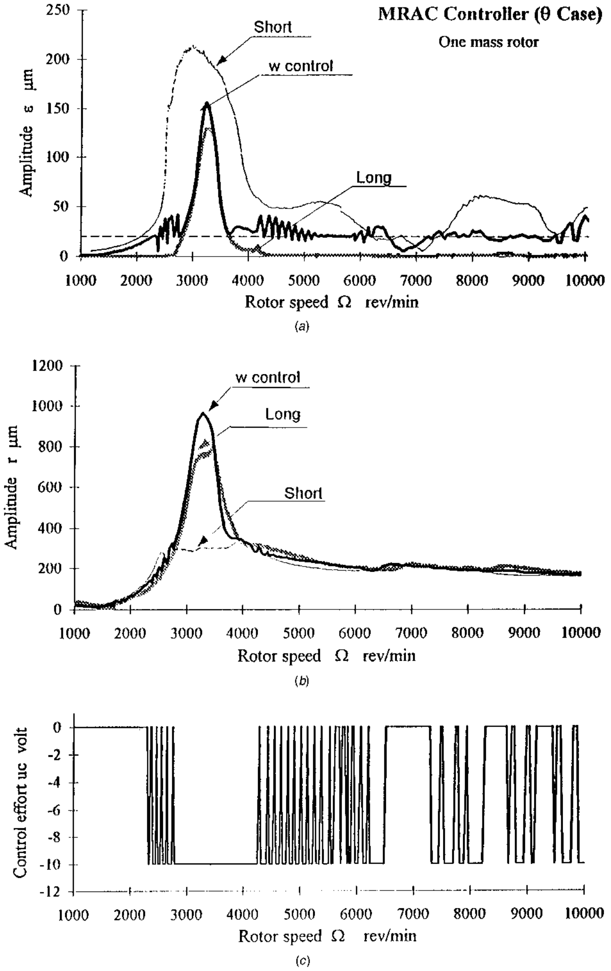

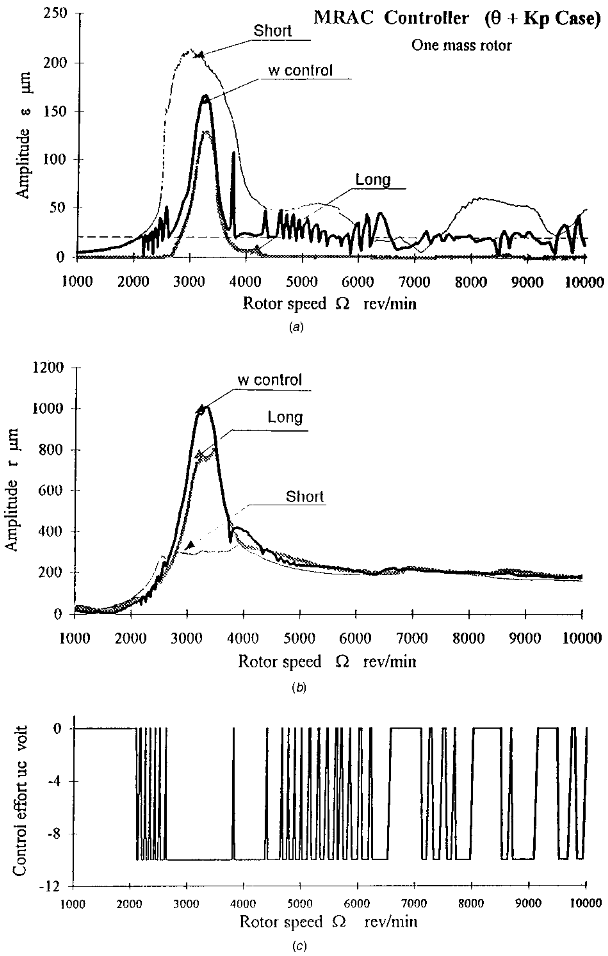

Fig. 13 Experimental results of model reference adaptive controller (*θ* case): (*a*) experimental response at D2 journal center; (*b*) experimental response at CM location; (*c*) controller actuating signal

Fig. 14 Experimental results of model reference adaptive controller (*θ*+Kp Case): (*a*) experimental response at D2 journal center; (*b*) experimental response at CM location; (*c*) controller actuating signal

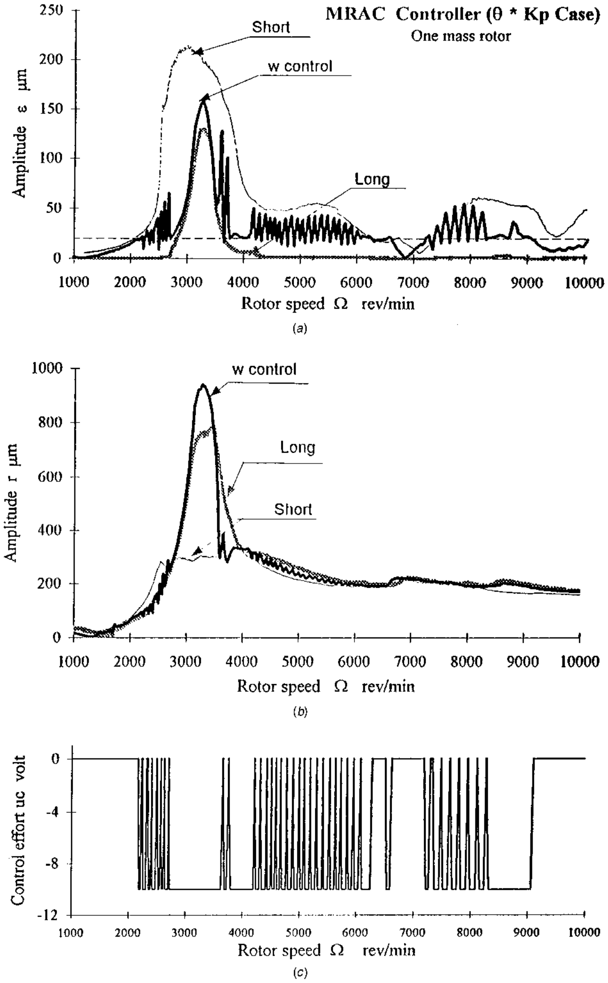

Fig. 15 Experimental results of model reference adaptive controller (*θ Kp Case): (*a*) experimental response at D2 journal center; (*b*) experimental response at CM location; (*c*) controller actuating signal**

mode provides a smaller amplitude value at the damper location at resonance. However, at the center mass the amplitude is higher for the long damper at resonance. Thus it may be foreseen that if feedback on the displacement of the center mass was used, and a reasonable reference value was chosen, then the controller would try to achieve this reference value throughout the speed range.

To complete the testing, another set of test runs was performed with a single disk rotor, for all three forms of the adaptation mechanism. In this case, the feedback also was on the damper eccentricity, but the reference value was set at 25 μm. Figures 13–15 illustrate the performance of the MRAC controller for all three forms of adaptation gain. It is clear that the controller behaved very well particularly in the multiplicative form of Eq. (5). Moreover, the controller tried to follow the reference value away from resonance and the long damper mode at resonance.

Discussion and Conclusion

The MRAC controller is one of the best suited controllers for the HSFD. The HSFD is essentially an adaptive device that changes the amount of damping provided to the rotor based on the operating conditions. The adaptive controller used this feature to try to control the rotor vibration, and was quite successful in attaining this objective. The test results illustrate the ability of the controller to follow the reference input, when possible, and to obtain the closest response to the reference input when not possible, particularly at resonance where the controller opted for the long damper mode.

Hathout and El-Shafei [10] used a nonlinear reference model in their simulations of the adaptive controller. However, in this experimental work, it became apparent that this is an unnecessary complication, and the tests were performed with an easily implementable second order reference model. The tests indicated that this simple reference model was adequate and performed very well.

One last point, Hathout and El-Shafei [10] were able to demonstrate the ability of the adaptive controller to accommodate sudden unbalance in HSFD supported rotors. This is another feature where the HSFD is capable of using its adaptive characteristics to control rotor vibration; however, tests with sudden unbalance require a different test rig. Such tests are planned in the near future, in the direction to illustrate the capabilities of the HSFD in controlling rotor vibration.

Acknowledgment

The authors would like to acknowledge the fruitful discussions with Professor M. Elaraby and Doctor A. T. Massoud. The work presented in this paper was supported by EOARD, US Air Force Office of Scientific Research, Grant No. F49620-92-J-0512, Dr. Charbel Raffoul and Dr. Nelson Forrestor, program managers. This support is gratefully acknowledged. The U.S. Government has certain rights to this material.

References

[1] White, D. C., 1972, ''The Dynamics of a Rigid Rotor Supported on Squeeze Film Bearings,'' *Conference on Vibrations in Rotating Machinery*, Proc. I. Mech. E., pp. 213–229.
[2] Gunter, E. J., Barrett, L. E., and Allaire, P. E., 1977, ''Design of Nonlinear Squeeze Film Dampers for Aircraft Engines,'' ASME J. Lubr. Technol., **99**, No. 1, pp. 57–64.
[3] Holmes, R., and Dogan, M., 1985, ''The Performance of a Sealed Squeeze Film Bearing in a Flexible Support Structure,'' Proc. I. Mech. E., **199**, No. 1.
[4] Burrows, C. R., Sahinkaya, M. N., and Turkay, O. S., 1983, ''An Adaptive Squeeze-Film Bearing,'' ASME Paper 83-Lub-23.
[5] Adams, M. L., and Zahloul, H., 1987, ''Attenuation of Rotor Vibration Using Controlled-Pressure Hydrostatic Squeeze-Film Dampers,'' presented at the Eleventh Biennial ASME Vibrations Conference, Boston, MA, September 1987.
[6] Mu, C., Darling, J., and Burrows, R., 1991, ''An Appraisal of a Proposed Active Squeeze Film Damper,'' ASME J. Tribol., **113**, No. 4, pp. 750–754.
[7] El-Shafei, A., 1991, ''Hybrid Squeeze Film Damper for Active Control of Rotors,'' U.S. Patent number 5.058.452.
[8] El-Shafei, A., 1993, ''Experimental and Analytical Investigation of Hybrid Squeeze Film Dampers,'' ASME J. Eng. Gas Turbines Power, **115**, No. 2, pp. 353–359.
[9] El-Shafei, A., and Hathout, J.-P., 1995, ''Modelling and Control of HSFDs for Active Control of Rotor-Bearing Systems,'' ASME J. Eng. Gas Turbines Power, **117**, No. 4, pp. 757–766.
[10] Hathout, J. P., and El-Shafei, A., 1996, ''Adaptive Control of Rotor-Bearing Systems Using Hybrid Squeeze Film Dampers,'' Proceedings of Sixth Int. Conf. On Vibration in Rotating Machinery, Oxford, England, I. Mech. E., pp. 671–690.
[11] Hathout, J.-P., and El-Shafei, A., 1997, ''PI Control of HSFDs for Active Control of Rotor-Bearing Systems,'' ASME J. Eng. Gas Turbines Power, **119**, No. 3, pp. 658–667.
[12] Hathout, J.-P., El-Shafei, A., and Youssef, R., 1997, ''Active Control of Multi-Mode Rotor-Bearing Systems Using HSFDs,'' ASME J. Tribol., **119**, No. 1, pp. 49–56.
[13] El-Shafei, A., and El-Hakim, M., 1995, ''Development of a Test Rig and Experimental Verification of the Performance of HSFDs for Active Control of Rotors,'' ASME Paper 95-GT-256.
[14] El-Shafei, A., El-Hakim, M., and Hathout, J.-P., 1993, ''Control of Rotor Vibrations Using Hybrid Squeeze Film Dampers,'' Report MDP-EOARD-2/94, Cairo University.
[15] El-Shafei, A., 1990, ''Unbalance Response of a Jeffcott Rotor Incorporating Short Squeeze Film Dampers,'' ASME J. Eng. Gas Turbines Power, **112**, No. 4, pp. 445–453.
[16] El-Shafei, A., Massoud, A. T., El-Hakim, M., Hathout, J.-P., Youssef, R., 1997, ''Control of Rotor Vibrations Using Hybrid Squeeze Film Dampers,'' Report MDP-EOARD-1/97, Cairo University.
[17] Astrom, K. J., and Wittenmark, B., 1989, *Adaptive Control*, Addison-Wesley, Reading, MA.

Angelo V. Koschier
e-mail: angelo.koschier@ae.ge.com

Hagen R. Mauch
e-mail: hagen.mauch@ae.ge.com

General Electric Company,
Aircraft Engines,
1000 Western Avenue,
Lynn, MA 01910

Advantages of the LV100 as a Power Producer in a Hybrid Propulsion System for Future Fighting Vehicles

The core of any hybrid propulsion system is a high power density, low weight, and fuel efficient electric energy producer. The LV100 recuperated turbine engine is such a system. This engine is well suited to provide electric power efficiently at a volume and weight significantly lower than current systems. Originally designed for vehicular use and environment to drive a Hydrokinetic transmission, the turbine's high output speed lends itself to incorporate into the engine design an advanced generating device. This LV100 engine-based electric energy producer will provide in excess of 1MW of electric power in a volume of under one cubic meter at a weight of about 2500 pounds at fuel efficiencies comparable to advanced vehicular diesel engines. Recent state-of-the-art improvements in materials and component technology will permit further reductions in volume/weight and increase the system fuel efficiency. The technologies required to reach a volume of under one cubic meter, the system performance projections obtainable by technology upgrades and the program achievements to date are discussed. [S0742-4795(00)03103-3]

Introduction

Hybrid propulsion for heavy military vehicles requires a highly efficient power producer to meet the large continuous power needs of such a vehicle on the move. This continuous power cannot be provided from energy storage devices alone.

This paper discusses the significant benefits of the LV100, a modern recuperated turbine engine, as a power producer. This engine, when combined with an integrated high speed generator, can become the electric power producer in Hybrid Systems in the 1 MW class and used for advanced armored vehicles, where volume and weight are premium.

The LV100 engine has completed approximately 75 percent of its development cycle and can be put into production at a fraction of the cost of a new engine development program.

1.0 Hybrid Systems in the 1 MW Class

Hybrid propulsion systems contain the building blocks shown in Fig. 1. The prime purposes of the hybrid system are to install a smaller electric power producer and on demand, draw peak energy from stored devices for occasional high power demand. In addition, the energy storage devices will be the sole power supplier for extended low power requirements such as ''silent watch,'' where minimum vehicle signatures are required. Depending on the energy storage system capability, some limited vehicle operation with a nonoperative electric power producer will also be feasible.

Armored vehicles mandate minimum power pack volume under armor. Consequently, the energy density and volume of energy storage devices currently under consideration will have to improve significantly to permit their use for propulsion in an armored vehicle and before these existing devices become volume competitive with a recuperated turbine engine system. A further concern is the survivability of energy storage devices under high ''*g*'' loads, typical for armored vehicles.

Armored vehicles have mission requirements which require sustained high power for speed on grade. This may limit engine size reduction and balance energy storage.

2.0 Forms of Electric Power Producers

Electric power for use in vehicles can be produced by fuel cells or by fuel burning (internal combustion) devices combined with an electric generator. For armored vehicles where power density is critical, the turbine with its inherently lower volume and weight, combined with high output speeds, has distinct advantages. Table 1 highlights the many advantages and the relatively low risk of a turbine-based high speed power producer.

3.0 Desired Characteristics of the Electric Power Producer

Consistent with the minimum under-armor volume requirement, the fuel tank uses valuable under-armor space. Thus fuel consumption over a wide range of power, including idle, has to

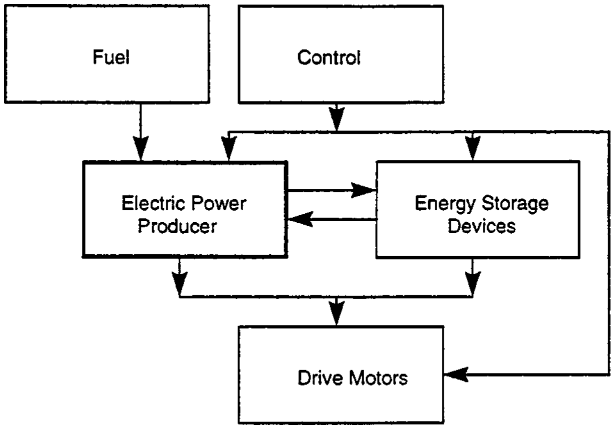

Fig. 1 Hybrid propulsion systems contain five major components

---

Contributed by the International Gas Turbine Institute (IGTI) of THE AMERICAN SOCIETY OF MECHANICAL ENGINEERS for publication in the ASME JOURNAL OF ENGINEERING FOR GAS TURBINES AND POWER. Paper presented at the International Gas Turbine and Aeroengine Congress and Exhibition, Indianapolis, IN, June 7–10, 1999; ASME Paper 99-GT-416. Manuscript received by IGTI March 9, 1999; final revision received by the ASME Headquarters May 15, 2000. Associate Technical Editor: D. Wisler.

Table 1 Turbine based power producers have many advantages

Design/Requirement	Turbine Advantage
High Output Speed	Direct Drive To High Speed Generator Possible/ No Speed-Up Gearbox Required
Low Volume/Low Weight	• Turbine Is Lowest • Further Reductions With High Speed Generator
Low O & S Cost	• Inherent High Reliability of Turbo Machinery • Direct Drive Reduces Parts Count
Low Cooling Losses/ Smaller Cooler Volume	• Turbines Require Much Less Supplemental Cooling Than Reciprocating Engines
Low Acquisition Cost	• Reduced Parts Count • High Volume Production for Large Commercial Market
Cold Day Start	Will Start Reliably at Down To -59°F Without Special Equipment
Survivability	• Low Emissions • Low Ambient Noise • Essentially Vibration Free
Multi Fuel Capability	• True Multi Fuel Capability - Liquid and Gaseous • No Corrosive Inhibitor Additives Required

be low. For vehicle survivability, low emissions and low noise are required. These characteristics are strengths of recuperative turbines.

Compared with high performance vehicular diesel engines, turbines in the 1500 SHP class are considerably smaller in size and over 1 ton lighter in weight. These advantages are magnified when the turbine is being used as an electric power producer, since it can be combined with a low volume, high speed generator. Figure 2, which is based on a 1992 vendor survey conducted by GE, illustrates the fact that changing to a high speed generator will result in a 3:1 generator power density improvement. As described in paragraph 5.0 of this paper, further power density improvements are possible if the high speed generator is integrated with the engine.

4.0 Advantages of the LV100 as a Power Producer in a Hybrid System

The LV100 engine as designed and built was the finalist in a Propulsion System Study [1] that investigated a large variety of turbomachinery configurations in the 1MW class. A recuperated engine configuration operating at a maximum cycle temperature of ~2500 °F and a 12.5/l cycle pressure ratio was found to be the best solution.

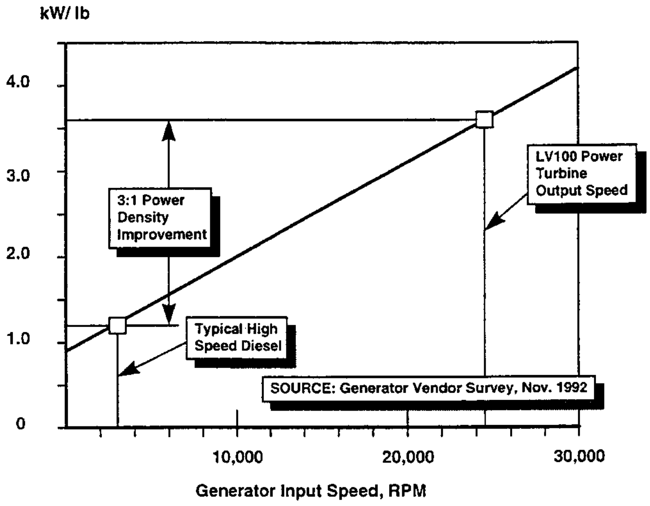

SOURCE: Generator Vendor Survey, Nov. 1992

Fig. 2 High speed generators permit a 3:1 power density improvement

The recuperated cycle required for successful vehicular engines offers the lowest under-armor system volume for all missions, except for very short duration missions where the amount of fuel carried becomes an insignificant part of the vehicle weight and volume. Levels of fuel consumption obtained at part power are unmatched by any simple cycle aircraft engine and are competitive with advanced technology diesel engines.

The LV100 engine has a ''built-in'' self cleaning inlet-air-filtration system and a state-of-the-art signature suppressor. As part of the Advanced Integrated Propulsion System (AIPS) program, discussed in [2], the engine was built and successfully tested.

Like all turbines, the LV100 is internally cooled and requires only small external coolers to handle the lube and accessory system heat rejection loads. Thus, coolers for turbines are a fraction of the size of reciprocating engine coolers.

The LV100 engine has successfully demonstrated the unique cycle requirements of the recuperated gas turbine engine and represents the only vehicular engine technology carrier available today. The engine was sized for 1500 SHP but could grow to 1800 SHP or, due to high component efficiencies, remain competitive with reciprocating engines at power levels down to 900 SHP. It is only cost effective to consider the design of brand new turbomachinery components if power requirements are below or above these limits. The engine is suitable for a high speed electric power producer in a hybrid propulsion system and provides an excellent basis for further technical developments.

4.1 Comparison of Aircraft and Vehicular Turbine Engines. Aircraft engines are designed for lowest possible weight and best performance in the 80 to 100 percent power range, which is the most significant range of engine operation for fixed wing or helicopter aircraft missions. Vehicular engines, for most operational use need to be optimized for the power range between idle and 60 percent of maximum power. This requires an engine with a recuperated cycle. Data obtained from typical operation of the Abrams main battle tank has confirmed that the vehicle spends a considerable amount of time with the engine at ''Idle.'' Low idle fuel consumption is therefore critical, an operating condition of little relevance on aircraft engines. In terms of cyclic engine use, vehicular operation subjects the engine to cycle counts many times higher than those of typical aircraft applications it also requires designing for continuous medium, and occasional high, ground shock loads during vehicle movement.

In addition to overall engine specific volume (volume/SHP), a successful military vehicular turbine engine must contain turbomachinery components which address the following requirements and constraints:

- optimized low pressure ratio recuperated cycle for good fuel efficiency at idle and part power
- provisions to reach high component efficiencies at low power settings by elevating cycle temperatures
- turbomachinery components with very wide operating mass flow range at high efficiency
- low cost components
- components designed for high thermal cycle counts and high shock loads
- means for power augmentation to cover short term system power needs to minimize engine (air flow) size and keep the system volume low

Durability, ease of maintenance, and logistics play major roles in the design of the engine. Consequently, a more robust design is favored. Weight is important, but system benefits are possibly, trading weight for lower acquisition cost. Due to the requirement for lowest possible mid power fuel economy on vehicular engines, the extra weight and volume of the recuperator can be justified.

4.2 Cycle Discussion. The design of a brand new recuperated vehicular turbine engine for the 2005/2010 time period will start with components with efficiencies similar to today's LV100 and the resulting mechanical configuration will be more or less identical. The following cycle discussion was documented in [3] and explains the reasons for this statement.

Figure 3 shows the results of a thermodynamic study for simple cycle and recuperated cycle turbomachinery with state-of-the-art component efficiencies obtainable for engines in the 1500 SHP power range and cycle temperatures reflecting the state of the art for small machines. The figure contains lines of constant cycle pressure ratio and constant cycle temperature (turbine inlet temperature) versus specific power (power per unit airflow) and specific fuel consumption (SFC). The results show that, at maximum power, the recuperated cycle has significant advantages over the simple, nonrecuperated cycle. At part load where cycle pressure ratios tend to decrease and where higher cycle temperatures can be maintained using variable geometry components, the SFC advantage of the recuperated cycle is even larger. At idle power, the LV100 burns about 25 percent of the fuel required for idling the T700 a simple cycle turbo shaft engine, which is in a similar power class and has similar component efficiency levels.

The Integrated High Performance Turbine Engine Technology (IHPTET) goals of improvements in specific power and fuel consumption of advanced aircraft engines (simple cycle) can be obtained by pushing to ever-increasing levels of temperatures and pressure ratios. Cycle temperatures approaching stoichiometric limits and pressure ratios of 60 and higher are targeted for future technology programs. Extrapolation of Fig. 3 suggests that at maximum power and at these cycle conditions, the simple cycle could get close to reaching the performance levels of the current recuperated cycle, however, at much higher specific power levels. Applying these techniques to an engine in the 1500 SHP class would result in an engine mass flow of slightly more than 3 lb/s. To make use of this cycle, turbomachinery components are getting too small to reach good efficiency levels. Airfoil heights will be less than 0.4 in. The necessity to cool such small airfoils to permit operation at the desired cycle temperatures will result in relatively thick airfoil trailing edges. Minimum tip clearances obtainable during operation for good component efficiencies will also be much larger than desirable. These effects will cause a reduction in obtainable component efficiencies which will negate the theoretical benefit from such an advanced cycle.

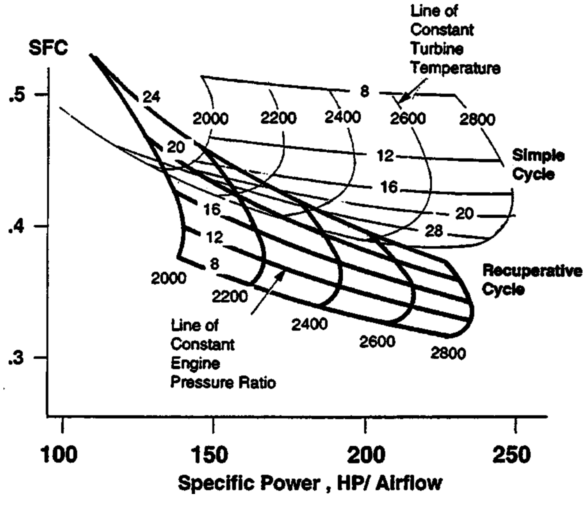

Fig. 3 For small turbine engines the recuperated cycle has significant SFC advantages

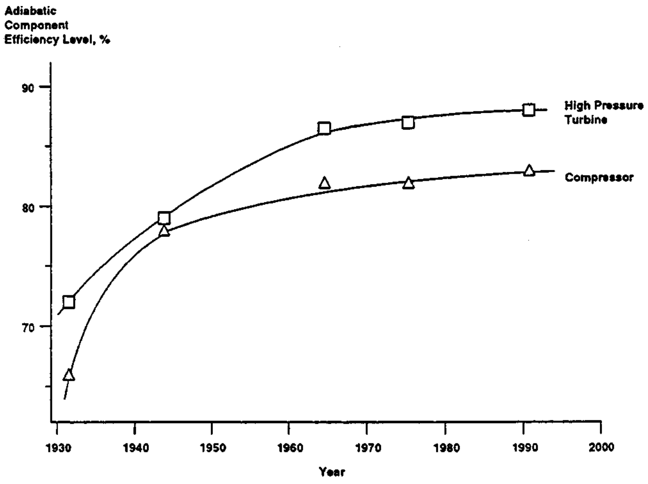

Fig. 4 Component efficiencies at design point for small engines have limited improvement potential

Figure 3 also shows that vehicular, recuperated engines optimize at much lower pressure ratios. This helps to reduce engine complexity, reduces the number of stages, and will result in comparatively higher component efficiencies when compared to the simple cycle. Temperature levels of 2800 °F will need to be traded off against the complexity of additional cooling, specific power increases, fuel burn reductions, and cost.

Attainable turbomachinery component efficiencies tend to decrease when the engine is scaled to a lower flow size. While flow passage dimensions can be scaled to obtain the appropriate Mach numbers in flow areas, operating clearances, usually expressed in percent of flow passage height, do not scale the same way. The necessary operational clearances, which have a strong impact on component efficiencies, are the result of radial growth due to centrifugal loading, thermal growth, and structural deflection of the support structure resulting from ''*g*'' and maneuver loads. The design process leading to minimum workable clearances is an iterative process. During the LV100 development effort, significant progress was made to optimize clearances.

References [4] and [5] indicate that over the last 50 years, gas turbine component efficiencies have improved dramatically. At the beginning of turbine development in the 1930s, components had efficiency levels in the 60 percent range, which were just sufficient for self sustaining operation. Since then, methodology has been developed which permits components to reach efficiency levels approaching, and in large engines exceeding, 90 percent. Figure 4 shows the state-of-the-art trend over the years for small machines. The curves illustrate that future component efficiency improvements on small turbomachinery will be limited. Progress will mostly be confined to increasing pressure ratio capability per stage (simplification), which will have little effect on machines which optimize at the low pressure ratios of recuperated engines.

For fighting vehicles that require massive short duration energy bursts, as will be required should an electric gun become part of the equipment, the combination of an electric power producer and energy storage of a hybrid system may not be sufficient. Means to provide additional engine power for short term power increases may be of interest. This may be obtainable with water injection and provisions for pressure loss reduction (recuperator bypass). Short duration power bursts of up to 50 percent over maximum continuous power may be achievable within the current engine volume envelope.

5.0 The Integrated High Speed Generator Concept

Figure 5 illustrates that simple modifications of the LV100 power turbine allow integration of a 24,000 rpm high speed generator with shared bearings, lubrication, and cooling systems. The generator is an integral part of the power turbine module. No speed-reducer gearbox is required. The integration of the genera-

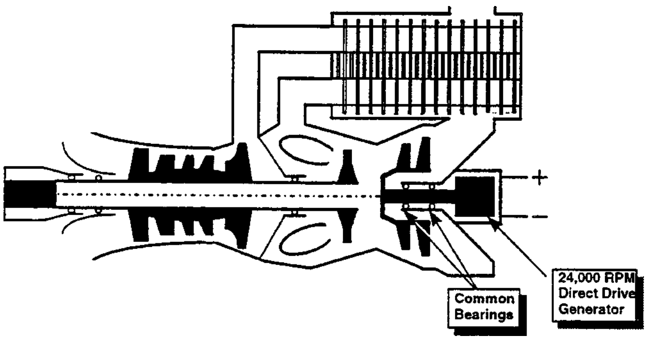

Fig. 5 The integrated high speed generator version of the LV100 features low weight, volume, complexity, and cost

tor with the engine allows the definition of an LV100 based electric power producer which, when compared to existing diesel based systems, has unmatched power densities. The system has the lowest weight and volume at minimum losses. The mechanical simplicity and reduced number of parts assure low acquisition and maintenance costs. The LV100 based electric power producer, as currently configured, will deliver 1 MW of DC power at approximately 700 volts and a system weight, including power electronics, of around 2500 pounds, well within the lifting range of modern helicopters. Inclusion of power generation increases the engine length by about 5 in.

Figure 6 shows the four main LV100 modules, including the power turbine/generator module under discussion.

Table 2 summarizes a preliminary weight roll-up based on the current LV100-2 engine and compares the results with a competing system diesel system. The LV100 high speed generator system weight is half the weight of competing diesel systems.

In ARPA research announcement (RA)94-24 [6], power densities for state-of-the-art generator sets and objectives for further improvements were discussed. Figure 7 illustrates that the LV100 based integrated high speed generator has power density potentials which represent a technical breakthrough.

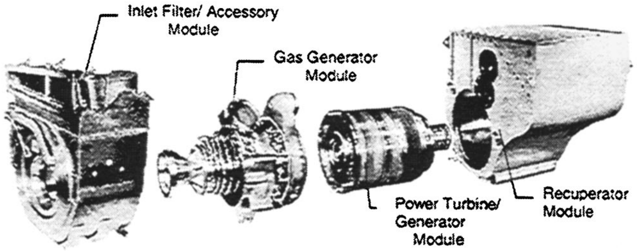

Fig. 6 The LV100 based electric power producer consists of four major modules

Table 2 The electric power producer based on the LV100 has half the weight of competing diesel systems

Component	Weight, lb LV100 High Speed Generator System	Weight, lb Advanced Diesel-Based Generator System
Engine	2,000	3,920
Generator	200	560
Electronics	130	130
Contingency (10%)	230	460
Total	**2,560**	**5,020**

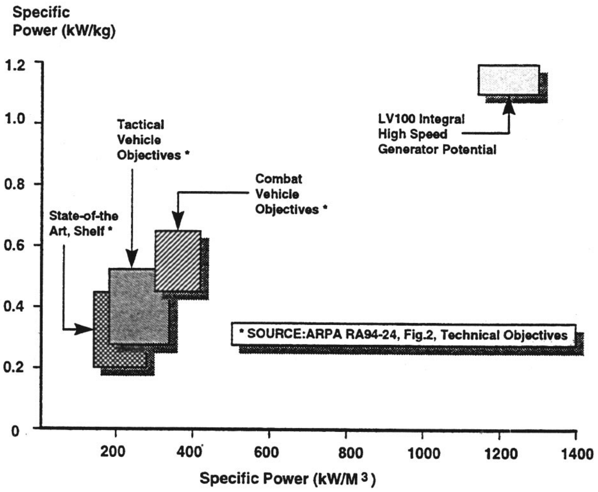

Fig. 7 The LV100 based integrated high speed generator represents a technical breakthrough

6.0 Potential Further Technical Developments

As illustrated in Fig. 8, the industry has made progress in reducing the fuel consumption of recuperated vehicular turbine engines.

The Joint Program Office (JPO), consisting of General Electric Aircraft Engines and Honeywell Systems, are under contract to develop advanced turbomachinery as part of the Integrated High Performance Turbine Engine Technology (IHPTET) initiative. The objectives of this initiative are lower fuel consumption, weight, and cost. This effort is targeted at aircraft engine cycles and components. No effort to improve vehicular engine performance exists at this time. However, as shown in Fig. 8, incorporation of selected emerging technologies such as fewer stages, higher cycle temperatures, and advanced materials into the LV100 engine are feasible and will lower the engine fuel consumption an estimated additional 10 percent. Table 3 illustrates that in addition to improved fuel efficiency, significant reductions in volume, weight, life cycle cost, and airflow are anticipated. In addition to reducing the size of the largest components of the engine system (inlet filter and recuperator), airflow reductions allow smaller inlet and exhaust ballistic grilles.

Introduction of novel intermittent or other high effectiveness advanced recuperators is expected to reduce the powerpack volume an additional 10 cubic feet. Advanced recuperators will require the use of high performance ceramics which, once developed, will reduce the engine weight by an additional 200 pounds.

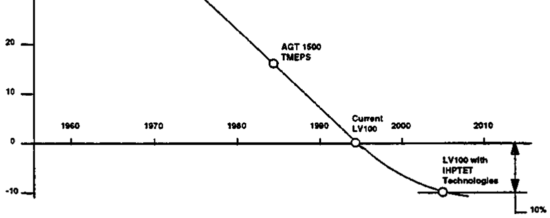

Fig. 8 Fuel burn reduction available using state-of-the-art technology

Table 3 IHPTET technologies allow significant LV100 improvements

	Current LV100 (ASM Config)	LV100 With Selected IHPTET Technologies	LV100 With Selected IHPTET Technologies Plus Advanced Recuperator
SFC	BASE	-10%	-15%
Powerpack Vol, Ft^3	157	147	136
Engine Weight, Lb	2,000	1,600	1,400
Life Cycle Cost	BASE	-8%	-10%
Airflow, Lb/Sec	7.5	6.0	6.0

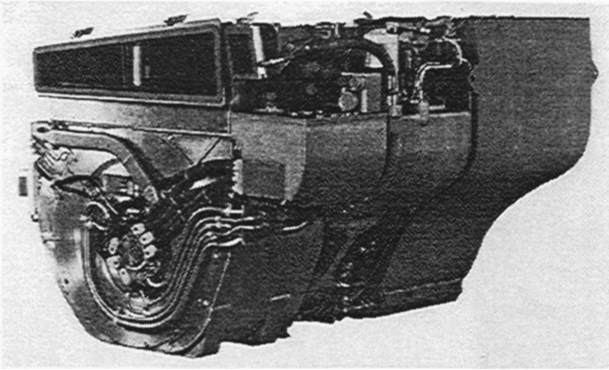

Fig. 10 The ASM engine demonstrated further power density reductions

7.0 Commercial Applications

With the enactment of electric power deregulation, private industry has shown interest in the commercial application of the LV100-based electric power producer discussed in this paper as a building block in a commercial and military Generator Set. Of particular interest are space/weight sensitive installations such as oil drilling platforms, emergency power supply situations requiring helicopter air lift, and supplementary power generators to meet peak energy demands.

If the LV100 engine is modified for operation on natural gas and equipped with a catalytic combustion device, mission levels, particularly NOx will drop into the ultra clean region which is not reachable with diesel engines. Such a device would open additional market opportunities.

A market study conducted by GE shows a combined military/commercial market of approximately 17,000 engines which justifies the low acquisition cost claimed in Table 1. These high production quantities will improve the competitive position of this engine among other 1 MW size power producers.

8.0 LV100 Development Status

The current LV100 engine configuration is the result of an optimization study which compared and ranked a great number of engine configurations for rear mounted installations. Simple cycle, recuperated, regenerated, inter-cooled, and combinations thereof, including engines with interturbine recuperators, were compared and ranked in an effort to determine the lowest propulsion system volume (including fuel, inlet air filtration, and exhaust treatment and accessory power generation). The study assumed a specified sprocket power and mission for a notional heavy vehicle over a specified ambient temperature and elevation range. The LV100 configuration, as it exists today, was the winner. Details of this effort are documented in [1].

A demonstrator of this winning configuration, the LV100-1 was built under the Advanced Integrated Propulsion System (AIPS) program for the U.S. Army Tank and Automotive Command (TACOM) and successfully tested in 1990 as a total system. This program was completed by a collaboration of GE, Textron-Lycoming, MTU, and Allison as principal players and resulted in the AIPS powerpack as shown in Fig. 9.

In the subsequent Armored Systems Modernization (ASM) program, this engine was selected by the winning contractor (Teledyne) to power its front drive common chassis. In order to meet demanding under-armor space allocations, the recuperator and inlet filter were reshaped to meet the desired envelope and powerpack compartment shape. This was successfully accomplished and resulted in the LV100-2 engine configuration, as shown in Fig. 10. Reference [7] contains additional information about this program.

Similar to the LV100-1, this engine had all-electric accessories including a newly designed resolverless engine integral starter/generator which successfully operated at gas generator speeds of 44,000 rpm and provided 36 KW electric energy to the vehicle. The new accessory package, as well as the novel and more space efficient rotating self-cleaning inlet filter and changes to the recuperator/engine interface, permitted a 9 percent powerpack volume reduction (from 171 ft^3 to 157 ft^3). This reduction brings this engine close to the Army's goal of 133 ft^3 for advanced vehicular engines in the 2000+ time frame as documented in [8].

The LV100-2 engine originally was to be mated to a hydrokinetic transmission. However, midway through the ASM program

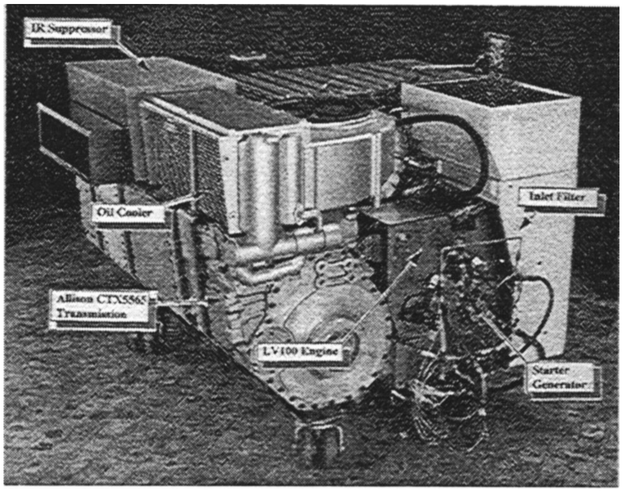

Fig. 9 The AIPS powerpack has demonstrated significant power density improvements

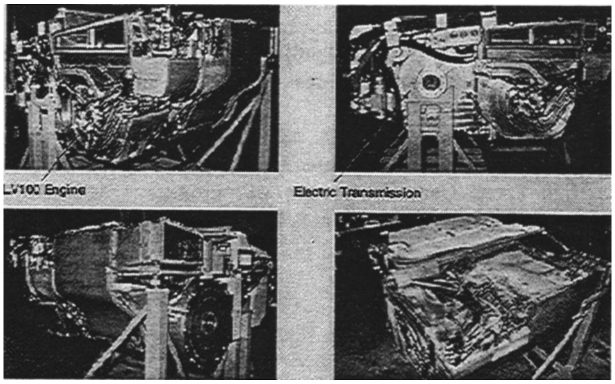

Fig. 11 The LV100 based electric drive powerpack has demonstrated the feasibility of electric drive

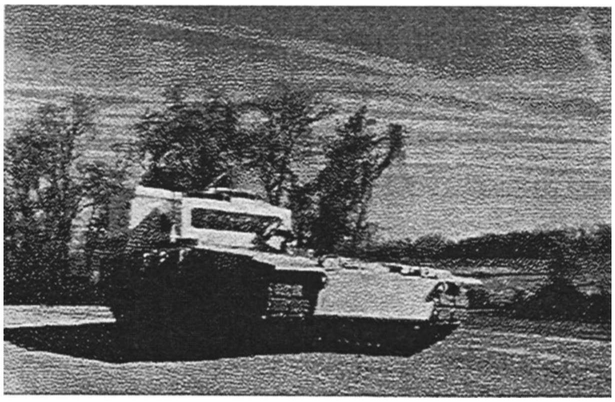

Fig. 12 The LV100 engine has proven its capability to perform in an armored vehicle environment

the effort was redirected towards an electric drive system demonstration and the engine subsequently was connected to a speed reduction gearbox to drive a permanent magnet (PM)1MW generator which was designed by EML, now Kaman Electromagnetics. The generator operated at design speeds of 7000 rpm. Figure 11 shows various views of the Electric Drive Powerpack.

This system was subsequently installed in an Automotive Test Rig (ATR) and was tested at the Army's Aberdeen Proving Grounds. Figure 12 shows the ATR vehicle.

9.0 Conclusion and Recommendations

The LV100 recuperated turbine engine, modified to operate with an advanced high speed generator, represents an ideal candidate for Electrical Power Producer in Hybrid Systems for future armored vehicles.

The LV100 engine has successfully demonstrated that it can meet the unique requirements of vehicular engines in the 1500 SHP class. The engine demonstrated high power densities, fuel efficiency, and low emissions, all characteristics of a good electric power producer for hybrid systems.

The Integrated High Speed Generator concept promises to deliver a low volume, low weight and low cost system at a system weight of about 2500 lb. Further technical developments have been identified which will allow significant additional reductions in volume, weight, and SFC.

Continuation of LV100 development will provide many military and commercial benefits. The LV100 based Integrated High Speed Generator system will produce 1 MW electric power at significantly lower volume and at half the weight of a diesel based system.

The U.S. Army currently considers the LV100 engine for a re-engining program of the M1 Main Battle Tank to reduce the system sustainment cost over the projected 40 years of fleet life. The engine is also considered for the Crusader self propelled howitzer vehicle which in line with the Army's intent of ''lightening the force'' is being downsized to 50 tons. This would satisfy the Army's desire to have a common engine for their heavy combat vehicles.

A military launch would create a large user base to underwrite the projected use of the LV100 for power generation use.

References

[1] ''Advanced Integrated Propulsion System (AIPS) Study Contract Final Report,'' 1983, U.S. Army Contract No. DAAE07-82-C-4067.

[2] ''AIPS Program Final Report,'' 1991, U.S. Army Contract No. DAAE07-84-C-R083.

[3] ''LV100 Vehicular Turbine Engine Technology Readiness Program,'' 1995, A White Paper Prepared for the U.S. Army Tank-Automotive and Armaments Command.

[4] Traupel, W., 1977, *Technische Turbomaschinen*, Springer-Verlag, New York.

[5] Franz, A., 1985, *From Jets To Tanks*, Avco Lycoming/Westbrook.

[6] ''Electric and Hybrid Vehicle Technology Program,'' ARPA Research Announcement (RA)-94-24, 1994.

[7] ''AMS Armor Modernization Program Final Report,'' 1994, AE/GE94-1, U.S. Army Contract DAAE07-91-C-R007.

[8] ''Research Needed For More Compact Intermittent Combustion Propulsion Systems For Army Combat Vehicles,'' 1995, Vols. I and II, U.S. Army Tank-Automotive Research, Development, and Engineering Center Fuels and Lubricants Research Facility (SwRI).